Modelling of wear and crack initiation in rails

This thesis is submitted for the degree of
Doctor of Philosophy

by

Gordana Vasić

School of Mechanical and Systems Engineering
Faculty of Science, Agriculture and Engineering
Newcastle University, United Kingdom

March 2013

This thesis is dedicated to my mother Bosiljka Vasić, my husband Francis Franklin and my daughter Ana-Sofia Franklin.

Abstract

The ‘Dynarat’ computer simulation of ratcheting wear and failure of rail steel has been developed at Newcastle University over the past decade based on laboratory tests and analysis of British normal grade (R220) rail steel. The aim of this thesis is to develop material models for Dynarat that can be used to predict wear and rail life for R260 rail steel, which is used widely in Europe and increasingly in Britain, and also for newer premium grade pearlitic rail steels.

Laboratory twin-disc testing and metallurgical material analysis were used to obtain data for characterising and modelling material response to repeated loading.

The relationship between material hardness and plastic shear strain is central to the material model used in the Dynarat simulation, and is determined for the materials tested here by studying the measured hardness and plastic strain. Additional calibration of the wear rate was achieved by performing Dynarat simulations that closely matched the laboratory tests.

In addition to the material model development, the contact stress model used by Dynarat for modelling wheel-rail contact is improved. Previously the driving stress for plastic strain accumulation was the orthogonal shear stress in the plane of the simulation. In the new model, plastic strain accumulation is now made directional, with components in the x and y directions. Partial slip is now implemented in the 3D simulation, to approximate the real wheel-rail contact, with both contact region and adhesive zone modelled as ellipses.

Two types of high-speed train at two curves on the UK’s East Coast Main Line have been simulated with the new computer model to study the effects of traffic mixtures. Wear rates and time until crack initiation are obtained.

The new model provides a tool to help rail/wheel manufacturers to choose the best steel, and for maintenance personnel to predict rail wear and cracks, and thus to help plan grinding schedules in order to optimise rail life and safety.

Acknowledgements

I would like to express my gratitude to my former supervisors Professor Ajay Kapoor and Dr David Fletcher for their guidance and helpful discussions and suggestions in the PhD process. I would like to thank my supervisor Dr George Kotsikos for his advice and big support in finishing the Thesis.

Thanks to Dr David Fletcher and Dr Francis Franklin for doing experiments on the SUROS twin-disc machine, with the assistance of the late Dr Mike Frolish of Sheffield University who is greatly missed. Thanks to InnoTrack project partners for letting me use results for my PhD. Thanks again to Dr Franklin for programming 'Dynarat' and for advice and being the first person to answer lists of questions. Thank you to everyone in NewRail, especially Professor Mark Robinson. Thanks to the Design Unit from Newcastle University, especially to Christopher Aylott and Dr Jishan Zhang for preparing samples and hardness measurements. Thank you to Pauline Carrick for ESEM images.

I thank my friends for being there for me when I needed them, especially Katarina Novaković.

I thank my family for their unconditional love and support. Especially to my mother Bosiljka Vasić who dedicated her life to me and my brother. I thank you for giving me guidance in life and encouragement to persist in doing my studies and PhD. Thanks to my brother Goran and his lovely family. Many thanks to my husband Francis Franklin for understanding, support and cuddles and giving me faith in myself, when I lost it. Special thanks to my daughter Ana-Sofia who made my life beautiful.

Publications

1. Fletcher, D.I., Franklin, F.J., Garnham, J.E., Muyupa, E., Papaelias, M., Davis, C.L., Kapoor, A., Widiyarta, M. and Vasic, G. (2008) 'Three-dimensional microstructural modelling of wear, crack initiation and growth in rail steel', *The 8th WCCR*, May 18 – 22, 2008, Seoul, Korea.
2. Fletcher, D.I., Franklin, F.J., Garnham, J.E., Muyupa, E., Papaelias, M., Davis, C.L., Kapoor, A., Widiyarta, M. and Vasic, G. (2008) 'Three-dimensional microstructural modelling of wear, crack initiation and growth in rail steel', *IJR International Journal of Railway*, 1 (3): pp.106-112.
3. Vasić, G., Franklin, F.J., Fletcher, D.I. and Kapoor, A. (2009) 'Effect of traffic on crack initiation in rails', *4th International Symposium on Speed-up, Safety and Service Technology for Railway and Maglev Systems 2009 (STECH'09),* 16-19 June 2009, Niigata, Japan.
4. Vasić, G., Franklin, F.J., Fletcher, D.I. and Kapoor, A. (2009) 'Effect of traffic on crack initiation in rails', *Journal of Mechanical Systems for Transportation and Logistics,* Vol.3, No. 1, 2010.
5. Vasić, G., Franklin, F.J. and Fletcher, D.I. (2009) 'Influence of partial slip and direction of traction on wear rate in wheel-rail contact', *8th International Conference on Contact Mechanics and Wear of Rail/Wheel Systems (CM2009)*, Firenze, Italy, September 15-18, 2009.
6. Vasić, G., Franklin, F.J. and Fletcher, D.I. (2011) 'Influence of partial slip and direction of traction on wear rate in wheel-rail contact', *Wear*, 270, pp.163–171.
7. Contribution in InnoTrack Report D4.2.5 (2009) '*Improved model for the influence of vehicle conditions (wheel flats, speed, axle load) on the loading and subsequent deterioration of rails*'.
8. Contribution in Chapters 5.3.3 and 5.3.4 in '*InnoTrack Concluding Technical Report*', Edited by Anders Ekberg and Björn Paulsson, Intellecta Infolog, Solna, 2010.
9. Contribution in Chapter 6: 'Wear', in InnoTrack Deliverable report D4.2.6 , *'Recommendation of, and scientific basis for, minimum action rules and maintenance limits'*
10. Contribution in Chapter 3.4: 'Wear prediction', in InnoTrack Deliverable report D.4.2.3, *'Improved model for loading and subsequent deterioration of insulated joints'*, 2009.
11. Vasić, G. and Franklin, F.J. (2011) 'Extended abstract – Plastic deformation and crack initiation in hard pearlitic rail steels' - *21st Century Rail, 1-3 November 2011, York, UK.*
12. Vasić, G. and Franklin, F.J. (2012) 'Modelling of plastic deformation and crack initiation in premium pearlitic rail steels', *9th International Conference on Contact Mechanics and Wear of Rail/Wheel Systems (CM2012)*, Chengdu, China, August 27-30, 2012.

Table of Contents

Nomenclature

Symbol	Unit	Paragraph	Description
a	m		Semi-contact width
a,b,c,d		§5.1.2	Hardness constants
A	m^2		Contact area
A	m^{-1}	§2.2.3	Curvature coefficient
A		§5.1.3	Roughness amplitude
b	m		Semi-contact width (in lateral direction)
B	m^{-1}	§2.2.3	Curvature coefficient
c	-		Constant
C			Empirical constant equal to 0.00237
d	m		Roughness affected depth
E	Pa		Modulus of elasticity (Young's modulus)
E^*	Pa		Elastic contact modulus
H	HV		Hardness
k	Pa		Shear yield stress
k_1 and k_2	Pa^{-1}	§2.2.3	Elastic constants
k_o	Pa		Initial shear yield stress
k_{eff}	Pa		Effective shear yield stress
K			Wear coefficient
K		§6.1.3	Scale factor in partial slip ellipses
L	m		Length
m		§2.2.3	Coefficient
n		§2.2.3	Coefficient
N	N		Normal load
N		§2.3.4	Number of cycles
p	Pa		Normal pressure
p_0	Pa		Maximum (Hertzian) contact pressure
p_r			Instantaneous probability of wear
$q(x)$	Pa		Shear traction
r		§5.1.1	Ratcheting constant
$r(z)$		§5.1.3	Roughness amplification equation
R	m		Radius
R_a	m		Roughness parameter: centre line average.
s	m		Sliding distance

Symbol	Unit	Paragraph	Description
t_c			Traction coefficient
T	N		Traction force
$T\gamma$	N		'T-gamma', the product of applied traction T and creep or slip γ
v	m/s		Velocity
w	m/cycle		Wear rate
W	m^3		Wear volume
α			Hardness parameter
β			Hardness parameter
γ			Shear strain
γ		§2.1.2	Creepage (slip) in Tγ model
γ	radians	§2.2.3	Angle of the direction of tangential force to the y-axis, the minor axis of the ellipse
γ_c			Critical plastic shear strain
ε			Strain
θ	radians		Angle
κ	m^{-1}		Curvature
μ			Friction coefficient
ν			Poisson´s ratio
σ	Pa		Direct normal stress
τ	Pa		Shear stress
ψ	radians		Angle

Glossary

Abbreviation/acronym	Description
InnoTrack	EU FP6 Project
AZ	Adhesive zone
BCC	Body-centred cubic crystal structure
BS	British Standard
C260 or P260	CORUS 260 Grade rail disc specimen or test identifier
C350	CORUS 350 Grade rail disc specimen or test identifier
C400	CORUS 400 Grade rail disc specimen or test identifier
CWR	Continuously welded rail
DB	'Deutsche Bahn' German Railways
ECML	East Coast Main Line
EMAT	Electromagnetic Acoustic Transducers
EN	'Standards'
ERA	European Railway Agency
ERADIS	European Railway Agency Database of Interoperability and Safety
ESEM	Environmental Scanning Electron Microscope
EUROSTAT	European Union database
FCC	Face-centred cubic crystal structure
FP6	Framework Programme 6
HB(W)	Brinell hardness
HCF	High cycle fatigue
HRC	Rockwell hardness ('C' scale)
HST	High speed train
HV	Vickers hardness
KAM	Kernal Average Misorientation
LCC	Life cycle cost
LCF	Low cycle fatigue
MGT	Mega gross tonnes
MHH	Mill head-hardened (steel)
MPI	Magnetic particle imaging
NIB	National Investigation Body
NRMI	Network Rail managed infrastructure
NSA	National Safety Authority

Abbreviation/acronym	Description
OOR	Out-of-round
ORR	The Office of Rail Regulation
OSS	Orthogonal shear stress
P260	*(see C260)*
PA	Prior-austenite
PE	Pro-eutectoid
PYS	Primary yaw stiffness
R260	260 grade rail material
R350HT	350 grade rail material
R370CrHT	370 grade rail material
R400HT	400 grade rail material
R7	R7 grade wheel disc specimen
R8T	R8 T grade wheel disc specimen
RAIB	Rail Accident Investigation Branch, Department for Transport, UK.
RCF	Rolling contact fatigue
RF	Ratcheting failure
RSSB	Rail Safety & Standards Board, UK
SEM	Scanning Electron Microscope
SUROS	Sheffield University Rolling Sliding [Twin-Disc Machine]
Track-Ex	Network Rail's expert track system model
UIC	International Union of Railways
UTS	Ultimate tensile strength
UTU	Ultrasonic Test Unit
V350	VA 350 ('Voestalpine Schienen GmbH') Grade rail disc specimen or test identifier
V400	VA 400 ('Voestalpine Schienen GmbH') Grade rail disc specimen or test identifier
VAMPIRE	Multibody simulation software for train-track interaction
VAS	Voestalpine Schienen GmbH

Chapter 1 Introduction

1.1 Problems arising at the wheel-rail interface

Requirements for safety, increased speed and loads on railways, and cost related to track repair or replacement, are constantly encouraging research to increase rail life. Problems arising at the wheel-rail interface, mostly from wear and the development of cracks in rails and wheels, can have devastating consequences. The most serious is catastrophic failure of a rail or wheel, which can lead to derailment of trains and loss of life, as has happened in several accidents, e.g., Hatfield, UK, 2000 (see Figure 1.1), and Eschede, Germany, 1998 (see Figure 1.2).

(a) (b)

Figure 1.1 The Intercity 225 train derailed roughly 0.8 km south of Hatfield Station on 17 October 2000. Four passengers were killed and over seventy people were injured. The immediate cause was the fracture and subsequent fragmentation of the high rail, due to the presence of multiple and pre-existing fatigue cracks in the rail. (a) Coach G showing extent of damage to seating area, (b) One of the fractures, with arrow indicating polished area (ORR, 2006).

Figure 1.2 Accident at Eschede, Germany, 1998. "101 people killed and a further 88 injured"[1]. "A cracking inside the ring of the wheel was responsible. There was no indication of material or production failure. This crack was caused by excessive load and wear."[2]

[1] http://danger-ahead.railfan.net/
[2] http://www.ndt.net/

Train operation and potential delays are also critical factors. Train derailments need to be investigated for cause, the site needs to be cleaned and the accident itself may also damage the track. In general, speed restrictions may be put in place where track quality is known to be substandard. Also, track maintenance and renewal are costly in terms of the need to close the line to normal operation, causing significant delays or time-table alterations.

The costs connected to infrastructure and wheels are high, even when it is just for regular maintenance, such as: rail or wheel replacement, grinding rails, turning wheels, track and vehicle inspection. Track renewal costs infrastructure managers more than regular maintenance. For example, Figure 1.3 shows the expenditure for Network Rail in the UK in 2009/2010, where £752 million was spent just on track renewal (Network Rail, 2011b). Regular renewal and maintenance should ensure safety and reliability.

£m (2011/12 prices)	Actual 2009/10	Forecast 2010/11	2011/12	2012/13	2013/14	Total
Operating expenditure						
Controllable opex	1,069	942	941	905	830	**4,687**
Non-controllable opex	469	433	426	466	492	**2,286**
Total	1,537	1,375	1,367	1,371	1,323	**6,972**
Maintenance	1,155	1,120	1,056	1,034	982	**5,347**
Renewals	2,365	2,276	2,621	2,530	2,450	**12,243**
Enhancements	1,050	1,217	1,662	1,990	1,774	7,692
Total PR08 funded expenditure	**6,107**	**5,987**	**6,707**	**6,925**	**6,529**	32,255
Expenditure deferred from 2008/09	204	87	77	0	3	**371**
Non PR08 funded enhancements	582	686	904	1,009	918	4,100
Total expenditure	**6,893**	**6,761**	**7,688**	**7,934**	**7,450**	36,726

(a)

in £m 2009/10 prices unless stated

	Actual	PR08	Difference
Core Maintenance (1)			
Track	464	459	(5)
Structures	33	42	9
Signalling	168	135	(33)
Telecoms	65	73	8
Electrification	46	37	(9)
Plant & machinery	38	16	(22)
Operational property	-	-	-
Other	49	36	(13)
Sub-total	**863**	**798**	**(65)**
Indirect costs	103	197	94
Other costs	105	116	11
Total maintenance expenditure	**1,071**	**1,111**	**40**

Notes:

(1) These costs only include direct costs.

(b)

Figure 1.3 (a) Expenditure (network), from (Network Rail, 2011b), (b) GB Summary analysis of maintenance expenditure for 2009/2010, where track maintenance cost is more than half of total costs, from (Network Rail, 2010a).

Accidents bring additional costs, which can be broken down in following categories:

- Human cost in terms of deaths and injuries
- Cost of replacement or repair of damaged rolling stock and railway installations
- Legal and litigation costs
- Cost of delays
- Loss of cargo (for freight)
- Cost of post-accident clean-up operation, especially if hazardous cargo was transported
- Cost of emergency services that attend after accident.

As one example, in court settlements and fees for the Hatfield accident, Balfour Beatty was fined £7.5 million and Network Rail (then Railtrack) was fined £3.5 million (ORR, 2006). Accident costs are gathered and published every year by ERA. For 2009 the total cost of accidents was reported to be €1,040,095,539 (ERA, 2011).

1.1.1 Track fault statistics

Improving safety on European railways is an ongoing aim of all EU member countries. According to European regulations, each state should report serious and significant accidents occurring on their territory, with causes leading to accidents, etc. Although data gathering is still not at a satisfactory level, it can give indications of safety issues and costs. The major problems are:

- Existence of two European databases (and forms for gathering data): ERADIS[3] and EUROSTAT[4];
- Definitions and terms are not uniform throughout Europe;
- Each country has several bodies working on statistics, analysis, reports;
- Countries are not submitting data to databases on time and in full.

The best source of information is ERA whose main task is gathering data, monitoring and analysing rail safety, and all data can be seen in their ERADIS database. From each country they have 2 bodies reporting: The national investigation body (NIB) that sends investigation reports on all serious accidents, and the national safety authority (NSA) which reports all significant accidents. ERA documents and reports are public domain.

ERA also collects data on 'precursors to accidents' which are defined as 'indicators measuring incidents that under other circumstances would have led to an accident', see

[3] http://pdb.era.europa.eu/
[4] http://ec.europa.eu/eurostat

Figure 1.4. Most countries still report precursors that actually led to an accident, and not the ones discovered in regular maintenance; they undergo changes of reporting practice and thresholds from year to year. Still, these statistics can be used as indicators. As can be seen in Figure 1.4, the number of broken rails is a major ongoing problem.

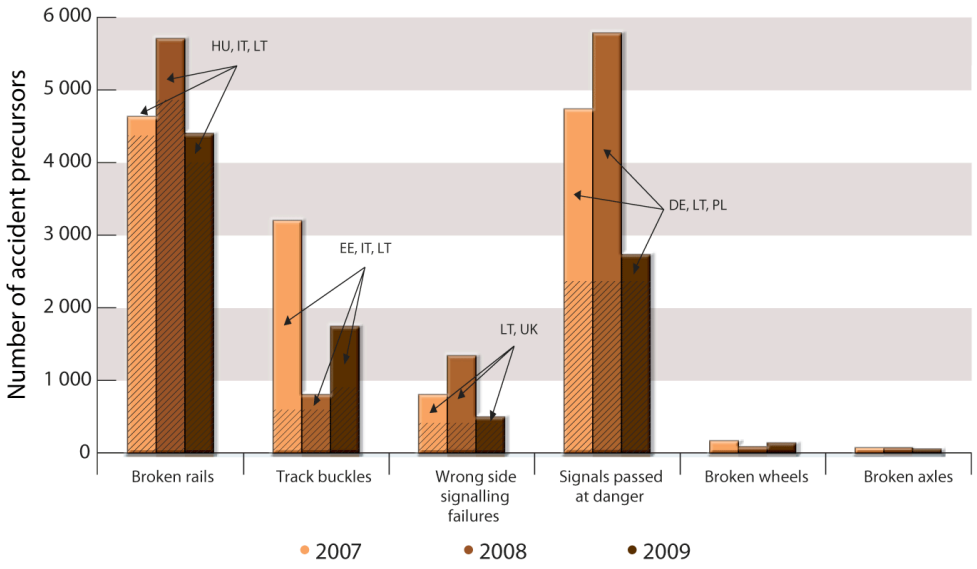

Figure 1.4 Accident precursors in all countries and in the subsets of countries (2007–2009), see (ERA, 2011).

In the UK, there are several organisations carrying out various statistics analysis and reports:

- RAIB[5] (Rail Accident Investigation Branch), is an independent railway accident investigation organisation for the UK and acts as UK's NIB.
- ORR[6] (The Office of Rail Regulation) is the independent safety and economic regulator for Britain's railways.
- RSSB[7] (Rail Safety and Standards Board) is a not-for-profit company owned and funded by major stakeholders in the railway industry (infrastructure manager company, passenger and freight operating companies, etc.), but is independent. It also receives grants for research from the Department for Transport.

In recent years, rail breaks have a declining trend (see Table 1.1). For the financial year 2010/11, covering the period 1 April 2010 to 31 March 2011, there were 171 rail breaks

[5] http://www.raib.gov.uk/
[6] http://www.rail-reg.gov.uk/
[7] http://www.rssb.co.uk/

reported on Network Rail managed infrastructure (NRMI). This is quite an improvement compared to 1998/1999 when 939 breaks were recorded (ORR, 2007).

Table 1.1 Risk from train accidents. After (RSSB, 2011).

Train accident precursors	**2006/07**	**2007/08**	**2008/09**	**2009/10**	**2010/11**
Environment: adhesion	93	80	137	104	184
Track: broken rails	192	182	164	154	171
Track: buckled rails	85	4	17	27	29

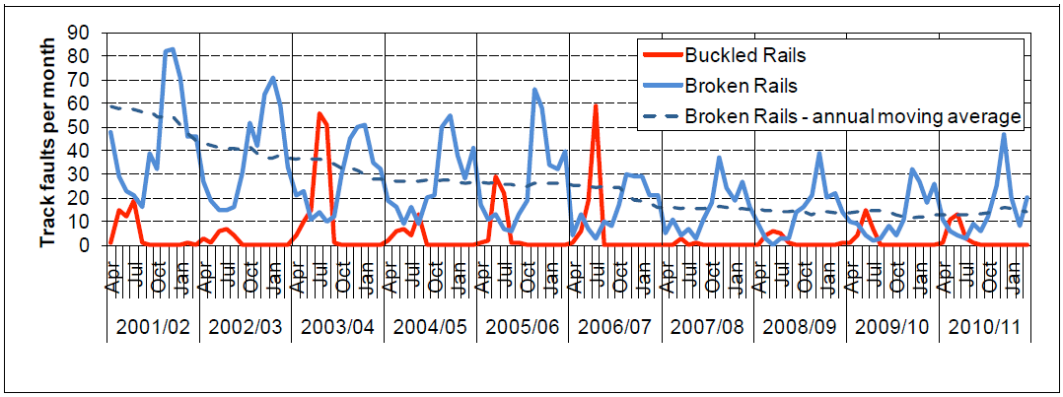

Figure 1.5 Trends in track failures, from (RSSB, 2011).

As can be seen from Figure 1.5, rail breaks occur more in the winter months, and rails are more prone to buckling in the summer months.

Taking into consideration both safety issues and maintenance costs, for both Europe and the UK, tracks still present major problems. More research is needed in this area in developing new materials for rails, and understanding their behaviour under different loads and environmental conditions.

1.1.2 Rail failures

According to (Cannon *et al.*, 2003), rail failures can be classified into three categories:

- ones that happen during manufacturing
- ones that are due to wrong handling
- ones that occur if material is no longer able to respond to fatigue: RCF.

UIC Leaflet 712 R (UIC712R, 2002) classifies rail defects using the 4-digit coding system in Figure 1.6.

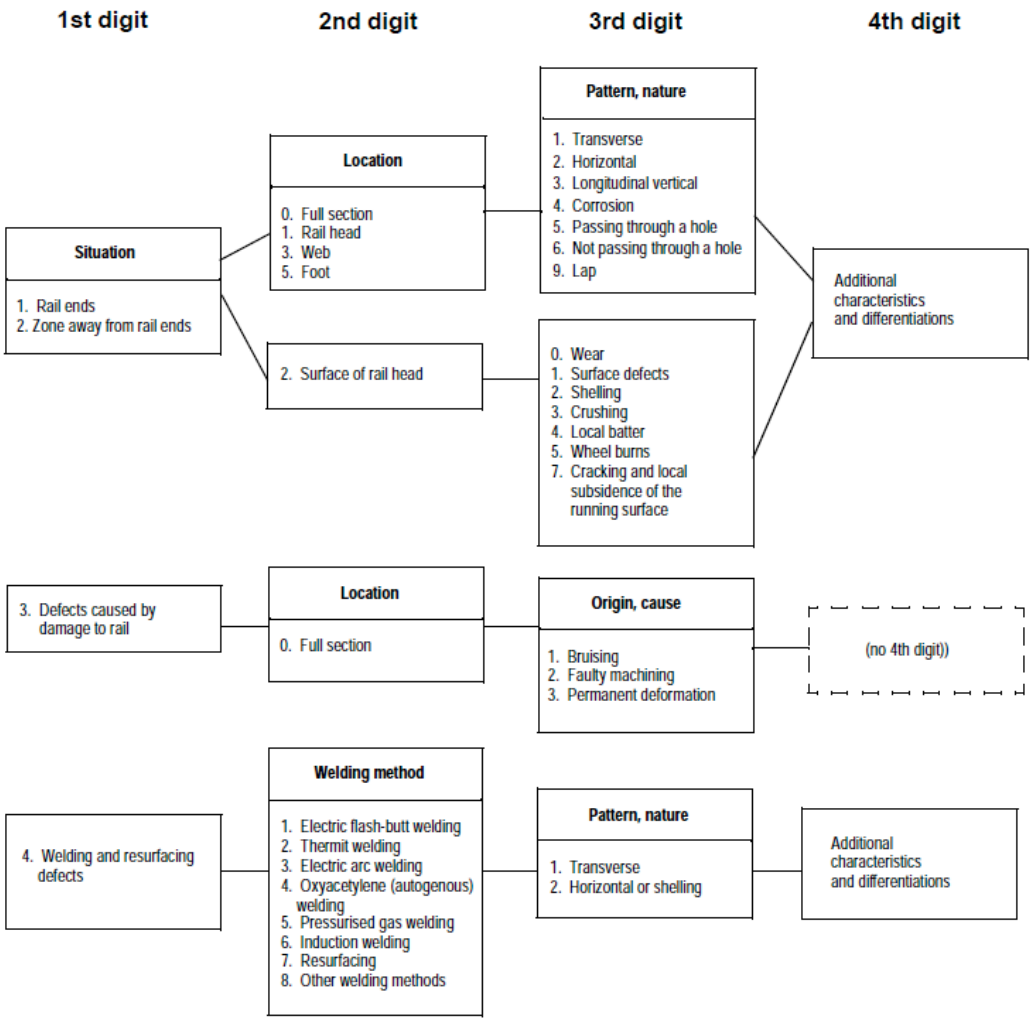

Figure 1.6 Rail defect coding system, from (UIC712R, 2002).

Wear defects are coded as:

- 2201 Short-pitch corrugation
- 2202 Long-pitch corrugation
- 2203 Lateral wear
- 2204 Abnormal vertical wear

Both short-pitch and long-pitch corrugation are defects due to traffic loads. They look like waves on rails, with bright ridges and dark hollows for short-pitch, see Figure 1.7a, and with no difference in appearance between ridges and hollows for long-pitch, see Figure 1.7b. The pitch generally varies between 3cm and 8cm for short-pitch, and 8cm to 30cm for long-pitch corrugation.

According to Grassie and Kalousek (1993) classification of corrugation only by wavelength is not sufficient, so they introduce the damage mechanism too, and according to these two critical characteristics they suggest six types of corrugation: heavy haul, light rail, booted sleeper, contact fatigue, rutting and roaring rails. Sato *et*

al. (2002) and Grassie (2005, 2009) did a comprehensive literature survey on rail corrugation. Xie and Iwnicki (2008), Baeza *et al.* (2008), Gomez and Vadillo (2003) and Afferrante and Ciavarella (2010) have created models to predict corrugation formation on railway rails.

Lateral and abnormal vertical wear result from rolling-stock stresses, the former appears in curves and the latter on line.

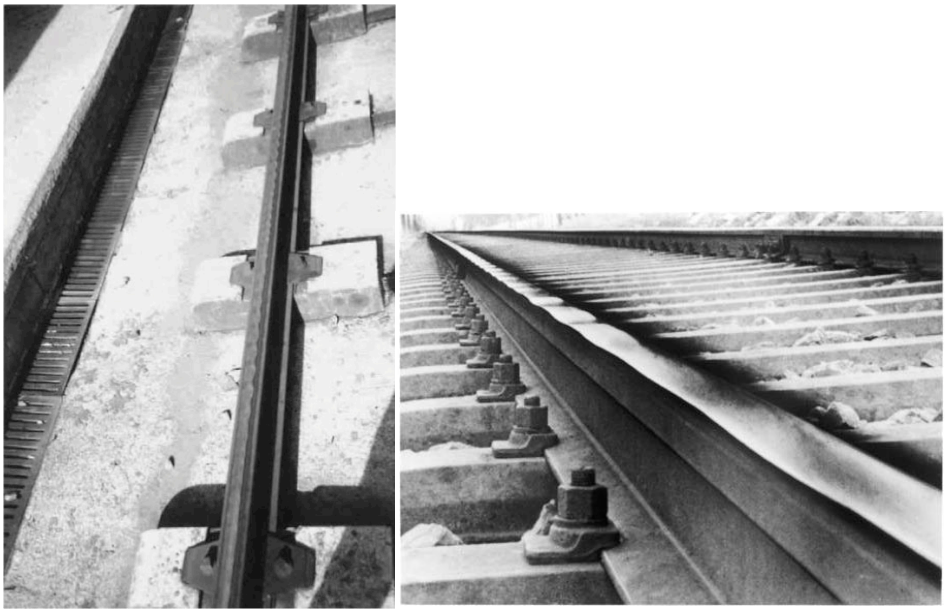

(a) (b)

Figure 1.7 (a) Detail of short-pitch corrugation, from (Gómez and Vadillo, 2003); (b) Detail of long-pitch corrugation, from (UIC712R, 2002).

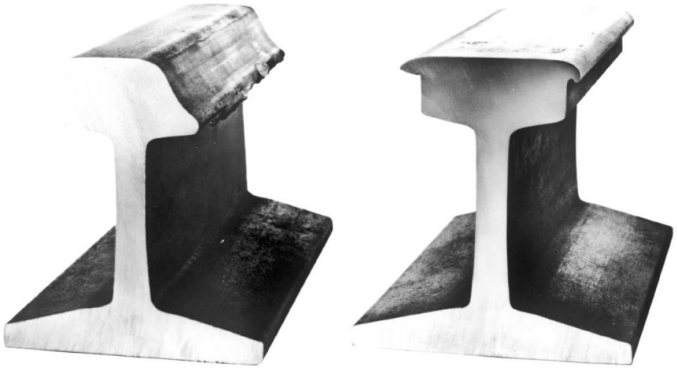

(a) (b)

Figure 1.8 (a) Lateral (or 'side') wear, and (b) abnormal vertical wear. From (UIC712R, 2002).

Coded as 2223, head-checks are cracks, usually equally spaced, that appear on the rail running surface, see Figure 1.9, generally at the gauge corner of the high rail in curves. The distance between cracks varies from 1mm to several centimetres, depending on local conditions, vehicle dynamics, track geometry and rail steel. Head checks develop as a consequence of rolling contact fatigue (RCF).

Single or a group of indentations on ridges of waves on short-wave-corrugation lines known as Belgrospi, happen on high speed lines with velocities over 200km/h, see Figure 1.10. Stresses are higher on crests and that is why they develop there. The work by Grohmann *et al.* (2002) showed highest vertical stress just before the corrugation peak.

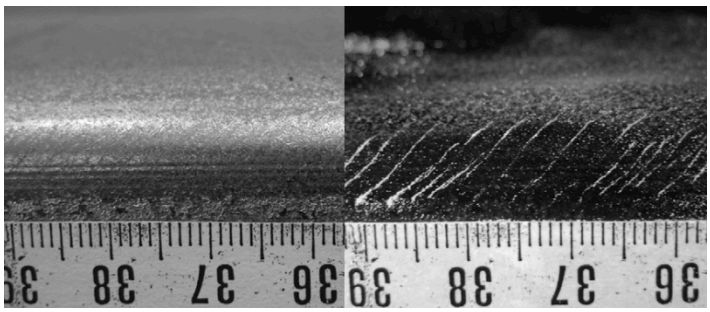

Figure 1.9 Head Checks: Standard photograph (left) and magnetic particle imaging (MPI) (right) of rail sample, used to enhance visualisation (example – R260 "dry" after 100k passes), from (Stock and Pippan, 2011).

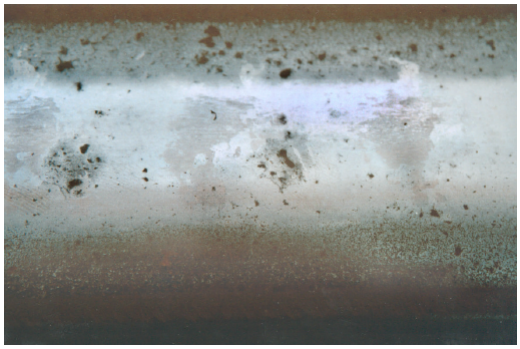

Figure 1.10 Belgrospies of category 3; source DB regulation 821.2007A02, from (InnoTrack, 2008b).

Figure 1.11 Squats (left figure from UIC712R (2002); right figure from InnoTrack (2009d))

Squats are defined in UIC 712R (2002) as a rail defect type 227, which occurs on the rail head (see Figure 1.11) and is usually a V-shaped crack with a dark circle surrounding it. Squats propagate first at a shallow angle, up to 3-5mm depth, then turn down transversely and eventually result in rail break. Both squats and corrugation and their modelling are described in InnoTrack Deliverable 4.2.4 (2009d). A research review of squats has been done by Grassie (2012) and numerical modelling by Li *et al.* (2011).

During the EU FP6 project InnoTrack (2008b), DB collected results of inspections and measurements of selected track sites. It was observed that the main maintenance cost drivers were wavelength-corrugation, belgrospies and head checks, and other failures were minimal.

In general, wear (including natural and grinding wear) is the main cause of rail replacements in almost all countries, (see Bhushan, 2001, §34.2.5).

1.1.3 Wheel failures

A good classification of wheel tread irregularities has been created by Nielsen and Johansson (2000):

- Eccentricity
- Discrete defect: "a deviation of the wheel radius that is present over a small part of the tread."
- Periodic non-roundness, with wavelengths from 14cm to the whole wheel circumference (about 3.5m), and amplitude of roughly 1mm. Also called polygonalization if wavelengths are long, 1-5 harmonics round circumference.
- Non-periodic (stochastic) non-roundness
- Corrugation, with wavelengths in the order of 3–10 cm, and amplitude less than 10μm.
- Roughness, with wavelength in the order of magnitude of 1mm and amplitude in the order of 10μm.
- Flats
- Spalling: when relatively large pieces of material come off the wheel tread. Researched in more detail by (Wen-jian *et al.*, 2006).
- Shelling is when material is lost from a tread as flakes.

Nielsen and Johansson (2000) concentrated on wheel out-of-roundness (OOR), but explained causes of other phenomena as well. The paper also presents numerical models

for prediction of development of OOR wheels, but concludes that there is still a need for a complete wear model that includes mechanisms like hardness and roughness, leading to periodic wear round the circumference.

OOR wheels cause higher contact forces and therefore the wear depth is much larger after a passage of corrugated wheels than round ones. Surprisingly, longer term influence on rail corrugation by OOR wheels can be neglected, taking into consideration the averaging effect of different irregularities, (see Johansson and Nielsen, 2007).

Both wheel and rail defects increase contact forces, as well as impact and rolling noise levels, reducing ride quality in general.

1.1.4 Rail inspection, maintenance and renewal

Train journeys have to be safe, on time and comfortable. To ensure that, infrastructure has to be inspected and maintained to the level required by standards or better, while looking at the same time at costs and environment, so effective planning and management is crucial. In the UK over 30,000km of track is maintained by Network Rail. Maintenance, renewal and enhancement works are defined in asset policies, which are currently based on practice, but it is planned to create future policies based on life cycle cost methods and tools (Network Rail, 2011a). DB uses an Intelligent Inspection System that collects and evaluates measurement results and helps infrastructure managers to plan maintenance work (InnoTrack, 2008b).

An extract from track asset policy (Network Rail, 2010b) is given in Table 1.2.

Network Rail, like most railways, inspects tracks at regular fixed intervals, according to track category. Inspection techniques used for detecting rail failures are mostly visual inspections, rail surface and profile measurements and ultrasonics. Other rail inspection technologies, as reviewed by (Papaelias *et al.*, 2010), are: Eddy Currents, Magnetic Flux Leakage, Alternating Current Field Measurement, Automated Vision Systems and Radiographic Inspection. Still in development are: Long-range Ultrasonics, Electromagnetic Acoustic Transducers (EMATs) and Laser Ultrasonics. High speed inspection techniques are in great demand and research has moved into this area.

Detection methods, treatments of rail defects and defect management recommendations are defined in UIC Leaflet 725R (UIC725R, 2007). The UK Ministry of Defence published their own documents to help manage their permanent way, see (Ministry-of-Defence, 1997; Ministry-of-Defence, 2001), and it again shows that maintenance depends on operating managers' skills and fixed schedules of inspection and works.

Regular preventative rail maintenance involves mostly lubrication and grinding. Rail grinding is primarily for maintaining profile, but is also performed to remove RCF-initiated defects, corrugation, and other head defects; and sometimes for reducing noise. Getting the interval right is tricky. It is usually based on experience and gross tonnage carried, which is not a reliable method. Cracks can be deeper than the thickness of the metal removed.

However, railways are faced with a number of future challenges to maintenance, including increase in number of travels, increased axle loads and increased traction of the new generation of rolling stock, and climate change, and further research is needed to face these.

Table 1.2 Policy Statements for Track Assets, from (Network Rail, 2010b)

No	Activity	Quadrant 1a High Cost of Incidents High Frequency	Quadrant 1b High Cost of Incidents Low Frequency	Quadrant 2a Low Cost of Incidents High Frequency	Quadrant 2b Low Cost of Incidents Low Frequency
Inspection					
30	Ultrasonic inspection	UTU compliant regimes shall be used for the ultrasonic inspection of rail in track categories 1A to 3. The balance of inspection shall be by UTU where practical, otherwise manual testing shall be used		Track categories 1 & 2: as for quadrants 1a & 1b. Track categories 3 to 6: UTU compliant regimes shall be considered for the ultrasonic inspection of rail in track category 3, depending on: • proportion of CWR/jointed track • age of rail • access for manual testing • deliverability of UTU programme nationally The balance of inspection shall be manual	
		Note: current UTU resources enable 100% of category 1A, 1 & 2 track and approximately 75% of all category 3 track to be covered			
Maintenance					
31	Lubrication	All curves with radii below 1500 metres shall be lubricated using non contact remote mounted lubricators. Existing mechanical lubricators shall be replaced when the rail is renewed		All curves with radii below 800 metres shall be lubricated. Curves with radii between 1500 and 801 metres shall be lubricated if the rail life due to sidewear without lubrication is (or would be) less than 5 years. Installation of non contact remote mounted lubricators should be considered on multiple curves when the rail is renewed	Curves with radii below 800 metres shall be lubricated if the rail life due to sidewear without lubrication is (or would be) less than 5 years. Lubricators shall be installed on unlubricated curves when the rail is renewed
32	Lubrication	The adequacy of existing lubrication shall be reviewed following significant changes to the type of rolling stock or tonnage of traffic along a route			

33	Grinding	Rail shall be ground using train based grinders to restore the specified transverse and longitudinal rail head profile at regular intervals, dependent upon: • whether the track is straight or curved • the passage of specified tonnages of traffic	Track categories 1 to 3: as for quadrants1a & 1b. Track categories 4 to 6: train based grinding shall be considered where inspection identifies problems due to poor transverse or longitudinal rail head profile	Train based grinding shall be considered where inspection identifies problems due to poor transverse or longitudinal rail head profile
34	Grinding	Rail grinding shall be used to prevent the formation of RCF by control of the rail head profile. Grinding heavy or severe high rail RCF shall only be used as temporary mitigation. Rail that exhibits heavy or severe high rail RCF shall be planned for replacement		
Renewal				
39	Renewal Criteria	Rail shall be renewed if specified replacement criteria are met for: • defect history (frequency of intervention) • safety (heavy or severe RCF, risk of broken rail, etc) • wear (sidewear, railhead profile grinding)		
40	Renewal Criteria	All pre-1976 rail in track categories 1A & 1 shall be renewed by the end of CP4 and in track categories 2 & 3 by the end of CP5. Note: approx. 1200 and 1500 track km respectively	N/A	N/A
41	Renewal Criteria	Rail in wet tunnels and other aggressive environments shall be replaced at specified frequencies to suit the rate of rail corrosion at each site. Coated rail shall be specified for the replacement of rails due to corrosion at level crossings, where justified by a site-specific business case		
42	Material Specification for Renewal	Premium rail steel shall be specified for the replacement of rails due to sidewear or RCF, where justified by a site-specific business case		

1.2 Wear and crack mechanisms

Wear and cracking in railway rails and wheels are interrelated damage mechanisms affecting the smooth and safe running of trains. Removal of material from the railhead, through wear, changes the railhead profile and influences the dynamic behaviour of passing trains. Rails need to be re-profiled periodically, and both wear and grinding reduce the structural strength of the railhead, necessitating eventual rail replacement. However, some wear can be beneficial. Surface-breaking cracks are shortened by wear, and very short cracks may be removed completely, and thus the risk of cracks growing to dangerous lengths and causing rail breaks is significantly reduced. Rail inspection for cracks, rail re-profiling and replacement are costly procedures, and tools for predicting wear and cracking of rails are essential for optimizing railway maintenance schedules.

Rolling contact fatigue (RCF) depends on wheel and rail materials, and also on wheel-rail contact conditions, especially the forces applied to the contact area. The combined influence of rail and wheel profiles and type of railway vehicle results in different sizes and shapes of contact area, mostly due to different suspension characteristics, bogie stiffness and vehicle load. Initiation and early growth of RCF cracks is the most important part of the progression of rail damage (Garnham and Davis, 2011).

Rails are subjected to cyclic loading by passing trains. Plastic shear strain accumulates, leading to wear and crack formation. Cracks usually initiate at the rail surface and follow the strained microstructure, typically making an angle of 5º-15º to the surface, in the highly strained region within about 20 microns of the surface, and growing thereafter at a steeper angle, typically about 30º (Fletcher *et al.*, 2003), (RSSB, 2002). The shallow angle increases the sensitivity of crack growth rate to wear.

The ‘Dynarat’ model (also known as the ‘brick’ model) was developed as a computer simulation of plastic shear strain accumulation in rails for predicting wear and crack initiation, based on ratcheting principles outlined by Kapoor (1994) and confirmed experimentally by Tyfour *et al.* (1996) and Clayton and Su (1996).

1.3 Thesis aim

The aim of this thesis is to develop a new material model for the Dynarat simulation, which includes new approach to stress, strain and damage evaluation, in order to be able to predict wear and crack initiation in R260 (‘standard’ grade) and four harder premium grade rail steels. The aim is to further knowledge of the new rail grade materials’ behaviour under cyclic loading, in order to help improve rail material characteristics in

future productions, and eventually to help with the selection of rail material for certain types of rail operation.

The ultimate goal is to be able to use the model developed in this thesis to help optimise maintenance schedules and strategies, and therefore to improve safety while reducing costs. The potential for practical implementation is discussed in Chapter 8.

1.4 Thesis structure

Chapter 2 provides a review of literature relevant for understanding the subject and the basis for the work in this thesis, covering wear, rail materials, wheel-rail contact properties and wear and RCF models and testing.

Chapter 3 describes the experimental work, the twin-disc testing of the five rail steels and two wheel steels, and the results of wear, adhesion and roughness. Note: A subset of the test data and metallurgical analysis has been published in reports for the EU FP6 Project 'InnoTrack' (primarily Deliverable D4.2.5).

Chapter 4 presents the results and discussion of the metallurgical analysis of the test samples, including microscopy and measurements of microhardness and plastic shear strain at various depths.

Chapter 5 uses the results of the metallurgical analysis to create strain-hardness equations for each rail material, and to drive development of the core ratcheting model used in the Dynarat simulation.

Chapter 6 develops aspects of the Dynarat model related to three-dimensional wheel-rail contact, including a new method for approximating partial slip. An equation for predicting wear rate, based on contact pressure and traction coefficient, is determined.

Chapter 7 presents a case study exploring the impact of different types of traffic on rail wear.

A short summary and discussion of the thesis is given in Chapter 8, along with the main conclusions and recommendations for future work.

The diagram in Figure 1.12 shows how the different parts of the thesis fit together.

The appendices support this thesis by providing full sets of laboratory results and simulation results.

Appendix A supplements Chapter 3 with twin-disc test results, i.e., wear and traction coefficients, and has images and observation of disc surfaces after testing, and surface roughness measurements.

Appendix B has micrographs of disc cross-sections.

Appendix C has data on microhardness measurements.

Appendix D shows simulation predictions of twin-disc tests in terms of hardness vs depth and shear strain vs depth for different materials and testing conditions.

Appendix E has selected rail material and profile definitions from standards.

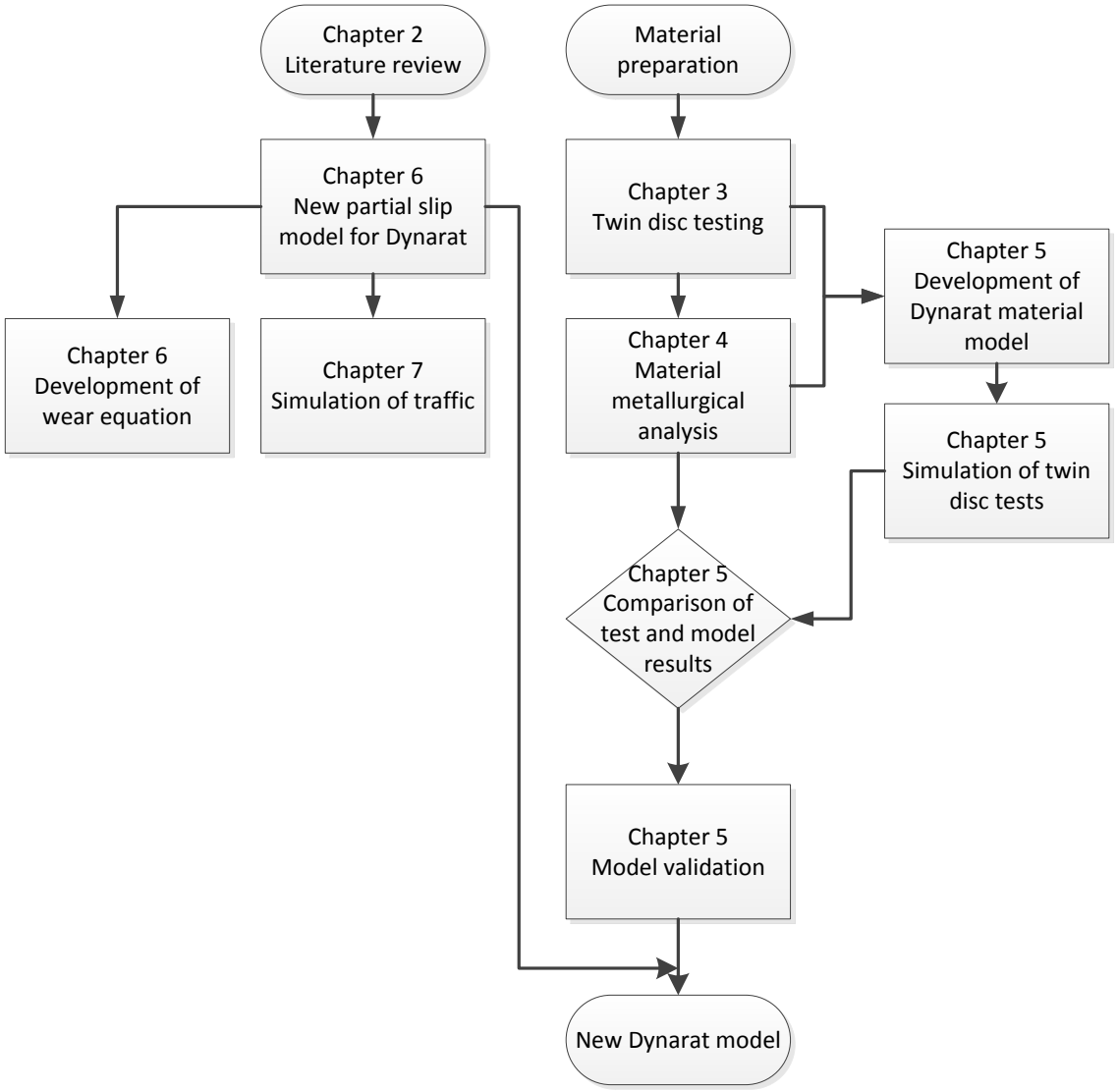

Figure 1.12 Diagram showing how the different parts of the thesis fit together.

Chapter 2 Literature Review

2.1 Wear

2.1.1 Different types of wear

Wear is the term that describes loss of material from a surface, and this can happen in various ways described below. It is a complex phenomenon and it is hard to categorise. There are four main mechanisms (also called modes, types or forms) of wear generally recognised, see Figure 2.1: adhesive, abrasive, fatigue and corrosive (Bhushan, 2001), (Rabinowicz, 1995). Other researchers categorise wear mechanisms in different ways. According to Johansson (2005) it is categorised into: delamination, oxidative, abrasive and adhesive. Halling (1989) classified wear in six types, adopted also by Alwahdi (2004) in his thesis, as: adhesive, abrasive, delamination, oxidative, fatigue and fretting. A review paper on wear mechanisms by Kato (2002) classifies wear in the following categories:

1. Wear types: mechanical, chemical and thermal wear
2. Wear modes: abrasive, adhesive, flow, fatigue, corrosive, melt and diffusive wear

Mechanical, chemical and thermal wear are governed respectively by the processes of deformation, growth rate of chemical film and local melting due to frictional heating.

Mechanisms mostly contributing to wheel and rail wear are adhesive, abrasive and fatigue (Bhushan, 2001).

Adhesive wear (see Figure 2.1a) occurs when there is strong adhesive bonding between clean surfaces (with no contaminant or lubricant) at contacting asperities. When bodies slide over each other, particles are pulled off one surface and transfer to the other. They can fall back and become loose wear fragments.

Abrasive wear (see Figure 2.1b) occurs when hard asperities, or hard particles, slide over and plough the softer surface. Grooves can be seen on the softer surface from which material is removed in the form of wear particles.

Fatigue wear (see Figure 2.1c) is a common mechanism in wheel rail contact. It occurs when material is exposed to either repeated rolling or sliding. Cracks initiate on, or under, the surface, propagate and eventually form flakes that separate as wear debris.

The wear mechanism can be either high cycle fatigue or low cycle fatigue. This will be described in more detail in the Sections 2.3.3 to 2.3.5.

Corrosive wear (see Figure 2.1d) occurs when an iron-oxide film forms on the material and is removed by sliding as a result of the following mechanisms: shear fracture of a ductile tribofilm, or 'shaving off' a soft tribofilm; accumulated plastic shear of soft tribofilm; or corrosive wear by delamination of brittle tribofilm (Kato, 2002).

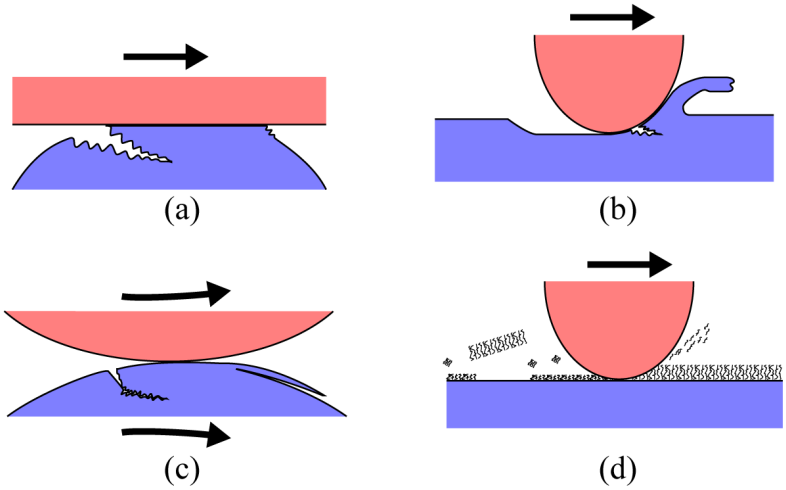

Figure 2.1 Schematic images of four representative wear mechanisms: a) adhesive wear, b) abrasive wear, c) fatigue wear, d) corrosive wear. Adapted from (Bhushan, 2001), p. 278.

2.1.2 Wear rate and categories

Archard (1953) states that the wear rate is proportional to load and inversely proportional to (rail) hardness; the wear coefficient (i.e., the 'constant' of proportionality) depends on other operating conditions, especially the sliding (or 'slip') velocity between wheel and rail. Archard describes this by the following equation:

$$W = K\frac{Ns}{H} \tag{2.1}$$

where:

- W wear volume,
- K wear coefficient,
- N normal load,
- s sliding distance,
- H material hardness.

The wear number or $T\gamma$ number [in N], is the product of applied traction T (normal force multiplied by the coefficient of friction) and creep or slip γ (percentage difference in

surface speeds between the wheel and rail or test specimens) developed in the contact patch. This term describes the energy inputted into wheel rail rolling/sliding contact. In literature (Clayton *et al.*, 1987; Lewis and Olofsson, 2004) it can be also seen in the form of $T\gamma/A$ [in N/mm^2], where A is Hertzian contact area (see Chapter 2.2.3).

Depending of the amount of wear and/or size of flakes, wheel and rail wear can be categorised as:

- Mild or Type I,
- Severe or Type II,
- Catastrophic or Type III.

This categorisation was a product of twin-disc tests and correlated to wear observed on track (Bolton and Clayton, 1984). A later review done by RSSB (2008) adopts the same categorisation and it is graphically presented in Figure 2.2.

Mild wear (Type I) happens at low stresses and creep at the interface. Wear debris is both metal oxide and metal, and its formation is associated with deformed manganese sulphide inclusions. Wear rate is independent of creep once the limiting coefficient of friction has been reached, but is proportional to sliding distance and contact stress. It is also independent of the type of material.

Mild wear is seen on lines with infrequent traffic (Schmid, 2010), and occurs on the rail head where the rail exhibits a smooth surface (Williams, 1999).

Severe wear (Type II) happens at medium stresses and creep at the interface. Wear debris is metallic. Wear depends on both stress and creep, i.e., it is a linear function of $T\gamma/A$. Severe wear is seen predominantly on the running band and gauge corner of the rail head.

Catastrophic (Type III) wear happens at high stresses and creep above 10% at the interface, where the wear rate increases rapidly for a small increase in $T\gamma$. This type of wear is explained by the reduction of yield strength of metals when the temperature rises to 250ºC due to high sliding speed. Catastrophic wear is seen on the gauge face, mostly on high rails under heavy axle load trains.

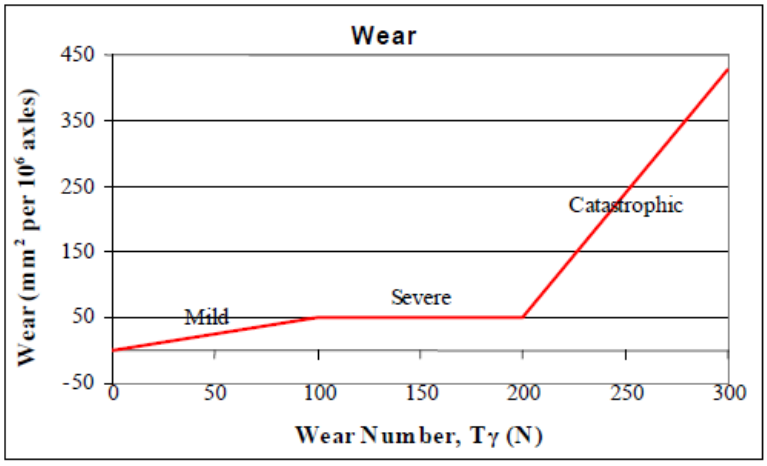

Figure 2.2 Variation of wear with wear number (RSSB, 2008)

Plotting wear data against $T\gamma$ or $T\gamma/A$ makes it easy to observe distinctions between types of wear and to compare wear of different types of materials. To analyse wear further and to include influencing parameters such as contact pressure and sliding speed, the usual method is to create wear maps for the coefficient K. An example of a wear map for rail material R260 versus R7 wheel material is shown in Figure 2.3, in the form of contour plots and 3D point graphs.

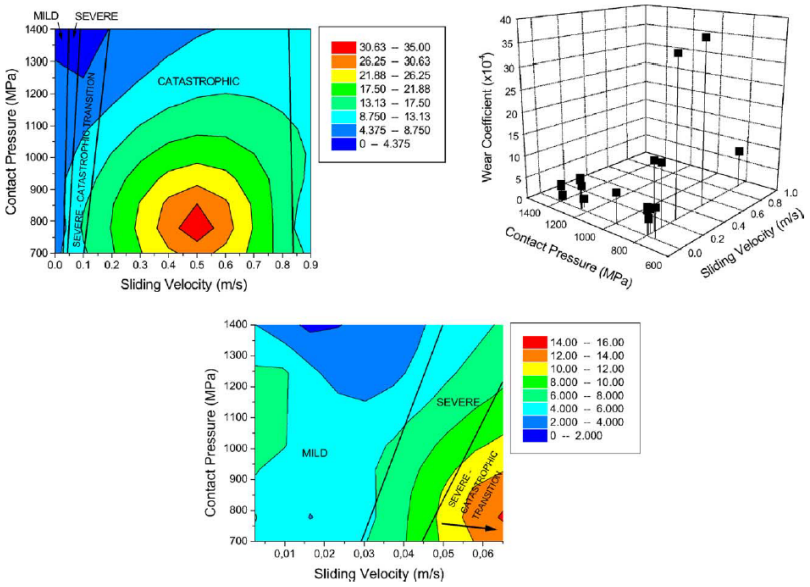

Figure 2.3 Wear coefficient maps for R260 rail material vs. R7 wheel material. Data from twin-disc and pin-on-disc tests, in Olofsson and Telliskivi (2003) (Olofsson and Telliskivi, 2003) (Olofsson and Telliskivi, 2003) (Olofsson and Telliskivi, 2003). Figure from Lewis and Olofsson (2004).

2.1.3 Factors influencing wear

Rails are subjected to repeated loading by the action of passing train wheels. The contact stresses, and how well the rail steel resists deterioration by wear and cracking, depend on several factors:

- the geometry of the wheel-rail contact patch,
- the geometry and substructure of the track,
- vehicle characteristics (load, suspension, etc.),
- type of traffic,
- wheel and rail materials,
- wheel-rail contact conditions (environmental factors, temperature, friction, adhesion).
- contaminants
- 3rd body layer

2.2 Wheel − rail contact

The wheel-rail contact patch is very small compared to the overall size of wheel and rail, typically having an area of 100-150mm^2 (Kapoor *et al.*, 2002b). (See photo of wheelsets and contact in Figure 2.4.) Its shape and dimension depend on: wheel and rail profiles (these change continuously due to wear and occasional turning/grinding); lateral position and angle of attack of the wheel in relation to the rail; train weight, speed, etc.

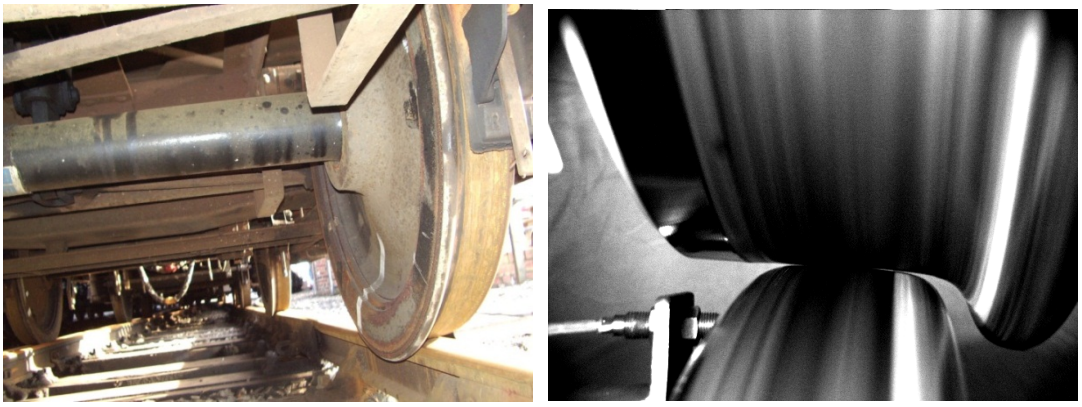

Figure 2.4 Left: Mark 1 coach wheelsets (courtesy of Francis Franklin). Right: wheel-on-rail contact (courtesy of Lucchini).

Many researchers have attempted to measure the real contact patch (Marshall *et al.*, 2006), (Pau, 2003), (Rovira *et al.*, 2011), but that is not an easy task. An example of how the contact patch changes with wheelset position is shown in Figure 2.5.

It can be modelled using contact mechanics, defined by Kalker (1990) as "the mechanics of the interaction of deformable bodies that touch each other in a contact

zone, which will also be named the ‘contact’, ‘contact region’ ‘contact patch’ or ‘contact area’.”

There are many rolling contact theories that can be used to describe the wheel − rail contact area (Garg and Dukipatti, 1984; Johnson, 1985; Halling, 1989; Kalker, 1990; Hills *et al.*, 1993). Some of the first research in this area was done by Hertz (1896) and Carter (1926). A review of several contact theories can be found in Johansson (2005). Wheel and rail, as contacting bodies, are usually approximated by half-spaces for easier computation of elasticity and stress.

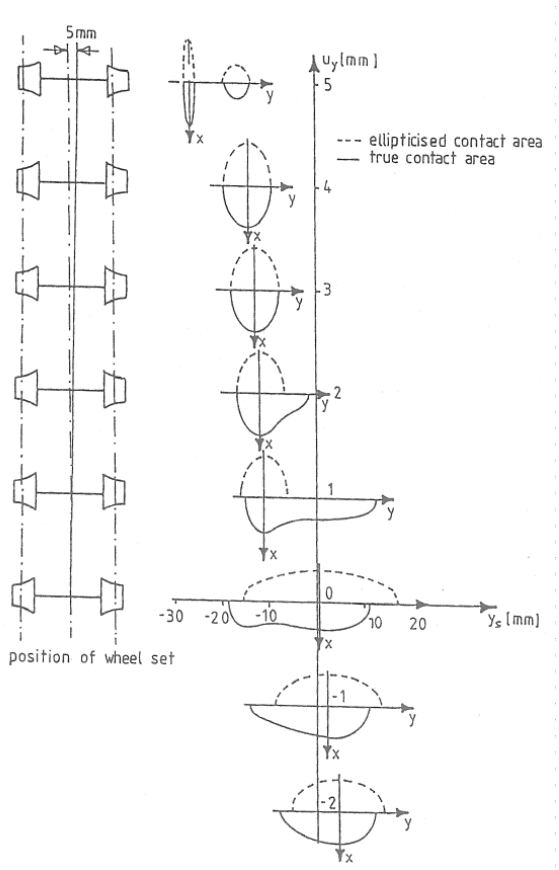

Figure 2.5 Position of the contact point as well as the elliptic and real areas of contact on the rail head at various positions of the wheelset (right wheel): upper part of each subfigure, elliptic contact; lower part, real contact, (Kalker, 1990).

2.2.1 Track geometry

“The railway track has the three functions: carrying the train, guiding it and absorbing the traction forces. These functions lead to vertical, lateral and longitudinal forces between train and track” (EN 13848-5, 2010).

Track geometry is important for wear and crack initiation, because it directly influences the position of the contact and forces acting between wheel and rail in the contact. Lateral track alignment has greater influence on rail wear and cracking than vertical.

The interaction is complex, and has been researched by Karttunen *et al*. (2012): "In more shallow curves, the general trend is that the portion of the high rail affected by RCF is increased as standard deviation of lateral track irregularities increases." Track geometry parameters have to be within safety limits as defined in the standards. Rail itself first has to be supplied within tolerances set in (EN 13674-1, 2011; UIC860R, 2008) for straightness, twist and vertical and horizontal flatness.

Cant deficiency

"The difference between the angle to which track would have to be canted on a curve to just counterbalance the centrifugal forces acting on a vehicle, and the actual cant angle of the track." (Definition is from GM/RT2141, 2009). All curves should be designed to operate with some cant deficiency to aid steering. Research has shown, e.g. (Dembosky *et al.*, 2006), that RCF on the high rail can be reduced by increasing cant deficiency on a curve, and it is most pronounced in curves with radius of 1000m to 2500m. In tighter curves the reduction in RCF is less significant but side wear can be reduced with increased cant deficiency. The mechanism that happens is as the cant deficiency increases, the angle of attack of the leading wheelset decreases, and hence reduces the contact patch forces generated during curving. See also (Burstow and Robinson, 2007; Schmid, 2010; Track-Ex, 2012).

2.2.2 Rail / wheel profiles

The railhead and wheel wear and change shape over time, which influences contact patch and stresses. Rail profiles are defined in UIC 861-1 and -3, and the most commonly used profile in Europe is 60E1, defined in (EN 13674-1, 2011); in the UK the traditional profile is BS113A (equivalent to 56E1) although 60E1 is used in new track. Drawings and tolerances are given in Appendix E. An illustration of a wheelset on rails is shown in Figure 2.6.

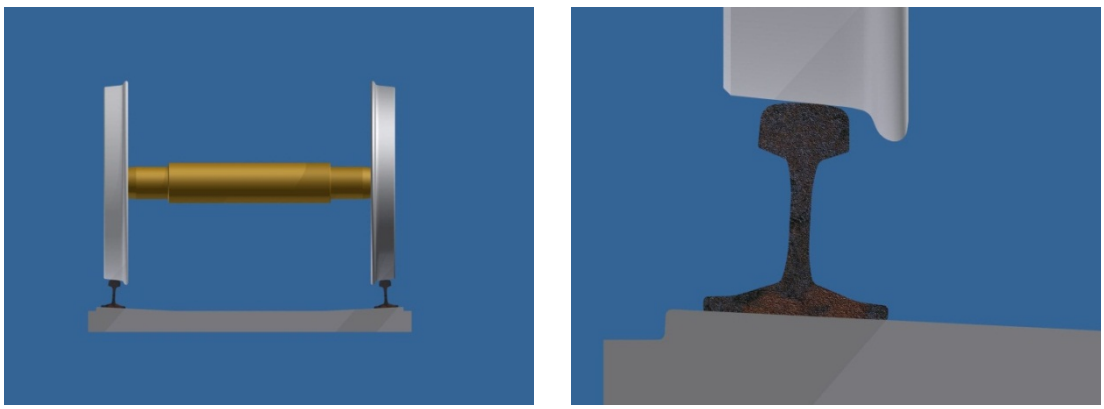

Figure 2.6 Drawings of wheelset on rails and detail of wheel-rail contact.

Rail grinding can restore profiles and it can be done in the way to introduce relief between the wheel and the rail where RCF forms, but to maintain good curving performance at the same time. Lubrication is sometimes applied to the gauge face of the rail or the flange of the wheel to reduce the friction where flange contact occurs, in order to reduce wear and profile change.

2.2.3 Hertz contact theory

Hertz contact theory takes its name from the pioneering work of Heinrich Hertz who, in 1882, started the study of contact mechanics while examining the interference fringes seen when a glass sphere (or lens) rests on a flat surface.

When two cylinders are brought into contact, without any load applied, if the cylinder axes are aligned then they make contact along a line. If a load is applied, the line of contact broadens into a rectangle. The contact pressure is highest along the centre line (i.e., the line of original contact) and drops to zero at the edges of the contact. This kind of contact is called ‘line’ contact. In its simplest mathematical form, the cylinders are assumed to be infinitely long and the contact mechanics theory is two-dimensional.

If the two cylinder axes are not aligned then, when no load is applied, they make contact at a point. As load is applied, the point of contact widens into an ellipse. Again the contact pressure is highest in the centre and drops to zero at the edge of the contact. This kind of contact is called ‘point’ contact. If the cylinder axes are perpendicular, and the radii are equal, the elliptic contact region is circular and the mathematics of contact simplifies considerably.

The idea of crossed cylinders is based on early experiments, and Hertz contact theory talks about cylinders or spheres with a given radius, but mathematically the contacting surfaces are parabolic and one basic assumption of the theory, therefore, is that the dimensions of the contact area are significantly smaller than the radii of the contacting bodies. Another assumption is that the contacting surfaces are completely smooth. (In engineering practice no surface is completely smooth. Surfaces which are not smooth will, of course, make contact at the high bumps or ‘asperities’.)

In addition, Hertz contact theory assumes the contacting bodies to be isotropic, homogenous and perfectly elastic, and neglects friction between the contacting surfaces. The study of contact mechanics has, of course, advanced beyond these various limitations, but Hertz contact theory is still the natural starting point.

Line (Cylindrical) Contact

When a cylinder of radius R_1 makes contact along its length with a cylinder of radius R_2, see Figure 2.7, the contact pressure distribution can be calculated by considering a cylinder of radius R making contact with an elastic half-space, where:

$$\frac{1}{R} = \frac{1}{R_1} + \frac{1}{R_2} \tag{2.2}$$

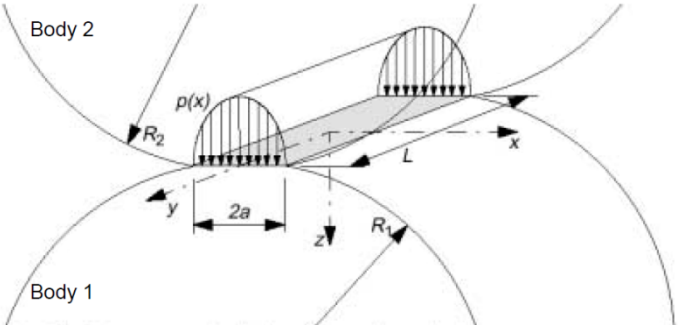

Figure 2.7 The Hertzian pressure distribution in the contact region of two elastic parallel cylinders (Alwahdi, 2004).

The equations of line contact assume the contacting cylinders to be of infinite length, but for practical purposes it is usual to consider them to be a certain length, L, and to consider a central cross-section through the contacting cylinders (since towards the ends of the cylinders the plane stress conditions will break down the assumptions of Hertz contact theory). For such a contact the peak (i.e., maximum and central) contact pressure is related to the load as follows:

$$p_0 = \sqrt{\frac{NE^*}{\pi LR}} \tag{2.3}$$

where:

p_0 peak contact pressure,

N normal load,

E^* elastic contact modulus,

L length of the contact.

The elastic contact modulus is related to the Young's elastic moduli (E_1,E_2) and Poisson's ratios (ν_1,ν_2) of the two contacting bodies:

$$\frac{1}{E^*} = \frac{1-\nu_1^2}{E_1} + \frac{1-\nu_2^2}{E_2} \tag{2.4}$$

The semi-contact width (or contact half-width) in this case is given by:

$$a = \sqrt{\frac{4NR}{\pi LE^*}} \tag{2.5}$$

or, alternatively, the peak pressure can be related to the semi-contact width by:

$$p_0 = \frac{4}{\pi}\frac{N}{2aL} \tag{2.6}$$

where:

a semi-contact width, i.e., half the width of the contact,

and the distribution of pressure within the contact is:

$$p(x) = p_0\sqrt{1-\left(\frac{x}{a}\right)^2}\ ,\ |x| \le a \tag{2.7}$$

Point (Spherical) Contact

Similarly to line contact, when a sphere of radius R_1 makes contact with a sphere of radius R_2, the contact pressure distribution can be calculated by considering a sphere of radius R (where again $1/R = 1/R_1 + 1/R_2$) making contact with an elastic half-space. For such a contact the peak contact pressure is related to the load as follows:

$$p_0 = \left(\frac{6NE^{*2}}{\pi^3 R^2}\right)^{\frac{1}{3}} \tag{2.8}$$

The semi-contact width (or contact radius) in this case is given by:

$$a = \left(\frac{3NR}{4E^*}\right)^{\frac{1}{3}} \tag{2.9}$$

or, alternatively, the peak pressure can be related to the semi-contact width by:

$$p_0 = \frac{3}{2}\frac{N}{\pi a^2} \tag{2.10}$$

and the distribution of pressure within the contact is given again by Equation (2.7).

Point (Elliptic) Contact

For more general shapes which are approximately parabolic in the region of contact, the surfaces touch initially at a point and, when loaded elastically, make contact over an elliptic region. When two such bodies, e.g., 1 and 2 in Figure 2.8 (or as a rail and wheel in Figure 2.9), are in contact, their contact geometry is defined by the principal radii of curvature of each body in two orthogonal planes.

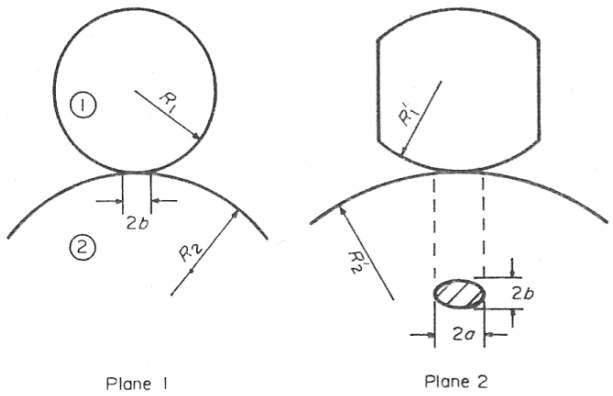

Figure 2.8 Principal radii of curvature of bodies 1 and 2 (Halling, 1989).

The semi-contact width dimensions (*a* and *b*) can be calculated using the following equations taken from (Timoshenko and Goodier, 1970; Garg and Dukipatti, 1984):

$$a = m\left(\frac{3\pi N}{4}\cdot\frac{k_1+k_2}{A+B}\right)^{1/3} \tag{2.11}$$

$$b = n\left(\frac{3\pi N}{4}\cdot\frac{k_1+k_2}{A+B}\right)^{1/3} \tag{2.12}$$

The elastic constants k_1 and k_2 are calculated using the following equations:

$$k_1 = \frac{1-\nu_1^2}{\pi E_1} \tag{2.13}$$

$$k_2 = \frac{1-\nu_2^2}{\pi E_2} \tag{2.14}$$

Note that $k_1 + k_2 = 1/\pi E^*$ – compare Equations (2.11) and (2.12) with the equivalent for spherical contact, Equation (2.9). The constants *A* and *B* are defined as:

$$A+B = \frac{1}{2}\left[\frac{1}{R_1}+\frac{1}{R_1'}+\frac{1}{R_2}+\frac{1}{R_2'}\right] \tag{2.15}$$

$$B-A = \frac{1}{2}\left[\left(\frac{1}{R_1}-\frac{1}{R_1'}\right)^2+\left(\frac{1}{R_2}-\frac{1}{R_2'}\right)^2+2\left(\frac{1}{R_1}-\frac{1}{R_1'}\right)\left(\frac{1}{R_2}-\frac{1}{R_2'}\right)\cos 2\psi\right]^{1/2} \tag{2.16}$$

where:

R_1 principal radius of curvature of body 1 (or wheel radius, see Figure 2.9)

R_1' principal radius of curvature of body 1 in plane 2 (or principal radius of wheel profile in the point of contact, which may be negative)

R_2 principal radius of curvature of body 2 (or principal rail diameter in the point of contact, $R_2=\infty$)

R_2' principal radius of curvature of body 2 in plane 2 (or principal radius of rail profile in the point of contact),

ψ angle between the normal planes which contain curvatures R_1 and R_2

In these equations curvature radius is taken as positive if the corresponding curvature centre is inside the body, as shown in Figure 2.8. The coefficients *m* and *n* in Equations (2.11) and (2.12) are numbers which depend on the ratio $(B-A)/(A+B)$, and these coefficients can be obtained by introducing an auxiliary angle defined by:

$$\theta = \cos^{-1}\left(\frac{B-A}{A+B}\right) \tag{2.17}$$

The constants *m* and *n* are given in Table 2.1 as a function of θ.

Table 2.1 Coefficients *m* and *n*. After (Garg and Dukipatti, 1984).

θ (deg)	*m*	*n*	θ (deg)	*m*	*n*	θ (deg)	*m*	*n*
0.5	61.4	0.1018	10	6.604	0.3112	60	1.486	0.717
1	36.89	0.1314	20	3.813	0.4123	65	1.378	0.759
1.5	27.48	0.1522	30	2.731	0.493	70	1.284	0.802
2	22.26	0.1691	35	2.397	0.530	75	1.202	0.846
3	16.5	0.1964	40	2.136	0.567	80	1.128	0.893
4	13.31	0.2188	45	1.926	0.604	85	1.061	0.944
6	9.79	0.2552	50	1.754	0.641	90	1.000	1.000
8	7.86	0.285	55	1.611	0.678			

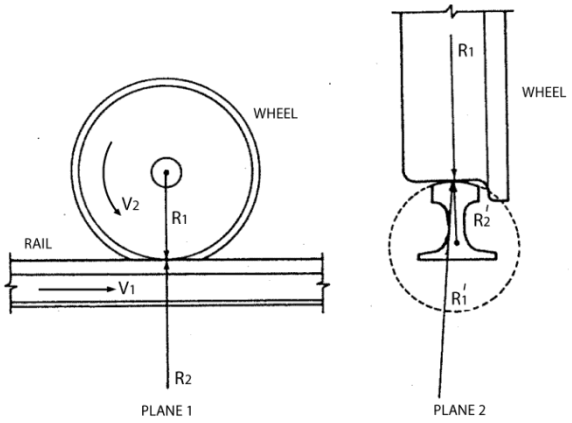

Figure 2.9 Principal radii of curvature and motion of wheel and rail (Garg and Dukipatti, 1984).

Elliptic point contact, with half-widths (i.e., semi-major and –minor axes) *a* and *b*, is represented in Figure 2.10, and ellipse equation is:

$$\left(\frac{x}{a}\right)^2 + \left(\frac{y}{b}\right)^2 = 1, \quad a \geq b \tag{2.18}$$

High forces are acting in this small contact, with components in three directions: vertical; longitudinal (i.e., in the direction of travel); and lateral (i.e., in the direction from rail to rail). The applied tangential force T acts at a general angle γ to the y-axis.

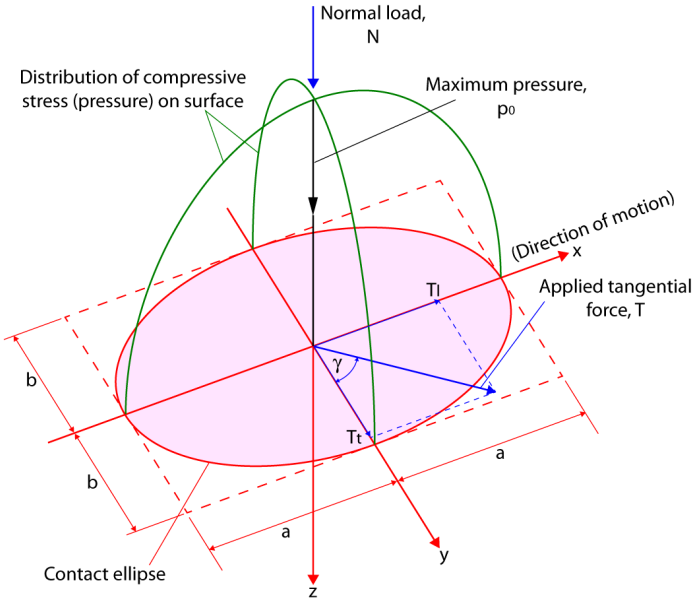

Figure 2.10 Top of the rail elliptic contact. Area of contact; forces: longitudinal and transverse traction; and pressure (modified from (ESDU, 1984)).

$$T_l = t_{cl} N \tag{2.19}$$

$$T_t = t_{ct} N \tag{2.20}$$

$$T = t_c N \tag{2.21}$$

$$F_{\max} = \mu N \tag{2.22}$$

where:

T_l	longitudinal traction force,
T_t	transversal traction force,
T	traction force,
$F_{\max}$	traction force – the limiting value of T,
N	normal load,
μ	coefficient of friction,
t_{cl}	longitudinal coefficient of traction,
t_{ct}	transversal coefficient of traction,
t_c	(resultant) coefficient of traction.

The contact pressure distribution over this contact is given by following equation (Johnson, 1985):

$$p(x,y) = p_0\sqrt{1-\left(\frac{x}{a}\right)^2-\left(\frac{y}{b}\right)^2}, \quad \left(\frac{x}{a}\right)^2+\left(\frac{y}{b}\right)^2 \le 1 \tag{2.23}$$

and the peak pressure can be related to the semi-contact width by:

$$p_0 = \frac{3}{2}\frac{N}{\pi ab} \tag{2.24}$$

For a fully sliding contact, $t_c=\mu$, and the resultant shear stress at the surface (i.e., tangential force per unit area applied at the surface) is everywhere equal to μp.

Bodies in contact are subjected to stresses within and on the surface of each body. In each plane there are two normal stresses and one shear stress. In total there are three normal stresses (σ_x, σ_y, σ_z) and three shear stresses (τ_{xy}, τ_{yz}, τ_{zx}), see Figure 2.11.

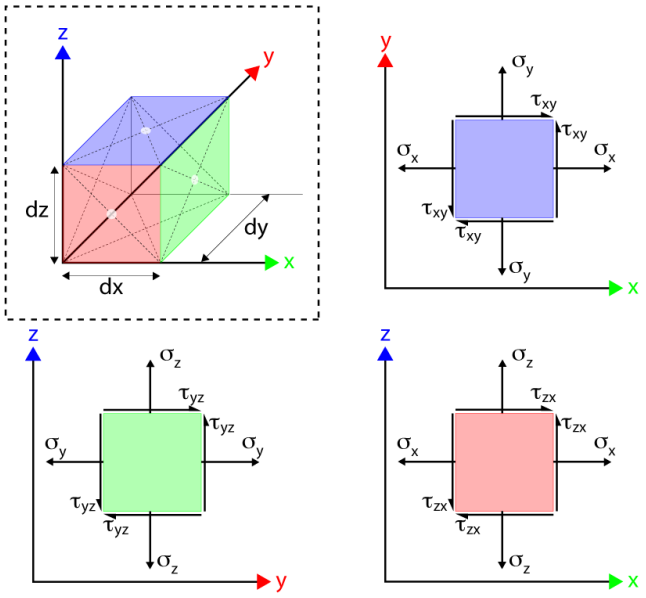

Figure 2.11 3D stress cube faces.

The z-axis is normal to the tangent plane at the centre of the wheel-rail contact ellipse and directed toward the interior of the body. Within the contact ellipse, σ_x, τ_{zx} and τ_{yz} are determined by the boundary conditions:

$$\begin{aligned} \sigma_z &= -p \\ \tau_{zx} &= -\mu p \sin\gamma \\ \tau_{yz} &= -\mu p \cos\gamma \end{aligned} \tag{2.25}$$

where:

p contact pressure,

μ coefficient of sliding friction,

γ angle of the direction of tangential force to the y-axis, the minor axis of the ellipse.

2.2.4 Partial slip

The wheel and rail are elastic bodies, which deform under rolling contact, so some of the contacting points may *slip* and others may *stick*. During free rolling, the whole of the contact is sticking. With tractive rolling, on the other hand, the contact patch is divided into 'stick' regions and 'slip' regions, and as the traction increases less and less of the contact patch sticks. For the case in Figure 2.12, the ellipse at the leading edge (left) sticks and the rest of the contact slips.

Partial slip will be explained in detail in Chapter 6.

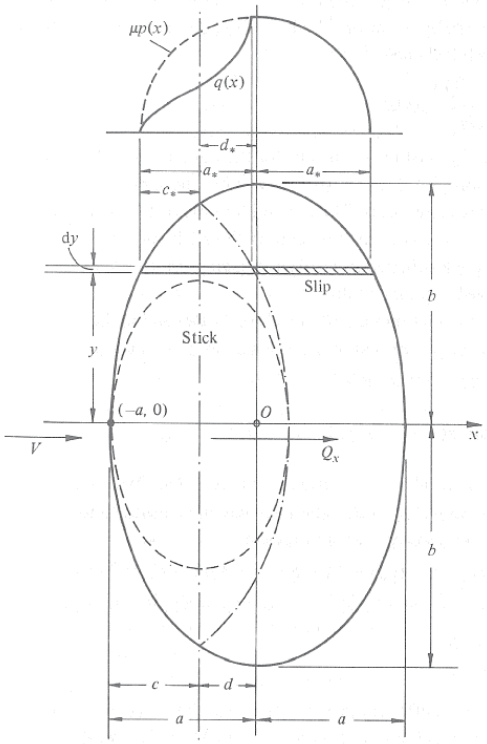

Figure 2.12 Tractive rolling of an elliptical contact region under a longitudinal force Qx $(=T_l)$. Broken line – elliptical stick (adhesive) zone, Johnson (1958a); chain line – strip theory, Haines and Ollerton (1963). After (Johnson, 1985).

2.2.5 Roughness

The surface of a rail and a wheel is not smooth, and they make contact at asperities (see Figure 2.13). Each contact area will be in the order of few square microns, so contact pressure will be much higher than the average Hertzian pressure (Kapoor and Johnson, 1994b). A thin layer under the surface (sometimes only few microns) will therefore have severe contact stresses even if applied loads are low. (Kapoor *et al.*, 2002a), tested

Japanese steels (275 HV rail, and 310 HV wheel), on a SUROS machine with turned and ground and polished surfaces, with a contact pressure of 1 GPa under pure rolling and water lubrication. They concluded that within 10μm from the surface material was plastically deformed after 100000 cycles, although it was run under the shakedown limit pressure, (which was calculated to be 2077MPa). Using a computer model, it was found that real surfaces compared to smooth surfaces give eight times higher pressures, both for real Shinkansen rail and SUROS discs. This leads to stresses high enough to create plastic deformation within a few microns of the rail surface. Their conclusion is that the thin plastically deformed layer in rails is the consequence of its surface roughness. The same conclusion that the surface roughness influences stresses and causes an increase in the depth of plastically deformed layer under the rail surface is shown in the study by Daves and Fischer (2002).

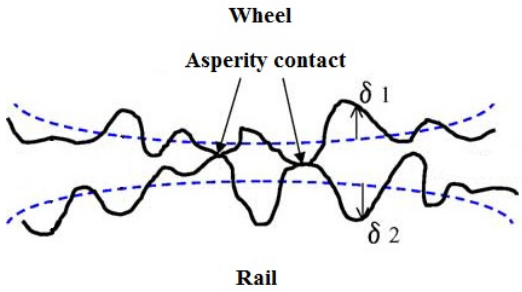

Figure 2.13 Asperity contact of rough wheel and rail. δ_1, δ_2 – random roughness amplitudes (heights) of wheel and rail surfaces. Adapted from (Chen *et al.*, 2005).

Distribution of contact pressure was calculated from ultrasonic wave reflection (Pau *et al.*, 2002). When they compared results for the minor and major axes of elliptic contact area, the pressure for minor axes was in agreement with Hertz theory, while the one for major axes had two pressure peaks, from irregularities in the wheel profile. They were also managing to plot 3D pressure distribution and see that consequently stress distribution is not ellipsoidal. For small contact pressures of 600-800MPa the real contact area is smaller than the nominal one and depends on the initial roughness of the contact areas. Pau (2003) did a series of tests varying load and roughness to investigate how the real contact area changes. The real contact area is proportional to applied load and decreases exponentially as the roughness increases, for all tested loads.

Alonsoa and Gimenez (2008) investigated the level of influence of roughness and heat generation in modelling of wheel-rail contact for dynamic railway simulations. When comparing rough surfaces with smooth (Hertzian) ones, their pressure distribution is similar. It will only differ if applied loads are 10 times lower than current static loads.

For tangential forces transmitted via the contact, they concluded that roughness again does not have significant influence.

With a number of passing wheels over rails, both components would experience wear and change of surface roughness with time. To maintain the profile of both wheel and rail, and to eliminate all defects, it is necessary to regrind them. By regrinding it is possible to establish the best roughness amplitude for the desired traction coefficient. Figure 2.14 shows that the surface roughness has a great influence on the traction coefficient, which reduces with a decrease in the surface roughness amplitude (Chen *et al.*, 2002).

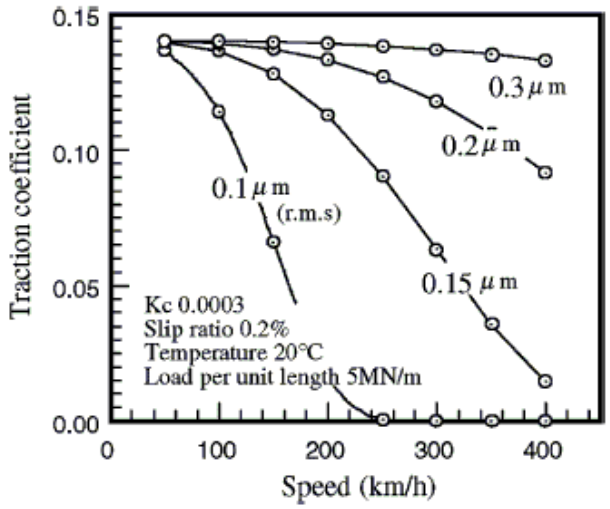

Figure 2.14 Effect of roughness on traction coefficient vs. rolling speed (Chen *et al.*, 2002).

Lundmark et al., (2009) conducted a series of twin disc tests where they changed the roughness of wheel and rail discs, as well as rail material. They have concluded that surface roughness has an influence on wear, friction and general surface damage. Research of surface roughness after grinding in site tests on Swedish heavy haul railway by (Lundmark *et al.*, 2006) showed that the roughness of the rail tended towards the steady state operating value after one day of traffic.

2.2.6 Type of traffic and individual vehicles

Deterioration of rails accumulates with each wheel pass, so by increasing traffic, rails will damage faster. Different vehicles will deteriorate rails differently, depending on axle load, steering behaviour of the bogies, and speed.

Effect of speed is related to wheel-rail dynamic forces, which can increase if wheels and rails are not smooth, e.g., out of round wheels.

Primary yaw stiffness (PYS) of the vehicle influences formation of RCF on curves. Damage is correlated to curve radius so stiffer vehicles create the most damage on 800-2000m curves, while softer PYS vehicles generate RCF on narrower curves, 600-800m radius, so it is important to choose correct vehicles for certain network routes (see Schmid, 2010, p. 4-50).

2.2.7 Adhesion

Traction is the actual driving force achieved by a locomotive, so that traction coefficient is the ratio of tractive force to normal load. The friction coefficient is the maximum value of the traction coefficient that is theoretically possible, given materials, geometry and environmental contaminants. Adhesion is specific to a vehicle, indicating the maximum achievable traction for that vehicle, so that: $traction \leq adhesion \leq friction$.

The available adhesion level between the locomotive wheels and rails is affected by many factors:

- Vehicle and track technological factors
- Wheel and rail material
- Environmental conditions (rolling speed, surface roughness, contaminants on rail surface). Adhesion levels for dry clean conditions are in the region 20%-40%, in wet conditions 10%-20%, and on British railways the adhesion levels are typically around 22% (Schmid, 2010).

The adhesion has a significant effect on wear. High locomotive adhesion is likely to increase wear and RCF damage, because it increases shear forces at the rail surface, producing material ratcheting and consequently surface cracks (Bhushan, 2001). On the other hand, poor adhesion, or even loss of adhesion during braking lead to wheel sliding, resulting in wheel flats and skidding marks on the rail surface. Adhesion management is very important for railways and has been researched significantly in the past.

2.3 Rail Steels

The wheel-rail contact is a small area, the size of a small coin ($100mm^2$), which is subjected to high cyclic loads. Rail material has to be resistant to wear, RCF and other damage and at the same time be low cost. The material has to be strong, hard and with a high elastic modulus (i.e., a high stiffness). An overview of rail steel characteristics and manufacturing is given in this section.

2.3.1 Manufacturing of rails

The manufacturing process influences the performance of the material, because there is a close relationship between heat treatment, microstructure and mechanical properties of the material. Nowadays rails have to be manufactured to fulfil EuroNorms and standards both for geometry, chemical and mechanical properties: e.g., (UIC 860 R, 2008; EN 13674-1, 2011).

The rail manufacturing process and rail materials are explained in (Schmid, 2010), (Mädler, 2008). The critical stage of the rail rolling process is the reheating of blooms in a furnace to a temperature of ~1250 ºC, which has to be done uniformly and continuously, through good control of atmosphere and temperature. Consequences can be poor internal and surface quality, residual stresses and decarburisation.

By a controlled process of rail steelmaking, the aim is to achieve consistency of chemical composition, minimise steel segregation, and also get uniformity of mechanical properties. With new rails it is very rare to have brittle inclusions as crack initiators, which almost stop 'tache ovale' (circular cracks growing out from defects deep within the rail) fatigue failure.

All stages of rail production have 'acceptance tests' to make sure that all defective rails will be eliminated.

Depending on the cooling-heating process, rails are produced with different hardness, roughness, mechanical properties and microstructure.

2.3.2 Rail material properties

Increasing numbers of rail journeys and train speeds, as well as higher axle loads of freight trains, has put even more demand on rail materials. The choice of material is also influenced by the duty a rail has to perform, like type of traffic, curve radius, high or low rail, or straight line, switches and crossings. Rail material manufacturers prefer to have material with high strength and higher resistance to RCF than to wear.

Pearlitic microstucture steels are most widely used for wheels and rails. Another microstructure tried in recent years is bainitic rail steel. In Japan and the USA for heavy haul railways Nippon steel is used too, which is a hardened specially formed high carbon (0.8-0.9 wt%C) pearlitic steel (Ueda *et al.*, 2004).

The standard rail material is low alloy, carbon-manganese steel with weight percentage carbon 0.4-0.6 (wt%C) and 1.0 manganese (wt%Mn), see D4.2.1 (InnoTrack, 2007).

Chemical composition of most used steels in the UK is given in Table 2.2, grades are classified according to material hardness. Data are from standard EN 13674-1 (2011). More comprehensive tables are given in Appendix E.

Table 2.2 Chemical composition and hardness of selected examples of UK currently installed rail steels

Steel grade	Chemical analysis, (wt%), i.e. (% in mass)									Hardness
	C	Si	Mn	S (max)	P (max)	Cr (max)	Al (max)	V (max)	H_2 (ppm max)	HBW
220	0.48-0.62	0.18-0.62	0.95-1.30	0.030	0.030	0.15	0.004	0.03	3.0	220-260
260	0.60-0.82	0.13-0.60	0.65-1.25	0.030	0.030	0.15	0.004	0.03	2.5	260-300
350HT	0.70-0.82	0.13-0.60	0.65-1.25	0.030	0.025	0.15	0.004	0.03	2.5	350-390

The mechanical properties of steel can vary according mostly to the content of carbon and then other alloying elements such as manganese, chromium, vanadium, and tungsten, and also time-temperature history. Different mixtures of iron and carbon and heat treatments can form microstructures with very different properties. This can be better explained looking at the iron-carbon phase diagram Figure 2.15.

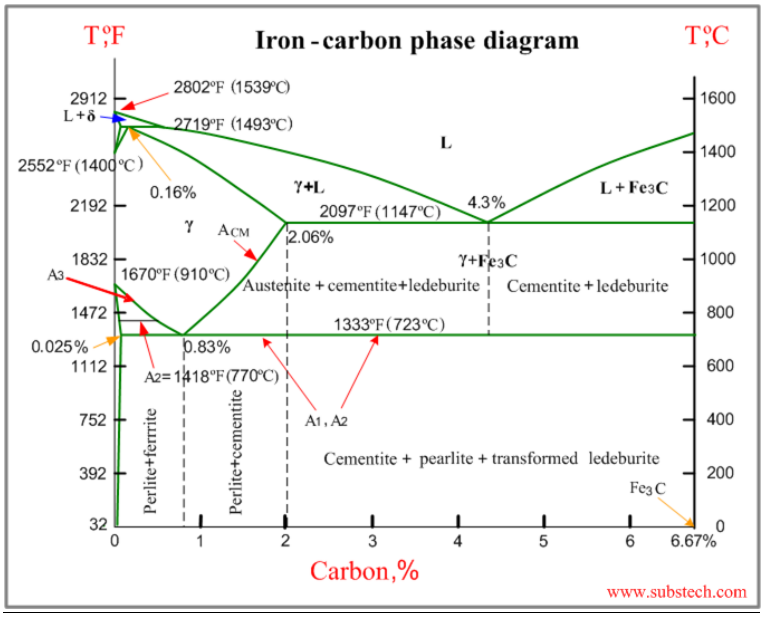

Figure 2.15 Iron-Carbon phase diagram (Kopeliovich, 2011). Rail steels are in the region of 0.4-0.9 %C in the diagram.

The most stable form of iron at room temperature is called ferrite (or α-iron) and has body-centred cubic (BCC) atomic structure, which has low carbon solubility (max 0.022 wt% at 727ºC). Austenite (or γ-iron) has face-centred cubic (FCC) atomic structure with high carbon solubility (max 2.14 wt% at 1147ºC). Pure iron (looking at the left vertical axis on the diagram) has first change in crystal structure from BCC to FCC at 912ºC,

and then again at 1394ºC, from FCC to δ-ferrite with BCC and finally melts at 1538ºC, (Callister and Rethwisch, 2011).

Most rail steels are hypo-eutectoid (less than eutectoid) alloys (0.40-0.60 wt% C) and their change in microstructure while cooling is better explained following vertical yy' line on part of Fe-C diagram shown on Figure 2.16.

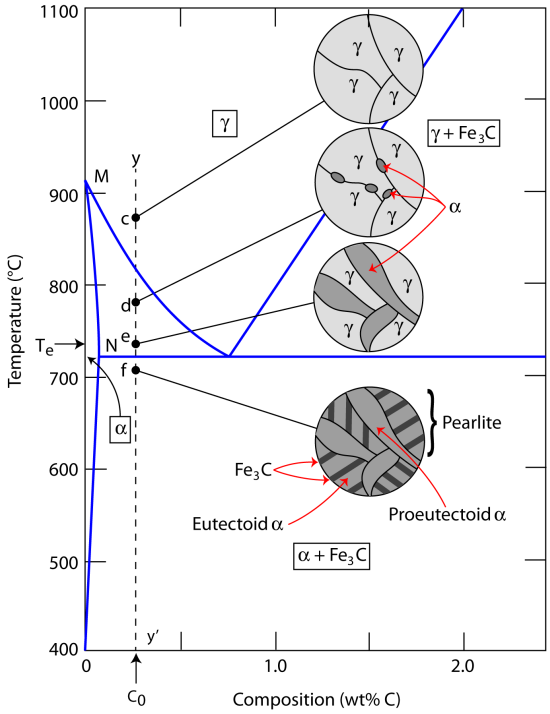

Figure 2.16 Schematic representation of microstructures for an iron-carbon alloy of hypo-eutectoid composition C_O (0.25-0.60 wt% C) as it is cooled from within the austenite phase region to below the eutectoid temperature. Nomenclature: γ - austenite; α - ferrite; Fe_3C – cementite (Callister and Rethwisch, 2011)

At temperatures of above 875ºC, point c, the steel is in the austenitic phase (γ-iron). On cooling to α+γ phase region, to just below 775ºC ferrite nucleates will form along austenite grain boundaries. While cooling down to point e, α grains will grow bigger. When the temperature is below the eutectoid of 727ºC, point f on the diagram, austenite will transform to pearlite. There will be no change in the ferrite (α phase) that existed in the material (point e) before crossing the eutectoid line. This ferrite is called proeutectoid (PE) that exists at the prior austenite (PA) grain boundaries, so now surrounding the pearlite colonies.

Pearlite is a sandwich structure consisting of lamellae of cementite (Fe_3C) and eutectoid ferrite (Fe), Figure 2.17. They have different mechanical properties, see Table 2.3. Ferrite is more ductile but has lower hardness and strength than cementite.

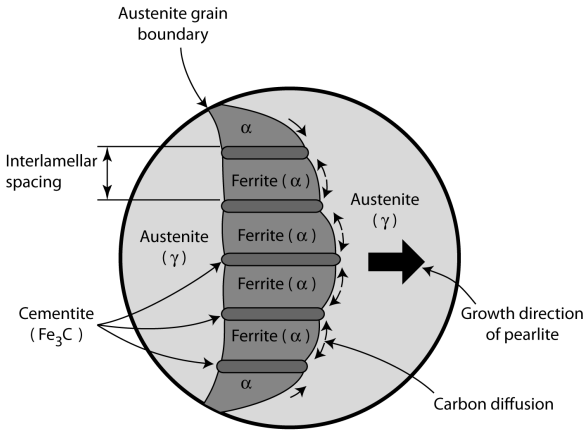

Figure 2.17 Pearlite structure: Schematic representation of the formation of pearlite from austenite; direction of carbon diffusion indicated by arrows. Adapted from (Callister and Rethwisch, 2011)

Table 2.3 Properties of ferrite and cementite

	Young's Modulus	Poisson's Ratio	Vickers Hardness
Cementite	160GPa [1)] 170GPa [3)]	0.26	630 [2)] 1230-1270 [1)] 1270 [3)]
Ferrite	190-210GPa	0.27-30	86 (hot-rolled) 95 (cold-drawn)

Note - data from:
[1)] (Li *et al.*, 1998)
[2)] (Carpene and Schaaf, 2002)
[3)] (Webb and Forgeng, 1958)

Interlamellar spacing in pearlite (Figure 2.17) has a significant effect on material strength. It can be controlled by the cooling rate of the manufacturing process. Wear rate can increase by reducing interlamellar spacing and with thinner cementite lamellae (Perez-Unzueta and Beynon, 1993).

2.3.3 Material response to repeated loading

Wheels and rails are subjected to repeated loading in service. Their material can respond in one of the four different ways to this repeated rolling and/or sliding contact stresses, (Bower and Johnson, 1991; Kapoor and Johnson, 1994a) (see Figure 2.18):

a) Elastic behaviour: If the loading in any cycle does not exceed the elastic limit, then the material will behave totally elastically and there will not be any plastic deformation.

b) Elastic shakedown: When a material is loaded above the elastic limit, but under the elastic shakedown limit, it will experience some plastic deformation in first

few cycles. At the same time, the material will develop protective residual stresses or strain harden, so when loaded again, it will behave in an elastic manner.

c) Plastic shakedown: If a material is loaded above the elastic shakedown limit, it will reach steady state behaviour after a few cycles in the form of a closed elastic-plastic loop, but with no net accumulation of plastic deformation. The limit under which this cyclic plasticity is happening is called the plastic shakedown limit or the ratcheting threshold.

d) Ratcheting: If loading exceeds the ratcheting threshold, the material will accumulate unidirectional plastic strain with each contact cycle. This process is called plastic ratcheting.

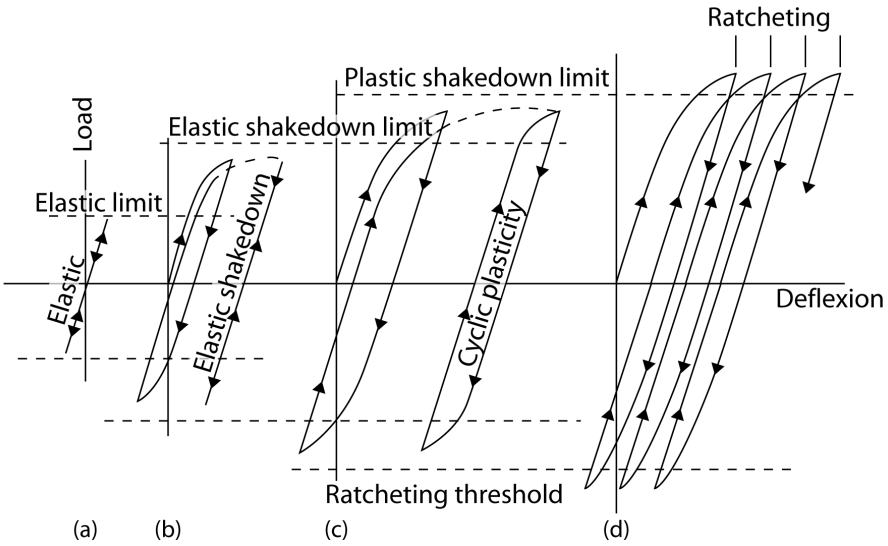

Figure 2.18 Response of material to repeated (cyclic) loading, (Kapoor and Johnson, 1994a). Ratcheting is associated with asymmetry in stresses.

2.3.4 Material failure

How a material fails if loaded repeatedly was analysed by (Bower and Johnson, 1989; Bower and Johnson, 1991; Kapoor, 1994; Kapoor, 1997). Within the elastic limit and also elastic shakedown limit, the life of the material will be very long and failure will occur most likely by high cycle fatigue (HCF). For the plastic shakedown response, a closed elastic-plastic loop, failure will be by low cycle fatigue (LCF). The number of cycles to failure, N_f, is related to plastic deformation involved, and can be estimated using the Coffin-Manson equation:

$$\frac{\Delta\varepsilon_p}{2} = \varepsilon'_f \left(N_f\right)^c \tag{2.26}$$

where:

c fatigue exponent, usually in the range -0.7 to -0.5 for metals,

ε'_f fatigue ductility (related to strain to failure in a monotonic test),

$\Delta\varepsilon_p$ the plastic strain range.

If a material accumulates plastic deformation with each cycle, then the cycles of plastic strain are open, and 'ratcheting failure' (RF) is possible. This occurs when the accumulated strain reaches a critical value ε_c. For a ratcheting strain per cycle of $\Delta\varepsilon_r$, the number of cycles to failure, N_r, is given by:

$$N_r = \frac{\varepsilon_c}{\Delta\varepsilon_r} \tag{2.27}$$

Kapoor (1994) also suggests that LCF and RF are competitive such that whichever corresponds to earlier failure governs the life of the specimen:

$$N = \min\left(N_f, N_r\right) \tag{2.28}$$

where N is the actual number of cycles to failure, and N_f and N_r are given by Equations (2.26) and (2.27) respectively. However, it is possible that the two mechanisms are additive, in which case life can be determined by using summative rule such as Miner's.

Wear and the initiation of fatigue cracks are direct consequences of ratcheting as the material accumulates strain up to its limiting ductility (Fletcher *et al.*, 2003). This happens in the wheel-rail contact under the repeated combined action of surface shear forces and high compressive loads.

2.3.5 Crack initiation and propagation

Microstructural analysis and investigation of fatigue crack initiation in R220 and R260 steels has been done recently by (Garnham and Davis, 2011) and (Eden *et al.*, 2005; Garnham *et al.*, 2007; Fletcher *et al.*, 2008; Franklin *et al.*, 2008; Garnham and Davis, 2008). This has shown that RCF crack initiation and early growth is dependent on microstructure. There are two types of crack initiation sites: surface and subsurface. For R220, cracks usually initiate and grow at the boundaries of strained prior-austenite (PA) grains at the surface, especially if there is pro-eutectoid (PE) ferrite present at the boundary. R260 has less PE ferrite at boundaries, but one of the cracking mechanisms is the same as in R220, while another seems to be along elongated PA boundaries and MnS inclusions. Beynon *et al.* (1996) also showed that crack growth was often associated with planes of weaknesses in particular manganese sulphide inclusions. The effect of inclusions on the rail cracks depends on their size, composition and distribution. Johnson (1989) identified major contributing factors to the initiation of

surface cracks being plastic flow in the material due to large traction on high-speed rails; and spin, due to conicity of the wheels.

Fracture mechanics describes three modes of crack propagation, Figure 2.19:

- Mode I - opening mode, where the forces pull the crack open
- Mode II - shearing mode, where the crack faces slide over one another in a direction perpendicular to the leading edge of the crack
- Mode III - tearing mode, is anti-plane shear where the crack surfaces move relative to one another and parallel to the leading edge of the crack

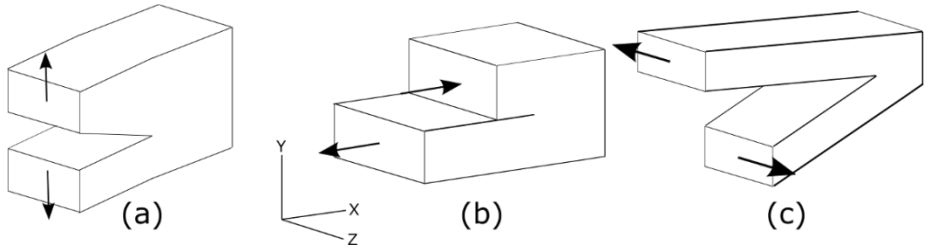

Figure 2.19 Fracture mechanics modes: (a) Mode I (opening); (b) Mode II (shearing); (c) Mode III (tearing). Figure from (Smith, 2007)

Bower (1988), studied mode I and mode II stress intensity factors in RCF and explained crack propagation by several mechanisms. In shear mechanism (mode II), see Figure 2.20a, there is relative motion between the two faces of the crack, making it propagate. If fluid is forced into the crack, the hydraulic pressure would produce tensile (opening - mode I) stresses at the crack tip and forcing it to propagate, see Figure 2.20b. Crack propagation by fluid entrapment in the crack is shown in Figure 2.21.

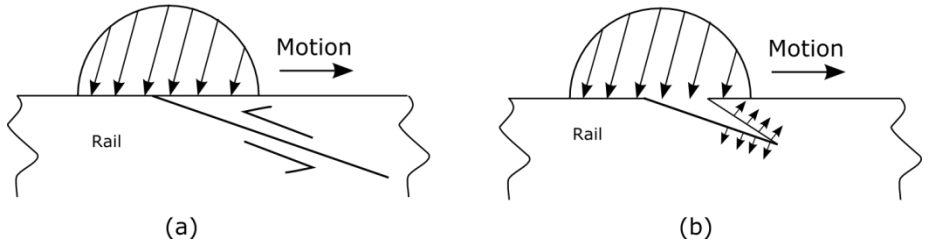

Figure 2.20 Schematic illustrating the stages involved in the propagation of a rolling contact fatigue crack proposed by (Bower, 1988): (a) The shear mechanism (mode II), (b) The hydraulic pressure mechanism (mode I). Figure from (Smith, 2007)

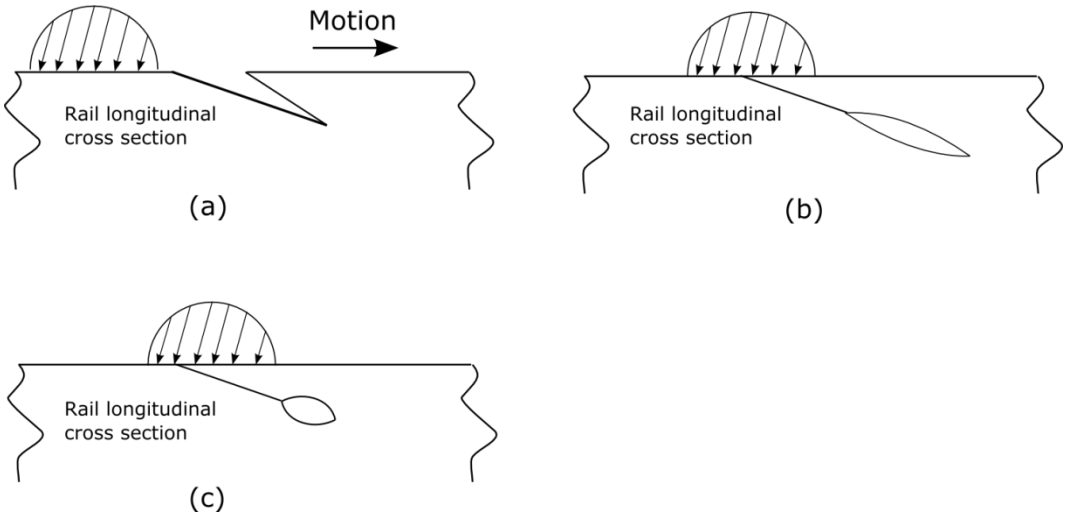

Figure 2.21 Schematic illustrating the stages involved in the propagation of a rolling contact fatigue crack by the fluid entrapment mechanism proposed by Bower (1988). (a) A wheel contact approaches a crack in the rail, under lubricated conditions, (b) The wheel contact closes the crack mouth, trapping fluid inside, (c) The fluid is driven to the crack tip and becomes pressurised until the contact has moved away and the crack can open allowing the fluid out. Figure from (Smith, 2007)

Propagation of RCF crack in rails can be separated into three phases, see Figure 2.22, with an example of a longitudinal cross-section of a rail containing a crack. This has been explained in several works, e.g. (Kapoor *et al.*, 2002b).

- Phase I - Initiation and early growth

  The train mass and steering behaviour of wheelsets impose large vertical and shear (longitudinal and lateral) forces in the wheel-rail interface. Strain accumulates in material near the surface, and when ductility of the material is exhausted, cracks will appear (usually following grain boundaries).

- Phase II - Shallow angle crack growth

  Crack growth is driven by contact stresses and initially growth is at an angle of 10-20° relative to the contact surface. Water or lubricant can increase crack growth. Deeper into the material, the crack tip moves away from the highest contact stresses and its growth rate drops.

- Phase III - Branch crack growth

  Dominating stresses in this phase are bending stresses, residual stresses from rail manufacturing and the continuous welded rail stresses. Cracks may branch up or down (see Figure 2.22). Bending-driven growth of longer cracks is fast, and rapid fracture is possible, leading to rail breaks.

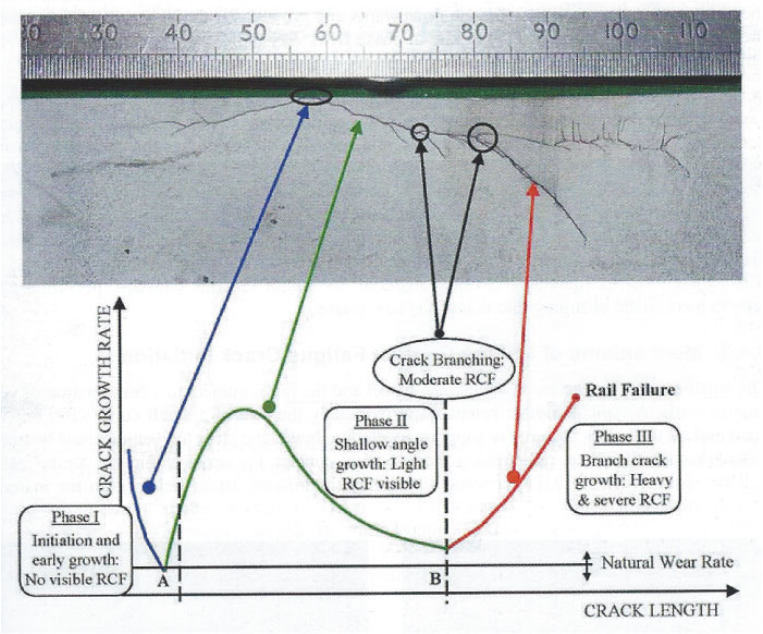

Figure 2.22 Phases of crack growth of a typical RCF crack (Schmid, 2010)

2.4 Interdependence of wear and crack formation and growth

Wear and crack growth are not independent. Surface-breaking cracks are truncated by wear, and short cracks can be removed by wear or grinding (see Figure 2.23). This interdependence has been researched by: (Donzella *et al.*, 2005), (Kapoor *et al.*, 2002b) (RSSB, 2008), (Hyde, 2012) and others. Wear can therefore be beneficial for rail life, but too much wear also shortens the life of the rail. Another consideration is the change of rail profile as a result of wear, which affects vehicle dynamics and passenger ride quality, so that rails have to be ground to correct the profile. In addition to correcting the profile, short cracks at the surface are removed, and longer cracks are shortened. However, since grinding removes material from the surface, excessive grinding shortens the life of the rail. Each grinding cycle removes about 0.2mm of the railhead, see (Network Rail, 2007), also reported by (Magel *et al.*, 2003) for US heavy haul. Using models to help optimise preventive maintenance it is possible to find the 'magic wear rate', i.e., the minimum sum of natural wear and grinding wear that will remove shallow cracks at the surface (Kalousek and Magel, 1997); in practice, there is too much variability in the railway system to achieve the 'magic wear rate', but it provides a useful target during optimisation.

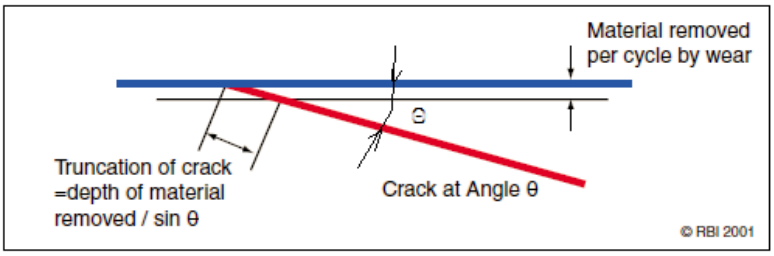

Figure 2.23 Truncation of a shallow angled crack by wear or grinding, after (Kapoor *et al.*, 2002b).

Although wear (and material loss through grinding or turning) leads to the need for rail or wheel replacement, which is expensive in terms of loss of access (i.e., taking the train out of service, or preventing traffic on a stretch of track), the removal or shortening of cracks can also increase the life, and certainly increase the safety, of the wheel or rail.

2.5 Experimental investigation of wear and RCF

Regular maintenance is necessary for the safety of the railway service. Railway authorities perform regular inspections of track using a combination of methods ranging from visual inspection to using special inspection vehicles equipped with several technologies, e.g., for recording track geometry. To understand rail wear and crack mechanisms better, focused rail research in the form of field and laboratory tests has continued over the years, e.g., see review paper by (Clayton, 1996). A quick, and certainly not exhaustive, overview is presented below, and concentrates mostly on the degradation behaviour of premium grade rail steels.

2.5.1 Field tests

Railways are experiencing higher axle loads and speeds in service, for which renewal of track with new steel grades that would reduce overall life cycle cost (LCC) is important. Rail grade selection for certain sites is often combined with field trials. Behaviour of certain steel grades over years in service is monitored, like wear and RCF, data collected and some overall conclusions could be made.

Research results from site tests reported in D4.1.3 (InnoTrack, 2008) show that harder pearlitic rail steels have in general higher resistance to wear and RCF. For example, the wear rate of R260 was found to be three times higher than that of R350HT, and the RCF resistance of the R260 was significantly lower. When examining behaviour in curves, wear is higher in tighter curves with radii of less than 1000m, while RCF-initiated 'head checks' are generally found in curves with a greater radius (ranging from 500m to 5000m). Lubrication has a significant impact on curve deterioration, although the impact on rail wear is less for premium grade rails (Muster *et al.*, 1996; Olofsson and

Telliskivi, 2003), so changing material with higher hardness will slightly improve wear resistance, up to the factor of 1.5. (Caution is needed here, however, because reducing the wear rate can result in an increase in RCF.) If cracks have been already initiated on rail when lubricant is applied, this can speed up cracking process due to hydraulic pressure mechanism, explained in Chapter 2.3.5.

Extensive test trials were done on DB AG high-speed lines to investigate and compare damage of rails, predominantly 'head checking' with material R220, R260 and R350HT, see (Heyder and Girsch, 2005). Rails with grade R350HT had 6 times lower depth of damage due to head checks and 3 times lower wear rate, compared to R220. R260 performed twice as well as R220, for both damage mechanisms.

Although track trial results depend on many factors, and differ from site to site, using harder steels has in general been shown to be advantageous for reducing LCC.

Wheel wear is not the focus of this thesis. Research and field measurements of wheel wear can be found in, e.g., (Jendel, 2002).

Premium grade trial by Network Rail

This discussion refers to field trials reported on by: Mark Burstow, 'Experience of premium grade rail steels to resist rolling contact fatigue (RCF) on the GB network,' IoM3-Rail, 1-3 November 2011, NRM, York, U.K.

During curving, the high angle of attack of the leading wheelset causes very high forces between wheel and rail. On the high rail, these forces drive RCF growth; on the low rail, the forces are still high and can cause plastic deformation, pitting, gauge corner cracking and corrugation.

A premium grade rail steel is being trialled by Network Rail in a 250m-radius curve. Previously the low rail at this site was experiencing spalling and cracking after only five years of service and required frequent grinding, whereas the high rail had no signs of damage or RCF after nine years in service. Both rails were 'normal' grade (probably R260, although 'normal' traditionally refers to R220; certainly the new premium grade rails are being compared with new R260 rails in place on the same curve).

Nine months after new R260 and MHH (the C400 grade – R370CrHT – studied in this thesis) rails were put in service in the curve, the MHH showed significantly less plastic deformation than the R260. On the high rail, the grinding marks were still clearly on the premium grade rail steel, but had been worn away on the R260, showing that the wear is

significantly higher for the R260. Also, on the low rail, the R260 showed signs of RCF on the field side, and some spalling in the running band.

The MHH clearly performs better than the R260 on the low rail, and is generally superior in terms of wear and plastic deformation. In the high rail, however, the MHH developed RCF within six weeks of service. The position of the cracks on the rail head is closer to the gauge face, where the contact pressure and creepage are generally higher. (Gauge corner radius is 12.7mm for the 56E1 rail profile and 13mm for the 60E1 rail profile.)

In the SUROS tests for InnoTrack and analysed in this thesis, the MHH (C400) developed cracks during dry testing, reaching depth 0.05mm after 5000 cycles and 0.1mm after 10000 cycles. The cracks grew to 0.5mm depth in the mixed dry-wet test – see Figure 4.21. The twin-disc contact is not properly comparable with wheel-rail because of the difference in scale, but the tests have shown clearly that the MHH will develop RCF if the pressure and creepage are high, and if water gets into the cracks (which is not unlikely given British weather).

It is worth noting also that both rails had gauge face lubrication, and since the cracks were close to the gauge face it is possible that the lubricant entered the cracks and this would accelerate shear mode crack growth (Fletcher and Beynon, 2000c).

As for why the MHH developed RCF when the R260 did not, this is probably down to the resistance of the MHH to wear and plastic deformation. The MHH would have maintained its original rail profile for longer than the R260, even the severely stressed gauge corner region where the cracks developed. To resolve this in future, the rail profile will need to be optimised for premium grades. An additional factor is the grinding roughness, which is usually ignored since it wears away quickly. In the trial, however, these grinding marks persisted for longer (still visible after nine months). Surface roughness acts to raise the stresses close to the surface (within about 0.05mm), and persistent grinding marks will therefore accelerate plastic deformation and crack initiation. The surface quality of premium grade rails following grinding needs special attention (Hyde, 2012).

2.5.2 Laboratory test rigs

Laboratory tests have various advantages over field tests, mostly in saving time and money. Conditions can be better controlled and parameters monitored. Materials' characteristics can be better compared and worse materials discarded, thus avoiding

early further expensive field tests. Several laboratory test rigs for testing rail and wheel material for wear, adhesion and RCF are noted here:

- DB test rig, see D4.3.7, (InnoTrack, 2009).
- Full-scale rail-wheel test rig at Voestalpine Schienen GmbH (VAS), see D4.3.7, (InnoTrack, 2009); also described in many papers, e.g. (Stock *et al.*, 2011)
- Lucchini test rig, see (Braghin *et al.*, 2005)
- Twin-disc machine, see (Takikawa and Iriya, 2008)
- Scaled car test facility, see (Zhang *et al.*, 2002)
- SUROS test rig was used to test materials for this thesis, and is explained in Chapter 3.

Comparison between four test rigs and their overall assessment is presented here in Table 2.4 and Table 2.5. Data for DB, VAS and SUROS tests and rigs is taken from D4.3.7 (InnoTrack, 2009) and this author's knowledge and data about Lucchini test rig BU300 is courtesy of Lucchini RS.

Table 2.4 Qualitative comparison of the wheel-rail test methods

	Rating	SUROS machine	Rating	VAS RSP test rig	Rating	DB test rigs	Rating	Lucchini test rig BU300
Test specimen								
Rail test sample	3	cylindrical disc; Ø47 mm	5	rail segment, 1.5m	2	bended or rolled rail material	2	Bended or rolled rail material
Rail material	5	any desired (even prototypes)	4	arbitrary	2	specific	2	Any desired if selected before a new mounting
Wheel counterpart	3	cylindrical disc; Ø47 mm	4	single wheel, original sized	5	wheelset, original sized	5	Wheelset in full-scale dimension
Wheel material	5	any desired (even prototypes)	5	arbitrary	5	arbitrary	5	Any steel grade in function of wheelset used
Contact conditions								
wheel and rail profiles	3	line contact	5	S1002/UIC 60	5	S1002/UIC 60	5	Wheel: in function of tested wheels Rail: different profiles. Normally UIC 60 profile but it can be changed re-profiling in different shape
Nominal contact forces	4	usually~7.14 kN (downscaled) Capable of load up to 29kN.	4	200 kN vertical 40 kN lateral (200% magnified)	5	2x80 kN vertical ~5 kN lateral (real sized)	5	Vertical contact force: 0 to 260 kN on each wheel Lateral contact force: -150kN to 150 kN on each wheel Longitudinal contact force: -40kN to 40 kN on each wheel
Lateral forces	2	none	5	<40 kN	3	<10 kN		

	Rating	SUROS machine	Rating	VAS RSP test rig	Rating	DB test rigs	Rating	Lucchini test rig BU300
slip	4	usually 1 % (too large for non-driven wheels) Could be run with pure rolling, or higher slip (e.g.5%)	4	none (too low for driven wheels or braking)	4	none (too low for driven wheels or braking)	4	None
lubrication	3	usually water Other lubricants could be used: e.g. water spray, oil.	3	(water)	4	Water spray	3	Normally not used but it is possible to mount a lubrication system
angle of attack	3	none	3	none	5	< 8 mrad	5	-30 to30 mrad
Quality of test results								
stability of test results	4	good	4	good	1	Mechanical failure	5	Good
correlation to simulation	4	good	4	good	3	Medium	5	Good
comparable material deformation	4	good	4	good	3	Medium	4	Good
comparability to field conditions	3	medium	4	good	-	Not evaluated	4	Good

The following rating was used in Table 2.4:

1, 2 – more or less far from practical requirements or expectations

3 – acceptable compromise between practical demands and testing capabilities

4, 5 – good or excellent agreement to practical requirements or expectations

The time needed for one test, including preparation, running and data collection, is presented in Table 2.5 for the four different test methods. Time for machining the rail specimen and the contacting wheel needs additional efforts for the tests, and is not included in the table.

SUROS twin-disc testing seems to be the method that is easiest to run, with the lowest overall costs, compared to full-scale roller rig tests, which have expensive specimens to prepare due to machining of profiles.

Table 2.5 Rough estimate of efforts needed for one test.

	Samples & material needed	**Estimated time for test preparation and follow-up (*)**	**Estimated duration of the test (**)**	**Estimated time for measurement and data collection (***)**
Twin disc, SUROS	special test sample, Ø47 mm	1 hour	In function of the test aim: 1 to 6 hours	1 hour
Linear test rig VAS RSP	rail segment, 1500 mm single wheel with new S1002 profile	3 man-day	5 days	2 man-days
Roller test rigs DB, C and A	2 rings of rail material newly profiled wheelset with bearing, new 1002 profiles	3 man-days	1 week	2 man-days
Lucchini test rig BU300	Two rings of rail material newly profiled Wheelset with bearing	3 man-days for standard mounting. Not included the time for the preparation, for example, of a wheelset with a particular devices mounted (i.e. strain gauges)	In function of the test aim: 5 days for a quick evaluation of wheelset behaviour, 6 months or more for the evaluation of wear	In function of the test aim, test duration and data dimension

* Includes all objects needed for performing the test, i.e., the samples to be tested and their counterpart.

** Includes the man-time needed for establishing one test configuration at the rig.

*** Includes the man-time needed for doing measurements, storing and evaluating data, etc. This does not include the time needed for an overall evaluation of all results after a test campaign.

2.5.3 Wear-hardness correlation

The influence of wheel hardness on rail wear rate, and vice versa, is not as widely researched as the influence of rail hardness on its own wear rate. Wheel hardness and rail hardness and their influence on wear are best studied as a system. It is difficult to compare results in the literature from modelling and from track tests and laboratory tests. Each researcher uses a slightly different method to calculate wear, and materials vary too.

Results obtained from research in the past show that there is not a straightforward dependence, because it is influenced by many other factors like contact load, slippage, direction of motion and material microstructure and chemical composition, i.e., interlamellar spacing and carbon content.

Dependence of rail hardness and wear, when wheel hardness is kept constant is shown in Figure 2.24. Both rail and system wear decrease as rail hardness increases (Pointner, 2008). Wheel wear, however, will at first increase for softer rails and, when using harder rails, will remain constant.

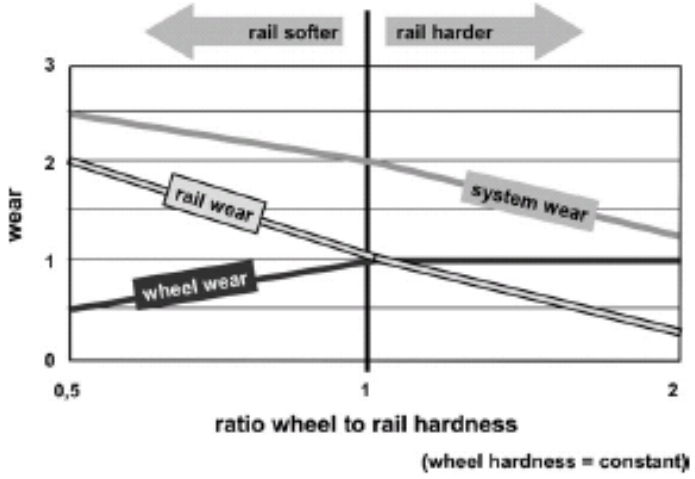

Figure 2.24 Wheel, rail and system wear as a function of rail hardness; wheel hardness is kept constant (Pointner, 2008).

Regarding wear resistance of material, the hardness of steel is closely connected to its microstructure. Research by Lee and Polycarpou (2005) shows that harder bainitic steels (J6) had worse wear performance in traffic than pearlitic steels, in contradiction to Archard's wear law (Archard, 1953; Jendel, 2002). This was connected to work hardening, where pearlitic steels hardened more. Hardness measurements were taken in detail on rail samples taken from new rail, from the low rail of a test track after 50 MGT, and from the high rail after 500 MGT. Cross-section SEM images of rail samples confirm findings from micro hardness Vickers tests, where the plastically deformed

layer of J6 is only 70μm and clearly visible from the undeformed layer, while there is no definite layer formation of distinct plastic deformation in pearlitic rail samples. J6 showed improved RCF in service compared to pearlitic steels, because of the absence of surface and near surface microcracks. As an indication of core hardness of materials, new pearlite rail had 38.52HRC and new J6 bainite had 41.65HRC. Although, this research did not present wheel wear behaviour, it provides good guidance for choosing the optimal rail/wheel material, working in a system, showing that relying on initial material hardness is not reliable for predicting wear rate, but steel work microhardening during operation has to be considered.

Strain-hardening behaviour of pearlitic rail steels was also observed by Tyfour *et al.* (1995). They performed twin-disc tests with W8A wheel material (275HV) for the driving disc, and BS11 rail material (240HV) for the driven disc. Contact pressure was 1500MPa and creepage of -1% in all dry air-cooled tests. Wear rates of both discs, in an experiment run for 40000 cycles, where the test was stopped every 2500 cycles for weight measurements, is shown in Figure 2.25. For the lower number of cycles wheel wear is slightly lower than rail wear and then increases significantly. The strain hardening of the pearlite steel in the rail disc specimen was at the maximum at the contact surface, 2.5 times higher that of the bulk material. It was also noted that most of the hardening is achieved during the first stages of rolling cycles. Wear results of other tests that were run for different number of cycles are shown in Table 2.6.

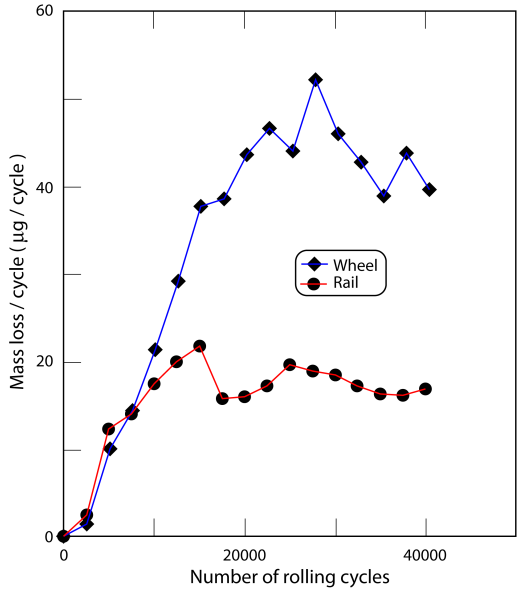

Figure 2.25 A comparison between the wear rates of the rail and wheel test discs for test 130. (Tyfour *et al.*, 1995)

Table 2.6 Wear results from twin-disc testing of R220 by (Tyfour *et al.*, 1995).

Test results

Results	Test number						
	134	136	137	135	138	130	139
Total number of cycles	500	1000	5000	10 000	17 500	40 000	40 000
Coefficient of traction							
Maximum	0.405	0.432	0.441	0.441	0.441	0.441	0.441
End of test	0.405	0.432	0.386	0.322	0.300	0.340	0.268
Contact area (mm^2)	6.11						
Total disc weight loss (g)							
Rail	0.0005	0.0029	0.0348	0.1341	0.2490	0.6520	0.6198
Wheel	0.0005	0.0001	0.0382	0.1694	0.6320	1.3650	1.6732
Total disc diameter loss (mm)							
Rail	NM	0.005	0.005	0.045	0.085	0.200	0.200
Wheel	NM	0.005	0.005	0.030	0.162	0.330	0.400
Total disc track width gain (mm)							
Rail	NM	0.130	0.220	0.385	0.720	1.060	1.145
Wheel	NM	0.080	0.170	0.215	0.485	0.960	0.675
Accumulated shear strain 0.2 mm below the contact surface of rail disc	2.0	2.4	4.3	5.7	11.4	11.4	NM
Total strain hardening 0.2 mm below the contact surface of rail disc (%)	29.2	37.9	69.6	80.8	88.8	88.8	NM
End-of-test surface roughness (rail) R_a (μm)	0.26	0.26	7.3	8.11	NM	NM	NM

NM: value not measured due to the limitation of the measuring equipment.

A series of laboratory twin-disc tests were conducted on Amsler-type testing machines by Markov (1995) with the aim of investigating the influence of wheel-rail hardness on wear rate. Test specimens were discs machined from rail heads and wheel rims, 40 mm in diameter and 6 mm in contact width. To achieve different hardness values, discs were oil quenched and tempered.[1] Test conditions, like contact pressure and slippage, were adjusted to resemble conditions on railway track, and so four test methods were used: rolling-sliding friction with longitudinal slippage, rolling-sliding friction with constant friction force, rolling-sliding friction with lateral slippage, and pure sliding friction. Wear rate (W) was calculated as the difference of disc radius (Δr) per revolution (n):

$$W = \Delta r / n$$

and presented in units of millimetres per revolution. Mass loss measurements were used to correct decrease in radius. Discs were cleaned in ethanol before testing to remove any contamination. Tests were performed with no lubrication (dry).

The first set of tests simulated rolling-sliding friction with constant longitudinal slippage of -10%, with load 700 N so the maximum contact pressure was 650 N/mm^2. The hardness of the rail rollers did not change and was 370 HV_{10} in all experiments, while the hardness of the wheel rollers changed from 250 to 850 HV. Wear rates of wheel and rail discs were calculated after 70000 revolutions. Experiments showed that the wear rate of the rail disc is influenced by the change of hardness of the wheel disc

[1] This kind of heat treatment is very uncommon for wheels. The disadvantage consists in changing the microstructure also in an uncommon way because of producing a quenched and tempered microstructure instead of a fine-pearlitic microstructure. Therefore the results do not represent the practice at all.

and increases when wheel hardness increases, while the wear rate of the wheel disc decreases.

Markov (1995) presented results from tests with constant friction force that were originally conducted by Larin in 1958-1965, in order to simulate locomotive rim wear. The moment of friction force and the friction coefficient were constant and in the first set of tests were: moment 400-450 Ncm, friction coefficient 0.27-0.30, maximum contact pressure 537 N/mm^2, and in the second set of tests moment 300-350 Ncm, friction coefficient 0.19-0.23, maximum contact pressure 619 N/mm^2. Tests were run for 50000 revolutions and wheel and rail roller hardness were varied. Both sets of tests showed that when the hardness of a roller increases, its own wear rate decreases, but its hardness also influences the wear rate of the opposite "counter-roller", which increases. The sum of the wear rates of both rollers was not sensitive to rail or wheel hardness.

Tests with constant lateral slippage of 5% were conducted for 70000 revolutions, with a maximum contact pressure of 950 N/mm^2. The same conclusion can be derived as from previous tests. The wear rate of a roller is related directly to the hardness of the counter-roller, and inversely proportional to its own hardness. The hardness of both discs show only small influence on the total wear rate.

Tests with pure sliding friction were done as simulation of flats on a wheel tread and the process is also similar to side wear at the gauge face of rails. The top rail roller was fixed so slippage was -100%, and the speed of the bottom roller was 100 rev/min. Tests were run for only 300 revolutions under an initial pressure of 600 N/mm^2. It was found that the wear rate of the top rail roller is 10 times higher than of the bottom wheel roller and that the wear rate of the top roller decreased with an increase of the hardness of either disc. In these experiments the influence of the hardness of the rail roller on the wear rate of the bottom wheel roller was negligible, but dependant on its own hardness. As the hardness of the wheel roller increased, its wear rate decreased.

The general conclusion by Markov (1995) is that the relationship between hardness and wear varies with different test conditions. In most of the experiments that were taken, rail wear rate depends on wheel hardness and it gets higher with harder wheels. Slippage has to be considered too. When components work under slippage of less than 5%, wear rate redistributes according to disc hardness but total wear remains almost the same. It is recommended to increase rail/wheel hardness to reduce wear rate if they work under higher slippages.

The effect of varying wheel/rail material hardness on wear behaviour was investigated by Singh and Singh (1993) using laboratory experiments on an Amsler twin-disc machine and a pin-on-disc machine. Rolling-sliding twin-disc Amsler test disc specimens were machined from three types of rail (235HB, 278HB and 322HB) and one wheel (227HB) and were 40 mm in diameter and the contact width was 10mm. The wheel disc was the driving specimen and the rail disc was the driven specimen. Tests were run dry for one hour with 10% slip, under contact pressures of 312 N/mm^2, 492 N/mm^2 and 696 N/mm^2, at two different speeds of 200 and 400 r.p.m. During test runs, wear debris was continuously removed with a woollen cloth. The wear rate was calculated as the ratio of loss of mass of a disc to total rolling distance, in μg/m. Comparing the wear of just the rail disc shows an increase of wear with an increase of rolling speed and contact pressure, and a decrease in wear with an increase of material hardness. In all experiments the wheel disc was wearing more than the rail disc. The wear rate of the wheel disc did not seem to be influenced by rail hardness, and even decreased when the rail hardness increased.

Pin-on-disc tests were used to simulate sliding wear. Two wheel materials were used for the disc, wrought wheel of hardness 227HB and cast wheel of hardness 324HB, and the same rail material as in the twin-disc tests for two pins 8mm in diameter. Pin load was 54, 65, 76 and 87 kg. When the softer rail material (235HB) was tested, its wear increased in all experiments using a harder wheel disc, for example by a factor of 5.75 in the experiment with 54 kg load and by a factor of 2 with 87 kg load. When harder rails were tested (278 and 322HB), their wear increased with wheel hardness only in tests with 54 kg load and 65 kg for rail of 322HB, and decreased in all other tests.

The general conclusion by Singh and Singh (1993) was that wear is dependent on both hardness of wheel and rail and those softer components will wear more. In most cases, increasing the hardness of one component will result in a decrease of wear of both components. Pearlite interlamellar spacing was also discussed in the paper and the relationship with wear was established that less wear will occur with smaller interlamellar spacing, and that relationship is more emphasised in sliding wear.

As part of answering a wider research problem of optimization of wheel and rail profiles Zakharov et al. (2006) did laboratory and field tests to see the influence of wheel-rail hardness on wear. Rolling/lateral sliding laboratory experiments of rail-wheel rollers distinguished three hardness levels for influencing wear. For softer material of less than 250HB, total wear does not depend on an increase of one component's

hardness. Testing harder rollers 250-450HB showed that if one disc's hardness increased, the total wear of wheel-rail rollers decreased. For a hardness level of more than 450HB, increase in hardness of one component reduced total wear dramatically. The experiments showed decrease of wear of the second component as well.

Field tests were in agreement with the laboratory tests for rail to wheel hardness ratio (HR/HW) from 0.7 to 1.6. This wide range of hardness ratios shows that no magic ratio can be found to provide minimal total wear. In general, wear rate of either component is inversely proportional to its hardness.

Rolling-sliding behaviour of rail steels was studied by Sato et al. (1993) using a twin-disc rolling contact test machine. The wheel disc (driven directly by the motor) was driving the rail disc; both discs were constrained to rotate at the same speed by a gear system. Rail material discs were heat treated to give pearlite (280HV, 340HV, and 360HV) and tempered martensite (280HV, 300HV and 360HV) microstructures. Wheel specimens' material was the same in all tests, with a hardness of 360HV. Tests were conducted under unlubricated and lubricated conditions, with 5% slip, load 750 N (maximum elastic contact stress 525 MPa) for 300000 cycles. The steel tested was Japanese Industrial Standard 60 kg for rail discs and 50 kg for wheel discs.

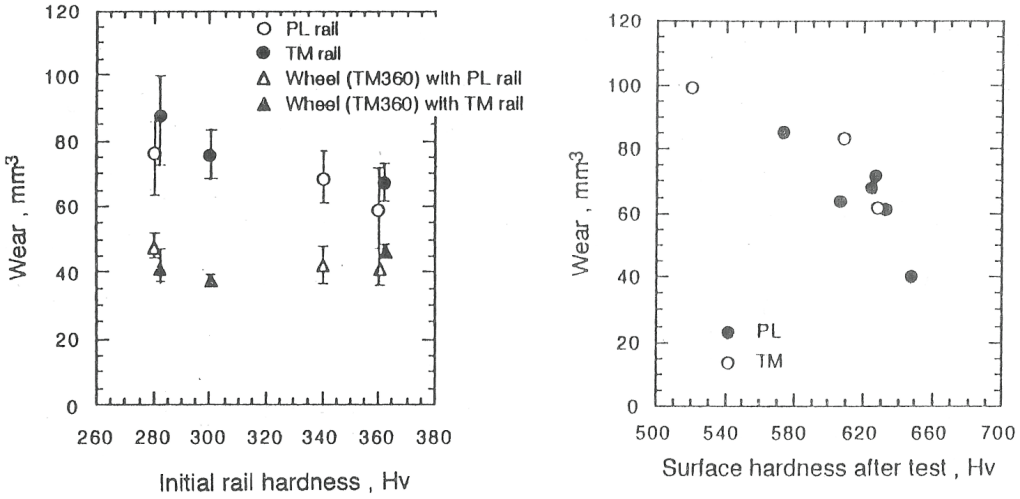

Figure 2.26 Left image: Comparison of wear of rail and wheel specimens for different microstructures and different values of rail hardness. Conditions: 750N, 5% slip, unlubricated. Error bars estimated from spread of two or three data points. Right image: Wear of rail specimens for different microstructures and different values of surface hardness after testing. Conditions: 750N, 5% slip, unlubricated. The trends are similar for the two microstructures. (Sato *et al.*, 1993)

The wear of rail discs decreased as initial hardness increased for both pearlite and martensite materials in unlubricated tests (see Figure 2.26).

The influence of the increase of surface hardness after testing on wear shows an even higher decrease. Wear of the wheel disc was smaller than that of rail discs. The initial rail hardness and microstructure did not influence wheel wear. In tests where water lubrication followed dry tests, the influence of hardness on volume loss was not very different when materials with different hardness were tested.

British Rail Research (Benson, 1993) conducted a literature survey – *Effect of differential hardness on wheel-rail wear*. Their conclusion was that material microstructure has a more significant role on wear than hardness, so laboratory experiments are needed to investigate the optimum hardness ratio for minimum system wear using materials in the same microstructure group. Across different structure groups, pearlite showed better wear resistance than martensite and bainite, when tested at the same hardness values. When investigating pearlitic steels, up to the level of 380HV, increasing rail hardness resulted in decreases in both rail and wheel wear; above this limit, wheel wear slightly increased. This is the opposite of the general belief that using harder rails wears wheels more. Also, some laboratory experiments showed that the optimum rail hardness should be 30% higher than the wheel, for minimum system wear, while track data suggested using the same hardness for both. However, increasing rail hardness of pearlitic steels more than 350HV does not have a significant influence on rail.

Mädler *et al.* (2008) performed a series of twin-disc tests on an Amsler-type rig, investigating the behaviour of 6 rail steels (three pearlitic and three bainitic) and 2 wheel steels. Disc samples had an external diameter of 46mm (both wheel and rail). Surface pressure was 1250N/mm^2, and discs rolled with slip of 3% (with the rail disc running at 450 r.p.m., the wheel disc at 436 r.p.m.). Tests were run wet with water lubrication 1 drop every 20s. Three tests were run for each material pair and the results presented are the average of three separate readings. Material loss of wheel and rail samples is presented in Figure 2.27. When comparing wear rates of wheel steels, using higher-strength B6 material results in lower wear not just for the wheel disc but also for the rail pearlitic steels. Looking at the influence of different rail materials, bainitic steels 1000B and 1100B wear the most and wear of counter wheel disc is slightly higher than when run against the pearlitic rail steels. Higher strength bainitic rail steel 1400B exhibits lower wear especially when run against R7 wheel. Comparing pearlitic rail steel wear against R7 wheel steel, the best wear resistance is with 350HT grade. There is not a clear trend that harder rail materials wear the wheel more. The general

conclusion, when looking at wheel-rail wear as a system, would be to use higher-strength steels for both wheels and rails to get the lowest wear rate of both to maintain profiles longer.

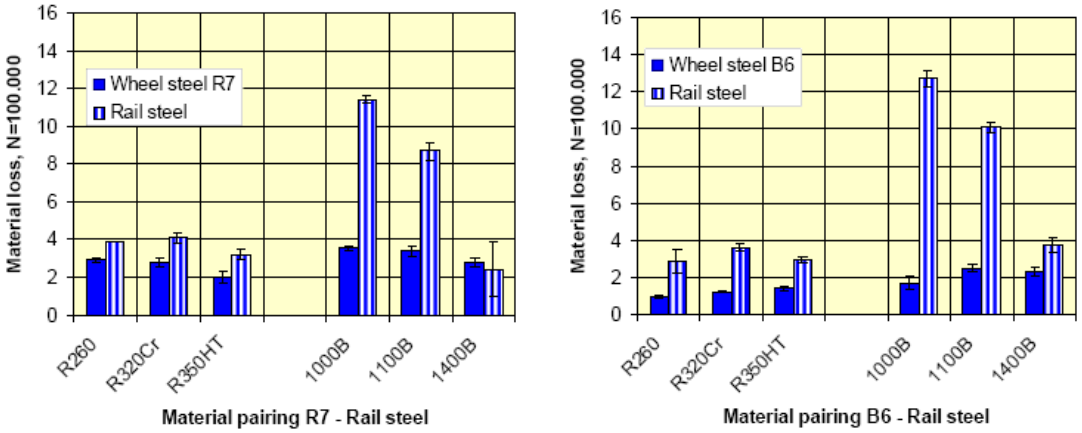

Figure 2.27 Material loss on wheel (R7) and (B6) and rail in Amsler test after 100000 roll-overs (Mädler, 2008)

Summary of wear-hardness correlation

In general, harder materials wear less. However, material hardness is not the only determining factor of wear performance; microstructure and strain-hardening behaviour are critical factors, and rolling contact fatigue performance is equally important. Regarding the influence of rail hardness on wheel wear, and vice versa, here are some key observations:

- **Pointner:** System wear (i.e., considering both wheel and rail) reduces as rail hardness increases – harder rails wear wheels more, but only up to a point, and wear less themselves.
- **Markov:** Increasing wheel hardness decreases wheel wear and increases rail wear. In general, the relationship between hardness and wear varies with different test conditions. In most of the experiments that were taken, rail wear rate depends on wheel hardness and it gets higher with harder wheels. When slip is less than 5%, wear rate redistributes according to disc hardness but total wear remains almost the same.
- **Singh and Singh:** In all experiments wheel disc wear was higher than rail disc wear. The wear rate of the wheel disc did not seem to be influenced by rail hardness, and even decreased when the rail hardness increased. In most cases, increasing the hardness of one component will result in a decrease of wear of

both components. Regarding sliding wear of pearlitic steel, less wear will occur with smaller interlamellar spacing.

- **Zhakarov et al.:** For softer material of less than 250HB, total wear does not depend on an increase of one component's hardness. Testing harder rollers 250-450HB showed that if one disc's hardness increased, the total wear of wheel-rail rollers decreased. For a hardness level of more than 450HB, an increase in hardness of one component reduced total wear dramatically. The experiments showed decrease of wear of the second component as well.
- **Sato et al.:** There is a clear correlation with rail wear decreasing as rail surface hardness following the test increases, regardless of initial hardness or microstructure. Wheel wear is not sensitive to the rail's initial hardness or microstructure.
- **Benson (BRR):** For pearlitic steels up to the level of 380HV, increasing rail hardness decreased both rail and wheel wear; above this limit, wheel wear increased slightly. Some laboratory experiments showed that the optimum rail hardness, for minimum system wear, is 30% higher than the wheel hardness, while track data suggest using the same hardness for both. However, increasing rail hardness of pearlitic steels more than 350HV does not have significant influence on rail wear.
- **Mädler et al.:** There is not a clear trend that harder rail materials wear the wheel more. The general conclusion, when looking at wheel-rail wear as a system, would be to use higher-strength steels for both wheels and rails to get the lowest wear rate of both to maintain profiles longer.

2.6 Simulation models for wheel-rail contact and wear and RCF

The aim of railways is always to reduce the LCC of the system while maintaining safety and reliability. To help that, and to further research in this area, numerous models have been created, but a huge number still remain available to small research groups at universities. One of the outputs of the InnoTrack project was to analyse capabilities of models, including those simulating dynamic train behaviour and wear and RCF. There has been a public database[2] created with over 230 models. Presented here is a

[2] http://www.innotrackdataentry.co.uk/DefaultQuestions.aspx

comparison and short description of a few models, some of which can also be found in the database.

2.6.1 Comparative review of wear and RCF models

Assessment of several whole life, wear and RCF models was done by infrastructure managers; how well they answer certain problems has been presented by Amoore (2007), see Table 2.7.

One of the theoretical approaches to modelling wear and RCF in rails is to use the T-gamma (Tγ) method – the 'wear number', explained in Section §2.1.2. By correlating predicted wear numbers (based on vehicle dynamics simulations) with field observations of wear and RCF, an empirical formula has been developed by Evans and Burstow (2006) for the UK rail network where R220 grade pearlitic rail steel is prevalent. For high values of the wear number (more than 170N) wear is the dominant damage mechanism, whereas RCF is dominant for wear numbers from 170N down to 20N. However, the formula does not necessarily translate to other rail networks where different rail and wheel materials and wheel-rail geometries are in use. Changes in wear behaviour can, to some extent, be predicted for different steel grades (Clayton, 1996) but crack initiation is very sensitive to microstructural properties, so RCF prediction is complicated.

Traffic simulation is possible by several methods and models, but this is not widely published. Enblom and Berg (2008) simulated traffic using a numerical wear model based on Archard's tribological model and compared results with site measurements; the predicted wear rates, relative to MGT of traffic, were higher than the measured wear rates, but the main trends could be seen. However, such wear modelling does not indicate severity of crack initiation and growth.

Track-Ex is a powerful tool (based again on the Tγ energy concept) which allows RCF and wear predictions to be generated quickly for large track mileages, and the effectiveness of maintenance measures to be tested. Track-Ex is supported by geometry measurements from recording cars, it has a vehicle database and it is able to simulate traffic. This is not a high precision tool but is fast and considered good for general predictions. Sweden has a similar tool called DeCoTrack.

There are many software tools for predicting the RCF of wheels, e.g., (Ekberg *et al.*, 2002; Ekberg and Kabo, 2005), and RCF and wear for wheels, e.g., (Dirks and Enblom, 2011).

Table 2.7 List of RCF and wear models and tools, problems that they are simulating, and 'resolution' indicating whether they apply across the whole system or are case-specific. After (Amoore, 2007).

Organisation (Owner of the model)	**Model Name**	**Resolution[1)]**	**Infrastructure Problem**
NewRail (Newcastle University)	Crack Growth	H	RCF
	'Dynarat'	H	Rail Wear
	Grinding	H*	Grinding
Corus	Critical defect size model (head, web, foot)	L	RCF
	SafeRail – crack initiation	L	RCF
Banverket	DeCAys (whole system model)	M	Poor track geometry
		M	Optimisation renewals
		M	Ballast wear
	Rail surface damage model	H*	Rail surface damage
Chalmers	IRID / FE[2)]	H	Stress/strain, plasticity (RCF)
	DIFF(3D)	H	Forces and contact patch, Corrugation
	FIERCE	H	RCF
RSSB	VTISM (whole system model)	M/H	Poor track geometry
		L/H	Wear in S & C[3)]
		L/H	Optimisation renewals
		L/H	Ballast wear
		L/H	S & C geometry
	WLRM	H	RCF
Network Rail	Track-Ex	M	RCF
Damill	DeCoTrack (whole system model)	L	Poor track geometry
		L	Optimisation renewals
		L	Ballast wear
MMU	VAMPIRE, Adams Rail	H	Low adhesion
	RoutEx	H	RCF
	Track System Model	H	Unstable substructure

[1)] **Resolution** National infrastructure managers had categorised models according to how well they matched to problems, as high (H), medium (M) or low (L) resolution.
- L: Based upon general findings - Easy to use - General trends - Global
- M: Based on general findings of high resolution models - Requires general technical competency - Medium accuracy - Good for parametric studies
- H: Require fine grain inputs - Require technical expertise - Provide high accuracy - Tend to be site specific - Good for identifying causal factors

[2)] **FE** – Finite Element

[3)] **S&C -** Switches and Crossings

[*] Not evaluated by infrastructure managers

VAMPIRE[3] is a well-known commercial multi-body dynamic simulation tool used for modelling and analysis of railway vehicle dynamic behaviour. Numerous papers were published about or modelling with VAMPIRE, e.g., (RSSB, 2003; RSSB, 2008; Evans, 2006; Burstow and Robinson, 2007; Sun *et al*., 2011).

Xie and Iwnicki (2008a and 2008b) used a time-domain wheel–track vertical interaction model integrated with a three dimensional wheel–rail contact model to simulate railhead wear.

Finite element models are also used for simulations of repeated sliding contacts between wheel and rail and wear (Lee and Polycarpou, 2011). Several other numerical models are described in (Rovira et al., 2011; Markov, 1995; Deters and Proksch, 2005; Zhong et al., 2011).

The Dynarat model is a computer simulation of plastic ratcheting, i.e., subsurface accumulation of plastic shear deformation, used to predict both wear and crack initiation simultaneously, and thus wear-fatigue interaction is modelled automatically; the simulation allows microstructural details of the rail steel to be simulated. For understanding material behaviour of new harder steels and predicting their wear rates, the Dynarat model is developed further in this thesis.

2.6.2 Ratcheting wear simulation – Dynarat model

The 'Dynarat' model (also known as the 'brick' model) was developed initially as a computer simulation of ratcheting wear, based on ratcheting principles outlined by (Kapoor, 1994), and confirmed experimentally by (Tyfour *et al.*, 1996).

The wear simulation was introduced by Kapoor and Franklin (2000), and then developed into a 2D simulation with elements (or 'bricks') which could be given different material properties to better reflect variability of material properties within pearlitic rail steel microstructure (Franklin *et al.*, 2001; Franklin *et al.*, 2003). In related work, the effect of surface micro-roughness (even on a polished surface) on ratcheting of near-surface material, i.e., within about 50μm of the surface, shows the importance of considering this effect when modelling wear (Kapoor *et al.*, 2002a).

This simulation was first used to look at crack initiation by Fletcher *et al.* (2003) who used image analysis to identify patterns of failed material elements, and subsequent

[3] http://www.vampire-dynamics.com

research has focussed on improving the model's ability to predict life to crack initiation (Franklin and Kapoor, 2007).

An important aspect of the model is its ability to represent rail steel microstructure and (Franklin and Kapoor, 2007; Garnham *et al.*, 2007) have provided detailed metallurgical data to improve the microstructural model. This research is based on careful analysis of twin-disc tests using samples machined from R220 rail sections, but extending the model's capabilities to predict rail life for other grades of rail steel has been discussed by Franklin *et al.* (2008). The inclusion of thermal effects in a similar ratcheting model has been explored by (Fletcher *et al.*, 2008; Widiyarta *et al.*, 2008; Widiyarta, 2010).

The Dynarat computer simulation has been used in collaboration with industry to calculate wear rates and crack initiation depths for a selection of vehicle cases for sites in the U.K., and also for different rail steel grades – see RSSB Project T355 (RSSB, 2008). The simulation has also been adapted for Health & Safety Laboratory (HSL) to study the life of rails with a decarburized surface layer (Fletcher *et al.*, 2006).

Basic Mechanism

In the Dynarat simulation, the wearing material is modelled as a mesh of elements (or 'bricks') that lie in a plane (i.e., a cross-section through the rail) parallel to the direction of traction (see Figure 2.28 and Figure 2.29). The rectangular mesh elements have equal size ($dx \times dz$), where x is the direction applied traction and z is into the material. In order to model variation of material properties at a microscopic level, each element is given individual material properties, such as initial shear yield stress (k_0) and critical plastic shear strain for failure (γ_c). ($\gamma_c = 11.5$ was estimated for R220 rail steel by Tyfour *et al.* (1995).

The width and depth of the simulated area are $Nx \times dx$ and $Nz \times dz$ respectively. For each load cycle, for each element ij in column i (i=1, …, Nx) and in row j (j=1, …, Nz), the model calculates the effective shear yield stress (k_{eff}) based on the current accumulated plastic shear strain (γ):

$$k_{eff}^{ij} = k_0 \max\left\{1, \beta\sqrt{1 - e^{-\alpha\gamma^{ij}}}\right\} \tag{2.29}$$

The constants α and β are material parameters; α is a measure of how quickly the material hardens, and β is a measure of how much it hardens. The increment of plastic shear strain ($\Delta\gamma$) is calculated using the current effective shear yield stress:

$$\Delta\gamma^{ij} = C\left[\left(\frac{\tau^{j}_{zx(\max)}}{k^{ij}_{\text{eff}}}\right) - 1\right] \tag{2.30}$$

where $\tau^{j}_{zx(\max)}$ is the maximum orthogonal shear stress occurring at the depth of row j, and C is a constant, estimated as 0.00237 for R220 rail steel by (Tyfour *et al.*, 1996).

Maximum orthogonal shear stress $\tau^{j}_{zx(\max)}$ is evaluated in the computer simulation as elastic, using the method outlined by the ESDU 78035 and ESDU 84017 (1984). If there is any plasticity, this is assumed to be very small and that calculation of stresses is a good approximation.

Finally, the new value of accumulated plastic shear strain is then calculated by adding the plastic shear strain increment:

$$\gamma^{ij} = \gamma^{ij} + \Delta\gamma^{ij} \tag{2.31}$$

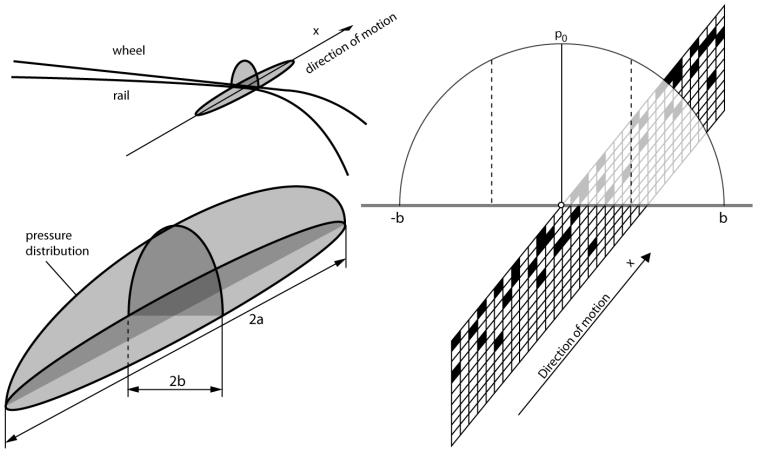

Figure 2.28 The rail/wheel contact patch can be approximated as elliptic. Here the plane of the simulation includes the centre-line of the contact; a transverse offset can be specified. After (Franklin and Kapoor, 2006).

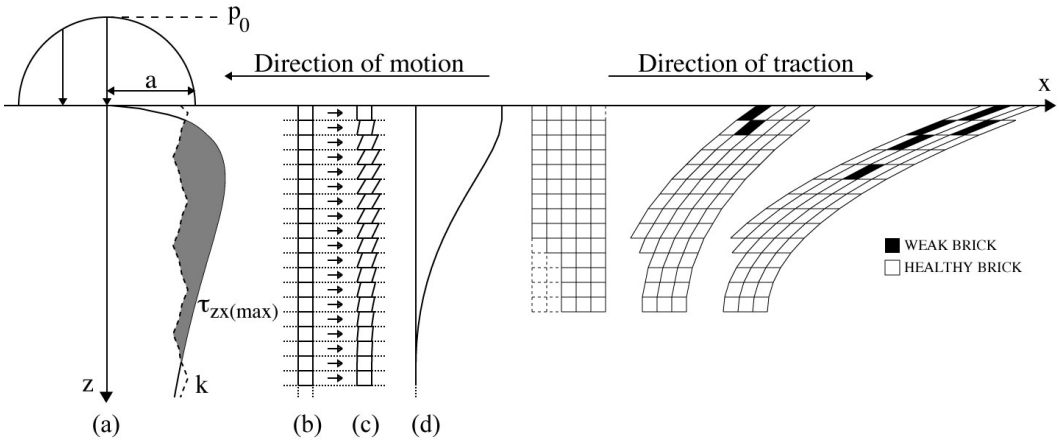

Figure 2.29 Each element (or 'brick') accumulates shear strain according to the current applied shear stress, $\tau_{zx(max)}$, and its effective shear yield stress, k_{eff}. Left: (a) Variation of shear stress with depth for a low coefficient of friction ($\mu<0.33$). The shaded region indicates where the shear stress exceeds the initial shear yield stress k, which varies from element to element. (b) and (c) Plastic flow occurs and there is an increment in plastic shear strain per cycle. (d) Material displacement per cycle as a result of the strain increment. Right: Elements are increasingly strained until failure occurs. After (Franklin and Kapoor, 2007).

The material is considered as 'failed' if the accumulated plastic shear strain exceeds the value for critical plastic shear strain for failure (γ_c). Because the shear yield stress varies between elements, each element accumulates shear strain at a different rate, independently from others.

Failed material is considered to be 'weak', i.e., unable to support tensile stresses and a potential site of crack initiation. Material at the surface which fails can be removed as wear debris, and thus the wear rate over time can be predicted. In the simulation, an element can be removed from the surface as wear debris depending on the surrounding material. In each load cycle, 3×3 groups of elements at the surface are compared with the heuristics shown in Figure 2.30, and if there is a match then there is a probability (p, dependent on thickness dz) that the central element is removed as wear. When all the elements in the top layer have been removed, all the layers move up and a new layer of elements is added to the bottom of the simulation with new properties and zero initial plastic strain.

Also, by examining elements which fail subsurface, the simulation can estimate the number of load cycles until the initiation of a 'significant' crack, i.e., a crack which is sufficiently long that further growth will be driven by the contact stresses rather than plastic strain accumulation (although crack growth may be accelerated by further plastic strain accumulation).

One approach used for predicting crack initiation depth is percentage 'damage depth'. The simulation calculates the maximum depth at which, for example, 10% of the elements at that depth have failed, which suggests that crack initiation to that depth is likely to happen. Damage depth prediction depends on how microstructure is modelled, see (Franklin and Kapoor, 2006), and is useful for comparing material response to different contact conditions.

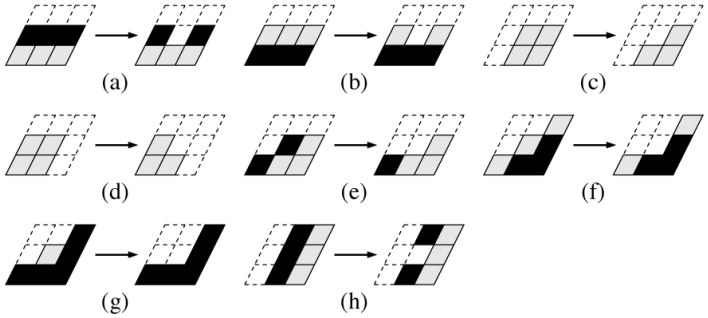

Figure 2.30 Block patterns of 3×3 elements which determine whether the central element may be removed as wear debris. 'Elements can be healthy, weak or non-existent. The grey elements in this figure are non-specific; they can have any of the three states. The black elements are weak. The uncoloured elements are non-existent, i.e., they have been removed as wear debris. (g), therefore, is a subset of (f), but different probabilities may be assigned to the two cases. These heuristics were chosen with a constant direction of shear in mind.'

Microstructure

To create a representation of rail steel microstructural in the simulation, elements are defined as pro-eutectoid ferrite (at the prior-austenite grain boundaries) or as 'pearlite' (a composite structure of ferrite and cementite). Figure 2.31a shows a 256×256 pixel two-colour image which is used as an input to the model. Each pixel represents a 1μm×1μm element of the material. The two colours represent two different materials, in this case the darker grey is pro-eutectoid ferrite and the lighter grey is 'pearlite'; to model the two constituent elements of pearlite separately would require a very fine mesh, so instead the pearlite is treated as a single material.

A sample image from a rail section is given in Figure 2.31b, in which the prior-austenite grain boundary can be seen clearly.

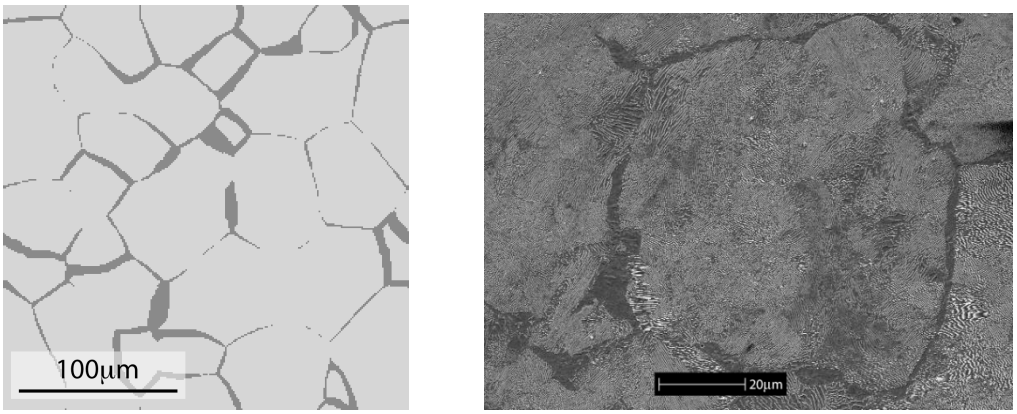

(a) (b)

Figure 2.31 Comparison of real and simulated pearlitic rail steel microstructure: (a) Input microstructure: 256×256 pixels, each pixel determines a 1μm×1μm element in the simulation model; the colour of the pixel determines the 'material' selected for the element (light grey for 'pearlite', dark grey for ferrite). (b) Real material microstructure: Scanning electron microscope image of a cross-section through a rail sample from Harringay.

(Franklin and Kapoor, 2007; Garnham *et al.*, 2007) used nanohardness measurements to estimate material properties of 'pearlite' and ferrite, based on a series of twin-disc tests with R220 rail steel specimens. Ferrite has a nano-hardness of 250kgf/mm^2, and hardening ratio (i.e., ratio of final to initial hardness) β=1.48. Pearlite has a nano-hardness of 370kgf/mm^2, and hardening ratio β=1.55. In both cases α=1 – see Equation (2.29). The initial shear yield stress, k_0, is related to the nano-hardness, H_n, by:

$$k_0 \approx 0.8 \times 10^6 H_n \tag{2.32}$$

The standard deviations of the initial hardness and critical shear strain are 15% and 5% of their respective means.

Roughness

In Dynarat, when modelling rail wear, for example, the rail roughness does not influence the stresses directly. Stresses near the surface can be amplified according to how much material has been removed, so any isolated remaining elements forming asperities on the rail surface will experience magnified stresses; but these asperities will not influence the stresses in the material below. The influence of roughness of the counterface, i.e., the wheel in this case, can be included by magnifying the stresses at each depth (Franklin and Kapoor, 2007). This magnification increases rail stresses only very close to the rail surface, i.e., within about fifty microns (see Kapoor *et al.*, 2002a).

2.7 Summary

Literature presented in this chapter covered basics about wheel-rail contact and rail materials. Material degradation – and wear, crack initiation and mechanisms that drive this – were explained too. Material testing in the field and in the laboratory, and modelling tools, have been presented.

One gap in rail material analysis is that new materials still have to be tested to determine how they behave under cyclic loading, and to determine the relationship between hardness and strain, in order to be able to predict wear and crack initiation.

Dynarat's past development has focussed on BS11 (R220) steel, but R260 and premium grade steels are much more commonly selected for new rail, so new material models are required for Dynarat to have the ability to predict wear and crack initiation for new rail materials. Also, the 3D contact model is limited to elliptical contact without proper partial slip, and this needs to be improved.

These gaps in new rail materials testing and analysis, as well as the need for improvement in the Dynarat model will be addressed in this thesis.

Chapter 3 Twin-Disc Tests

3.1 Introduction

New rail and wheel materials have to be tested in laboratories before they go into field trials and mass production. There are various tests needed, one of which is testing the material behaviour under cyclic loading that simulates the rolling of wheels over rails. This chapter presents the SUROS machine twin-disc testing of R260 rail steel, which has widespread use in Europe and increasingly in the UK, and four premium grade pearlitic rail steels. These discs were machined from sections of rail, and run against discs machined from wheels. R7 wheel steel was used for most tests; R8T wheel steel was used for one test condition. In this chapter, test equipment, procedure and samples will be presented along with test measurements: wear data, traction coefficients throughout tests, and roughness measurements of disc surfaces before and after tests.

Samples were machined from the rail head and wheel rim and run against each other for a specified number of cycles. In all cases, the peak pressure was 1500MPa and a driving wheel was simulated with -1% slip. 'Dry' tests were air-cooled, and 'wet' tests were water-lubricated. A total of 25 twin-disc tests were performed (five rail steels; five test conditions) and full data for each test and images of disc surfaces after the test are presented in Appendix A. Metallurgical analysis will be presented in Chapter 4. Results of wear, traction coefficients and metallurgical analysis are used for development, calibration and validation of new Dynarat material models in Chapter 5.

A subset of the data and metallurgical analysis for these SUROS tests has been published in several reports for the EU FP6 Project 'InnoTrack' (primarily Deliverable D4.2.5). Twin-disc tests on the SUROS machine were done by Dr David Fletcher and Dr Francis Franklin, with the assistance of the late Dr Mike Frolish. All subsequent analysis presented here was done by the author. The aims of this thesis were chosen both to complement the work in InnoTrack D4.2.5 (the new 3D partial slip model was developed for this thesis prior to its use in D4.2.5) and to extend the metallurgical analysis and wear model development.

3.2 Sheffield University Rolling-Sliding (SUROS) test machine

Processes that take place during wheel and rail motion are complex, so it is useful to study them in controlled laboratory conditions. The SUROS twin-disc test machine is designed to simulate this rail/wheel contact, with fair representation of the contact

pressure, creepage and environment to which rail and wheel materials are subjected. (However, the conditions used in these tests represent a particularly severe contact, with higher pressure and slip ratio than normally seen.) It has been used extensively for research of material rolling contact fatigue (RCF), wear, early detection of cracks and friction. This kind of twin-disc testing is also cheaper and faster than track trials.

Operation and characteristics of the machine are described in detail by (D.I. Fletcher and Beynon, 2000a). A photograph of the SUROS machine is shown in Figure 3.1 and a schematic representation is given in Figure 3.2. Test conditions are closely controlled and monitored.

Figure 3.1 Photograph of the SUROS test machine.

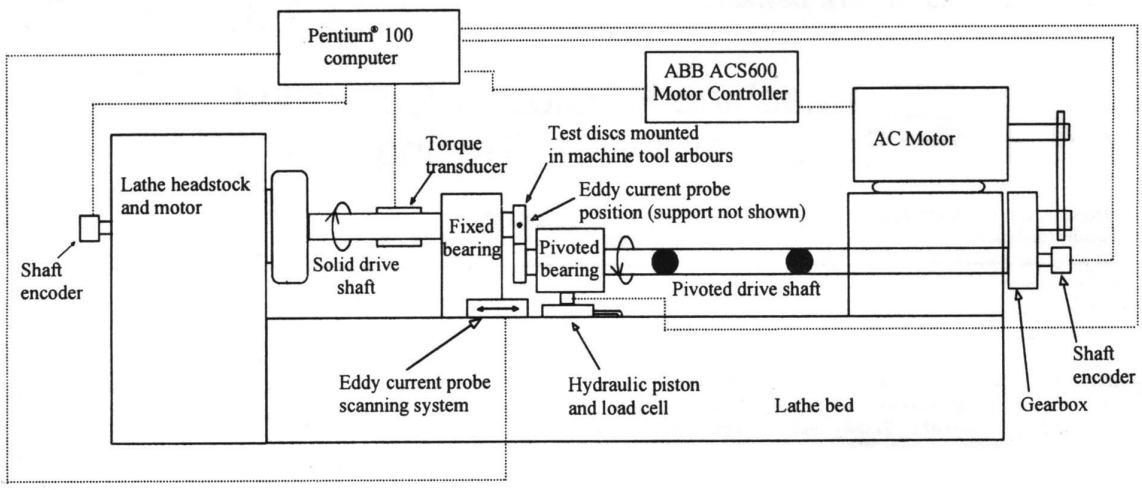

Figure 3.2 Schematic representation of SUROS twin-disc machine (D.I. Fletcher and Beynon, 2000a).

The machine is based on a Colchester Mascott 1600 lathe, which was modified for use as a test rig. The rail and wheel specimen discs are mounted on the machine one above the other with their axes horizontal and parallel. The rail material disc (braking disc –

top) is mounted at the end of the lathe arbour, so it is driven by the lathe motor through its gearbox. The wheel disc (driving disc – bottom) is driven by a separate 7kW AC motor mounted at the tailstock end of the machine bed.

Normal loads up to 29kN can be applied to the discs by a hydraulic system. Load is controlled manually and it is measured directly by a load cell fitted in line with the hydraulic loading piston, below the pivoted bearing housing.

Shaft encoders are fitted to the machine directly in line with the drive shafts and are used for monitoring disc speed and revolution. Shaft encoders give 2500 output pulses per revolution for accurate determination of shaft speed even at low speed. The slip ratio can therefore be controlled precisely and it is achieved by adjusting the rotational speed of the shaft connected to the AC motor.

The torque of the top disc drive shaft is measured by a torque transducer, which is mounted in the mid-section of the upper shaft and connected to the computer using an amplifier identical to that used with the load cell. The torque is induced by the rolling – sliding contact of the discs, i.e., caused by their different rotational speeds. The measurement of the torque and normal load enables the calculation of the traction (adhesion) coefficient.

The test rig has a calibrated eddy current unit, which is used for the early detection of cracks. The unit has a probe that moves across the specimen surface throughout tests, detecting cracks at any location. The computer controls the position of the probe and readings can be seen on the oscilloscope.

The speed of the AC motor is computer-controlled over a range of 0 to 1600 r.p.m. The computer also collects and processes data from the shaft encoder (rotation speed), torque transducer (torque) and load cell (load).

3.3 Material and disc specimens

The increased traffic and load on railways demands improved materials that will withstand the increase of stresses that lead to wear and cracking. These days, most rail steels used are pearlitic, with different hardness levels. Microstructure characteristics have an important influence on wear and RCF. The standard names of the materials tested here, and the codes (i.e., short names) used to identify them in the thesis are given in Table 3.1.

Data of the Corus rail materials and VAS wheel material tested are presented in Table 3.2 and Table 3.3. General information about European rail steel chemical composition and mechanical properties (from European standard EN 13674-1:2011) is given in Appendix E.

Table 3.1 Material names and codes

	Code according to EU standard	**Supplier**	**Code in Thesis**
rail	R260	Corus	**P260**
	R350HT	Corus	**C350**
	R370CrHT (a.k.a. MHH400)	Corus	**C400**
	R350HT	Voestalpine Schienen	**V350**
	R400HT	Voestalpine Schienen	**V400**
wheel	ER7 (supplied as R7)	Given by Voestalpine Schienen (Origin unknown)	**R7**
	ER8 (supplied as R8T)	Given by Voestalpine Schienen (Origin unknown)	**R8T**

Test specimens were cut from the rail head and wheel rim as shown in Figure 3.3a to the dimensions shown in Figure 3.3b. A photograph of a disc specimen is shown in Figure 3.4. Both wheel and rail discs have the diameter (47mm), which is the maximum diameter obtainable from the rail head, and track width (10mm), i.e., the width of the disc running surface. All machining and cutting operations were conducted to maintain the original microstructure and properties.

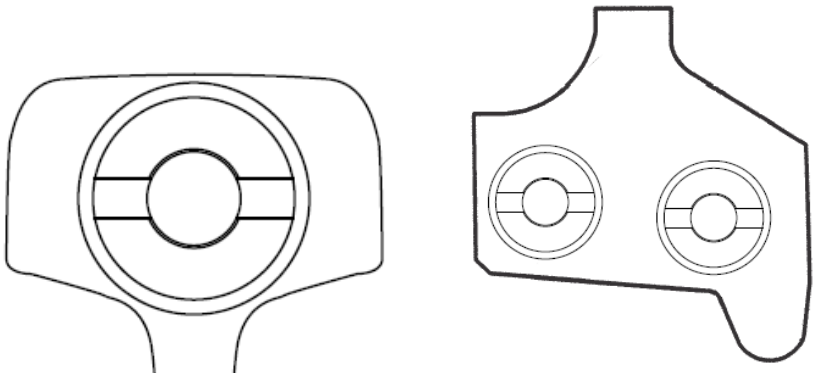

(a)

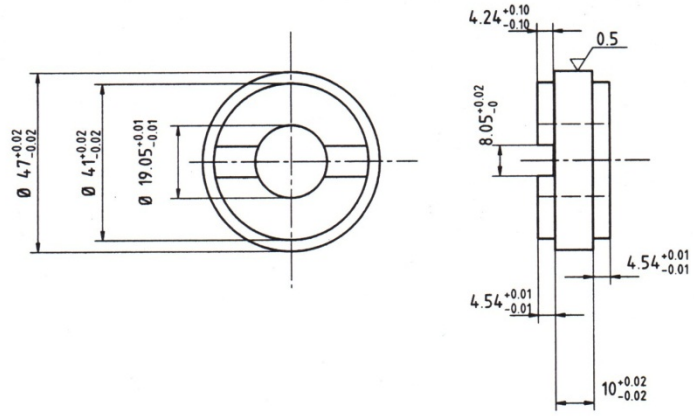

(b)

Figure 3.3 (a) Typical original locations of test specimens in cross-sections of wheel and rail (personal communication from David Fletcher); (b) SUROS test specimen dimensions [in mm] (after Fletcher and Beynon, 2000a).

Figure 3.4 Photograph of a test disc sample, dimension Ø47mm.

Table 3.2 Material chemical analysis data (courtesy of Rob Carroll).

	7TR19	7TR35	8TR76	8TR78	
Manufacturer	**Corus MSM**	**Corus HY**	**Corus HY**	/	/
Grade	**260**	**MHH400**	**350HT**	**R7 Wheel**	**R8T Wheel**
C	0.76	0.78	0.79	0.51	0.53
Si	0.26	0.62	0.43	0.34	0.31
Mn	1.03	0.91	1.13	0.74	0.83
P	0.015	0.016	0.012	0.011	0.019
S	0.02	0.014	0.019	0.006	0.010
Cr	0.02	0.51	0.02	0.24	0.25
Mo	0.005	0.005	0.005	0.005	<0.02
Ni	0.02	0.03	0.02	0.02	0.05
Cu	0.01	<.01	0.01	0.05	
Sn	<.005	<.005	<.005	<.005	
Al	0.004	0.003	0.003	0.028	
As	<.005	<.005	<.005	0.005	
B	0.0005	<.0005	<.0005	<.0005	
Ca	<.0005	<.0005	<.0005	0.001	
Co	0.004	0.005	0.004	0.003	
N	0.0046	0.005	0.005	0.005	
Nb	0.001	0.001	0.001	0.001	
Sb	0.0005	0.0005	0.0005	0.001	
Ti	0.0003	0.012	0.0004	0.0017	
V	0.001	0.002	0.001	0.001	<0.01
W	0.001	0.001	0.001	0.001	

Note: Grade R8T wheel steel is according to standard BS5892-3, which is equivalent to EN13262 ER8, with hardness HV 257.
Wheel materials R7 and R8T are supplied by VAS, but manufacturer is unknown.

Table 3.3 Grade comparison (courtesy of Rob Carroll).

	UTS(MPa)	0.2% Proof (MPa)	Elongation(%)	Running surface Hardness Brinell
260	962	514	11	277
	983	580	10	276
	966	535	10	271
	980	521	12	293
	977	521	11	267
400MHH	1315		13	388
	1296		13	394
	1335		12.2	401
	1341		12.2	401
	1347		12.4	398
	1357		12.2	398
R350HT	1210	763	12	360

3.4 Test procedure and conditions

All discs used for testing were engraved with an identification code (see Table 3.4), examined for surface defects and checked for dimensional accuracy. Discs were then cleaned and degreased in a beaker of methanol placed in ultrasonic bath, to ensure that there were no contaminants.

The wheel disc (aligned vertically below the rail disc) was connected to the drive shaft of the A/C motor and acted as the driving disc while the rail disc was driven. The test discs were loaded by force 7.16kN, to achieve a peak contact pressure of 1500MPa. This resulted in a contact patch of dimensions 10mm (i.e., the track width) by approximately 0.7mm. The rail disc was set to rotate at the lathe setting of 400 r.p.m. and the wheel disc rotation was controlled to give a constant slip ratio of –1%.

Weather conditions that can be experienced on track were simulated in the laboratory. Discs were submitted to either dry and/or wet conditions. For the dry tests the discs were air-cooled. The air compressor was switched on, and the air jet directed at the contact between the top and bottom discs. For simulating wet conditions distilled water was applied in the form of drops, onto the top of rail disc at a rate of 1 drop per second.

Temperature and air humidity were measured before and after each test run.

All data including number of cycles, torque, load and coefficient of traction were automatically collected and processed by the computer. The test parameters and traction graph were monitored during the test on the computer screen.

The following is the summary of the twin-disc tests performed:

- Five different rail materials (P260, C350, C400, V350 and V400) and 2 wheel materials (R7 and R8T) were tested.
- For each of the five selected rail steels, five twin-disc tests were performed (i.e., a total of twenty five tests):

  1. 5000 cycles dry (i.e., without water or other lubrication).
  2. 5000 cycles dry, followed by 5000 cycles wet (with water lubrication).
  3. 15000 cycles dry.
  4. 20000 cycles wet.
  5. 15000 cycles dry (with different wheel material disc R8T).

For each test description, see Table 3.4.

The choice to run discs 5000 cycles dry before running wet was because it was expected that these harder materials would develop initial cracks after a longer number of cycles than what was experienced with R220 steel. Longer tests of 15000 cycles were chosen because it was assumed to achieve a steady state wear rate. Just running wet would result in least deterioration, which is why this test is run for the longest number of cycles.

- Tests were performed at contact pressure 1500MPa and slip -1% (to simulate a driving wheel), conditions which have been used extensively with the SUROS machine in the past.

Table 3.4 Summary table of test and disc codes.

Test name	Rail disc id	Wheel disc id	Material type	Test cycles
INNOT-01	INR1	INW1	C400	5000 dry
INNOT-02	INR2	INW2	C400	5000 dry + 5000 wet
INNOT-03	INR3	INW3	C400	15000 dry
INNOT-04	INR10	INW4	V350	5000 dry
INNOT-05	INR11	INW5	V350	5000 dry + 5000 wet
INNOT-06	INR12	INW6	V350	15000 dry
INNOT-07	INR24	INW14	P260	5000 dry
INNOT-08	INR23	INW13	P260	5000 dry + 5000 wet
INNOT-09	INR22	INW9	P260	15000 dry
INNOT-10	VA400(1)	INW7	V400	5000 dry
INNOT-11	VA400(2)	INW8	V400	15000 dry
INNOT-12	VA400(3)	INW12	V400	5000 dry + 5000 wet
INNOT-13	INR30	INW21	C350	5000 dry
INNOT-14/41	INR31	INW16	C350	5000 dry + 5000 wet
INNOT-51	INR34	INW20	C350	15000 dry
INNOT-16	INR36	INW17	C350	20000 wet
INNOT-17	INR26	INW10	P260	20000 wet
INNOT-18	INR7	INW15	C400	20000 wet
INNOT-19	INR40	INW23	V400	20000 wet
INNOT-21	INR16	INW24	V350	20000 wet
INNOT-22	INR25	WB35 (R8T)	P260	15000 dry
INNOT-23	INR33	WB47 (R8T)	C350	15000 dry
INNOT-24	INR4	WB46 (R8T)	C400	15000 dry
INNOT-25	INR14	WB37 (R8T)	V350	15000 dry
INNOT-26	INR41	WB45 (R8T)	V400	15000 dry

Note: Most wheel discs were R7 material. It is stated in table when material was different (R8T).

3.5 Wear data

Discs were weighed before and after each test run. Prior to measurement, discs were cleaned in an ultrasonic bath with methanol and then air-dried.

Wear rate was calculated as mass loss per cycle and this then converted to thickness of material removed (i.e., reduction of radius) per cycle.

Wear rates for rail and wheel discs for each test are given in Table 3.5 and Table 3.6.

Images of disc surface are given in Appendix A. An example of how much surface deteriorates is given in Figure 3.5.

Observations of material surface deformation from images of 25 rail and 25 wheel samples are summarised in Table 3.7. For all discs that had damage, it runs in the same direction around the circumference, so that when a finger is run across the surface, in one direction it feels smooth, and in the opposite direction it feels rough. The same start of the cracks appears in service and is connected to the direction of motion / traction (see Section §1.1.2).

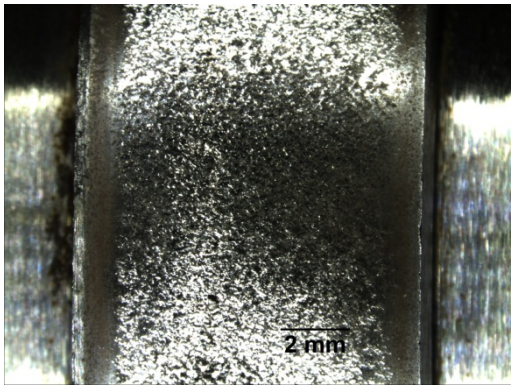

Figure 3.5 Surface image of (rail) disc INR31. C350, after 5000 dry + 5000 wet.

Table 3.5 Summary of rail disc wear rates in SUROS twin-disc tests.

Rail Disc		Steel Density	7.95	[g/cm3]						
		Track Width	10	[mm]						
Test	**Description**	**Material**	**Lubrication**	[mm] **Diameter**	**#Cycles**	[g] **Original Mass**	[g] **Final Mass**	[g] **Mass Loss**	[µg/cycle] **Wear Rate**	[nm/cycle] **Wear Rate**
INNOT-07	C260-5k	P260	Dry	46.98	5014	180.5581	180.5271	0.031	6.183	0.527
INNOT-08 a	C260-10kDry	P260	Dry	46.97	5014	180.7453	180.7166	0.0287	5.724	0.488
INNOT-08 b	C260-10kWet	P260	Wet	46.97	5010	180.7166	180.4612	0.2554	50.978	4.346
INNOT-09	C260-15k	P260	Dry	46.98	15015	181.2587	181.0745	0.1842	12.268	1.046
INNOT-17	C260-20k	P260	Wet	46.99	20014	180.8887	180.869	0.0197	0.984	0.084
INNOT-22	C260-15kR8T	P260	Dry	46.95	15011	181.0554	181.0124	0.043	2.865	0.244
INNOT-13	C350-5k	C350	Dry	46.98	5000	180.9874	180.9744	0.013	2.600	0.222
INNOT-14	C350-10kDry	C350	Dry	46.98	5016	180.9493	180.9366	0.0127	2.532	0.216
INNOT-41	C350-10kWet	C350	Wet	46.98	5013	180.9366	180.9215	0.0151	3.012	0.257
INNOT-51	C350-15k	C350	Dry	46.98	15015	181.0456	181.0062	0.0394	2.624	0.224
INNOT-16	C350-20k	C350	Wet	46.96	20000	180.7043	180.6978	0.0065	0.325	0.028
INNOT-23	C350-15kR8T	C350	Dry	46.96	15013	181.0057	180.971	0.0347	2.311	0.197
INNOT-01	C400-5k	C400	Dry	46.97	5013	180.3178	180.3054	0.0124	2.474	0.211
INNOT-02 a	C400-10kDry	C400	Dry	46.99	5013	180.4118	180.3979	0.0139	2.773	0.236
INNOT-02 b	C400-10kWet	C400	Wet	46.99	5016	180.3979	180.3506	0.0473	9.430	0.803
INNOT-03	C400-15k	C400	Dry	47	15014	180.1083	180.0715	0.0368	2.451	0.209
INNOT-18	C400-20k	C400	Wet	46.99	20013	180.4047	180.3932	0.0115	0.575	0.049
INNOT-24	C400-15kR8T	C400	Dry	46.97	15012	180.7436	180.7265	0.0171	1.139	0.097
INNOT-04	V350-5k	V350	Dry	46.98	5011	180.6997	180.6741	0.0256	5.109	0.435
INNOT-05 a	V350-10kDry	V350	Dry	46.99	5014	180.4083	180.392	0.0163	3.251	0.277
INNOT-05 b	V350-10kWet	V350	Wet	46.98	5013	180.392	180.3861	0.0059	1.177	0.100
INNOT-06	V350-15k	V350	Dry	47	15014	180.3917	180.315	0.0767	5.109	0.435
INNOT-21	V350-20k	V350	Wet	46.99	20013	180.6961	180.6872	0.0089	0.445	0.038
INNOT-25	V350-15kR8T	V350	Dry	46.96	15014	180.6293	180.6072	0.0221	1.472	0.126
INNOT-10	V400-5k	V400	Dry	46.99	5011	180.4915	180.4818	0.0097	1.936	0.165
INNOT-12a	V400-10kDry	V400	Dry	46.99	5013	180.5027	180.4879	0.0148	2.952	0.252
INNOT-12b	V400-10kWet	V400	Wet	47	5012	180.4879	180.4752	0.0127	2.534	0.216
INNOT-11	V400-15k	V400	Dry	47	15011	180.7681	180.7348	0.0333	2.218	0.189
INNOT-19	V400-20k	V400	Wet	47.01	20012	180.5551	180.5493	0.0058	0.290	0.025
INNOT-26	V400-15kR8T	V400	Dry	46.95	15012	180.5263	180.5021	0.0242	1.612	0.137

Table 3.6 Summary of wheel disc wear rates in SUROS twin-disc tests.

Wheel Disc		Steel Density	7.95	[g/cm3]						
		Track Width	10	[mm]						
Test	**Description**	**Material**	**Lubrication**	[mm] **Diameter**	**#Cycles**	[g] **Original Mass**	[g] **Final Mass**	[g] **Mass Loss**	[µg/cycle] **Wear Rate**	[nm/cycle] **Wear Rate**
INNOT-07	C260-5k	R7	Dry	46.99	5063	181.1096	181.0855	0.0241	4.760	0.406
INNOT-08 a	C260-10kDry	R7	Dry	46.99	5062	180.9138	180.9016	0.0122	2.410	0.205
INNOT-08 b	C260-10kWet	R7	Wet	46.98	5060	180.9016	180.8819	0.0197	3.893	0.332
INNOT-09	C260-15k	R7	Dry	46.99	15163	181.0548	180.9018	0.153	10.090	0.860
INNOT-17	C260-20k	R7	Wet	47	20210	180.9091	180.8786	0.0305	1.509	0.129
INNOT-22	C260-15kR8T	R8T	Dry	46.96	15159	181.1844	181.0489	0.1355	8.939	0.762
INNOT-13	C350-5k	R7	Dry	46.99	5050	180.9149	180.8921	0.0228	4.515	0.385
INNOT-14	C350-10kDry	R7	Dry	47	5065	181.02	180.9967	0.0233	4.600	0.392
INNOT-41	C350-10kWet	R7	Wet	46.98	5061	180.9967	180.9901	0.0066	1.304	0.111
INNOT-51	C350-15k	R7	Dry	46.99	15163	180.9471	180.8481	0.099	6.529	0.556
INNOT-16	C350-20k	R7	Wet	46.99	20200	181.0133	180.9773	0.036	1.782	0.152
INNOT-23	C350-15kR8T	R8T	Dry	46.97	15161	181.5728	181.4332	0.1396	9.208	0.785
INNOT-01	C400-5k	R7	Dry	46.96	5065	181.0489	181.0230	0.0259	5.114	0.436
INNOT-02 a	C400-10kDry	R7	Dry	46.98	5066	180.8339	180.8051	0.0288	5.685	0.485
INNOT-02 b	C400-10kWet	R7	Wet	46.96	5069	180.8051	180.8010	0.0041	0.809	0.069
INNOT-03	C400-15k	R7	Dry	46.99	15169	180.9945	180.8929	0.1016	6.698	0.571
INNOT-18	C400-20k	R7	Wet	46.99	20214	180.9726	180.9294	0.0432	2.137	0.182
INNOT-24	C400-15kR8T	R8T	Dry	46.95	15170	181.1207	180.9740	0.1467	9.670	0.825
INNOT-04	V350-5k	R7	Dry	47.01	5059	180.224	180.1879	0.0361	7.136	0.608
INNOT-05 a	V350-10kDry	R7	Dry	47	5064	181.3028	181.279	0.0238	4.700	0.400
INNOT-05 b	V350-10kWet	R7	Wet	46.96	5066	181.279	181.2718	0.0072	1.421	0.121
INNOT-06	V350-15k	R7	Dry	47	15165	180.9953	180.8197	0.1756	11.579	0.986
INNOT-21	V350-20k	R7	Wet	46.99	20215	180.7882	180.7418	0.0464	2.295	0.196
INNOT-25	V350-15kR8T	R8T	Dry	46.97	15162	181.293	181.1565	0.1365	9.003	0.767
INNOT-10	V400-5k	R7	Dry	46.99	5062	180.9727	180.9467	0.026	5.136	0.438
INNOT-12a	V400-10kDry	R7	Dry	47	5062	180.9348	180.9063	0.0285	5.630	0.480
INNOT-12b	V400-10kWet	R7	Wet	46.98	5061	180.9063	180.9034	0.0029	0.573	0.049
INNOT-11	V400-15k	R7	Dry	46.99	15166	180.8324	180.7228	0.1096	7.227	0.616
INNOT-19	V400-20k	R7	Wet	46.99	20222	180.8415	180.7974	0.0441	2.181	0.186
INNOT-26	V400-15kR8T	R8T	Dry	46.95	15163	181.3085	181.1812	0.1273	8.395	0.716

Table 3.7 Observations of material surface of rail steels and wheel steels. Most wheel discs were material R7. It is stated in the table where wheel material was different (R8T).

Test name INNOT-	**Test cycles**	**Rail disc id**	**Material type**	**Observation of material surface of rail steels**	**Wheel disc id**	**Observation of material surface of wheel steels**
01	5000 dry	INR1	C400	Minor damages, as tiny pits.	INW1	Wheel disc damaged more than rail disc, and has visibly rough surface.
02	5000 dry + 5000 wet	INR2	C400	Rail disc damaged a lot by flaking, and very rough in the middle band of 8mm, while 1mm edges are smooth.	INW2	Wheel disc damaged on the running band of 5mm but closer to one edge. End edges of 1mm width are smooth.
03	15000 dry	INR3	C400	Minor damages, as tiny pits.	INW3	Minor damages, as tiny pits, but more than rail disc.
04	5000 dry	INR10	V350	Damaged at the surface evenly as pits, removed by very small amounts of surface flaking.	INW4	Damaged very unevenly at the surface with bits rough and smooth.
05	5000 dry + 5000 wet	INR11	V350	The disc surface had a light brown colouration, which varied darker and lighter around the disc. Minor damages, as tiny pits.	INW5	Discoloured but much smoother surface, with tiny patches of pits.
06	15000 dry	INR12	V350	Considerable surface flaking has taken place. Very deformed surface with deeper pits and bigger surface cracks.	INW6	Rough surface with small bits of smooth surface but mostly all damaged round circumference.
07	5000 dry	INR24	P260	Damaged at the surface evenly as pits, removed by very small amounts of surface flaking.	INW14	Damaged round surface like layer of material has been removed but left not that rough surface to feel.
08	5000 dry + 5000 wet	INR23	P260	Severe damage, cracked and flaking of the disc surface. Very rough at the surface.	INW13	Corresponding wheel disc surface, showing some minor transfer of rail material to the wheel surface after test but was removed in cleaning. Running middle band 2mm wide discoloured and feels smooth. Disc has damage but feels smooth to touch.
09	15000 dry	INR22	P260	Rough surface with pits, created by large amounts of surface flaking.	INW9	Rough surface not evenly damaged round the most of circumference, with a few small patches of very smooth

Test name INNOT-	**Test cycles**	**Rail disc id**	**Material type**	**Observation of material surface of rail steels**	**Wheel disc id**	**Observation of material surface of wheel steels**
						surface.
10	5000 dry	VA400(1)	V400	*(no surface observations made)*	INW7	*(no surface observations made)*
11	15000 dry	VA400(2)	V400	*(no surface observations made)*	INW8	*(no surface observations made)*
12	5000 dry + 5000 wet	VA400(3)	V400	*(no surface observations made)*	INW12	*(no surface observations made)*
13	5000 dry	INR30	C350	Smooth surface with tiny dots.	INW21	Smooth surface with tiny dots.
14/41	5000 dry + 5000 wet	INR31	C350	Severe damage, cracked and flaking of the disc surface. Very rough at the surface.	INW16	Disc is smooth except for a contact running band of 4mm moved roughly 2mm away from centre line. Contact band is little rough with pits.
51	15000 dry	INR34	C350	Rough surface with clear pits and cracks.	INW20	Rough surface with pits, slightly less damaged than rail disc.
16	20000 wet	INR36	C350	Very smooth surface, discoloured a bit.	INW17	Even smoother surface than rail disc. All shiny.
17	20000 wet	INR26	P260	Very smooth surface with distinguished brighter lines round discoloured disc.	INW10	Very smooth surface with distinguished brighter lines round disc.
18	20000 wet	INR7	C400	Very smooth surface, discoloured a bit.	INW15	Very smooth shiny surface.
19	20000 wet	INR40	V400	Very smooth surface, discoloured a bit.	INW23	Very smooth surface, discoloured a bit, but still shiny.
21	20000 wet	INR16	V350	Very smooth surface, discoloured a bit.	INW24	Very smooth shiny surface.
22	15000 dry (R8T)	INR25	P260	Rough surface with pits.	WB35 (R8T)	Rough surface with pits, but they are smaller and denser.
23	15000 dry (R8T)	INR33	C350	Rough surface with pits and parts round circumference are rougher and cracks are more wavy and perpendicular to motion, but not that deep.	WB47 (R8T)	Rough surface with pits.
24	15000 dry (R8T)	INR4	C400	Rough surface with pits.	WB46 (R8T)	Much rougher surface than at rail disc with pits, but they are smaller and denser.
25	15000 dry (R8T)	INR14	V350	Minor surface roughness with shallow pits.	WB37 (R8T)	Minor surface roughness with shallow pits, but they are smaller and denser than in rail disc.
26	15000 dry (R8T)	INR41	V400	Minor surface roughness with shallow pits.	WB45 (R8T)	Very rough surface with pits.

3.6 Traction coefficient data

The measured traction coefficient during twin-disc tests is plotted in Figure 3.6 - Figure 3.10 below, for each material grade. This data is used as an input into the Dynarat model simulations in Chapter 5.

Independent of material, some general conclusions about adhesion can be made. For all materials tested under dry conditions, air-cooled, the traction coefficient has values between 0.38 – 0.47. From the start of the test the coefficient increases and reaches a maximum of 0.42-0.47, and then drops and stabilises roughly round 1000 cycles to the value 0.4-0.42, depending on the test. The reason for this is that discs are machined to a certain roughness and during running they get a polished surface, meaning that roughness drops and consequently traction coefficient also. When wheel material R8T was used in the tests, the coefficient of traction is very slightly lower than with R7.

In wet conditions, distilled water was applied at a rate of one drop per second. For all wet tests, the coefficient of traction is significantly lower than in the dry tests, in the region of 0.15-0.22. The obvious difference in the coefficient is between tests of 20000 cycles wet, and 5000 cycles wet that followed 5000 cycles dry test, where tests of 20000 cycles show more stability in the coefficient. For materials P260, C350 and C400 it stabilises at around 0.2, and for V350 and V400 is slightly higher, around 0.21-0.22. All 5000 cycles wet tests have coefficient under 0.2 but it varies during the test. For each material it is a different trend, either rising, falling or both.

Dry contact gives the highest and most stable levels of traction, in the range 0.4 - 0.42, while in wet tests they are lower, 0.15-0.22. The same traction coefficient behaviour was observed in previous research on SUROS machine (Franklin *et al.,* 2005; Alwahdi, 2004; Vasic, 2004). If the traction coefficients measured in the lab are also seen, with only a slight difference, in practice, for uncontaminated wheels and rails, then traction levels are sufficiently high for safe operation, whether dry or wet. Coefficient of traction changes with number of rolling cycles, observed also by (Krause and Lehna, 1987; Tyfour *et al.*, 1995).

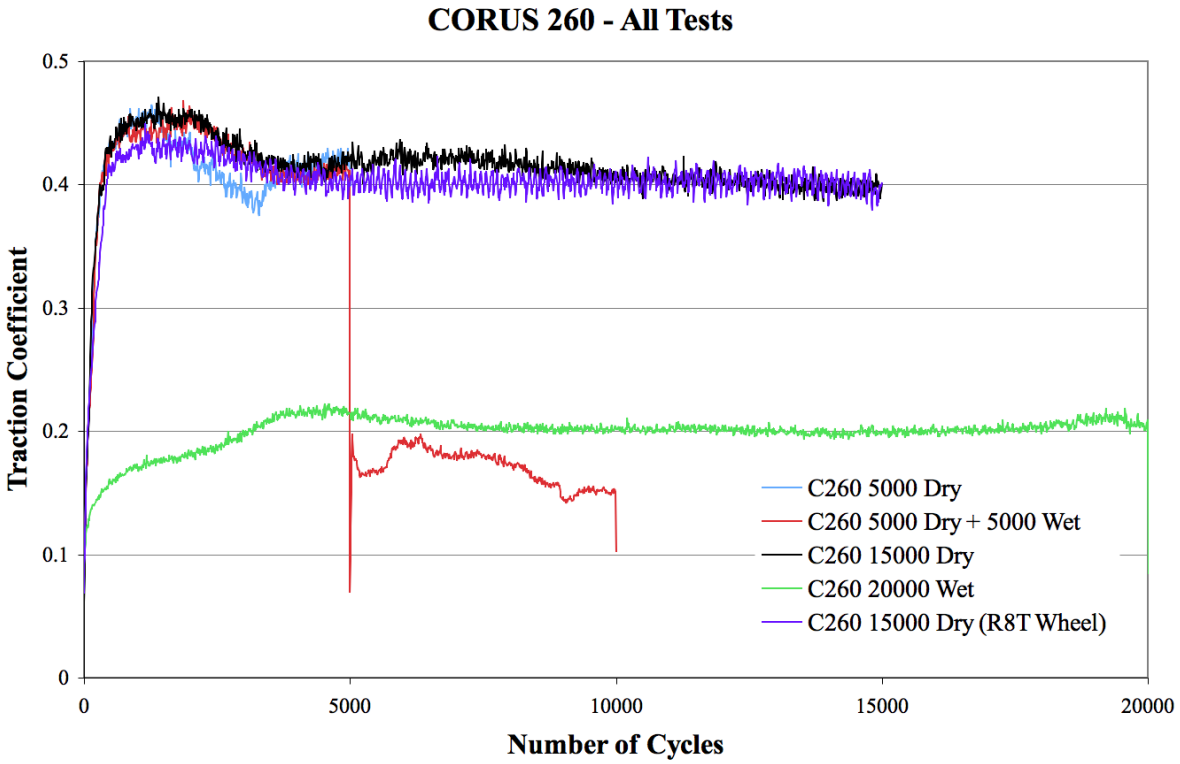

Figure 3.6 Traction curves for P260 rail steel (see Appendix A).

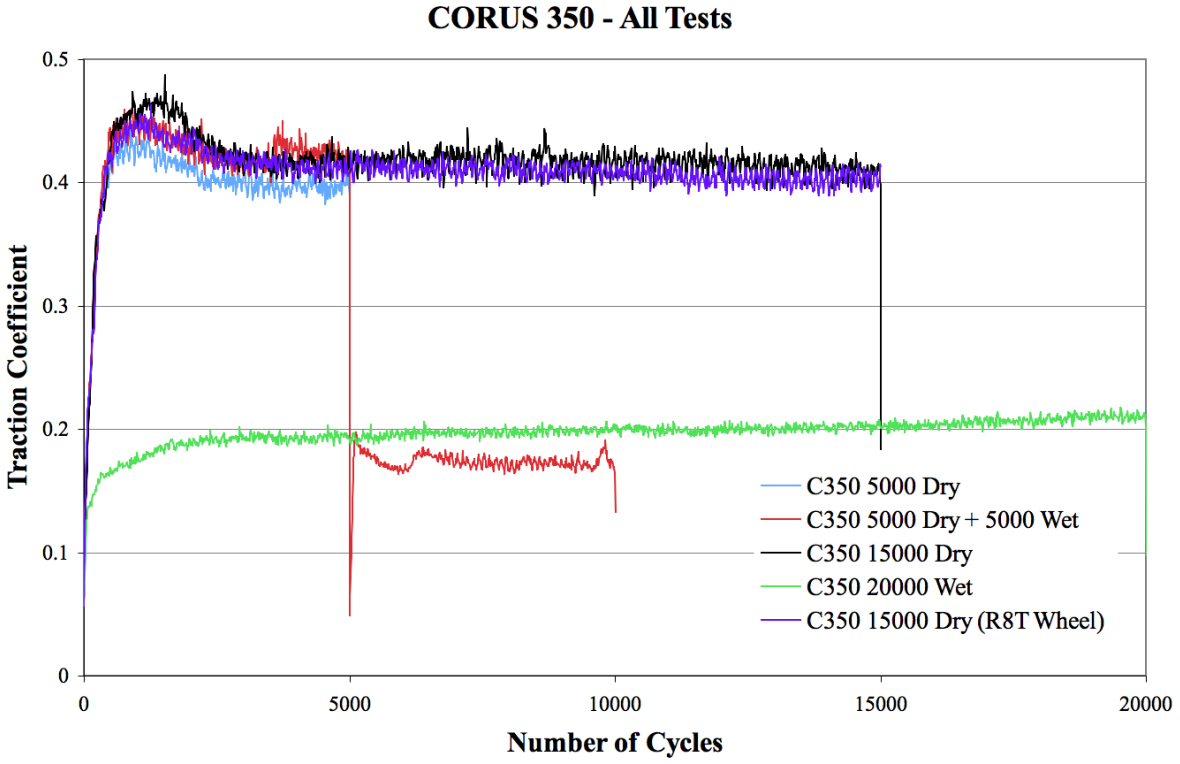

Figure 3.7 Traction curves for C350 rail steel (see Appendix A).

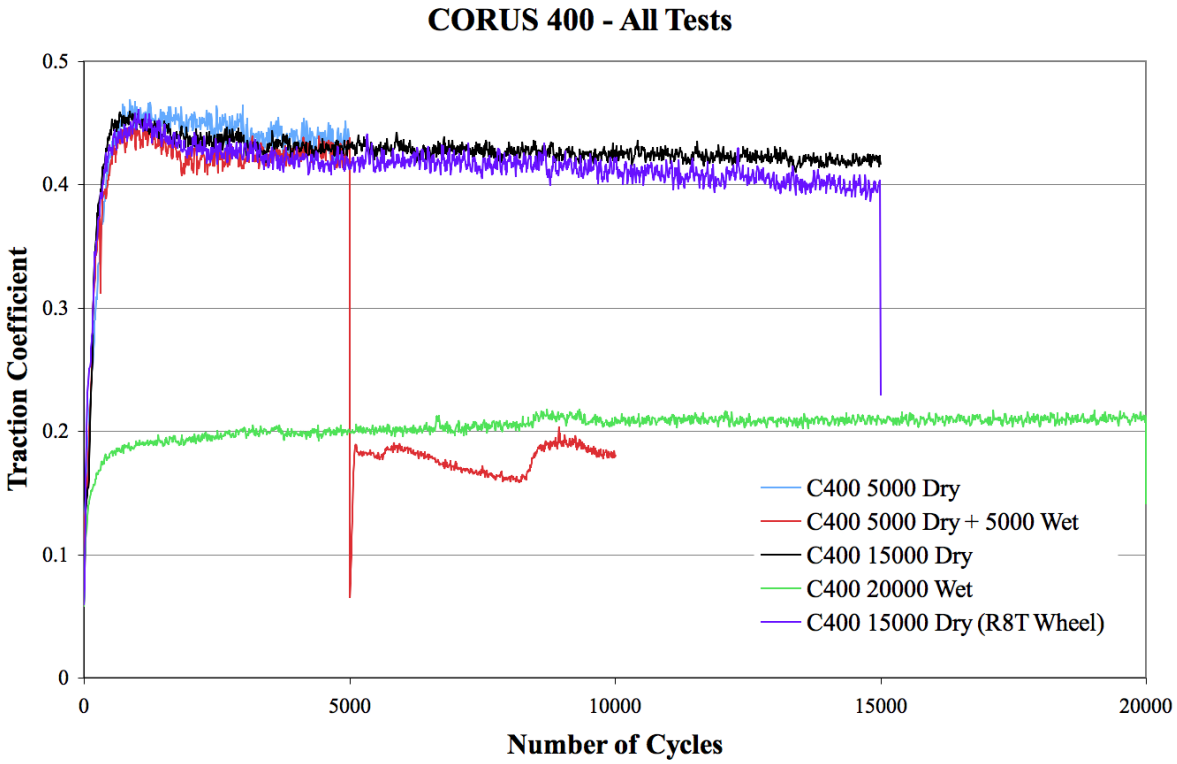

Figure 3.8 Traction curves for C400 rail steel (see Appendix A).

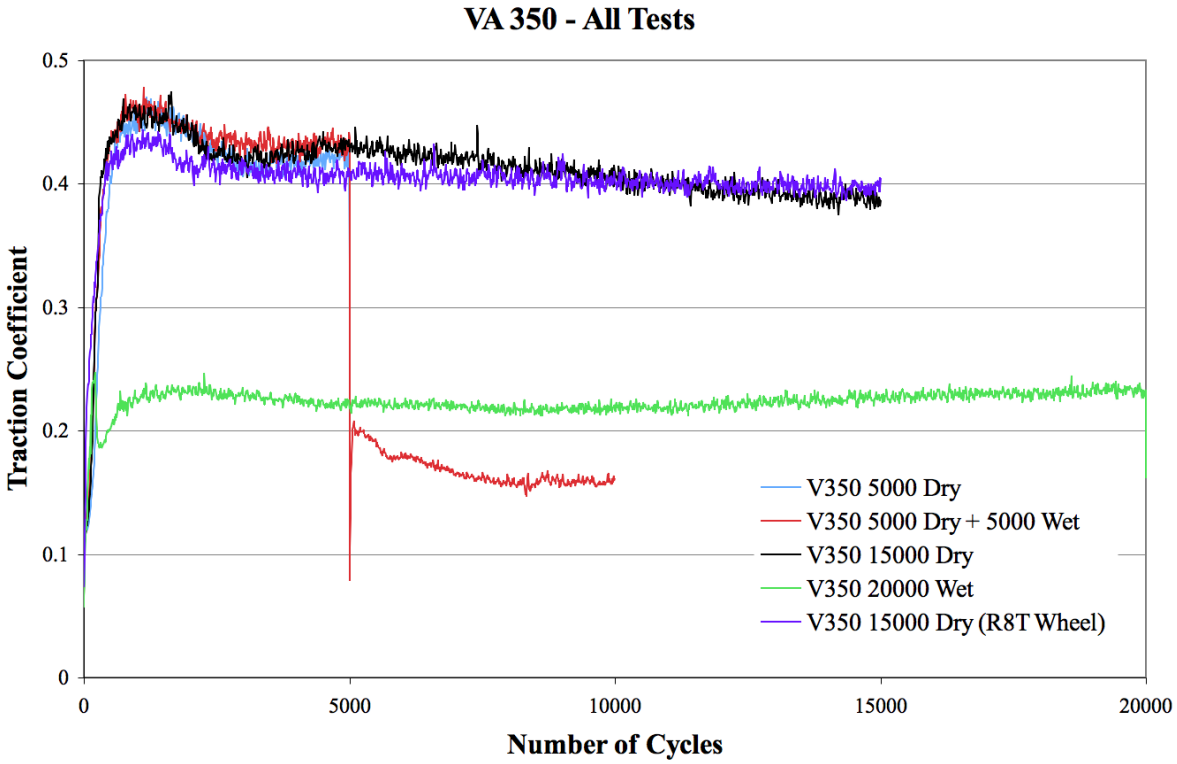

Figure 3.9 Traction curves for V350 rail steel (see Appendix A)..

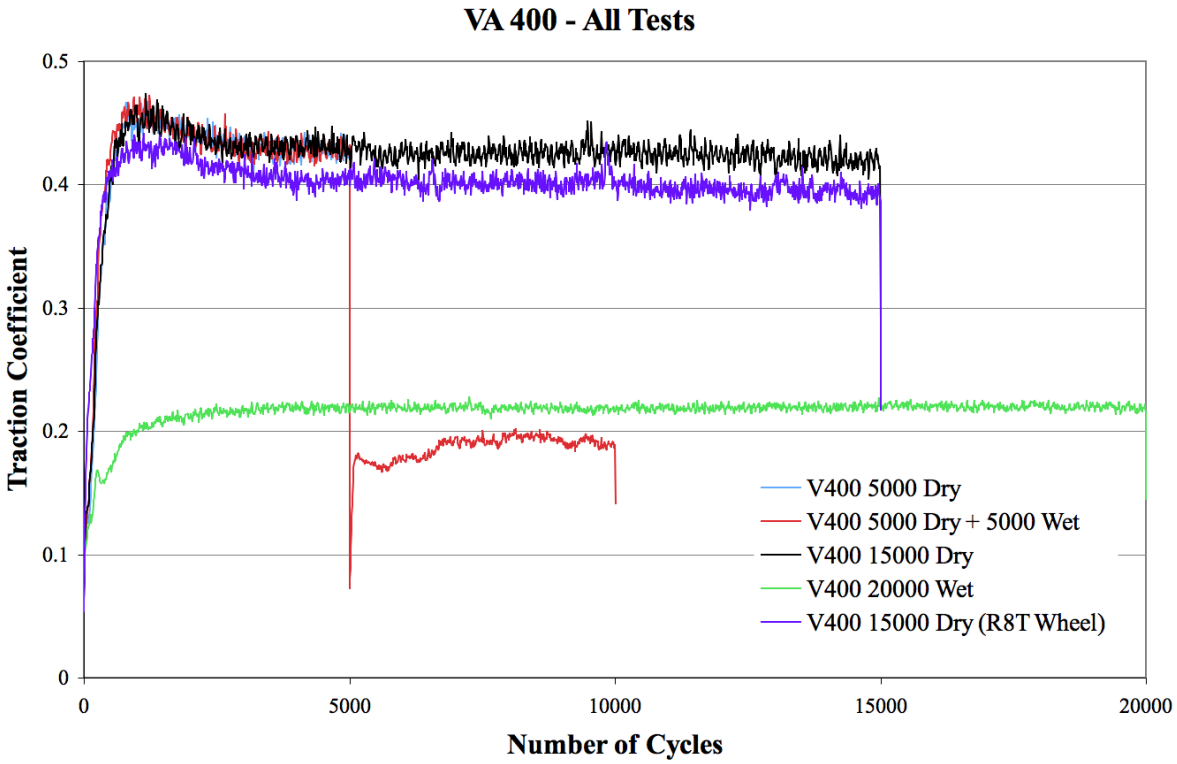

Figure 3.10 Traction curves for V400 rail steel (see Appendix A).

3.7 Roughness data

3.7.1 Measurement

Micro-scale surface roughness in the form of grinding marks, or as a result of uneven wear during operation, is often neglected as a source of raised contact stresses, but with the introduction of harder, premium grade rail steels the persistence of grinding marks and other damage needs to be considered.

Prior to roughness measurement, discs were cleaned in an ultrasonic bath. The instrument used for roughness measurement was a "Taylor Hobson – Surtronic 25". The measuring stylus (tip radius 5µm) was run transversely across the disc circumference (the curvature of the disc makes it difficult to measure the roughness around the circumference), using a sample length of 4mm in the middle of the disc track. Note: The sample length determines the maximum wavelength that can be measured, while the style tip radius determines the minimum wavelength. Kwon and Cho (2006) found that the minimum wavelength of the traced profile and the stylus tip radius have a power-law relationship.

The surface roughness (*Ra*, or centre-line average) of the disc's contact surface was recorded at four positions around the disc and average value was calculated. The roughness for new discs

was checked on only one disc for each different material. All discs were done to the same surface finish. The complete set of results is given in Appendix A, and the averages are presented in Table 3.8 for new discs and in Table 3.9 for discs after testing. These are summarised also in Figure 3.11.

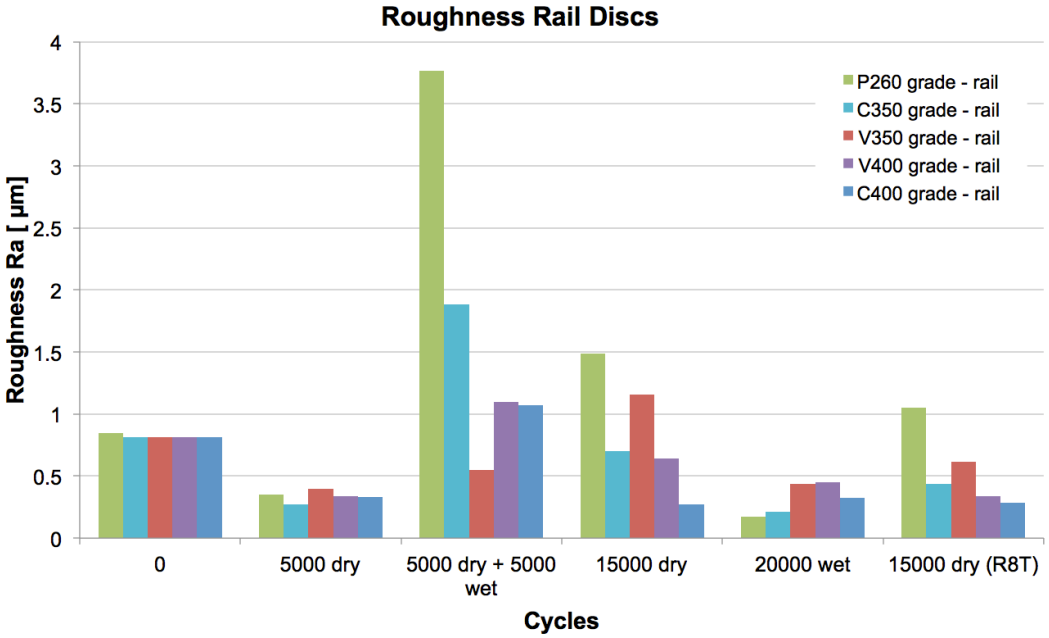

(a)

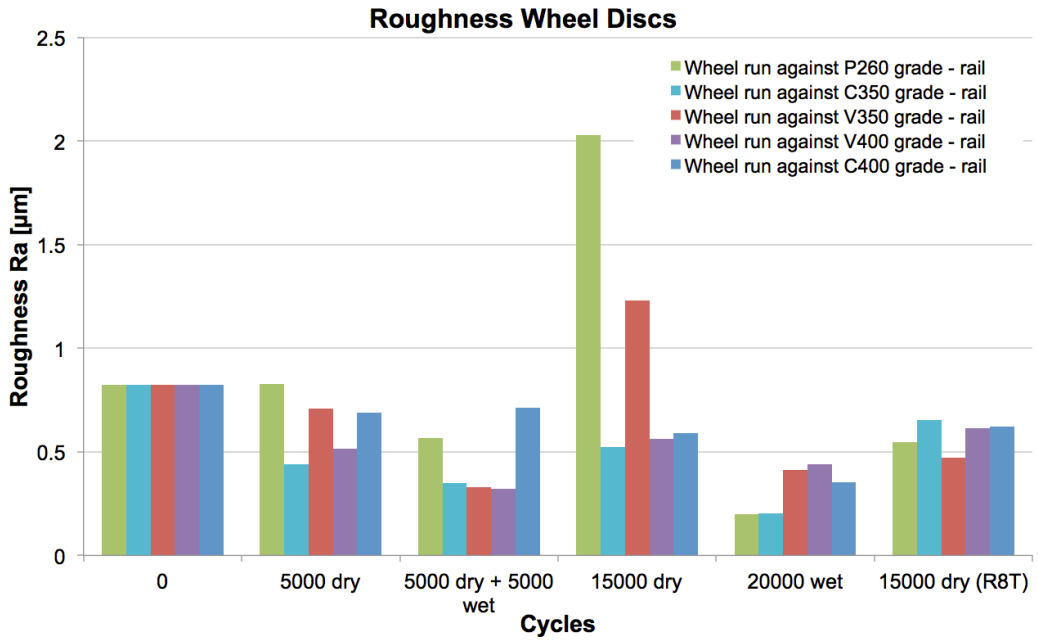

(b)

Figure 3.11 Average measured transverse roughness of (a) the rail discs, and (b) the wheel discs following testing. Reference values prior to testing are given as category '0'.

Table 3.8 Transverse surface roughness measurements – value *Ra* in μm. New discs.

New material	**Disc label**	**Average**
wheel	INW 10	0.824
C400 – Rail	INR 5	0.811
V350 – Rail	INR 13	0.817
P260 – Rail	INR 20	0.845

Table 3.9 Transverse surface roughness measurements – value *Ra* in μm. Discs after testing.

Test Duration (cycles)	**Rail Disc label**	**Rail roughness average**	**Wheel Disc label**	**Wheel roughness Average**
C400 – rail				
5000 dry	INR 1	0.332	INW 1	0.688
5000 dry + 5000 wet	INR 2	1.073	INW 2	0.713
15000 dry	INR 3	0.273	INW 3	0.592
20000 wet	INR 7	0.327	INW 15	0.355
15000 dry	INR 4	0.283	WB46 (R8T)	0.621
V350 – rail				
5000 dry	INR 10	0.397	INW 4	0.709
5000 dry + 5000 wet	INR 11	0.552	INW 5	0.331
15000 dry	INR 12	1.156	INW 6	1.230
20000 wet	INR 16	0.439	INW 24	0.411
15000 dry	INR 14	0.616	WB37 (R8T)	0.471
P260 – rail				
5000 dry	INR 24	0.353	INW 14	0.826
5000 dry + 5000 wet	INR 23	3.768	INW 13	0.565
15000 dry	INR 22	1.485	INW 9	2.030
20000 wet	INR 26	0.171	INW 10	0.198
15000 dry	INR 25	1.054	WB35 (R8T)	0.546
V400 – rail				
5000 dry	VA400(1)	0.337	INW 7	0.514
5000 dry + 5000 wet	VA400(3)	1.096	INW 12	0.321
15000 dry	VA400(2)	0.641	INW 8	0.561
20000 wet	INR 40	0.450	INW 23	0.442
15000 dry	INR 41	0.341	WB45 (R8T)	0.613
C350 – rail				
5000 dry	INR 30	0.274	INW 21	0.441
5000 dry + 5000 wet	INR 31	1.884	INW 16	0.349
15000 dry	INR 34	0.701	INW 20	0.522
20000 wet	INR 36	0.211	INW 17	0.202
15000 dry	INR 33	0.436	WB47 (R8T)	0.653

3.7.2 Discussion

The results show that all rail steels, except V350, behave similarly. The roughness values (average of *Ra*) decline after 5000 cycles (dry) from the original value, reaching a minimum of 0.332μm and 0.353μm. For C400, the disc surface after 15000 cycles dry is in much better condition than after 5000 cycles dry, with roughness dropping to 0.273μm. Discs are rougher after 15000 cycles than 5000 dry for the other four materials (P260, V350, V400 and C350), e.g., roughness after 15000 cycles is 1.485μm for P260. Therefore, the softer steel deteriorates more.

The dry-wet combination deteriorates surfaces the most, giving a significant rise in roughness to approximately 1μm for harder steels, 1.9μm for C350 and 3.768μm for P260. V350 behaves differently in dry-wet testing, where roughness is 0.552μm, significantly less than for other materials.

When tests are run wet for the whole duration of the test of 20000 cycles, all materials have low roughness values. An interesting observation can be made looking at both wheel and rail discs, that roughness is almost identical for all wheel-rail disc pairs in wet tests.

Wheel material behaves differently in every test, so it may be important to test atmospheric conditions as well as corresponding material. In tests with rail steel C400, roughness does not change a lot, but in tests with P260 and V350, it drops slightly at 5000 cycles from the initial value, and then drops more in dry-wet tests after 10000 cycles. For 15000 cycles dry, roughness increases, and comes close to the value of the 5000 cycles tests. Note: Wheel discs do not deteriorate like rail discs in dry-wet tests. (Because the wheel disc is driving, the alignment of short cracks at the wheel disc surface prevents the fluid entrapment and pressurisation that accelerates short crack growth at the driven rail surface.)

There were not enough tests with various number of cycles (only 0, 5000 and 15000 dry) to properly plot how roughness changes with number of cycles and to make a proper conclusion about how it correlates with type of material and wear. The best approximation is polynomial trend, where roughness initially drops up to round 6000-8000 cycles in the running-in process, depending on material, and then rises. For rail materials (see Figure 3.12) it is a sharper rise, i.e., the material surface deteriorates more if the material is softer, and roughness is steadier for harder materials. For wheel materials, see Figure 3.13, roughness does not change much with number of cycles for dry tests. The biggest difference in results is obtained when discs are run against softer rail material – P260 and then V350. The reason that roughness of the wheel

material is not changing that much, is because it is the same material run under different conditions, so deterioration of surface (and roughness) depends greatly on material itself.

Hyde (2012) has tested on the same materials how rail roughness changes with time as a locomotive is driven over repeatedly. Special implants were inserted in a gap between rails and roughness measured several times up to 100 wheel passes. It was seen that roughness reduces from initial values for all materials and comes to steady state faster for softer materials than harder, but for all it is more or less stable after 100 cycles. It would be good to see development of roughness for more cycles to be comparable to results from Figure 3.12.

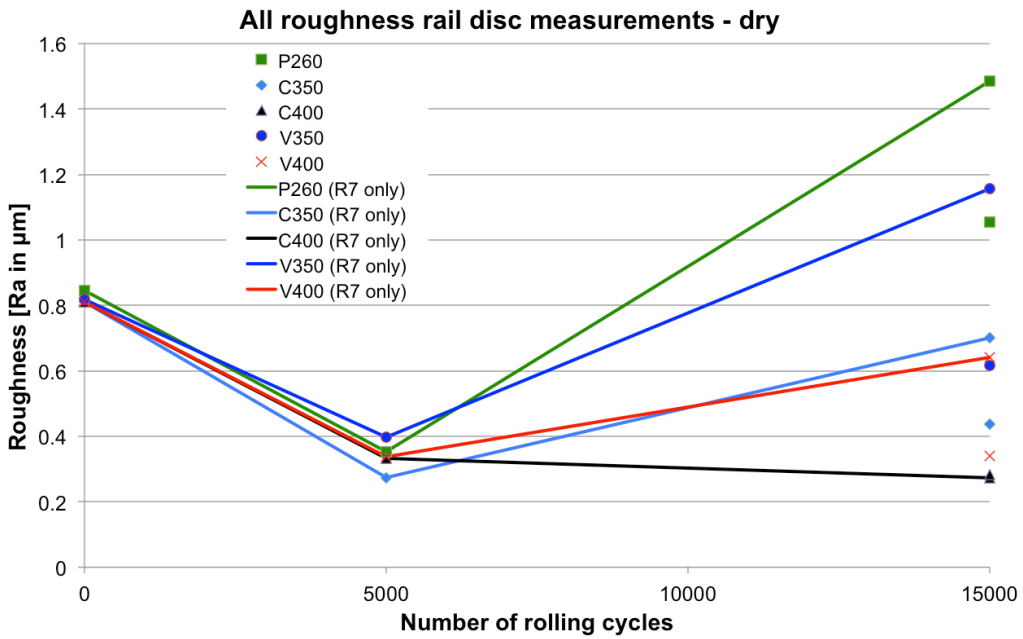

Figure 3.12 Roughness measurements for rail discs – dry tests. Lines connect measurements for tests with R7 wheel steel. Additional data points are plotted for roughness measurements of rail discs after the tests 15000 cycles dry against R8T wheel steel.

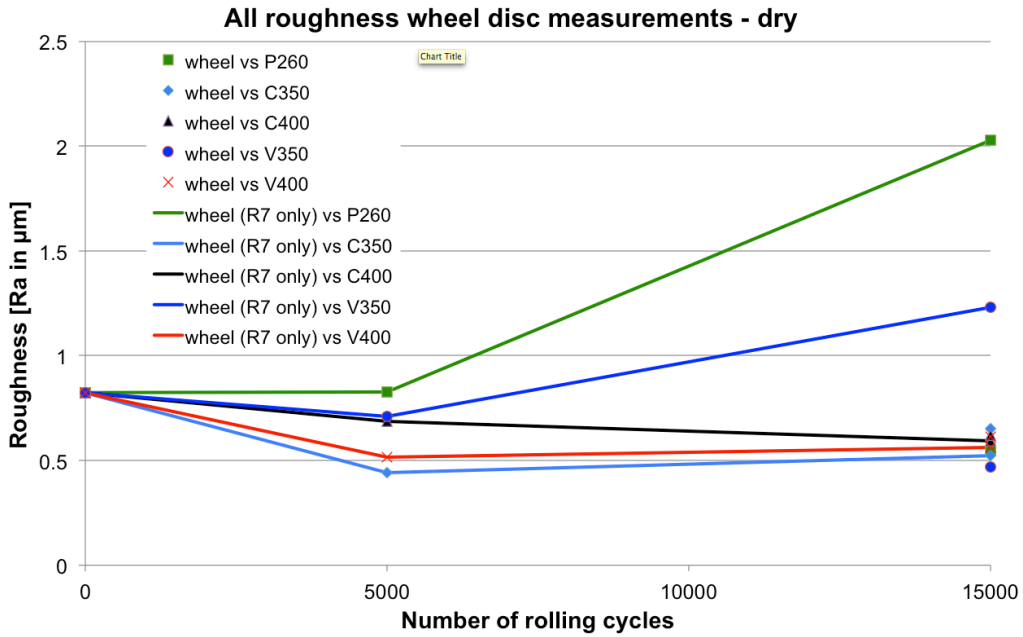

Figure 3.13 Roughness measurements for wheel discs – dry tests. Lines connect measurements for tests with R7 wheel steel. Additional data points are plotted for roughness measurements of R8T wheel steel discs after the tests 15000 cycles dry.

3.8 Discussion – twin-disc tests

3.8.1 Comparison of wear rates with BS11

Twin-disc testing of BS 11 rail steel (British 'normal' grade, R220) has been done by (Tyfour *et al.*, 1995). Material and conditions were similar to SUROS testing, and were as follows:

Rail: BS 11

average hardness (Hv0.5kg)	240-250
ultimate tensile strength	781MPa
yield strength	406MPa
total plastic elongation	21.9%
Young's modulus	209GPa
roughness (Ra)	0.10-0.49μm
disc diameter	47mm
track width	10mm

Wheel: W8A

Young's modulus	199GPa
roughness (Ra)	0.12-0.55μm

Operating conditions

peak pressure	1500MPa
creepage	-1%
speed (r.p.m.)	406-410

Contact was dry (i.e., unlubricated) and air-cooled.

Estimated density of rail steel: $\rho = 7.85 mg/mm^3$

Contact surface area: $A = \pi \times 47mm \times 10mm = 470\pi mm^2$

Wear rates of new material discs after SUROS dry testing, see Table 3.5 and summarised in Table 3.10, are compared with Tyfour's results, see Table 3.11. For 5000 cycles dry testing, materials C350, C400 and V400 have roughly 2-3 times lower wear rates than the BS11. The 15000 cycles dry test can be compared to Tyfour's 10000 and 17500 cycles tests. Except for the P260-R7 test, all other materials' wear rates are significantly lower than for BS11 steel; roughly 3-12 times, depending on test and material.

For similar tests it can be confirmed, therefore, that the newer premium grade rail steels have better wear performance than the older traditional rail steel.

Table 3.10 Wear rate [µg/cycle] of rail discs from SUROS tests.

	5000 Cycles [R7]	**5000 Cycles [R7]** (from mixed test)	**15000 Cycles [R7]**	**15000 Cycles [R8T]**
P260	6.183	5.724	12.268	2.865
C350	2.600	2.532	2.624	2.311
C400	2.474	2.773	2.451	1.139
V350	5.109	3.251	5.109	1.472
V400	1.936	2.952	2.218	1.612

Table 3.11 Wear rate of rail discs BS11, calculated from (Tyfour *et al.*, 1995).

Test Number	134	136	137	135	138	130	139
Number of cycles	500	1000	5000	10000	17500	40000	40000
Mass loss (mg)	0.5	2.9	34.8	134.1	249	652	619.8
Wear rate (µg / cycle)	1	2.9	6.96	13.41	14.2	16.3	15.5
Wear rate (nm / cycle)	0.0863	0.250	0.600	1.157	1.228	1.406	1.337

3.8.2 Wear rates according to different environmental conditions

When tests are performed under different environment conditions, the idea was to simulate dry and rainy days as happens on railways. How much material will wear out and how the surface will deteriorate according to operating conditions can be discussed by looking at surface observations, wear and roughness measurements, as well as at traction coefficient. It is well known that the coefficient of friction has a significant effect on wear.

The twin-disc tests reported in this thesis show the same trends as seen in practice and in literature (Franklin *et al.*, 2005; Alwahdi, 2004; Vasic, 2004). For dry conditions, traction coefficient is the highest, and all materials show higher wear rates for dry than for wet conditions, see Table 3.12, by a factor of 3-12.

That is why on curves where flange contact between wheel and rail may occur, with significant sliding at the interface and high pressure, the wheel or rails are often lubricated to reduce wear.

Another observation is that the average ratio dry wear to wet wear is 8.8 for rail discs and 4.4 for wheel discs. The reason is the orientation of discs in the machine, wheel disc being driving disc and rail disc driven, so the hydro effect (fluid entrapment and crack pressurisation) does not have the same influence on both discs, because of the opposite direction of traction with respect to motion. Only in the driven disc (rail) does the fluid pressurise the cracks, accelerating growth.

Table 3.12 Comparison of wear rates for dry 15k and wet 20k tests.

Rail material No. cycles		Wear Rate [µg/cycle] rail	Wear Rate [µg/cycle] wheel
P260-15k	Dry	12.268	10.090
P260-20k	Wet	0.984	1.509
	ratio	*12.5*	*6.69*
C350-15k	Dry	2.624	6.529
C350-20k	Wet	0.325	1.782
	ratio	8.07	3.66
C400-15k	Dry	2.451	6.698
C400-20k	Wet	0.575	2.137
	ratio	*4.27*	*3.13*
V350-15k	Dry	5.109	11.579
V350-20k	Wet	0.445	2.295
	ratio	*11.5*	*5.04*
V400-15k	Dry	2.218	7.227
V400-20k	Wet	0.290	2.181
	ratio	*7.65*	*3.31*

3.9 Conclusions

A series of twin-disc tests have been performed to investigate the behaviour under cyclic loading of some new rail materials. Compared to older BS 11 (R220) material, the new premium grades have lower wear rates. For all materials traction coefficient and wear are higher for dry tests than for wet ones, the same thing is observed on track. If test discs are run dry, followed by lubricated runs, deterioration of the surface (and subsequent wear and crack growth) accelerates. Similar behaviour has been observed by others (Franklin *et al.*, 2005; D.I. Fletcher, Beynon J.H., 1998; Tyfour *et al.*, 1996; Alwahdi, 2004).

In this thesis, these SUROS tests are used for development and calibration of the Dynarat ratcheting simulation model for use with R260 and premium grade rail steels. The traction coefficient recorded during the tests is used as an input for simulations of the twin-disc tests and the predicted wear rates compared with the measured wear rates. The hardness and strain data required for development of the new material models is determined from microstructural measurements and analysis of the test specimens, presented in Chapter 4.

Chapter 4 Metallurgical Analysis

This chapter presents a metallurgical description of material plastic deformation and crack initiation in the twin-disc tested harder pearlitic steels. Similar work on microstructure investigations and development of models has been done previously for BS11 (British 'normal' grade, R220) and R260 ('standard' grade) rail steels, see (Fletcher *et al*., 2008; Franklin *et al*., 2008; Garnham and Davis, 2008; Garnham *et al*., 2007; Eden *et al*., 2005), and this thesis extends the research to the harder pearlitic steels.

These results are important for understanding material behaviour under cyclic loading and are needed for developing the 'Dynarat' model for simulating wear and crack initiation of these new steels.

4.1 Introduction

After testing of the materials on the SUROS twin-disc machine, the disc specimens were subjected to further analysis. First, images were taken of the disc surfaces to obtain a visual record of deterioration. (Photographs of disc surfaces are given in Appendix A.) After that, the discs were sectioned and prepared for microhardness measurements and metallographic (microscopic) analysis. Optical microscopy and electron microscopy – using an Environmental Scanning Electron Microscope (ESEM) – were used to observe plastic deformation of the five rail materials closer to the surface, and crack formation. Hardness measurements were done up to 10mm under the surface, to show variation of material hardening with depth. Shear strain measurements were estimated in the severely strained material close to the surface, to determine variation of plastic shear strain with depth.

4.2 Preparation of specimens

Disc specimens were sectioned, mounted in bakelite, polished and etched (with 2% Nital), and cross-sections analysed under the microscope. Discs were sectioned under the running contact, normal to the surface (see Figure 4.1). The cutting procedure and etching chemical did not deform the material microstructure. Before disc sections were examined under the microscope, they were cleaned: first in soapy water in the ultrasonic bath, then rinsed under cold running water, immersed in methanol in the ultrasonic bath again, and finally air-dried.

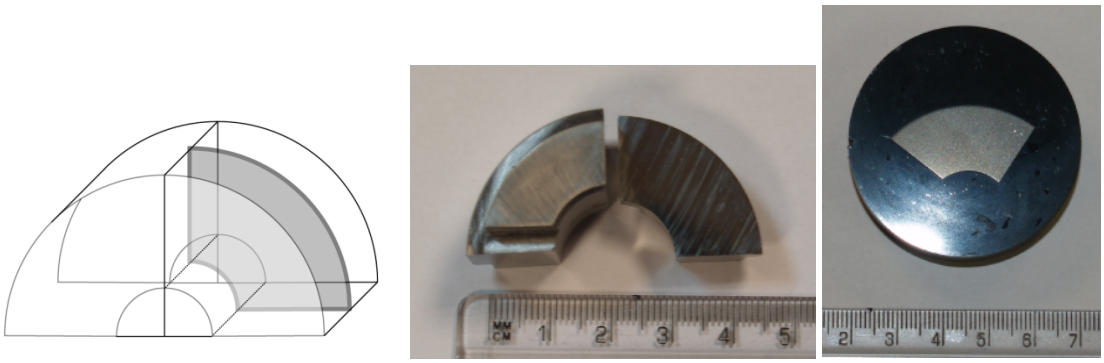

(a) (b) (c)

Figure 4.1 (a) Sketch showing how discs were sectioned. (b) Sample section. (c) Sample in bakelite, polished and etched.

Experimental procedure:

1. The discs were sectioned and polished.
2. The specimens were photographed (unetched) using the optical microscope to examine for any cracks.
3. Microhardness measurements were made on the (unetched) sections – 200g load (300g used in some cases).
4. The discs were etched with 2% Nital.
5. The specimens were photographed (etched) using the optical microscope to see the microstructure and measure deformation angles (i.e., to estimate plastic shear strain).
6. A selection of specimens was studied using electron microscopy (ESEM).

4.3 Hardness measurements and results

4.3.1 The dependence of microhardness measurements on load

The generally accepted assumption is that the Vickers test produces a hardness number that is independent of load. However, this is only true for tests performed with loads above 100g. For very light loads, microhardness value increases with increasing load (see Figure 4.2).

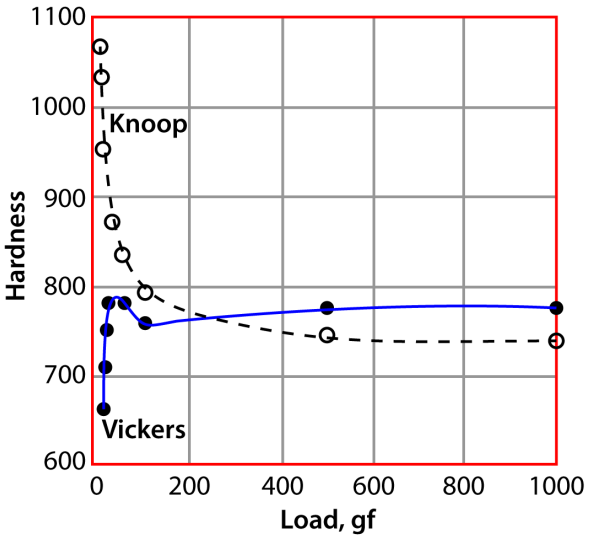

Figure 4.2 Dependence of Vickers hardness on load. (Adapted from Boyer, Hardness testing, 1990; and in turn from Metals Handbook, Mechanical Testing, 1985.)

4.3.2 Vickers hardness testing

Bulk hardness measurements were taken at the side of the specimen. Microhardness measurements were taken at a series of depths on the circumferential cross-section, using the Vickers hardness method, which is widely used in industry and standardised.

Bulk hardness measurements, using a Vicker's hardness indenter, were done with a 10kg load on disc parts. This measurement is largely independent of local variations in the material microstructure. 2-3 measurements were taken, and the average calculated.

In addition, microhardness measurements taken at depth 10mm from the surface (in the undeformed part of the specimen) were used as a reference / core hardness value for the microhardness measurements.

Microhardness measurements were taken along four lines normal to the surface, to a depth of 10mm. Two of the four lines are shown in the sample in Figure 4.3. Within 0.5mm of the surface, starting at either 50 microns or 80 microns, the measurements are close together and need to be staggered (alternate measurements offset) to prevent interference; the distance between indentations was required to be more than 2.5 indentation diameters.

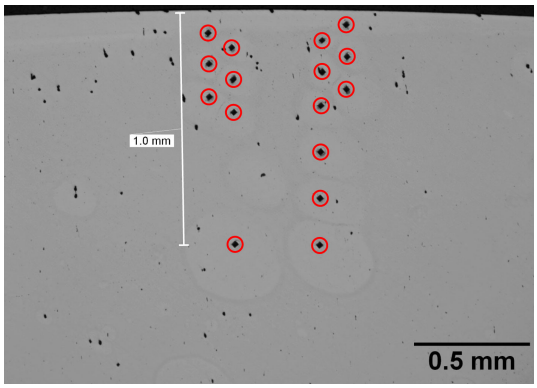

Figure 4.3 Micrograph showing microhardness indents down to 1mm – two out of four lines total shown. Left: 80, 150, 220, 290, 360, 430, 1000 [microns]. Right: 50, 120, 190, 260, 330, 400, 600, 800, 1000. Alternate measurements staggered within 0.5mm of surface to prevent interference.

4.3.3 Hardness results

Bulk/core hardness measurements for each test disc are given in Table 4.1. They should show similar values for the same material independent of the test. Differences between min and max value are 83 for C400, 16 for V350, 25 for P260, 7 for V400. Of the three C400 hardness measurements, INR1 appears to be suspiciously small (295 HV10 compared with 354 HV10 and 378 HV10); however, the wear rate of INR1 is consistent with other C400 discs, so this is unlikely to be a mix-up of samples with a different rail steel grade.

Microhardness measurements were done to determine near-surface strain hardening of the material. The rail disc microhardness data are plotted in Figure 4.4 - Figure 4.8. The complete set of microhardness measurements is tabulated in Appendix C. (Note: A load of 200g was used for measuring Vickers microhardness of all rail discs and corresponding wheel discs, except for VA400(1), VA400(2) and VA400(3) and corresponding wheel discs where the load was 300g.) Two hardness measurements are taken at each depth under disc surface, except at depths of 1mm and 5mm, where four were taken. Values shown in Figure 4.4 - Figure 4.8 are the averages of the readings at each depth.

All discs show material hardening characteristics at the surface. The rail material exhibits an increase in hardness with an increase in cycles. When comparing tests with 15000 cycles run against softer wheel material R7, Figure 4.6, and harder R8T, Figure 4.7, the rail material hardens more against R7. Although R8T is initially harder than R7, by the end of the test the surface hardness of the R7 is higher than that of the R8T. The softer P260 steel hardens more at the surface (i.e., at a depth of 50 microns) than harder steels in dry tests, while the harder materials have similar hardening rates at all depths.

In wet tests, the P260 deteriorated rapidly and is almost always softer than the other harder materials when measured from the surface into the depth of material.

One unusual observation, which may be nothing more than measurement error or an indication of hardness variation in the original railhead, is that hardness measurements are slightly lower (93-96%) at 2-5mm compared with the measurements at 10mm which are used as a baseline / core hardness reference, for almost all measured rail discs. If this is a real effect, it suggests that the materials soften slightly for very small strains. (Softening of some steels at small strains has been noted by other researchers; see, e.g., Sankaran *et al*., 2003.)

Table 4.1 Bulk hardness – HV10 (10kg load) – average of 2-3 measurements. Also, for comparison, average wear rates (dry only).

	Rail disc id	**Rail hardness [HV]**	**Rail wear rate [nm/cycle]**	**Wheel disc id**	**Wheel hardness [HV]**	**Wheel wear rate [nm/cycle]**
C400	**rail**			**wheel**		
5000 dry	INR1	295	*0.211*	INW1	215	*0.436*
5000 dry + 5000 wet	INR2	354		INW2	206	
15000 dry	INR3	378	*0.209*	INW3	238	*0.571*
V350	**rail**			**wheel**		
5000 dry	INR10	373	*0.435*	INW4	225	*0.608*
5000 dry + 5000 wet	INR11	389		INW5	211	
15000 dry	INR12	375	*0.435*	INW6	217	*0.986*
P260	**rail**			**wheel**		
5000 dry	INR24	277	*0.527*	INW14	203	*0.406*
5000 dry + 5000 wet	INR23	283		INW13	235	
15000 dry	INR22	258	*1.046*	INW9	217	*0.860*
V400	**rail**			**wheel**		
5000 dry	VA400(1)	326	*0.165*	INW7	233	*0.438*
5000 dry + 5000 wet	VA400(3)	329		INW12	201	
15000 dry	VA400(2)	322	*0.189*	INW8	235	*0.616*

The original hardness of material C350, estimated by averaging all microhardness measurements of all 5 discs at 10mm under the surface, is 358HV; the difference between the minimum and maximum measured values was 64.

Standard hardness reference values for these materials are given in Appendix E.

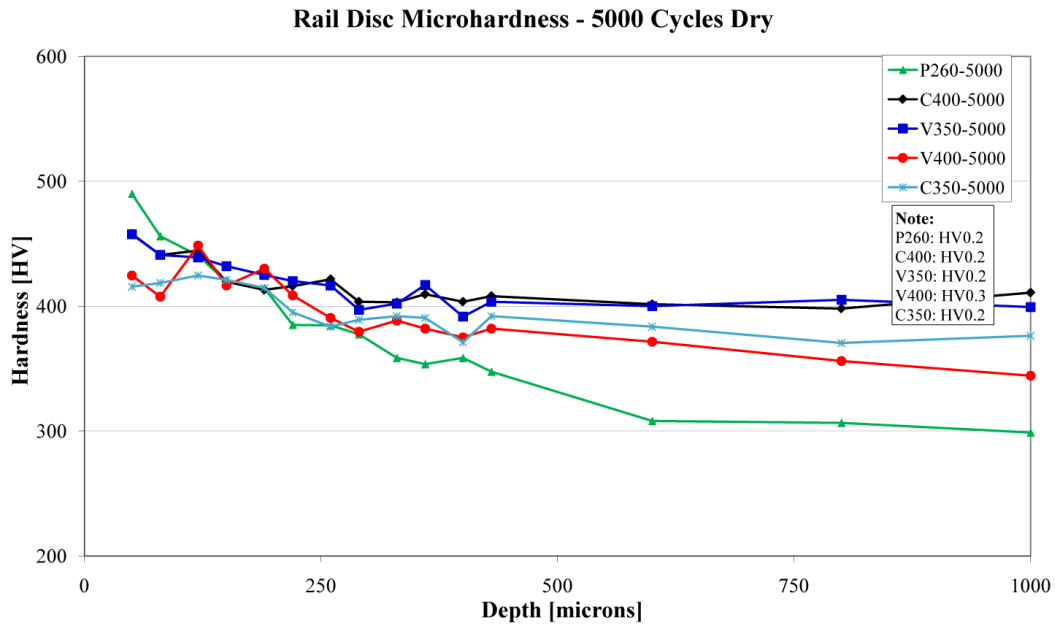

Figure 4.4 Microhardness measurements at various depths on circumferential cross-sections through rail disc specimens following 5000 cycles dry. Rail discs run against R7 wheel disc.

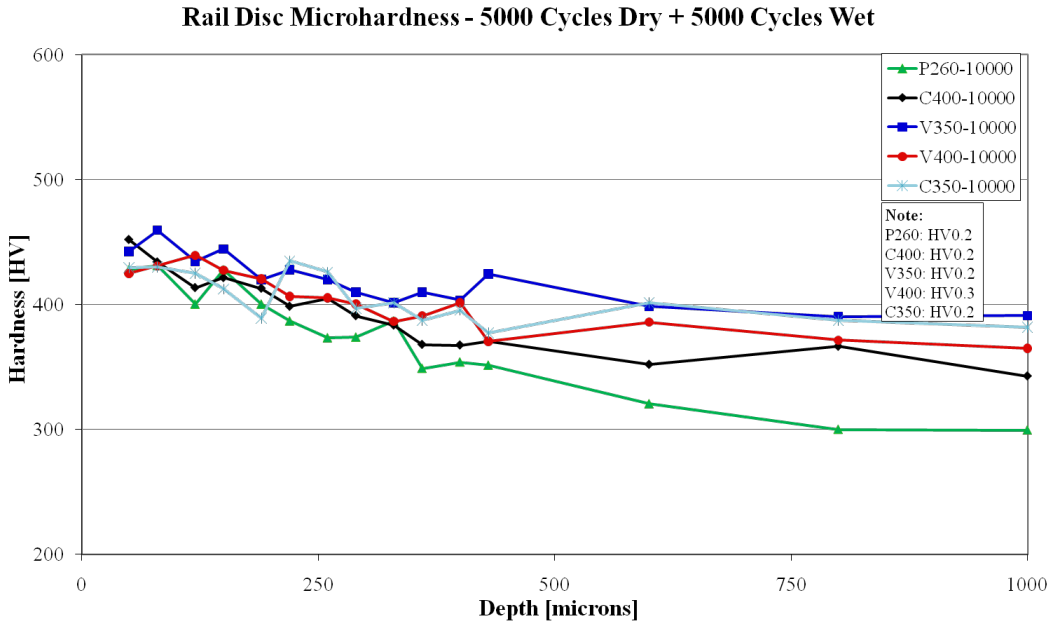

Figure 4.5 Microhardness measurements at various depths on circumferential cross-sections through rail disc specimens following 5000 cycles dry and 5000 cycles wet. Rail discs run against R7 wheel disc.

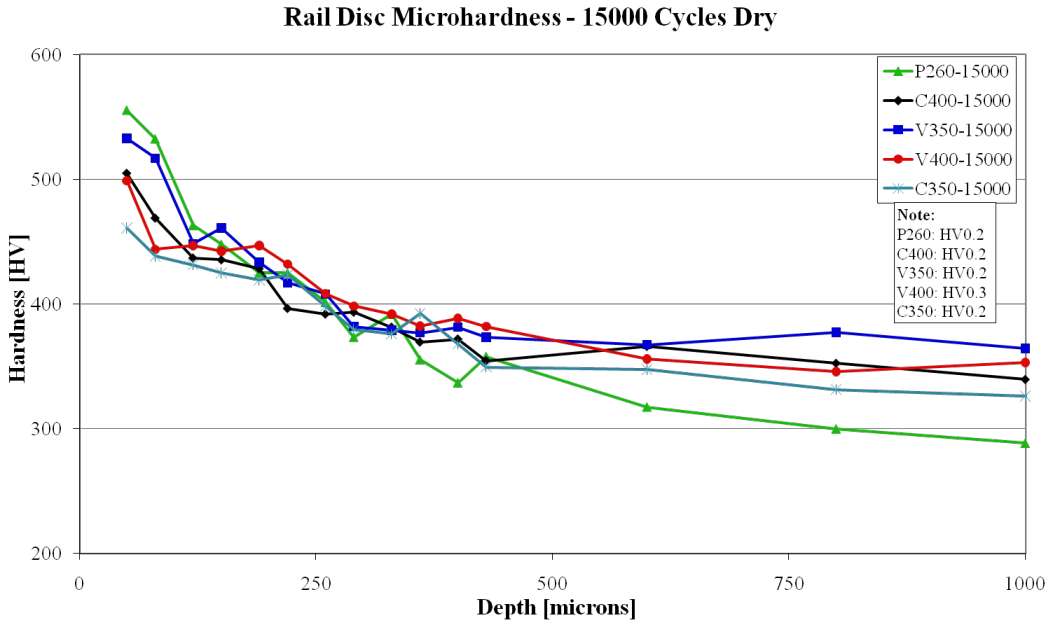

Figure 4.6 Microhardness measurements at various depths on circumferential cross-sections through rail disc specimens following 15000 cycles dry. Rail discs run against R7 wheel disc.

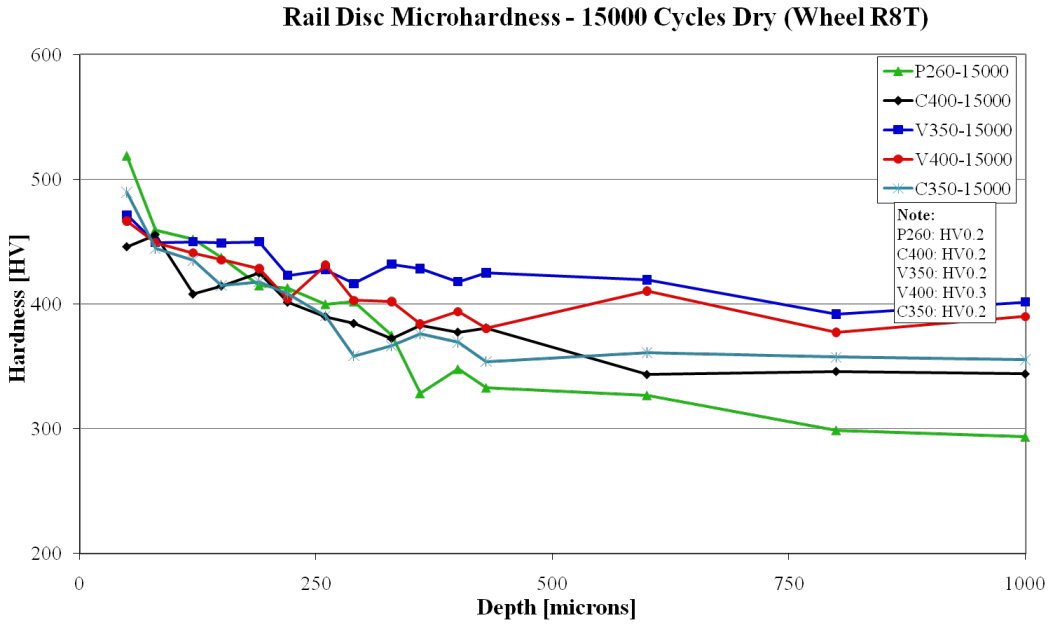

Figure 4.7 Microhardness measurements at various depths on circumferential cross-sections through rail disc specimens following 15000 cycles dry. Rail discs run against R8T wheel disc.

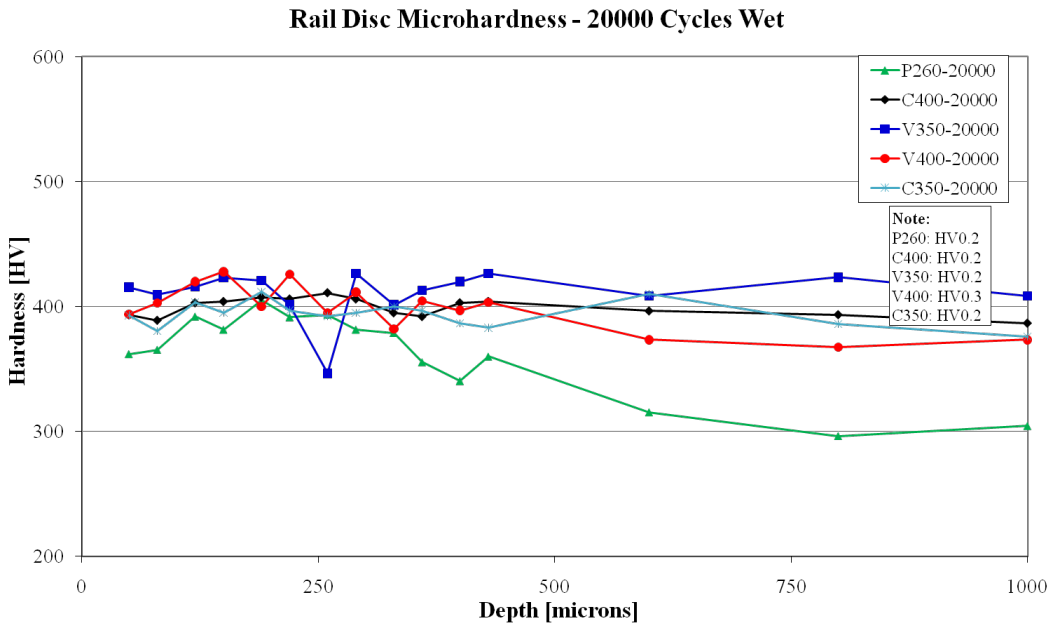

Figure 4.8 Microhardness measurements at various depths on circumferential cross-sections through rail disc specimens following 20000 cycles wet. Rail discs run against R7 wheel disc.

Graphs of microhardness measurements to 10000 microns in depth for each rail and wheel material are given in Appendix C.

Microhardness of the R7 wheel discs run for 15000 cycles dry is given in Figure 4.9, and microhardness of the R8T wheel discs run for 15000 cycles dry is given in Figure 4.10. Both figures show the same hardening trend, where discs harden at the surface and hardness drops with the depth into the material. On average, wheel steel material R7 hardens slightly more than R8T, but the difference is minimal. Average hardness of these 2 materials before twin-disc testing is 219HV for R7 and 257HV for R8T, so the latter is harder. Looking at the microhardness measured after the tests, the materials hardened the most for 15000 cycles dry then 10000 (5000 dry + 5000 wet) and the least for 5000 cycles dry.

There is no obvious difference in hardening behaviour of these 2 materials when run against different rail steels. After 15000 cycles dry, the wheel disc microhardness at depth 50 microns correlates with the rail disc microhardness at depth 50 microns, i.e., the P260 was the hardest at this depth, then the V350, and finally the C400 and V400, and the corresponding wheel discs matched this order of hardness. However, there is no matching trend after 5000 cycles.

From just looking at hardness, there is no clear conclusion about how different rail materials influence hardening of the wheel material in cyclic loading.

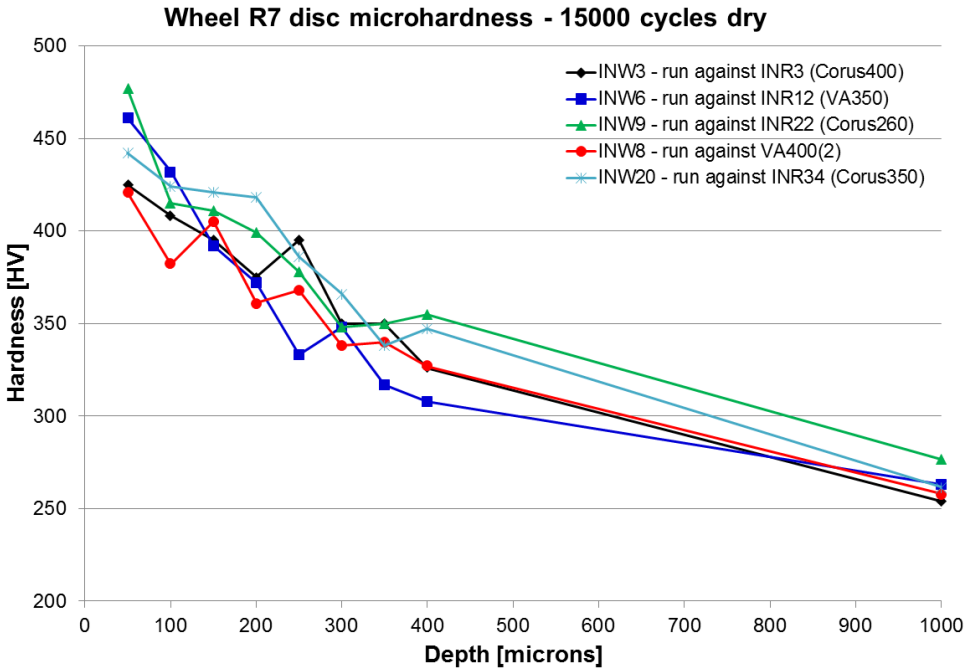

Figure 4.9 Microhardness measurements at various depths on circumferential cross-sections through wheel disc specimens, material R7, following 15000 cycles dry.

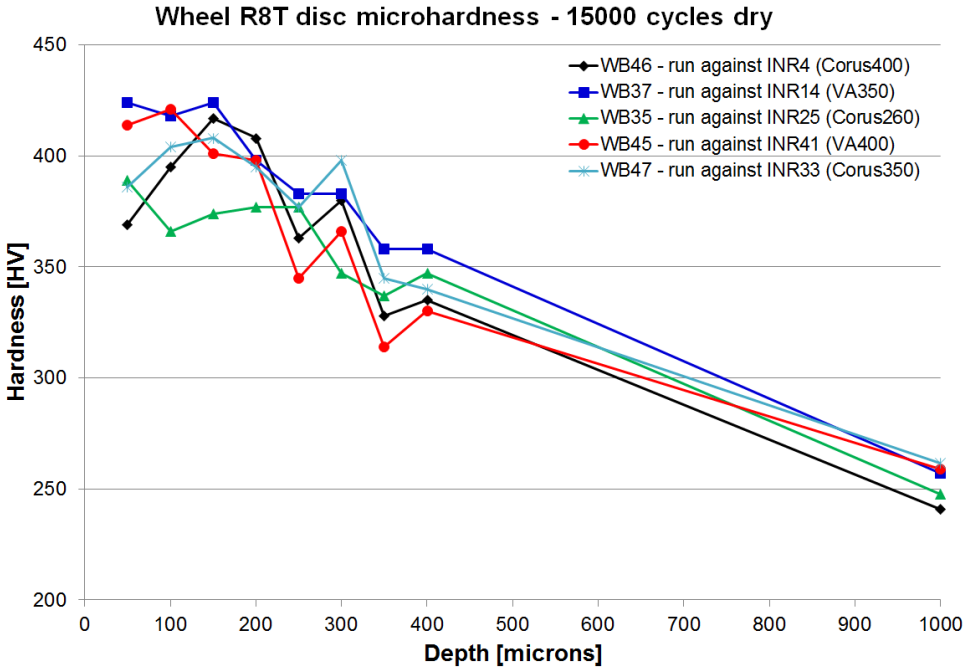

Figure 4.10 Microhardness measurements at various depths on circumferential cross-sections through wheel disc specimens, material R8T, following 15000 cycles dry.

4.4 Plastic deformation measurements and results (strain)

During tractive rolling, material below the contact surface gets plastically deformed and shear strain accumulates. This deformation plays an important role in wear and crack initiation. In this chapter, metallographic techniques are used to study microstructural changes of material after twin-disc testing in order to determine the plastic shear strain distribution.

Images were taken using an optical microscope with an integrated camera connected to a computer.

Optical micrographs of cross-sections of rail discs tested for 15000 cycles, and some images with measurements, are given in this chapter; images of all tested samples are presented in Appendix B.

4.4.1 Shear strain measurement technique

The strains are estimated using a method similar to those explained by Menezes *et al*., 2009, Garnham and Davis, 2008, and Tyfour *et al.*, 1995; see Figure 4.11. Figure 4.12 shows an optical micrograph of the disc section cut circumferentially, i.e., parallel to sliding/rolling direction (as explained previously in Chapter 4.2). Lines have been traced on the image which follow the visibly strained microstructure. The direction of traction is indicated by an arrow and it can be observed that strain lines are 'flowing' in the same direction. Deformation is more severe close to the surface, so flow lines become increasingly parallel towards the worn surface and then slightly curve out of the traction direction towards the normal to the surface (see Figure 4.12).

To measure shear strain as objectively as possible, several measurements were taken at each depth. Lines were drawn following material strain 'flow' lines (where these were visible), and angles and depths were measured (see Figure 4.12). In some cases, the image had to be rotated by up to three degrees, because the surface 0-line did not match perfectly the surface of the specimen (which is curved and cracked). Angles were measured to the horizontal (horizontal being parallel to the surface) so they had to be transformed to strain angles θ first (the strain angle is the angle to the vertical). Calculation of mean strain at each depth under the surface was done by averaging strain angles for each depth and then calculating shear strain as:

$$\gamma = \tan\theta,$$

where θ is the shear angle between the tangent to the deformed grain boundaries (flow line) and the normal to the contact surface (see Figure 4.11).

Graphs for average values at depths from the surface up to 170 microns for strain line, deformation angle to the horizontal and shear strain are presented for one disc specimen, V350 grade steel, 15000 dry, as an example in Figure 4.13.

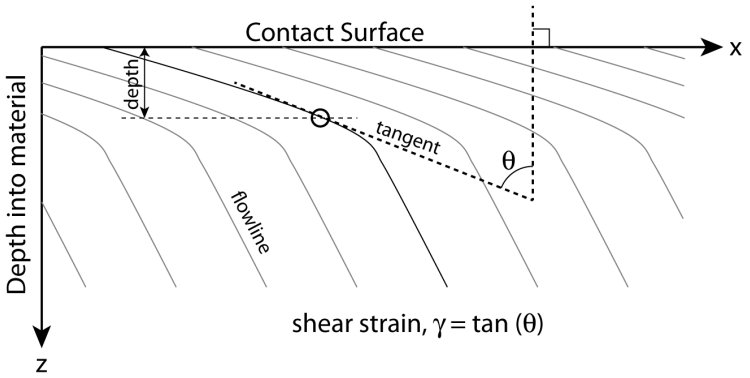

Figure 4.11 A sketch illustrating the method for estimating an angle θ, used for calculating shear strain γ beneath the surface.

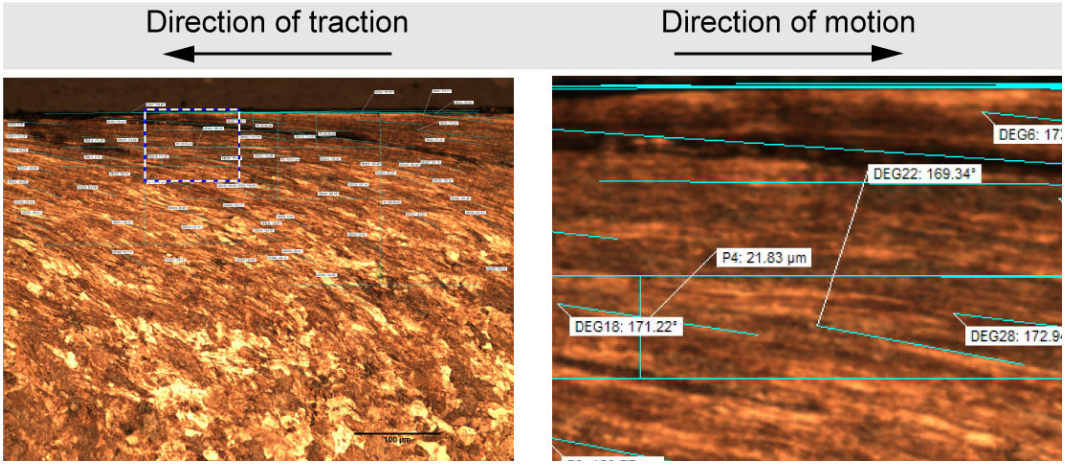

Figure 4.12 Microscope image of INR4, C400 grade steel, 15000 dry. Drawn lines follow material strain lines. Some depths and angles are presented for interpretation of data reading method. Right image is enlargement of the area within the white rectangle in the left image.

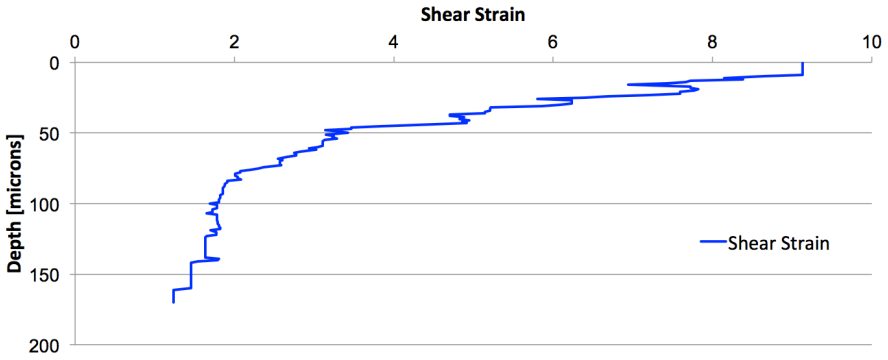

(a)

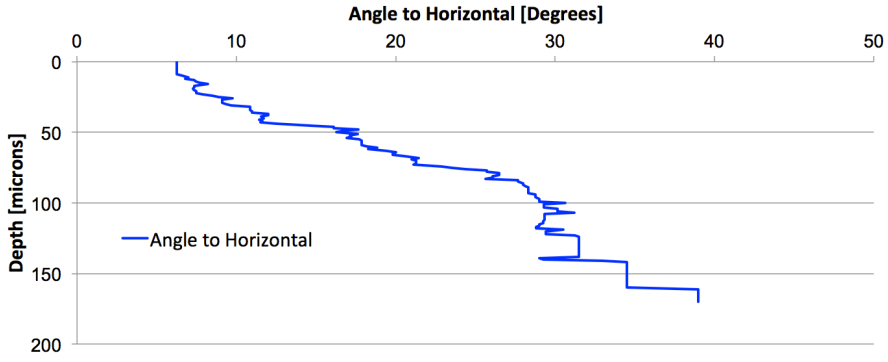

(b)

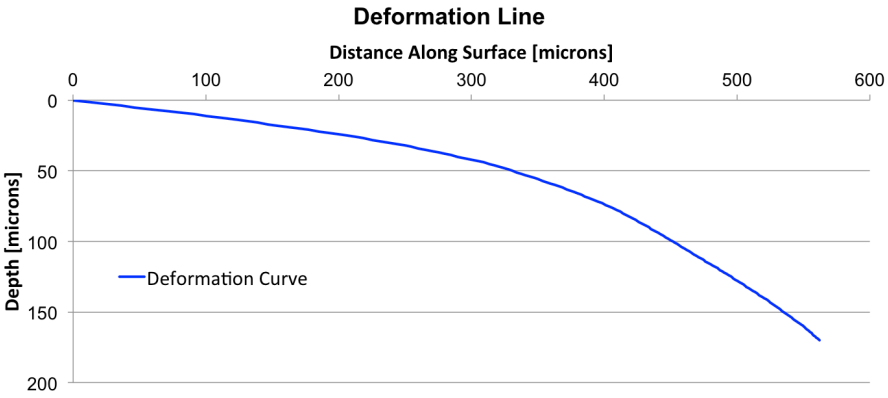

(c)

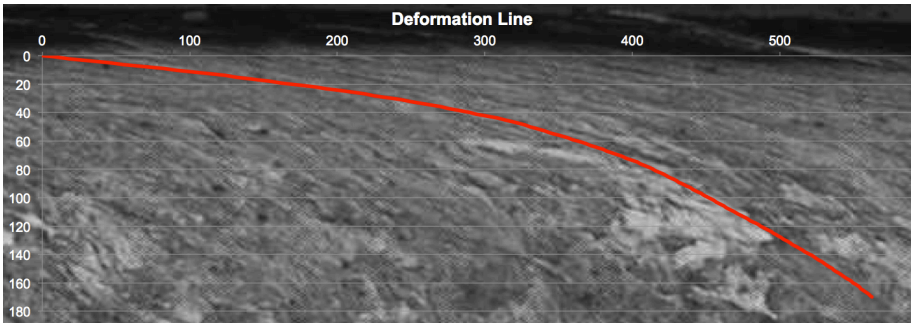

(d)

Figure 4.13 INR12, V350 Grade, 15000 cycles dry, average value at certain depth: (a) Shear strain vs depth, (b) Angle of flow lines to horizontal vs depth, (c) Deformation line vs depth, (d) deformation line with microstructure image in the background.

Some limitations of this method are:

- The depth of the deformed layer is not easily observed, because the flow lines become increasingly indistinct as the material is less and less deformed.
- The method may not be very accurate at, or closely beneath, the surface (within 50 μm), where a small change in shear angle results in a significant change of calculated strain.
- The edge of the surface is not easy to determine, because it is usually worn and cracked.
- The diameter of disc specimens is 47mm and the curvature can be seen even on the small width of the image, which makes it more difficult to determine shear angles and the normal to the surface.

4.4.2 Shear strain measurement results

Measured shear strains for the five investigated rail materials are presented in Figure 4.14 to Figure 4.18. Steel P260 plastically deforms and strains significantly more than the other steels. Under 20000 cycles wet, although the test is run for the longest period, the materials strain less than in other test types. For C400 and V400 it was not possible to measure strain after test 20000 cycles wet, because those materials experienced very low strain. C400 has variable performance: strains more than C350 for 15000 cycles dry tests and 10000 dry-wet test (see Figure 4.14, Figure 4.15 and Figure 4.17); less for 5000 cycles dry (see Figure 4.16), and not strained for 20000 cycles wet test (see Figure 4.18). The same variability is seen in core hardness (see Table 4.1).

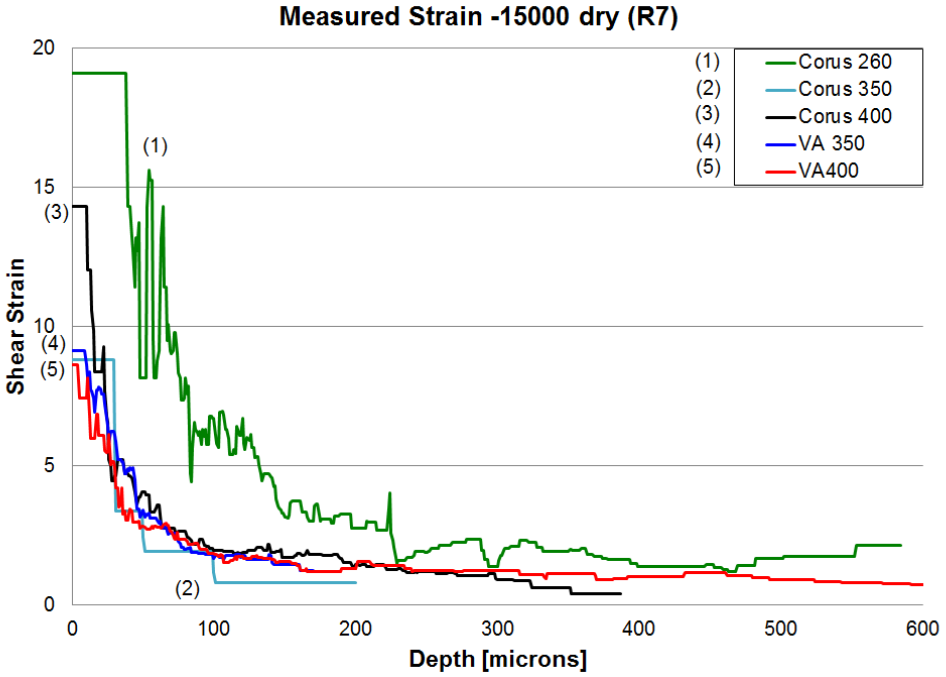

Figure 4.14 Measured strain vs depth. Conditions: 15000 cycles dry. Rail material discs run against wheel R7.

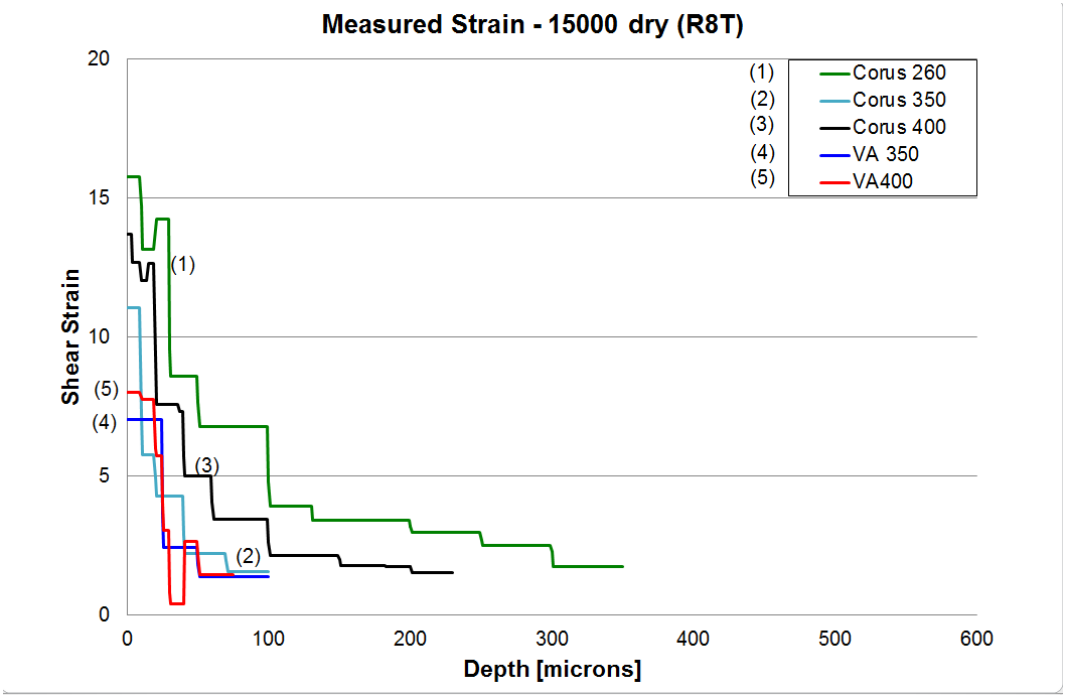

Figure 4.15 Measured strain vs depth. Conditions: 15000 cycles dry. Rail material discs run against wheel R8T.

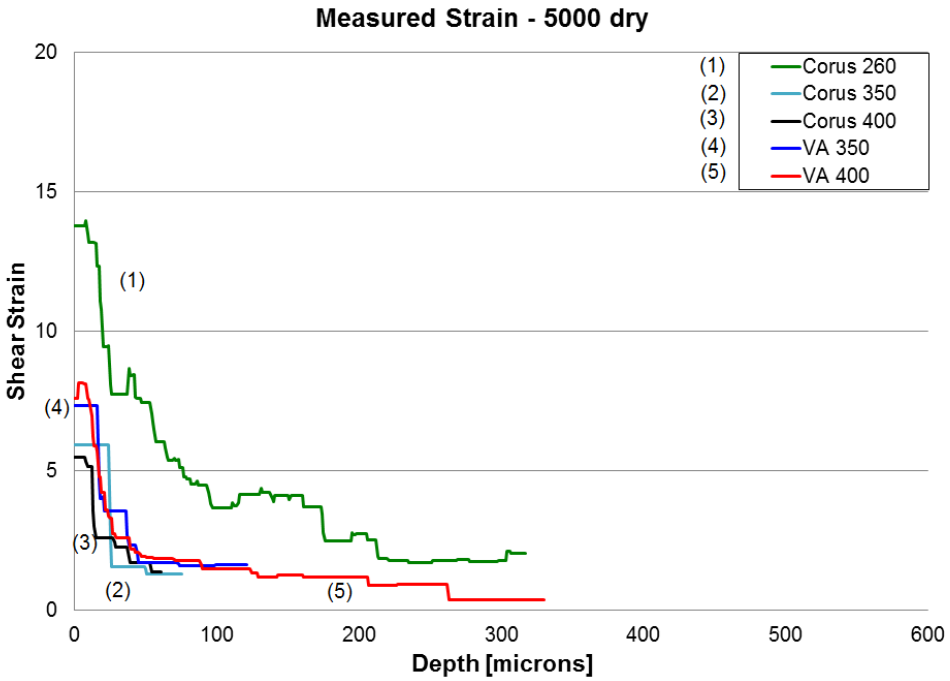

Figure 4.16 Measured strain vs depth. Conditions: 5000 cycles dry.

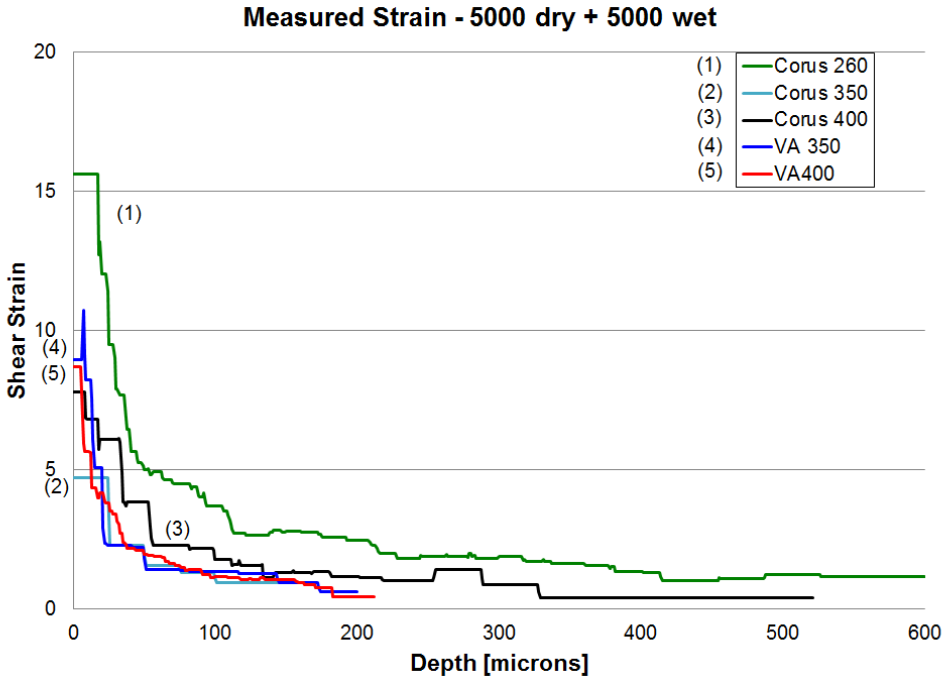

Figure 4.17 Measured strain vs depth. Conditions: 5000 cycles dry + 5000 cycles wet.

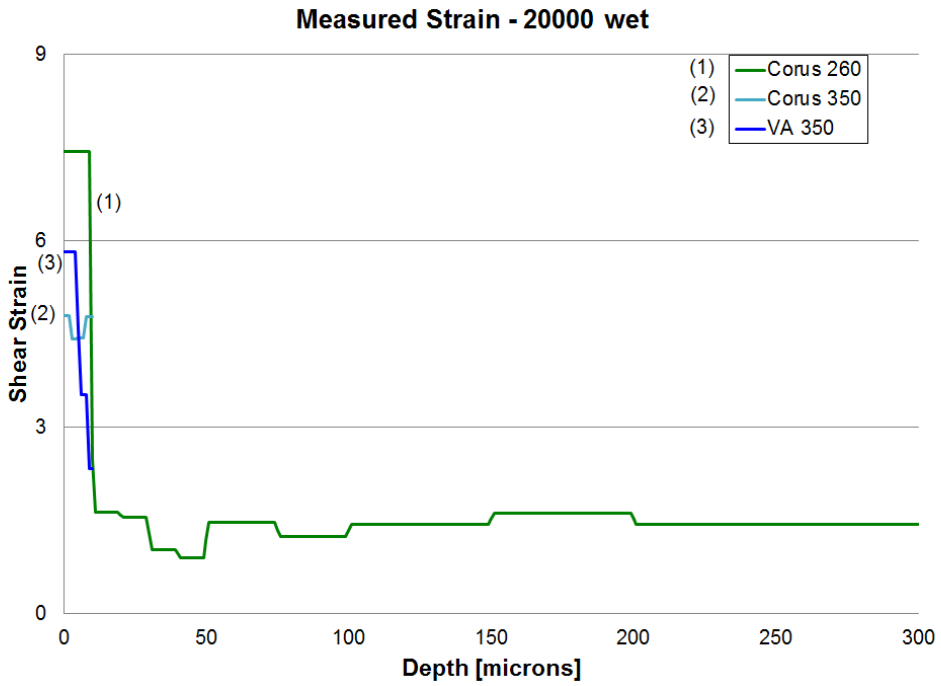

Figure 4.18 Measured strain vs depth. Conditions: 20000 cycles wet. C400 and V400 could not be measured, since no clear residual strain could be distinguished.

4.4.3 Subsurface microstructure of tested steels

Optical micrographs of all disc cross-sections, unetched and etched, are given in Appendix B. Unetched images show cracks more clearly. The 5000 dry – 5000 wet tests damage the rail disc surfaces the most and produce the deepest cracks for all materials, compared to other types of testing; see example images in Figure 4.19 - Figure 4.22. The P260 steel cracks the most of all materials under these conditions, and the cracks go to the greatest depth, 0.65mm. Observations of material cracking and plastic deformation from microscopic images of 25 rail samples are summarised in Table 4.2 and Table 4.3. (Note: When reading comments in the table, it is useful to look at microscopic images given in Appendix B at the same time.)

Observations of material plastic deformation from the microscopic images of the 25 wheel samples are summarised in Table 4.4.

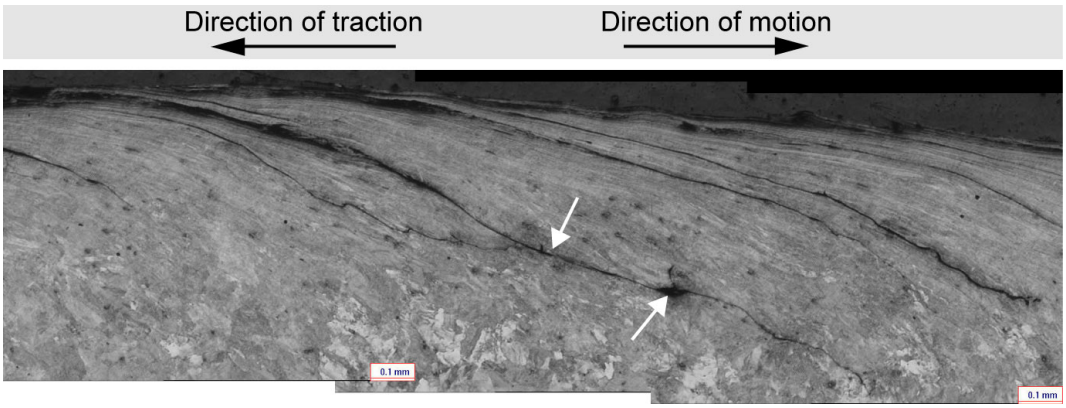

a) INR23 etched

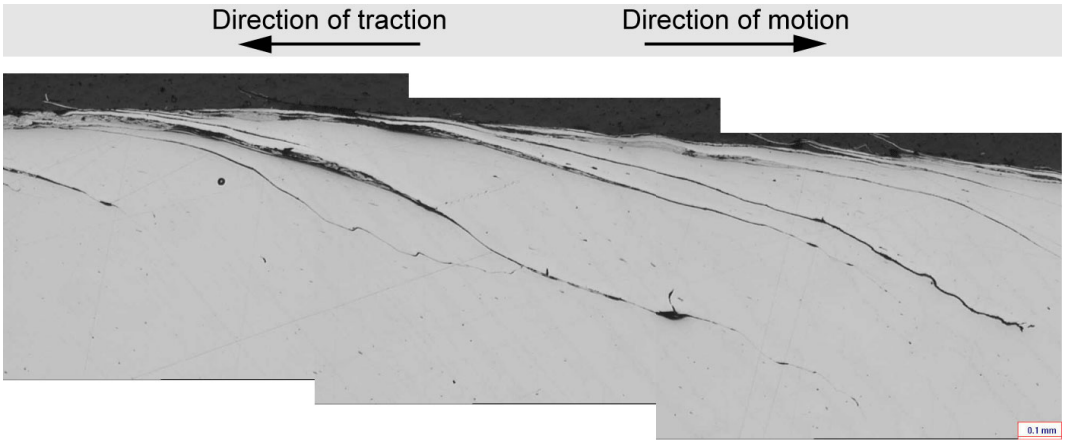

b) INR23 unetched

Figure 4.19 Optical microscope images INR23 (a) etched - top image and (b) unetched - bottom image, P260, 5000 cycles dry and 5000 cycles wet.

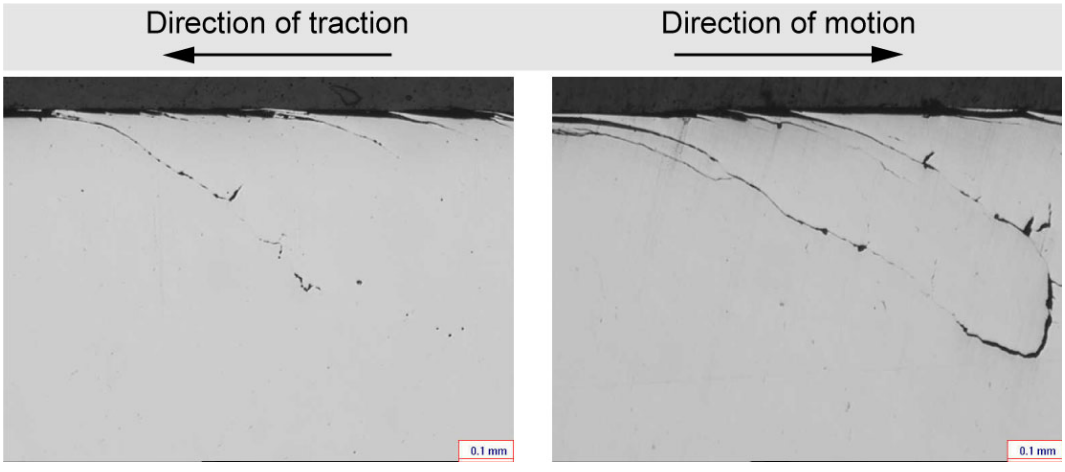

Figure 4.20 Optical microscope image INR2, C400, 5000 cycles dry and 5000 cycles wet.

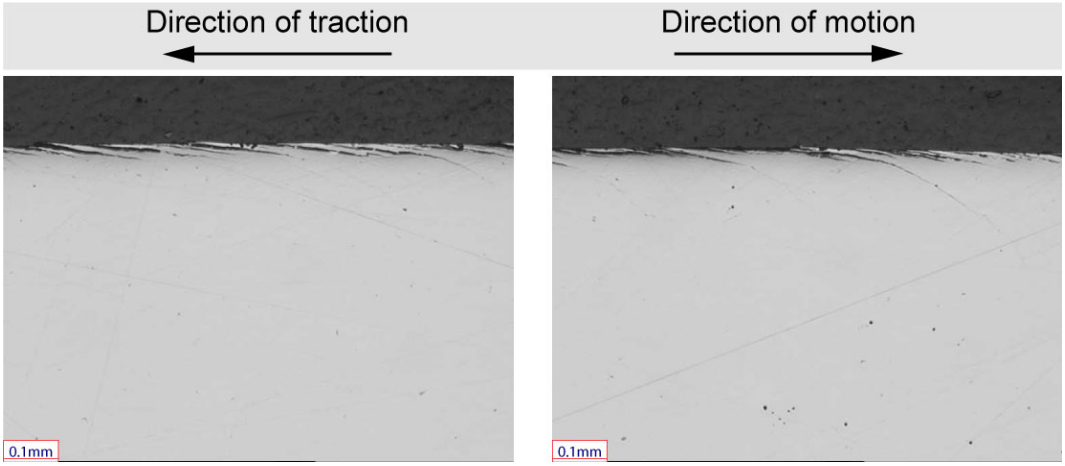

Figure 4.21 Optical microscope image INR11, V350, 5000 cycles dry and 5000 cycles wet.

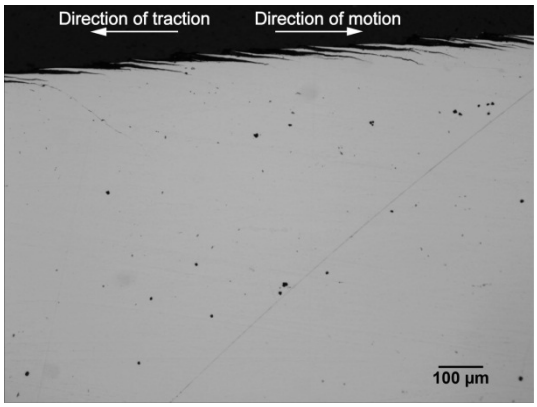

Figure 4.22 Optical microscope image INR31, C350, 5000 cycles dry and 5000 cycles wet.

Table 4.2 Severity of cracking, a qualitative judgment based on visual observation of spacing and depth of cracks.

	Material				
Condition	**P260**	**C350**	**C400**	**V350**	**V400**
5000 dry 5000 wet					
15000 dry R7					
15000 dry R8T					
5000 dry					
20000 wet					

Description	**Severely cracked**	**Very cracked**	**Moderately Cracked**	**Few cracks**	**Not cracked**
Colour code					

Table 4.3 Observations of cracks and material plastic deformation of rail steels

Test name INNOT-	**Rail disc id**	**Material type**	**Test cycles**	**Observation of cracks, depth and spacing**	**Plastic deformation and depth**
01	INR1	C400	5000 dry	Hardly any cracks. Some don't have pattern and go to depth of 0.05mm.	Severe: 0.04mm. Deformed: 0.1mm.
02	INR2	C400	5000 dry + 5000 wet	Cracked a lot. Crack after crack. Space between mouths 0.15-0.20mm.	
03	INR3	C400	15000 dry	Some cracks. Not equal spacing. At some point 0.25mm distance. Few cracks go to depth of 0.1mm.	
04	INR10	V350	5000 dry	Usually no cracks, only few. At some point 3 cracks in a row.	
05	INR11	V350	5000 dry + 5000 wet	Regular cracks on surface. Space between mouths 0.06-0.1mm.	
06	INR12	V350	15000 dry	Severe cracks. Distance between not uniform 0.2-0.5mm.	
07	INR24	P260	5000 dry	Not cracked.	
08	INR23	P260	5000 dry + 5000 wet	Cracked a lot. Crack after crack with tips between cracks at un- uniform distance . Deep cracks up to 0.65mm.	
09	INR22	P260	15000 dry	Cracked a lot, but shallow cracks at the surface.	
10	VA400(1)	V400	5000 dry	Only few cracks.	Plastically uniformly deformed at the surface
11	VA400(2)	V400	15000 dry	Few deep cracks, not uniformly spaced.	
12	VA400(3)	V400	5000 dry + 5000 wet	Cracked a lot.	
13	INR30	C350	5000 dry	Not cracked at all.	
14/41	INR31	C350	5000 dry + 5000 wet	Cracked a lot. Cracks next to each other, usual depth 0.07mm. Peeks peel off. Cracks follow plastic deformation. Crack goes deep as 0.29mm.	0.020mm severely damaged.

Table 4.3-continuing Observations of cracks and material plastic deformation of rail steels

Test	**Rail disc**	**Material**	**Test cycles**	**Observation of cracks, depth and spacing**	**Plastic deformation and depth**

name INNOT-	**id**	**type**			
51	INR34	C350	15000 dry	Cracked with shallow cracks at the surface that are separating. Spacing is more or less uneven.	
16	INR36	C350	20000 wet	Not cracked at all.	Hardly any deformation
17	INR26	P260	20000 wet	Not cracked at all.	Sub-surface deformation
18	INR7	C400	20000 wet	Not cracked at all.	
19	INR40	V400	20000 wet	Not cracked at all.	
21	INR16	V350	20000 wet	Not cracked at all.	Tiny deformation at surface
22	INR25	P260	15000 dry (R8T)	Cracked on surface, but not deep cracks.	
23	INR33	C350	15000 dry (R8T)	Cracked.	Severe: 0.05mm Deformed: 0.2mm
24	INR4	C400	15000 dry (R8T)	Not cracked much, few surface cracks.	
25	INR14	V350	15000 dry (R8T)	Uneven surface, tiny cracks on surface. More or less evenly spaced (0.15mm).	
26	INR41	V400	15000 dry (R8T)	Cracked on surface. More or less evenly spaced (0.2mm) cracks or crack initiations. Cracks are different shapes, sizes lengths.	

Table 4.4 Observations of material plastic deformation of wheel steels, most discs were material R7. It is stated in the table where the material was different (R8T)

Test name INNOT-	**Wheel disc id**	**Tested against rail material type**	**Test cycles**	**Observation of cracks**
01	INW1	C400	5000 dry	Usually not cracked. Few tiny cracks on surface unevenly spaced. Rough surface.
02	INW2	C400	5000 dry + 5000 wet	Cracked at surface, evenly spaced shallow cracks (0.4mm).
03	INW3	C400	15000 dry	Shallow cracks at the surface, at places evenly spaced (0.25mm).
04	INW4	V350	5000 dry	Uneven rough surface with several shallow cracks with different lengths.
05	INW5	V350	5000 dry + 5000 wet	Few short shallow cracks.
06	INW6	V350	15000 dry	Uneven cracked surface with long shallow cracks.
07	INW14	P260	5000 dry	Surface uneven, but not cracked. Only few short shallow cracks.
08	INW13	P260	5000 dry + 5000 wet	Part of the surface not cracked and smooth. Few parts of the surface have long shallow cracks.
09	INW9	P260	15000 dry	Cracked at surface, evenly spaced shallow cracks (0.15-0.25 mm), delaminating.
10	INW7	V400	5000 dry	*No observations made.*
11	INW8	V400	15000 dry	*No observations made.*
12	INW12	V400	5000 dry + 5000 wet	*No observations made.*
13	INW21	C350	5000 dry	Not cracked at all.
14/41	INW16	C350	5000 dry + 5000 wet	Cracked at surface, evenly spaced shallow cracks (0.28mm), delaminating.
51	INW20	C350	15000 dry	Cracked a little, not evenly spaced cracks.
16	INW17	C350	20000 wet	Not cracked at all.
17	INW10	P260	20000 wet	Not cracked at all.
18	INW15	C400	20000 wet	Not cracked at all.
19	INW23	V400	20000 wet	Not cracked at all.
21	INW24	V350	20000 wet	Not cracked at all.
22	WB35 (R8T)	P260	15000 dry	Cracked with uneven cracks, but not severely. Rough surface.
23	WB47 (R8T)	C350	15000 dry	Usually not cracked. Tiny cracks on surface, unevenly spaced.

24	WB46 (R8T)	C400	15000 dry	Not cracked. Shallow cracks on surface, uneven distance between cracks: 0.155, 0.233, 0.375, 0.164mm.
25	WB37 (R8T)	V350	15000 dry	Not cracked at all, only few minor cracks.
26	WB45 (R8T)	V400	15000 dry	Cracked a little, just few small cracks.

The micrographs in Figure 4.23a – Figure 4.27a show undeformed microstructure, and are taken from discs tested for 5000 cycles dry, 10mm under the running surface (except for C350 grade, which was taken 5mm under surface), because material deformation should not have had a 'visible' effect at this depth. Figure 4.23b – Figure 4.27b show surfaces of discs with the same material and magnification, for comparison of how much grains changed after tests. Comparing the undeformed structure between these 5 materials, it can be seen that material P260 has the largest grains and mixture of different sizes, shapes and colour (material). Both C350 and C400 have the finest grains, the smallest and more uniform. V350 and V400 are somewhere in the middle, with V400 having finer, smaller grains than V350.

The most plastic deformation is observed on the samples that were tested for 15000 dry cycles, so subsurface microstructure of 5 different materials, after this type of test, is presented here. All samples show the highest plastic deformation under the surface with changed microstructure properties from the rest of the material. Grains are so elongated that they form layers of material lying under the shallow angle (roughly 3-10º) to the surface. The depth of this layer is different for each material.

The flow lines of strain are apparent in micrographs of sections of specimens through the distortion of the microstructure and the paths of near-surface cracks. This is more noticeable with tests performed dry than lubricated conditions.

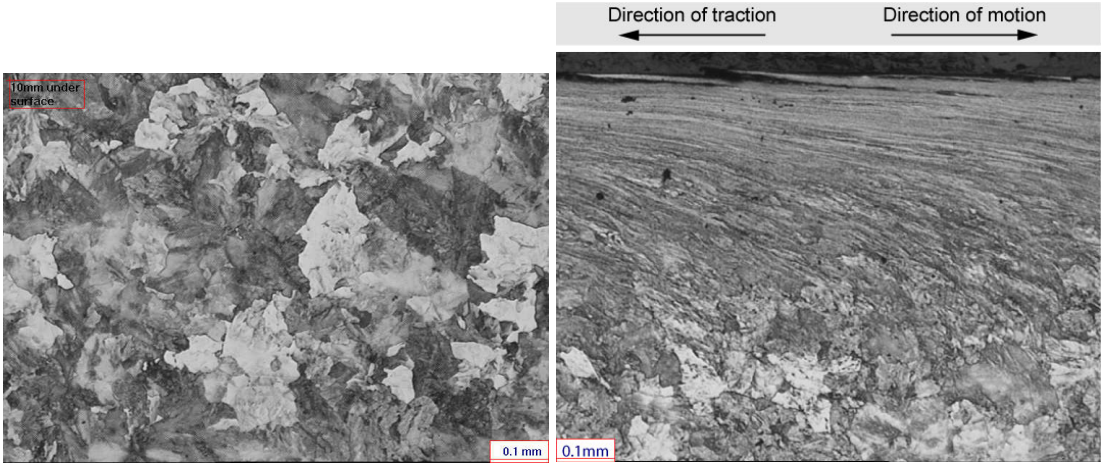

(a) (b)

Figure 4.23 Optical microscope image, material Corus 260 grade: (a) rail disc INR24, 10mm under the surface, test 5000 cycles dry; (b) rail disc INR22, test 15000 cycles dry.

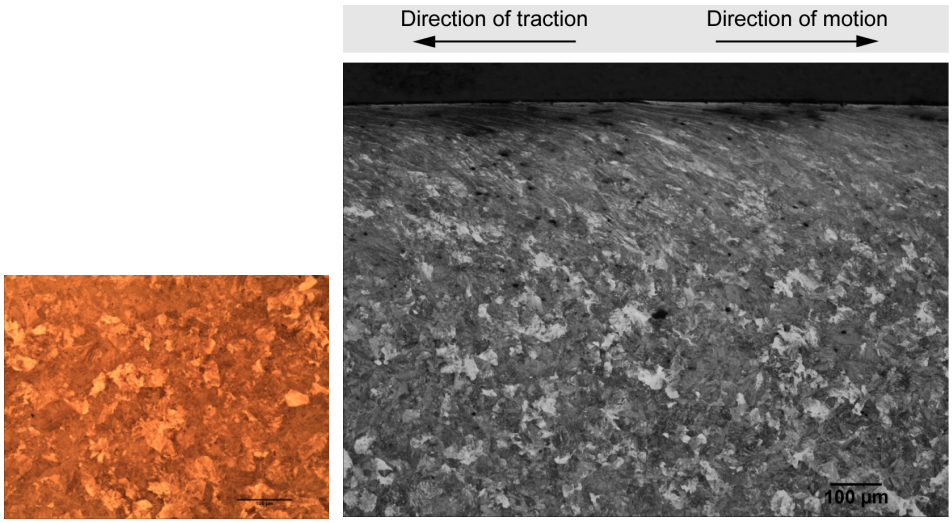

(a) (b)

Figure 4.24 Optical microscope image, material C350 grade: a) rail disc INR30, 5mm under the surface, test 5000 cycles dry; b) rail disc INR34, test 15000 cycles dry.

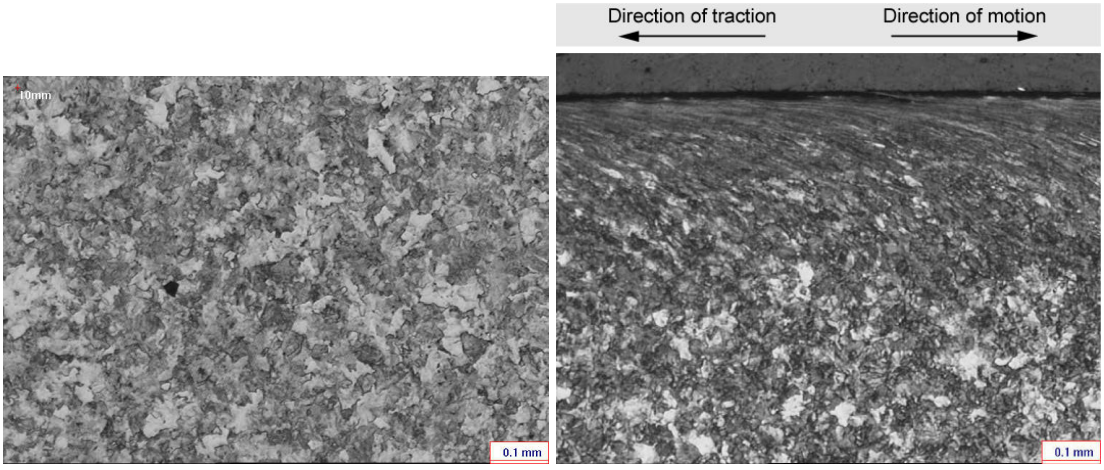

(a) (b)

Figure 4.25 Optical microscope image, material C400 grade: (a) rail disc INR1, 10mm under the surface, test 5000 cycles dry; (b) rail disc INR3, test 15000 cycles dry.

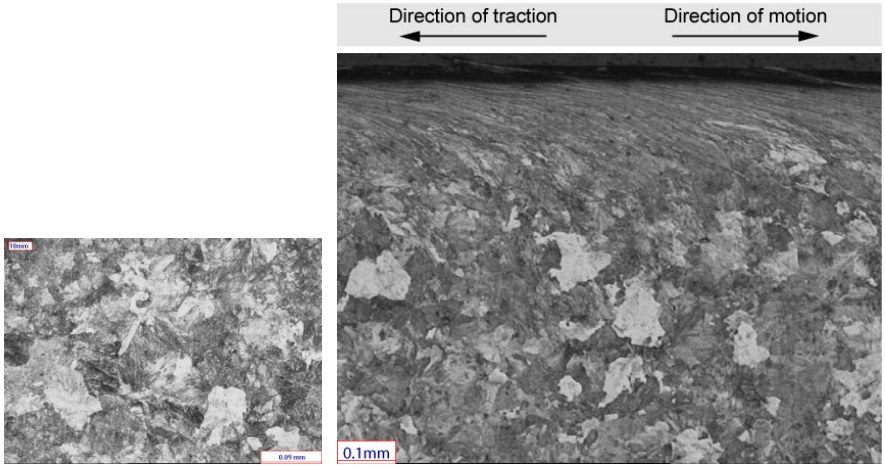

(a) (b)

Figure 4.26 Optical microscope image, material V350 grade: (a) rail disc INR10, 10mm under the surface, test 5000 cycles dry; (b) rail disc INR12, test 15000 cycles dry.

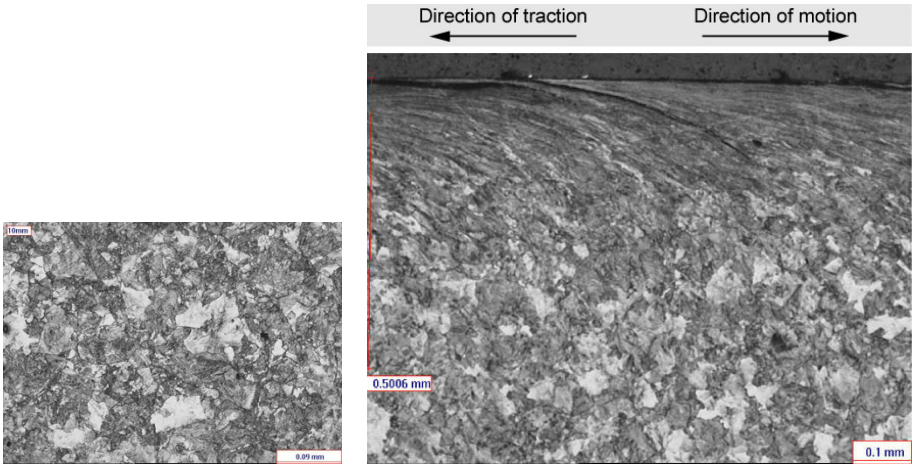

(a) (b)

Figure 4.27 Optical microscope image, material V400 grade: (a) rail disc VA400(1), 10mm under the surface, test 5000 cycles dry; (b) rail disc VA400(2), test 15000 cycles dry.

4.5 ESEM images

ESEM images were taken of disc surfaces to compare deterioration under same testing condition, 15000 cycles dry, of different materials, see Figure 4.28, and of the same material C350 grade, under different testing conditions, see Figure 4.29. These images show how cracks form on the surface. The start of the crack is a flattened grain, and it has different size for different materials, see Figure 4.28. It gives different impression of surface cracking when looked at magnification 100x or 500x. Looking at Figure 4.29, the C350 has different surface texture for different conditions. The dry-wet test causes the most surface damage. The material is flaked and cracks are circular with rough wavy edges. If looked at with magnification of 500x, grains are flattened and overlap,

and it is clear how they delaminate and flake. Dry tests also cause surface damage, where the cracks start forming in the same way as semi-circular with a wavy edge, and grow bigger with number of cycles. The texture is very different in wet tests. Although the duration of the test was the longest, 20000 cycles, the surface is not cracked much. It has more dense shallow pits with only a few cracks opening, and they are more linear than circular. This wet test showed the least wear.

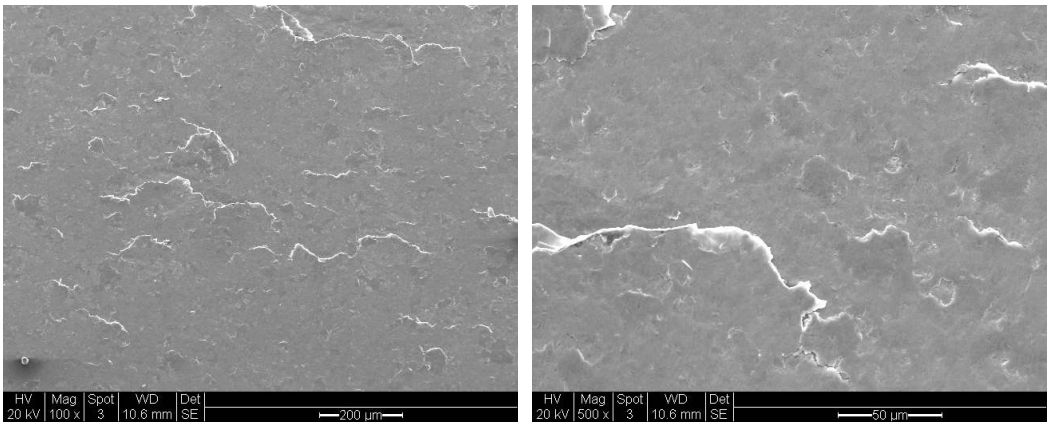

Disc number INR4, material C400

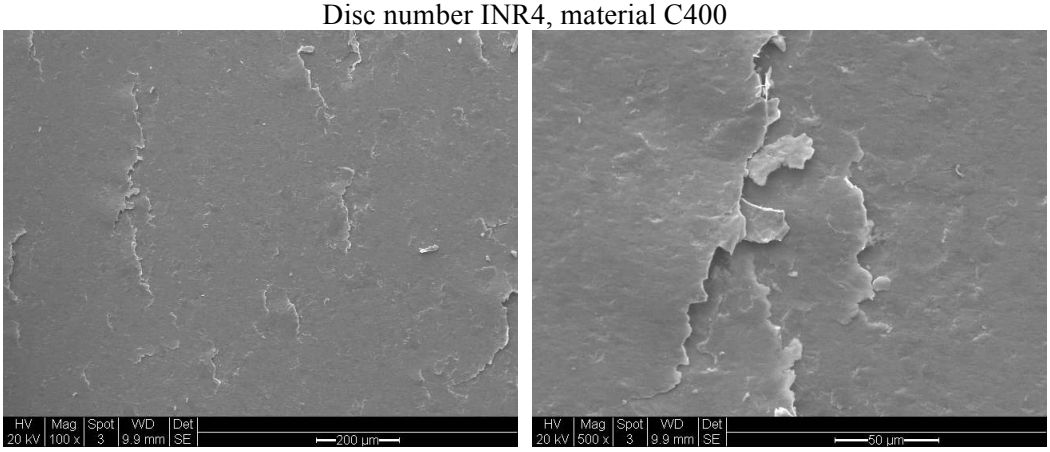

Disc number INR25, material P260

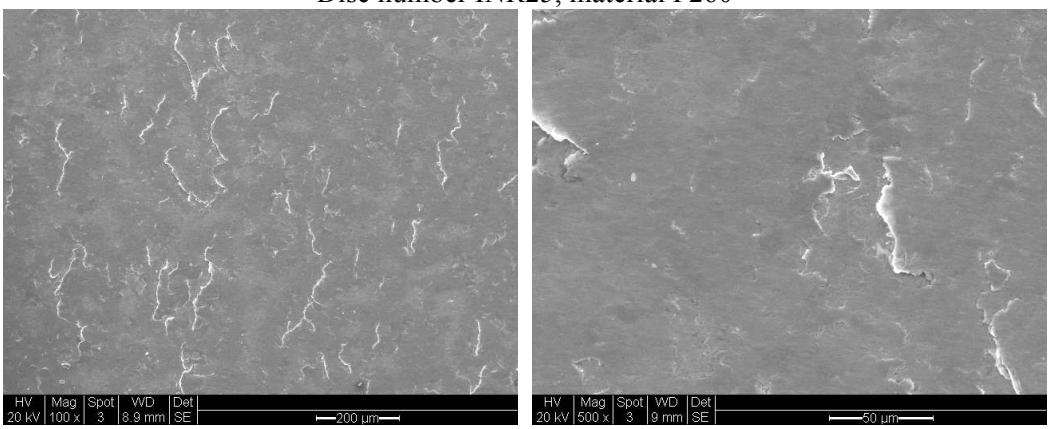

Disc number INR41, material, V400

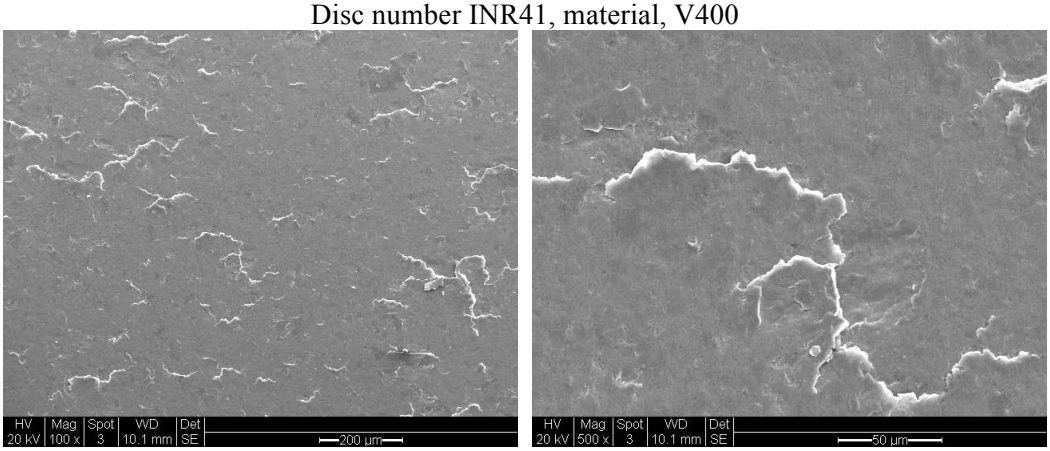

Disc number INR33, material, C350

Figure 4.28 Comparative ESEM views of track surfaces for 4 steels run for 15000 cycles, dry, against wheel material R8T. Left images are 100x magnification and right are 500x magnification of the same material.

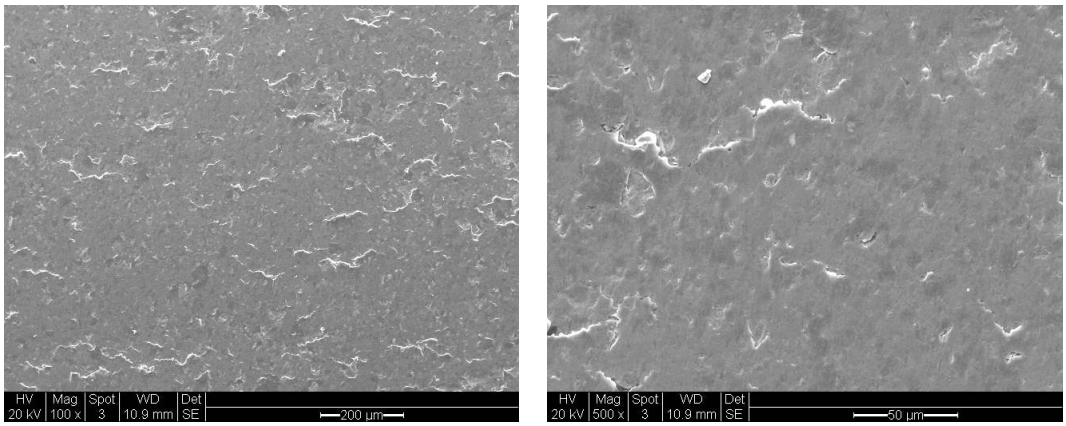

Disc number INR30, 5000 dry

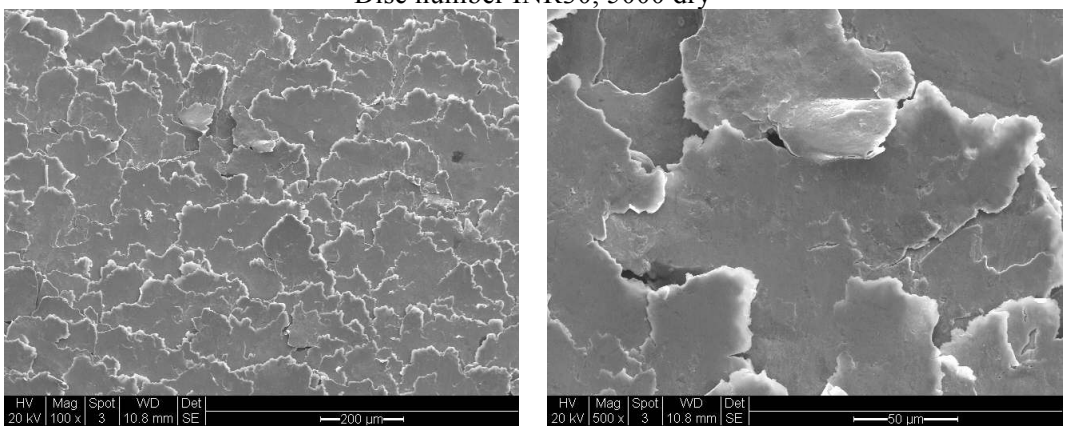

Disc number INR31, 5000 dry + 5000 wet

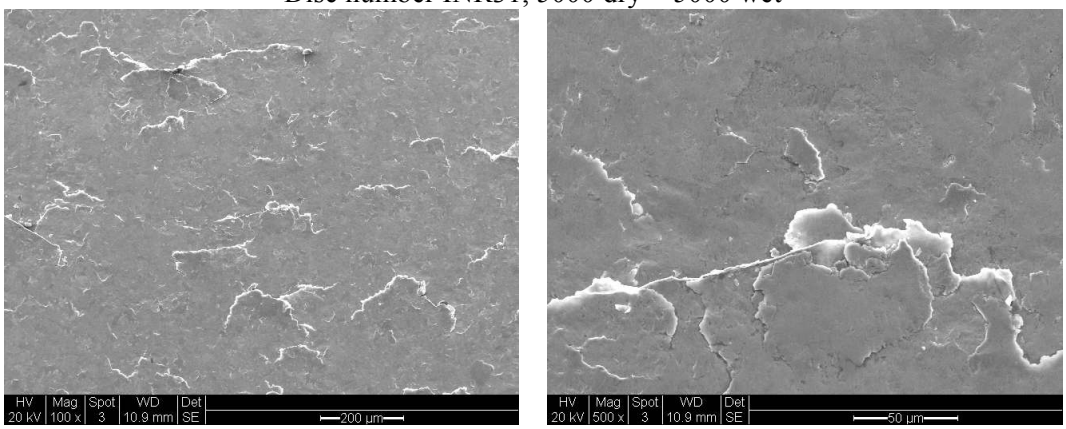

Disc number INR34, 15000 dry

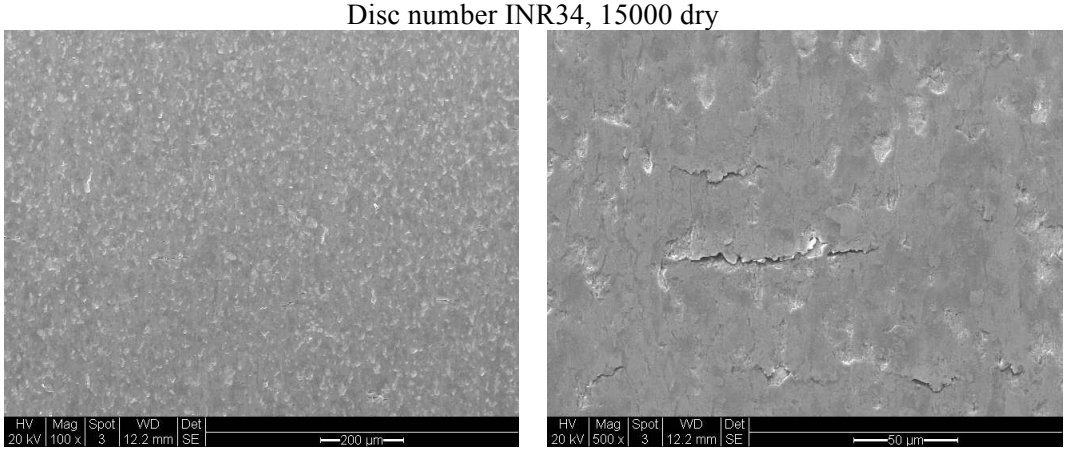

Disc number INR36, 20000 wet

Figure 4.29 Comparative ESEM views of track surfaces for steel C350, for different test conditions. Discs are run against wheel material R7. Left images are 100x and right are 500x magnification of the same disc.

Cross-section of the same material C350 under 2 distinctive test conditions where the most cracking would be expected, is shown for INR 31 for 5000 dry + 5000 wet in Figure 4.30, and INR33 for 15000 dry in Figure 4.31. A close up is given of one of subsurface cracks. It is possible that these belong to larger surface-breaking cracks not visible in the cross-section.

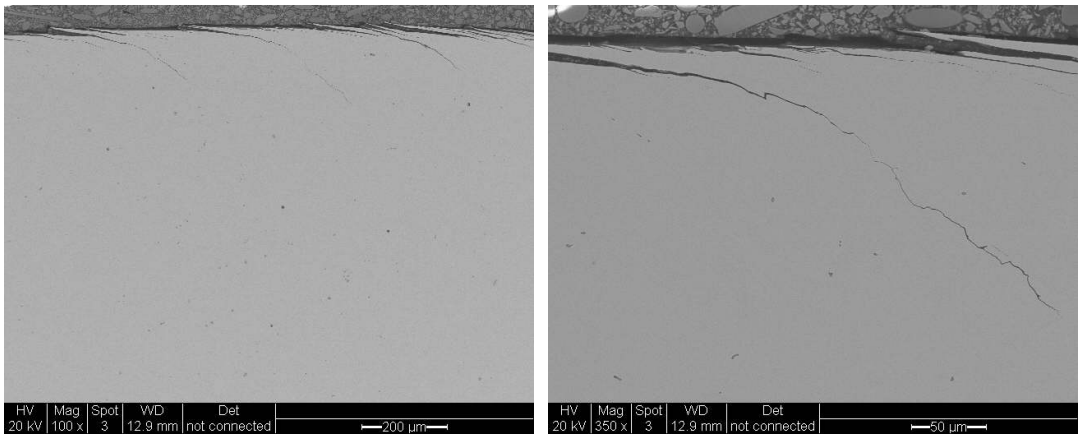

Figure 4.30 ESEM images of INR31, C350, 5000 dry + 5000 wet, cross-section. Left image is section of cracks starting at surface. Right image of cracks magnified. Cracks are separating from the surface. Crack on the right image goes to a depth of 200 microns.

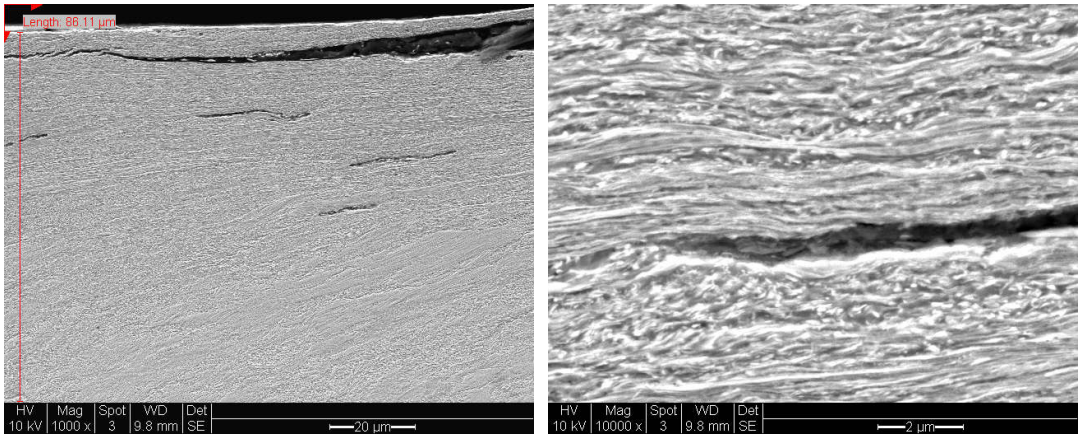

Figure 4.31 ESEM images of INR33, C350, 15000 dry, cross-section. Left image is section of crack just under surface. Crack is separating from the surface. Right image of subsurface crack magnified. Both cracks follow flow lines of strained material.

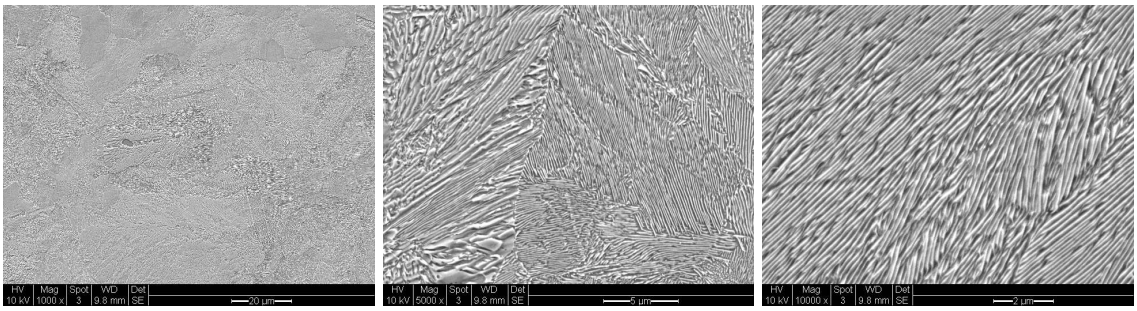

Figure 4.32 ESEM images of INR33, C350, 15000 dry, cross-section at 2mm depth of material, different magnification. Pearlitic microstructure with visible lamellae.

Sizes of grains of INR33, Figure 4.32, are not easy to measure since it is a fully pearlitic structure with no ferrite boundaries like in R220 steel. Thus it is difficult to make out boundaries. Lamellae within grains are, however, oriented in different directions.

4.6 Discussion

Comparing microscopic images and micro-hardness graphs (see Figure 4.4 to Figure 4.8), it can be seen that hardening goes to much greater depths than indicated by material strain distortion.

The depth of hardening and plastic deformation is greater in rails in service than in rail samples from twin-disc tests. As an example, for R260, the hardening depth of the rail is 5mm compared with 1mm for test discs, measured by Garnham *et al*., 2010.

4.6.1 Hardness – wear correlation

The influence of the hardness of the rail material on deformation, wear and cracking of the wheel material, and vice versa, is not as widely researched as the influence of rail hardness on its own wear rate.

For example, see Figure 4.6 and Figure 4.7, the near surface material of the rail discs hardens slightly more against the R7 wheel discs than against the R8T.

When looking at SUROS test wear data (see Table 3.4) and disc material hardness, some conclusions on their correlation can be made, although the dependence is not straightforward.

Wear rates for all materials and tests are presented in Figure 4.33. Dry-wet tests deteriorated the softer material more so the wear rate is significantly higher than in dry tests. For all discs run just wet for 20000 cycles, the wear is negligible, one order of magnitude smaller than in the dry tests, with values ranging from 0.984μg/cycle for the P260 to 0.290μg/cycle for V400 (the hardest of the rail steels). V400 steel showed the lowest wear in general and its wear rate did not vary much with test duration or

environment, except for 20000 cycles wet. Initial dry wear of all discs is larger within the first 5000 cycles than in longer tests of 15000 cycles, for running against R8T only. Rail disc wear, depending on its own hardness in dry tests (see Figure 4.34), decreases when rail hardness increases. The same conclusion was reached by many researchers (e.g., Pointner, 2008) and it is in agreement with Archard's wear law (Archard, 1953). The difference in the rail disc wear rate in dry tests (against R7 wheel discs) between 5000 and 15000 cycles is greater for P260 than for the harder materials. However, it is possible that this is an anomaly (the wear rate of the P260 running against the R8T wheel disc is significantly lower) and further testing is recommended.

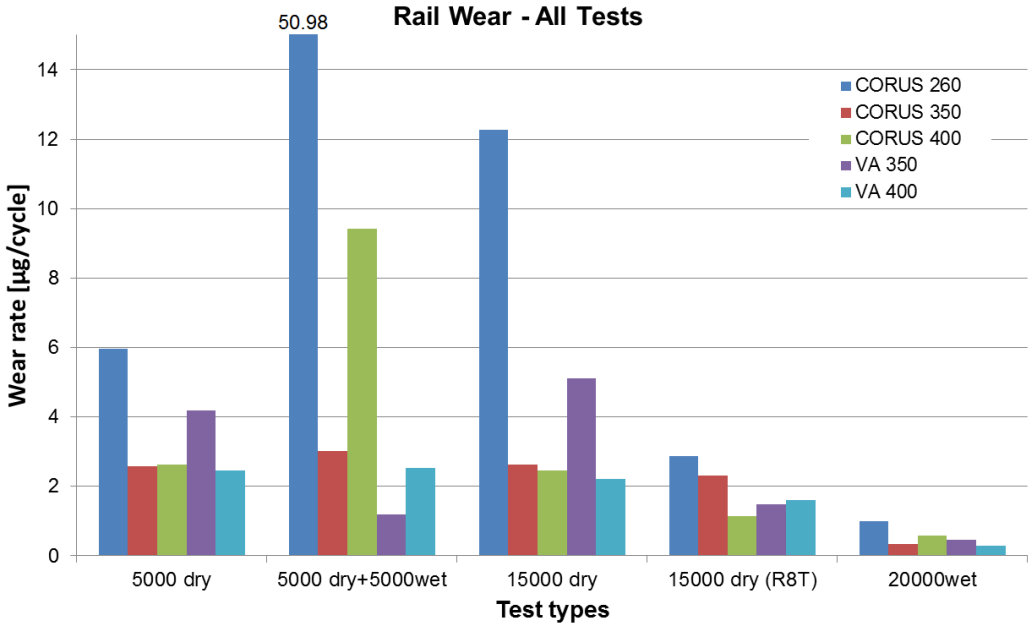

Figure 4.33 Rail wear – all tests. Note: 5000 cycles dry is average of 2 tests.

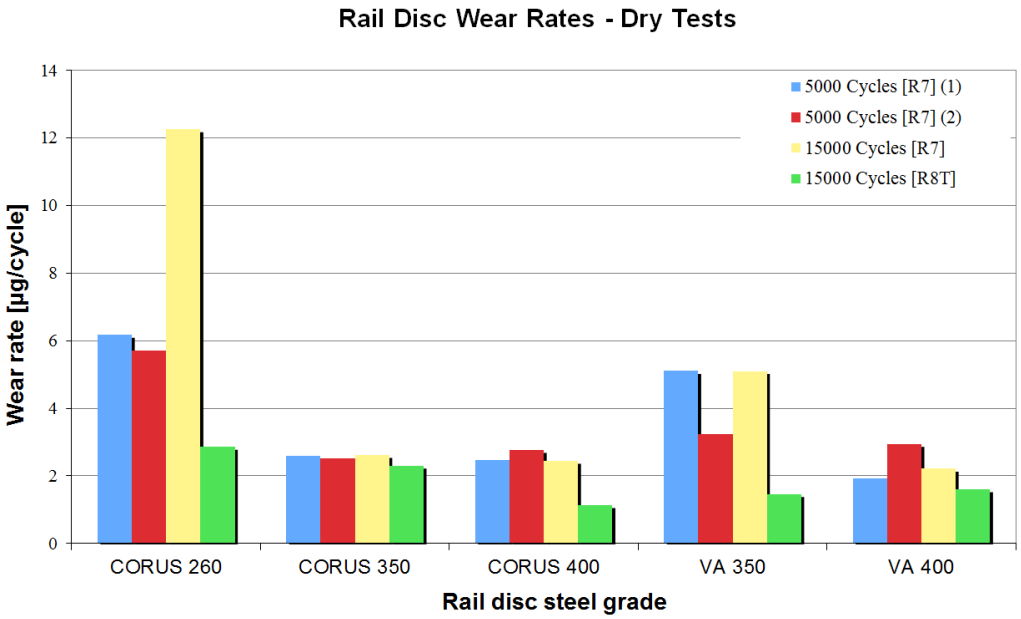

Figure 4.34 Rail disc wear rates during dry SUROS tests.

Wheel disc wear in dry tests (Figure 4.35) increased when run against the harder material V350 compared to the P260, but dropped when run against harder steels C400 and V400. However, for 5000 cycles, wheel wear is lowest when run against P260. In wet tests, wear rate drops as hardness of the rail material increases.

For the system as a whole, using harder C400 and V400 rail steels lowers the wear rate, and in practice would maintain wheel/rail profiles for longer; wear rate did not increase significantly when discs were run from 5000 to 15000 cycles, as observed with tests when P260 and V350 rail materials were used (see Figure 4.36). Similar behaviour was observed by Mädler *et al*. (2008).

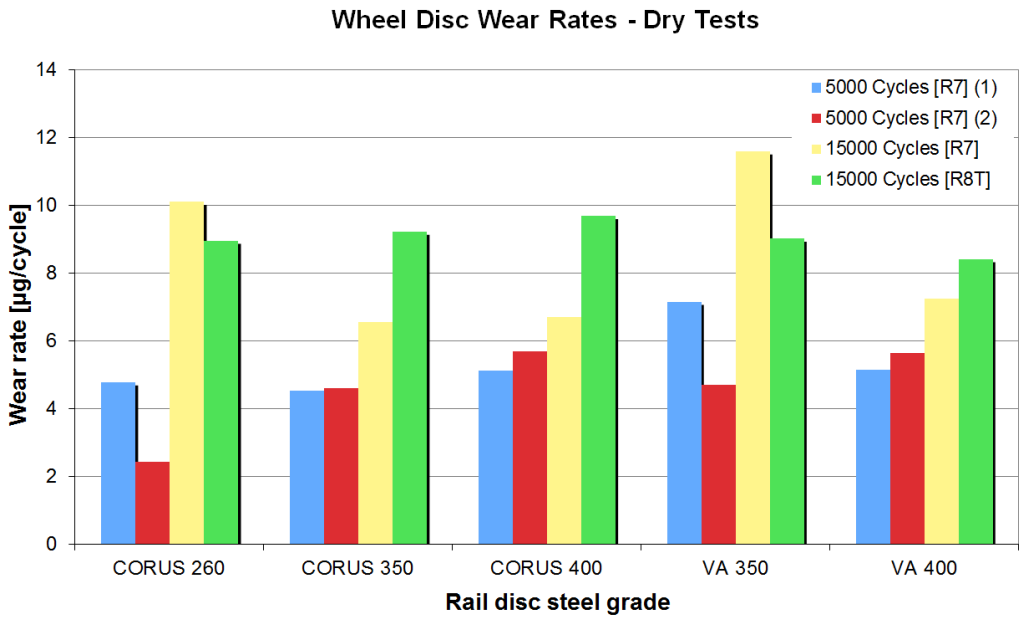

Figure 4.35 Wheel discs wear rates after dry SUROS tests

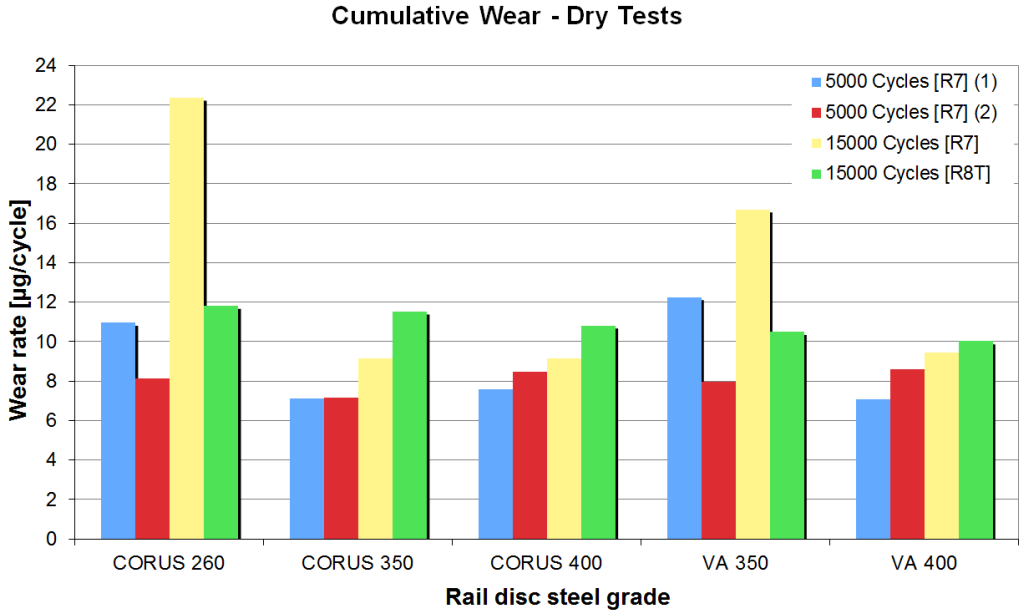

Figure 4.36 Cumulative material wear of both wheel and rail discs in SUROS dry tests.

4.6.2 Summary from the results of the wear and hardness tests

- Rail disc wear decreased when rail steel hardness increased.
- In general, the harder the rail disc material becomes at the surface, the harder the wheel disc material becomes at the surface.
- Wheel disc wear in dry tests was higher than the corresponding rail disc wear, except for P260 which had the highest wear rate.

- In the system as a whole (i.e., considering both wheel and rail discs), using harder C400 and V400 rail steels lowers the total wear rate; also, for C400 and V400, the wear rate averaged over the first 15000 cycles was not significantly higher than the wear rate averaged over the first 5000 cycles.

4.6.3 Strain-hardness relationship

Hardening depth and depth of visibly deformed microstructure are clearly correlated. As an example, for the 15000 cycles dry test of P260 material (see hardness graph Figure 4.6 and microscope image Figure 4.23), the depth of the severely deformed layer and the depth of hardening is the same, about 0.35 mm, and the depth of less but still clearly visible deformation/hardening is about 0.6 mm. Materials, in general, are the most strained and hardened at the surface, the values dropping with the depth into the material.

Both strain and hardening depend on:

- Both materials (wheel and rail)
- Number of rolling cycles
- Environment or testing conditions: load, lubrication, creepage, coefficient of friction/adhesion; here only lubrication (and coefficient of adhesion) has changed throughout tests (wet, dry + wet, dry)

Comparing materials, the most strained is the softest steel P260. A comparison of how strain of rail material changes when run against softer wheel steel R7 and harder R8T, is presented in Table 4.5. P260 has the biggest difference in values from the surface to 0.073 mm depth, and strains more when run against softer R7 wheel. For the other steels, the biggest difference is subsurface, at a depth of 0.010-0.030 mm for C350 and mostly 0.025-0.040 mm for other materials.

The twin-disc samples analysed in this thesis have been examined also by Corus (now Tata Steel) and some results are presented in InnoTrack D4.3.6 (2009c). A plot of Kernal Average Misorientation (KAM), which indicates the degree of microstructural damage, against depth is given in Figure 4.37. This shows that the R260 twin-disc samples experienced significant strain to a depth of at least 0.6mm, and the measurements correlate with the applied stresses and test durations, i.e., for the 20000 cycles wet test sample there is a dip near the surface where there is also a dip in the contact stresses, and for the 15000 cycles dry the damage occurs at greater depths than for any other tests.

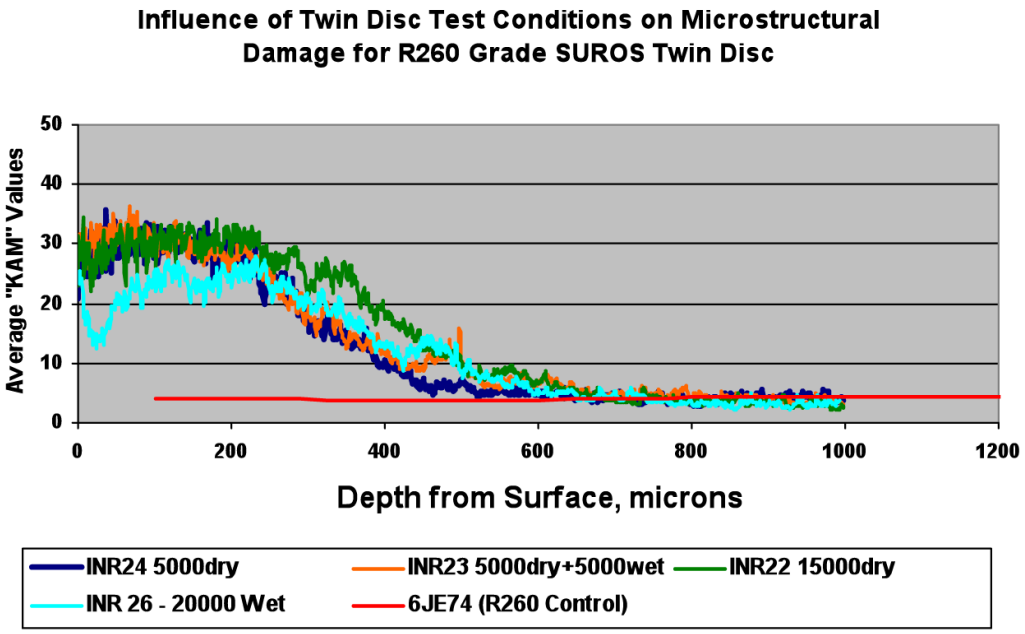

Figure 4.37 Kernal Average Misorientation (KAM) from electron back scatter diffraction analysis of SUROS twin-disc samples; analysis by Corus. The KAM value is a measure of variation in crystal alignment between neighbouring points, with high values indicating microstructural damage, e.g., severe plastic strain. From InnoTrack D4.3.6 (2009c).

The strain-hardness relationship is a core part of the ratcheting model described in Chapter 5.

4.6.4 Crack initiation and early stage of crack growth

This chapter presents a metallurgical description of cracks in twin-disc tested harder pearlitic steels and builds upon previous work using the same techniques as in researching softer materials, see (Garnham and Davis, 2011).

Surface flaking is a result of flattened elongated grains that delaminate from the surface. These surface flake structures are starters of surface cracks that propagate into the material. The tips of the cracks are opening at the same side, in the running direction, so when you run a finger over the specimen surface in the running direction it feels sharp and rough, while in the opposite direction it feels smooth, best seen in images Figure 4.21 and Figure 4.22. Crack initiation observations for all steels showed that cracks follow elongated grain boundaries, mostly prior austenite (PA) grains at the surface, as observed by Garnham and Davis (2011), for R220 and R260 steels. In material cross-sections, these cracks can be seen following material flow lines. Cracks can branch along grain boundaries instead of being semi-circular in shape, see Figure 4.31, which show cracks that do not propagate all the way to the surface.

Table 4.5 Difference in rail strain for 15000 cycles dry: rail strain run against wheel R8T minus rail strain run against wheel R7

Depth	Difference strain R8T-R7				
[microns]	Corus 260	Corus 350	Corus 400	VA 350	VA400
0	-3	2	-1	-2	-1
1	-3	2	-1	-2	-1
2	-3	2	-1	-2	-1
3	-3	2	-1	-2	-1
4	-3	2	-2	-2	-1
5	-3	2	-2	-2	1
6	-3	2	-2	-2	1
7	-3	2	-2	-2	1
8	-3	2	-2	-2	1
9	-3	2	-2	-2	1
10	-4	-2	-2	-2	0
11	-6	-3	0	-1	0
12	-6	-3	0	-1	1
13	-6	-3	0	-1	2
14	-6	-3	1	-1	2
15	-6	-3	3	0	2
16	-6	-3	4	0	2
17	-6	-3	4	-1	1
18	-6	-3	4	-1	1
19	-6	-3	4	-1	2
20	-5	-4	1	-1	0
21	-5	-5	-1	-1	0
22	-5	-5	-2	-1	0
23	-5	-5	0	0	0
24	-5	-5	1	0	0
25	-5	-5	1	-3	-2
26	-5	-5	2	-3	-3
27	-5	-5	3	-4	-2
28	-5	-5	3	-4	-2
29	-5	-5	3	-4	-2
30	-10	-1	3	-4	-4
31	-10	1	3	-3	-4
32	-10	1	2	-3	-4
33	-10	1	2	-3	-3
34	-10	1	2	-3	-3
35	-10	1	2	-3	-4
36	-10	1	2	-3	-3
37	-10	1	3	-2	-3
38	-10	1	3	-2	-3
39	-6	1	3	-2	-3
40	-6	-1	1	-2	-3
41	-6	-1	0	-3	-1
42	-5	-1	0	-2	-1
43	-4	-1	1	-2	0
44	-3	-1	1	-2	0
45	-5	-1	1	-1	0
46	-4	-1	1	-1	0
47	-5	-1	1	-1	0
48	0	-1	1	-1	0
49	0	-1	1	-1	0
50	0	0	1	-2	-1
51	-1	0	1	-2	-1
52	-1	0	1	-2	-1
53	-8	0	1	-2	-1
54	-9	0	1	-2	-1
55	-8	0	2	-2	-1
56	-8	0	2	-2	-1
57	-3	0	2	-2	-1
58	-1	0	2	-2	-1
59	-1	0	2	-2	-1
60	-2	0	0	-2	-1
61	-2	0	0	-2	-1
62	-5	0	0	-2	-1
63	-6	0	1	-1	-1
64	-8	0	1	-1	-1
65	-5	0	1	-1	-1
66	-5	0	1	-1	-1
67	-3	0	1	-1	-1
68	-3	0	1	-1	-1
69	-2	0	1	-1	-1
70	-2	0	1	-1	-1
71	-2	0	1	-1	-1
72	-3	0	1	-1	-1
73	-3	0	1	-1	-1

Difference	
0	
1	
2	
3	
4	
5	
6	
7	
8	
9	
10	

PA grain boundaries can contain pro-eutectoid (PE) ferrite, but not necessarily. The new premium grade pearlitic rail steels have very little PE ferrite. However, pearlite grains will have different orientation of lamellae, which sometimes stops cracks, because they need more energy to propagate through pearlite transverse to the lamellae, so propagation along grain boundaries is still relatively easy.

Cracks can initiate at elongated non-metallic inclusions, or propagate through them when they come to their path (see arrows pointing to inclusions in Figure 4.19). Also, cracks start branching towards these inclusions but stop when encountering elongated grains. New steels are produced with minimum amount of inclusions, and examining etched microstructure images it can be seen that the P260 has very few inclusions, but more than the harder steels. The importance of inclusions was researched by Garnham *et al.* (2010) and they also found that strain-flattened ductile inclusions are initiating flake cracks at the surface and that cracks propagate along the inclusion boundaries.

Cracks usually grow quickly to the depth of visible plastic deformation. Looking at cracks in 5000 cycles dry tests comparing to 15000 dry tests, they are shallow and less dense.

When comparing different materials under the same testing conditions, in dry-wet tests the softest material (P260) cracks the most.

When comparing dry, dry-wet and wet tests it is necessary to look at the coefficient of traction (Figure 3.6 - Figure 3.10) and see how that influences cracking and what other mechanisms are involved there. Rail and wheel discs are cracking differently for the same test conditions, due to the wheel disc being the driving disc. All materials crack the most and the developed cracks penetrate the deepest for dry-wet tests, except for V350, test 15000 dry (INR12).

For the dry-wet tests, in the initial dry run, the coefficient of traction is over 0.4 and this increases the roughness of the disc surface. On average Ra=0.339 μm for rail discs and Ra=0.636 μm (more variation here, see Table 3.7) for wheel discs. At this point some shallow pits appear and only few cracks initiate for rail discs, while the surface of the wheel discs deteriorates more; it is rougher but still only few cracks develop on some discs, see images in Appendices A and B.

The test is then run for 5000 cycles wet. The coefficient of adhesion varies between 0.15-0.19, which is a lot lower than in the dry tests but more deterioration of the surface takes place. Water penetrates into these irregularities and now an opposite deterioration

pattern for rail and wheel discs takes place. All rail discs had an increase in roughness values, and now there are bigger variations in Ra between materials, while all wheel discs (except INW2, run against C400) had a decrease in Ra. Looking at the surfaces, all rail discs except INR11 (V350) deteriorated more compared to the 5000 cycle dry test. Wheel disc surfaces deteriorated less than in the dry tests. For all rail discs, except INR11 (V350), wear rates increased, while for all wheel discs they decreased. Similar observations were made for cracking.

While rail discs cracked a lot, see Figure 4.19 - Figure 4.22, wheel discs have not. This behaviour appears odd at first since in the dry tests the wheel surface deteriorated more. The explanation lies in the direction of traction and motion between discs and that the wheel disc provides the driving force. Water gets trapped and compressed into the cracks of rail discs, but is squeezed out and acts like a lubricant for wheel discs. For these dry-wet tests, only slight hardening of rail material occurred at the surface (Figure 4.5), but much more significant hardening of the wheel surface (Appendix C, Figure C.13 and Figure C.14), noting that hardness mechanisms play a role in the deterioration process. Hardening of the surface protects the material from further deterioration in general.

4.7 Summary

Detailed metallurgical analysis on sectioned SUROS twin-disc test discs has been presented in this chapter. Five rail grades with high hardness were tested and results of hardness, cracking and plastic deformation from the surface into the bulk of the material investigated and compared. The softer P260 steel plastically deformed to the greatest depth under the surface. For all steels RCF crack initiation and early propagation is determined by microstructure.

These results are important for understanding material behaviour under cyclic loading and are needed for creating the Dynarat model for wear and crack initiation for these new steels.

Chapter 5 Model Development and Calibration

Development of the material models used by the in-house wear and crack initiation prediction software, 'Dynarat', is presented in this chapter. First, the principle of the old model will be explained briefly, and then improvements, calibration and validation of the new model. (The development of the old model is explained in more detail in Section §2.6.2.) Further improvements of the model, more relevant to wheel-rail contact, including a new 3D partial slip model, are presented later in Chapter 6.

The Dynarat computer model is used to simulate accumulation of plastic shear strain (ratcheting) in rails and to predict wear and crack initiation. Prior to this work, the Dynarat wear model calibration and development focused on models of microstructure and strain hardening characteristics, based on twin-disc tests with British 'normal' grade (R220) rail steel, which has a significant proportion of pro-eutectoid ferrite at prior-austenite grain boundaries, and which therefore is best modelled as a two-material (ferrite / 'pearlite') microstructure. In Europe, and increasingly in Britain, the harder R260 rail steel is more common. However, the R260 grade and the harder premium grade pearlitic rail steels do not have such a high proportion of pro-eutectoid ferrite and in this work a single material microstructure is used in the modelling. Data from the twin-disc tests and metallurgical analysis in previous chapters are used here to develop a new strain-hardening model. Calibration has led to developments in the core ratcheting model, including the ratcheting equation, the criterion for material failure and the influence of surface micro-roughness.

The flow chart of model development and calibration process is presented in Figure 5.1. It shows the basic logic of this modelling chapter, where test data for P260 steel are used for model calibration. For the premium grade steels, a strain-hardness equation is determined in the same way, but to make validation easier other parts of the model are not changed.

- For all five rail steel grades tested, the principal aim is to determine the initial hardness and strain-hardening behaviour.
- For the 260 grade only, the aim is also to calibrate the wear rate against twin-disc results.
- Wear rate predictions will be made for the premium grade rail steels, and compared against measured twin-disc results. This part is validation of the model.

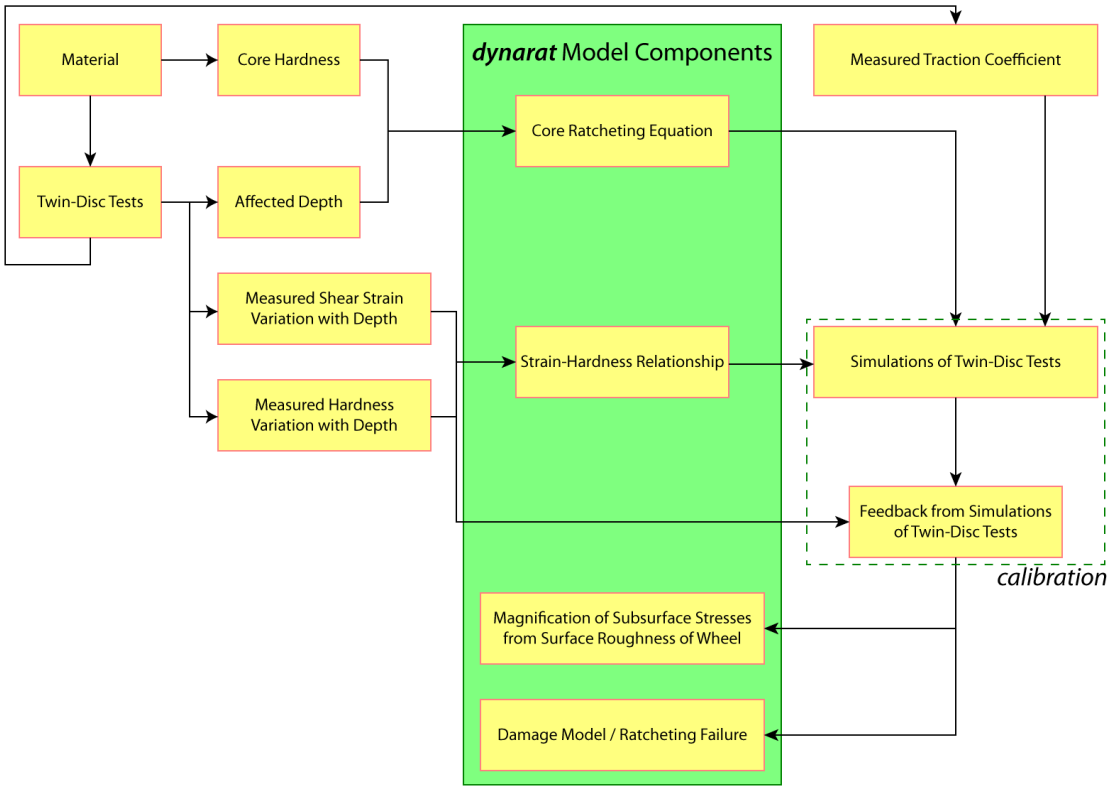

Figure 5.1 Flow chart of material model development and calibration process.

5.1 Model development

5.1.1 Ratcheting equation

The Dynarat ratcheting model (see Section §2.6.2) is based on plastic flow following shakedown, when the dominant stress is the orthogonal shear stress. The ratcheting strain increment ($\Delta\gamma$) for the element in row j column i of the simulation matrix is calculated using:

$$\Delta\gamma^{ij} = Cf\left(\frac{\tau^{j}_{zx(\max)}}{k^{ij}_{eff}}\right) \tag{5.1}$$

where:

- C = 0.00237, determined for British 'normal' grade rail steel (R220) by (Tyfour *et al.*, 1996);
- $\tau_{zx(\max)}$ is the maximum orthogonal shear stress occurring at the depth corresponding to row j;
- k_{eff} is the effective shear yield stress (following any hardening or softening) of the element, see (Franklin *et al.*, 2003).

The traditional form of the ratcheting function, $f(x)$ in Equation (5.1), see Figure 5.2, is:

$$f(x) = \begin{cases} 0, & x \le 1 \\ x - 1, & x \ge 1 \end{cases} \tag{5.2}$$

where x is $\tau_{zx(\max)} / k_{\text{eff}}$.

This has a sharp cut-off at the shear yield stress, and therefore the computer simulation predicts zero strain accumulation if the applied orthogonal shear stress drops below the shear yield stress (i.e., if $\tau_{zx(\max)} \le k_{\text{eff}}$.). In effect, this predicts that there will be no shear strain accumulation below a certain depth, depending on the applied contact load.

The initial shear yield stress, k_0, is derived from the measured Vickers hardness H_V as follows, see (Franklin *et al.*, 2008):

$$k_0\left[\text{MPa}\right] = \frac{1}{3\sqrt{3}} H = \frac{9.81}{3\sqrt{3}\sin\left(136° / 2\right)} H_V \approx 2.04 H_V \tag{5.3}$$

where:

- H [MPa] – bulk hardness;
- H_V – Vickers hardness number;
- the hardness is typically three times the yield strength for metals: $H = c\sigma_y \approx 3\sigma_y$, where the constant c is determined by geometrical factors, usually ranging between 2 and 4 (Tabor, 1951);
- $\sqrt{3}$ is from the von Mises yield criterion, relating shear yield stress to yield stress – the magnitude of shear yield stress in pure shear is lower than the tensile yield stress by a factor of $\sqrt{3}$ in the case of uniaxial tension, i.e.:

$$k = \frac{\sigma_y}{\sqrt{3}}$$

(Franklin *et al.*, 2008) explain the $\sin(136^o/2)$ term as follows: "the conversion factor from Vickers hardness number follows from the definition of hardness in terms of force per unit surface contact area for a pyramid shaped indenter, but of yield stress in terms of plan view area over which the same force is applied" – see also (Garnham *et al.*, 2007) – but this is an approximation.

Equation (5.3) uses Vickers hardness in the sense of mean pressure. In the literature, the usual method for converting hardness from HV number to MPa is just multiplication by 9.807, so the formula should be:

$$k_0\left[\text{MPa}\right] = \frac{9.807}{3\sqrt{3}} H_V \approx 1.887 H_V \tag{5.4}$$

There is not a huge difference between Equation (5.3) and Equation (5.4); so, the previously calculated k_0 value in Equation (5.3) will be used in the model for consistency with earlier calibration work of the 'Dynarat' model.

For the P260, the measured hardness is 296 (HV0.2 at 10mm) so the corresponding shear yield stress is 603MPa. For a rolling/sliding contact with peak contact pressure 1500MPa and friction coefficient 0.4 (dry contact, fully sliding), for instance, the shear stress is 600MPa at the surface, at the centre of the contact where the pressure is the peak value:

$$\tau_{zx} = \mu p_0 = 0.4 \times 1500\text{MPa} = 600\text{MPa}$$

The shear stress reduces quickly with depth. Because ratcheting is driven by the shear stress and the ratcheting equation has a sharp cut-off, the depth of material subject to ratcheting deformation is only about 20 microns (the roughness influence zone). However, analysis of the twin-disc specimens reveals plastic deformation below the expected cut-off. This indicates that the stresses are higher than expected, or perhaps the material is softer than expected, or perhaps that there is no sharp cut-off. (Surface roughness increases stresses, but only very close to the surface. Equation (5.4) could be used instead of Equation (5.3), and a slightly higher friction coefficient could be argued, but this only lessens the problem, it doesn't solve it.)

In order to reproduce the observed increase in micro-hardness at depths down to 600 microns, the micro-hardness readings would need to be scaled by a factor of about 0.4. A similar factor was needed when calibrating the Grade 220 (R220) against nanohardness measurements, see (Franklin *et al.*, 2008) and (Garnham *et al.*, 2007), justified because hardness readings scale with indent size.

However, rather than introduce an arbitrary scale factor, a new ratcheting equation is proposed here:

$$f(x) = x - 1 + e^{-x(1+rx)} \tag{5.5}$$

where r ≈ 0.439.

Equations (5.2) and (5.5) are shown in Figure 5.2.

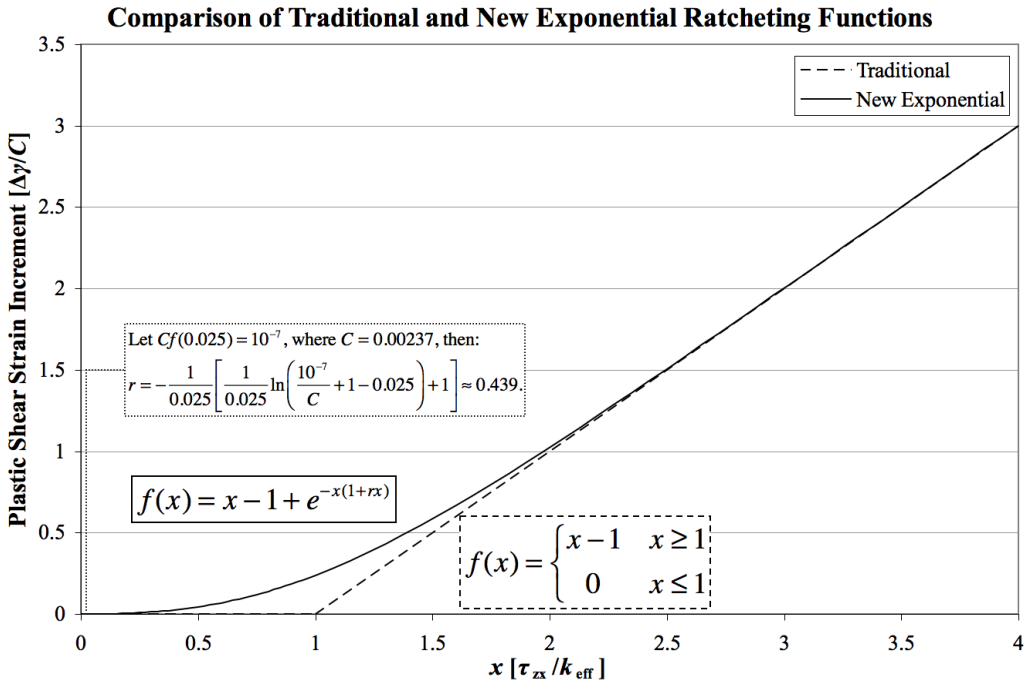

Figure 5.2 Comparison of traditional and new ratcheting equations

The new ratcheting equation has been chosen to meet the following requirements:

- It is asymptotically equivalent to the traditional equation (and tends to the asymptote quickly) as the shear stress increases;
- It drops rapidly towards zero (but remains finite) as the shear stress decreases;
- The shear strain increment is still significant when the ratio of shear stress to shear yield stress is 0.4 (i.e., rather than scale the hardness by 0.4, ensure that strain will accumulate when the shear stress is 0.4 times the shear yield stress); and
- The shear strain increment is 10^{-7} (so that the accumulated shear strain is approximately 10^{-3} after 10000 cycles) when the ratio of shear stress to shear yield stress is 0.025, i.e., at a depth of about 5mm):

$$C f(0.025) = 10^{-7} \tag{5.6}$$

Equation (5.6) can be rearranged to find the exact value of r in Equation (5.5):

$$r = -\frac{1}{0.025}\left[1 + \frac{1}{0.025}\ln\left(\frac{10^{-7}}{C} + 1 - 0.025\right)\right] \tag{5.7}$$

The last bullet point above is specified so that the accumulated shear strain is 10^{-3} after 10000 cycles at a depth of about 5mm; this is to provide a mechanism for including strain softening in the strain-hardening curve, which will then be chosen to have a minimum when the strain is about 10^{-3}. This makes it easier to reproduce the observed softening behaviour if an appropriate strain-hardening equation is chosen. (Of course, this has negligible effect on the wear rate.)

5.1.2 Strain-hardness equation

The relationship between the accumulated shear strain and the effective shear yield stress (or alternatively the hardness, which is assumed to be proportional) is a core component of the ratcheting model. The shear yield stress is assessed through measurements of hardness, see Chapter 4, and equations describing the strain-hardness relationship are required for each material.

An appropriate strain-hardening equation needs to be chosen to reproduce the observed softening behaviour. The modified Voce equation, used traditionally in Dynarat, does not permit softening, but the following equation has a reasonable fit to the data:

$$H(\gamma) = H_0\left[a\ln\left(1+\gamma^b\right)+c+(1-c)e^{-\gamma/d}\right] \tag{5.9}$$

where:

H_0 [HV]	core hardness
γ	shear strain
a, b, c, d	parameters from curve-fit

The five constants in the equation are given in Table 5.1, and the curve fit for the P260 is shown in Figure 5.3. (For comparison, the curve fit for BS11 rail steel, using a Voce equation, is shown also.)

Strain–hardness curves are shown in Figure 5.4 for all five materials. This data is based on 15000 cycles R7 dry tests. Hardness data is normalised as measured values divided with core hardness, the value taken from 10mm depth measurement. For material C350 softening is not obvious, so it was decided not to include softening in this equation (i.e., coefficient c=1 for C350).

Table 5.1 Strain-hardening parameters for the pearlitic rail steels tested.

Rail Steel	Core Hardness H_o [HV]	a	b	c	d
P260	296.0	0.260177580	1.292291910	0.96	0.0001
C350	327	0.36	0.9	1.00	0.0001
C400	347.0	0.224138139	1.399843934	0.95	0.0001
V350	364.0	0.396849778	0.823357015	0.95	0.0001
V400	371.5	0.206666114	1.310212528	0.93	0.0001

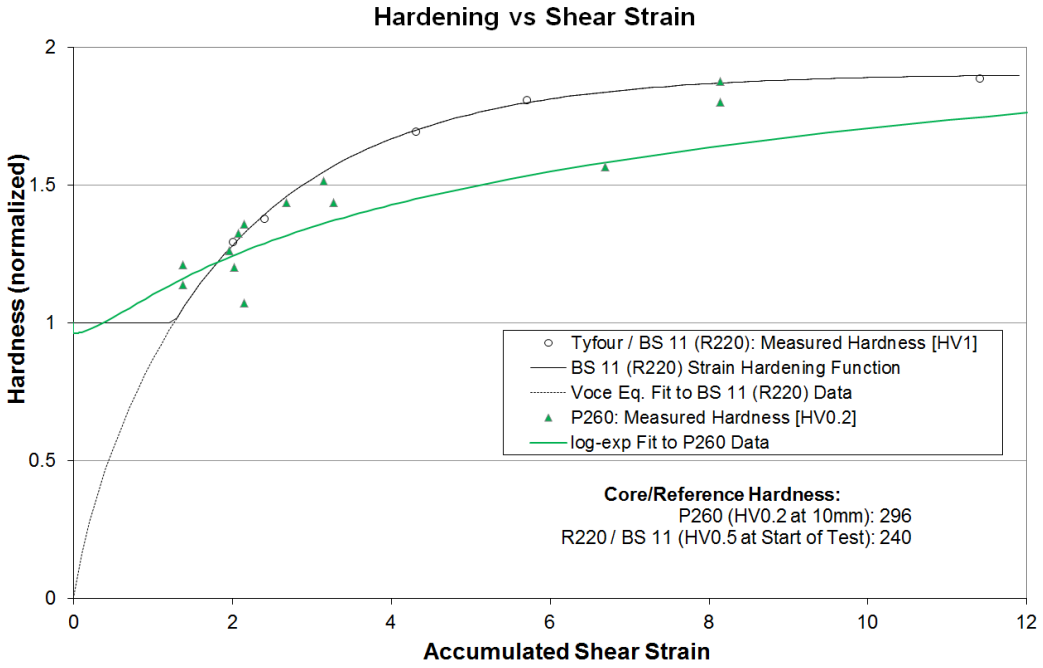

Figure 5.3 Strain-hardening curves and measured data from twin-disc tests on BS 11 by (Tyfour *et al.*, 1995) and on the P260.

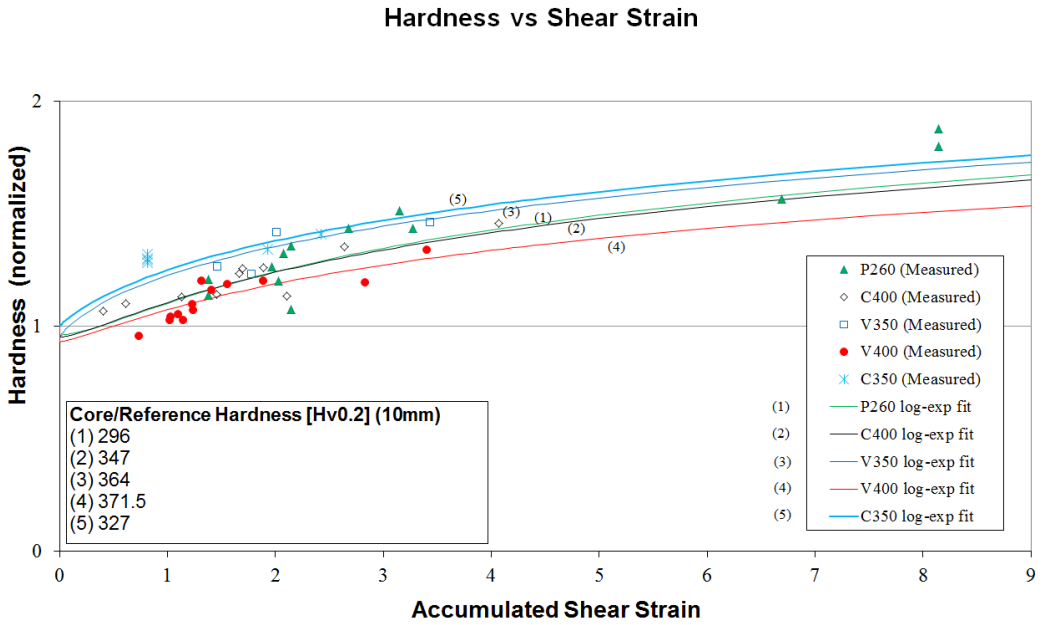

Figure 5.4 Strain-hardening curves and measured data from twin-disc tests. (All curves start at 1. Softening occurs rapidly for all materials except C350.)

5.1.3 Effect of surface roughness

The orthogonal shear stress calculated without the effect of roughness at each depth is denoted $\tau_{zx}(z)$. To account for the effect of surface micro-roughness of the opposite contacting surface, the current Dynarat model uses an approximation of rough contact by multiplying the orthogonal shear stress τ_{zx} at each depth by factor $r(z)$. (Franklin and Kapoor, 2007) suggested an exponential form of roughness amplification as:

$$r(z) = A^{1-z/d}, \quad 0 \le z \le d \tag{5.10}$$

where:

- A the amplification factor at the surface
- d the affected depth
- z depth below the surface.

$r(z)$ has a maximum value A at the surface (z=0), and value $r = 1$ when $z \ge d$.

A smoother transition between the near-surface roughness-influenced zone and the deeper unaffected zone can be achieved using the following 'quadratic' formula:

$$r(z) = 1 + (A-1)(1 - z/d)^2, \quad 0 \le z \le d \tag{5.11}$$

If, as an example, the following values are used:

A = 3.5 is the amplification factor at the surface, and

d = 200 μm is the affected depth,

then the functions described with Equations (5.10) and (5.11) are as in Figure 5.5.

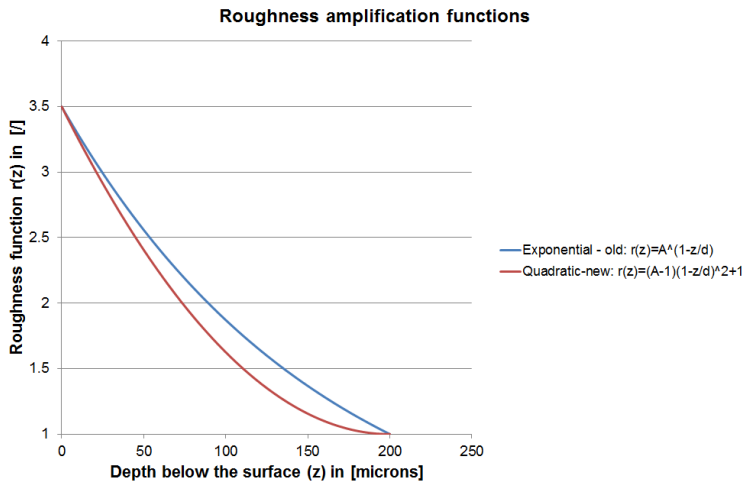

Figure 5.5 Roughness amplification functions: exponential and quadratic.

The current Dynarat model uses an approximation of rough contact by multiplying the orthogonal shear stress τ_{zx} at depth z by Equation (5.11). The function is maximum at the surface (value A) and decays to one at depth d, where the gradient is zero so that the

transition to the non-amplified region is smooth (the previous roughness function was exponential and the transition was not smooth). The constants (A and d) were estimated by comparing simulation predictions, performed over a range of amplifications and depths, with micro-hardness and strain measurements.

5.1.4 Continuous damage wear model

A new wear methodology has been developed for the computer simulation. Instead of defining the critical shear yield strain (γ_c) as a threshold value below which material is healthy and above which material is weak, i.e., a binary scenario (see Figure 2.29), it is defined as a reference value and a 'weakness' value between 0 and 1 is calculated for each material element:

$$p_r \propto \frac{\gamma / \gamma_c}{1+\gamma / \gamma_c} \tag{5.12}$$

For each element at the exposed surface, this weakness value, p_r, is then used to calculate the instantaneous probability of wear. This continuous damage approach allows a very small wear rate even when there is very little plastic deformation, but also allows severely strained material to retain some resistance to wear.

5.2 Twin-disc simulations

Strain, hardness and wear simulations were performed for the P260 grade using the new core ratcheting and strain-hardness equations developed above.

- A cross-sectional area of 0.5mm (width) × 10mm (depth), with element size 1μm ×1μm, was modelled, with one simulation corresponding to each twin-disc test.
- In addition, higher-resolution simulations with a cross-sectional area of 0.05mm × 0.05mm, with element size 0.1μm × 0.1μm, were performed to confirm that element size does not affect predicted wear rate significantly.
- The contact was Hertzian 'line' (two-dimensional) with peak pressure 1500MPa and semi-contact width 0.3mm.
- In some simulations, the contact was modelled as partial slip, with the friction coefficient fixed at 0.6 and the traction coefficient varying. In other simulations, the contact was modelled as fully slipping, with the friction coefficient equal to the traction coefficient. (At -1% slip, the contact between the discs has generally

been assumed to be fully sliding, but this is not necessarily the case for dry contact.)

- The traction coefficient was derived from the measured history of traction coefficient for each of the respective SUROS tests (5000 and 15000 cycles dry tests against R7 wheel steel). The recorded test data was split into blocks of approximately 50 cycles and the average traction coefficient in each block used as input to the model.
- Various roughness equations and/or parameters were tested to study how the shear strain and hardness predicted by the simulation compare with the measured distributions.

Parameters of simulations are given in Table 5.2, and one example of simulations for 15000 dry test in Figure 5.6.

The fully slipping contact condition with the quadratic roughness equation was chosen for further simulations of these twin disc tests.

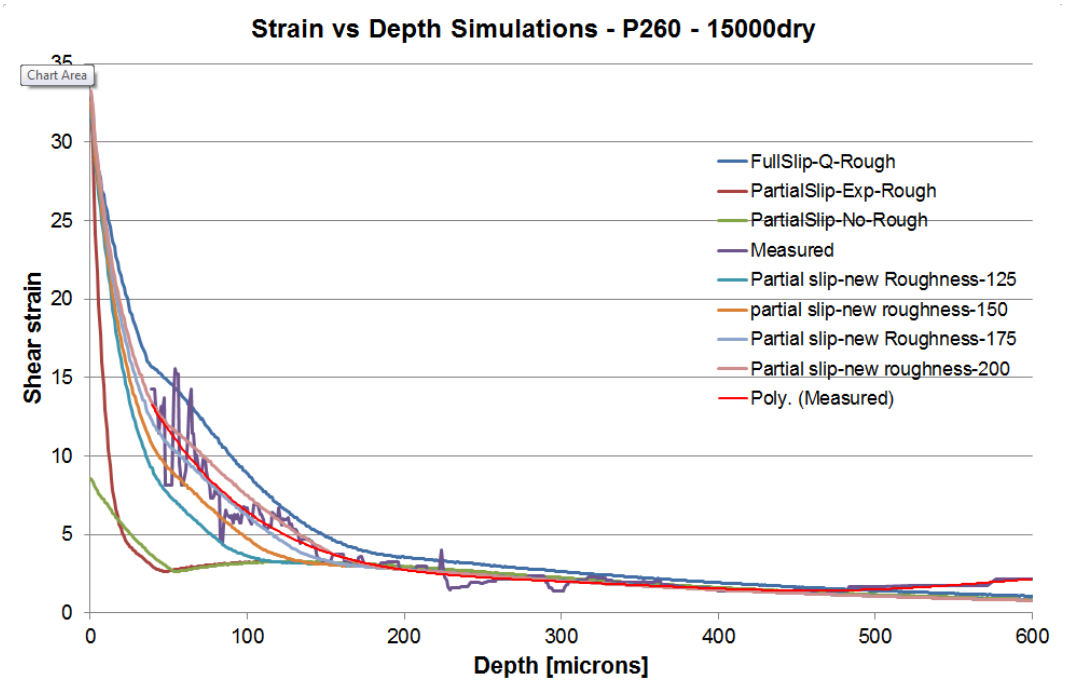

Figure 5.6 Strain vs depth, from several simulations of the P260 material tests with curve 'Measured' representing measured strain values for 15000 dry test.

Table 5.2 Parameters for simulations of twin disc tests and curves in Figure 5.6

		Roughness			
Simulation types from Figure 5.6	**Slip**	**Equation**	**Affected depth d**	**Amplification factor A**	**Traction-t_c and friction-μ**
Full slip-Q-Rough	Full	Q-Quadratic (Eq 5.11)	200	3.5	$t_c = \mu$ = measured value
Partial slip-No-Rough	Partial	No	0		μ_{dry} =0.6 μ_{wet} =0.202 t_c = measured value
Partial slip-Exp-Rough	Partial	Exponential (Eq 5.10)	25	4	μ_{dry} =0.6 μ_{wet} =0.202 t_c = measured value
Partial slip-new roughness-125	Partial	Exponential (Eq 5.10)	125	4	μ_{dry} =0.6 μ_{wet} =0.202 t_c = measured value
Partial slip-new roughness-150	Partial	Exponential (Eq 5.10)	150	4	μ_{dry} =0.6 μ_{wet} =0.202 t_c = measured value
Partial slip-new roughness-175	Partial	Exponential (Eq 5.10)	175	4	μ_{dry} =0.6 μ_{wet} =0.202 t_c = measured value
Partial slip-new roughness-200	Partial	Exponential (Eq 5.10)	200	4	μ_{dry} =0.6 μ_{wet} =0.202 t_c = measured value

5.3 Model calibration

5.3.1 Material model calibration

Material properties (specifically hardness and critical shear strain) were allowed to vary by 5% between elements in the mesh. (This is typical for the standard deviation in micro-hardness measurements.) Material properties for the P260 grade, that are the same in all simulations, are summarised in Table 5.3.

Hardness simulation results for P260 are presented in Figure 5.7. This shows how hardness increases towards the surface, with hardening visible even to a depth of 1000 microns. Hardness increases with number of cycles, which is also observed in measurements (see Section §4.3.3 and Figure C.1 in Appendix C).

Strain simulation results for P260 are presented in Figure 5.8. This shows similarly how strain is greatest at the surface and is visible to a depth of 500 microns. Strain increases over time, which is also observed in measurements (see Section 4.4.2).

Table 5.3 Properties of P260 rail steel used in simulations.

Property	**Value**	**Assumed standard deviation**
Young's modulus, E [GPa]	209	
Poisson's ratio, ν	0.3	
Core hardness, H_0 [HV]	296	14.8 (5%)
Ratcheting constant, C	0.00237	
Critical shear strain for failure, γ_c	29	1.45 (5%)

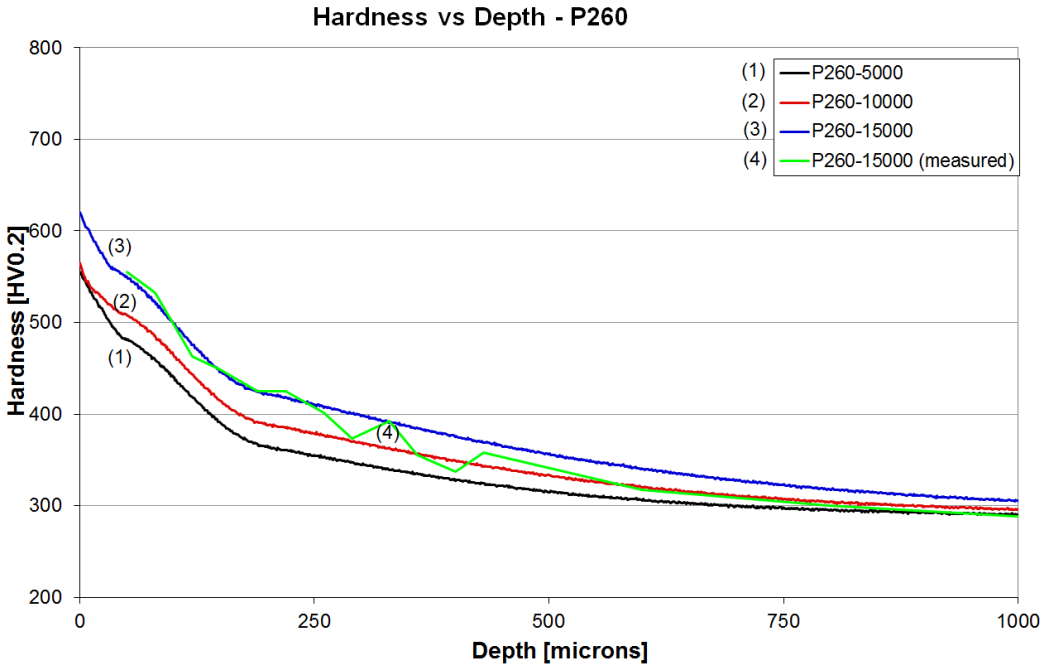

Figure 5.7 Hardness vs depth, from simulations of the P260 material tests with curve 4 representing measured hardness values for 15000 dry test, put here for comparison of simulated and measured results.

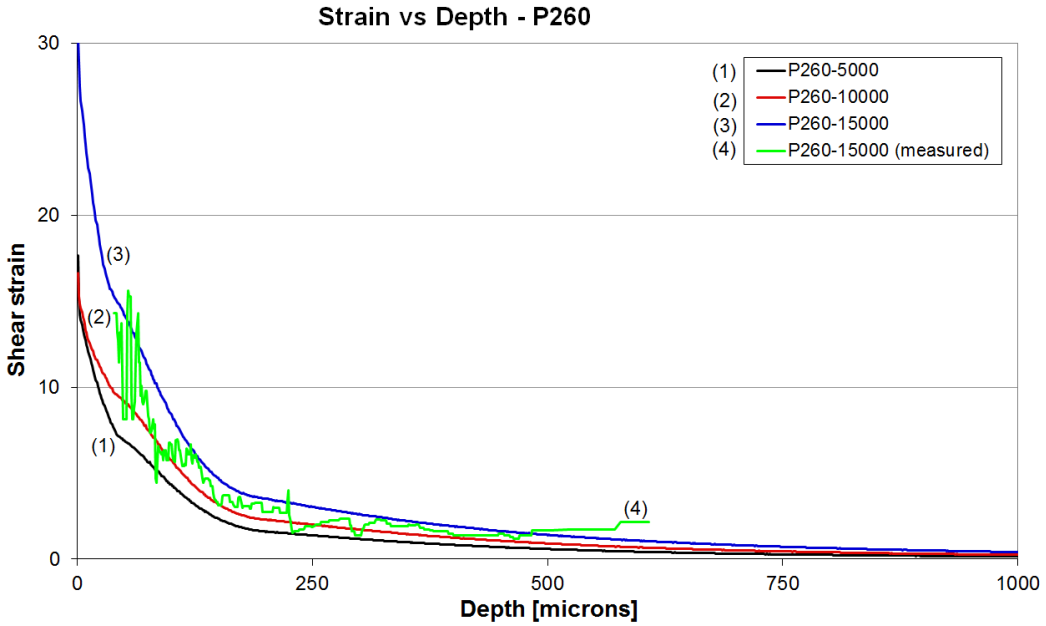

Figure 5.8 Strain vs depth, from simulations of the P260 material tests with curve 4 representing measured strain values for 15000 dry test, put here for comparison of simulated and measured results.

5.3.2 Wear model calibration

The wear rate can be calibrated by adjusting the critical shear strain; increasing this will reduce the wear rate. Unfortunately, this method is not sufficient to get a good match to experimental data, since both the time until significant wear occurs and the eventual 'steady-state' wear rate are affected by the critical shear strain.

A value of critical shear strain, $\gamma_c = 29$, was chosen for the new continuous damage model so that predicted wear rate of the P260 matched the wear measurements of the two tests reasonably well (5000 dry, and 15000 dry). Wear rates (measured and predicted) are given in Table 5.4 for P260.

Table 5.4 Measured wear rates from twin-disc tests, and predicted wear rates [nm/cycle] from simulations of the same twin-disc tests for material P260.

Material P260 **Wear rates**	**Number of cycles**		
Type of simulation	**5000 dry**	**10000 (dry + wet)**	**15000 dry**
Measured	0.527	4.833	1.046
Predicted – full slip	0.314	0.550	0.972

5.4 Model validation

The same full slip model and value of critical shear strain, $\gamma_c = 29$, was then used when simulating other rail steel grades; wear rates are given in Table 5.5. The complete set of figures showing the predicted micro-hardness with depth, and the predicted accumulated plastic shear strain with depth, are given in Appendix D. An example for material V350 is given in Figure 5.9 and Figure 5.10.

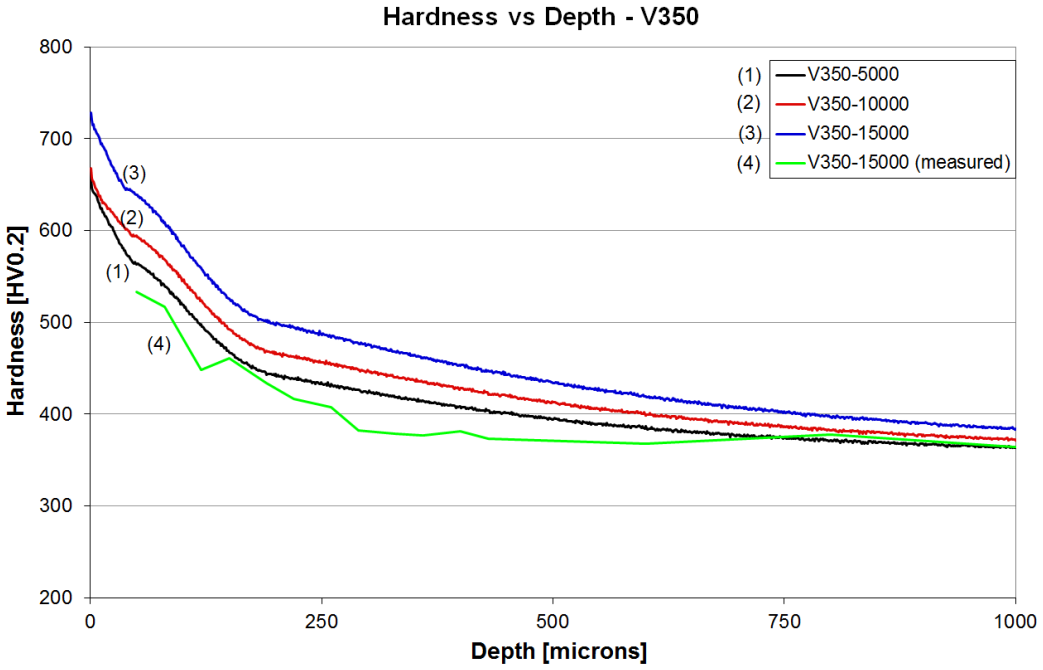

Figure 5.9 Hardness vs depth from simulations of the V350 material grade test.

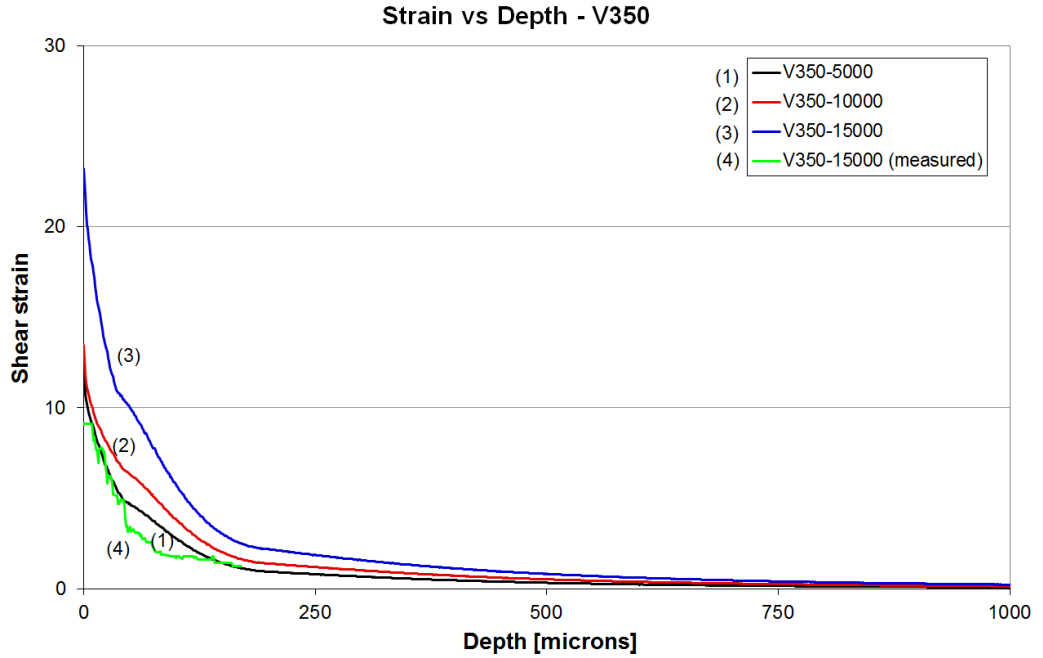

Figure 5.10 Strain vs depth from simulations of the V350 material grade test.

Table 5.5 Predicted wear rates [nm/cycle] from simulations of the twin-disc tests, and measured wear rates (from Table 3.4).

Predicted	**5000**	**10000**	**15000**
C350	0.209	0.403	0.867
C400	0.271	0.409	0.809
V350	0.169	0.344	0.629
V400	0.226	0.426	0.898

Measured	**5000**	**10000**	**15000**
C350	0.222	0.473	0.224
C400	0.211	1.040	0.209
V350	0.435	0.377	0.435
V400	0.165	0.467	0.189

The wear rate predictions for the premium grade rail steels match measured values for the 5000 cycles dry tests (only V350 is under-predicted with a factor 0.39 of measured value), but over-predict the wear rates for the 15000 cycles dry tests by a factor of 2 to 3. (The dry-wet test predictions do not match for P260 and C400, but are not expected to, since the ratcheting wear model does not account for major surface deterioration caused by significant lubricant assisted surface cracking.)

5.5 Discussion

Development of the model and simulations are explained in this chapter, but some points should be noted and may require further research:

- The constant C = 0.00237 was determined for British 'normal' grade rail steel by Tyfour et al., 1996, and was assumed here as well.
- For harder materials, the model uses hardening Equation (5.9) developed for this thesis. In future this equation can be improved further or even to develop a new hardening equation for each material, not just to change the parameters within the equation.
- In the simulations, the value for critical shear strain was $\gamma_c = 29$ for all materials. In future it could be better adjusted for each material separately, instead of using the same value for all.

Predictions for wear are in the same order of magnitude as those measured from twin-disc tests, but for some tests the simulations over-predict the wear rate (i.e., for V400, 15000 dry, the model over-predicts wear by a factor of 4.7). This is an early analysis, and more tests are needed to better calibrate and validate the model. Parameters can be further adjusted to get better model predictions. The number of tests was small (one or two tests with the same materials and parameters) and the technique used to measure strain is subjective. With more data, it will be easier to exclude outliers and improve confidence.

5.6 Summary

A material model has been developed for harder pearlitic rail steels. New core ratcheting, roughness effect and strain-hardness equations are developed. Predictions for wear are of the same order of magnitude as measured from twin-disc tests, but for some tests simulations over-predict the wear rate by a factor of 4 or more. This is an initial analysis, and more tests are needed to better calibrate and validate the model.

Chapter 6 Wear Prediction in Wheel-Rail Contact

Chapter 5 focussed on calibrating the model using twin-disc data. The main aim of this work is to predict wear rates and crack initiation in rails, and wheel-rail contact is three-dimensional in contrast to twin-disc tests which can be modelled as two-dimensional. The partial slip model used for two-dimensional contact was developed by Carter (1926), who argued that for heavily worn (i.e., flattened) rails the wheel-rail contact could be considered approximately two-dimensional. Modern, well-maintained rails have a more complex geometry and this approximation is not valid.

In this chapter:

- A quasi-static model of partial slip in three-dimensional wheel-rail contact, that retains the simplicity of Carter's approach, is presented.
- The ratcheting model is developed to include transverse traction and strain accumulation.
- Wear rates are predicted for a set of generic wheel-rail contacts.

6.1 New Dynarat wheel-rail contact model

6.1.1 Introduction

Three improvements are made to the contact stress model used by the Dynarat model:

(1) Previously the driving stress for plastic strain accumulation was the orthogonal shear stress (OSS) in the plane of the simulation, τ_{zx}, where x is the direction of motion and z is normal to the rail surface; now the OSS in the plane normal to this, τ_{yz}, is also considered and the resultant stress used to drive plastic strain accumulation.

(2) Plastic strain accumulation is now made directional, with components in the x and y directions.

(3) Partial slip is now implemented in the 3D simulation, with both contact region and adhesive zone (AZ) modelled as ellipses – similar to the method of Vermeulen and Johnson (1964) but with an AZ ellipse selected to approximate the real (i.e., observed) AZ.

6.1.2 Partial slip – introduction

In general in wheel-rail contact, the traction coefficient (i.e., the ratio of the tractive force to the normal load) is less than the limiting friction coefficient, and for part of the contact patch the surfaces stick. This type of contact is called partial slip. The 2D computer simulation has been used to study the influence of partial slip on wear (Franklin *et al.*, 2003; Alwahdi *et al.*, 2005) using the theory developed independently by Carter, 1926, Poritsky and others (see Johnson, 1985 [§8.3] and Figure 6.1).

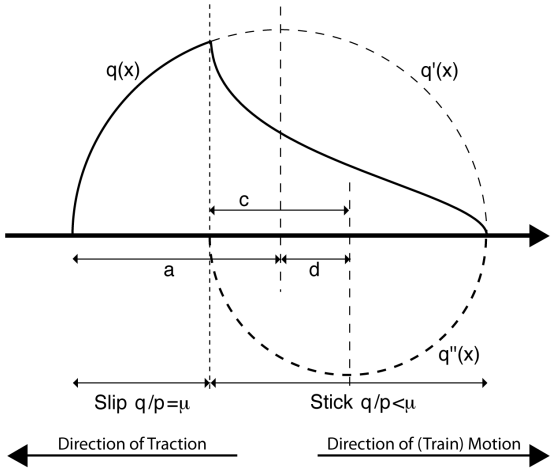

Figure 6.1 Partial slip in 2D, where a is the half-width of the contact, c is the half-width of the adhesive zone, $d=a-c$ is the offset, $q(x)$ is the shear traction, $q'(x)$ is the shear traction for a fully slipping contact and $q''(x)$ is the difference. (Note: Since the traction is opposite the direction of x-axis, these distributions should properly have the opposite sign.) (Based on Figure 8.6 in Johnson, 1985.)

However, previously the study of partial slip was restricted to the 2D model. In 3D, partial slip could only be simulated by replacing the friction coefficient with the traction coefficient, giving an incorrect distribution of traction in the contact, even though overall friction force was correct. In this thesis, a superior implementation of a 3D model of partial slip is presented. In this new model, traction direction is a variable, and the orthogonal shear stress and the ratcheting strain are treated as vectors.

For partial slip conditions (i.e., when the traction coefficient is less than the limiting friction coefficient) the wheel-rail contact region can be divided into 'stick' regions and 'slip' regions. In general, these regions move dynamically, making it difficult to model the contact patch. A new static model of partial slip has been developed for the Dynarat wear model.

The assumption made in the new model for the contact region is that it is elliptic, and the stress distribution in the rail fully three-dimensional. Within the ellipse is a partial

slip mechanism so there are slip and stick regions. The contact patch size and shape will depend on location on track, vehicle suspension characteristics, weather conditions, type of vehicle, wheel profile and other variables. The traction coefficient can vary widely and can have transverse and longitudinal components.

This computer model is used for simulations of different train configurations. Wear rate, sub-surface strain and crack initiation are calculated out of these contact data.

6.1.3 3D elliptic contact and the partial slip model in Dynarat

Tractive rolling of an elastic sphere on a plane was studied by Johnson (1958a and 1958b). When the tractive force, T, is less than the limiting friction force, μN (where μ is the coefficient of friction and N is the normal load), there is relative slip between the two contact surfaces over part of the contact. In the other part, called the Adhesive Zone (AZ), there is no relative slip, and the surfaces are said to stick. Johnson modelled the AZ as a circular region, tangential to the (also circular) contact region at the leading edge of the contact, but concluded that the difference between this assumed shape of the AZ and the real shape was responsible for inaccuracies in the model's predictions. Vermeulen and Johnson (1964) extended this model to contact over an elliptical region, where the AZ was assumed to be an ellipse similar to the contact ellipse, i.e., the axes of the AZ ellipse are similarly proportional and aligned with the axes of the contact ellipse, and the AZ ellipse is tangential to the leading edge of contact ellipse. This is illustrated in Figure 6.2.

Haines and Ollerton (1963) developed the strip method to model the AZ in elliptical contacts. The contact ellipse is subdivided into thin strips (parallel to the direction of motion) and the 2D partial slip model (Figure 6.1) is applied to each strip. The strip method predicts that the adhesive zone has a 'lemon' shape, following and reflecting the leading edge of the contact ellipse (see Figure 6.2). Photoelastic experiments studying the stresses arising from tractive rolling contact agreed closely with the strip method's predictions.

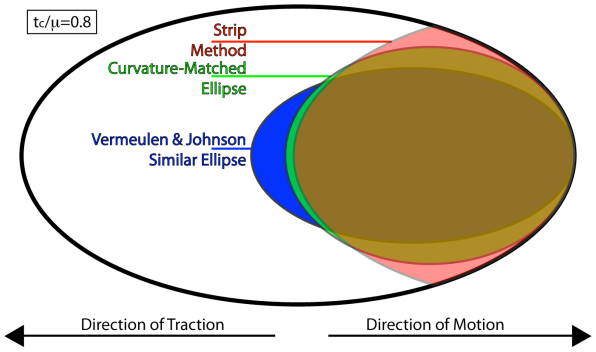

Figure 6.2 The outer ellipse represents an elliptic contact patch which approximates wheel-rail contact. Slip occurs in the non-shaded interior region. Adhesive zones (inner shaded regions) for the three models: the strip method's 'lemon'-shaped AZ follows the leading edge of the contact; Vermeulen and Johnson's similar ellipse AZ is a poor fit to the strip method's AZ; the curvature-matched ellipse AZ is a better approximation to the strip method AZ.

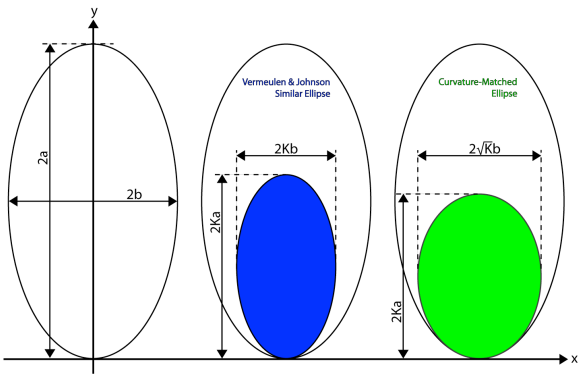

Figure 6.3 Three models for the adhesive ('stick') zone in a partially slipping contact.

Both the above analyses are based on traction parallel to the direction of motion. Haines and Ollerton note (in the Author's Reply) that the shape and size of the AZ are the same when the traction is transverse. Johnson (1985 [§8.4]) reported a 'pear'-shaped AZ for a rubber ball rolling with spin. These are all steady-state solutions achieved under controlled laboratory conditions. In practice, certainly for wheel-rail contact where contact size, shape and forces are continually varying, a detailed dynamic analysis is required to get the transient solutions for stick/slip in the contact; a technique for this has been pioneered by Kalker (1990).

Although Vermeulen and Johnson's assumption of a similar ellipse for the AZ satisfies theoretical constraints, the AZ ellipse is a poor match to the experimentally observed AZ. However, sub-surface stress distributions can be calculated for elliptic regions more easily than for, e.g., the strip method's predicted 'lemon'. A compromise, therefore, is to assume an elliptic AZ, but to choose an ellipse that adheres as closely as possible to

the leading edge of the contact – this is achieved by matching the curvature of the AZ ellipse to the curvature of the contact ellipse at the point where they meet.

The three AZ are illustrated in Figure 6.3.

If the longitudinal width of the contact ellipse is 2*a* and the transverse width is 2*b*, at the point where the AZ ellipse touches the curvature of the contact ellipse, κ_C, is:

$$\kappa_C = \frac{a}{b^2}. \tag{6.1}$$

This formula (6.1) can be derived as:

$$\kappa_C = y''(0),$$

i.e., to calculate the curvature of an ellipse at its lowest point, located at the origin (as in Figure 6.3):

$$\left(\frac{y-a}{a}\right)^2 + \left(\frac{x}{b}\right)^2 = 1 \tag{6.2}$$

$$y = a\left(1 + \sqrt{1 - \frac{x^2}{b^2}}\right) \tag{6.3}$$

$$\kappa_C = y''(0) = \frac{a}{b^2},$$

Alternatively, this can be obtained using direct formula for radius from Savic (1992):

$$R = a^2 b^2 \left(\frac{x^2}{a^4} + \frac{y^2}{b^4}\right)^{3/2} \tag{6.4}$$

where the ellipse is centred at the origin and has horizontal and vertical axes *a* and *b* respectively. The equivalent point is therefore $x=a$, $y=0$:

$$\kappa_C = \frac{1}{R} = \frac{a}{b^2} \tag{6.5}$$

Vermeulen and Johnson's similar ellipse has longitudinal and transverse widths 2*Ka* and 2*Kb* respectively, for same scale factor *K* ($0 < K < 1$), so the corresponding curvature, κ_{VJ}, is:

$$\kappa_{VJ} = \frac{Ka}{(Kb)^2} = \frac{\kappa_C}{K}, \tag{6.6}$$

i.e., the curvature increases as the ellipse is scaled down. If instead the transverse width is scaled by $\sqrt{K}$, the curvature, κ_{CM}, remains the same as the ellipse is scaled down:

$$\kappa_{CM} = \frac{Ka}{\left(\sqrt{K}b\right)^2} = \kappa_C. \tag{6.7}$$

The curvature-matched ellipse is shown in Figure 6.2 and Figure 6.3.

For the strip method, the scale factor K is the ratio of the width of the AZ to the longitudinal width of the contact ellipse. The relationship between scale factor K and the traction coefficient is plotted for the above three AZ models in Figure 6.4(a). For a contact ellipse with a=6.5mm and b=3.5mm, friction coefficient μ=0.45, traction coefficient t_c=0.8μ=0.36 (opposite the direction of motion) and peak pressure p_0=1500MPa, the shear traction along the centreline of the contact is plotted for the three models in Figure 6.4(b). Both plots in Figure 6.4 show that the curvature-matched ellipse is a significantly better match than the similar ellipse to the strip method.

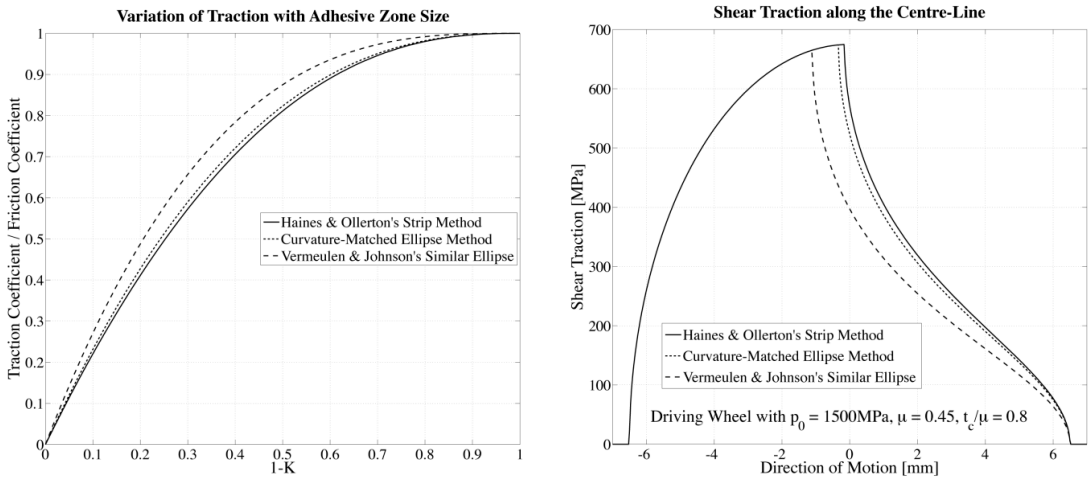

(a) (b)

Figure 6.4 Comparison of the Haines & Ollerton strip method, the curvature-matched ellipse method and the Vermeulen & Johnson similar ellipse method. (a) Relationship between the scaling factor K and the ratio of the traction coefficient to the friction coefficient (where t_c/μ=0 indicates pure rolling and t_c/μ=1 indicates a fully slipping contact). (b) Shear traction distribution along the centre-line of the contact, for the case t_c/μ=0.8. (Note: Since the traction is opposite the direction of x-axis, these distributions should properly have the opposite sign.)

Surface shear traction distributions for the three cases are shown in Figure 6.5(a-c). Figure 6.5(d) shows the orthogonal shear stress, τ_{zx}, in the plane parallel to the surface at depth 0.1mm. (This orthogonal shear stress was used to drive the ratcheting in the previous model, i.e., before transverse shear traction was included in the model.)

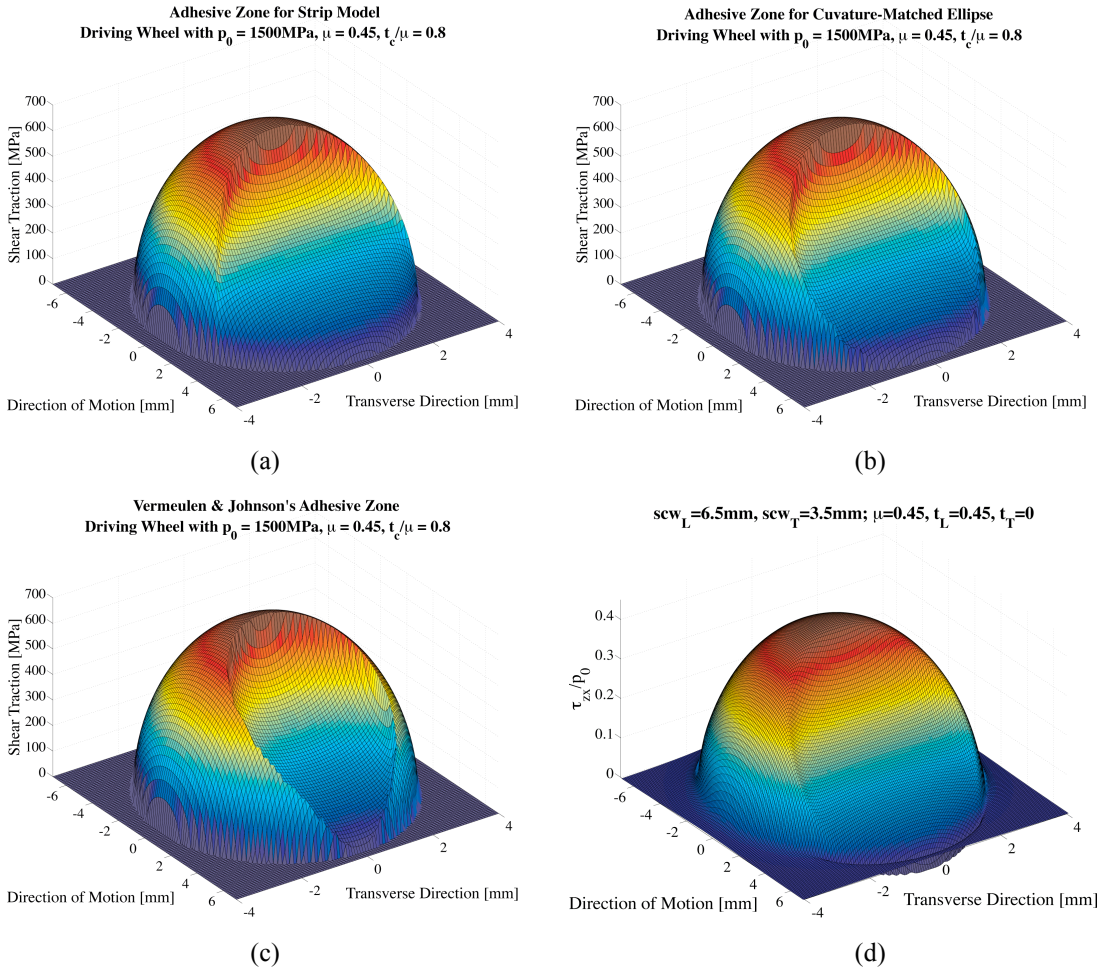

Figure 6.5 (a-c) Surface shear traction distributions for the three partial slip models. (Note: Since the traction is opposite the direction of x-axis, these distributions should properly have the opposite sign.) (d) Distribution of the orthogonal shear stress (normalized w.r.t. peak pressure), τ_{zx}/p_0, in the plane z=0.1mm, i.e., subsurface, parallel to the x-y plane; adhesive zone is curvature-matched ellipse. (Note: Sign of distribution is correct.)

The pressure distribution over the contact ellipse is:

$$p(x,y) = p_0\sqrt{1-(x/a)^2-(y/b)^2}\,, \tag{6.8}$$

taking the origin at the centre of the contact ellipse. The shear traction in the slip zone is:

$$q(x,y) = -\mu p(x,y)\,, \tag{6.9}$$

while the shear traction in the AZ for curvature matched ellipse is:

$$q_{AZ}(x,y) = -\mu p(x,y) + \mu p_0 K\sqrt{1-\left(\frac{x-(1-K)a}{Ka}\right)^2-\left(\frac{y}{\sqrt{K}b}\right)^2} \tag{6.10}$$

i.e., the peak shear force is scaled by the same amount as the longitudinal axis, as in the 2D partial slip model and Vermeulen and Johnson's model. The total tractive force is:

$$T = \mu\left(K^{3/2}-1\right)N \tag{6.11}$$

and so the traction coefficient can be expressed in terms of K (or vice versa):

$$t_c = \frac{T}{N} = \mu\left(K^{5/2} - 1\right). \tag{6.12}$$

From this equation, the sign of t_c is negative, but t_c/μ is plotted with opposite sign in Figure 6.4(a). Only the magnitude of the tractive force is considered in the above equations, but in practice there are longitudinal and transverse components; in general, the longitudinal component arising from train acceleration or braking, and the transverse component arising from curving. The tractive force is negative when accelerating because it is opposite the motion; during braking, the tractive force is positive. The transverse component of the traction does not affect the location of the AZ. Equation (6.10) is assumed here to be valid for any direction of traction, although Haines and Ollerton (1963) report that the distribution of shear traction is a function of Poisson's ratio.

For the elliptic contact pressure and traction described in Equations (6.8) and (6.9), the subsurface distribution of stress is given by Hills *et al.* (1993). The computer simulation uses the method outlined by the ESDU 85007 (1985).

6.2 Directional strain accumulation

In the old model (i.e., without transverse shear traction), ratcheting was driven by the orthogonal shear stress in the *zx*-plane (where *x* is the direction of motion and *z* is depth). The maximum absolute value of the orthogonal shear stress, $\tau_{zx(\max)}$, was calculated at each depth in the simulation plane, and the corresponding shear strain increment, $\Delta\gamma$, calculated:

$$\Delta\gamma^{ij} = Cf\left(\frac{\tau^{j}_{zx(\max)}}{k^{ij}_{eff}}\right)$$

See Equations (5.1) and (5.2). With direction of traction taken as a variable, the direction of ratcheting strain accumulation also needs to be considered. Combined with the orthogonal shear stress in the *yz*-plane, τ_{yz}, the ratcheting is driven by a vector of shear stress, (τ_{zx},τ_{yz}), which has magnitude:

$$\tau = \sqrt{\tau_{zx}^2 + \tau_{yz}^2}\,. \tag{6.14}$$

The maximum absolute value of the shear stress, $\tau_{(\max)}$, at each depth in the simulation plane, drives the ratcheting, so Equation (5.1) needs to be updated:

$$\Delta\gamma^{ij} = Cf\left(\frac{\tau^{j}_{(\max)}}{k^{ij}_{eff}}\right), \tag{6.15}$$

but just as the stress is a vector so the strain (γ_{zx},γ_{yz}) and the strain increment ($\Delta\gamma_{zx}$,$\Delta\gamma_{yz}$) are vectors also, i.e.:

$$\frac{\Delta\gamma^{ij}_{zx}}{\Delta\gamma^{ij}} = \frac{\tau^{j}_{zx(\max)}}{\tau^{j}_{(\max)}}, \quad \frac{\Delta\gamma^{ij}_{yz}}{\Delta\gamma^{ij}} = \frac{\tau^{j}_{yz(\max)}}{\tau^{j}_{(\max)}}, \tag{6.16}$$

where $\tau_{zx(\max)}$ is the value of τ_{zx} when τ is maximum, and similarly for $\tau_{yz(\max)}$. The resultant strain is:

$$\gamma = \sqrt{\gamma^{2}_{zx} + \gamma^{2}_{yz}}\ . \tag{6.17}$$

The strain increments and components are directional, so it is possible for the resultant strain to decrease.

6.3 General head-of-rail simulations and wear equation development

Simulations with the new ratcheting model and new 3D partial slip model have been performed to study trends in the wear rate with variation of the load and the magnitude and direction of the applied traction.

The wear model is sensitive to vehicle characteristics through their effect on the wheel-rail contact patch, in particular contact patch size and shape, normal load and traction coefficient. Unless otherwise stated, this study makes the following assumptions:

- The contact patch shape is elliptical and the pressure distribution is Hertzian. Longitudinal semi-contact width (a) and transverse semi-contact width (b) are calculated from the normal load using the following relation derived for an elliptic contact patch representing wheel-rail contact on top of the railhead, i.e., appropriate for straight track, not curves (Kabo *et al.*, 2009):

$$\begin{aligned} a &= 1.57\times10^{-4}\times\sqrt[3]{N} \\ b &= 1.19\times10^{-4}\times\sqrt[3]{N} \end{aligned} \tag{6.18}$$

  where N is the normal load. The peak pressure is given as usual by:

$$p_0 = \frac{3}{2}\frac{N}{\pi ab} \tag{6.19}$$

- The friction coefficient (as distinct from traction coefficient) is assumed to be constant and equal to 0.45.
- Effects of lubrication, rainwater and track contaminants are not included.

- The vehicle condition selected as a 'standard' case for this study is a normal load of 100 kN (approximating a 20-tonne axle load) and traction coefficient 0.3. Only longitudinal traction is considered.

The Dynarat wear model used here is applied with input parameters corresponding to R260 grade rail steel under dry contact conditions (see Chapter 4).

6.3.1 Contact offset

Using the model the effect of traction coefficient and transverse offset of the contact (see Figure 6.6) were studied for normal load 100 kN and for a range of longitudinal traction coefficients. Wear rate, averaged over 100000 cycles, is shown in Figure 6.7. Wear rate is maximum at the centreline of the contact, dropping to zero at the edges of the contact. The average wear rate across the full width of the contact is about 75 % of the wear rate at the centreline.

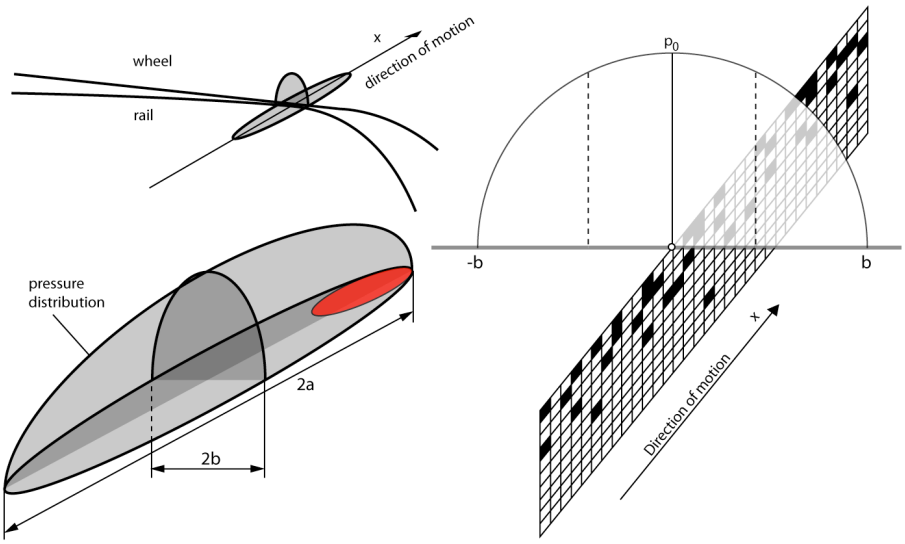

Figure 6.6 Variation on Figure 2.24 including the adhesive zone for the curvature-matched ellipse used in the partial slip model.

Traction coefficient has a significant effect on the wear rate. For unpowered coaches there should be no traction on straight track (except for steering forces, or when braking, on approach to a station, for example).

For distributed traction systems the traction coefficient may often be about 0.1. For the corresponding curve in Figure 6.7, the average wear rate is about 0.75 nm/cycle. For locomotives the traction coefficient may be 0.3 or even higher, i.e., an average wear rate of 1.5 nm/cycle or more.

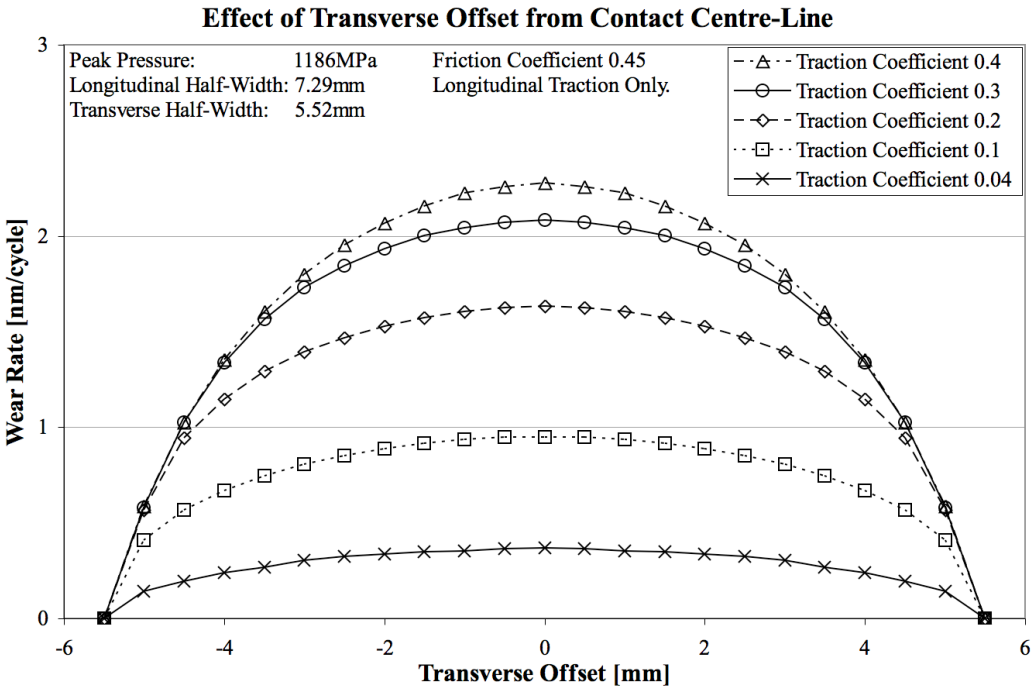

Figure 6.7 Predicted wear rates, averaged over 100000 cycles, for a range of (longitudinal) traction coefficients (with friction coefficient 0.45) and normal load 100 kN. The transverse half-width is 5.52 mm, and wear rates are evaluated in 0.5 mm intervals from the centreline to the edge of the contact.

The results in Figure 6.7 have been studied for trends of wear rate against traction coefficient, and these are shown in Figure 6.8. A second order polynomial has been fit to the centre wear rates, while a straight line has been fit to the average wear rate (the average across the transverse width of the contact, in proportion to the centre wear rate). The product of these, i.e., the average wear rate across the transverse width of the contact, is given in Figure 6.8(b), along with a best-fit cubic polynomial (constrained to pass through the origin). Since the applied tractive force increases with t_c/μ, wear rate should also increase with t_c/μ. The best fit, however, is not continuously increasing on the range [0,1], so an alternative fit has been proposed, a cubic polynomial passing through the origin with a stationary maximum when $t_c=\mu$. The two curve fits are very similar, within the range of the data fitted; the main difference is the projected behaviour as t_c approaches μ.

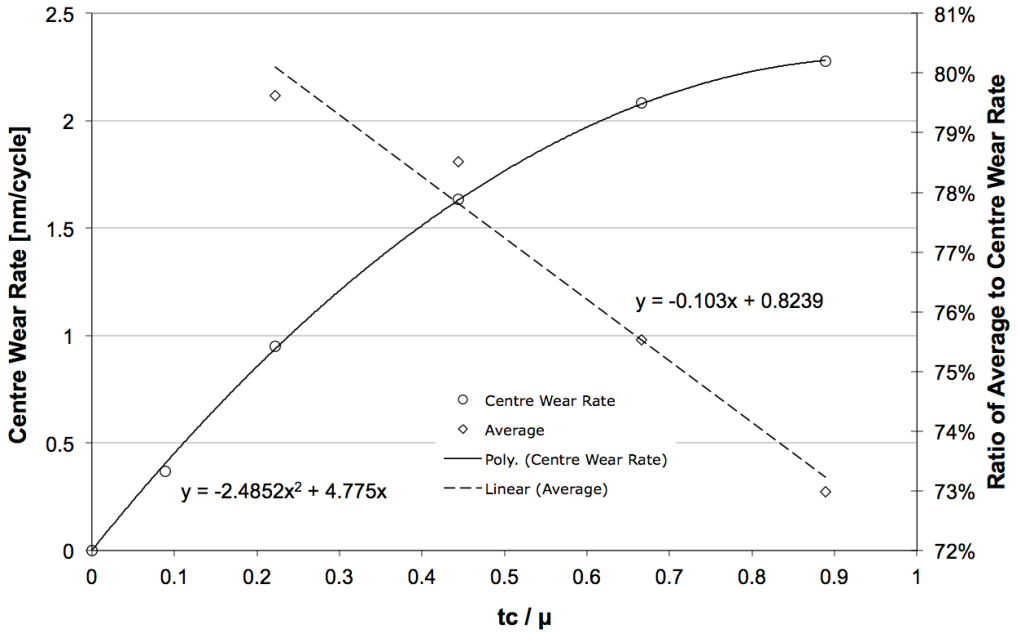

(a)

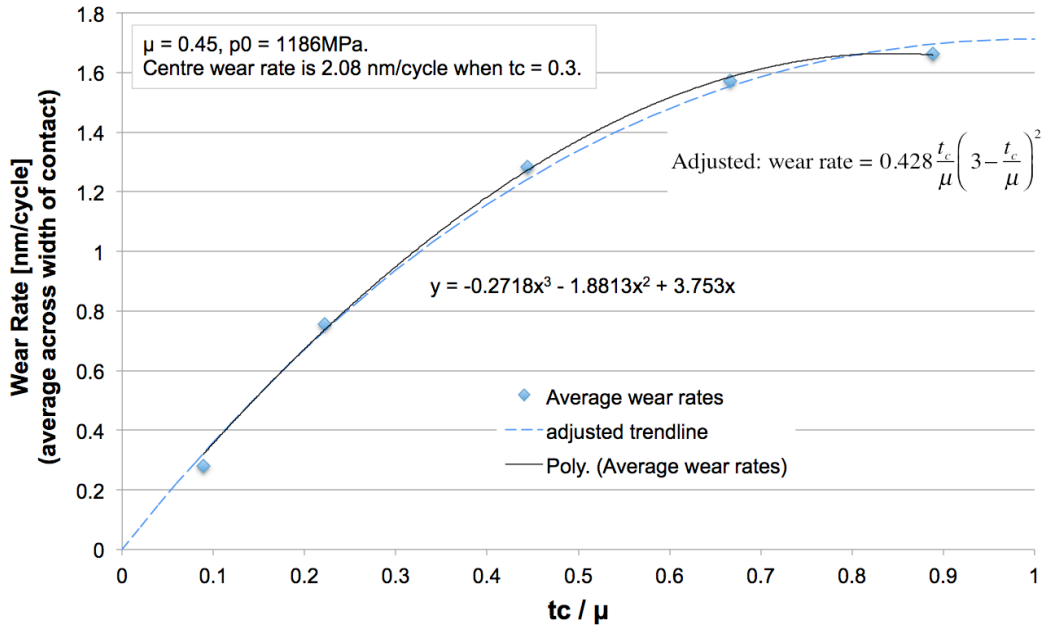

(b)

Figure 6.8 Wear rate trend with traction coefficient as a proportion of the limiting friction coefficient. (a) Wear rate at the centre line, and average across the transverse width of the contact as a proportion of the centre line wear rate. (b) Wear rate average across the transverse width of the contact, and comparison with adjusted trendline.

6.3.2 Transverse traction

Direction of traction has only a very slight influence on the wear rate. Figure 6.9 shows full slip contact with three directions of traction (at 0°, 45° and 90°, 0° being longitudinal-only and 90° being transverse-only), and also partial slip contact with three directions of traction (at 30°, 45° and 60°).

The results suggest that direction of traction can be neglected. Note, however, that in these simulations the same contact is repeated for all load cycles, and the effect of the wear rate of changing traction direction with each load cycle is not investigated but may be significant.

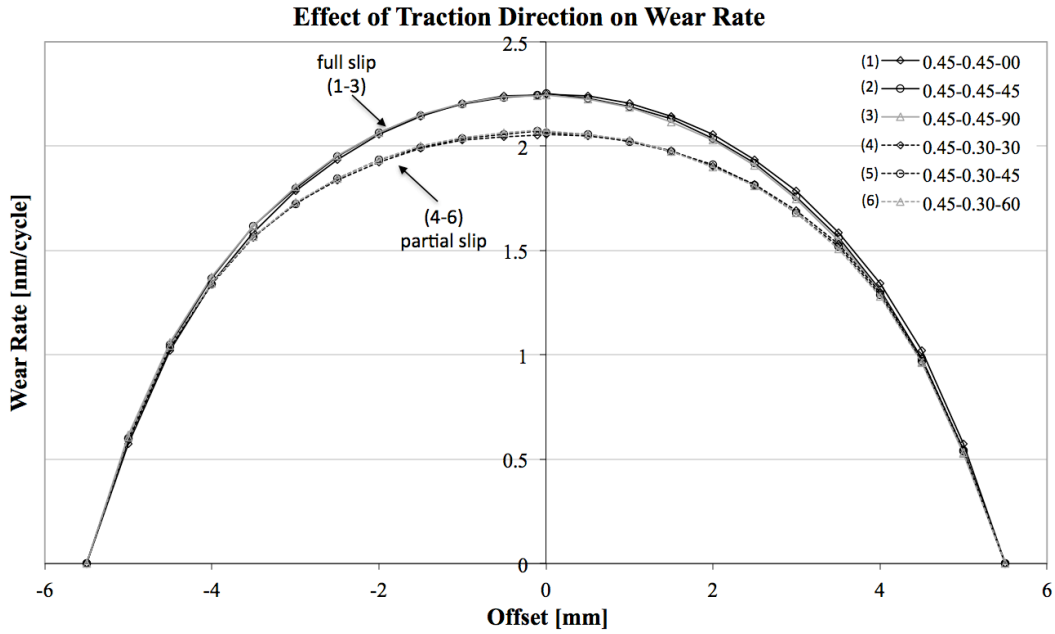

Figure 6.9 Effect of traction direction on wear rate. Three directions each of fully and partially slipping contact (traction coefficient 0.3), both with friction coefficient 0.45. (0°=longitudinal; 90°=transverse).

6.3.3 Pressure variation

To study the effect of contact pressure on the wear rate, and also to study the effect of contact force variation caused by out-of-round wheels, a distribution of pressures representing variation of contact force was selected (see Figure 6.10). A wear simulation was performed for each pressure, and Figure 6.11 shows the centre-line wear rate averaged (a) over the whole 100000 cycles (b) over the first 10000 cycles, and (c) over the last 10000 cycles. The last is taken as a prediction of the asymptotic 'steady state' wear rate. For all three averaging periods, there is a clear linear trend, and the equations of the linear fits are given in Figure 6.11. Figure 6.8(b) and Figure 6.11 suggest the following wear equation relating wear to traction coefficient:

$$w = 0.2\frac{t_c}{\mu}\left(3-\frac{t_c}{\mu}\right)^2\left(2.3p_0-0.68\right) \tag{6.20}$$

where p_o is peak pressure in GPa, and w is average wear rate in nm/cycle; friction coefficient $\mu = 0.45$. To calculate profile area loss, the wear rate should be multiplied by the width of the contact.

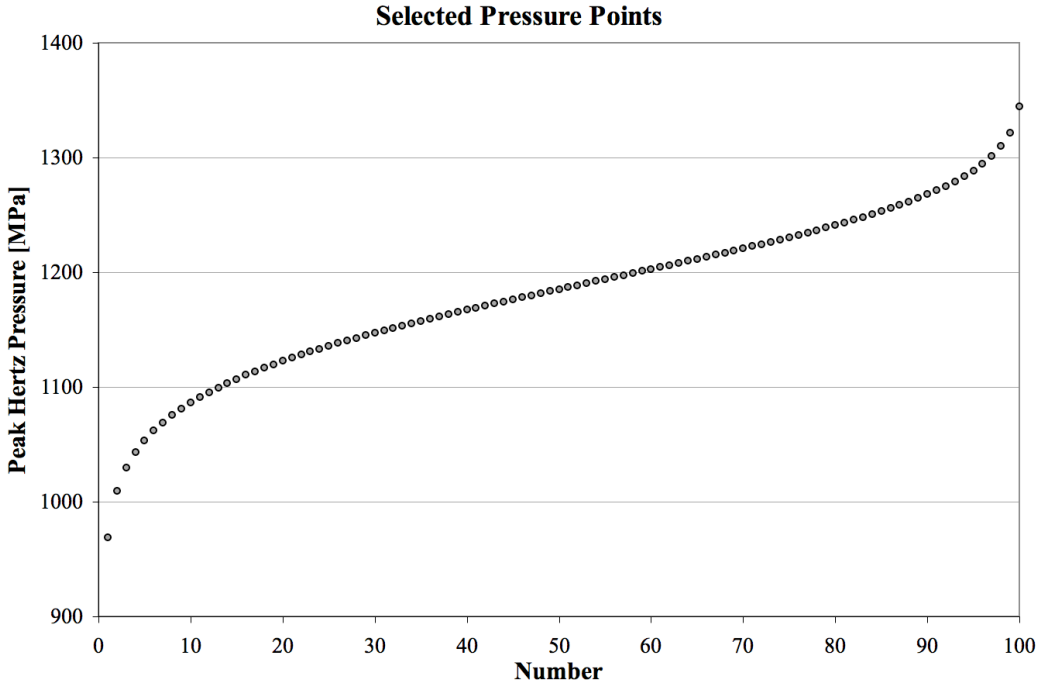

Figure 6.10 100 pressures selected to represent a normal (i.e., Gaussian) variation of contact loads (mean: 100 kN; standard deviation 25 kN).

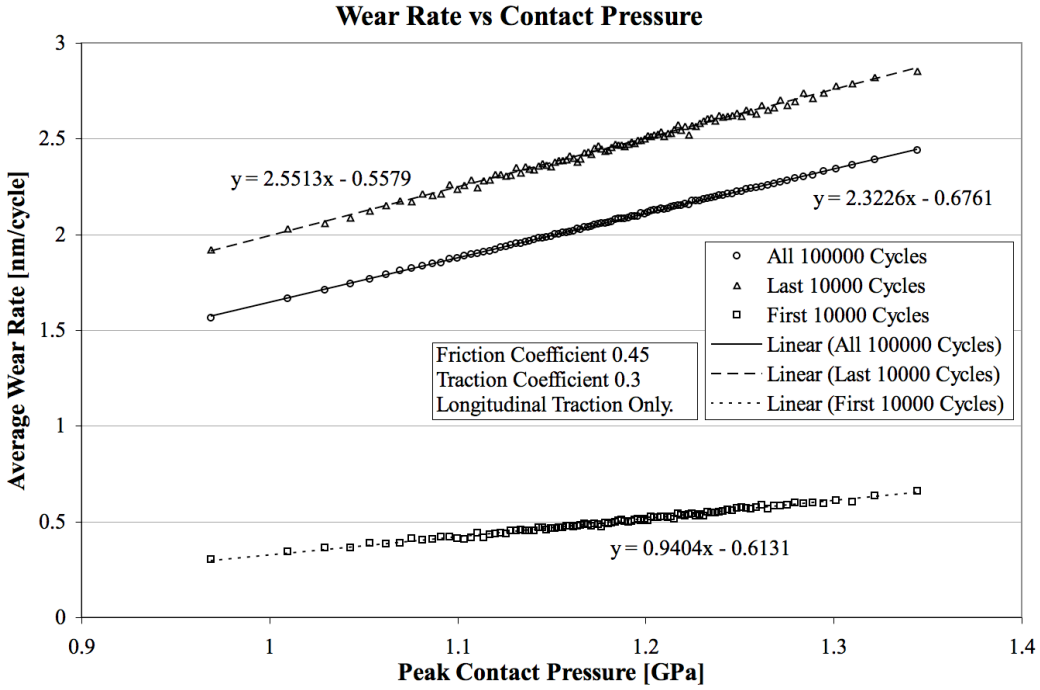

Figure 6.11 Wear rates from simulations over 100000 cycles showing the effect of pressure.

6.4 Comparison of average and variable loading

In Figure 6.11 the contact pressure was the same for each wheel pass during the simulation. To study the effect of out-of-round wheels on the wear rate, simulations were performed in which each wheel pass had a different pressure chosen at random from the selection in Figure 6.10. This was done for two traction coefficients, 0.2 and

0.3, constant throughout the simulation, and the results are compared in Figure 6.12 with simulations in which the contact pressure was constant (the average pressure) for each wheel pass.

The pressure variation does not have a significant effect on the wear rate in either case, suggesting that out-of-round wheels do not need to be considered in wear rate calculations. This is a consequence of the choice of a normal distribution of loads, and the linear relationship between peak pressure and wear rate; the large loads are balanced out by the low loads. In practice, a different distribution of loads is likely, skewed so that significantly higher loads are possible. In addition, the linear relationship is predicted by the ratcheting model which does not account for high impact loads which cause severe plastic damage to the rail. Also, the effect of out-of-round wheels on crack growth cannot be neglected – see InnoTrack Deliverable D4.2.5.

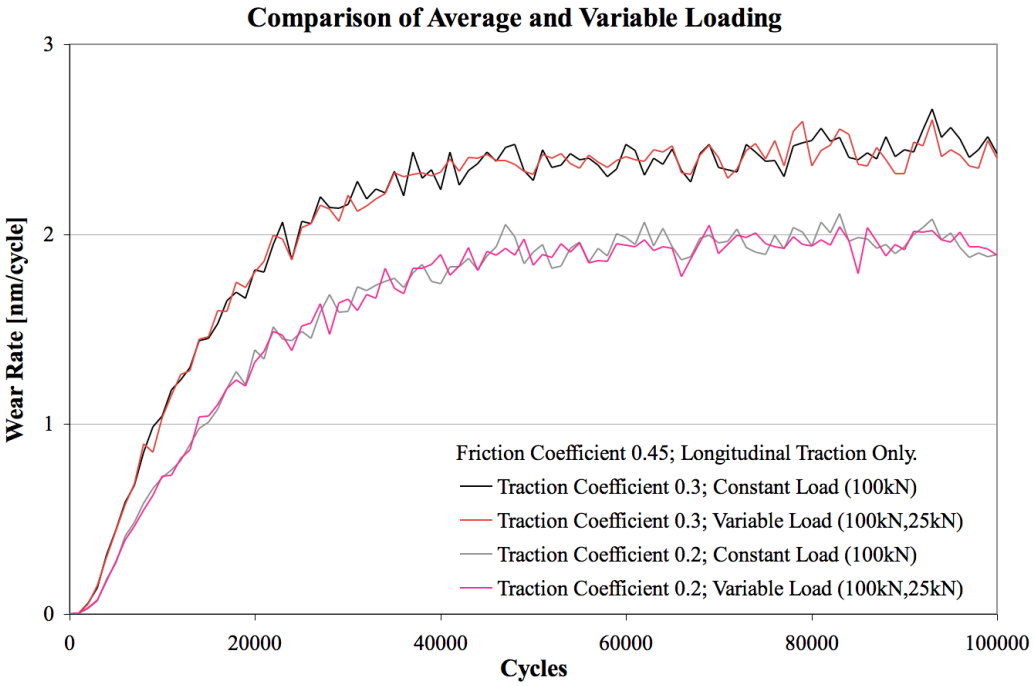

Figure 6.12 Effect of contact pressure variation (between wheel passes) caused by out-of-roundness. Simulations with (longitudinal) traction coefficients 0.2 and 0.3, compared with respective constant pressure equivalent cases.

6.5 Summary

A new partial slip model has been implemented in the 3D Dynarat computer simulation in which the adhesive zone (stick region) is elliptical, like in Vermeulen and Johnson's (1964) model, but which is curvature-matched rather than similar. This provides a superior approximation to the strip method's adhesive zone which has good agreement

with experimental observation of the adhesive zone in rolling contact (Haines and Ollerton, 1963).

In addition, the model has been developed to make direction of traction a variable, and the orthogonal shear stresses and the accumulating shear strain are therefore calculated in both the *zx*- and *yz*-planes.

The main conclusions are:

- A brief study of traction direction in full and partially slipping contact suggests that traction direction is not significant for wear. However, the effect of variation of traction direction between wheel passes needs further study.
- Traction coefficient has a significant effect on the wear rate. For example, in distributed traction systems where the traction coefficient is typically about 0.1, the model predicts an average wear rate of about 0.75 nm/cycle. For locomotives, where the traction coefficient may be 0.3 or even higher, the model predicts an average wear rate of 1.5 nm/cycle or more.
- There was a very clear linear trend of wear rate against peak contact pressure (for the range of pressures studied). For the range of contact conditions studied, wear rate is found to vary linearly with peak contact pressure, and an equation for estimating wear rate as a function of peak pressure and traction coefficient is fitted to the simulation data.

Chapter 7 Traffic Simulation and Wear Prediction

Different vehicles have different dynamic loading characteristics and damage the rail to a greater or lesser extent. In practice, traffic is a mixture of different vehicle types, and any given point on the rail is subjected to a range of contacts. This chapter presents a case study of how the model can be implemented to predict wear and crack initiation for real traffic.

During Rail Safety & Standards Board's Project T355, 2006, vehicle dynamics simulations were performed using 'VAMPIRE'[1] with four vehicle types – Class 43 locomotive, Mark 3 coach, Class 91 power car and Mark 4 coach – at two curves (a 1250m-radius curve at Harringay and a 3000m-radius curve at Sandy) on the East Coast Main Line (ECML) in the UK. (The Class 365 EMU was also simulated in VAMPIRE for the RSSB project, but is not included in the present study.) This provided data on contact patch area (the contact patch is approximated as an ellipse) and forces – sufficient for calculation of peak pressure, traction coefficient and contact stresses – for one wheel each on the high rail at three locations at these two sites. This was used as an input to the ratcheting simulation for this chapter.

The material model used for the simulations is that developed for British standard grade 220 (R220) rail steel by Franklin & Kapoor (2007), not the new material model used in the previous chapters. The likelihood of crack initiation is studied using a new prediction method 'PC-Depth'. Simulations are performed using both the original wheel-rail contact model, assuming a fully slipping contact with no transverse component, and the new partial slip model described in Chapter 6. Results from both models are discussed.

7.1 Input Data

7.1.1 Location

Harringay and Sandy are names for locations on the East Coast Main Line (ECML) in the UK. Harringay is a curve with radius of 1250m and Sandy of 3000m. Data for the two curves have been used as input to the Dynarat model. Three locations at each curve are considered:

[1] DeltaRail's railway vehicle and track dynamics simulator, used by Network Rail.

Harringay: 2179.03, 2188 and 2196.96

Sandy: 871.057, 879.998 and 888.939

The numbers represent distances along the curves.

7.1.2 Wheel profiles

The three wheel profiles used in the vehicle dynamics analysis are based on the P8 wheel profile which is used widely in the UK. As a result of wheel wear, profiles vary during the life of the wheel, with periodic maintenance (i.e., turning or grinding of the wheel) re-applying the original profile. The three profiles used in the analysis represent the original P8 profile ('P8 new'), and profiles typical of worn ('P8 average') and heavily worn ('P8 worn') wheels which started with a P8 profile.

7.1.3 Rail material

Rail material at Harringay and Sandy curves was R220 rail steel and the material model used for the simulations is that developed by Franklin & Kapoor (2007). The microstructure is described in detail in Section §2.6.2.

7.1.4 Traffic mixture

The following four vehicles are considered here:

Class 91 Electric locomotive, weight 84t, modern design

Class 43 HST (high speed train) diesel power car, weight 70t, has higher primary jaw stiffness than Class 91

Mark 4 Coach, with bogie that has high primary jaw stiffness

Mark 3 Coach, which has modern bogie design with moderate primary jaw stiffness

The wheel-rail data provided gives contact data for one wheel on the outer (high) rail, where gauge corner cracking is usually a problem. In this work, the other three wheels of the vehicle (on the same rail) are assumed to have the same contact data (although in practice the leading wheelset of each bogie generally produces higher forces than the trailing wheelset).

For the simulation, the trains are composed as follows:

Intercity[2] 125: First power car – Class 43 (4 wheels); followed by 9 coaches (Mark 3), four wheels each; and at the end, the power car – Class 43 (4 wheels). No distinction is made between the two locomotives.

Intercity 225: Locomotive – Class 91 (4 wheels); followed by 9 coaches (Mark 4), four wheels each; and at the end, the power car – Class 91 (4 wheels). No distinction is made between the locomotive and the Class 91 driving van trailer.

Each train, therefore, will have 44 wheel/rail contacts. The data for the individual vehicles has been structured in the input data for Dynarat to simulate these two trains. The input files for these simulations specify a sequence of 176 contacts, i.e., the equivalent of four trains; the sequence is then repeated until the total number of load cycles reaches the requested number.

Different proportions of the two intercity trains in the total traffic are considered. In the following results, these proportions are represented as follows:

0%	Only Intercity 225,
25%	25% of Intercity 125 and 75% of Intercity 225,
50%	50% of Intercity 125 and 50% of Intercity 225,
75%	75% of Intercity 125 and 25% of Intercity 225,
100%	Only Intercity 125.

7.1.5 Contact conditions

The wheel-rail contact patch is modelled as elliptical. Contact data provided by the multibody simulation software VAMPIRE includes contact patch area and ellipticity.

At Harringay, for both coaches and locomotives, the longitudinal and lateral creep forces were approximately equal at all three locations. At Sandy, the forces were generally lower, and for the Mark 4 and the Class 43 at Location 888.939 (F) the longitudinal force was in the direction of motion (representing a slight braking effect). Creepage, or slip ratio, is presented in Table 7.1.

Wheel-rail contact data for the three locations at Harringay are presented in Table 7.2, and for the three locations at Sandy in Table 7.3.

[2] 'Intercity' is an old term, but used here for convenience.

This data has been used in modelling wear and crack initiation for this thesis. There are differences between fully slipping and partial slipping contact modelling, so it is specified throughout the thesis which data from these tables are used.

Table 7.1 Vehicle speed and creepage (slip ratio), and identifiers (A-F) used for each track location studied.

Harringay (85mph)	**Location (Identifier)**		
Vehicle	**2179.03 (A)**	**2188 (B)**	**2196.96 (C)**
Mark 4 Coach	0.30%	0.23%	0.20%
Mark 3 Coach	0.27%	0.30%	0.32%
Class 43	0.30%	0.22%	0.24%
Class 91	0.28%	0.24%	0.25%
Sandy (125mph)	**Location (Identifier)**		
Vehicle	**871.057 (D)**	**879.998 (E)**	**888.939 (F)**
Mark 4 Coach	0.04%	0.08%	0.02%
Mark 3 Coach	0.05%	0.12%	0.02%
Class 43	0.06%	0.08%	0.01%
Class 91	0.12%	0.09%	0.02%

7.1.6 Simulation length

Simulations are run for 4,000 trains (176,000 cycles), which is approximately 2 million gross tonnes (MGT), at each of the three locations at Harringay; and for 8,000 trains (352,000 cycles), at each of the three locations at Sandy. Therefore, there have been 90 simulations performed with the new model, see Section §7.4, and 30 simulations with the old model (restricted to average P8 wheel profile), see Section §7.3.

Table 7.2 Wheel-rail contact data for three locations at Harringay. Vehicle speed is 85mph. Friction coefficient is 0.45.

Vehicle	Profile	Distance	Peak Pressure (MPa)	Longitudinal Semi-Width (mm)	Transverse Semi-Width (mm)	Traction Coefficient (Longitudinal)	Traction Coefficient (Transverse)	Traction Coefficient (Combined)
Mk4	worn P8	2179.03	1554.58	7.06	2.32	0.261	0.227	0.346
Mk4	worn P8	2188	1313.93	6.78	3.01	0.213	0.229	0.312
Mk4	worn P8	2196.96	1634.67	7.47	2.48	0.230	0.229	0.324
Mk4	average P8	2179.03	1283.73	6.67	2.97	0.274	0.247	0.369
Mk4	average P8	2188	1725.31	7.32	2.12	0.205	0.201	0.287
Mk4	average P8	2196.96	1655.51	7.47	2.47	0.184	0.193	0.267
Mk4	new P8	2179.03	1284.54	6.65	2.99	0.240	0.222	0.327
Mk4	new P8	2188	1396.07	6.90	2.81	0.199	0.207	0.287
Mk4	new P8	2196.96	1351.21	7.04	3.21	0.215	0.220	0.308
Mk3	worn P8	2179.03	1529.21	6.86	2.23	0.273	0.201	0.339
Mk3	worn P8	2188	1515.24	6.89	2.30	0.269	0.196	0.333
Mk3	worn P8	2196.96	1597.84	7.23	2.33	0.253	0.201	0.324
Mk3	average P8	2179.03	1453.11	6.75	2.38	0.256	0.197	0.323
Mk3	average P8	2188	1460.27	6.82	2.41	0.274	0.191	0.333
Mk3	average P8	2196.96	1508.33	7.08	2.51	0.270	0.212	0.343
Mk3	new P8	2179.03	1251.34	6.43	2.88	0.246	0.210	0.323
Mk3	new P8	2188	1388.26	6.68	2.58	0.229	0.175	0.288
Mk3	new P8	2196.96	1338.62	6.83	3.00	0.217	0.184	0.284
Class 43	worn P8	2179.03	1387.63	8.08	3.66	0.262	0.244	0.358
Class 43	worn P8	2188	1423.08	8.09	3.59	0.176	0.203	0.268
Class 43	worn P8	2196.96	1348.08	8.00	3.93	0.206	0.239	0.315
Class 43	average P8	2179.03	1372.55	8.06	3.70	0.268	0.261	0.374
Class 43	average P8	2188	1739.39	8.61	2.76	0.180	0.215	0.281
Class 43	average P8	2196.96	1820.07	8.82	2.68	0.183	0.227	0.291
Class 43	new P8	2179.03	1370.00	8.02	3.76	0.256	0.227	0.342
Class 43	new P8	2188	1646.07	8.45	2.97	0.186	0.191	0.267
Class 43	new P8	2196.96	1465.81	8.27	3.53	0.230	0.238	0.331

Vehicle	Profile	Distance	Peak Pressure (MPa)	Longitudinal Semi-Width (mm)	Transverse Semi-Width (mm)	Traction Coefficient (Longitudinal)	Traction Coefficient (Transverse)	Traction Coefficient (Combined)
Class 91	worn P8	2179.03	1594.98	8.77	3.57	0.236	0.243	0.339
Class 91	worn P8	2188	1664.74	8.96	3.61	0.183	0.177	0.255
Class 91	worn P8	2196.96	1640.34	9.01	3.68	0.204	0.233	0.309
Class 91	average P8	2179.03	1497.19	8.59	3.89	0.255	0.239	0.350
Class 91	average P8	2188	1934.21	9.36	2.97	0.195	0.198	0.278
Class 91	average P8	2196.96	1532.74	8.77	3.94	0.229	0.252	0.340
Class 91	new P8	2179.03	1512.23	8.57	3.92	0.206	0.162	0.262
Class 91	new P8	2188	1742.82	9.07	3.40	0.171	0.162	0.235
Class 91	new P8	2196.96	1499.84	8.51	3.91	0.158	0.218	0.269

Table 7.3 Wheel-rail contact data for three locations at Sandy. Vehicle speed is 125mph. Friction coefficient is 0.45.

Vehicle	Profile	Distance	Peak Pressure (MPa)	Longitudinal Semi-Width (mm)	Transverse Semi-Width (mm)	Traction Coefficient (Longitudinal)	Traction Coefficient (Transverse)	Traction Coefficient (Combined)
Mk4 coach	worn P8	871.057	1021.53	6.33	5.01	0.037	0.060	0.070
Mk4 coach	worn P8	879.998	1418.38	7.17	3.10	0.160	0.126	0.203
Mk4 coach	worn P8	888.939	825.14	5.78	7.60	-0.037	-0.006	0.037
Mk4 coach	average P8	871.057	1182.69	6.73	4.05	0.078	0.077	0.109
Mk4 coach	average P8	879.998	1661.96	7.53	2.55	0.109	0.092	0.142
Mk4 coach	average P8	888.939	747.73	5.47	8.92	-0.022	0.024	0.032
Mk4 coach	new P8	871.057	1385.42	7.13	3.25	0.118	0.084	0.145
Mk4 coach	new P8	879.998	1015.60	6.28	4.95	0.088	0.057	0.105
Mk4 coach	new P8	888.939	829.04	5.81	7.45	0.010	0.033	0.034
Mk3 coach	worn P8	871.057	931.43	5.83	4.84	0.041	0.034	0.054
Mk3 coach	worn P8	879.998	1383.14	6.86	2.87	0.177	0.110	0.208
Mk3 coach	worn P8	888.939	712.31	5.14	8.06	0.004	0.038	0.038
Mk3 coach	average P8	871.057	990.86	5.99	4.44	0.062	0.035	0.071
Mk3 coach	average P8	879.998	1374.07	6.83	2.89	0.157	0.087	0.180
Mk3 coach	average P8	888.939	703.42	5.11	8.21	0.033	0.039	0.051
Mk3 coach	new P8	871.057	767.92	5.26	6.42	-0.017	-0.008	0.019
Mk3 coach	new P8	879.998	1256.30	6.64	3.28	0.114	0.044	0.123
Mk3 coach	new P8	888.939	905.94	5.87	5.62	0.086	0.057	0.103
Class 43	worn P8	871.057	1136.87	7.58	5.39	0.071	0.051	0.087
Class 43	worn P8	879.998	1429.91	8.31	3.98	0.117	0.107	0.158
Class 43	worn P8	888.939	962.74	7.11	7.45	-0.012	0.030	0.032
Class 43	average P8	871.057	1171.58	7.66	5.14	0.076	0.059	0.096
Class 43	average P8	879.998	1734.73	8.84	3.06	0.110	0.102	0.150
Class 43	average P8	888.939	986.52	7.20	7.20	-0.004	0.049	0.049
Class 43	new P8	871.057	1038.16	7.27	6.10	0.077	0.044	0.089
Class 43	new P8	879.998	1461.28	8.36	3.84	0.118	0.092	0.150

Vehicle	Profile	Distance	Peak Pressure (MPa)	Longitudinal Semi-Width (mm)	Transverse Semi-Width (mm)	Traction Coefficient (Longitudinal)	Traction Coefficient (Transverse)	Traction Coefficient (Combined)
Class 43	new P8	888.939	998.83	7.27	7.12	0.010	0.025	0.027
Class 91	worn P8	871.057	1205.71	7.79	5.32	0.084	0.082	0.118
Class 91	worn P8	879.998	1484.92	8.62	4.30	0.114	0.104	0.154
Class 91	worn P8	888.939	766.41	6.26	12.49	0.016	0.014	0.021
Class 91	average P8	871.057	1872.02	9.07	2.93	0.148	0.104	0.181
Class 91	average P8	879.998	1822.96	9.16	3.23	0.105	0.121	0.160
Class 91	average P8	888.939	1082.29	7.67	7.31	0.030	0.053	0.061
Class 91	new P8	871.057	1790.67	9.01	3.14	0.182	0.108	0.211
Class 91	new P8	879.998	1943.70	9.30	2.99	0.119	0.109	0.161
Class 91	new P8	888.939	1043.78	7.55	7.74	0.046	0.058	0.074

7.2 Traffic simulations using old 3D model with full slip

7.2.1 Input data

- Wheel profiles: Only average P8 wheel profile was used in simulations.
- Contact conditions:
  - Full slip contact is assumed in the Dynarat simulations.
  - The predicted traction coefficient (combined) is used as the friction coefficient.
- Simulations:
  - That means that 30 simulations are run, i.e., 2 sites × 3 locations × 5 train proportions × 1 wheel profile.

Accumulated shear strain, stress and wear rates are calculated in each simulation.

7.2.2 Simulation results and discussion

Wear rate predictions for the different traffic mixtures and locations are given in Table 7.4. Wear rates at Sandy (radius 3000m) are significantly lower than those at Harringay (radius 1250m). Comparing different proportions of Class-43/Mark-3 traffic, only in one of the six cases (Harringay Location C) does the Class-43/Mark-3 cause a higher wear rate than the Class-91/Mark-4.

The variation of the wear rate with traffic mix is almost linear. The linear relationship means that wear rates can be calculated for individual trains and then a weighted average of these used to calculate wear rates of different combinations of trains.

Table 7.4 Predicted wear rates [nm/cycle], averaged over 4,000 trains at Harringay, and 8,000 trains at Sandy.

Percentage of Traffic as 43/Mk-3	Harringay Locations			Sandy Locations		
	A	B	C	D	E	F
0%	1.693	1.966	1.435	0.086	0.07	0
25%	1.666	1.869	1.674	0.058	0.067	0
50%	1.637	1.782	1.871	0.036	0.066	0
75%	1.612	1.696	2.054	0.013	0.066	0
100%	1.581	1.629	2.220	0	0.067	0

The current simulations have a 1024×2048 mesh of square 1μm×1μm elements (i.e., approximately 1mm horizontally × 2mm depth). At each depth below the rail surface, according to the microstructure model – the pattern in Figure 2.31(a) repeated – a proportion of the elements have been given properties of ferrite, and the remainder have

been given properties of pearlite. Figure 7.1 shows the accumulated shear strain, averaged at each depth over the ferrite elements (Figure 7.1(a,c)) and, separately, the pearlite elements (Figure 7.1(b,d), for Location A at Harringay (after 4,000 trains) and for Location D at Sandy (after 8,000 trains). Pearlite is harder than the ferrite and accumulates shear strain more slowly.

For both locations the shear strain is clearly greater when the traffic is Class-91/Mark-4 compared to when the traffic is Class-43/Mark-3. For Location A at Harringay the traction coefficient is relatively high, and close to the surface (i.e., within 0.5mm) there is considerable shear strain in the harder pearlite as well as in the ferrite. For Location D at Sandy the traction coefficient is low and the accumulated shear strain is larger subsurface than at the surface.

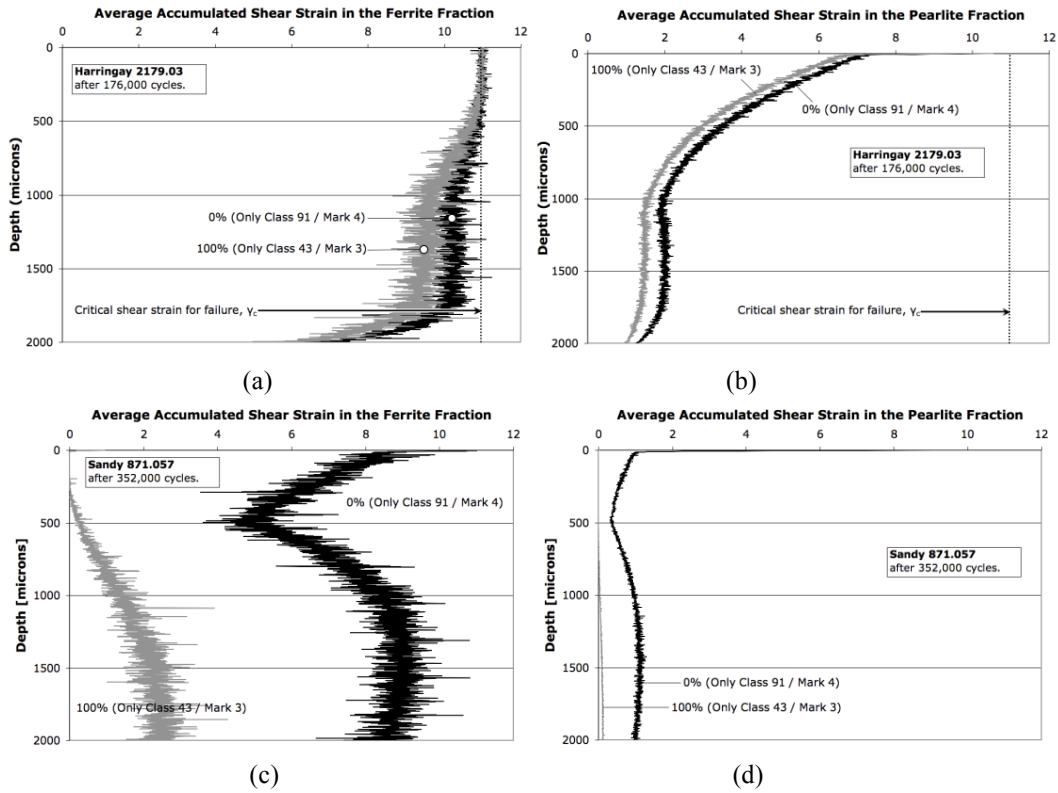

Figure 7.1 Accumulated shear strain with depth, averaged across the ferrite and pearlite elements separately at each depth. (a-b) Harringay: Location A. (c-d) Sandy: Location D

Shear stress

The distributions of maximum orthogonal shear stress for Locations B and C at Harringay are compared in Figure 7.2. In both these cases, three of the four stress distributions are very similar. At Location B, the stress distribution for the Class 91 is significantly greater than for the other vehicles, so the Class-91/Mark-4 would be expected to be more damaging. At Location C, however, the stress distribution for the

Mark 4 is significantly lower than for the other vehicles, so the Class-91/Mark-4 would be expected to be less damaging. The stress distributions for Location D at Sandy are shown in Figure 7.2(c). The stress distribution for the Class 91 is significantly higher than for the other vehicles, especially at the surface; but for all vehicles the stress is lower than at Harringay.

Crack Initiation Prediction

Three methods of predicting crack initiation and probable depth were used:

- Analysis of the shear strain plots
- '10% Damage Depth' (10DD)
- 'PC Depths'

The probable depth of initiating cracks can be estimated from the accumulated shear strain. When the shear strain reaches the critical strain for failure, the material is regarded as 'weak', unable to support tensile stresses, so crack initiation in this region is likely.

For these two cases, the shear strain reaches the critical shear strain for failure (γ_c =11) only at Harringay, and only in the top 0.5mm of the ferrite fraction. Figure 7.1 indicates that after 4,000 trains (irrespective of type), cracks of depth 0.5mm (or, at least, initiation of damage to this depth) would be expected at Location A at Harringay, but no cracks are indicated at Location D at Sandy, even after 8,000 trains.

Snap-shots of the simulation at Location A after 20,000 cycles are shown in Figure 7.3. The snap-shot in Figure 7.3(a) is the internal representation, which does not indicate the accumulated plastic shear strain. When the shear strain is considered (see Figure 7.3(b)), the ferrite grain boundaries (where failure occurs soonest) are elongated and can become natural paths for crack initiation and propagation. Unlike the regular hexagonal microstructure used in earlier versions of this model (Franklin and Kapoor, 2007; Garnham *et al.*, 2007), the irregular structure does provide some resistance to crack growth, especially when both crack and microstructure are treated as three-dimensional; however, 3D microstructure is not modelled here.

Crack initiation can be predicted by using image analysis techniques to identify clusters of failed elements in the simulation matrix (Fletcher *et al.*, 2003).

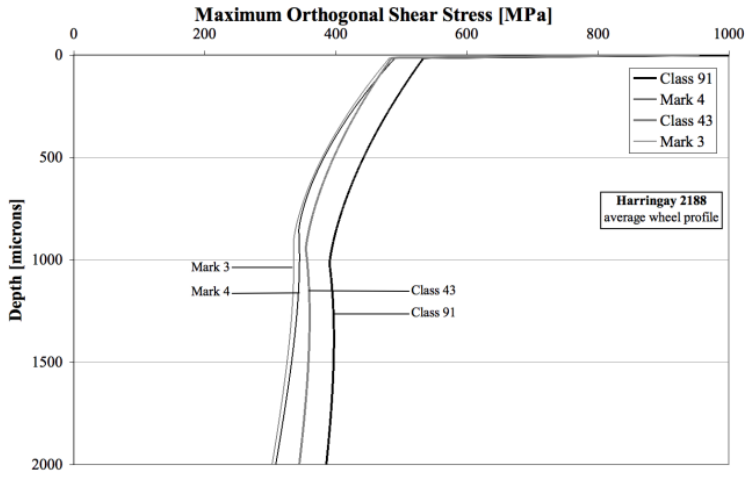

(a)

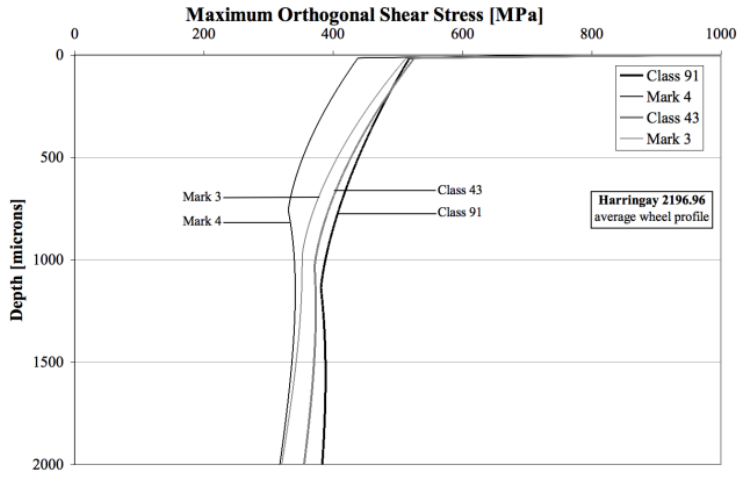

(b)

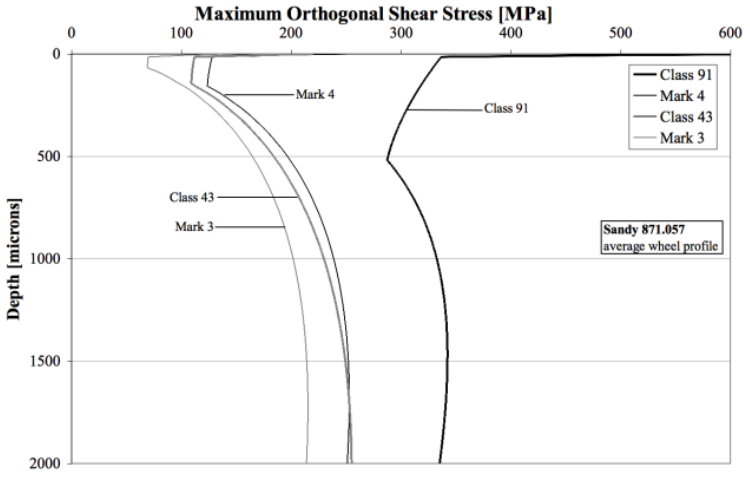

(c)

Figure 7.2 Variation of the maximum orthogonal shear stress with depth. (a) Location B at Harringay, (b) Location C at Harringay, and (c) Location D at Sandy.

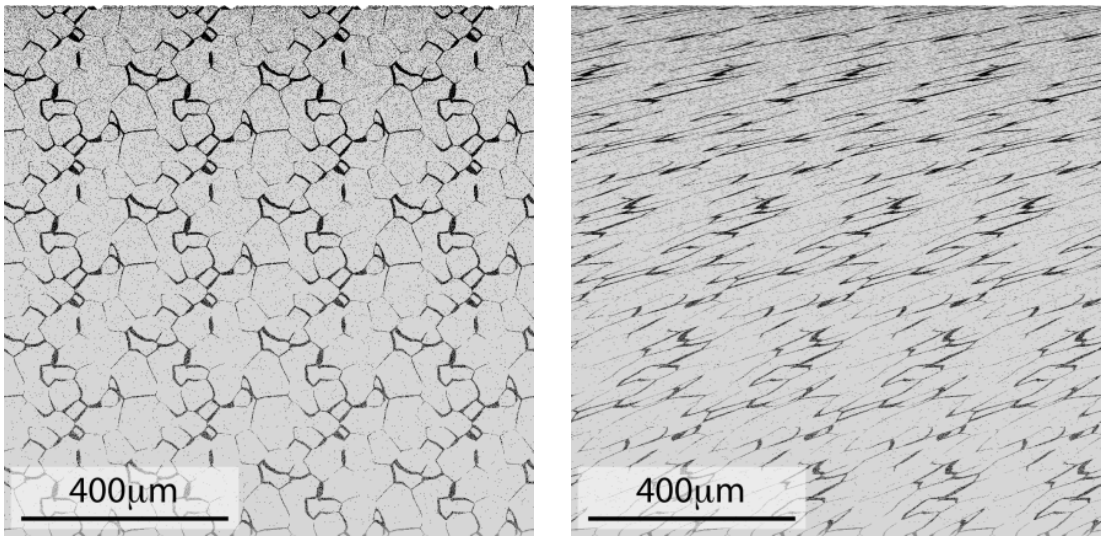

(a) (b)

Figure 7.3 Snap-shots of the simulation, representing a 1mm×1mm area of the cross-section. Traffic is Class-43/Mark-3 only. Shown (a) un-sheared, and (b) sheared. Elements which have failed are black; elements (at the top surface) which have been removed as wear debris are white.

Another approach to predicting crack initiation depth is to use percentage 'damage depth': the simulation calculates the maximum depth at which, e.g., 10% of elements have failed in one layer, which suggests that crack initiation to that depth is likely to happen (Franklin and Kapoor, 2007).

At Harringay, at Locations A and B the "10% Damage Depth" (10DD) jumps from 25µm to about 200µm after 8,800 cycles (200 trains) – regardless of the traffic mixture. At Location C, for only Class-43/Mark-3, the 10DD jumps to 200µm earlier, after 7,040 cycles (160 trains); and for only Class-91/Mark-4, the 10DD jumps to 198µm later, after 10,560 cycles (240 trains). At this location, therefore, the time until crack initiation is likely to reduce as the percentage of Class-43/Mark-3 increases.

At Sandy Locations D and E, the 10DD jumped from less than 10µm (the severely strained region close to the surface where micro-roughness causes very high stresses) to over 1.5mm, suggesting crack initiation is likely to occur sub-surface in the region where the shear stress is a maximum. (In practice subsurface crack initiation is typically associated with a metallurgical defect). For both locations, the 0% case (i.e., only Class-91/Mark-4) caused the 10DD to jump soonest, after 107,360 cycles (2,440 trains) at Location D, and after 65120 cycles (1,480 trains) at Location E. No jump occurred at Location F. At Sandy, therefore, increasing the percentage of Class-43/Mark-3 trains increases the number of cycles until crack initiation.

However, the damage depth percentage is arbitrary and the damage depth method sensitive to statistical anomalies.

PC-Depths

A new method is proposed here: probable crack depths ('PC-depths') are calculated such that in 95% of layers closer to the surface the average strain in the ferrite exceeds 10.5. PC-depths are presented in Table 7.5 for all locations and traffic mixtures at Harringay after 4,000 trains; at Sandy (after 8,000 trains) the PC-depths were zero. The results for Harringay are in the range 485-800 microns.

Because the definition of PC-depth is related to ferrite (which accumulates strain faster than the pearlite, and thus fails sooner), the method is also sensitive to statistical anomalies, since the ferrite fraction is low. Furthermore, for premium grade rail steels the ferrite fraction is even lower still, to the point where the microstructure can be modelled as fully pearlitic – in which case, PC-depth will not apply. Therefore, an alternative definition based on strain in the pearlite has been found by comparing predictions for the Harringay cases; for pearlite, selecting a threshold value of 2.7 (rather than 10.5 for the ferrite) results in similar PC-depth predictions. These results are presented in Table 7.6 for Harringay; pearlite PC-depths for Sandy are zero again.

In general, the Class-91/Mark-4 creates conditions for crack initiation sooner than the Class-43/Mark-3. It is worth noting that this ranking of traffic in terms of crack initiation can differ from their ranking for crack propagation (Hyde and Fletcher, 2010) since the mechanisms of initiation and propagation differ.

Table 7.5 'PC-depth' – ferrite [microns].

Percentage of Traffic as Class-43/Mark-3	Harringay Locations		
	A	B	C
0%	785	790	800
25%	716	672	764
50%	687	580	730
75%	630	545	709
100%	620	485	690

Table 7.6 'PC-depth' – pearlite [microns].

Percentage of Traffic as Class-43/Mark-3	Harringay Locations		
	A	B	C
0%	727	740	745
25%	703	691	708
50%	675	630	672
75%	634	538	635
100%	594	422	611

7.3 Traffic simulations using new 3D model with partial slip

7.3.1 Input data

- Wheel profiles: Average, worn and new P8 wheel profiles were used in simulations
- Contact conditions:
  - Partial slip contact model used in simulations (see Chapter 6)
  - Both longitudinal and transverse traction coefficients are considered (see Table 7.2 and Table 7.3.
  - Friction coefficient 0.45 was assumed during the vehicle dynamics simulations.
- Simulations: In total, 90 simulations are run: 2 sites × 3 locations × 5 traffic mixtures × 3 wheel profiles.

7.3.2 Simulation results and discussion

Wear

The wear rates presented in Table 7.7 are the average wear rate calculated by Dynarat over the full duration of the simulation. The stress distribution which drives the ratcheting model is calculated in the plane, perpendicular to the rail surface, which runs through the centre-line of the contact ellipse. (Franklin and Kapoor, 2007) showed that the wear rate is maximum at the centre-line. In the new model, where traction is not aligned with the direction of motion, the relationship between wear rate and location within the contact is likely to be more complex.

At Harringay, for all combinations of traffic and location, the new profile gives the lowest wear rates, all around 4 nm/cycle. At Locations C and A, the worn profile causes higher wear rates than the average profile. At Location B, the average profile causes a higher wear rate than the worn profile.

At Sandy, the wear rates are significantly lower than at Harringay, and the differences in wear rates are not as clear.

In general, the influence of traffic proportion on wear is linear, but the trends depend on individual cases.

Table 7.7 Wear rates [nm/cycle] predicted by new model with partial slip.

Wheel profile	Percentage of traffic	Harringay			Sandy		
		2179.03 (A)	2188 (B)	2196.96 (C)	871.057 (D)	879.998 (E)	888.939 (F)
new	0%	3.658	4.907	4.237	2.729	1.447	0.001
	25%	3.568	4.856	4.152	2.016	1.214	0.007
	50%	3.478	4.801	4.086	1.233	0.972	0.012
	75%	3.382	4.758	4.032	0.481	0.759	0.018
	100%	3.279	4.714	3.997	0.004	0.667	0.024
average	0%	4.973	11.292	8.394	1.778	2.317	0.001
	25%	5.270	10.543	8.618	1.293	2.141	0
	50%	5.584	9.642	8.848	0.768	1.969	0
	75%	5.901	8.634	9.069	0.309	1.802	0
	100%	6.221	7.569	9.290	0.053	1.658	0
worn	0%	9.649	4.432	10.645	0.093	1.909	0
	25%	9.274	5.265	10.237	0.075	1.878	0
	50%	8.879	6.051	9.811	0.059	1.843	0
	75%	8.490	6.749	9.352	0.031	1.806	0
	100%	8.099	7.371	8.866	0.018	1.782	0

Shear strain and PC depths

Stresses in rail steel are calculated to a depth of 2mm in the *zx*-plane, i.e., parallel with the direction of motion and under the centreline of the contact. The rail steel is modelled as pearlite grains with ferrite grain boundaries. Each element in the simulation is assigned properties of either ferrite or pearlite according to an underlying representation of the rail steel microstructure. During the simulation the stress distribution(s) are applied to each element and the plastic strain increments (if any) added, until the absolute value of the strain (which is directional in the new model) exceeds the critical strain for failure – at which point the element is labelled as having failed. Once the element fails, it accumulates no further strain.

At the end of each simulation, the program outputs the numbers of ferrite and pearlite elements at each depth, and for each material the average shear strain at that depth. As more and more elements reach failure, the average shear strain approaches the critical shear strain for failure.

Pearlite is significantly harder than ferrite. In all the simulations presented here, the average shear strain in the pearlite elements does not reach the critical shear strain for failure (i.e., γ_c =11). However, in several cases the average shear strain in the ferrite elements does reach the critical shear strain for failure; when this happens for all (or most) layers for a significant depth, this can be interpreted as the probable depth of surface-initiated cracks. In Table 7.8, these probable crack depths ('PC-depths') are presented for two extremes of traffic combination; the PC-depths are calculated such that in 95% of layers closer to the surface the average strain in the ferrite exceeds 10.5.

At Harringay, the PC-depths are all in the range 625-930 microns. (The depth of cracks observed in rail sections from this curve at Harringay was typically about 700 microns.) Comparing wheel profiles, in general the average profile causes the greatest PC-depths while the new profile causes the lowest. At Sandy, new wheel profiles cause the greatest PC-depths, and worn profiles cause the lowest; the 0% vehicle combination (Class 91 / Mark 4 only) is significantly worse here.

Table 7.8 Probable crack depth ('PC-depth') [microns] based on average shear strain in ferrite elements

Wheel profile	Vehicle combination	Harringay			Sandy		
		2179.03	2188	2196.96	871.057	879.998	888.939
new	0%	670	790	630	1130	665	0
	100%	635	625	665	0	65	0
average	0%	845	930	805	835	370	0
	100%	700	725	805	0	275	0
worn	0%	825	795	880	0	350	0
	100%	740	705	780	0	285	0

7.4 Discussion

7.4.1 Wear

Wear rates using the old and new models are shown in Figure 7.4, and wear rates for the new model are given also in Table 7.7. The new model gives wear rates three times higher.

In general, wear rates are significantly higher when the new model is used for simulations, partly because orthogonal shear stresses in the *yz*-plane are also being considered, and partly because contact shear stresses in the slip zone are higher than in the previous model. In the previous model, fully slipping contact was assumed and the traction coefficient was used as the friction coefficient. In the new model, the friction

coefficient is set to be 0.45, the value used in the VAMPIRE dynamics simulations, and the traction coefficients are calculated from results of the dynamics simulations.

7.4.2 Stresses

Examples of the change in stresses between the previous and new models are given in Figure 7.5. The results show that, when different vehicles are compared, higher stresses are produced by power cars than coaches; this was observed also by (Evans and Iwnicki, 2002). Class 91 has slightly higher stresses than Class 43. When different wheel profiles are compared, for locations at Harringay, average and worn wheels give higher stresses than new, but at Sandy worn profile is better. Evans and Burstow (2006) simulated different wheel profiles for a Mark 3 coach and showed that RCF damage increases gradually for average and then worn P8 profile. Findings at Sandy location agree with the results in the report (RSSB, 2003).

In practice, the number of locomotives is a lot less than the number of coaches, so the influence of locomotives is not as great as might be expected. However, the high stresses cannot be discounted since they will cause ratcheting and may contribute to eventual failure of the rail material.

Looking at the variation of maximum resultant orthogonal shear stress with depth (down to 2mm), at Harringay stresses are higher at the surface, gradually drop and stabilise around 1mm under the surface (e.g., see stresses for average profile at Harringay 2196.96 in Figure 7.5(a)). At Sandy (Locations 871.057 and 888.939), the stresses drop until 100-200 microns under the surface, and then start to increase up to a second maximum at 1mm (Location 871.057 – see Figure 7.5(b)) and 2mm (Location 888.939). At Location 879.998, the stresses show the same trend as at Harringay.

Comparing previous and new models, the stresses are similar at depths below about 1mm, but closer to the surface the stresses for the new model increase significantly. In some cases, the order of vehicles changes, e.g., in Figure 7.5(a), for the new model Mark 3 and Mark 4 have almost identical stresses, but in the old model there was a clear difference (Mark 4 having lower stress).

7.4.3 Shear strain and probable crack depth

Comparing previous and new models (see Table 7.5, Table 7.6 and Table 7.8), the new model gives greater probable depths of cracks. In both models, if the combination of traffic is looked at, for proportion of traffic 0% (only Intercity 225) the depth to which the ferrite fraction reaches critical strain for failure is greater.

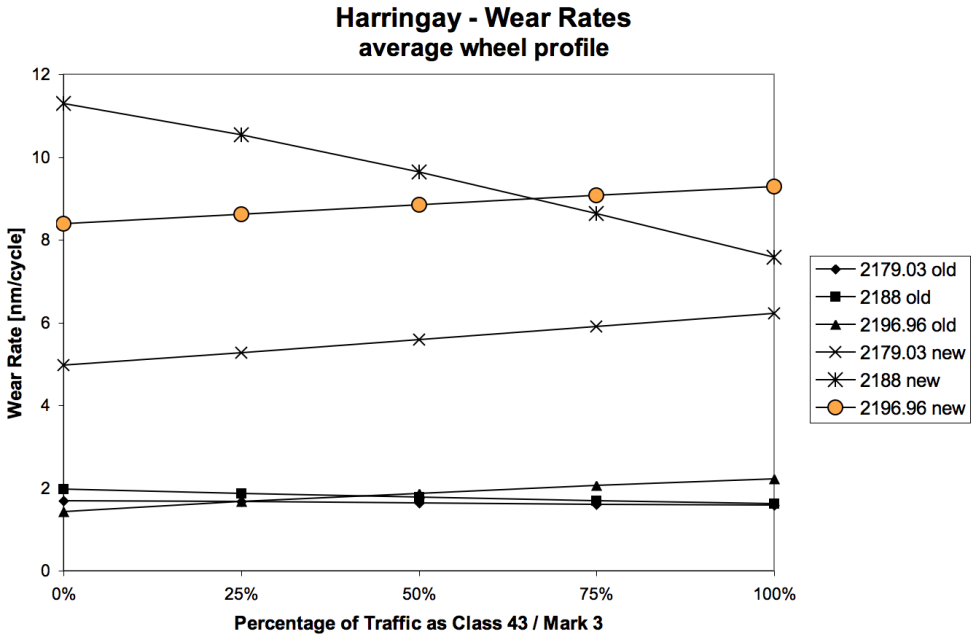

(a)

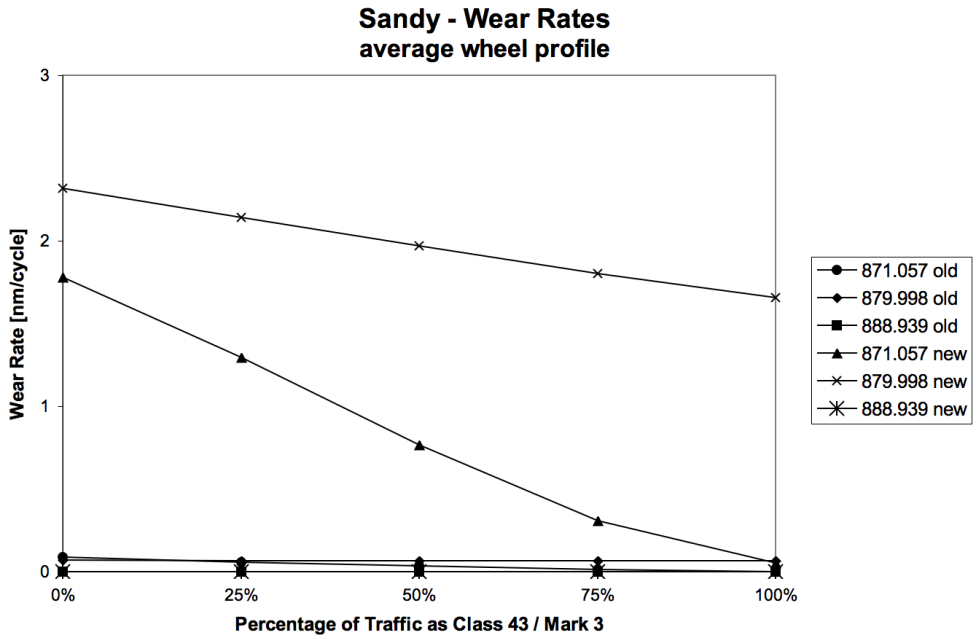

(b)

Figure 7.4 Predicted wear rates for average wheel profile using old and new model at 3 locations at (a) Harringay, and (b) Sandy.

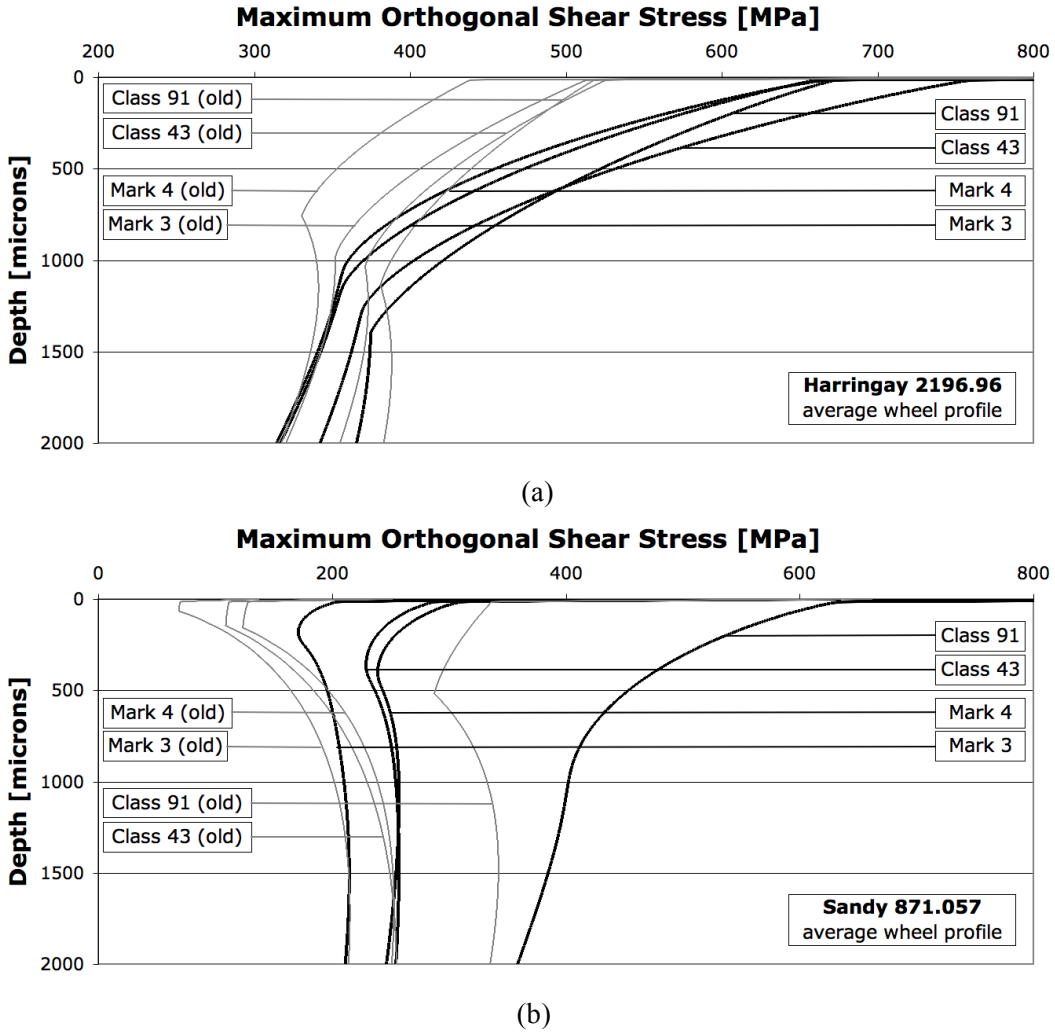

Figure 7.5 Variation of the maximum orthogonal shear stress with depth. Comparison of stresses between old and new model (a) Location 2196.96 at Harringay, (b) Location 871.057 at Sandy.

7.5 Summary

A new partial slip model has been used to simulate Intercity 125 and Intercity 225 trains at two curves, Harringay and Sandy on the East Coast Main Line, and the results compared with results from the previous full slip model. Using the new model, the influence of new and worn P8 profiles has also been studied.

The stresses calculated by the new model are significantly higher than those in the previous model, especially within 1mm of the surface. This has increased the wear rates by an order of magnitude, and the wear rates are now much higher than are observed in practice. The new model needs to be recalibrated.

A new, more reliable measure of probable crack depths ('PC-depths'), based on shear strain and failure in the ferrite fraction, is presented. The PC-depth at Harringay is

predicted to be 625-930 microns, and cracks unlikely to occur at Sandy – both in agreement with site observations.

This model gives predictions of wear and crack initiation, and (once properly calibrated and validated) can be used as a tool to assess the effect of different mixtures of vehicles, site locations and in principle the rail material, to predict maintenance requirements and optimise rail grinding strategy.

Chapter 8 Conclusions

Premium grade rail steels are generally regarded as having superior wear and rolling contact fatigue (RCF) characteristics. However, rail wear has an impact on rail profile, and rail profile influences vehicle dynamics, and the wheel-rail contact causes wear and RCF. Therefore, changes to rail metallurgy can influence the stresses that the rail is subject to, and a combination of reduced wear and raised stresses, for example, will increase the potential for RCF. It is essential to choose an initial rail profile that is appropriate for the steel grade used. The response of rail steels to rolling/sliding contact when the contact is continuously dry or continuously wet can be determined from testing. The response to intermittent rainfall is harder to test for. The twin-disc tests used as a basis for the development work in this thesis used relatively severe conditions: high pressure, high creepage and (in the case of mixed dry-wet contact) a long initial dry sequence. Although the premium grades performed better than the 'standard' grade, significant cracks developed.

Despite improvements in rail steels, RCF is still an issue for the railways, and there is need for a better understanding of crack initiation and propagation in rails.

This thesis has focussed on developing the 'Dynarat' software for simulating plastic ratcheting (accumulation of plastic strain with repeated cyclic loading) of rail steels and predicting wear rates and crack initiation. The main findings in this work can be summarised as follows:

- Metallurgical analysis of R260 and four premium grade pearlitic rail steels has led to new material models, and accompanying changes to the core ratcheting model and wear mechanism.
- A new partial slip model has been developed for simulating wheel-rail contact more accurately, and the method of strain accumulation in three-dimensional simulations has been developed to allow strain accumulation transversely as well as longitudinally.
- A wear equation has been determined for wheel-rail contact and R260 rail steel; the wear rate is linear with peak pressure and cubic with the traction coefficient.

One of the aims in the thesis is to further knowledge of new rail grade materials' behaviour under cyclic loading, in order to help improve rail material characteristics in future production. The methodology and models developed could be used to aid

selection of rail material for certain types of rail operation and/or for certain track sections.

8.1 Tests and analysis

8.1.1 Wear-hardness correlation

One of the motivations for the twin-disc tests was to study both wheel and rail steel wear rates, in response to the general belief that harder rail wears wheels faster, and vice versa. Based on the twin-disc test results, the following can be concluded:

- Rail disc wear is higher for the P260 than for the (harder) premium grades.
- In general, after 15000 cycles dry, the harder the rail disc material becomes at the surface, the harder the wheel disc material becomes at the surface.
- Wheel disc wear in dry tests was higher than the corresponding rail disc wear, except for P260 which had the highest wear rate.
- In the system as a whole (i.e., considering both wheel and rail discs), using harder C400 and V400 rail steels lowers the total wear rate; also, for C400 and V400, the wear rate averaged over the first 15000 cycles was not significantly higher than the wear rate averaged over the first 5000 cycles.

As a general rule, therefore, it is best to use harder steels for both wheels and rails. However, this conclusion is based on twin-disc tests, which are essentially a two-dimensional scenario and remain so even as the discs wear; some caution is needed when extrapolating to rails and wheels in practice.

8.1.2 Strain and hardness measurement

In general, the materials accumulated the most strain, and hardened most, at the surface, the values dropping with the depth into the material. Softer materials accumulated more strain than the harder; the most strained was the P260.

Hardening depth, and depth of visibly deformed microstructure, are clearly correlated, e.g., for the 15000 cycles dry test of the P260 material the depth of the severely deformed layer and the depth of hardening is the same, about 0.35mm, and the depth of less but still clearly visible deformation/hardening is about 0.6mm.

8.1.3 Cracking

Microscopy of the twin-disc test samples led to the following observations:

- For all steels, cracks follow elongated grain boundaries.
- Cracks can be seen following material flow lines.

- Cracks can initiate at elongated non-metallic inclusions, or propagate through them when they come to their path.
- Cracks usually grow quickly to the depth of visible plastic deformation.
- Material cracks the most, and cracks propagate the deepest, for dry-wet tests in all materials; the VA350 developed severe cracking also for the 15000 cycles dry test.
- Materials don't crack when they are run 20000 cycles wet, and there is very little plastic deformation observed, only very slightly at the surface, and for P260 sub-surface.

There is no clear conclusion about which steel performs best, but all the premium grade steels perform better than the P260, both in terms of wear and cracking. The C400 has very good resistance to wear and cracking in dry contact, but still develops cracks during mixed dry-wet contact.

8.2 Partial slip and traffic simulation

Fully slipping wheel-rail contact is a rare and generally undesired event, for example flange contact or wheel slip (or wheel slide). Fully slipping contact generates very high temperatures that can affect the steel microstructure, causing significant wear; wheels are more susceptible to increased temperatures. For unpowered coaches, there is usually no traction at the wheel-rail interface and therefore little or no slip; however, transverse traction will arise when the vehicle curves, and longitudinal traction will arise during vehicle braking.

Traction and slip are important for the driving wheels of locomotives and multiple units, where sometimes a large amount of traction is required but a fully slipping contact is undesirable.

Previously, Dynarat could simulate partial slip only in two-dimensional contact, e.g., twin-disc simulations, and modelled wheel-rail contact as fully slipping, using a friction coefficient equal to the predicted traction coefficient, and without including any thermal effects. The new partial slip contact model produces a very different distribution of traction to the old approximation, which has consequences for wear and crack prediction. However, it is restricted to an elliptic contact with an elliptic 'stick' region, and in practice wheel-rail contacts often deviate significantly from these approximations.

Direction as well as magnitude of traction can be included in the new partial slip contact model, and subsurface accumulation of shear strain can be transverse as well as longitudinal.

Dynarat does not simulate dynamic train-track interaction, and is dependent on VAMPIRE or similar multibody simulation software to provide details on contact size and shape and forces. However, once contact data is provided for a particular point on a rail, the contacts can be applied in any desired order. This made it possible to take the measured traction data from the SUROS twin-disc tests and create an input file where the traction coefficient varied in 50-cycle segments to match the test. It also makes it possible to study different mixtures of traffic. Even on lines with a traffic monoculture, there will likely be a significant difference between the impacts of the leading and trailing wheelsets of each bogie.

The new partial slip model has been used to simulate Intercity 125 and 225 trains at two curves, Harringay and Sandy, on the East Coast Main Line, and the results compared with results from the previous full slip model. Using the new model, the influence of new and worn P8 profiles has also been studied. The conclusions from these traffic simulations are:

- In general the Class-91/Mark-4 causes greater wear than the Class-43/Mark-3, and creates conditions for earlier crack initiation.
- The full slip model predicts wear rates that are observed in practice, while the partial slip model predicts wear rates which are higher by an order of magnitude.
- A new, more reliable measure of probable crack depths ('PC-depths'), based on shear strain and failure in the ferrite fraction, was developed for this work. The PC-depth at Harringay is predicted to be 625-930 microns, and cracks unlikely to occur at Sandy – both in agreement with site observations.

The high wear rates predicted by the partial slip model are a point of concern and need further investigation. However, the capability to model traffic mixtures and study wear-fatigue interaction makes Dynarat a tool worth developing.

8.3 Further work

8.3.1 Planning rail maintenance

Rail grinding is performed regularly to maintain rail profile, and also to remove cracks, corrugation or other rail surface damage. Models of crack growth can be used to

optimise grinding intervals and depths (Hyde and Fletcher, 2010; Hyde, 2012) but these may need to assume a certain initial crack length. Dynarat predicts both wear and crack initiation, and development of appropriate material models makes it a useful tool for estimating time to initiation of cracks and the depth of penetration, and this could be an input to the crack propagation models used to optimise grinding operations.

The wear equation developed here for R260 is for top-of-rail contact and needs to be extended to cover (a) a wider range of contacts, and (b) premium grade steels. Similarly, a set of 'crack depth' equations (i.e. equations predicting the depth to which cracks are likely to initiate after a specific number of cycles) could also be developed, and this would allow the results to be applied throughout the rail network.

8.3.2 Track tests

It is difficult to obtain data collected from sites on the rail network in sufficient detail to validate models. The approach used in this thesis has been to use twin-disc tests for both calibration and validation, and to extrapolate to wheel-rail contact. However, it would be good to document a variety of sites (single/double track; passenger/freight; high/low speed; etc.), perform regular MiniProf measurements of rail profile and even wheel profiles for the vehicles operating across these locations, perhaps also wayside measurement of axle loads. This would also require data on vehicle types and wheel materials, track recording car measurements, and even daily weather reports. This data could then be used to build detailed vehicle dynamics simulations.

In fact, something like this has been done in RSSB's Project T613 (2010), and it would be good to reuse the extensive dataset to evaluate (and, therefore, possibly validate against field data) the models developed in this thesis.

8.3.3 Laboratory tests

The twenty-five tests discussed in this thesis cover five test conditions and five rail materials. There is a degree of repetition, in that there are two wear rate results for the 5000 cycles dry test, and the 15000 cycles dry test was run twice, but for two different wheel steels. For the R260, the wear rate against R7 is very high, but the wear rate against the R8T is low. The validity of these tests needs to be explored through additional tests with these materials for 15000 cycles dry, and ideally a range of other durations also. It would be useful also to do a range of tests at other peak pressures (e.g., 900MPa, 1200MPa) and at lower slip ratios (e.g., −0.3%).

For the premium grades, dry and wet tests for longer durations would also be useful to determine long-term behaviours, and mixed tests should have a range of shorter initial dry test durations.

In any future tests, the discs should be machined with their axis normal to the rail top surface, and as close to the top surface as possible, to ensure material properties are representative of the top of the rail head. For the tests discussed in this thesis, the disc axis was parallel to the rail, and it is possible that parts of the discs examined do not fairly represent the rail's performance in track.

A careful 3D analysis of the cracks in the premium grade samples should be undertaken (using focused ion beam milling with electron microscopy, for example). This would provide data on early crack growth in the different rail steels that could be used to develop predictive models of crack initiation.

8.3.4 Modelling, simulations and software development

Temperature effects (i.e. heat generated by the sliding contact) are likely to be significant when the contact is sliding, e.g. during wheel slip or flange contact. This has recently been added to Dynarat for modelling 2D contact, based on (Widiyarta *et al.*, 2008), but needs further study.

In this thesis, the traffic simulations were modelled with R220 steel, but R260 is used increasingly these days in the UK so it would be an interesting comparison to redo simulations with R260.

Ultimately, the wear equations developed here and the grinding optimisation methodology developed by (Hyde, 2012) should be integrated with tools like Track-Ex, in order to compare results between models and with real measured track and vehicle data from railway operators.

A new method of strain-based crack initiation depth estimates, called 'PC – depths' was developed for this thesis and used with the R220 material model for traffic simulations. This new approach needs to be extended to cover the new material models.

On a separate note, it would be useful to develop software for automatic and precise reading of plastic flow in material, from micrographs. For this thesis, material strain was measured from micrographs, drawing lines over material flow lines and measuring their angle to the surface and their depth under surface. This is a good method, but it is a manual and slow process, and quite subjective. The image analysis software 'ImageJ'

used by (Stock and Pippan, 2011) only enhances changes in the image; shear strain measurements are still made manually.

8.3.5 A new twin-'wheelset' test rig

The standard twin-disc test rig uses cylindrical discs, creating an approximately two-dimensional contact, but one which stays more or less constant through the test. Full scale railway wheel-rail contact is three-dimensional, however, and the interaction between wheel and rail profiles is both widely varying (depending on curving behaviour, for example) and evolving over time as wear causes the profiles to change.

Twin-disc tests which imitate a 3D contact suffer from the way in which wear causes the profiles to become more conformal over time, because the location of the contact patch generally remains the same.

A better representation of wheel-rail contact can be achieved by controlling lateral and even angular position of the wheel disc relative to the rail disc, and allowing this to vary during the test. Even better is to have two twin-disc contacts connected by shafts, a miniature representation of a train's wheelset on rails.

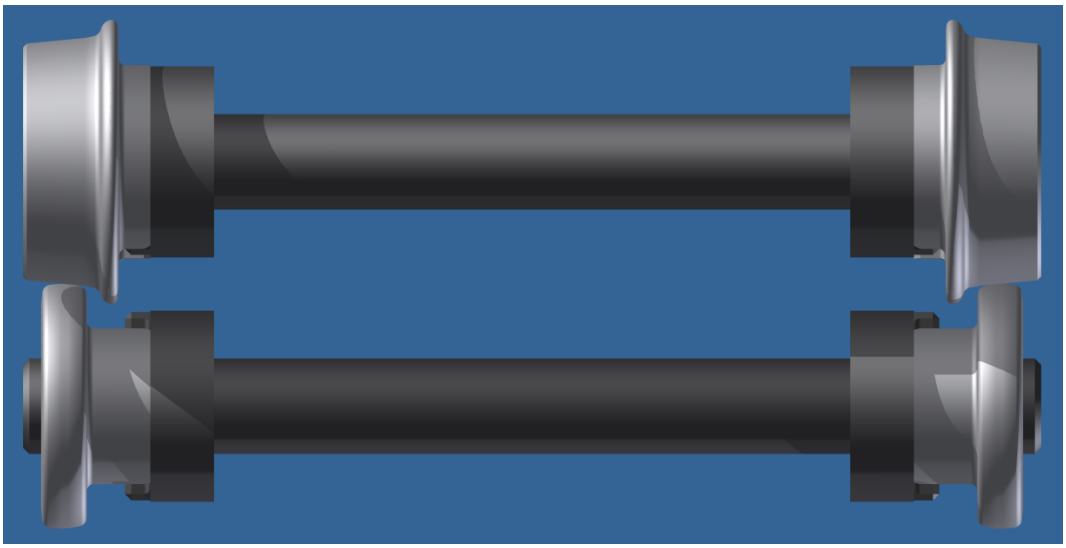

Figure 8.1 Test rig representing scaled-down wheelset on rails.

The twin-'wheelset' rig will require:

- Precise control of lateral and angular displacement of one wheelset with respect to the other;
- Precise control of load;
- Precise control of speed (to be able to choose different slip/creep ratios);
- Discs will need to be precision manufactured with scaled wheel and rail profiles, and equipment for measuring the profile after the test will be required;

- Equipment for precise measurement of speed and vibration during the test will be useful;
- Climate chamber to control temperature and humidity;
- Eddy current or other check of cracks;
- Recording on a computer during test: adhesion coefficient, load, force, torque, speed, etc.;
- Inclination of rails.

The results will provide predictions of profile evolution under various track conditions. The conicity of the wheelsets will enable study of stick-slip phenomena and torsional vibration.

References

Afferrante, L. and Ciavarella, M. (2010) 'Short pitch corrugation of railway tracks with wooden or concrete sleepers: An enigma solved?', Tribology International, 43(3), pp. 610-622.

Alonsoa, A. and Gimenez, J.G. (2008) 'Wheel–rail contact: Roughness, heat generation and conforming contact influence', Tribology International, 41, pp. 755 - 768.

Alwahdi, F. (2004) Wear and rolling contact fatigue of ductile materials. PhD thesis. University of Sheffield.

Alwahdi, F., Franklin, F.J. and Kapoor, A. (2005) 'The effect of partial slip on the wear rate of rails', Wear, 258(7-8), pp. 1031-1037.

Amoore, J. (2007) 'InnoTrack. SP1 Duty. The Vehicle and Track System' [Presentation]. 28 November 2007. UIC - Paris.

Archard, J.F. (1953) 'Contact and rubbing of flat surfaces', Journal of applied physics, 24, pp. 981-988.

Baek, K.-S., Kyogoku, K. and Nakahara, T. (2007) 'An experimental investigation of transient traction characteristics in rolling-sliding wheel/rail contacts under dry-wet conditions', Wear, 263(1-6), pp. 169-179.

Baeza, L., Vila, P., Roda, A. and Fayos, J. (2008) 'Prediction of corrugation in rails using a non-stationary wheel-rail contact model', Wear, 265(9-10), pp. 1156-1162.

Benson, M. (1993) Effect of differential hardness on wheel/rail wear – Literature survey.

Beynon, J.H., Garnham, J.E. and Sawley, K.J. (1996) 'Rolling contact fatigue of three pearlitic steels', Wear, 192 pp. 94-111.

Bhushan, B. (ed.) (2001) Modern Tribology Handbook (2 vols). Boca Raton, London, New York, Washington D.C.: CRC Press.

Bolton, P.J. and Clayton, P. (1984) 'Rolling—sliding wear damage in rail and tyre steels', Wear, 93(2), pp. 145-165.

Bower, A.F. (1988) ' The influence of crack face friction and trapped fluid on surface initiated rolling contact fatigue cracks', Transactions of the ASME, Journal of Tribology, 110, pp. 704-711.

Bower, A.F. and Johnson, K.L. (1989) 'The influence of strain hardening on cumulative plastic deformation in rolling and sling line contact', JMPS, 37, pp. 471-493.

Bower, A.F. and Johnson, K.L. (1991) 'Plastic flow and shakedown of the rail surface in repeated wheel–rail contact', Wear, 144, pp. 1-18.

Boyer, H (ed.) (1987), ‘Hardness testing’, Metals park, OH: ASM International.

Braghin, F., Bruni, S. and Diana, G. (2005) 'Experimental and numerical investigation on the derailment of a railway wheelset with solid axle', Vehicle System Dynamics, 00, pp. 1-21.

Brouzoulis, J., Torstensson, P.T., Stock, R. and Ekh, M. (2011) 'Prediction of wear and plastic flow in rails--Test rig results, model calibration and numerical prediction', Wear, 271(1-2), pp. 92-99.

Burstow, M. and Robinson, S. (2007) 'Management and understanding of rolling contact fatigue (RCF) damage on the low rail of curves', Railway Engineering - 2007, 9th International Conference,. London, 20th-21st June 2007.

Callister, W. and Rethwisch, D. (2011) Materials Science and Engineering. Asia: John Wiley and Sons.

Cannon, D.F., Edel, K., S.L., G. and Sawley, K. (2003) 'Rail defects: an overview', Fatigue & Fracture of Engineering Materials & Structures, 26(10), pp. 865-886.

Carpene, E. and Schaaf, P. (2002) 'Formation of Fe3C surface layers by laser plasma cementation', Applied Physics Letters, 80(5), pp. 891-893.

Carter, F.W. (1926) 'On the action of a locomotive driving wheel', Proccedings of the royal society London, 112, pp. 151-157.

Chen, H., Bana, T., Ishida, M. and Nakahara, T. (2002) 'Adhesion between rail/wheel under water lubricated contact', Wear 253, pp. 75-81.

Chen, H., Ishida, M. and Nakahara, T. (2005) 'Analysis of adhesion under wet conditions for three-dimensional contact considering surface roughness', Wear, 258, pp. 1209-1216.

Clayton, P. (1996) 'Tribological aspects of wheel-rail contact: a review of recent experimental research', Wear, 191, pp. 170-183.

Clayton, P., Sawley, K.J., Bolton, P.J. and Pell, G.M. (1987) 'Wear behavior of bainitic steels', Wear, 120(2), pp. 199-220.

Clayton, P. and Su, X. (1996) 'Surface initiated fatigue of pearlitic and bainitic steels under water lubricated rolling/sliding contact', Wear, 200(1-2), pp. 63-73.

Daves, W. and Fischer, F.D. (2002) 'Modelling of the plastification near the rough surface of a rail by the wheel-rail contact', Wear, 253(1-2), pp. 241-246.

Dembosky, M., Doherty, A., Urban, C., Walker, R. and Gurule, S. (2006) 'Management of Rolling Contact Fatigue (RCF) in the UK Rail system: A systems solution', Proceedings of the 7th World Congress on Railway Research (WCRR 2006). Montreal, Canada 4th-8th June 2006.

Deters, L. and Proksch, M. (2005) 'Friction and wear testing of rail and wheel material', Wear, 258(7-8), pp. 981-991.

Dinnar, U. (1976) 'Two-porous-layers lubrication in human synovial joints', Annals of Biomedical Engineering, 4, pp. 91-107.

Dirks, B. and Enblom, R. (2011) 'Prediction model for wheel profile wear and rolling contact fatigue', Wear, 271, pp. 210-217.

Donzella, G., Faccoli, M., Ghidini, A., Mazzù, A. and Roberti, R. (2005) 'The competitive role of wear and RCF in a rail steel', Engineering Fracture Mechanics, 72(2), pp. 287-308.

Eden, H.C., Garnham, J.E. and Davis, C.L. (2005) 'Influential microstructural changes on rolling contact fatigue crack initiation in pearlitic rail steels', Materials Science and Technology, 21(6), pp. 623-629.

Ekberg, A. and Kabo, E. (2005) 'Fatigue of railway wheels and rails under rolling contact and thermal loading—an overview', Wear 258 pp. 1288-1300.

Ekberg, A., Kabo, E. and Andersson, H. (2002) 'An engineering model for prediction of rolling contact fatigue of railway wheels', Fatigue & Fracture of Engineering Materials & Structures, 25, pp. 899-909.

Ekh, M., Johansson, A., Thorberntsson, H. and Josefson, B.L. (2000) 'Models for Cyclic Ratchetting Plasticity—Integration and Calibration', Transactions of the ASME, Journal of Engineering Materials and Technology, 122.

EN 13262:2004+A2:2011 (2011) Railway applications – Wheelsets and bogies – Wheels – Product requirements.

EN 13674-1 (2011) Railway applications —Track — Rail. Part 1: Vignole railway rails 46 kg/m and above.

EN 13848-5:2008+A1:2010 (2010) Railway applications —Track — Track geometry quality —Part 5: Geometric quality levels — Plain line.

Enblom, R. and Berg, M. (2008) 'Proposed procedure and trial simulation of rail profile evolution due to uniform wear', Proc. IMechE Part F: J. Rail and Rapid Transit (special issue), 222, pp. 15-25.

ERA (2011) Railway safety performance in the European Union.

ESDU Contact phenomena. I: stresses, deflections and contact dimensions for normally-loaded unlubricated elastic components. Item No. 78035

ESDU (1984) Contact phenomena. II: stress fields and failure criteria in concentrated elastic contacts under combined normal and tangential loading. Item No. 84017.

ESDU (1985) Contact Phenomena III: Calculation of Individual Stress Components in Concentrated Elastic Contacts Under Combined Normal and Tangential Loading. Item No. 85007. London.

Evans, J. and Iwnicki, S.D. (2002) 'Vehicle Dynamics and the Wheel/Rail Interface', Wheels on Rails - An update, Understanding and managing the Wheel/Rail Interface, IMechE Seminar. London, April 2002.

Evans, J.R., Burstow, M.C. (2006) 'Vehicle/Track Interaction and Rolling Contact Fatigue in Rails in the UK', Vehicle System Dynamics, 44(Supplement), pp. 708-717.

Fletcher, D.I., Beynon J.H. (1998) 'The influence of lubricant type on rolling contact fatigue of pearlitic rail steel.' In: Dowson, D. et al. Lubrication at the frontier – The role of the interface and surface layers in the thin film and boundary regime: Proceedings ', 25th Leeds-Lyon symposium on tribology. The Institut National des Sciences Appliquees de Lyon, Lion, France, September 8-11. pp. 299-310.

Fletcher, D.I. and Beynon, J.H. (2000a) 'Development of a machine for closely controlled rolling contact fatigue and wear testing', Journal of Testing and Evaluation, pp. 267-275.

Fletcher, D.I. and Beynon, J.H. (2000b) 'Equilibrium of crack growth and wear rates during unlubricated rolling-sliding contact of pearlitic rail steel', Proceedings of the Institution of Mechanical Engineers, Part F: Journal of Rail and Rapid Transit, 214(2), pp. 93-105.

Fletcher, D.I. and Beynon, J.H. (2000c) 'The effect of intermittent lubrication on the fatigue life of pearlitic rail steel in rolling-sliding contact', Proceedings of the Institution of Mechanical Engineers, Part F: Journal of Rail and Rapid Transit, 214, pp. 145-158.

Fletcher, D.I., Franklin, F.J., Garnham, J.E., Muyupa, E., Papaelias, M., Davis, C.L., Kapoor, A., Widiyarta, M. and Vasic, G. (2008) 'Three-Dimensional Microstructural Modelling of Wear, Crack Initiation and Growth in Rail Steel, in Proceedings', 8th World Congress on Railway Research. COEX, Seoul, Korea, May 18-22.

Fletcher, D.I., Franklin, F.J. and Kapoor, A. (2003) 'Image analysis to reveal crack development using a computer simulation of wear and rolling contact fatigue', Fatigue and Fracture of Engineering Materials and Structures, 26(10), pp. 957-967.

Fletcher, D.I., Hyde, P. and Kapoor, A. (2004) 'Growth of multiple rolling contact fatigue cracks driven by rail bending modelled using a boundary element technique', Proceedings of the Institution of Mechanical Engineers, Part F: Journal of Rail and Rapid Transit, 218(3), pp. 243-253.

Fletcher, D.I. and Kapoor, A. (2006) 'Rapid method of stress intensity factor calculation for semi-elliptical surface breaking cracks under three-dimensional contact loading', Proceedings of the Institution of Mechanical Engineers, Part F: Journal of Rail and Rapid Transit, V220(3), pp. 219-234.

Fletcher, D.I., Kapoor, A., Franklin, F.J., Smith, L. and Hyde, P. (2006) 'Comparison of the Hatfield and alternative UK rails using models to assess the effect of residual stress on crack growth from rolling contact fatigue'. Health & Safety Laboratory's project JR31.086.

Franklin, F.J., Chung, T. and Kapoor, A. (2003) 'Ratcheting and fatigue-led wear in rail-wheel contact', Fatigue and Fracture of Engineering Materials and Structures, 26(10), pp. 949-955.

Franklin, F.J., Garnham, J.E., Fletcher, D.I., Davis, C.L. and Kapoor, A. (2008) 'Modelling rail steel microstructure and its effect on wear and crack initiation', Wear, 265, pp. 1332-1341.

Franklin, F.J. and Kapoor, A. (2006) 'Modelling wear and crack initiation in rails', Journal of rail and rapid transit, 220.

Franklin, F.J. and Kapoor, A. (2007) 'Modelling Wear and Crack Initiation in Rails', Proc. IMechE Part F: J. Rail and Rapid Transit (special issue), 221(1), pp. 23-33.

Franklin, F.J., Weeda, G.J., Kapoor, A. and Hiensch, E.J.M. (2005) 'Rolling contact fatigue and wear behaviour of the infrastar two-material rail', Wear, 258(7-8), pp. 1048-1054.

Franklin, F.J., Widiyarta, I.M. and Kapoor, A. (2001) 'Computer simulation of wear and rolling contact fatigue', Wear, 251, pp. 949-955.

Gallardo-Hernandez, E.A. and Lewis, R. (2008) 'Twin disc assessment of wheel/rail adhesion', Wear, 265, pp.1309-1316.

Garg, V. and Dukipatti, R. (1984) Dynamics of railway vehicle systems. Toronto: Academic Press.

Garnham, J.E. and Davis, C.L. (2008) 'The role of deformed rail microstructure on rolling contact fatigue initiation', Wear, 265, pp. 1363-1372.

Garnham, J.E. and Davis, C.L. (2011) 'Very early stage rolling contact fatigue crack growth in pearlitic rail steels', Wear, 271(1-2), pp. 100-112.

Garnham, J.E., Ding, R.G. and Davis, C.L. (2010) 'Ductile inclusions in rail, subject to compressive rolling-sliding contact', Wear, 269(11-12), pp. 733-746.

Garnham, J.E., Franklin, F.J., Fletcher, D.I., Kapoor, A. and Davis, C.L. (2007) 'Predicting the life of steel rails', IMechE, Part F: Journal of Rail and Rapid Transit, 221, pp. 45-58.

GM/RT2141 (2009) Resistance of railway vehicles to derailment and roll-over. Railway Group Standard.

Gómez, I. and Vadillo, E.G. (2003) 'A linear model to explain short pitch corrugation on rails', Wear 255, pp. 1127-1142.

Grassie, S.L. and Kalousek, J. (1993) 'Rail corrugation:characteristics, causes and treatments', Proceedings of the Institution of Mechanical Engineers, Part F: Journal of Rail and Rapid Transit, 207, pp. 57-68.

Grassie, S.L. (2005) 'Rail corrugation: Advances in measurement, understanding and treatment', Wear, 258(7-8), pp. 1224-1234.

Grassie, S.L. (2009) 'Rail corrugation: Characteristics, causes and treatments', Proceedings of the Institution of Mechanical Engineers, Part F: Journal of Rail and Rapid Transit, 223(6), pp. 581-596.

Grassie, S.L. (2012) 'Squats and squat-type defects in rails: the understanding to date', Proceedings of the Institution of Mechanical Engineers, Part F: Journal of Rail and Rapid Transit, 226, pp. 235-242.

Grohmann, H.D., Hempelmann, K., Groß-Thebing, A. (2002) 'A new type of RCF, experimental investigations and theoretical modelling', Wear, 253, pp.67–74.

Haines, D.J. and Ollerton, E. (1963) 'Contact Stress Distributions on Elliptical Contact Surfaces Subjected to Radial and Tangential Forces', Proc. Instn Mech. Engrs, 177(4), pp. 95-114.

Halling, J. (1989) The principles of tribology. Macmillan education Ltd.

Hertz, H. (1896) 'On the contact of elastic solids,' J. reine und angewandte mathematik 92 (1882) 156-171 (for English trans. See Misc. papers by H. Hertz, Jones and Schott, Macmillan, London 1896).

Heyder, R. and Girsch, G. (2005) 'Testing of HSH® rails in high-speed tracks to minimise rail damage', Wear, 258, pp. 1014-1021.

Hiensch, M., Larsson, P.-O., Nilsson, O., Levy, D., Kapoor, A., Franklin, F., Nielsen, J., Ringsberg, J.W. and Josefson, B.L. (2005) 'Two-material rail development: field test results regarding rolling contact fatigue and squeal noise behaviour', Wear, 258(7-8), pp. 964-972.

Hills, D.A., Nowell, D. and Sackfield, A. (1993) Mechanics of elastic contacts. Oxford: Butterworth-Heinemann.

Hou, K., Kalousek, J. and Magel, E. (1997) 'Rheological model of solid layer in rolling contact', Wear, 211(1), pp. 134-140.

Hyde, P. (2012) Numerical Techniques for Optimising Rail Grinding. PhD Thesis. Newcastle University.

Hyde, P. and Fletcher, D.I. (2010) 'Planning Rail Grinding Using Crack Growth Predictions', Journal of Mechanical Systems for Transportation and Logistics, 3(1), pp. 216-225.

Ignesti, M., Malvezzi, M., Marini, L., Meli, E. and Rindi, A. (2012) 'Development of a wear model for the prediction of wheel and rail profile evolution in railway systems', Wear, 284–285(0), pp. 1-17.

InnoTrack (2007) D4.2.1 'The impact of vertical train-track interaction on rail and joint degradation'. Available at: http://www.innotrack.eu/

InnoTrack (2008a) D4.1.3 'Interim Guidelines on the selection of rail grades'. Available at: http://www.innotrack.eu/

InnoTrack (2008b) D1.2.2 'Track Sections and Track Irregularities - Analysis of DB Sites'. Available at: http://www.innotrack.eu/

InnoTrack (2009a) D4.2.5 'Improved model for the influence of vehicle conditions (wheel flats, speed, axle load) on the loading and subsequent deterioration of rails'. Available at: http://www.innotrack.eu/

InnoTrack (2009b) D4.3.7 'Innovative laboratory tests for rail steels'. Available at: http://www.innotrack.eu/.

InnoTrack (2009c) D4.3.6 'Characterisation of Microstructural Deformation as a function of Rail Grade'. Available at: http://www.innotrack.eu/.

InnoTrack (2009d) D4.2.4 'Improved model for loading and subsequent deterioration due to squats and corrugation'. Available at: http://www.innotrack.eu/.

Jendel, T. (2002) 'Prediction of wheel profile wear--comparisons with field measurements', Wear, 253(1-2), pp. 89-99.

Johansson, A. (2005) Out-of-round railway wheels - causes and consequences. PhD Thesis. Chalmers University of Technology.

Johansson, A. (2006) 'Out-of-round railway wheels--assessment of wheel tread irregularities in train traffic', Journal of Sound and Vibration, 293(3-5), pp. 795-806.

Johansson, A. and Nielsen, J.C.O. (2003) 'Out-of-round railway wheels - wheel-rail contact forces and track response derived from field tests and numerical simulations', J. Rail and Rapid Transit, 217, pp. 135-146.

Johansson, A. and Nielsen, J.C.O. (2007) 'Rail corrugation growth--Influence of powered wheelsets with wheel tread irregularities', Wear, 262(11-12), pp. 1296-1307.

Johnson, K.L. (1958a) 'The Effect of a Tangential Contact Force Upon the Rolling Motion of an Elastic Sphere on a Plane', Trans ASME, J. Appl. Mech., pp. 339-346.

Johnson, K.L. (1958b) 'The Effect of Spin upon the Rolling Motion of an Elastic Sphere on a Plane', Trans ASME, J. Appl. Mech, pp. 332-338.

Johnson, K.L. (1985) Contact Mechanics. Cambridge: Cambridge University Press.

Johnson, K.L. (1989) 'The strength of surfaces in rolling contact', Instn Mech Engrs, Part F, Journal of Rail and Rapid Transit, 203, pp. 249-264.

Johnson, K.L. (2005) Selected papers of K.L.Johnson.

Kabo, E., Enblom, R. and Ekberg, A. (2009) 'Assessing risks of subsurface initiated rolling contact fatigue from field measurements', Proceedings of the 8th International Conference "Contact Mechanics and Wear of Rail/Wheel Systems". Firenze, Italy, 15th-18th September, 2009.

Kalker, J.J. (1990) Three-dimensional elastic bodies in rolling contact. Dordrecht: Kluwer Academic Publishers.

Kalker, J.J. (1991) 'Wheel-rail rolling contact theory', Wear, 144, pp. 243-261.

Kalousek, J. and Magel, E. (1997) 'The magic wear rate', Railway track and structures.

Kang, G. and Gao, Q. (2002) 'Uniaxial and non-proportionally multiaxial ratcheting of U71Mn rail steel: experiments and simulations', Mechanics of Materials, 34(12), pp. 809-820.

Kapoor, A. (1994) 'Re-evaluation of the life to rupture of ductile metals by cyclic plastic strain', Fatigue and Fracture of Engineering Materials and Structures, 17(2), pp. 201-219.

Kapoor, A. and Johnson, K.L. (1994) 'Plastic ratchetting as a mechanism of metalic wear', Proccedings of the royal society London, A 445, pp. 367-384.

Kapoor, A. (1997) 'Wear by plastic ratchetting', Wear, 212, pp. 119-130.

Kapoor, A. and Franklin, F.J. (2000) 'Tribological layers and the wear of ductile materials', Wear, 245, pp. 204-215.

Kapoor, A., Fletcher, D., Schmid, F., Sawley, K.J., Ishida, M. (2001) 'Tribology of Rail Transport', in Bhushan, B. (ed.) Modern Tribology Handbook. CRC Press, USA, pp. 1271-1308.

Kapoor, A., Franklin, F.J., Wong, S.K. and Ishida, M. (2002a) 'Surface roughness and plastic flow in rail wheel contact', Wear, 253(1-2), pp. 257-264.

Kapoor, A., Schmid, F. and Fletcher, D.I. (2002b) 'Managing the critical wheel/rail interface', Railway Gazette International, pp. 25-28.

Kapoor, A., Beynon, J.H., Fletcher, D.I. and Loo-Morrey, M. (2004) 'Computer simulation of strain accumulation and hardening for pearlitic rail steel undergoing repeated contact', The Journal of Strain Analysis for Engineering Design, V39(4), pp. 383-396.

Karttunen, K., Kabo, E., Ekberg, A. (2012) ‘A numerical study of the influence of lateral geometry irregularities on mechanical deterioration of freight tracks’, Proceedings of the Institution of Mechanical Engineers, Part F: Journal of Rail and Rapid Transit, 226(6), pp. 575-586.

Kato, K. (2002) 'Classification of wear mechanisms/models', Journal of engineering tribology, 216(J), pp. 349-355.

Knothe, K. and Grassie, S.L. (1999) 'Workshop on rail corrugations and out-of-round wheels', Journal of Sound and Vibration, 227(5), pp. 895-897.

Knothe, K. and Liebelt, S. (1995) 'Determination of temperatures for sliding contact with applications for wheel-rail systems', Wear, 189(1-2), pp. 91-99.

Kopeliovich, D. (2011) 'Iron-carbon phase diagram', www.substech.com [Online] (Accessed: 10.5.2012.).

Krause, H. and Juhe, H.H. (1977) 'Internal stresses during rolling friction and their evaluation', Wear, 41(1), pp. 15-23.

Krause, H. and Lehna, H. (1987) 'Investigation of the tribological characteristics of rolling-sliding friction systems by means of systematic wear experiments under well-defined conditions', Wear, 119, pp. 153-174.

Krause, H. and Poll, G. (1986) 'Wear of wheel-rail surfaces', Wear, 113(1), pp. 103-122.

Kwon, K.H. and Cho, N.G. (2006) 'Assesing th effect of stylus tip radius on surface roughness measurement by accumulation spectral analysis', International journal of precision engineering and manufacturing, 7(1), pp. 9-12.

Lee, K.M. and Polycarpou, A.A. (2005) 'Wear of conventional pearlitic and improved bainitic rail steels', Wear, 259(1-6), pp. 391-399.

Lee, K.M. and Polycarpou, A.A. (2011) 'Microscale experimental and modeling wear studies of rail steels', Wear, 271(7-8), pp. 1174-1180.

Lewis, R. and Olofsson, U. (2004) 'Mapping rail wear regimes and transitions', Wear, 257(7-8), pp. 721-729.

Li, S.J., Ishihara, M., Yumoto, H., Aizawa, T. and Shimotomai, M. (1998) 'Characterisation of cementite films prepared by electron shower assisted PVD method', Thin Solid FIlms, 316, pp. 100-104.

Li, Z., Dollevoet, R., Molodova, M., and Zhao, X. (2011) 'Squat growth – some observations and the validation of numerical predictions'. Wear, 271, 148–157.

Lundmark, J., Höglund, E. and Prakash, B. (2006) 'Running-in Behaviour of Rail and Wheel Contacting Surfaces', Proceedings from the 5th International Conference on Tribology AITC-AIT 2006. Parma, Italy, September 2006.

Lundmark, J., Kassfeldt, E., Hardell, J. and Prakash, B. (2007) 'Influence of Initial Surface Topography on Tribological Performance of the Wheel/Rail Interface During Rolling/Sliding conditions. ', Proceedings from the conference IHHA STS 2007. ISBN: 978-91-633-0607-5. Kiruna, Sweden, June 2007.

Lundmark J., E Kassfeldt, J Hardell and Prakash, B. (2009) 'The influence of initial surface topography on tribological performance of the wheel/rail interface during rolling/sliding conditions', Proc. IMechE J. Rail and Rapid Transit, 223 Part F, pp. 181-187.

Mädler, K., Zoll A., Heyder R., Brehmer M. (2008) ' Rail Materials - Alternatives and Limits', WCRR Conference 2008. Korea.

Magel, E., Roney, M., Kalousek, J. and Sroba, P. (2003) 'The blending of theory and practice in modern rail grinding', Fatigue & Fracture of Engineering Materials & Structures, 26, pp. 921-929.

Markov, D. (1995) 'Laboratory tests for wear of rail and wheel steels', Wear, 181-183(Part 2), pp. 678-686.

Marshall, M.B., Lewis, R., Dwyer-Joyce, R.S., Olofsson, U. and Björklund, S. (2006) 'Experimental Characterization of Wheel-Rail Contact Patch Evolution', Journal of Tribology, 128, pp. 493-504.

Matsumoto, A., Sato, Y., Ono, H., Tanimoto, M., Oka, Y. and Miyauchi, E. (2002) 'Formation mechanism and countermeasures of rail corrugation on curved track', Wear, 253(1-2), pp. 178-184.

Menezes, P.L., Kishore and Kailas, S.V. (2009) 'Role of surface texture of harder surface on subsurface deformation', Wear, 266, pp. 103-109.

Ministry-of-Defence (1997) Design and Maintenance Guide 09 - Permanent Way. London.

Ministry-of-Defence (2001) Permanent Way –frequency of inspection and maintenance operations.

Morys, B. (1999) 'Enlargement of out-of-round wheel profiles on high speed trains', Journal of Sound and Vibration, 227(5), pp. 965-978.

Muster, H., Schmedders, H., Wick, K. and Pradier, H. (1996) 'Rail rolling contact fatigue: the performance of naturally hard and head-hardened rails in track', Wear 191 pp. 54-64.

Network Rail (2007) Network Rail October 2007 Strategic Business Plan - Supporting document - Asset management.

Network Rail (2010a) 2010 Regulatory Financial Statements.

Network Rail (2010b) Track asset policy part 4 update March 2010.

Network Rail (2011a) Asset Management Strategy.

Network Rail (2011b) Control Period 4 Delivery Plan update 2011.

Nielsen, J.C.O., Ekberg, A. and Lunden, R. (2005) 'Influence of short-pitch wheel/rail corrugation on rolling contact fatigue of railway wheels', Proceedings of the Institution of Mechanical Engineers, J. Rail Rapid Transit, part F, 219(3), pp. 177-187.

Nielsen, J.C.O. and Johansson, A. (2000) 'Out-of-round railway wheels-a literature survey', Proceedings of the Institution of Mechanical Engineers, Part F: Journal of Rail and Rapid Transit, 214, p. 79.

Nielsen, J.C.O., Lunden, R., Johansson, A. and Vernersson, T. (2003) 'Train-Track Interaction and Mechanisms of Irregular Wear on Wheel and Rail Surfaces', Vehicle System Dynamics, 40(1), pp. 3-54.

Olofsson, U. and Sundvall, K. (2004) 'Influence of leaf, humidity and applied lubrication on friction in the wheel-rail contact: pin-on-disc experiments', Journal of rail and rapid transit, 218.

Olofsson, U. and Telliskivi, T. (2003) 'Wear, plastic deformation and friction of two rail steels—a full-scale test and a laboratory study', Wear, 254(1-2), pp. 80-93.

ORR (2006) Train Derailment at Hatfield: A Final Report by the Independent Investigation Board.

ORR (2007) Railway safety statistical report 2007.

Papaelias, M., Roberts, C. and Davis, C. (2010) 'Rail inspection technology', Railway Strategies, (December-January 2010), www.railwaystrategies.co.uk [Online] (Accessed: 26.9.2011.).

Pau, M. (2003) 'Estimation of real contact area in a wheel-rail system by means of ultrasonic waves', Tribology International, 36(9), pp. 687-690.

Pau, M., Aymerich, F. and Ginesu, F. (2002) 'Distribution of contact pressure in wheel–rail contact area', Wear, 253(1–2), pp. 265-274.

Perez-Unzueta, A.J. and Beynon, J.H. (1993) 'Microstructure and wear resistance of pearlitic rail steels', Wear, 162-164, pp. 173-182.

Pointner, P. (2006) Contact mechanics and wear of rail/wheel systems. Brisbane, Australia.

Pointner, P. (2008) 'High strength rail steels--The importance of material properties in contact mechanics problems', Wear, 265(9-10), pp. 1373-1379.

Rabinowicz, E. (1995) Friction and wear of materials. New York: John Wiley & Sons.

Reddy, V., Chattopadhyay, G., Larsson-Kraik, P.-O. and Hargreaves, D.J. (2007) 'Modelling and analysis of rail maintenance cost', International Journal of Production Economics, 105(2), pp. 475-482.

Rigney, D.A. (1994) 'The roles of hardness in the sliding behavior of materials', Wear, 175, pp. 63-69.

Rovira, A., Roda, A., Marshall, M.B., Brunskill, H. and Lewis, R. (2011) 'Experimental and numerical modelling of wheel–rail contact and wear', Wear, 271(5-6), pp. 911-924.

RSSB (2002) T023 Rolling Contact Fatigue of Rail: Review of Current Understanding, Available at: http://www.rssb.co.uk/.

RSSB (2003) T115 Whole Life Rail Model: Initial Assessment of the Influence of Wheel Profile Changes on RCF Formation", Available at: http://www.rssb.co.uk/.

RSSB (2008) T355 Management and Understanding of Rolling Contact Fatigue: Literature Survey; WP1: Mechanisms of Crack Initiation; WP2: Crack Growth.

RSSB (2010) T613 Trials of wheel and rail rolling contact fatigue control measures. Site monitoring and sustainable operation limits.

RSSB (2011) Annual Safety Performance Report 2010/11.

Sandstrom, J. and Ekberg, A. (2009) 'Predicting crack growth and risks of rail breaks due to wheel flat impacts in heavy haul operations', J. Rail and Rapid Transit, 223, pp. 153-161.

Sankaran, S., Subramanya Sarma, V., Padmanabhan,K.A. (2003) 'Low cycle fatigue behavior of a multiphase microalloyed medium carbon steel: comparison between ferrite/pearlite and quenched and tempered microstructures ', Materials Science and Engineering A345, pp. 328-335.

Sato, M., Anderson, P.M. and Rigney, D.A. (1993) 'Rolling-sliding behavior of rail steels', Wear, 162-164(Part 1), pp. 159-172.

Sato, Y., Matsumoto, A. and Knothe, K. (2002) 'Review on Rail Corrugation Studies', Wear 253, pp. 130–139.

Savic, Z. (ed.) (1992) Inzenjersko-masinski prirucnik, [Mechanical engineering manual] (3 vols). Beograd: Zavod za udzbenike i nastavna sredstva, "Novi Dani".

Savkoor, A.R. and Ouwerkerk, H. (1995) 'Tribological transitions due to heat dissipation during braking on contaminated rails', Wear, 181-183(1), pp. 391-396.

Savkoor, A.R. and van der Schoor, G.H. (1993) 'Slip-time history influences on the interaction between friction and wear in contaminated rolling contacts of wheel-rail systems', Wear, 162-164(Part 2), pp. 980-984.

Sawley, K. and Kristian, J. (2003) 'Development of bainitic rail steels with potential resistance to rolling contact fatigue', Fatigue and Fracture of Engineering Materials and Structures, 26(10), pp. 1019-1029.

Schmid, F. (ed.) (2010) Wheel-rail best practice handbook. Hampshire: University of Birmingham Press.

Sheng, X., Iwnicki, S. D. (2006) 'Simulations of roughness initiation and growth on railway rails', Journal of Sound and Vibration, 293, pp. 819-829.

Singh, U.P. and Singh, R. (1993) 'Wear investigation of wheel and rail steels under conditions of sliding and rolling-sliding contact with particular regard to microstructural parameters', Wear, 170(1), pp. 93-99.

Smith, L. (2007) Rolling contact fatigue in wheel - rail contact. Newcastle University.

Stock, R., Eadie, D.T., Elvidge, D. and Oldknow, K. (2011) 'Influencing rolling contact fatigue through top of rail friction modifier application – A full scale wheel–rail test rig study', Wear, 271(1–2), pp. 134-142.

Stock, R. and Pippan, R. (2011) 'RCF and wear in theory and practice--The influence of rail grade on wear and RCF', Wear, 271(1-2), pp. 125-133.

Su, X. and Clayton, P. (1997) 'Ratchetting strain experiments with a pearlitic steel under rolling/sliding contact', Wear, 205(1-2), pp. 137-143.

Sun, Y.Q., Cole, C. and Boyd, P. (2011) 'A numerical method using VAMPIRE modelling for prediction of turnout curve wheel-rail wear', Wear, 271(1-2), pp. 482-491.

Sundh, J. and Olofsson, U. (2011) 'Relating contact temperature and wear transitions in a wheel–rail contact', Wear, 271(1-2), pp. 78-85.

Surtronic 'Surtronic S25 User's Guide'.

Tabor, D. (1951) The hardness of metals. Oxford: Oxford University Press.

Takikawa, M. and Iriya, Y. (2008) 'Laboratory simulations with twin-disc machine on head check', Wear, 265(9–10), pp. 1300-1308.

Telliskivi, T. and Olofsson, U. (2004) 'Wheel-rail wear simulation', Wear, 257(11), pp. 1145-1153.

Thelen, G. and Lovette, M. (1996) 'A parametric study of the lubrication transport mechanism at the rail-wheel interface', Wear, 191(1-2), pp. 113-120.

Timoshenko, S.P. and Goodier, J.N. (1970) Theory of Elasticity, 3rd ed. London: McGraw-Hill.

Track-Ex (2012) Track-Ex course notes. Network Rail.

Tyfour, W., Beynon, J. and Kapoor, A. (1995) 'The steady state wear behaviour of pearlitic rail steel under dry rolling-sliding contact conditions', Wear, 180(1-2), pp. 79-89.

Tyfour, W., Beynon, J. and Kapoor, A. (1996) 'Deterioration of rolling contact fatigue life of pearlitic rail steel due to dry-wet rolling-sliding line contact', Wear, 197, pp. 255-265.

Tyfour, W.R. and Beynon, J.H. (1994) 'The effect of rolling direction reversal on the wear rate and wear mechanism of pearlitic rail steel', Tribology International, 27(6), pp. 401-412.

Uchino, K., Ueda, M., Kutaragi, K. and Babazono, K. (1997) Mechanical Working and Steel Processing Conference Proceedings. Indianapolis, IN, USA. Iron & Steel Soc of AIME.

Ueda, M. and Uchino, K. (1997) Proceedings of the TMS Fall Meeting. Indianapolis, IN, USA. Minerals, Metals & Materials Soc (TMS).

Ueda, M., Uchino, K. and Kobayashi, A. (2002a) 'Effects of carbon content on wear property in pearlitic steels', Wear, 253(1-2), pp. 107-113.

Ueda, M., Uchino, K., Matsushita, K. and Kobayashi, A. (2002b) 'Development of HE rails with high wear and damage resistance for heavy haul railways', Nippon Steel Technical Report, (85), pp. 167-172.

Ueda, M., Uchino, K. and Senuma, T. (2001) 'Influence of hardness and carbon content on rolling contact wear in pearlitic steels', Tetsu-To-Hagane/Journal of the Iron and Steel Institute of Japan, 87(4), pp. 190-197.

Ueda, M., Uchino, K. and Senuma, T. (2004) 'Influence of microstructure on rolling contact wear in high carbon steels', Tetsu-To-Hagane/Journal of the Iron and Steel Institute of Japan, 90(12), pp. 1023-1030.

UIC 860R (2008) Technical specification for the supply of rails, 9th edition.

UIC 861-1 (1969) Standard 54 kg/m rail profiles - Types UIC 54 and 54E.

UIC 861-3 (1969) Standard 60 kg/m rail profiles - Types UIC 60 and 60E.

UIC 861-5 (1977) Standard UIC type 71 (71 kg/m) rail section.

UIC 712R (2002) Rail defects.

UIC 725R (2007) Treatment of rail defects.

Vasic, G. (2004) Influence of leaf contamination of rail surface on wheel/rail adhesion. MSc Thesis. University of Belgrade.

Vasic, G., Franklin, F.J. and Fletcher, D.I. (2011) 'Influence of partial slip and direction of traction on wear rate in wheel-rail contact', Wear, 270(3-4), pp. 163-171.

Vermeulen, P.J. and Johnson, K.L. (1964) 'Contact of Nonspherical Elastic Bodies Transmitting Tangential Forces', Trans ASME, J. Appl. Mech, pp. 338-340.

Viafara, C.C., Castro, M.I., Velez, J.M. and Toro, A. (2005) 'Unlubricated sliding wear of pearlitic and bainitic steels', Wear, 259(1-6), pp. 405-411.

Wang, W.J., Shen, P., Song, J.H., Guo, J., Liu, Q.Y. and Jin, X.S. (2011a) 'Experimental study on adhesion behavior of wheel/rail under dry and water conditions', Wear, 271(9-10), pp. 2699-2705.

Wang, W.J., Zhang, H.F., Wang, H.Y., Liu, Q.Y. and Zhu, M.H. (2011b) 'Study on the adhesion behavior of wheel/rail under oil, water and sanding conditions', Wear, 271(9-10), pp. 2693-2698.

Webb, W.W. and Forgeng, W.D. (1958) 'Mechanical behavior of microcrystals', Acta Metallurgica, 6(7), pp. 462-469.

Wen-jian, W., Jun, G., Qi-yue, L. and Zhong-rong, Z. (2006) Contact mechanics and wear of rail/wheel systems. Brisbane, Australia.

Widiyarta, I.M. (2010) Simulation of Wear and Crack Initiation in Line Contact with Thermal Stresses. PhD Thesis. Newcastle University.

Widiyarta, M., Franklin, F.J. and Kapoor, A. (2008) 'Modelling thermal effect in ratcheting-led wear and rolling contact fatigue', Wear, 265, pp. 1325 - 1331.

Williams, J.A. (1999) 'Wear modelling: analytical computing and mapping - a continuum mechanics approach', Wear 225-229, pp. 1-17.

Wu, T.X. and Thompson, D.J. (2005) 'An investigation into rail corrugation due to micro-slip under multiple wheel/rail interactions', Wear, 258(7-8), pp. 1115-1125.

Xie, G. and Iwnicki, S.D. (2008a) 'Calculation of wear on a corrugated rail using a three-dimensional contact model', Wear, 265(9-10), pp. 1238-1248.

Xie, G. and Iwnicki, S.D. (2008b) 'Simulation of wear on a rough rail using a time-domain wheel-track interaction model', Wear, 265(11-12), pp. 1572-1583.

Zakharov, S., Bogdanov, V., Goryachea, I., Pogorelov, D., Zharov, I., Yasikov, V., Torskaya, E. and Soshenkov, S. (2006) Contact mechanics and wear of rail/wheel systems. Brisbane, Australia.

Zakharov, S. and Zharov, I. (2002) 'Simulation of mutual wheel/rail wear', Wear, 253(1-2), pp. 100-106.

Zhang, W., Chen, J., Wu, X. and Jin, X. (2002) 'Wheel/rail adhesion and analysis by using full scale roller rig', Wear, 253(1–2), pp. 82-88.

Zhong, W., Hu, J.J., Shen, P., Wang, C.Y. and Lius, Q.Y. (2011) 'Experimental investigation between rolling contact fatigue and wear of high-speed and heavy-haul railway and selection of rail material', Wear, 271(9-10), pp. 2485-2493.

Appendix A: SUROS tests

Introduction

The first part (Chapter 1) of this Appendix A was included as an Annex of Deliverable 4.2.5: "SUROS Twin-Disc Test Results" of InnoTrack EU FP6 Project, but not made public. The twin-disc testing on the SUROS machine reported below in Chapter 1 was done primarily by Dr Francis Franklin and Dr David Fletcher, with some assistance from the author of this thesis.

This Appendix A is included in this thesis because the wear results are used for development and validation of the Dynarat model. Adhesion coefficients are used as input in model simulations.

The second part of this Appendix A (Chapter 2) gives disc surface images after SUROS testing, taken by author of this Thesis. These images show how much the surface deteriorated after each test. Some of the images in this Chapter 2 are taken with the digital camera and some with the optical microscope. The reason is the time difference between tests and what equipment was available at certain moment.

Chapter 3 has results of transverse surface roughness measurements – value *Ra* in μm of discs before and after twin-disc testing. Four measurements were done before testing on new discs (See Table A.4) and four after testing for each disc (See Table A.5).

Metallurgical analysis: optical micrographs are presented in Appendix B and micro-hardness measurements are presented in Appendix C.

Table of Contents – Appendix A

Glossary

Abbreviation/acronym	Description
SUROS	Sheffield University Rolling Sliding [Twin-Disc Machine]
"gate-triggering" cracks	Cracks producing eddy current equipment signals equal in magnitude to those from the calibration disc, which is used to set a "gate" level on the test equipment.
C260 or P260	CORUS 260 Grade rail disc specimen or test identifier
C350	CORUS 350 Grade rail disc specimen or test identifier
C400	CORUS 400 Grade rail disc specimen or test identifier
V350	VA 350 Grade rail disc specimen or test identifier
V400	VA 400 Grade rail disc specimen or test identifier

1 SUROS Twin-Disc Test Results

SUROS twin disc test machine is described in detail in (Fletcher and Beynon, 2000).

The equipment used to measure mass for determining wear loss was calibrated prior to use, and has an accuracy to be within 0.5mg.

Photos of a rail disc sample are shown in Figure A.1.

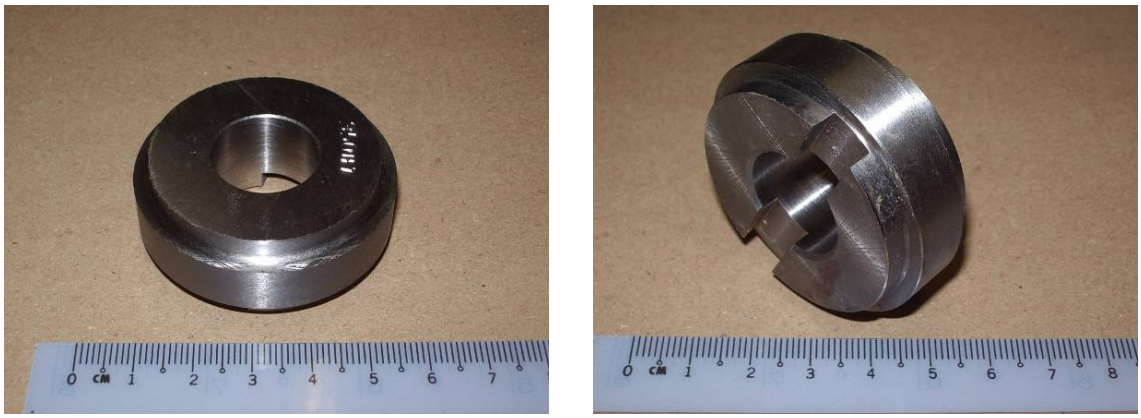

Figure A.1 Rail disc sample.

Test names and corresponding marked wheel and rail disc IDs are summarized in Table A.1. Details of each test are presented in the Sections §1.1 to §1.5 below; traction and wear rate data are summarized in Section §1.6.

Table A.1. Summary table of disc and test codes

Test name	Rail disc id	Wheel disc id	Material type	Test cycles
INNOT-01	INR1	INW1	Corus 400 Grade	5000 dry
INNOT-02	INR2	INW2	Corus 400 Grade	5000 dry + 5000 wet
INNOT-03	INR3	INW3	Corus 400 Grade	15000 dry
INNOT-04	INR10	INW4	VA 350 Grade	5000 dry
INNOT-05	INR11	INW5	VA 350 Grade	5000 dry + 5000 wet
INNOT-06	INR12	INW6	VA 350 Grade	15000 dry
INNOT-07	INR24	INW14	Corus 260 Grade	5000 dry
INNOT-08	INR23	INW13	Corus 260 Grade	5000 dry + 5000 wet
INNOT-09	INR22	INW9	Corus 260 Grade	15000 dry
INNOT-10	VA400(1)	INW7	VA 400 Grade	5000 dry
INNOT-11	VA400(2)	INW8	VA 400 Grade	15000 dry
INNOT-12	VA400(3)	INW12	VA 400 Grade	5000 dry + 5000 wet
INNOT-13	INR30	INW21	Corus 350 Grade	5000 dry
INNOT-14/41	INR31	INW16	Corus 350 Grade	5000 dry + 5000 wet
INNOT-51	INR34	INW20	Corus 350 Grade	15000 dry
INNOT-16	INR36	INW17	Corus 350 Grade	20000 wet
INNOT-17	INR26	INW10	Corus 260 Grade	20000 wet
INNOT-18	INR7	INW15	Corus 400 Grade	20000 wet
INNOT-19	INR40	INW23	VA 400 Grade	20000 wet
INNOT-21	INR16	INW24	VA 350 Grade	20000 wet
INNOT-22	INR25	WB35 (R8T)	Corus 260 Grade	15000 dry
INNOT-23	INR33	WB47 (R8T)	Corus 350 Grade	15000 dry
INNOT-24	INR4	WB46 (R8T)	Corus 400 Grade	15000 dry
INNOT-25	INR14	WB37 (R8T)	VA 350 Grade	15000 dry
INNOT-26	INR41	WB45 (R8T)	VA 400 Grade	15000 dry

1.1 Corus 260 Grade

The measured traction coefficient for the Corus 260 grade tests is plotted in Figure A.2 below.

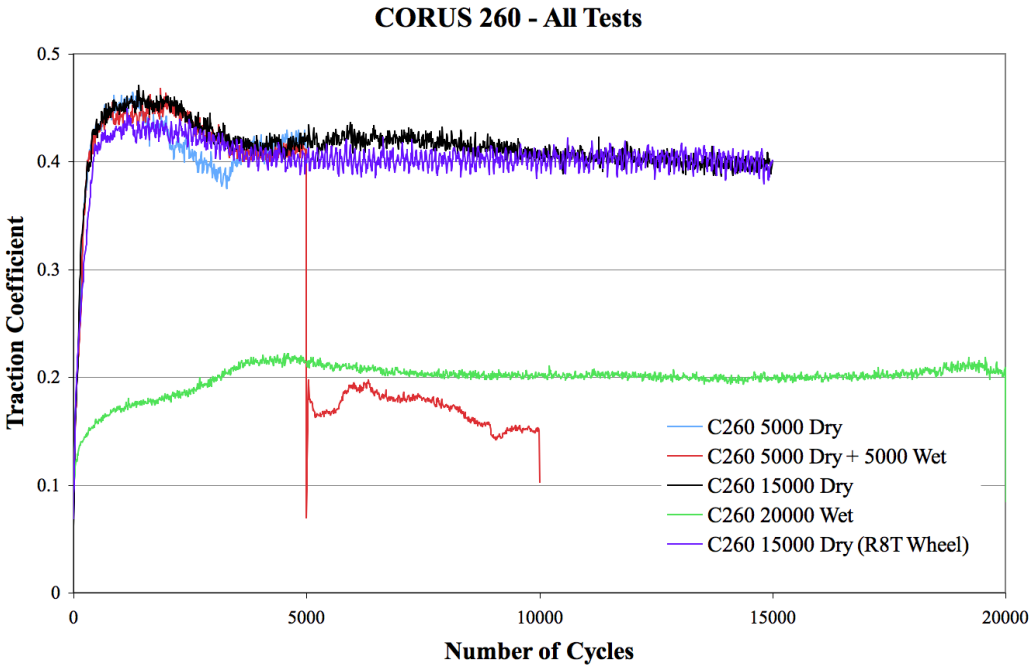

Figure A.2 Traction curves for Corus 260 Grade rail steel.

1.1.1 5000 Dry

Twin-disc testing parameters							
Test name	INNOT-07			**Test date**	20th July 2008		
Rail (top) id.	INR24			**Wheel (bottom) id.**	INW14		
Rail (base) material	Corus 260 Grade			**Wheel material**	VAS R7		
General description of test	5000 cycles dry (air-cooled)						
Measurement	**Initial**	**1. (dry)**					
Rail cycles	0	+5014					
Wheel cycles	0	+5063					
Rail diameter (mm)	46.98	46.96					
Wheel diameter (mm)	46.99	46.97					
Rail mass (g)	180.5581	180.5271					
Wheel mass (g)	181.1096	181.0855					

A/C Parameter	**11.4**	**11.5**	**22.4**	**22.5**
dry	2800	3200	15.00	15.00

E	212GPa	**Pressure**	1500MPa	**Slip**	-1%		
υ	0.3	**Force**	7.14kN	**Lub. feed**	-		
Eddy program	-	**Stand-off**	-	**Calibration disc**	-		

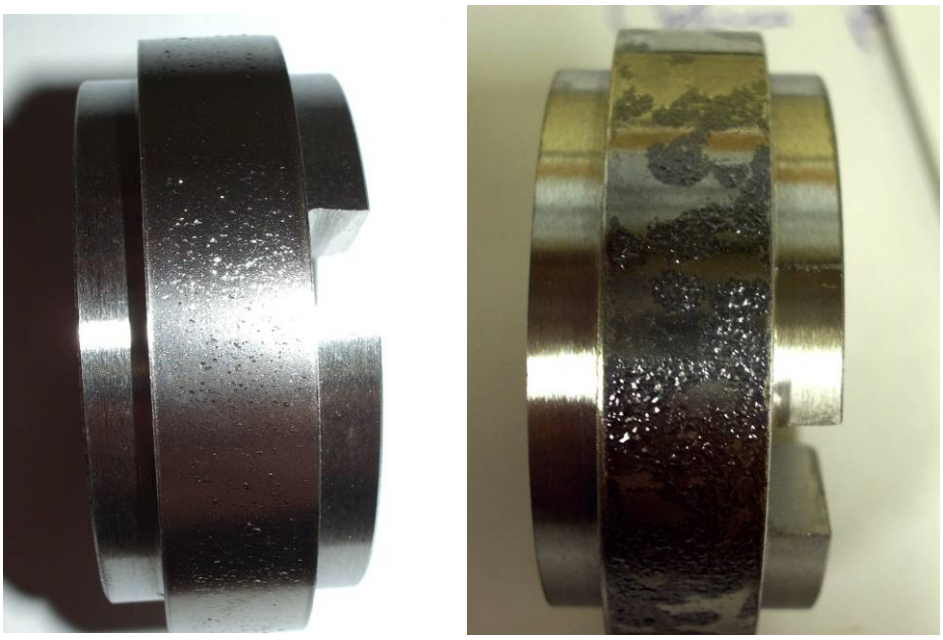

Figure A.3 5000 cycles under dry conditions, test INNOT-07. Left: Corus 260 Grade rail disc after testing, showing small amounts of surface flaking. Right: Wheel disc from test INNOT-07. Black patches thought to be loosely attached oxide were found on the wheel disc after testing. The majority of these patches were removed when the discs were cleaned ultrasonically in ethanol, leaving shallow depressions on the wheel disc surface.

1.1.2 5000 Dry + 5000 Wet

Twin-disc testing parameters						
Test name	INNOT-08		**Test date**	20th July 2008		
Rail (top) id.	INR23		**Wheel (bottom) id.**	INW13		
Rail (base) material	Corus 260 Grade		**Wheel material**	VAS R7		
General description of test	5000 cycles dry (air-cooled) + 5000 cycles wet					
Measurement	**Initial**	**1. (dry)**	**2. (wet)**			
Rail cycles	0	+5014	+5010			
Wheel cycles	0	+5062	+5060			
Rail diameter (mm)	46.97	46.97	46.87 (at disc edge) 46.94 (on flakes)			
Wheel diameter (mm)	46.99	46.98	46.92			
Rail mass (g)	180.7453	180.7166	180.4612			
Wheel mass (g)	180.9138	180.9016	180.8819			

A/C Parameter	**11.4**	**11.5**	**22.4**	**22.5**
dry	2800	3200	15.00	15.00
wet	2700	3200	20.00	20.00

E	212GPa	**Pressure**	1500MPa	**Slip**	-1%		
υ	0.3	**Force**	7.14kN	**Lub. feed**	1 drip / s (distilled water)		
Eddy program	-	**Stand-off**	-	**Calibration disc**	-		

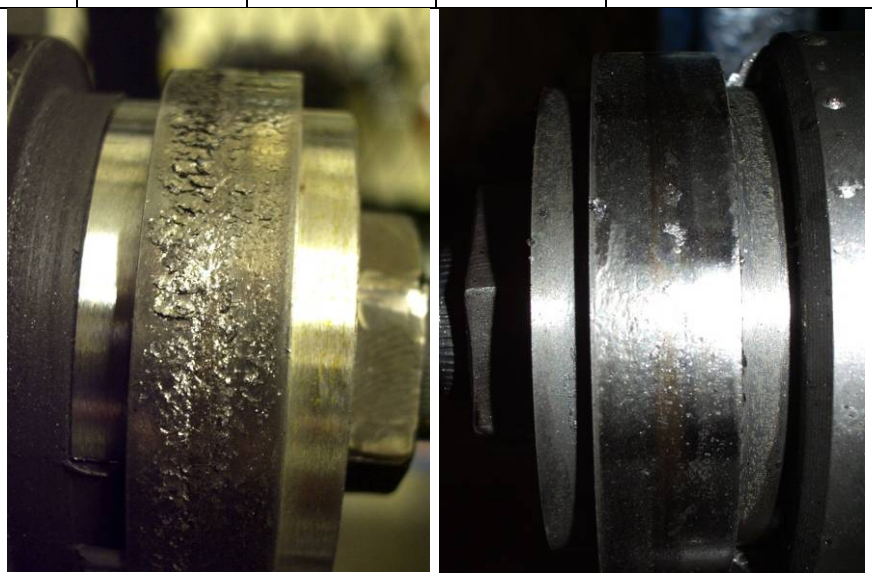

Figure A.4 Disc appearance following test INNOT-08. Left: 260 grade rail steel showing severe cracked and flaking of the disc surface was found after 5000 dry contact cycles followed by 5000 water lubricated cycles. Right: Corresponding wheel disc surface, showing some minor transfer of rail material to the wheel surface.

1.1.3 15000 Dry

Twin-disc testing parameters							
Test name	INNOT-09			**Test date**	20th July 2008		
Rail (top) id.	INR22			**Wheel (bottom) id.**	INW9		
Rail (base) material	Corus 260 Grade			**Wheel material**	VAS R7		
General description of test	15000 cycles dry (air-cooled)						
Measurement	**Initial**	**1. (dry)**					
Rail cycles	0	+15015					
Wheel cycles	0	+15163					
Rail diameter (mm)	46.98	46.91					
Wheel diameter (mm)	46.99	46.94					
Rail mass (g)	181.2587	181.0745					
Wheel mass (g)	181.0548	180.9018					
A/C Parameter	**11.4**	**11.5**	**22.4**	**22.5**			
dry	2800	3200	15.00	15.00			
E	212GPa	**Pressure**	1500MPa	**Slip**	-1%		
υ	0.3	**Force**	7.14kN	**Lub. feed**	-		
Eddy program	-	**Stand-off**	-	**Calibration disc**	-		

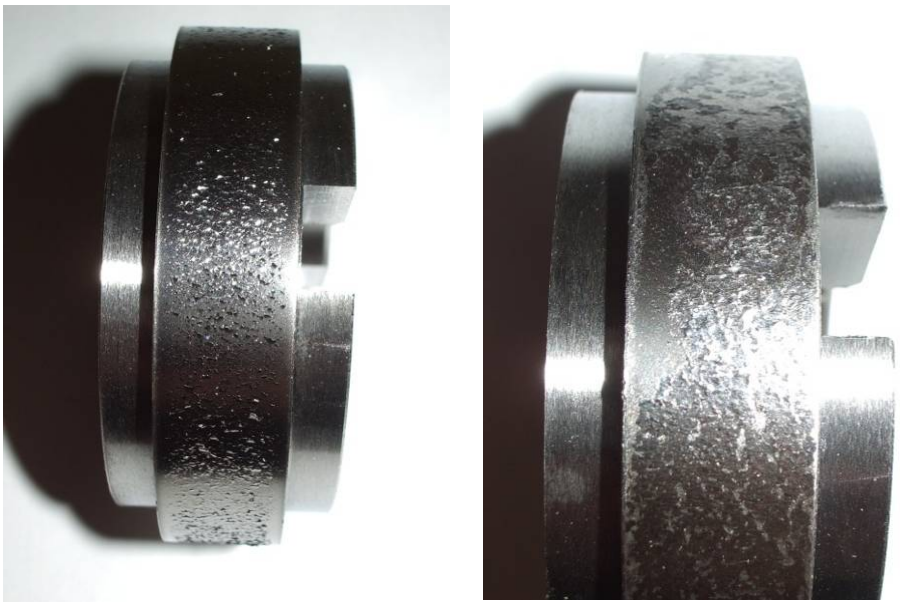

Figure A.5 15000 cycles under dry conditions, test INNOT-08. Left: 260 Grade rail disc after testing, showing large amounts of surface flaking. Right: Black regions believed to be oxide on the wheel disc surface, with pitting where cleaning has removed this loose material.

1.1.4 20000 Wet

Following the test, the wheel disc had unusual intermittent clean facets, although faceting could not be sensed by touch.

Twin-disc testing parameters							
Test name	INNOT-17		**Test date**	3rd August 2009			
Rail (top) id.	INR26		**Wheel (bottom) id.**	INW10			
Rail (base) material	Corus 260 Grade		**Wheel material**	VAS R7			
General description of test	20000 cycles wet						
Measurement	**Initial**	**1. (dry)**					
Rail cycles	0	+20014					
Wheel cycles	0	+20210					
Rail diameter (mm)	46.99	46.98					
Wheel diameter (mm)	47.00	46.98					
Rail mass (g)	180.8887	180.8690					
Wheel mass (g)	180.9091	180.8786					

A/C Parameter	**11.4**	**11.5**	**22.4**	**22.5**
wet	2700	3200	20.00	20.00

E	212GPa	**Pressure**	1500MPa	**Slip**	-1%		
υ	0.3	**Force**	7.14kN	**Lub. feed**	-		
Eddy program	-	**Stand-off**	-	**Calibration disc**	-		

1.1.5 15000 Dry (R8T Wheel)

Rail disc appeared to be highly polished between 1000 and 4500 cycles. As with other R8T tests, thin silvery flakes of steel (up to 1mm across) were blown out from the contact.

Twin-disc testing parameters											
Test name		INNOT-22			**Test date**			11th August 2009			
Rail (top) id.		INR25			**Wheel (bottom) id.**			WB35			
Rail (base) material		Corus 260 Grade			**Wheel material**			R8T			
General description of test		15000 cycles dry (air-cooled)									
Measurement		**Initial**	**1. (dry)**								
Rail cycles		0	+15011								
Wheel cycles		0	+15159								
Rail diameter (mm)		46.95	46.93								
Wheel diameter (mm)		46.96	46.88								
Rail mass (g)		181.0554	181.0124								
Wheel mass (g)		181.1844	181.0489								
A/C Parameter		**11.4**		**11.5**		**22.4**		**22.5**			
dry		2800		3200		15.00		15.00			
E	212GPa	**Pressure**	1500MPa		**Slip**	-1%					
υ	0.3	**Force**	7.13kN		**Lub. feed**	-					
Eddy program		-	**Stand-off**	-		**Calibration disc**	-				

1.2 CORUS 350 Grade

The measured traction coefficient for the Corus 350 grade tests is plotted in Figure A.6 below.

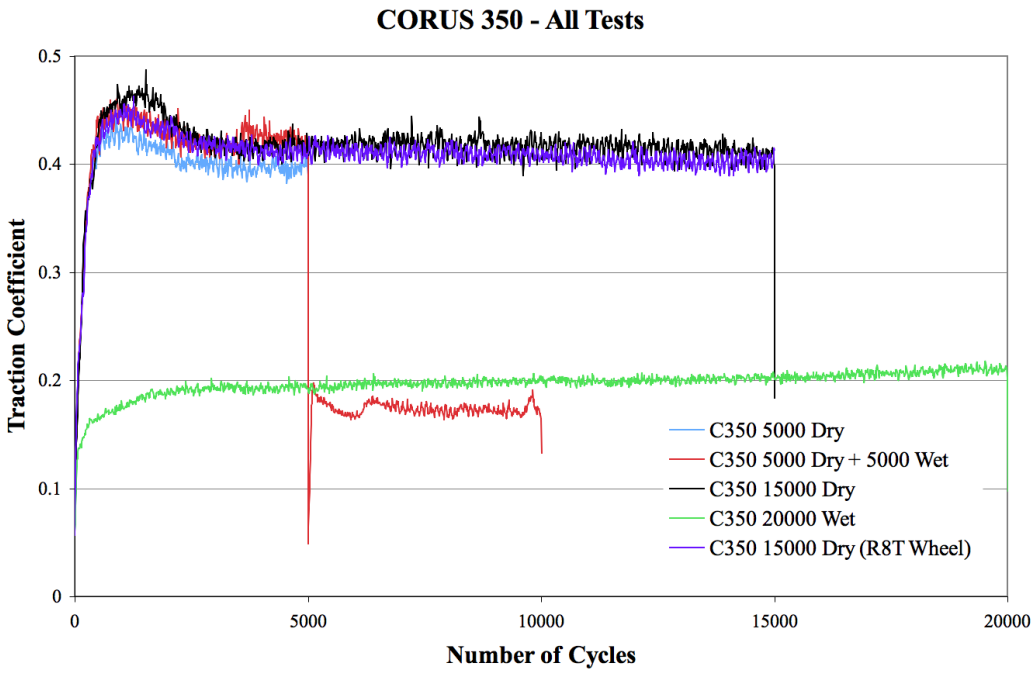

Figure A.6 Traction curves for Corus 350 Grade rail steel.

1.2.1 5000 Dry

3000 cycles: Wheel disc nut is unscrewed, but discs still aligned; test continued.

Twin-disc testing parameters						
Test name	INNOT-13		**Test date**	30th July 2009		
Rail (top) id.	INR30		**Wheel (bottom) id.**	INW21		
Rail (base) material	Corus 350 Grade		**Wheel material**	VAS R7		
General description of test	5000 cycles dry (air-cooled)					
Measurement	**Initial**	**1. (dry)**				
Rail cycles	0	+5000(?)				
Wheel cycles	0	+5050(?)				
Rail diameter (mm)	46.98	46.98				
Wheel diameter (mm)	46.99	46.94				
Rail mass (g)	180.9874	180.9744				
Wheel mass (g)	180.9194	180.8921				

A/C Parameter	**11.4**	**11.5**	**22.4**	**22.5**
dry	2800	3200	15.00	15.00

E	212GPa	**Pressure**	1500MPa	**Slip**	-1%	
υ	0.3	**Force**	7.14kN	**Lub. feed**	-	
Eddy program	-	**Stand-off**	-	**Calibration disc**	-	

1.2.2 5000 Dry + 5000 Wet

After 900 cycles: Thin silvery flakes of steel (up to 1mm across) were blown out from the contact.

Twin-disc testing parameters										
Test name		INNOT-14 / INNOT-41			**Test date**			30th July 2009		
Rail (top) id.		INR31			**Wheel (bottom) id.**			INW16		
Rail (base) material		Corus 350 Grade			**Wheel material**			VAS R7		
General description of test		5000 cycles dry (air-cooled) + 5000 cycles wet								
Measurement		**Initial**		**1. (dry)**	**2. (wet)**					
Rail cycles		0		+5016	+5013					
Wheel cycles		0		+5065	+5061					
Rail diameter (mm)		46.98		46.98	46.98					
Wheel diameter (mm)		47.00		-	46.96					
Rail mass (g)		180.9493		180.9366	180.9215					
Wheel mass (g)		181.0200		180.9967	180.9901					
A/C Parameter	**11.4**		**11.5**		**22.4**		**22.5**			
dry	2800		3200		15.00		15.00			
wet	2700		3200		20.00		20.00			
E	212GPa	**Pressure**	1500MPa	**Slip**	-1%					
υ	0.3	**Force**	7.14kN	**Lub. feed**	1 drip / s (distilled water)					
Eddy program	-	**Stand-off**	-	**Calibration disc**	-					

1.2.3 15000 Dry

After 2980 cycles: Thin silvery flakes of steel (up to 1mm across) were blown out from the contact.

About 8500 cycles: Slip went from -1% to +1.9% briefly, and traction coefficient jumped slightly – possibly E-M interference.

Twin-disc testing parameters						
Test name	INNOT-51		**Test date**	30th July 2009		
Rail (top) id.	INR34		**Wheel (bottom) id.**	INW20		
Rail (base) material	Corus 350 Grade		**Wheel material**	VAS R7		
General description of test	15000 cycles dry (air-cooled)					
Measurement	**Initial**	**1. (dry)**				
Rail cycles	0	+15015				
Wheel cycles	0	+15163				
Rail diameter (mm)	46.98	46.97				
Wheel diameter (mm)	46.99	46.95				
Rail mass (g)	181.0456	181.0062				
Wheel mass (g)	180.9471	180.8481				

A/C Parameter	**11.4**	**11.5**	**22.4**	**22.5**
dry	2800	3200	15.00	15.00

E	212GPa	**Pressure**	1500MPa	**Slip**	-1%		
υ	0.3	**Force**	7.13kN	**Lub. feed**	-		
Eddy program	-	**Stand-off**	-	**Calibration disc**	-		

1.2.4 20000 Wet

7000 cycles: Wheel disc looks polished; rail disc looks dull with dark edges.

18000 cycles: Wheel disc looks bright; rail disc looks dark.

Twin-disc testing parameters						
Test name	INNOT-16		**Test date**	30th July 2009		
Rail (top) id.	INR36		**Wheel (bottom) id.**	INW17		
Rail (base) material	Corus 350 Grade		**Wheel material**	VAS R7		
General description of test	20000 cycles wet					
Measurement	**Initial**	**1. (dry)**				
Rail cycles	0	+20000(?)				
Wheel cycles	0	+20200(?)				
Rail diameter (mm)	46.96	46.97				
Wheel diameter (mm)	46.99	46.97				
Rail mass (g)	180.7043	180.6978				
Wheel mass (g)	181.0133	180.9773				

A/C Parameter	**11.4**	**11.5**	**22.4**	**22.5**
wet	2700	3200	20.00	20.00

E	212GPa	**Pressure**	1500MPa	**Slip**	-1%		
υ	0.3	**Force**	7.13kN	**Lub. feed**	-		
Eddy program		-	**Stand-off**	-	**Calibration disc**	-	

1.2.5 15000 Dry (R8T Wheel)

Rail disc appeared to be highly polished between 850 and 7700 cycles. As with other R8T tests, thin silvery flakes of steel (up to 1mm across) were blown out from the contact (starting at 1841, particularly frequent at 2500).

Twin-disc testing parameters											
Test name		INNOT-23			**Test date**			11th August 2009			
Rail (top) id.		INR33			**Wheel (bottom) id.**			WB47			
Rail (base) material		Corus 350 Grade			**Wheel material**			R8T			
General description of test		15000 cycles dry (air-cooled)									
Measurement		**Initial**	**1. (dry)**								
Rail cycles		0	+15013								
Wheel cycles		0	+15161								
Rail diameter (mm)		46.96	46.94								
Wheel diameter (mm)		46.97	46.87								
Rail mass (g)		181.0057	180.9710								
Wheel mass (g)		181.5728	181.4332								
A/C Parameter	**11.4**		**11.5**		**22.4**		**22.5**				
dry	2800		3200		15.00		15.00				
E	212GPa	**Pressure**	1500MPa		**Slip**	-1%					
υ	0.3	**Force**	7.13kN		**Lub. feed**	-					
Eddy program	-	**Stand-off**	-		**Calibration disc**	-					

1.3 CORUS 400 Grade

The measured traction coefficient for the Corus 400 grade tests is plotted in Figure A.7 below.

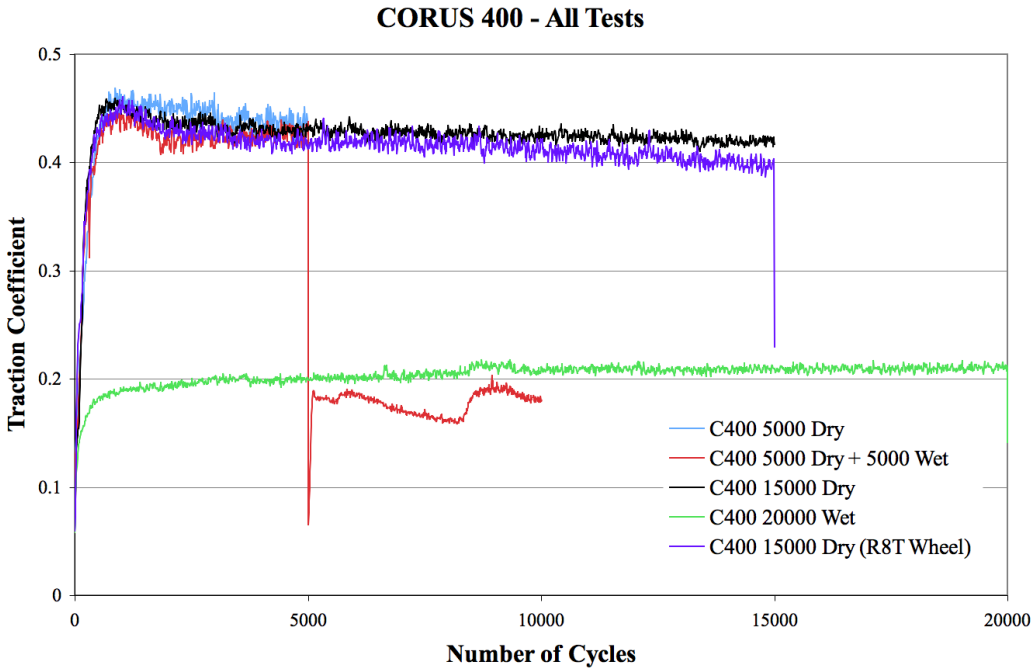

Figure A.7 Traction curves for Corus 400 Grade rail steel.

1.3.1 5000 Dry

Figure A.8 shows the discs mounted on the machine prior to the test. Figure A.9 shows the discs following the test; the damage to the rail disc surface can be seen clearly.

Discs were cooled with compressed air during the test; the air supply was started after 200 cycles.

Twin-disc testing parameters						
Test name	INNOT-01		**Test date**	20th February 2008		
Rail (top) id.	INR1		**Wheel (bottom) id.**	INW1		
Rail (base) material	Corus 400 Grade †		**Wheel material**	VAS R7		
General description of test	5000 cycles dry					
Measurement	**Initial**	**1. (dry)**				
Rail cycles	0	+5013				
Wheel cycles	0	+5065				
Rail diameter (mm)	46.97	46.97				
Wheel diameter (mm)	46.96	46.96				
Rail mass (g)	180.3178	180.3054				
Wheel mass (g)	181.0489	181.0230				

A/C Parameter	**11.4**	**11.5**	**22.4**	**22.5**
dry	2800	3200	15.00	15.00
wet	2700	3200	20.00	20.00

E	212GPa	**Pressure**	1500MPa	**Slip**	-1%		
υ	0.3	**Force**	7.13kN	**Lub. feed**	(none - air-cooled dry test)		
Eddy program	DIF30	**Stand-off**	0.2mm	**Calibration disc**	R1(45)		

† *Disc stamped incorrectly as 350HT.*

Additional Data

Humidity: -%

Temperature: -°C

Eddy current: (not used for dry test)

Figure A.8 Discs INR1 and INW1 mounted on the machine before testing.

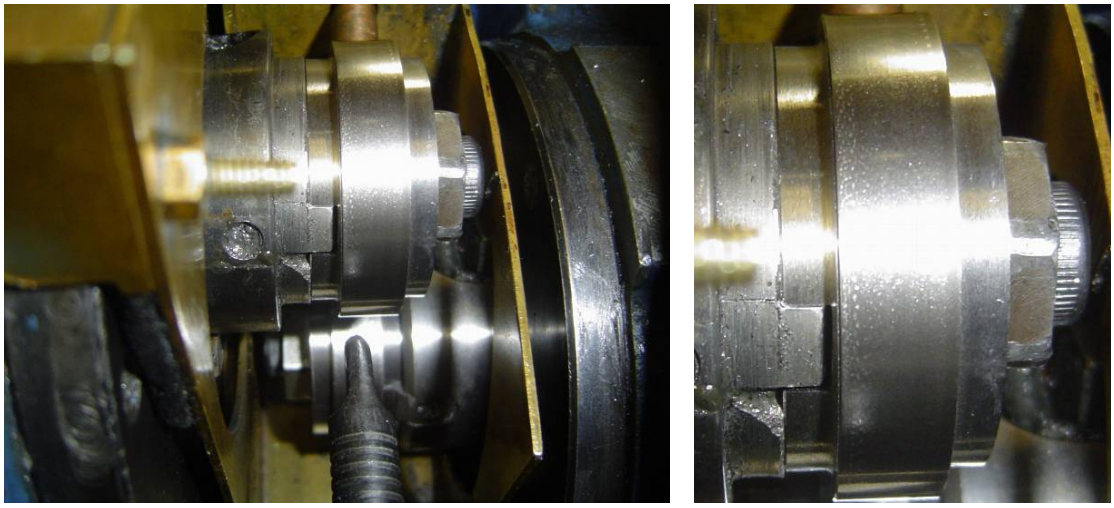

Figure A.9 Left: Discs INR1 and INW1 mounted on the machine after testing. Right: Disc surface after 5000 dry cycles. 400 grade disc INR1.

1.3.2 5000 Dry + 5000 Wet

Discs were cooled with compressed air during the test; the air supply was started immediately.

Discs were removed after 5000 cycles dry to be cleaned (using ethanol in an ultrasonic bath followed by warm air drying, no mechanical contact with the disc surface) and measured before continuing with the wet test.

The test was stopped prematurely after 5000 dry + 5000 wet. After 4000 wet cycles the eddy-current probe registered multiple "gate-triggering" cracks for which eddy current signals grew noticeably during the following 1000 wet cycles – at which point the test was stopped. The surface of the rail disc had undergone damage by flaking (see Figure A.10). Depending on the steel and crack orientation, previous tests have shown a gate triggering crack will have a depth of between 100 and 400μm.

Twin-disc testing parameters						
Test name	INNOT-02		**Test date**	20th February 2008		
Rail (top) id.	INR2		**Wheel (bottom) id.**	INW2		
Rail (base) material	Corus 400 Grade †		**Wheel material**	VAS R7		
General description of test	5000 cycles dry (air-cooled) + 10000 cycles wet (terminated prematurely after 5000)					
Measurement	**Initial**	**1. (dry)**	**2. (wet)**			
Rail cycles	0	+5013	+5016			
Wheel cycles	0	+5066	+5069			
Rail diameter (mm)	46.99	46.99	47.00			
Wheel diameter (mm)	46.98	46.96	46.96			
Rail mass (g)	180.4118	180.3979	180.3506			
Wheel mass (g)	180.8339	180.8051	180.8010			

A/C Parameter	**11.4**	**11.5**	**22.4**	**22.5**
dry	2800	3200	15.00	15.00
wet	2700	3200	20.00	20.00

E	212GPa	**Pressure**	1500MPa	**Slip**	-1%		
υ	0.3	**Force**	7.13kN	**Lub. feed**	1 drip / s (distilled water)		
Eddy program	DIF30	**Stand-off**	0.2mm	**Calibration disc**	R1(45)		

† *Disc stamped incorrectly as MHH.*

Additional Data

Humidity: 23%

Temperature: 22.2°C

Eddy current: (not used for dry test) Wet: Registered multiple gate-triggering cracks by 4000 cycles.

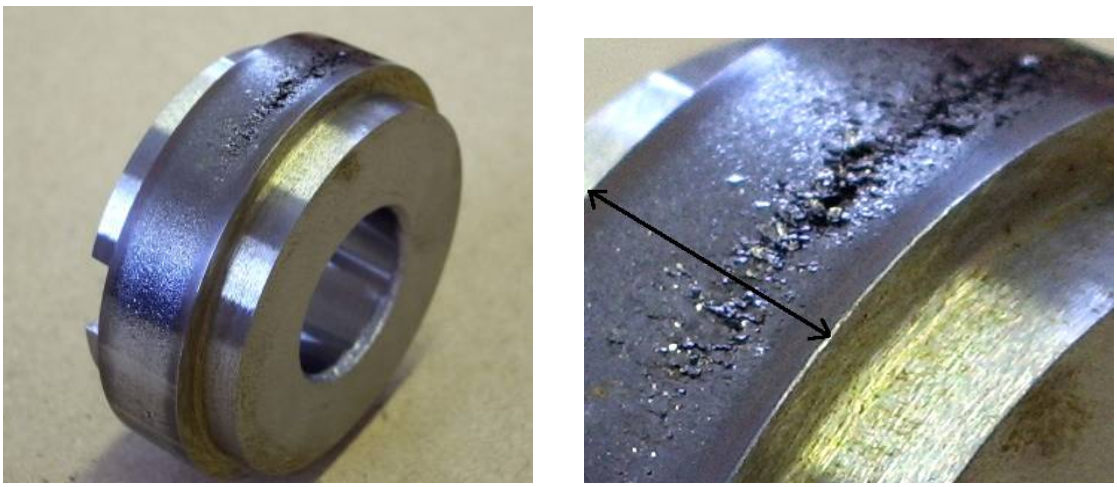

Figure A.10 Left: Disc INR2 after testing. Right: Expanded view of surface flaking damage on disc INR2. The line indicating the width of the disc track (10mm) can be used as a scale.

1.3.3 15000 Dry

Discs were cooled with compressed air during the test; the air supply was started immediately.

Twin-disc testing parameters						
Test name	INNOT-03		**Test date**	20th February 2008		
Rail (top) id.	INR3		**Wheel (bottom) id.**	INW3		
Rail (base) material	Corus 400 Grade †		**Wheel material**	VAS R7		
General description of test	15000 cycles dry (air-cooled)					
Measurement	**Initial**	**1. (dry)**				
Rail cycles	0	+15014				
Wheel cycles	0	+15169				
Rail diameter (mm)	47.00	46.98				
Wheel diameter (mm)	46.99	46.95				
Rail mass (g)	180.1083	180.0715				
Wheel mass (g)	180.9945	180.8929				

A/C Parameter	**11.4**	**11.5**	**22.4**	**22.5**
dry	2800	3200	15.00	15.00
wet	2700	3200	20.00	20.00

E	212GPa	**Pressure**	1500MPa	**Slip**	-1%		
υ	0.3	**Force**	7.14kN	**Lub. feed**	1 drip / s (distilled water)		
Eddy program	DIF30	**Stand-off**	0.2mm	**Calibration disc**	R1(45)		

† *Disc stamped incorrectly as 350HT.*

Additional Data

Humidity: 23%

Temperature: 23.2°C

Eddy current: (not used for dry test)

1.3.4 20000 Wet

8200 cycles: Wheel disc looks polished; rail disc has dark edges.

Twin-disc testing parameters							
Test name	INNOT-18			**Test date**	3rd August 2009		
Rail (top) id.	INR7			**Wheel (bottom) id.**	INW15		
Rail (base) material	Corus 400 Grade			**Wheel material**	VAS R7		
General description of test	20000 cycles wet						
Measurement	**Initial**	**1. (dry)**					
Rail cycles	0	+20013					
Wheel cycles	0	+20214					
Rail diameter (mm)	46.99	46.99					
Wheel diameter (mm)	46.99	46.96					
Rail mass (g)	180.4047	180.3932					
Wheel mass (g)	180.9726	180.9294					

A/C Parameter	**11.4**	**11.5**	**22.4**	**22.5**
wet	2700	3200	20.00	20.00

E	212GPa	**Pressure**	1500MPa	**Slip**	-1%		
υ	0.3	**Force**	7.14kN	**Lub. feed**	-		
Eddy program	-	**Stand-off**	-	**Calibration disc**	-		

1.3.5 15000 Dry (R8T Wheel)

Rail disc appeared to be highly polished between 600 and 4900 cycles. As with other R8T tests, thin silvery flakes of steel (up to 1mm across) were blown out from the contact (starting about 2000).

Twin-disc testing parameters						
Test name	INNOT-24		**Test date**		11th August 2009	
Rail (top) id.	INR4		**Wheel (bottom) id.**		WB46	
Rail (base) material	Corus 400 Grade		**Wheel material**		R8T	
General description of test	15000 cycles dry (air-cooled)					
Measurement	**Initial**	**1. (dry)**				
Rail cycles	0	+15012				
Wheel cycles	0	+15170				
Rail diameter (mm)	46.97	46.95				
Wheel diameter (mm)	46.95	46.87				
Rail mass (g)	180.7436	180.7265				
Wheel mass (g)	181.1207	180.9740				

A/C Parameter	**11.4**	**11.5**	**22.4**	**22.5**
dry	2800	3200	15.00	15.00

E	212GPa	**Pressure**	1500MPa	**Slip**	-1%		
υ	0.3	**Force**	7.13kN	**Lub. feed**	-		
Eddy program	-	**Stand-off**	-	**Calibration disc**	-		

1.4 VA 350 Grade

The measured traction coefficient for the VA 350 grade tests is plotted in Figure A.11 below.

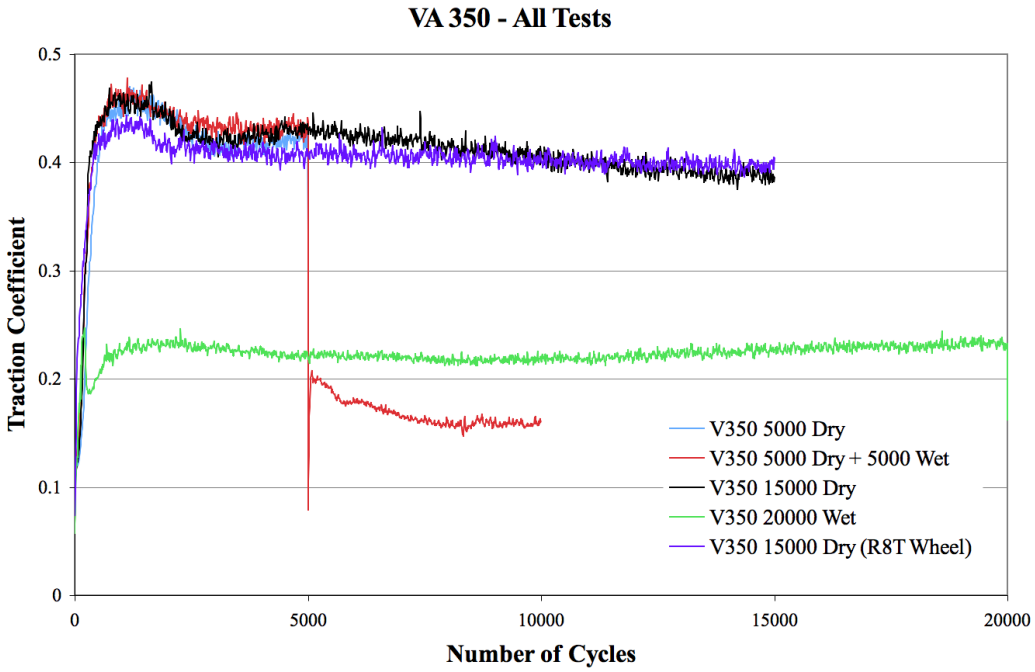

Figure A.11 Traction curves for VA 350 Grade rail steel.

1.4.1 5000 Dry

Twin-disc testing parameters							
Test name	INNOT-04			**Test date**		19th July 2008	
Rail (top) id.	INR10			**Wheel (bottom) id.**		INW4	
Rail (base) material	VA 350 Grade			**Wheel material**		VAS R7	
General description of test	5000 cycles dry (air-cooled)						
Measurement	**Initial**	**1. (dry)**					
Rail cycles	0	+5011					
Wheel cycles	0	+5059					
Rail diameter (mm)	46.98	46.99					
Wheel diameter (mm)	47.07	46.99					
Rail mass (g)	180.6997	180.6741					
Wheel mass (g)	180.2240	180.1879					

A/C Parameter	**11.4**	**11.5**	**22.4**	**22.5**
dry	2800	3200	15.00	15.00

E	212GPa	**Pressure**	1500MPa	**Slip**	-1%		
υ	0.3	**Force**	7.14kN	**Lub. feed**	-		
Eddy program	-	**Stand-off**	-	**Calibration disc**	-		

Figure A.12 VA 350 Grade rail disc after testing for 5000 cycles under dry conditions in test INNOT-04. Very small amounts of surface flaking could be seen.

1.4.2 5000 Dry + 5000 Wet

Twin-disc testing parameters						
Test name	INNOT-05		**Test date**	20th July 2008		
Rail (top) id.	INR11		**Wheel (bottom) id.**	INW5		
Rail (base) material	VA 350 Grade		**Wheel material**	VAS R7		
General description of test	5000 cycles dry (air-cooled) + 5000 cycles wet					
Measurement	**Initial**	**1. (dry)**	**2. (wet)**			
Rail cycles	0	+5014	5013			
Wheel cycles	0	+5064	5066			
Rail diameter (mm)	46.99	46.98	46.98			
Wheel diameter (mm)	47.00	46.96	46.96			
Rail mass (g)	180.4083	180.3920	180.3861			
Wheel mass (g)	181.3028	181.2790	181.2718			

A/C Parameter	**11.4**	**11.5**	**22.4**	**22.5**
dry	2800	3200	15.00	15.00
wet	2700	3200	20.00	20.00

E	212GPa	**Pressure**	1500MPa	**Slip**	-1%		
υ	0.3	**Force**	7.14kN	**Lub. feed**	1 drip / s (distilled water)		
Eddy program	-	**Stand-off**	-	**Calibration disc**	-		

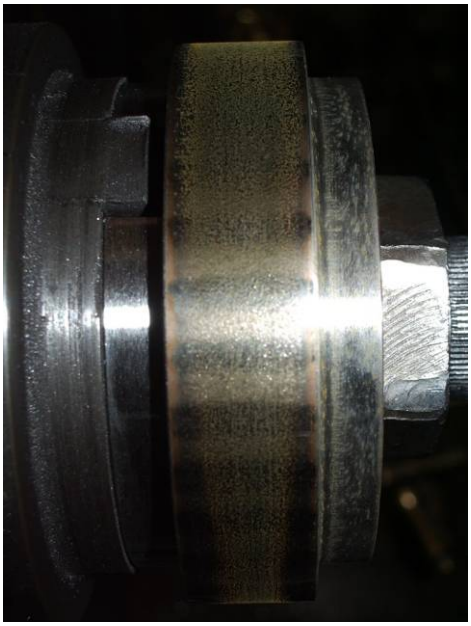

Figure A.13 VA 350 Grade rail disc still mounted on the SUROS test machine after testing for 5000 cycles under dry conditions + 5000 cycles under water lubricated conditions in test INNOT-05. The disc surface had a light brown colouration, which varied darker and lighter around the disc.

1.4.3 15000 Dry

Twin-disc testing parameters							
Test name	INNOT-06		**Test date**		19th July 2008		
Rail (top) id.	INR10		**Wheel (bottom) id.**		INW4		
Rail (base) material	VA 350 Grade		**Wheel material**		VAS R7		
General description of test	15000 cycles dry (air-cooled)						
Measurement	**Initial**	**1. (dry)**					
Rail cycles	0	+15014					
Wheel cycles	0	+15165					
Rail diameter (mm)	47.00	46.97					
Wheel diameter (mm)	47.00	46.93					
Rail mass (g)	180.3917	180.3150					
Wheel mass (g)	180.9953	180.8197					

A/C Parameter	**11.4**	**11.5**	**22.4**	**22.5**
dry	2800	3200	15.00	15.00

E	212GPa	**Pressure**	1500MPa	**Slip**	-1%		
υ	0.3	**Force**	7.14kN	**Lub. feed**	-		
Eddy program	-	**Stand-off**	-	**Calibration disc**	-		

Figure A.14 VA 350 grade rail disc from test INNOT-06, after 15000 cycles dry contact. Considerable surface flaking has taken place.

1.4.4 20000 Wet

The slip oscillated unusually during the first 1000 cycles; traction coefficient is relatively high during this period also.

Twin-disc testing parameters							
Test name	INNOT-21			**Test date**	3rd August 2009		
Rail (top) id.	INR16			**Wheel (bottom) id.**	INW24		
Rail (base) material	VA 350 Grade			**Wheel material**	VAS R7		
General description of test	20000 cycles wet						
Measurement	**Initial**	**1. (dry)**					
Rail cycles	0	+20013					
Wheel cycles	0	+20215					
Rail diameter (mm)	46.99	46.99					
Wheel diameter (mm)	46.99	46.94					
Rail mass (g)	180.6961	180.6872					
Wheel mass (g)	180.7882	180.7418					

A/C Parameter	**11.4**	**11.5**	**22.4**	**22.5**
wet	2700	3200	20.00	20.00

E	212GPa	**Pressure**	1500MPa	**Slip**	-1%		
υ	0.3	**Force**	7.14kN	**Lub. feed**	-		
Eddy program	-	**Stand-off**	-	**Calibration disc**	-		

1.4.5 15000 Dry (R8T Wheel)

Rail disc appeared to be highly polished between 650 and 3000 cycles. As with other R8T tests, thin silvery flakes of steel (up to 1mm across) were blown out from the contact (starting at 1691).

Twin-disc testing parameters							
Test name	INNOT-25		**Test date**		11th August 2009		
Rail (top) id.	INR14		**Wheel (bottom) id.**		WB37		
Rail (base) material	VA 350 Grade		**Wheel material**		R8T		
General description of test	15000 cycles dry (air-cooled)						
Measurement	**Initial**	**1. (dry)**					
Rail cycles	0	+15014					
Wheel cycles	0	+15162					
Rail diameter (mm)	46.96	46.94					
Wheel diameter (mm)	46.97	46.89					
Rail mass (g)	180.6293	180.6072					
Wheel mass (g)	181.2930	181.1565					

A/C Parameter	**11.4**	**11.5**	**22.4**	**22.5**
dry	2800	3200	15.00	15.00

E	212GPa	**Pressure**	1500MPa	**Slip**	-1%		
υ	0.3	**Force**	7.13kN	**Lub. feed**	-		
Eddy program	-	**Stand-off**	-	**Calibration disc**	-		

1.5 VA 400 grade

The measured traction coefficient for the VA 400 grade tests is plotted in Figure A.15 below. The dry tests with the VAS R7 wheel discs are very consistent with each other, while the dry test with the R8T wheel disc is distinctly lower.

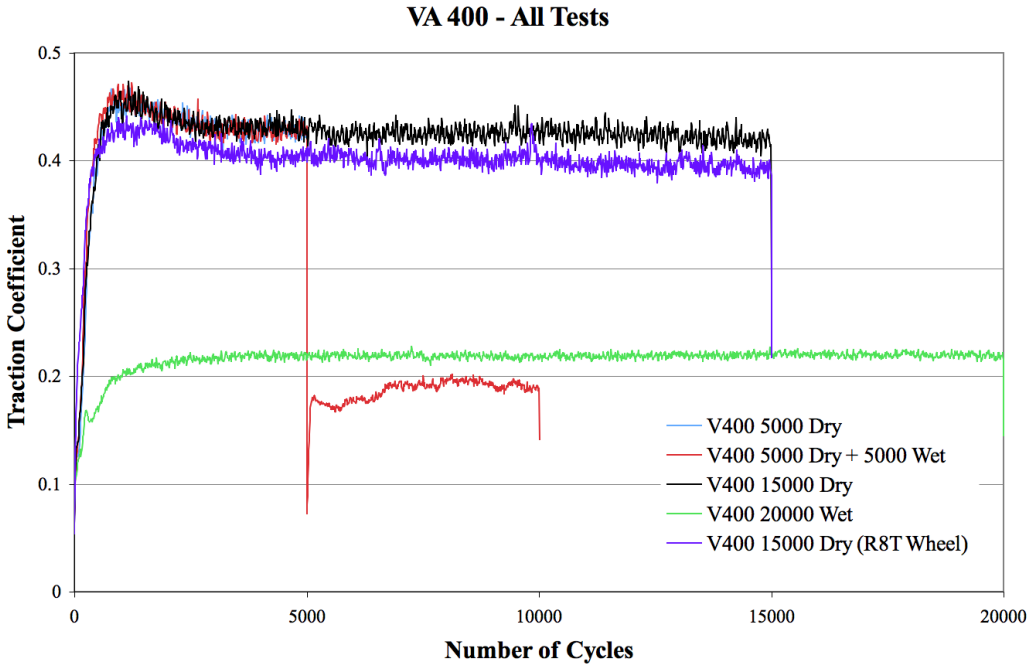

Figure A.15 Traction curves for VA 400 Grade rail steel.

1.5.1 5000 Dry

Twin-disc testing parameters							
Test name	INNOT-10			**Test date**		12th Nov 2008	
Rail (top) id.	VA400(1)			**Wheel (bottom) id.**		INW7	
Rail (base) material	VA 400 Grade			**Wheel material**		VAS R7	
General description of test	5000 cycles dry (air-cooled)						
Measurement	**Initial**	**1. (dry)**					
Rail cycles	0	+5011					
Wheel cycles	0	+5062					
Rail diameter (mm)	46.99	46.99					
Wheel diameter (mm)	46.99	46.97					
Rail mass (g)	180.4915	180.4818					
Wheel mass (g)	180.9727	180.9467					

A/C Parameter	**11.4**	**11.5**	**22.4**	**22.5**
dry	2800	3200	15.00	15.00

E	212GPa	**Pressure**	1500MPa	**Slip**	-1%		
υ	0.3	**Force**	7.14kN	**Lub. feed**	-		
Eddy program	-	**Stand-off**	-	**Calibration disc**	-		

Figure A.16 Rail disc after testing.

1.5.2 5000 Dry + 5000 Wet

Twin-disc testing parameters						
Test name	INNOT-12		**Test date**	12th NOV 2008		
Rail (top) id.	VA400(3)		**Wheel (bottom) id.**	INW12		
Rail (base) material	VA 400 Grade		**Wheel material**	VAS R7		
General description of test	5000 cycles dry (air-cooled) + 5000 cycles wet					
Measurement	**Initial**	**1. (dry)**	**2. (wet)**			
Rail cycles	0	+5013	+5012			
Wheel cycles	0	+5062	+5061			
Rail diameter (mm)	46.99	47.00	46.98			
Wheel diameter (mm)	47.00	46.98	46.96			
Rail mass (g)	180.5027	180.4879	180.4752			
Wheel mass (g)	180.9348	180.9063	180.9034			

A/C Parameter	**11.4**	**11.5**	**22.4**	**22.5**
dry	2800	3200	15.00	15.00
wet	2700	3200	20.00	20.00

E	212GPa	**Pressure**	1500MPa	**Slip**	-1%		
υ	0.3	**Force**	7.14kN	**Lub. feed**	1 drip / s (distilled water)		
Eddy program	-	**Stand-off**	-	**Calibration disc**	-		

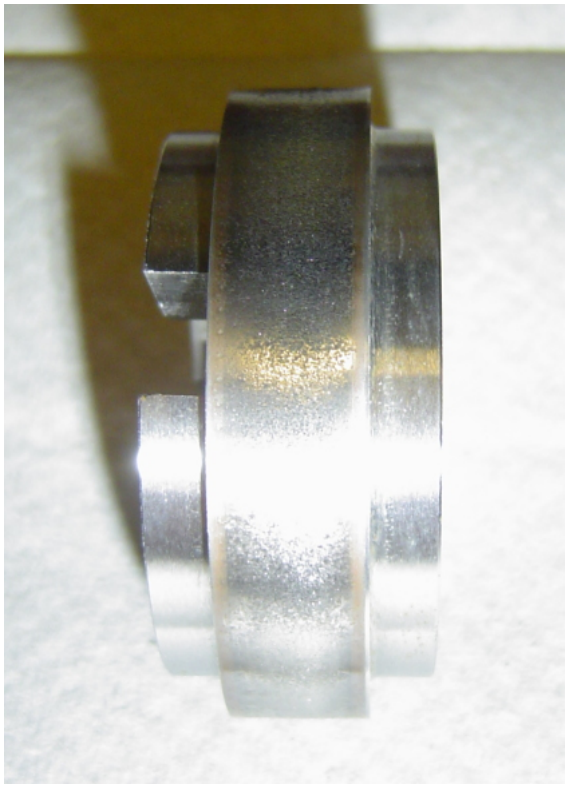

Figure A.17 Rail disc after testing.

1.5.3 15000 Dry

Twin-disc testing parameters										
Test name	INNOT-11			**Test date**	12^{th} Nov 2008					
Rail (top) id.	VA400(2)			**Wheel (bottom) id.**	INW8					
Rail (base) material	VA 400 Grade			**Wheel material**	VAS R7					
General description of test	15000 cycles dry (air-cooled)									
Measurement	**Initial**	**1. (dry)**								
Rail cycles	0	+15011								
Wheel cycles	0	+15166								
Rail diameter (mm)	47.00	46.99								
Wheel diameter (mm)	46.99	46.94								
Rail mass (g)	180.7681	180.7348								
Wheel mass (g)	180.8324	180.7228								
A/C Parameter	**11.4**		**11.5**		**22.4**		**22.5**			
dry	2800		3200		15.00		15.00			
E	212GPa	**Pressure**	1500MPa		**Slip**	-1%				
υ	0.3	**Force**	7.14kN		**Lub. feed**	-				
Eddy program	-	**Stand-off**	-		**Calibration disc**	-				

Figure A.18 Rail disc after testing.

1.5.4 20000 Wet

12700 cycles: Wheel disc looks polished; rail disc looks dark.

Following the test, the wheel disc has polished patches.

Twin-disc testing parameters							
Test name	INNOT-19		**Test date**	3rd August 2009			
Rail (top) id.	INR40		**Wheel (bottom) id.**	INW23			
Rail (base) material	VA 400 Grade		**Wheel material**	VAS R7			
General description of test	20000 cycles wet						
Measurement	**Initial**	**1. (dry)**					
Rail cycles	0	+20012					
Wheel cycles	0	+20222					
Rail diameter (mm)	47.01	46.99					
Wheel diameter (mm)	46.99	46.96					
Rail mass (g)	180.5551	180.5493					
Wheel mass (g)	180.8415	180.7974					

A/C Parameter	**11.4**	**11.5**	**22.4**	**22.5**
wet	2700	3200	20.00	20.00

E	212GPa	**Pressure**	1500MPa	**Slip**	-1%		
υ	0.3	**Force**	7.14kN	**Lub. feed**	-		
Eddy program	-	**Stand-off**	-	**Calibration disc**	-		

1.5.5 15000 Dry (R8T Wheel)

Rail disc appeared to be highly polished between 800 and 5500 cycles. As with other R8T tests, thin silvery flakes of steel (up to 1mm across) were blown out from the contact (starting at 1700).

Twin-disc testing parameters						
Test name	INNOT-26		**Test date**	11^{th} August 2009		
Rail (top) id.	INR41		**Wheel (bottom) id.**	WB45		
Rail (base) material	VA 400 Grade		**Wheel material**	R8T		
General description of test	15000 cycles dry (air-cooled)					
Measurement	**Initial**	**1. (dry)**				
Rail cycles	0	+15012				
Wheel cycles	0	+15163				
Rail diameter (mm)	46.95	46.94				
Wheel diameter (mm)	46.95	46.87				
Rail mass (g)	180.5263	180.5021				
Wheel mass (g)	181.3085	181.1812				

A/C Parameter	**11.4**	**11.5**	**22.4**	**22.5**
dry	2800	3200	15.00	15.00

E	212GPa	**Pressure**	1500MPa	**Slip**	-1%		
υ	0.3	**Force**	7.13kN	**Lub. feed**	-		
Eddy program	-	**Stand-off**	-	**Calibration disc**	-		

1.6 Summary

Traction curves for the first 5000 cycles dry, averaged over all three tests (5000 dry, 15000 dry, and the first 5000 cycles of the dry-wet test) with R7 wheel discs, are shown in Figure A.19(a); traction curves for dry contact with the R8T wheel discs are shown in Figure A.19(b). Traction curves for the 5000 cycles wet are shown in Figure A.20 below; wet tests following dry contact are shown in Figure A.20(a), and tests wet from the start are shown in Figure A.20(b). Wear rates are summarized in Table A.2 and Table A.3.

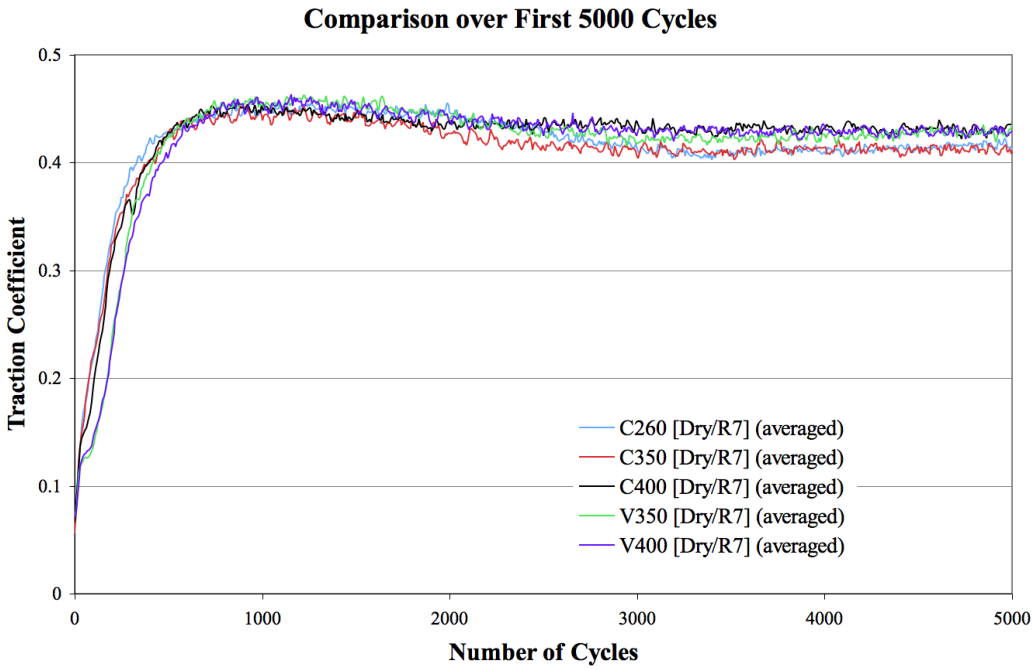

(a)

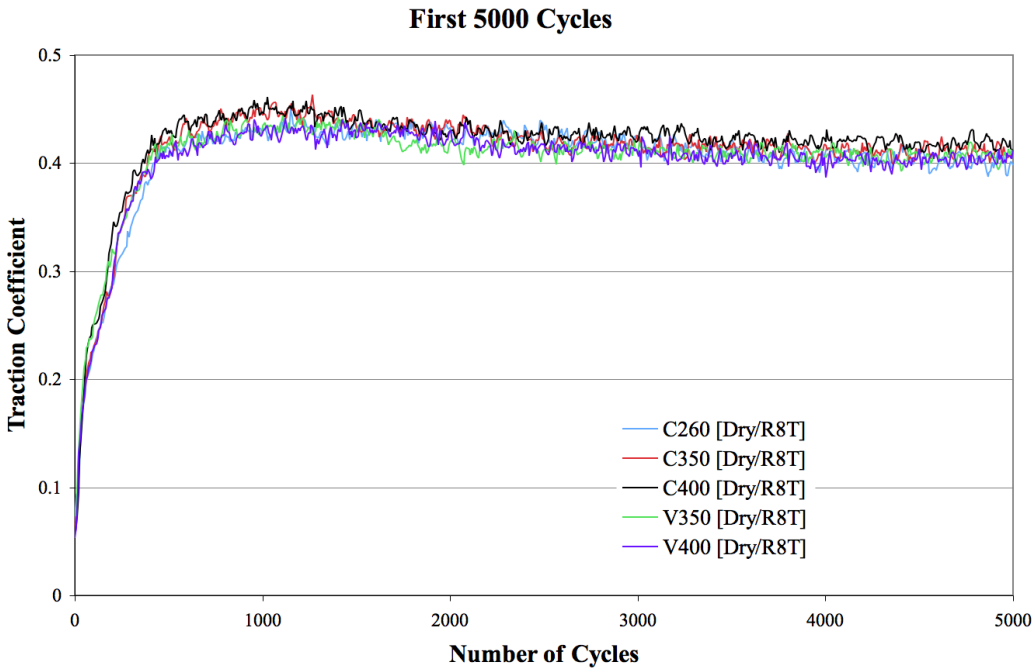

(b)

Figure A.19 Traction curves for all five grades of rail steel tested for first 5000 cycles dry contact: (a) averaged over all three tests (5000 dry, 15000 dry, and the first 5000 cycles of the dry-wet test) with R7 wheel discs; (b) tests with the R8T wheel discs.

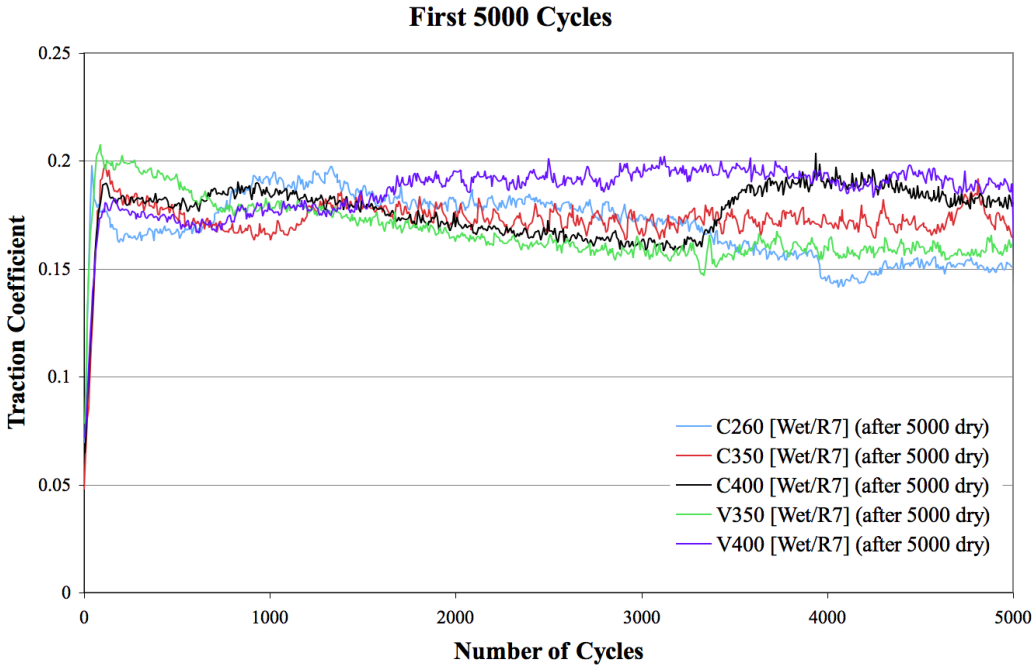

(a)

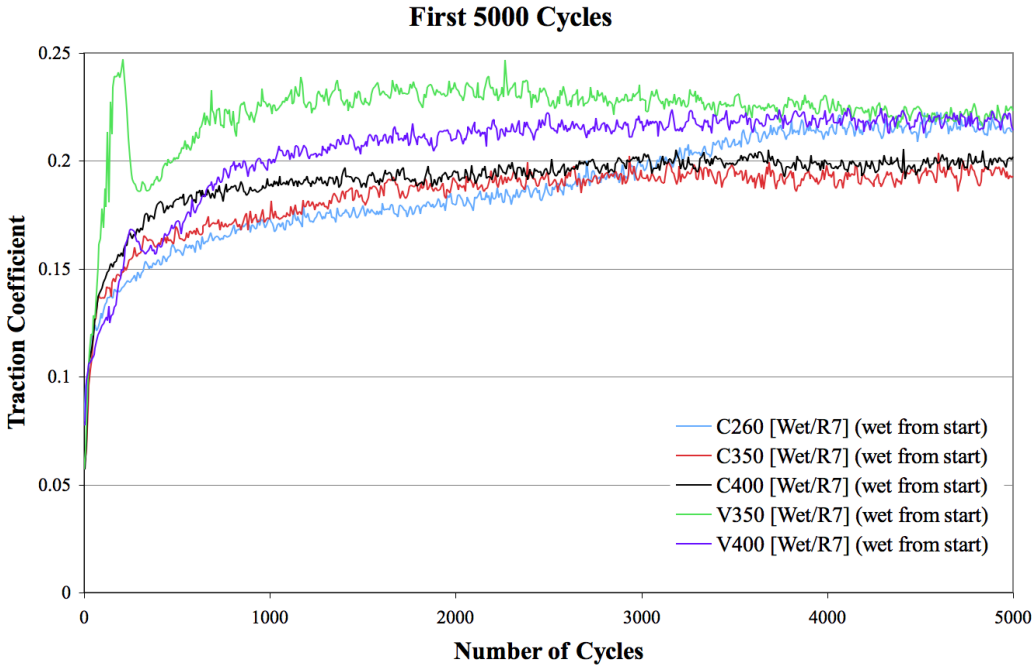

(b)

Figure A.20 First 5000 cycles for wet contact: (a) 5000 cycles wet following 5000 cycles dry in dry-wet tests; (b) first 5000 cycles of 20000 cycles wet test.

Table A.2. Summary of rail disc wear rates in InnoTrack SUROS twin-disc tests.

Rail Disc

Steel Density	7.95	[g/cm3]
Track Width	10	[mm]

Test	Description	Material	Lubrication	[mm] Diameter	#Cycles	[g] Original Mass	[g] Final Mass	[g] Mass Loss	[µg/cycle] Wear Rate	[nm/cycle] Wear Rate
INNOT-07	C260-5k	CORUS 260	Dry	46.98	5014	180.5581	180.5271	0.031	6.183	0.527
INNOT-08 a	C260-10kDry	CORUS 260	Dry	46.97	5014	180.7453	180.7166	0.0287	5.724	0.488
INNOT-08 b	C260-10kWet	CORUS 260	Wet	46.97	5010	180.7166	180.4612	0.2554	50.978	4.346
INNOT-09	C260-15k	CORUS 260	Dry	46.98	15015	181.2587	181.0745	0.1842	12.268	1.046
INNOT-17	C260-20k	CORUS 260	Wet	46.99	20014	180.8887	180.869	0.0197	0.984	0.084
INNOT-22	C260-15kR8T	CORUS 260	Dry	46.95	15011	181.0554	181.0124	0.043	2.865	0.244
INNOT-13	C350-5k	CORUS 350	Dry	46.98	5000	180.9874	180.9744	0.013	2.600	0.222
INNOT-14	C350-10kDry	CORUS 350	Dry	46.98	5016	180.9493	180.9366	0.0127	2.532	0.216
INNOT-41	C350-10kWet	CORUS 350	Wet	46.98	5013	180.9366	180.9215	0.0151	3.012	0.257
INNOT-51	C350-15k	CORUS 350	Dry	46.98	15015	181.0456	181.0062	0.0394	2.624	0.224
INNOT-16	C350-20k	CORUS 350	Wet	46.96	20000	180.7043	180.6978	0.0065	0.325	0.028
INNOT-23	C350-15kR8T	CORUS 350	Dry	46.96	15013	181.0057	180.971	0.0347	2.311	0.197
INNOT-01	C400-5k	CORUS 400	Dry	46.97	5013	180.3178	180.3054	0.0124	2.474	0.211
INNOT-02 a	C400-10kDry	CORUS 400	Dry	46.99	5013	180.4118	180.3979	0.0139	2.773	0.236
INNOT-02 b	C400-10kWet	CORUS 400	Wet	46.99	5016	180.3979	180.3506	0.0473	9.430	0.803
INNOT-03	C400-15k	CORUS 400	Dry	47	15014	180.1083	180.0715	0.0368	2.451	0.209
INNOT-18	C400-20k	CORUS 400	Wet	46.99	20013	180.4047	180.3932	0.0115	0.575	0.049
INNOT-24	C400-15kR8T	CORUS 400	Dry	46.97	15012	180.7436	180.7265	0.0171	1.139	0.097
INNOT-04	V350-5k	VA 350	Dry	46.98	5011	180.6997	180.6741	0.0256	5.109	0.435
INNOT-05 a	V350-10kDry	VA 350	Dry	46.99	5014	180.4083	180.392	0.0163	3.251	0.277
INNOT-05 b	V350-10kWet	VA 350	Wet	46.98	5013	180.392	180.3861	0.0059	1.177	0.100
INNOT-06	V350-15k	VA 350	Dry	47	15014	180.3917	180.315	0.0767	5.109	0.435
INNOT-21	V350-20k	VA 350	Wet	46.99	20013	180.6961	180.6872	0.0089	0.445	0.038
INNOT-25	V350-15kR8T	VA 350	Dry	46.96	15014	180.6293	180.6072	0.0221	1.472	0.126
INNOT-10	V400-5k	VA 400	Dry	46.99	5011	180.4915	180.4818	0.0097	1.936	0.165
INNOT-12a	V400-10kDry	VA 400	Dry	46.99	5013	180.5027	180.4879	0.0148	2.952	0.252
INNOT-12b	V400-10kWet	VA 400	Wet	47	5012	180.4879	180.4752	0.0127	2.534	0.216
INNOT-11	V400-15k	VA 400	Dry	47	15011	180.7681	180.7348	0.0333	2.218	0.189
INNOT-19	V400-20k	VA 400	Wet	47.01	20012	180.5551	180.5493	0.0058	0.290	0.025
INNOT-26	V400-15kR8T	VA 400	Dry	46.95	15012	180.5263	180.5021	0.0242	1.612	0.137

Table A.3. Summary of wheel disc wear rates in InnoTrack SUROS twin-disc tests.

Wheel Disc		Steel Density	7.95	[g/cm3]
		Track Width	10	[mm]

Test	**Description**	**Material**	**Lubrication**	[mm] **Diameter**	**#Cycles**	[g] **Original Mass**	[g] **Final Mass**	[g] **Mass Loss**	[µg/cycle] **Wear Rate**	[nm/cycle] **Wear Rate**
INNOT-07	C260-5k	VAS R7	Dry	46.99	5063	181.1096	181.0855	0.0241	4.760	0.406
INNOT-08 a	C260-10kDry	VAS R7	Dry	46.99	5062	180.9138	180.9016	0.0122	2.410	0.205
INNOT-08 b	C260-10kWet	VAS R7	Wet	46.98	5060	180.9016	180.8819	0.0197	3.893	0.332
INNOT-09	C260-15k	VAS R7	Dry	46.99	15163	181.0548	180.9018	0.153	10.090	0.860
INNOT-17	C260-20k	VAS R7	Wet	47	20210	180.9091	180.8786	0.0305	1.509	0.129
INNOT-22	C260-15kR8T	R8T	Dry	46.96	15159	181.1844	181.0489	0.1355	8.939	0.762
INNOT-13	C350-5k	VAS R7	Dry	46.99	5050	180.9149	180.8921	0.0228	4.515	0.385
INNOT-14	C350-10kDry	VAS R7	Dry	47	5065	181.02	180.9967	0.0233	4.600	0.392
INNOT-41	C350-10kWet	VAS R7	Wet	46.98	5061	180.9967	180.9901	0.0066	1.304	0.111
INNOT-51	C350-15k	VAS R7	Dry	46.99	15163	180.9471	180.8481	0.099	6.529	0.556
INNOT-16	C350-20k	VAS R7	Wet	46.99	20200	181.0133	180.9773	0.036	1.782	0.152
INNOT-23	C350-15kR8T	R8T	Dry	46.97	15161	181.5728	181.4332	0.1396	9.208	0.785
INNOT-01	C400-5k	VAS R7	Dry	46.96	5065	181.0489	181.0230	0.0259	5.114	0.436
INNOT-02 a	C400-10kDry	VAS R7	Dry	46.98	5066	180.8339	180.8051	0.0288	5.685	0.485
INNOT-02 b	C400-10kWet	VAS R7	Wet	46.96	5069	180.8051	180.8010	0.0041	0.809	0.069
INNOT-03	C400-15k	VAS R7	Dry	46.99	15169	180.9945	180.8929	0.1016	6.698	0.571
INNOT-18	C400-20k	VAS R7	Wet	46.99	20214	180.9726	180.9294	0.0432	2.137	0.182
INNOT-24	C400-15kR8T	R8T	Dry	46.95	15170	181.1207	180.9740	0.1467	9.670	0.825
INNOT-04	V350-5k	VAS R7	Dry	47.01	5059	180.224	180.1879	0.0361	7.136	0.608
INNOT-05 a	V350-10kDry	VAS R7	Dry	47	5064	181.3028	181.279	0.0238	4.700	0.400
INNOT-05 b	V350-10kWet	VAS R7	Wet	46.96	5066	181.279	181.2718	0.0072	1.421	0.121
INNOT-06	V350-15k	VAS R7	Dry	47	15165	180.9953	180.8197	0.1756	11.579	0.986
INNOT-21	V350-20k	VAS R7	Wet	46.99	20215	180.7882	180.7418	0.0464	2.295	0.196
INNOT-25	V350-15kR8T	R8T	Dry	46.97	15162	181.293	181.1565	0.1365	9.003	0.767
INNOT-10	V400-5k	VAS R7	Dry	46.99	5062	180.9727	180.9467	0.026	5.136	0.438
INNOT-12a	V400-10kDry	VAS R7	Dry	47	5062	180.9348	180.9063	0.0285	5.630	0.480
INNOT-12b	V400-10kWet	VAS R7	Wet	46.98	5061	180.9063	180.9034	0.0029	0.573	0.049
INNOT-11	V400-15k	VAS R7	Dry	46.99	15166	180.8324	180.7228	0.1096	7.227	0.616
INNOT-19	V400-20k	VAS R7	Wet	46.99	20222	180.8415	180.7974	0.0441	2.181	0.186
INNOT-26	V400-15kR8T	R8T	Dry	46.95	15163	181.3085	181.1812	0.1273	8.395	0.716

2 Surface images

2.1 Corus 260 tests - images

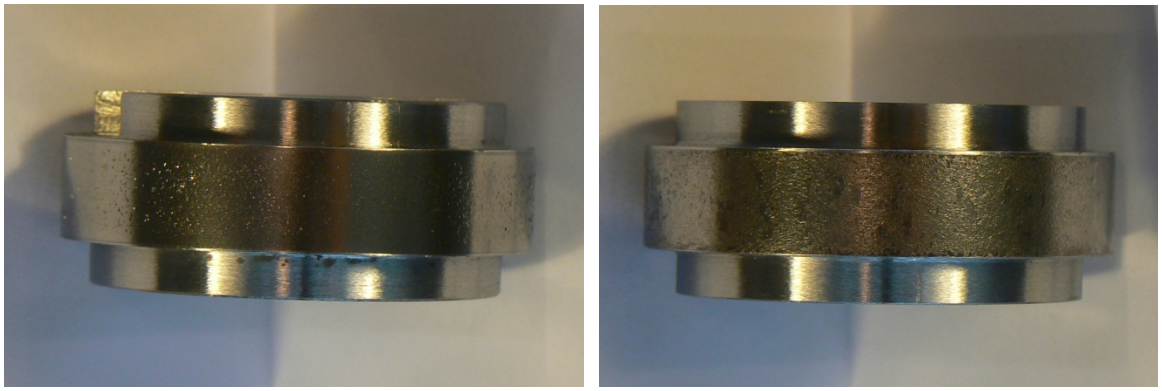

Figure A.21 Test INNOT-07. 5000 dry. Left: rail C260 – INR 24. Right: wheel – INW14

Figure A.22 Test INNOT-08. 5000dry + 5000wet. Left: rail C260 – INR23. Right: wheel – INW13

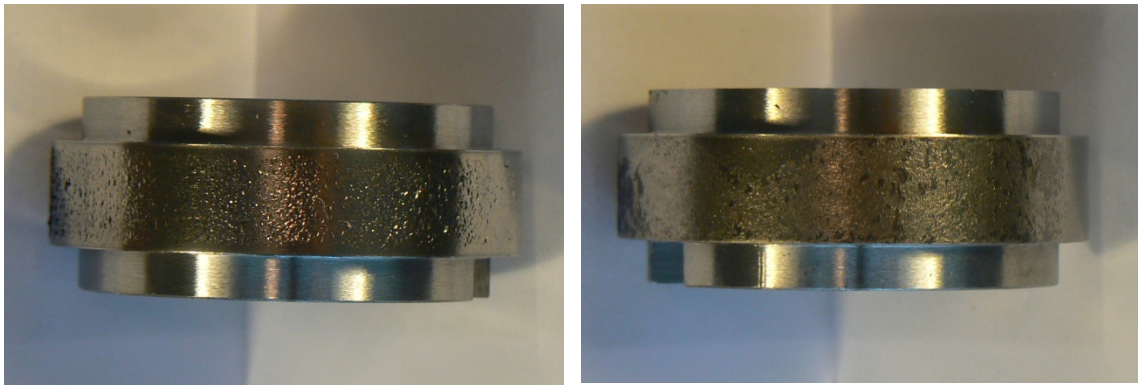

Figure A.23 Test INNOT-09. 15000 dry. Left: rail C260 – INR22. Right: wheel – INW9

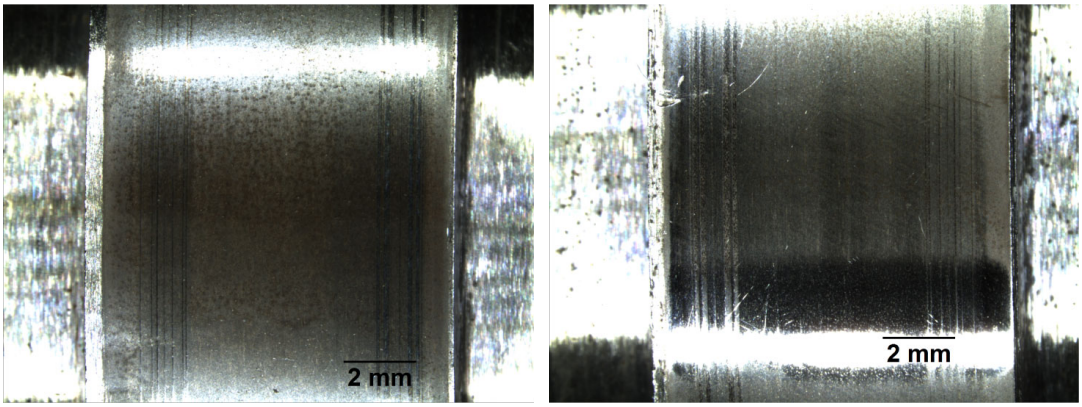

Figure A.24 Test INNOT-17. 20000wet. Left: rail C260 – INR26. Right: wheel – INW10

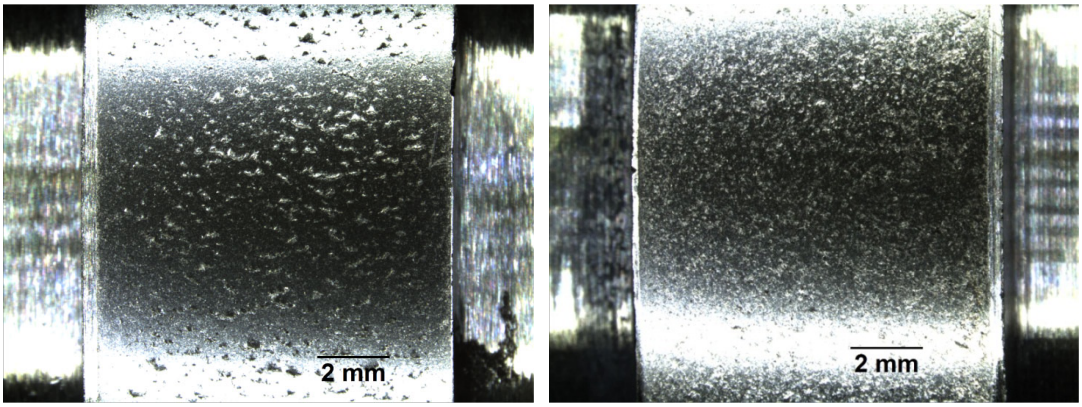

Figure A.25 Test INNOT-22. 15000 dry. Left: rail C260 – INR 25. Right: wheel –WB35(R8T)

2.2 Corus 350 tests – images

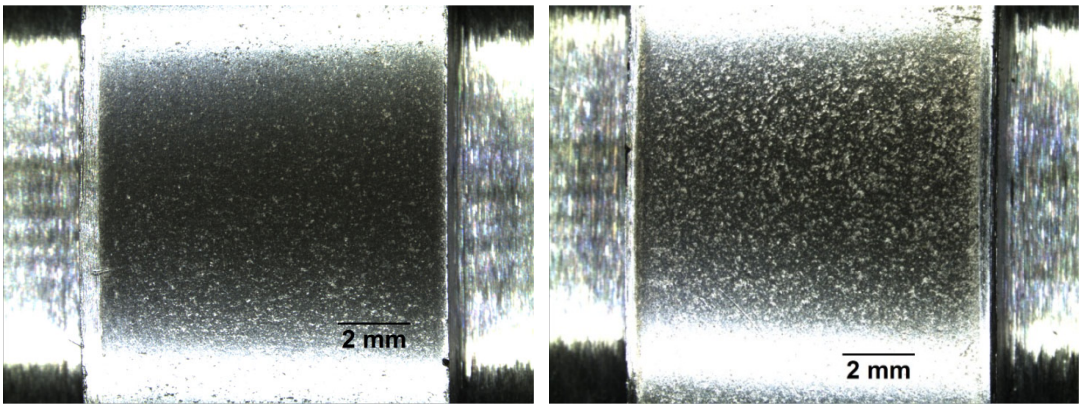

Figure A.26 Test INNOT-13. 5000 dry. Left: rail C350 – INR30. Right: wheel – INW21

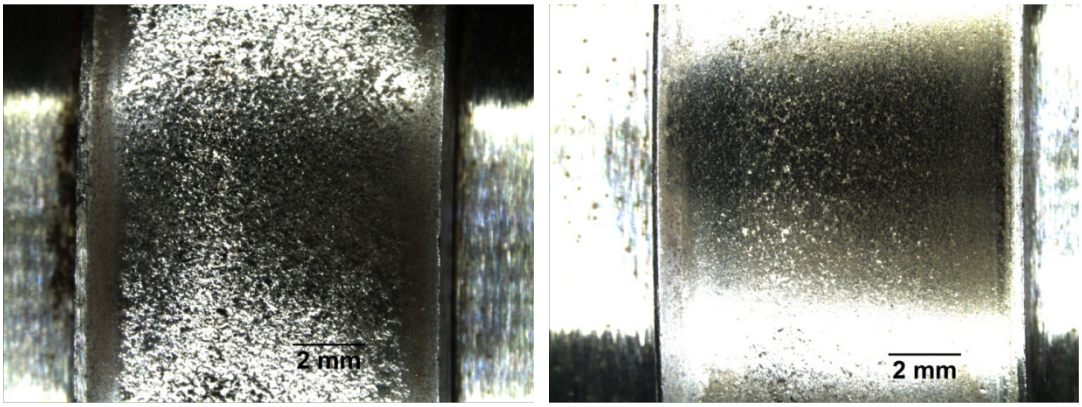

Figure A.27 Test INNOT-14/41. 5000dry+5000wet. Left: rail C350 – INR31. Right: wheel – INW16

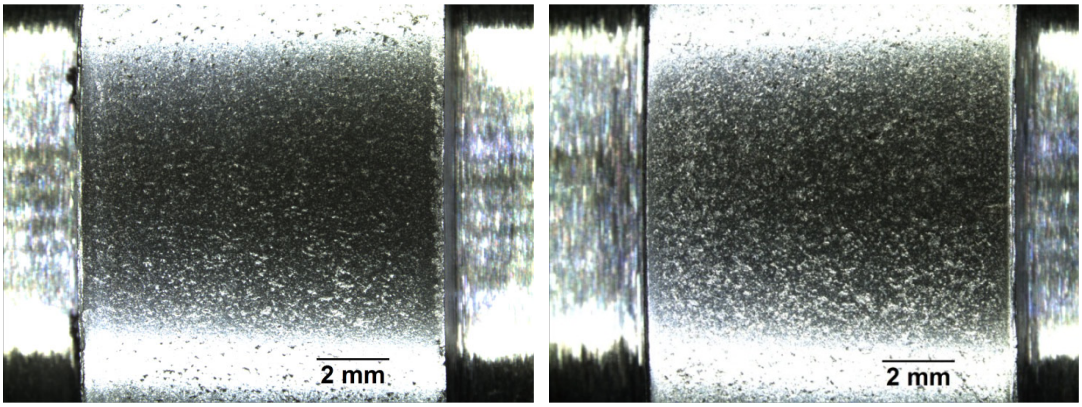

Figure A.28 Test INNOT-51. 15000 dry. Left: rail C350 – INR34. Right: wheel – INW20

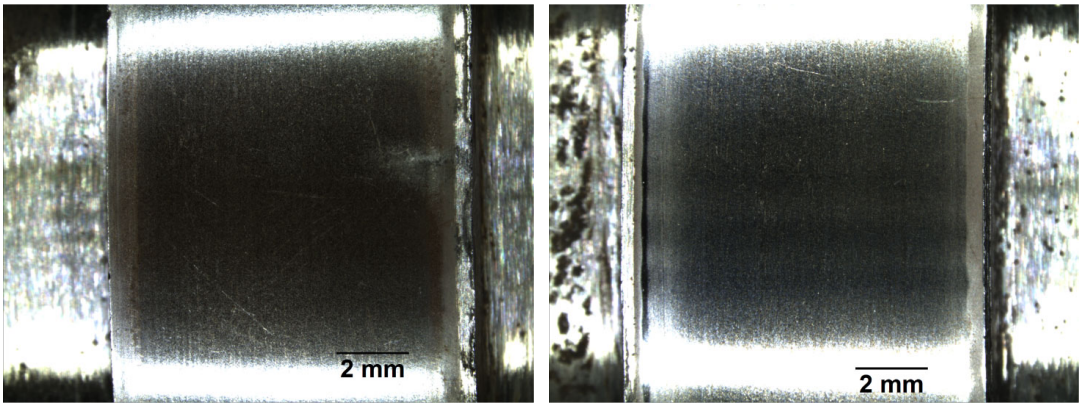

Figure A.29 Test INNOT-16. 20000 wet. Left: rail C350 – INR36. Right: wheel – INW17

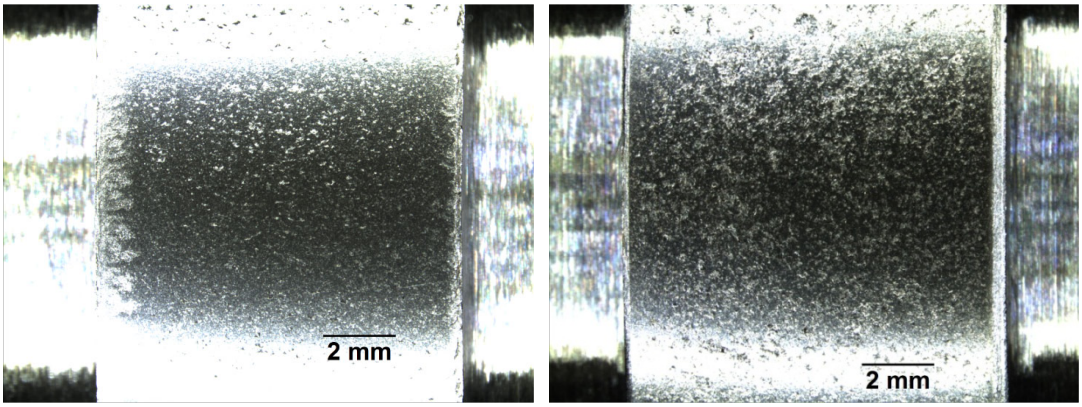

Figure A.30 Test INNOT-23. 15000 dry. Left: rail C350 – INR33. Right: wheel – WB47(R8T)

2.3 Corus 400 tests – images

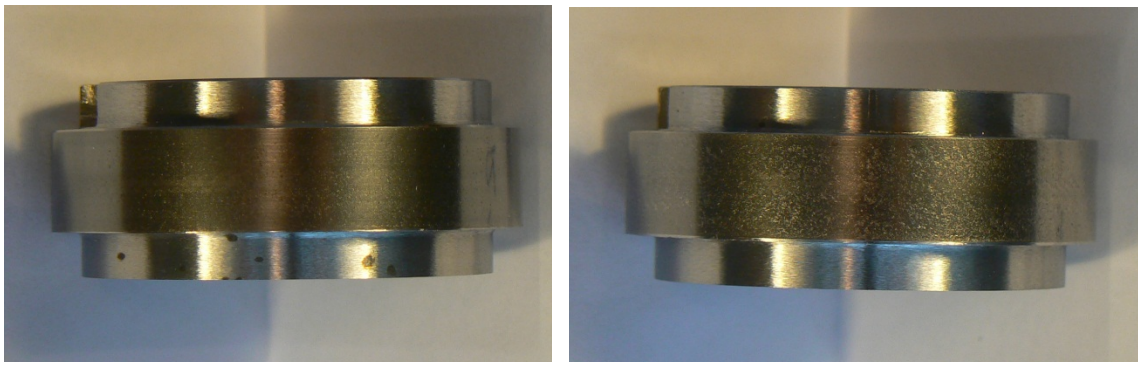

Figure A.31 Test INNOT-01. 5000 dry. Left: rail C400 – INR1. Right: wheel – INW1

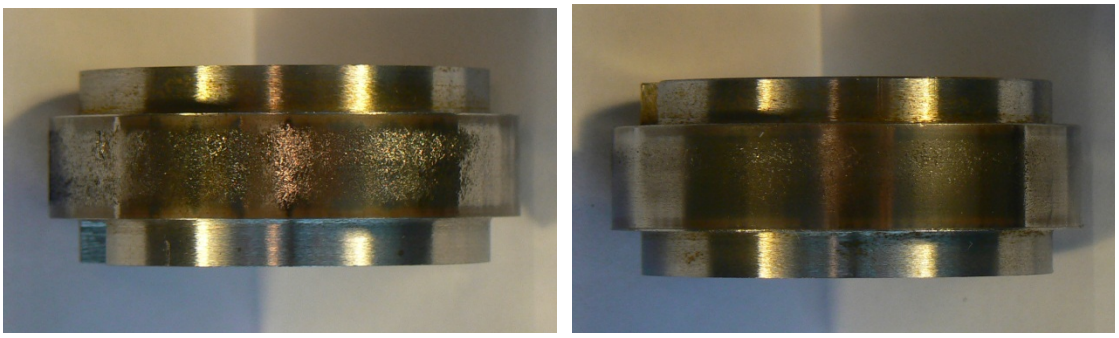

Figure A.32 Test INNOT-02. 5000dry+5000wet. Left: rail C400 – INR2. Right: wheel – INW2

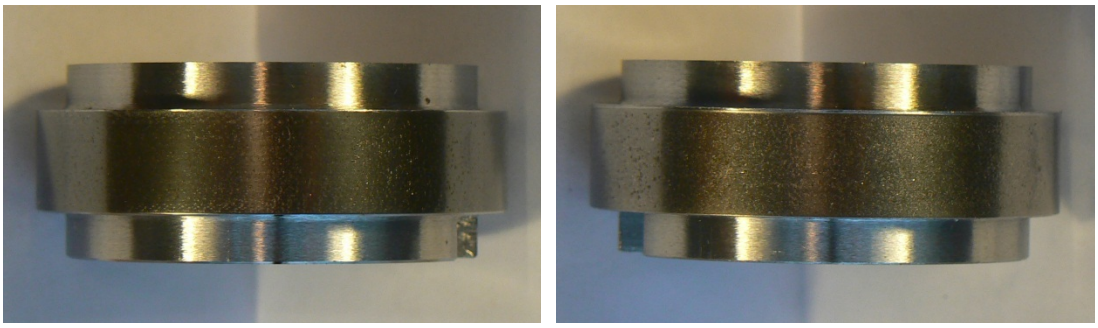

Figure A.33 Test INNOT-03. 15000 dry. Left: rail C400 – INR3. Right: wheel – INW3

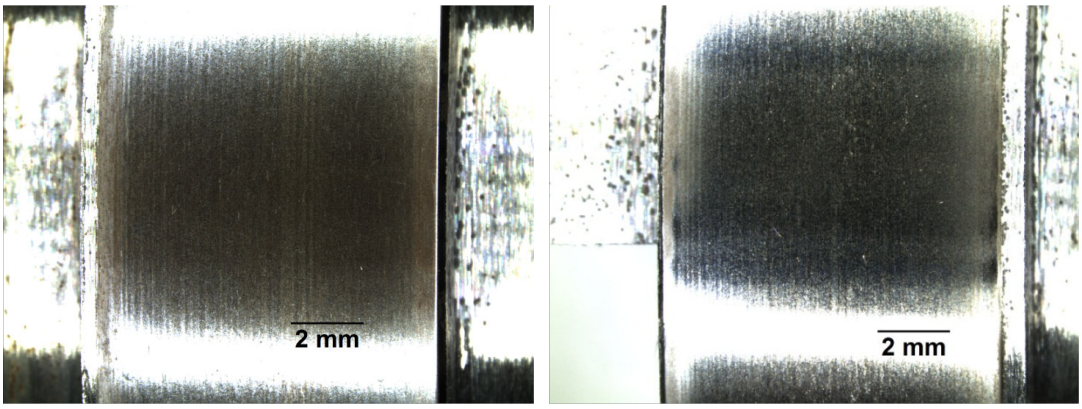

Figure A.34 Test INNOT-18. 20000 wet. Left: rail C400 – INR7. Right: wheel – INW15

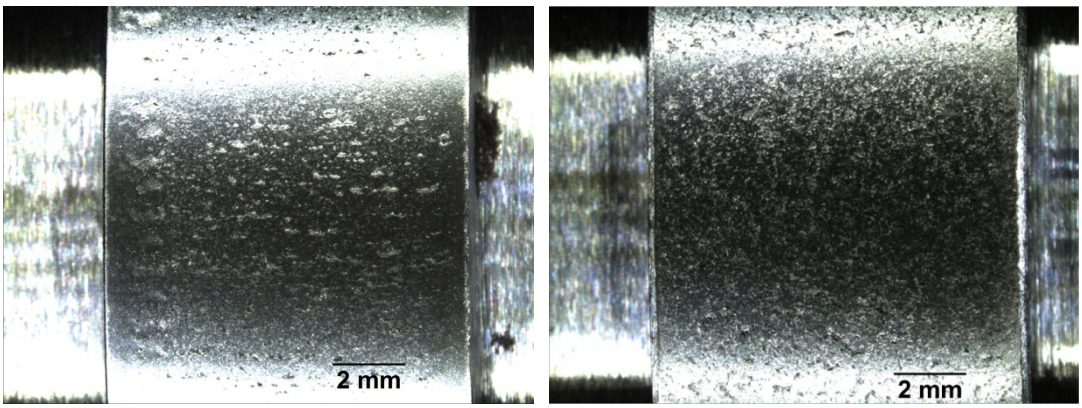

Figure A.35 Test INNOT-24. 15000 dry. Left: rail C400 – INR4. Right: wheel – WB46(R8T)

2.4 VA350 tests – images

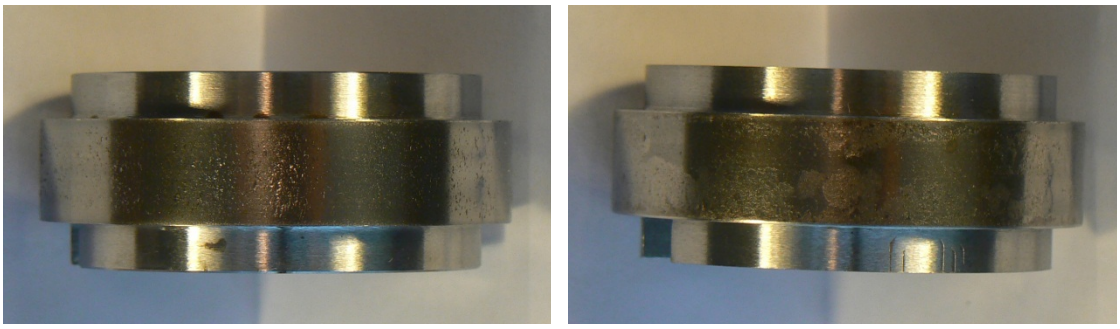

Figure A.36 Test INNOT-04. 5000 dry. Left: rail V350 – INR10. Right: wheel – INW4

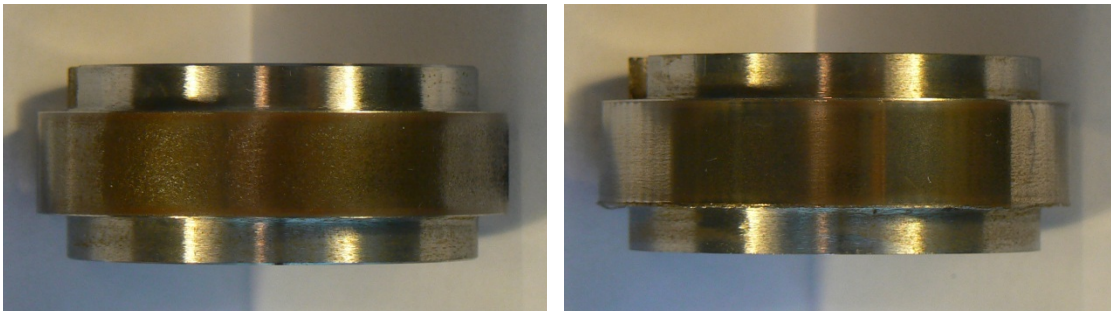

Figure A.37 Test INNOT-05. 5000 dry+5000wet. Left: rail V350 – INR11. Right: wheel – INW5

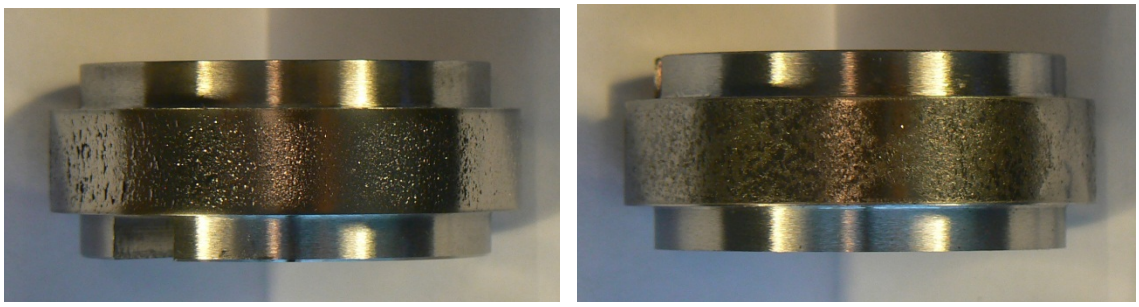

Figure A.38 Test INNOT-06. 15000 dry. Left: rail V350 – INR12. Right: wheel – INW6

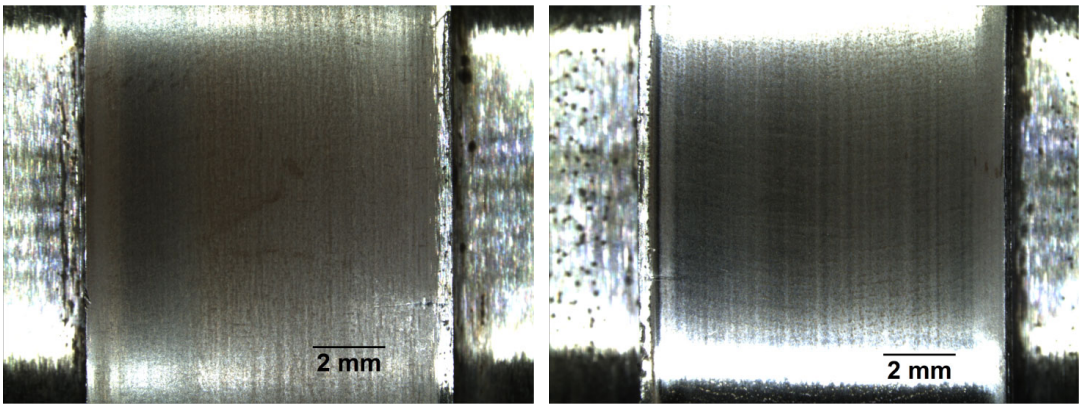

Figure A.39 Test INNOT-21. 20000wet. Left: rail V350 – INR16. Right: wheel – INW24

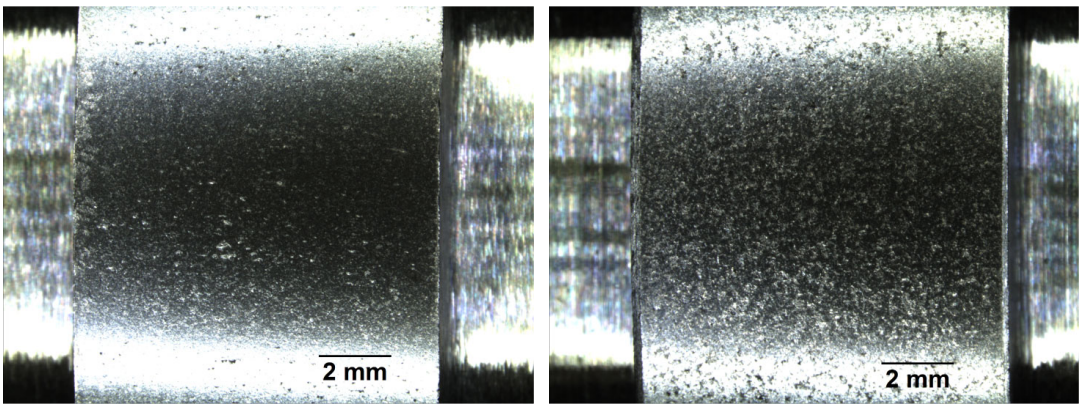

Figure A.40 Test INNOT-25. 15000 dry. Left: rail V350 – INR14. Right: wheel – WB37(R8T)

2.5 VA400 tests – images

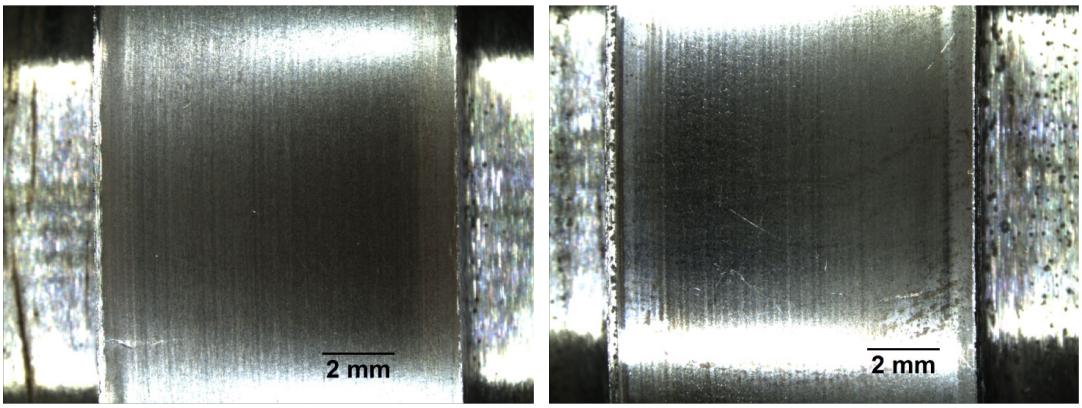

Figure A.41 Test INNOT-19. 20000wet. Left: rail V400 – INR40. Right: wheel – INW23

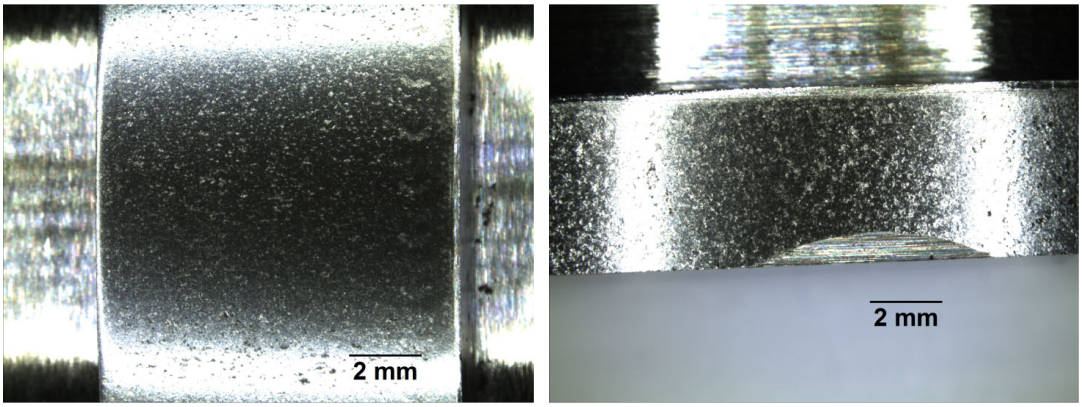

Figure A.42 Test INNOT-26. 15000 dry. Left: rail V400 – INR41. Right: wheel – WB45(R8T)

3 Roughness results

Transverse surface roughness measurements – value *Ra* in µm, 4 measurements before testing on new discs (See Table A.4) and 4 after testing for each disc (See Table A.5).

Table A.4. Transverse surface roughness measurements – value Ra in µm. New discs.

New material	Disc label	1	2	3	4	Average
wheel	INW 10	0.762	0.876	0.888	0.771	0.824
Corus 400 - Rail	INR 5	0.771	0.796	0.774	0.901	0.811
VA 350 – Rail	INR 13	0.799	0.844	0.789	0.837	0.817
Corus 260 - Rail	INR 20	0.72	0.869	0.877	0.915	0.845

Table A.5. Transverse surface roughness measurements – value Ra in µm. Discs after testing. Test conditions: pressure 1500MPa, slip -1%.

Disc label	1	2	3	4	5	Average	Comment
INR 1	0.359	0.425	0.293	0.252		0.332	
INR 10	0.363	0.399	0.395	0.43		0.397	
INR 11	0.67	0.445	0.687	0.404		0.552	
INR 12	0.727	0.94	2.12	0.835		1.156	
INR 14	0.361	0.807	0.406	0.395	1.11	0.616	5 is repeated 2
INR 15	0.432	0.468	0.41	0.375		0.421	
INR 16	0.418	0.495	0.43	0.412	0.44	0.439	
INR 2	0.987	1.46	0.939	0.905		1.073	ok
INR 22	1.3	2.26	1.47	0.908		1.485	
INR 23	2.52	2.16	6.78	2.38	5	3.768	
INR 24	0.268	0.37	0.428	0.346		0.353	
INR 25	1.33	1.21	1.04	0.637		1.054	
INR 26	0.157	0.176	0.174	0.178		0.171	
INR 3	0.305	0.285	0.267	0.236		0.273	
INR 30	0.17	0.436	0.266	0.222		0.274	spot 2 is more damaged
INR 31	0.939	1.18	1.79	1.63	3.88	1.884	5 over damaged spot
INR 32	0.372	0.334	0.301	0.276		0.321	
INR 33	0.491	0.24	0.664	0.349		0.436	unevenly rough, discarded 1 high measurement of 1.83
INR 34	0.535	0.365	0.567	1.27	0.768	0.701	repeated 4
INR 36	0.203	0.217	0.222	0.201		0.211	
INR 4	0.262	0.257	0.235	0.379		0.283	
INR 40	0.385	0.428	0.469	0.498	0.472	0.450	5 is 1 repeat
INR 41	0.443	0.252	0.337	0.331		0.341	
INR 7	0.299	0.391	0.289	0.328		0.327	
INW 1	0.683	0.731	0.708	0.628		0.688	
INW 10	0.153	0.19	0.321	0.128		0.198	
INW 12	0.282	0.302	0.383	0.318		0.321	slightly corroded
INW 13	0.431	0.758	0.491	0.579		0.565	
INW 14	0.979	1.15	0.838	0.335		0.826	ok
INW 15	0.352	0.331	0.372	0.363		0.355	spot 4 over polished surface

Disc label	1	2	3	4	5	Average	Comment
INW 16	0.427	0.405	0.279	0.286		0.349	
INW 17	0.206	0.187	0.238	0.175		0.202	
INW 19	0.549	0.618	0.45	0.368		0.496	
INW 2	0.509	0.668	0.829	0.845		0.713	no
INW 20	0.649	0.539	0.543	0.358		0.522	
INW 21	0.465	0.456	0.611	0.232		0.441	big difference between measurements
INW 22	0.361	0.343	0.336	0.361	0.383	0.357	1 spot is over polished part, 5 is spot 1 over unpolished part
INW 23	0.453	0.442	0.42	0.454		0.442	
INW 24	0.417	0.406	0.41	0.411		0.411	
INW 3	0.496	0.626	0.6	0.646		0.592	
INW 4	0.859	0.543	0.925	0.509		0.709	
INW 5	0.339	0.289	0.379	0.318		0.331	
INW 6	1.36	1.1	1.13	1.33		1.230	
INW 7	0.465	0.646	0.526	0.418		0.514	
INW 8	0.636	0.451	0.584	0.574		0.561	
INW 9	2.13	1.85	1.97	2.17		2.030	
VA400(1)	0.298	0.361	0.31	0.379		0.337	
VA400(2)	0.587	1.12	0.304	0.829	0.363	0.641	
VA400(3)	1.27	1.07	0.963	1.08		1.096	
WB35	0.774	0.551	0.488	0.371		0.546	
WB37	0.55	0.433	0.471	0.428		0.471	
WB45	0.581	0.588	0.477	0.807		0.613	4 is a little bit rougher
WB46	0.599	0.764	0.529	0.593		0.621	
WB47	0.692	0.483	0.821	0.615		0.653	

Bibliography:

Fletcher D.I. and Beynon J.H., Development of a machine for closely controlled rolling contact fatigue and wear testing, *Journal of Testing and Evaluation*, 2000, 267-275.

Appendix B: Metallurgical Results

Optical microscope images (etched)

List of figures:

Optical microscope images (unetched)

List of figures:

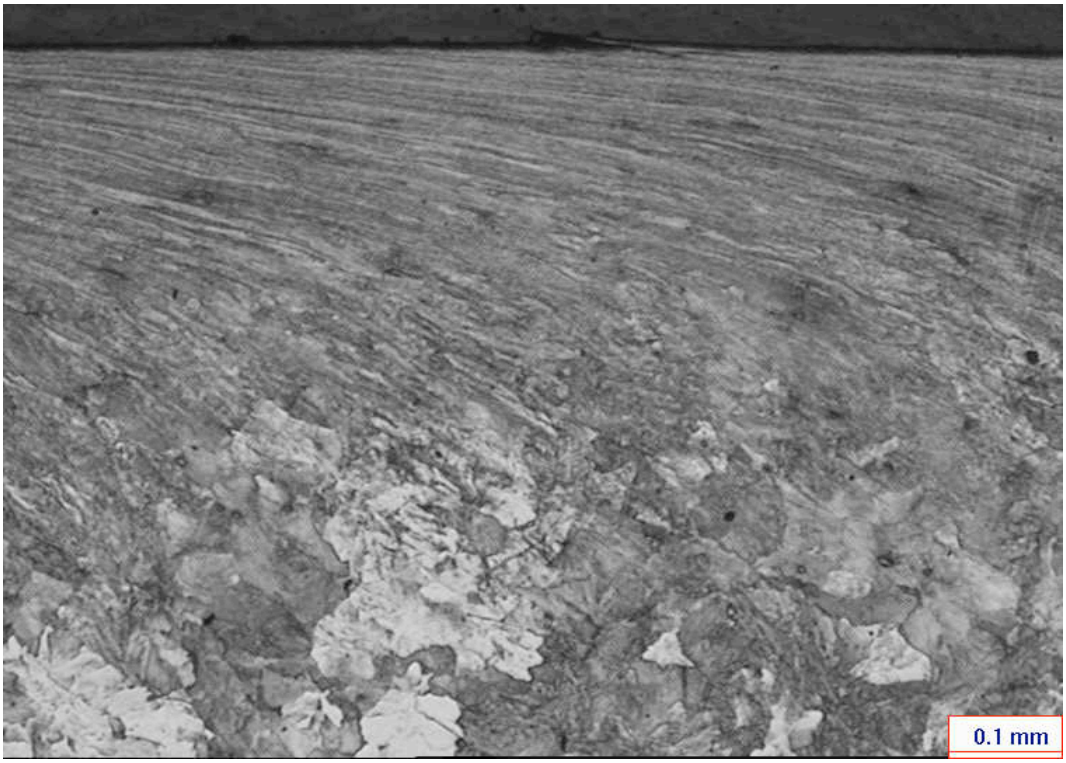

Figure B.1 Optical microscope image, P260, 5000 cycles dry.

Figure B.2 Optical microscope image, P260, 5000 cycles dry and 5000 cycles wet.

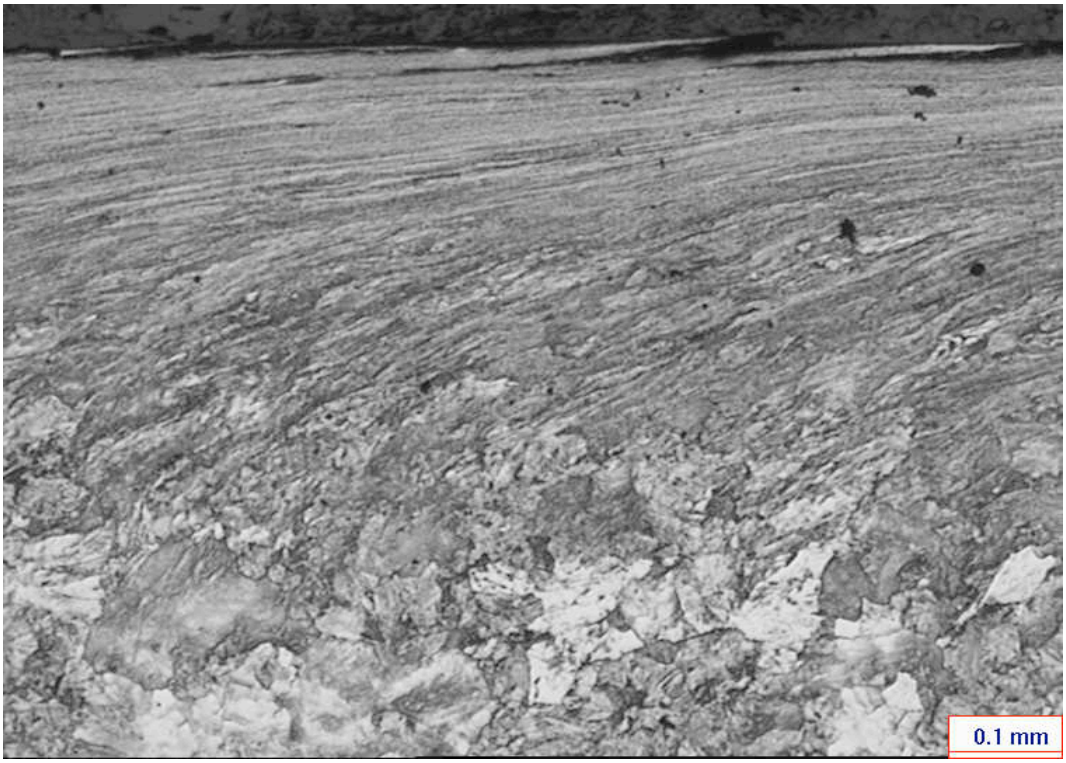

Figure B.3 Optical microscope image, P260, 15000 cycles dry.

Figure B.4 Optical microscope image, C400, 5000 cycles dry.

Figure B.5 Optical microscope image, C400, 5000 cycles dry and 5000 cycles wet.

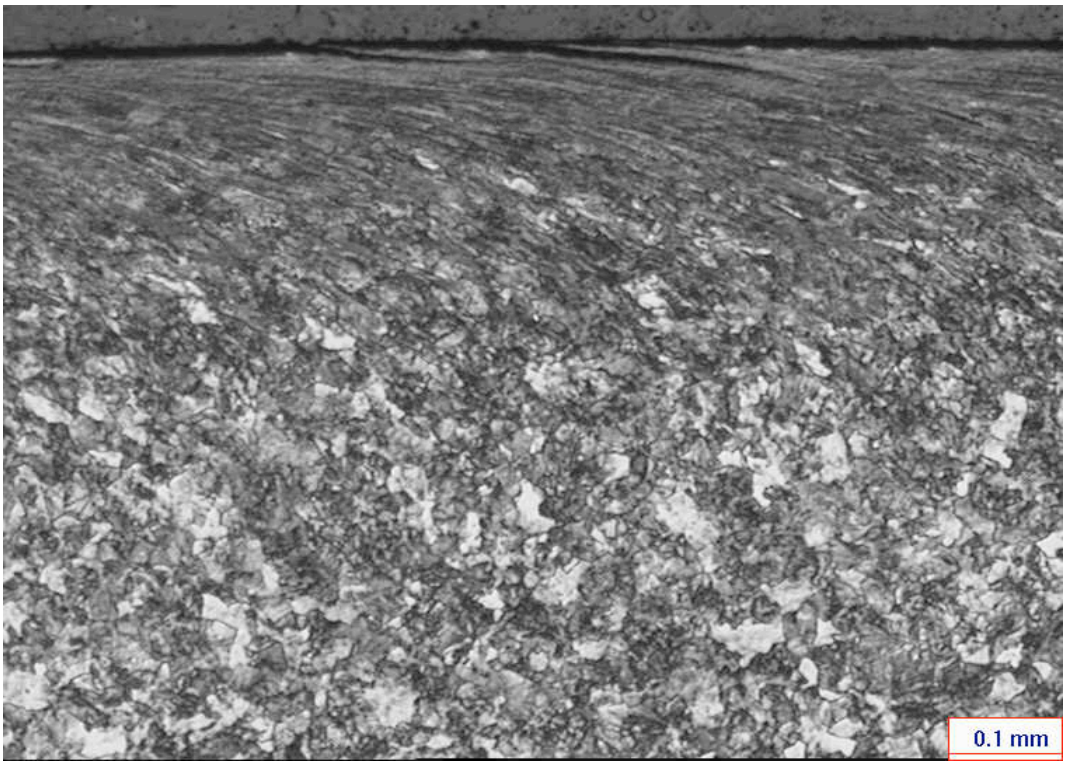

Figure B.6 Optical microscope image, C400, 15000 cycles dry.

Figure B.7 Optical microscope image, V350, 5000 cycles dry.

Figure B.8 Optical microscope image, V350, 5000 cycles dry and 5000 cycles wet.

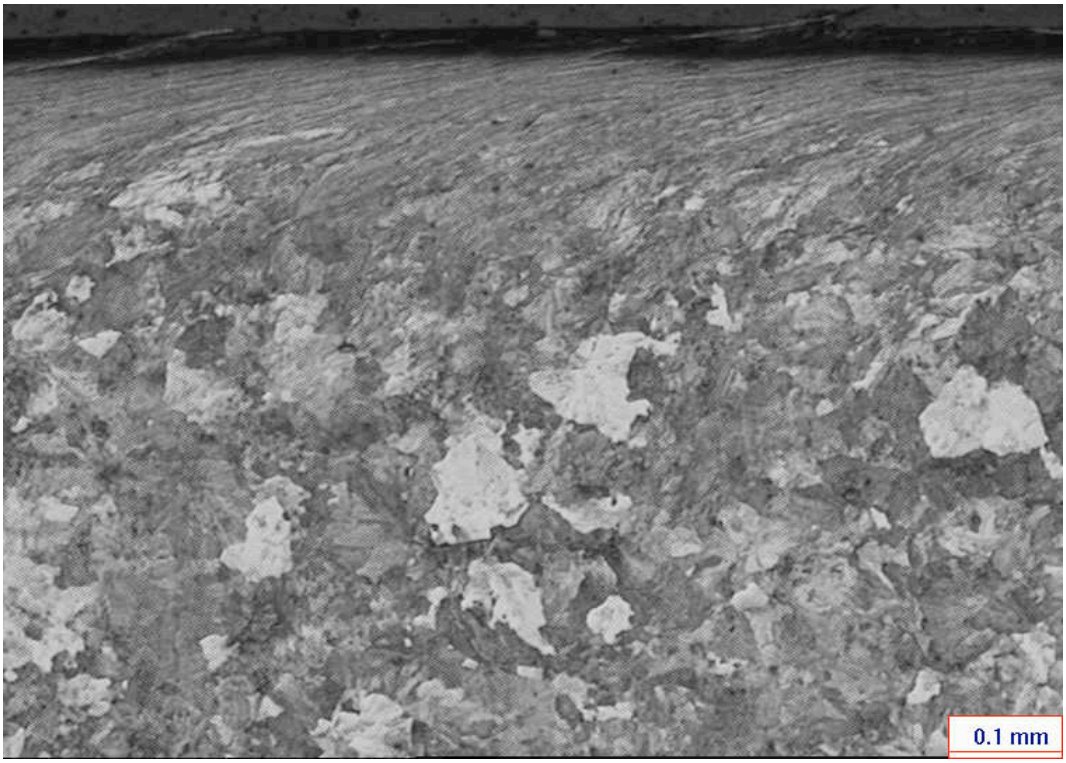

Figure B.9 Optical microscope image, V350, 15000 cycles dry.

Figure B.10 Optical microscope image, V400, 5000 cycles dry.

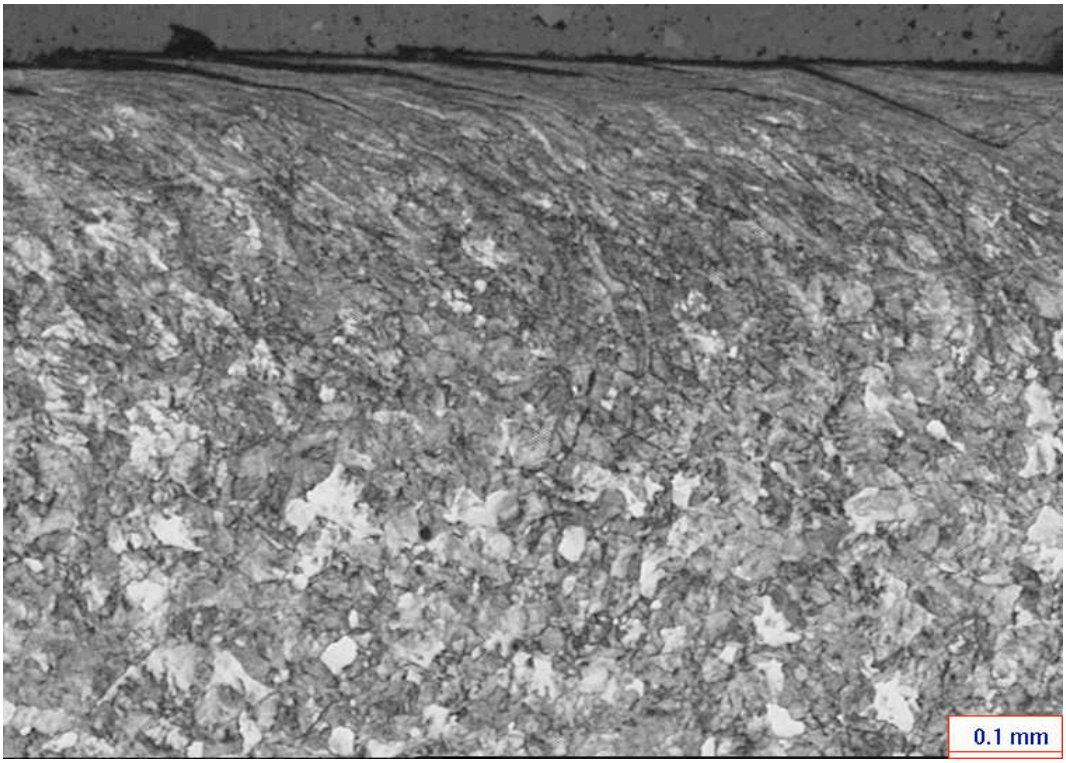

Figure B.11 Optical microscope image, V400, 5000 cycles dry and 5000 cycles wet.

Figure B.12 Optical microscope image, V400, 15000 cycles dry.

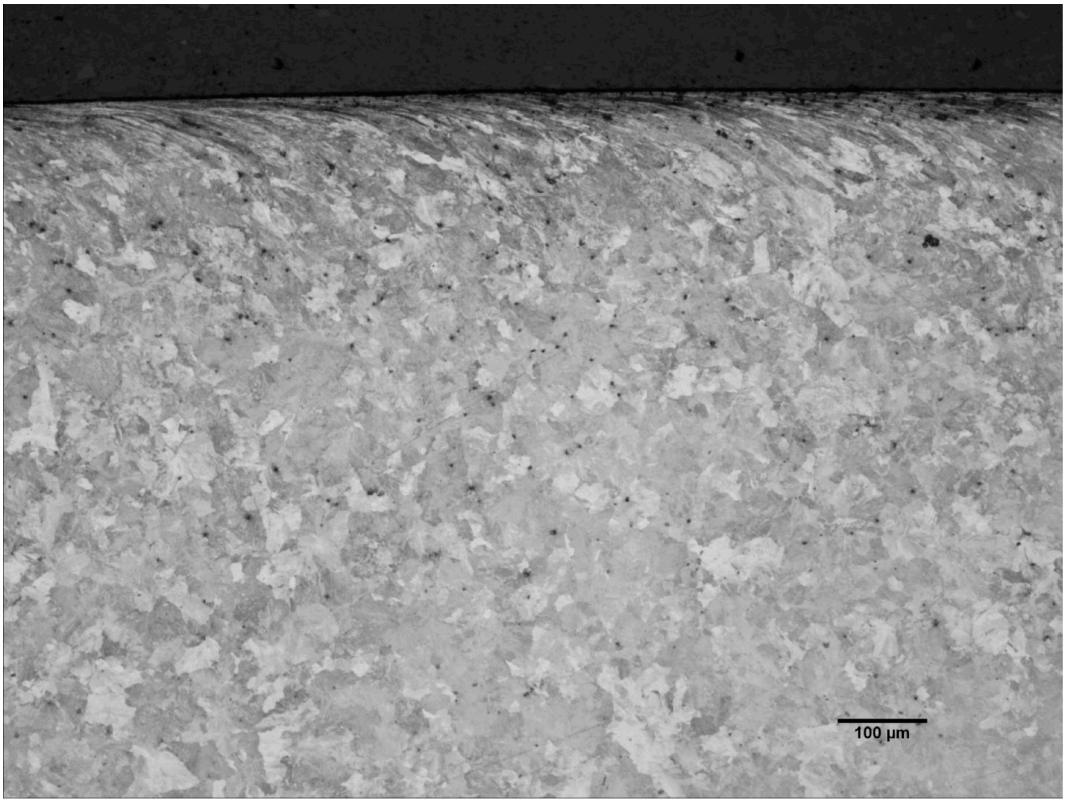

Figure B.13 Optical microscope image, C350, 5000 cycles dry

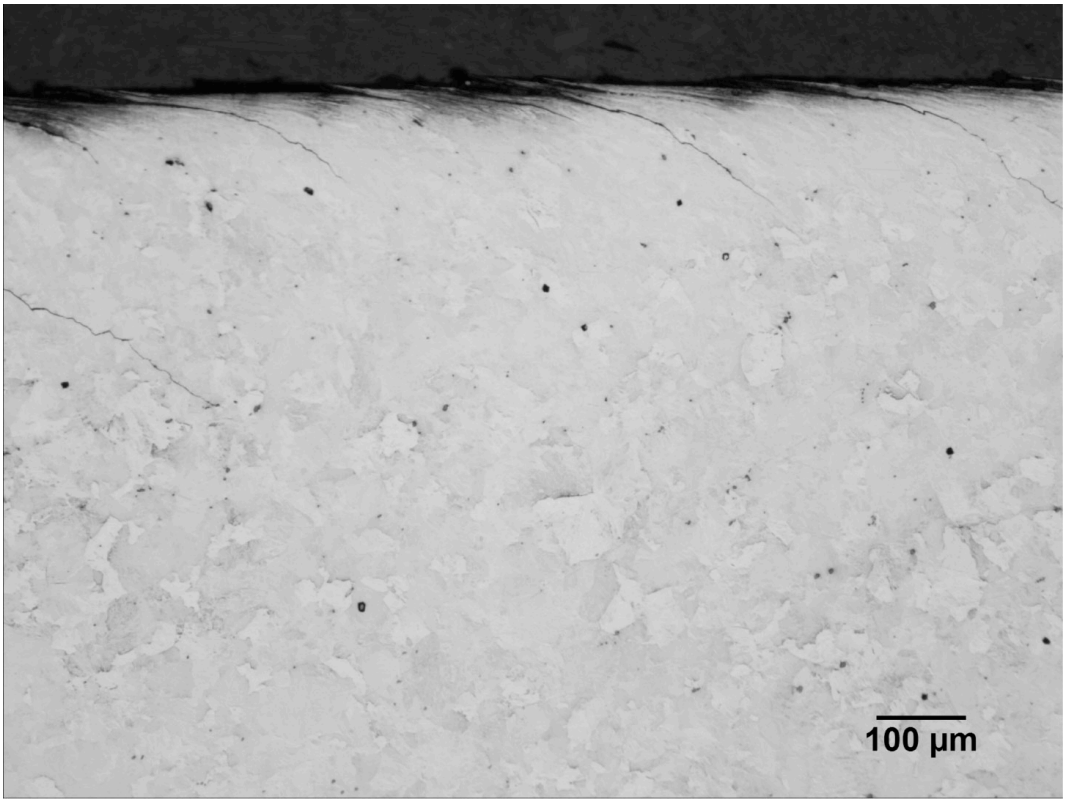

Figure B.14 Optical microscope image, C350, 5000 cycles dry and 5000 cycles wet

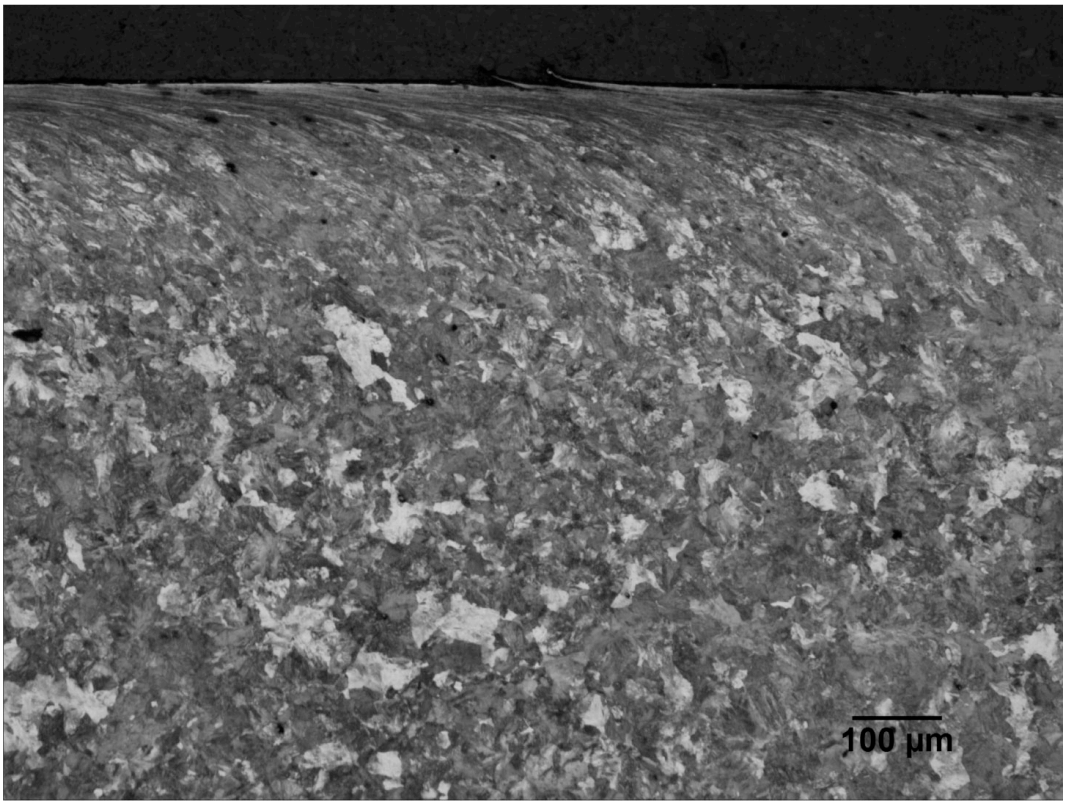

Figure B.15 Optical microscope image, C350, 15000 cycles dry

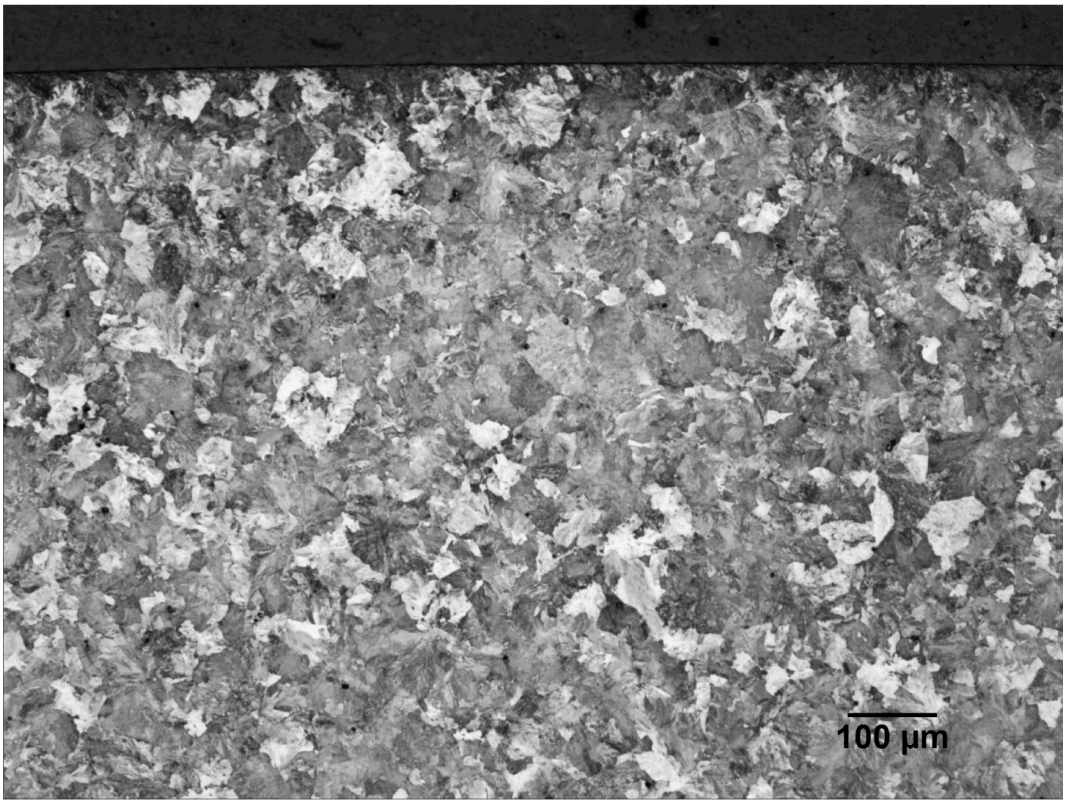

Figure B.16 Optical microscope image, C350, 20000 cycles wet

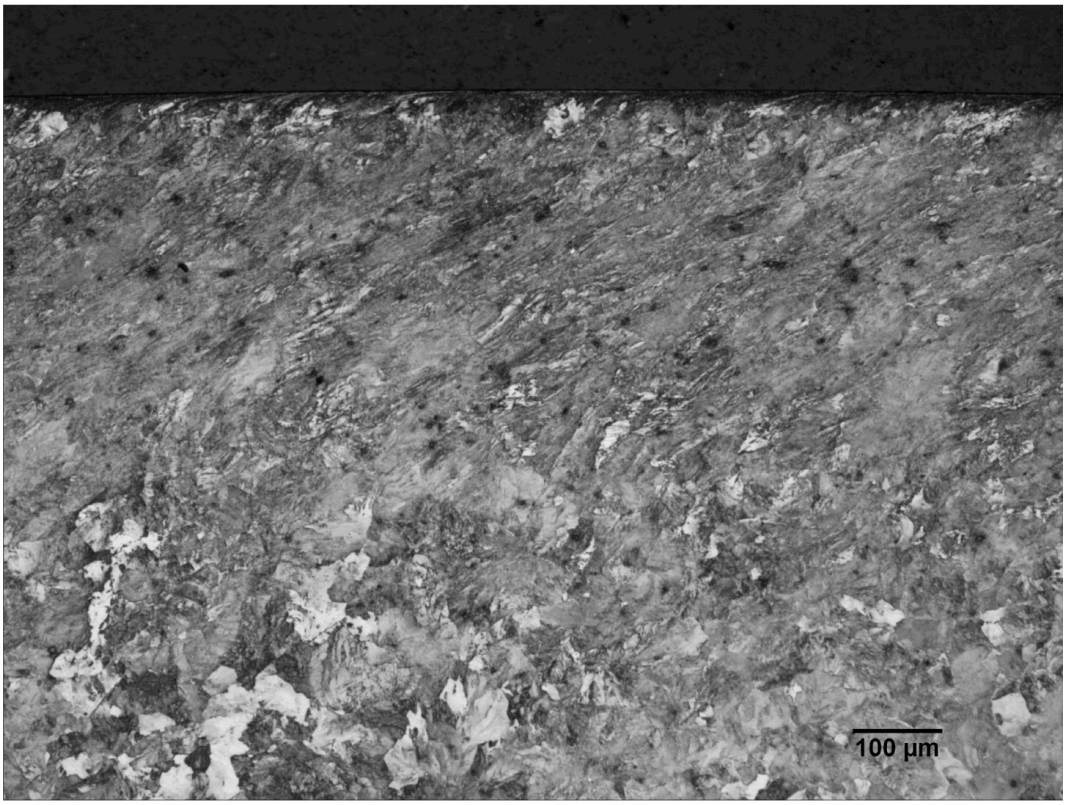

Figure B.17 Optical microscope image, P260, 20000 cycles wet

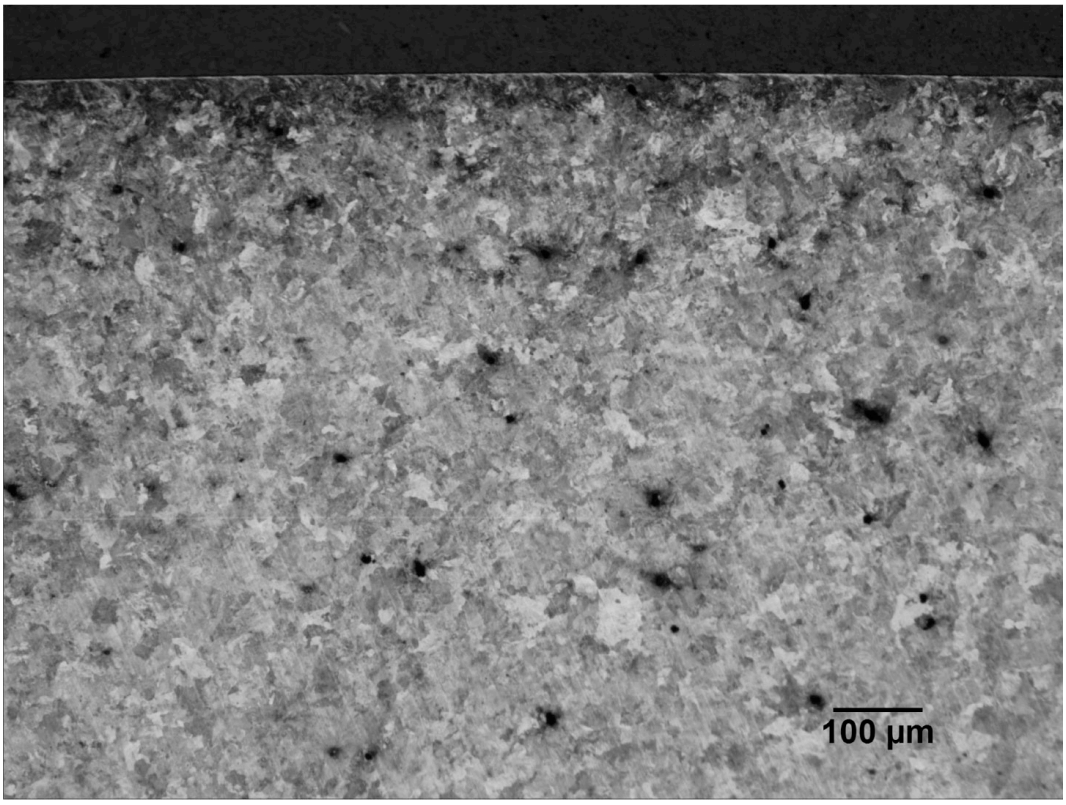

Figure B.18 Optical microscope image, C400, 20000 cycles wet

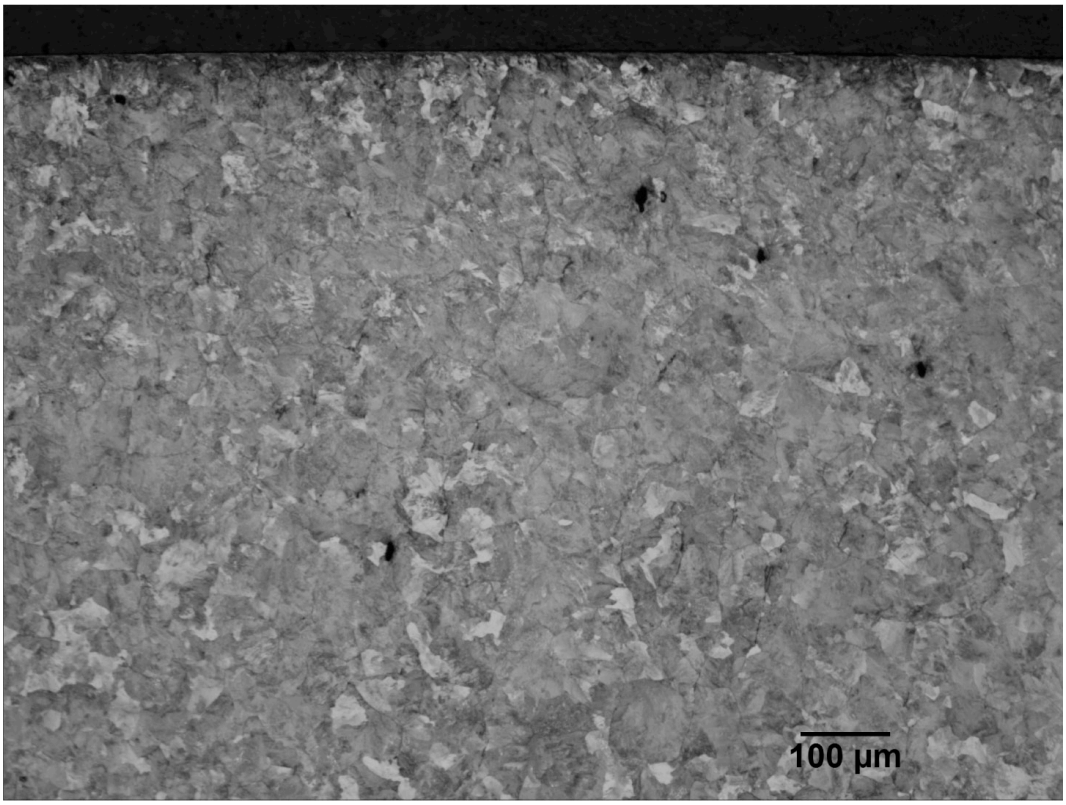

Figure B.19 Optical microscope image, V400, 20000 cycles wet

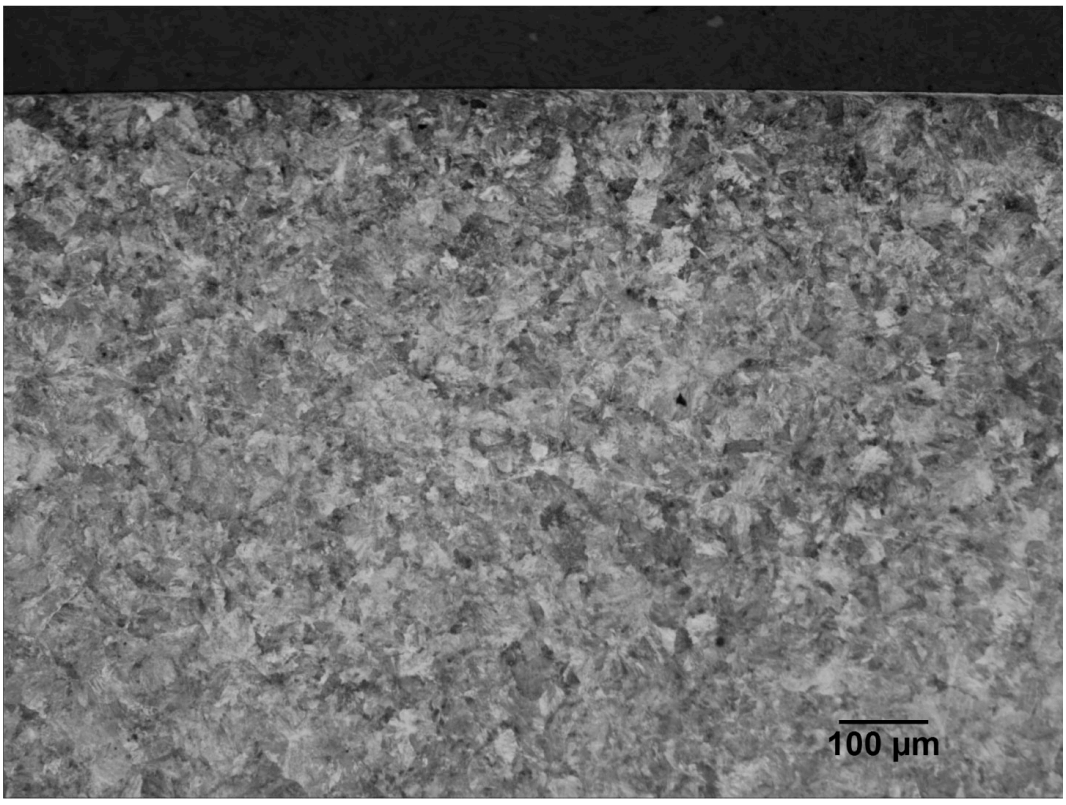

Figure B.20 Optical microscope image, V350, 20000 cycles wet

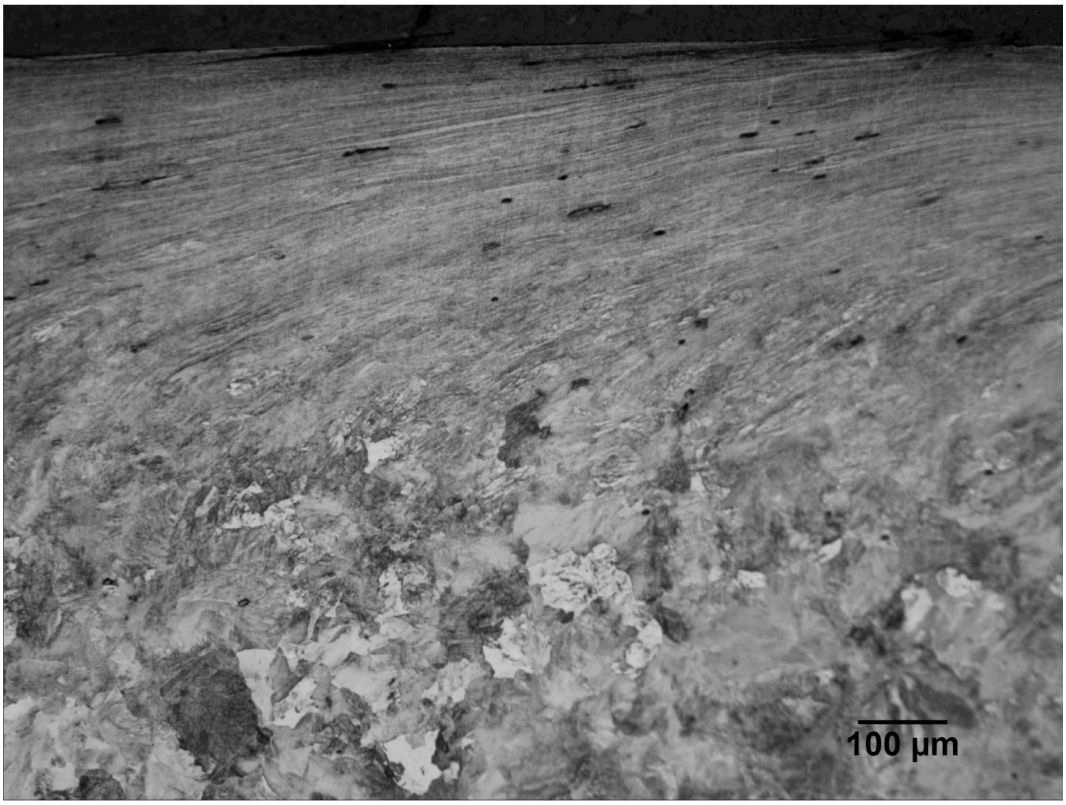

Figure B.21 Optical microscope image, P260, 15000 cycles dry, INNOT-22

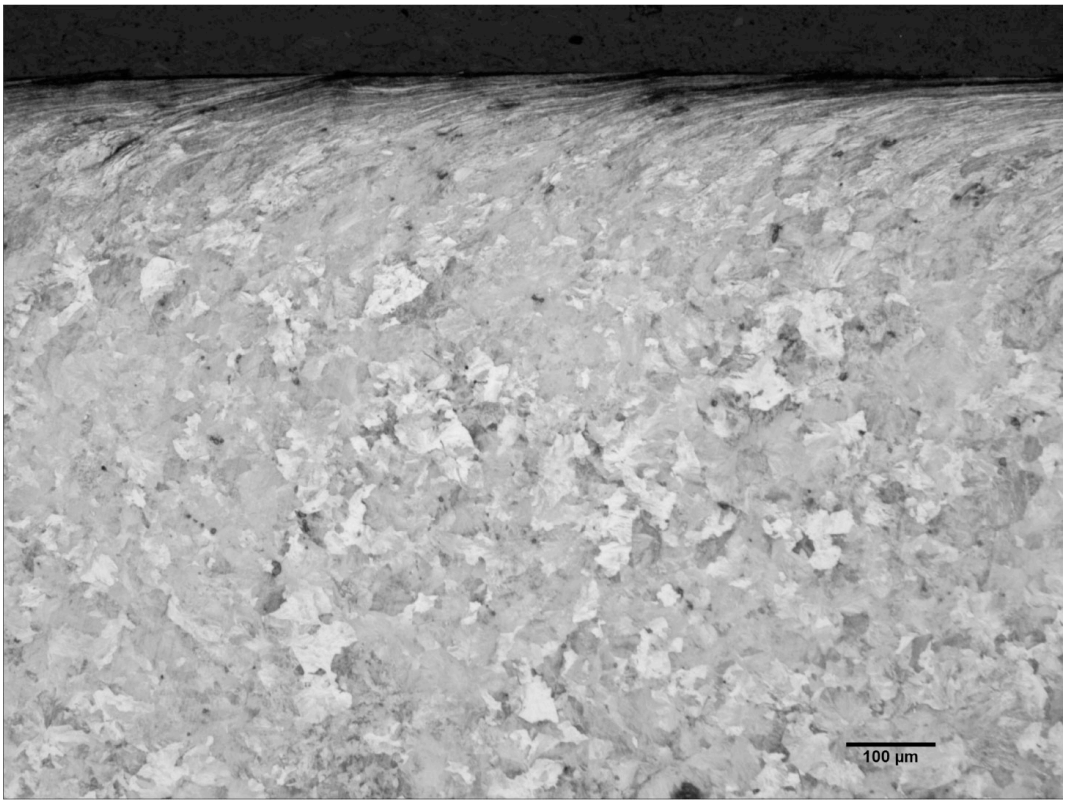

Figure B.22 Optical microscope image, C350, 15000 cycles dry, INNOT-23

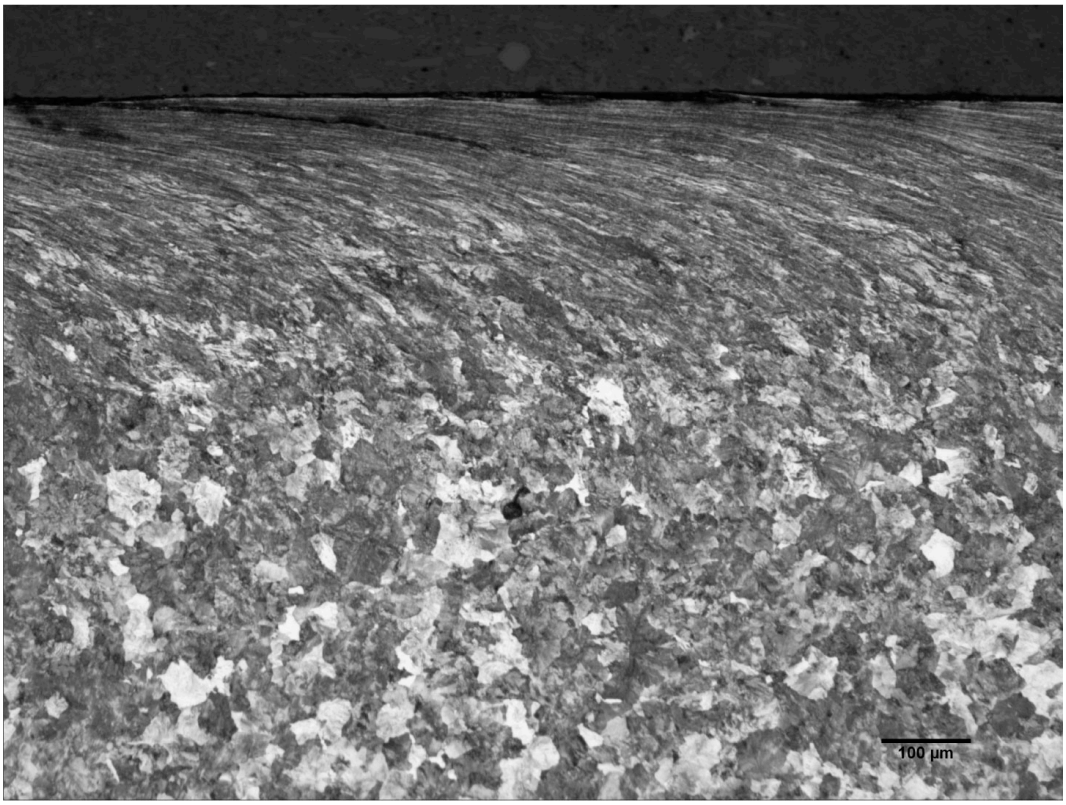

Figure B.23 Optical microscope image, C400, 15000 cycles dry, INNOT-24

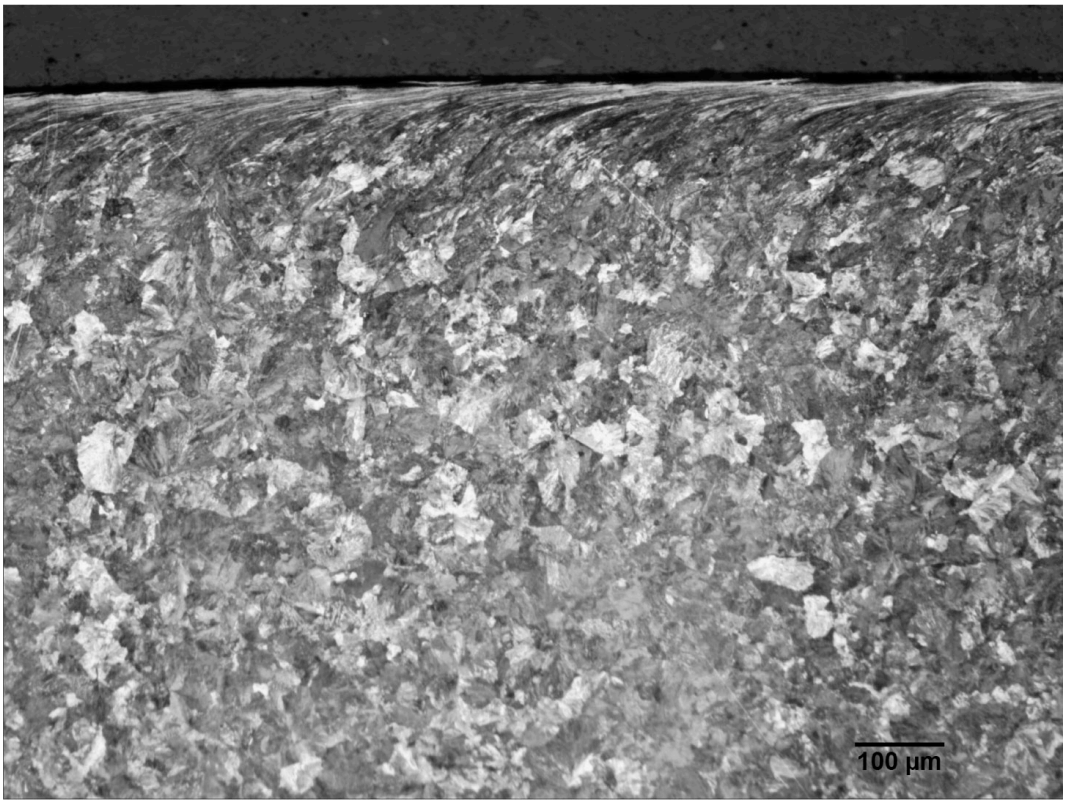

Figure B.24 Optical microscope image, V350, 15000 cycles dry, INNOT-25

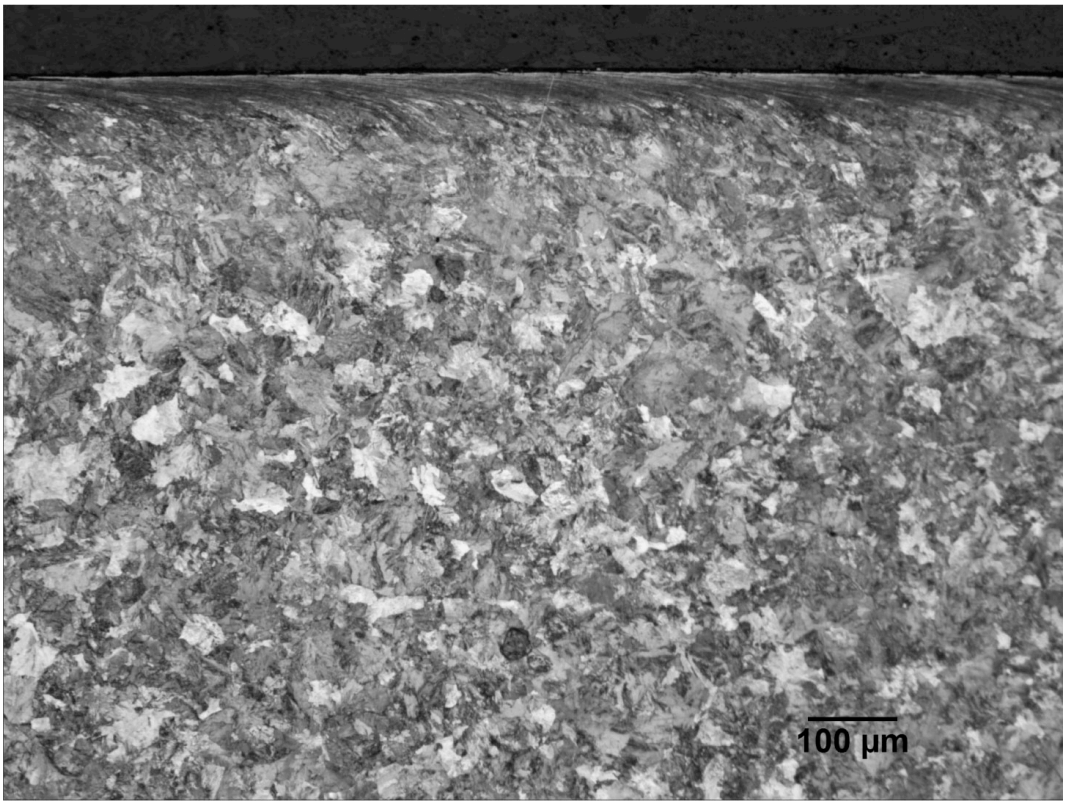

Figure B.25 Optical microscope image, V400, 15000 cycles dry, INNOT-26

Optical microscope images (unetched)

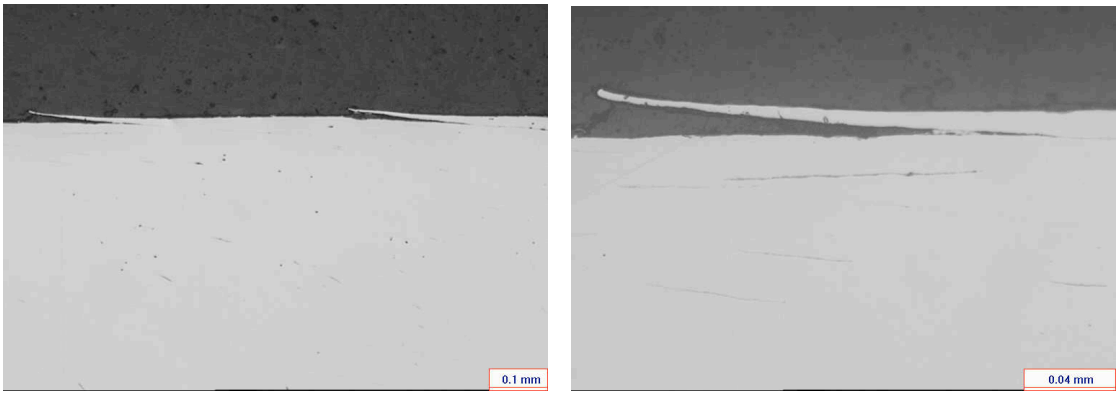

Figure B.26 Optical microscope image, P260, 5000 cycles dry

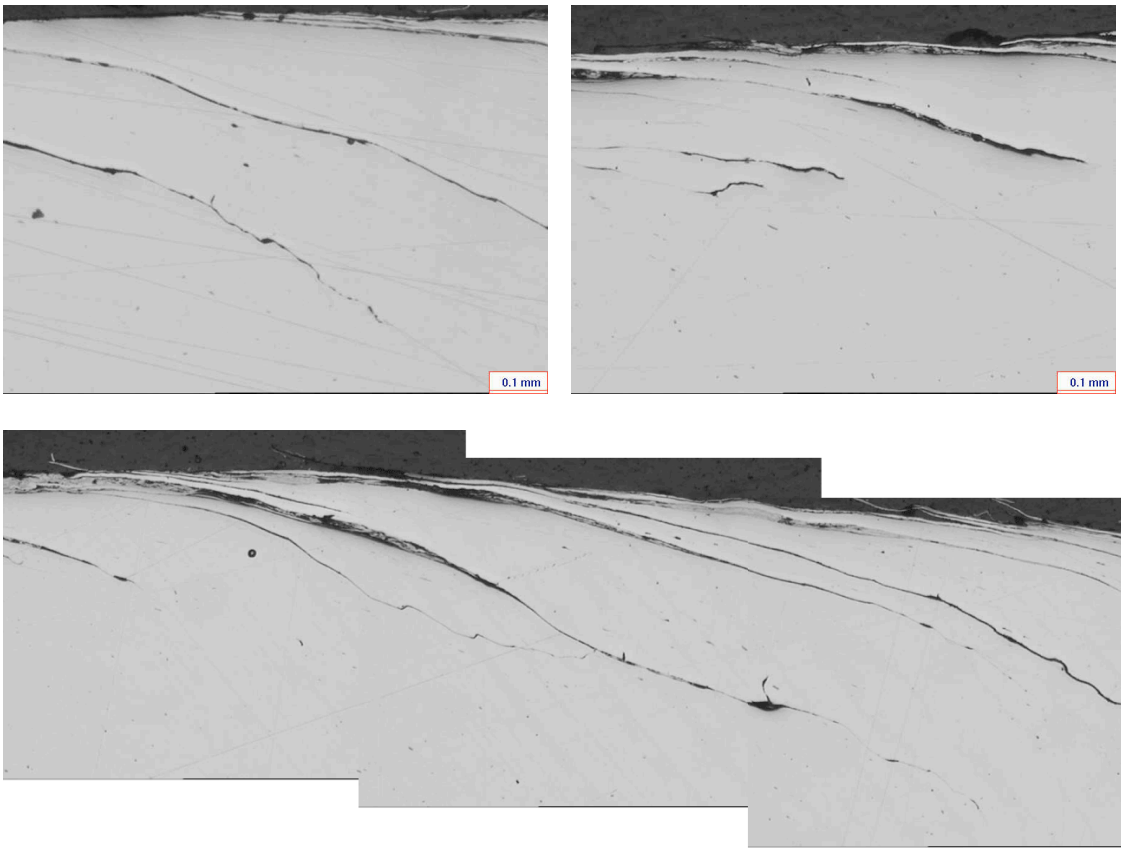

Figure B.27 Optical microscope image, P260, 5000 cycles dry and 5000 cycles wet

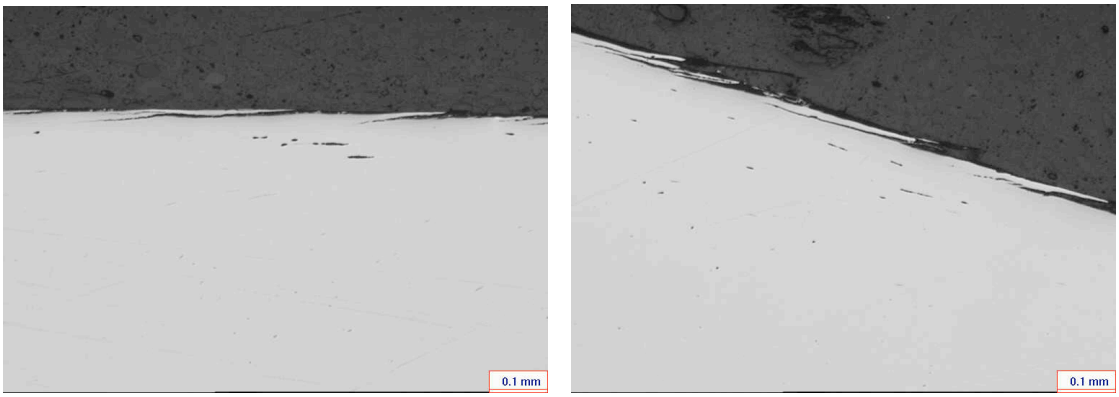

Figure B.28 Optical microscope image, P260, 15000 cycles dry

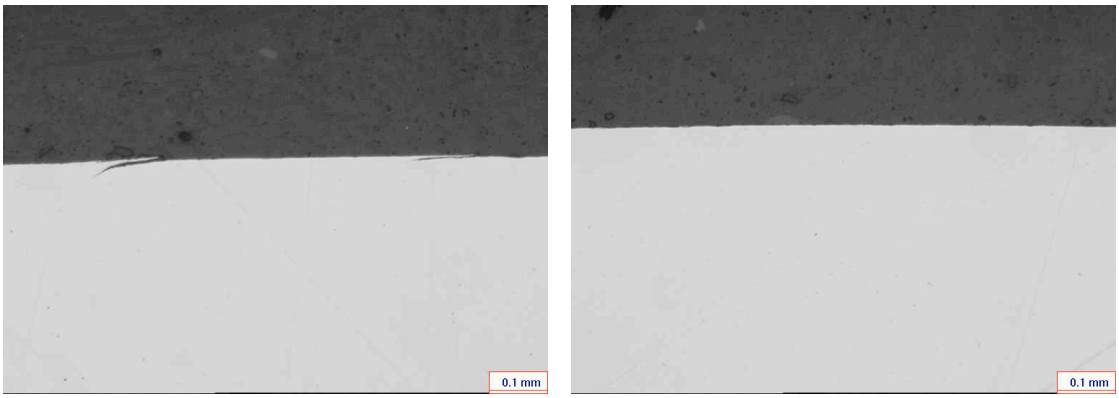

Figure B.29 Optical microscope image, C400, 5000 cycles dry

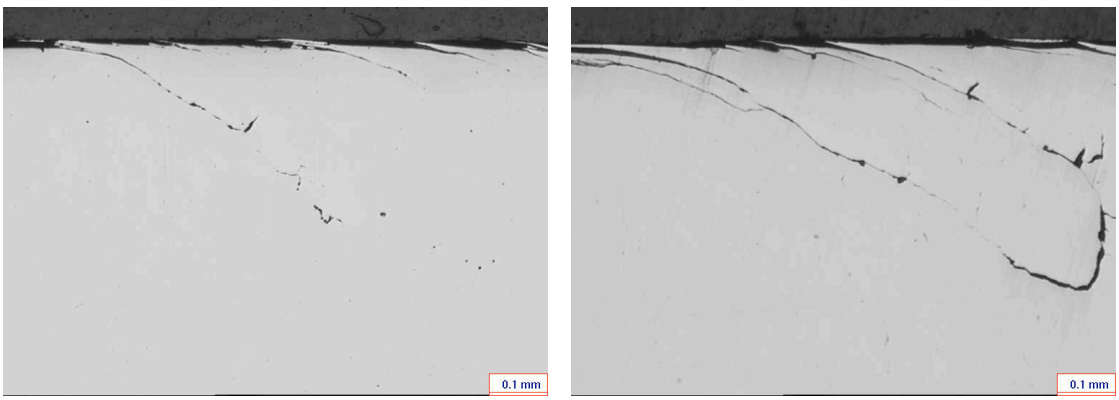

Figure B.30 Optical microscope image, C400, 5000 cycles dry and 5000 cycles wet

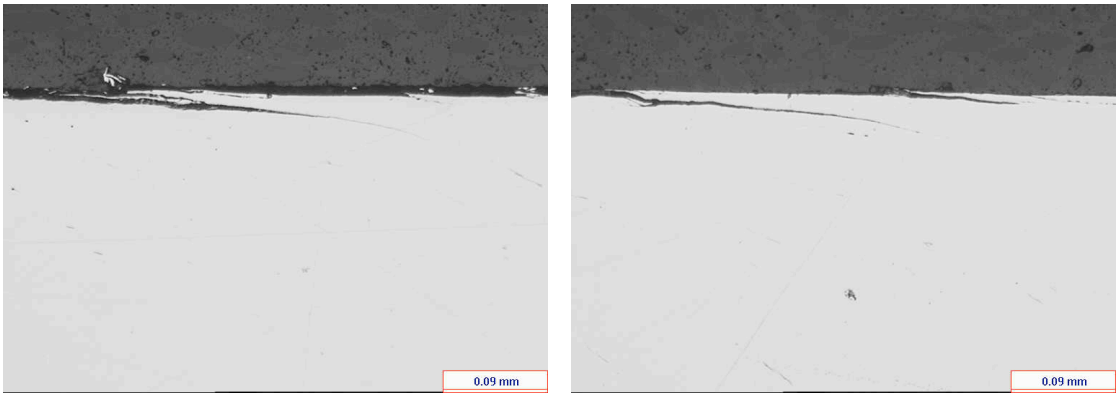

Figure B.31 Optical microscope image, C400, 15000 cycles dry

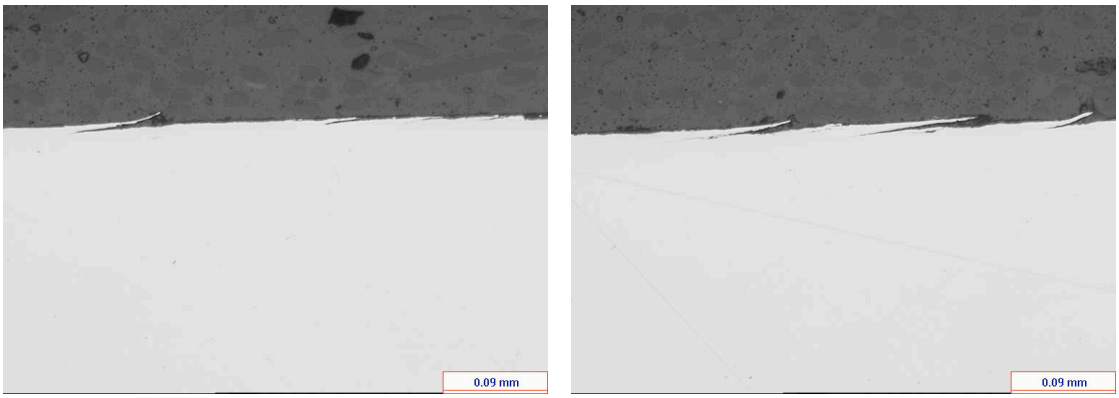

Figure B.32 Optical microscope image, V350, 5000 cycles dry

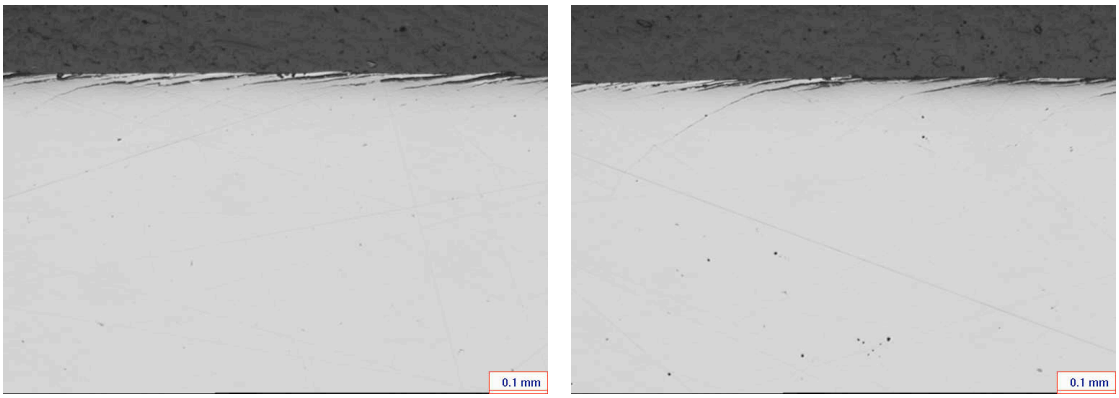

Figure B.33 Optical microscope image, V350, 5000 cycles dry and 5000 cycles wet

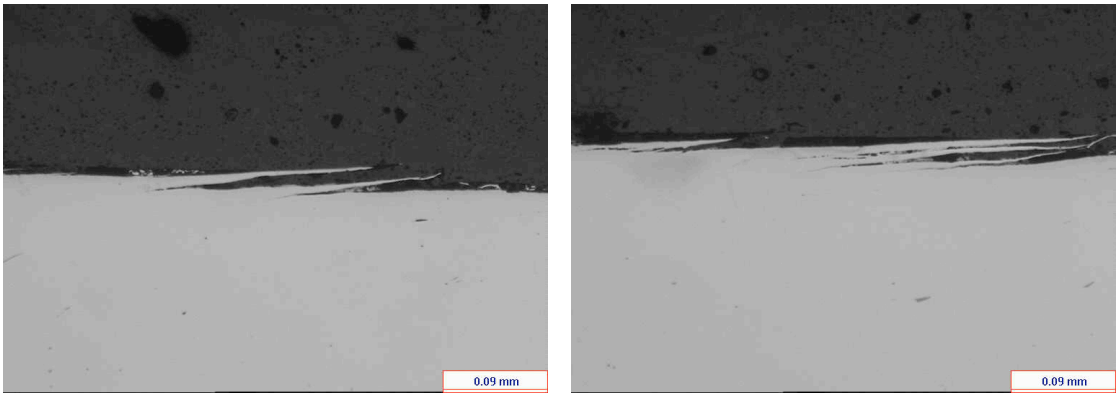

Figure B.34 Optical microscope image, V350, 15000 cycles dry

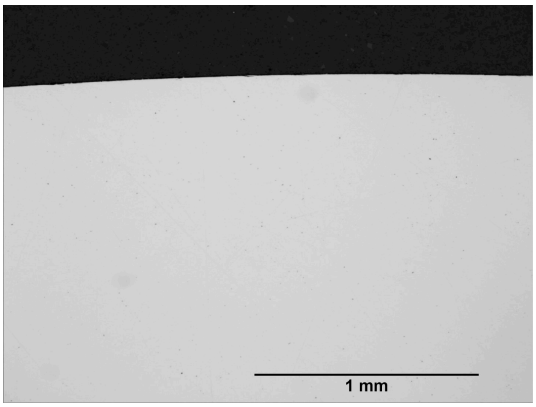

Figure B.35 Optical microscope image, C350, 5000 cycles dry

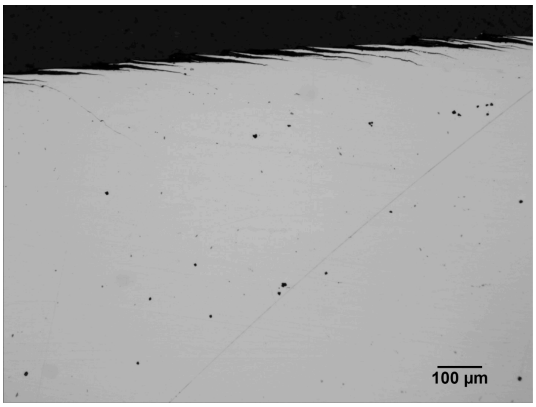

Figure B.36 Optical microscope image, C350, 5000 cycles dry and 5000 cycles wet

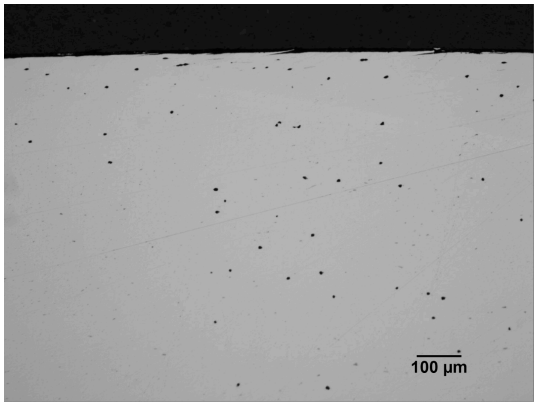

Figure B.37 Optical microscope image, C350, 15000 cycles dry

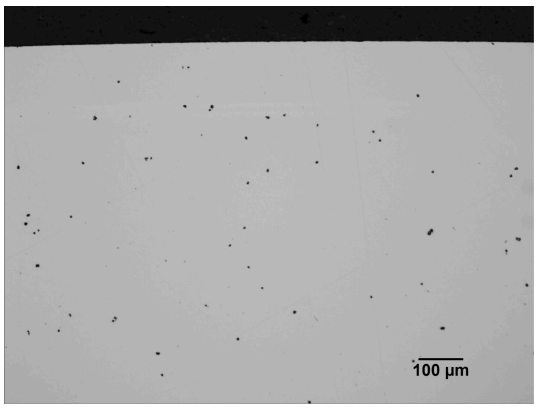

Figure B.38 Optical microscope image, C350, 20000 cycles wet

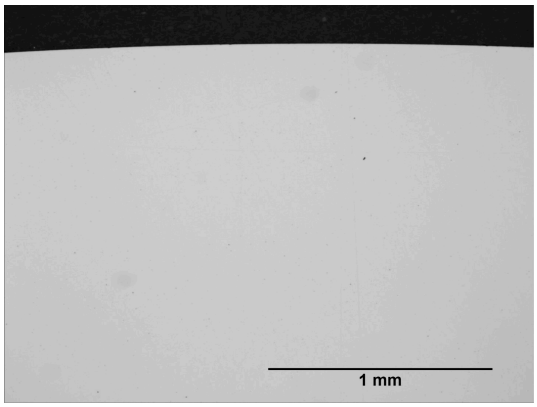

Figure B.39 Optical microscope image, P260, 20000 cycles wet

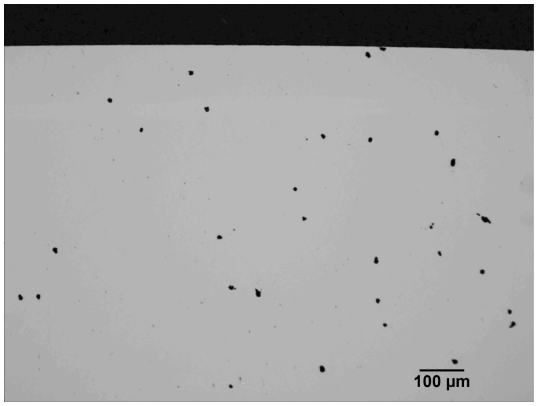

Figure B.40 Optical microscope image, C400, 20000 cycles wet

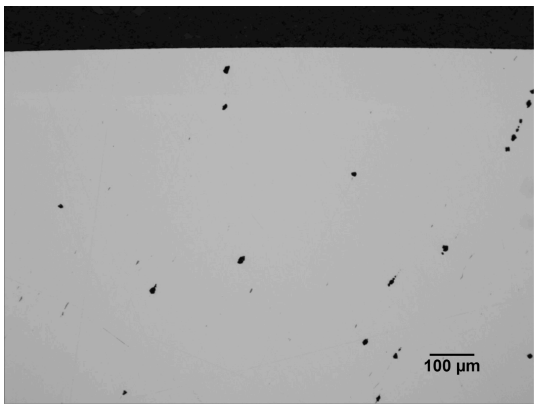

Figure B.41 Optical microscope image, V400, 20000 cycles wet

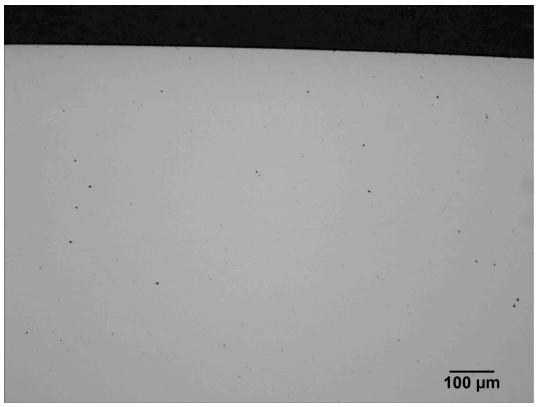

Figure B.42 Optical microscope image, V350, 20000 cycles wet

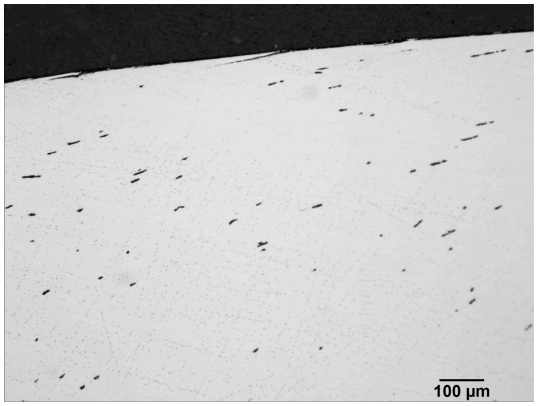

Figure B.43 Optical microscope image, P260, 15000 cycles dry, INNOT-22

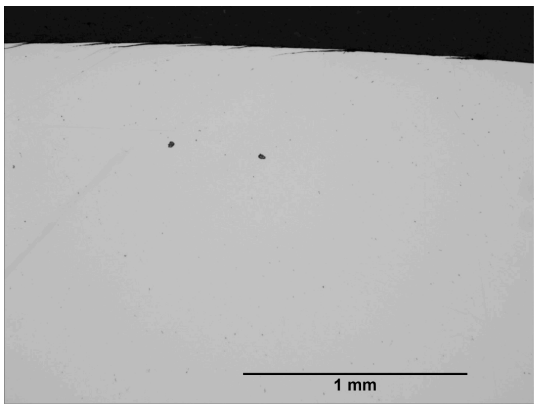

Figure B.44 Optical microscope image, C350, 15000 cycles dry, INNOT-23

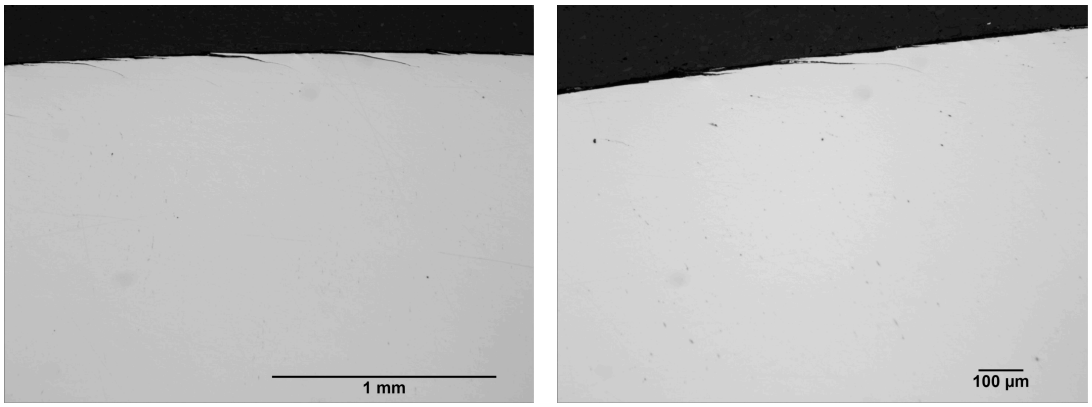

Figure B.45 Optical microscope image, C400, 15000 cycles dry, INNOT-24

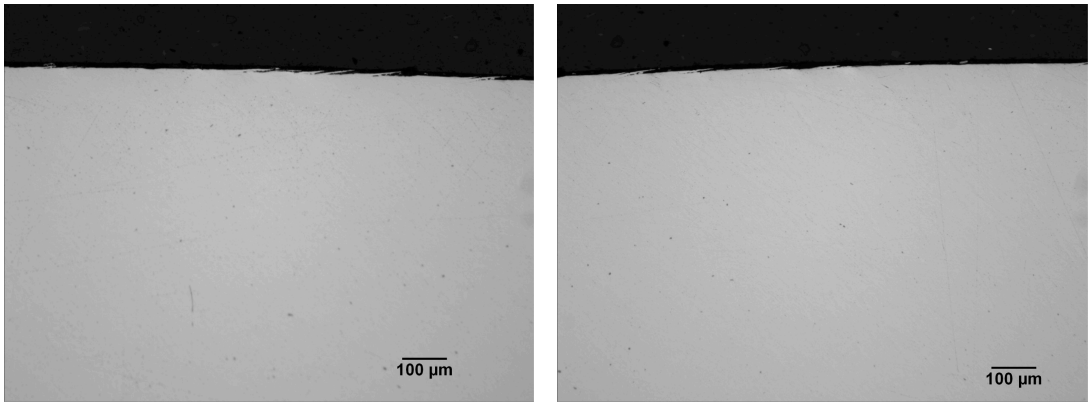

Figure B.46 Optical microscope image, V350, 15000 cycles dry, INNOT-25

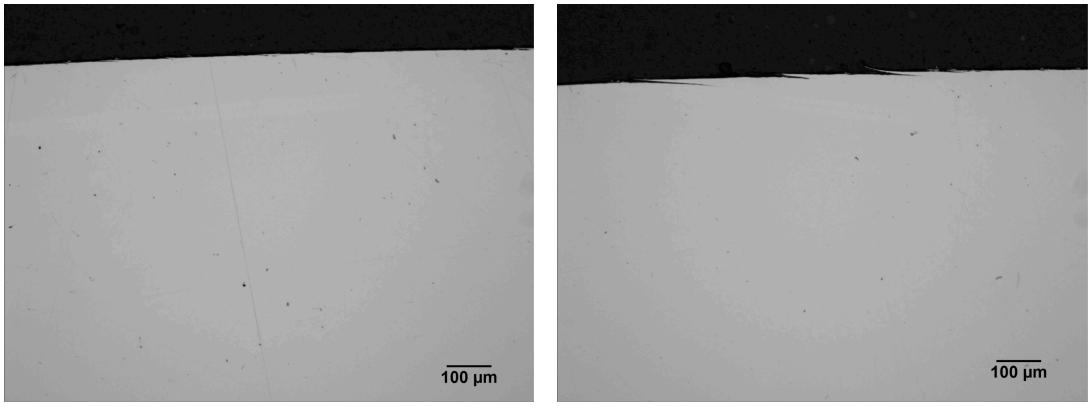

Figure B.47 Optical microscope image, V400, 15000 cycles dry, INNOT-26

Appendix C: Hardness Measurements

Microhardness measurements

List of tables:

Table C.22	Hardness vs depth measurements, V400 material grade, test 5000 cycles dry+5000 cycles wet, INNOT-12
Table C.23	Hardness vs depth measurements, V400 material grade, test 15000 cycles dry, INNOT-11
Table C.24	Hardness vs depth measurements, V400 material grade, test 20000 cycles wet, INNOT-19
Table C.25	Hardness vs depth measurements, V400 material grade, test 15000 cycles dry, INNOT-26
Table C.26	Hardness vs depth measurements, R7, test 5000 cycles dry, INNOT-07
Table C.27	Hardness vs depth measurements, R7, test 5000 cycles dry+5000 wet, INNOT-08
Table C.28	Hardness vs depth measurements, R7, test 15000 cycles dry, INNOT-09
Table C.29	Hardness vs depth measurements, R7, test 20000 cycles wet, INNOT-17
Table C.30	Hardness vs depth measurements, R8T, test 15000 cycles dry, INNOT-22
Table C.31	Hardness vs depth measurements, R7, test 5000 cycles dry, INNOT-13
Table C.32	Hardness vs depth measurements, R7, test 5000 cycles dry+5000 wet, INNOT-14/41
Table C.33	Hardness vs depth measurements, R7, test 15000 cycles dry, INNOT-51
Table C.34	Hardness vs depth measurements, R7, test 20000 cycles wet, INNOT-16
Table C.35	Hardness vs depth measurements, R8T, test 15000 cycles dry, INNOT-23
Table C.36	Hardness vs depth measurements, R7, test 5000 cycles dry, INNOT-01
Table C.37	Hardness vs depth measurements, R7, test 5000 cycles dry+5000 wet, INNOT-02
Table C.38	Hardness vs depth measurements, R7, test 15000 cycles dry, INNOT-03
Table C.39	Hardness vs depth measurements, R7, test 20000 cycles wet, INNOT-18
Table C.40	Hardness vs depth measurements, R8T, test 15000 cycles dry, INNOT-24
Table C.41	Hardness vs depth measurements, R7, test 5000 cycles dry, INNOT-04
Table C.42	Hardness vs depth measurements, R7, test 5000 cycles dry+5000 wet, INNOT-05
Table C.43	Hardness vs depth measurements, R7, test 15000 cycles dry, INNOT-06
Table C.44	Hardness vs depth measurements, R7, test 20000 cycles wet, INNOT-21

Table C.45	Hardness vs depth measurements, R8T, test 15000 cycles dry, INNOT-25
Table C.46	Hardness vs depth measurements, R7, test 5000 cycles dry, INNOT-10
Table C.47	Hardness vs depth measurements, R7, test 5000 cycles dry+5000 wet, INNOT-12
Table C.48	Hardness vs depth measurements, R7, test 15000 cycles dry, INNOT-11
Table C.49	Hardness vs depth measurements, R7, test 20000 cycles wet, INNOT-19
Table C.50	Hardness vs depth measurements, R8T, test 15000 cycles dry, INNOT-26

Bulk hardness measurements

Table C.51	Bulk hardness measurements, rail discs, 10 kg load
Table C.52	Bulk hardness measurements, wheel discs, 10 kg load

Microhardness measurements

List of figures:

Microhardness measurements

Measurements were taken in 4 columns, starting from the surface (0 microns). These columns of measurements are marked in tables as 1, 2, 3 and 4.

Table C.1 Hardness vs depth measurements, P260 material grade, test 5000 cycles dry

Specimen No:	**INR24**	**Material:**	**P260**	**Test:**	**5000 dry**	**Test Name:**	**INNOT-07**
1		**2**		**3**		**4**	
Depth	**Hardness**	**Depth**	**Hardness**	**Depth**	**Hardness**	**Depth**	**Hardness**
microns	HV	microns	HV	microns	HV	microns	HV
50	494	80	454	50	486	80	458
120	446	150	421	120	435	150	418
190	421	220	395	190	408	220	375
260	389	290	389	260	380	290	366
330	369	360	364	330	348	360	343
400	369	430	345	400	348	430	350
600	308			600	308		
800	315			800	298		
1000	294	1000	300	1000	284	1000	317
2000	296			2000	312		
5000	270	5000	277	5000	304	5000	302
10000	288			10000	277		

Table C.2 Hardness vs depth measurements, P260 material grade, test 5000 cycles dry+5000 cycles wet

Specimen No:	**INR23**	**Material:**	**P260**	**Test:**	**5000+5000**	**Test Name:**	**INNOT-08**
1		**2**		**3**		**4**	
Depth	**Hardness**	**Depth**	**Hardness**	**Depth**	**Hardness**	**Depth**	**Hardness**
microns	HV	microns	HV	microns	HV	microns	HV
50	428	80	405	50	428	80	458
120	399	150	421	120	402	150	435
190	402	220	369	190	399	220	405
260	375	290	353	260	372	290	395
330	402	360	343	330	372	360	355
400	375	430	353	400	333	430	350
600	324			600	317		
800	298			800	302		
1000	343	1000	277	1000	292	1000	286
2000	286			2000	298		
5000	247	5000	275	5000	273	5000	296
10000	288			10000	298		

Table C.3 Hardness vs depth measurements, P260 material grade, test 15000 cycles dry

Specimen No:	**INR22**	**Material:**	**P260**	**Test:**	**15000 dry**	**Test Name:**	**INNOT-09**
1		**2**		**3**		**4**	
Depth	**Hardness**	**Depth**	**Hardness**	**Depth**	**Hardness**	**Depth**	**Hardness**
microns	HV	microns	HV	microns	HV	microns	HV
50	550	80	5.3	50	561	80	535
120	465	150	461	120	461	150	435
190	425	220	425	190	425	220	425
260	395	290	378	260	408	290	369
330	395	360	343	330	389	360	368
400	321	430	361	400	353	430	355
600	300			600	335		
800	290			800	310		
1000	271	1000	300	1000	306	1000	277
2000	290			2000	302		
5000	292	5000	298	5000	286	5000	288
10000	280			10000	312		

Table C.4 Hardness vs depth measurements, P260 material grade, test 20000 cycles wet

Specimen No:	**INR26**	**Material:**	**P260**	**Test:**	**20000 wet**	**Test Name:**	**INNOT-17**
1		**2**		**3**		**4**	
Depth	**Hardness**	**Depth**	**Hardness**	**Depth**	**Hardness**	**Depth**	**Hardness**
microns	HV0.2	microns	HV0.2	microns	HV0.2	microns	HV0.2
50	355	80	375	50	369	80	356
120	404	150	392	120	380	150	371
190	424	220	375	190	386	220	408
260	395	290	380	260	392	290	383
330	383	360	358	330	375	360	353
400	348	430	345	400	333	430	375
600	319			600	312		
800	303			800	290		
1000	303	1000	325	1000	292	1000	298
2000	302			2000	310		
5000	290	5000	312	5000	288	5000	288
10000	308			10000	298		

Table C.5 Hardness vs depth measurements, P260 material grade, test 15000 cycles dry

Specimen No:	**INR25**	**Material:**	**P260**	**Test:**	**15000 dry**	**Test Name:**	**INNOT-22**
1		**2**		**3**		**4**	
Depth	**Hardness**	**Depth**	**Hardness**	**Depth**	**Hardness**	**Depth**	**Hardness**
microns	HV0.2	microns	HV0.2	microns	HV0.2	microns	HV0.2
50	503	80	454	50	535	80	465
120	465	150	443	120	439	150	432
190	405	220	405	190	425	220	421
260	392	290	418	260	408	290	386
330	378	360	353	330	372	360	304
400	358	430	331	400	338	430	335
600	326			600	328		
800	306			800	292		
1000	296	1000	275	1000	310	1000	294
2000	277			2000	292		
5000	270	5000	290	5000	277	5000	288
10000	277			10000	265		

Table C.6 Hardness vs depth measurements, C350 material grade, test 5000 cycles dry

Specimen No:	**INR30**	**Material:**	**C350**	**Test:**	**5000 dry**	**Test Name:**	**INNOT-13**
1		**2**		**3**		**4**	
Depth	**Hardness**	**Depth**	**Hardness**	**Depth**	**Hardness**	**Depth**	**Hardness**
microns	HV0.2	microns	HV0.2	microns	HV0.2	microns	HV0.2
50	392	80	398	50	439	80	439
120	414	150	431	120	435	150	411
190	408	220	398	190	421	220	392
260	375	290	392	260	392	290	386
330	386	360	395	330	398	360	386
400	364	430	389	400	378	430	395
600	389			600	378		
800	361			800	380		
1000	383	1000	386	1000	372	1000	364
2000	378			2000	383		
5000	350	5000	378	5000	375	5000	389
10000	369			10000	380		

Table C.7 Hardness vs depth measurements, C350 material grade, test 5000 cycles dry+5000 cycles wet

Specimen No:	**INR31**	**Material:**	**C350**	**Test:**	**5000+5000**	**Test Name:**	**INNOT-14/41**
1		**2**		**3**		**4**	
Depth	**Hardness**	**Depth**	**Hardness**	**Depth**	**Hardness**	**Depth**	**Hardness**
microns	HV0.2	microns	HV0.2	microns	HV0.2	microns	HV0.2
50	398	80	421	50	461	80	439
120	404	150	414	120	446	150	411
190	392	220	435	190	386	220	435
260	438	290	408	260	414	290	386
330	382	360	386	330	421	360	389
400	389	430	392	400	402	430	363
600	411			600	392		
800	386			800	389		
1000	378	1000	398	1000	383	1000	369
2000	361			2000	378		
5000	323	5000	371	5000	386	5000	364
10000	360			10000	383		

Table C.8 Hardness vs depth measurements, C350 material grade, test 15000 cycles dry

Specimen No:	**INR34**	**Material:**	**C350**	**Test:**	**15000 dry**	**Test Name:**	**INNOT-51**
1		**2**		**3**		**4**	
Depth	**Hardness**	**Depth**	**Hardness**	**Depth**	**Hardness**	**Depth**	**Hardness**
microns	HV0.2	microns	HV0.2	microns	HV0.2	microns	HV0.2
50	461	80	431	50	461	80	446
120	424	150	425	120	439	150	425
190	424	220	425	190	415	220	422
260	398	290	395	260	398	290	364
330	383	360	380	330	369	360	405
400	375	430	361	400	361	430	338
600	364			600	331		
800	348			800	315		
1000	345	1000	343	1000	319	1000	298
2000	372			2000	319		
5000	345	5000	340	5000	335	5000	298
10000	335			10000	319		

Table C.9 Hardness vs depth measurements, C350 material grade, test 20000 cycles wet

Specimen No:	**INR36**	**Material:**	**C350**	**Test:**	**20000 wet**	**Test Name:**	**INNOT-16**
1		**2**		**3**		**4**	
Depth	**Hardness**	**Depth**	**Hardness**	**Depth**	**Hardness**	**Depth**	**Hardness**
microns	HV0.2	microns	HV0.2	microns	HV0.2	microns	HV0.2
50	405	80	378	50	381	80	383
120	402	150	398	120	405	150	392
190	431	220	402	190	393	220	392
260	399	290	392	260	386	290	398
330	411	360	402	330	389	360	392
400	395	430	386	400	378	430	380
600	425			600	395		
800	411			800	361		
1000	380	1000	380	1000	378	1000	366
2000	402			2000	398		
5000	386	5000	378	5000	356	5000	366
10000	364			10000	380		

Table C.10 Hardness vs depth measurements, C350 material grade, test 15000 cycles dry

Specimen No:	**INR33**	**Material:**	**C350**	**Test:**	**15000 dry**	**Test Name:**	**INNOT-23**
1		**2**		**3**		**4**	
Depth	**Hardness**	**Depth**	**Hardness**	**Depth**	**Hardness**	**Depth**	**Hardness**
microns	HV0.2	microns	HV0.2	microns	HV0.2	microns	HV0.2
50	485	80	435	50	494	80	454
120	424	150	405	120	446	150	425
190	418	220	424	190	418	220	392
260	389	290	364	260	392	290	353
330	380	360	383	330	353	360	369
400	383	430	380	400	356	430	328
600	389			600	333		
800	372			800	343		
1000	378	1000	366	1000	340	1000	338
2000	386			2000	378		
5000	389	5000	350	5000	315	5000	377
10000	356			10000	330		

Table C.11 Hardness vs depth measurements, C400 material grade, test 5000 cycles dry, INNOT-01

Specimen No:	**INR1**	**Material:**	**C400**	**Test:**	**5000 dry**	**Test Name:**	**INNOT-01**
1		**2**		**3**		**4**	
Depth	**Hardness**	**Depth**	**Hardness**	**Depth**	**Hardness**	**Depth**	**Hardness**
microns	HV	microns	HV	microns	HV	microns	HV
50	458	80	432	50	458	80	450
120	439	150	411	120	450	150	428
190	418	220	421	190	408	220	411
260	415	290	405	260	428	290	402
330	395	360	408	330	411	360	411
400	399	430	411	400	408	430	405
600	395			600	408		
800	378			800	418		
1000	399	1000	415	1000	421	1000	408
2000	369			2000	415		
5000	372	5000	372	5000	415	5000	405
10000	364			10000	392		

Table C.12 Hardness vs depth measurements, C400 material grade, test 5000 cycles dry+5000 cycles wet

Specimen No:	**INR2**	**Material:**	**C400**	**Test:**	**5000+5000**	**Test Name:**	**INNOT-02**
1		**2**		**3**		**4**	
Depth	**Hardness**	**Depth**	**Hardness**	**Depth**	**Hardness**	**Depth**	**Hardness**
microns	HV	microns	HV	microns	HV	microns	HV
50	454	80	425	50	450	80	443
120	432	150	418	120	395	150	425
190	415	220	402	190	411	220	395
260	411	290	399	260	399	290	383
330	395	360	375	330	372	360	361
400	366	430	380	400	369	430	361
600	369			600	335		
800	369			800	364		
1000	348	1000	328	1000	355	1000	340
2000	358			2000	333		
5000	338	5000	338	5000	335	5000	338
10000	335			10000	326		

Table C.13 Hardness vs depth measurements, C400 material grade, test 15000 cycles dry

Specimen No:	**INR3**	**Material:**	**C400**	**Test:**	**15000 dry**	**Test Name:**	**INNOT-03**
1		**2**		**3**		**4**	
Depth	**Hardness**	**Depth**	**Hardness**	**Depth**	**Hardness**	**Depth**	**Hardness**
microns	HV	microns	HV	microns	HV	microns	HV
50	503	80	477	50	507	80	461
120	435	150	446	120	439	150	425
190	432	220	418	190	425	220	375
260	395	290	415	260	389	290	372
330	408	360	378	330	355	360	361
400	389	430	340	400	355	430	369
600	389			600	343		
800	386			800	319		
1000	353	1000	338	1000	319	1000	348
2000	340			2000	319		
5000	361	5000	326	5000	350	5000	335
10000	366			10000	328		

Table C.14 Hardness vs depth measurements, C400 material grade, test 20000 cycles wet

Specimen No:	**INR7**	**Material:**	**C400**	**Test:**	**20000 wet**	**Test Name:**	**INNOT-18**
1		**2**		**3**		**4**	
Depth	**Hardness**	**Depth**	**Hardness**	**Depth**	**Hardness**	**Depth**	**Hardness**
microns	HV0.2	microns	HV0.2	microns	HV0.2	microns	HV0.2
50	383	80	377	50	404	80	401
120	392	150	404	120	414	150	404
190	414	220	408	190	401	220	404
260	414	290	414	260	408	290	398
330	398	360	395	330	392	360	389
400	402	430	404	400	404	430	404
600	389			600	404		
800	383			800	404		
1000	374	1000	383	1000	395	1000	395
2000	355			2000	395		
5000	363	5000	355	5000	360	5000	398
10000	347			10000	350		

Table C.15 Hardness vs depth measurements, C400 material grade, test 15000 cycles dry

Specimen No:	**INR4**	**Material:**	**C400**	**Test:**	**15000 dry**	**Test Name:**	**INNOT-24**
1		**2**		**3**		**4**	
Depth	**Hardness**	**Depth**	**Hardness**	**Depth**	**Hardness**	**Depth**	**Hardness**
microns	HV0.2	microns	HV0.2	microns	HV0.2	microns	HV0.2
50	442	80	454	50	450	80	457
120	395	150	408	120	421	150	421
190	425	220	389	190	425	220	414
260	375	290	364	260	405	290	405
330	356	360	380	330	389	360	386
400	350	430	364	400	405	430	398
600	298			600	389		
800	317			800	375		
1000	294	1000	338	1000	372	1000	372
2000	340			2000	378		
5000	298	5000	331	5000	375	5000	364
10000	330			10000	364		

Table C.16 Hardness vs depth measurements, V350 material grade, test 5000 cycles dry

Specimen No:	**INR10**	**Material:**	**V350**	**Test:**	**5000 dry**	**Test Name:**	**INNOT-04**
1		**2**		**3**		**4**	
Depth	**Hardness**	**Depth**	**Hardness**	**Depth**	**Hardness**	**Depth**	**Hardness**
microns	HV	microns	HV	microns	HV	microns	HV
50	454	80	443	50	461	80	439
120	428	150	425	120	450	150	439
190	418	220	425	190	432	220	415
260	415	290	402	260	418	290	392
330	405	360	432	330	399	360	402
400	408	430	418	400	375	430	389
600	411			600	389		
800	402			800	408		
1000	395	1000	408	1000	395	1000	399
2000	372			2000	432		
5000	402	5000	392	5000	408	5000	408
10000	395			10000	411		

Table C.17 Hardness vs depth measurements, V350 material grade, test 5000 cycles dry+5000 cycles wet

Specimen No:	**INR11**	**Material:**	**V350**	**Test:**	**5000+5000**	**Test Name:**	**INNOT-05**
1		**2**		**3**		**4**	
Depth	**Hardness**	**Depth**	**Hardness**	**Depth**	**Hardness**	**Depth**	**Hardness**
microns	HV	microns	HV	microns	HV	microns	HV
50	446	80	454	50	439	80	465
120	454	150	443	120	415	150	446
190	415	220	428	190	425	220	428
260	415	290	399	260	425	290	421
330	411	360	405	330	392	360	415
400	389	430	421	400	418	430	428
600	392			600	405		
800	389			800	392		
1000	378	1000	402	1000	383	1000	402
2000	355			2000	380		
5000	361	5000	369	5000	386	5000	399
10000	369			10000	378		

Table C.18 Hardness vs depth measurements, V350 material grade, test 15000 cycles dry

Specimen No:	**INR12**	**Material:**	**V350**	**Test:**	**15000 dry**	**Test Name:**	**INNOT-06**
1		**2**		**3**		**4**	
Depth	**Hardness**	**Depth**	**Hardness**	**Depth**	**Hardness**	**Depth**	**Hardness**
microns	HV	microns	HV	microns	HV	microns	HV
50	531	80	531	50	535	80	503
120	443	150	461	120	454	150	461
190	432	220	432	190	435	220	402
260	405	290	375	260	411	290	389
330	353	360	355	330	405	360	399
400	383	430	361	400	380	430	386
600	355			600	380		
800	372			800	383		
1000	378	1000	350	1000	361	1000	369
2000	338			2000	372		
5000	315	5000	345	5000	345	5000	372
10000	375			10000	353		

Table C.19 Hardness vs depth measurements, V350 material grade, test 20000 cycles wet

Specimen No:	**INR16**	**Material:**	**V350**	**Test:**	**20000 wet**	**Test Name:**	**INNOT-21**
1		**2**		**3**		**4**	
Depth	**Hardness**	**Depth**	**Hardness**	**Depth**	**Hardness**	**Depth**	**Hardness**
microns	HV0.2	microns	HV0.2	microns	HV0.2	microns	HV0.2
50	399	80	411	50	432	80	408
120	400	150	435	120	432	150	411
190	431	220	392	190	411	220	411
260	295	290	439	260	398	290	414
330	428	360	418	330	375	360	408
400	432	430	432	400	408	430	421
600	389			600	428		
800	439			800	408		
1000	380	1000	408	1000	414	1000	432
2000	421			2000	340		
5000	414	5000	408	5000	404	5000	392
10000	411			10000	425		

Table C.20 Hardness vs depth measurements, V350 material grade, test 15000 cycles dry

Specimen No:	**INR14**	**Material:**	**V350**	**Test:**	**15000 dry**	**Test Name:**	**INNOT-25**
1		**2**		**3**		**4**	
Depth	**Hardness**	**Depth**	**Hardness**	**Depth**	**Hardness**	**Depth**	**Hardness**
microns	HV0.2	microns	HV0.2	microns	HV0.2	microns	HV0.2
50	457	80	446	50	486	80	453
120	443	150	449	120	457	150	449
190	439	220	411	190	461	220	435
260	405	290	428	260	450	290	405
330	418	360	418	330	446	360	439
400	418	430	418	400	418	430	432
600	408			600	431		
800	386			800	398		
1000	392	1000	402	1000	405	1000	408
2000	415			2000	411		
5000	386	5000	395	5000	411	5000	414
10000	361			10000	414		

Table C.21 Hardness vs depth measurements, V400 material grade, test 5000 cycles dry

Specimen No:	**V400(1)**	**Material:**	**V400**	**Test:**	**5000 dry**	**Test Name:**	**INNOT-10**
1		**2**		**3**		**4**	
Depth	**Hardness**	**Depth**	**Hardness**	**Depth**	**Hardness**	**Depth**	**Hardness**
microns	HV0.3	microns	HV0.3	microns	HV0.3	microns	HV0.3
50	426	80	423	50	423	80	392
120	435	150	410	120	462	150	423
190	450	220	402	190	410	220	415
260	387	290	377	260	394	290	382
330	375	360	384	330	402	360	380
400	384	430	382	400	366	430	382
600	366			600	377		
800	361			800	351		
1000	353	1000	340	1000	342	1000	342
2000	351			2000	361		
5000	353	5000	321	5000	330	5000	355
10000	346			10000	346		

Table C.22 Hardness vs depth measurements, V400 material grade, test 5000 cycles dry+5000 cycles wet

Specimen No:	**V400(3)**	**Material:**	**V400**	**Test:**	**5000+5000**	**Test Name:**	**INNOT-12**
1		**2**		**3**		**4**	
Depth	**Hardness**	**Depth**	**Hardness**	**Depth**	**Hardness**	**Depth**	**Hardness**
microns	HV0.3	microns	HV0.3	microns	HV0.3	microns	HV0.3
50	421	80	441	50	429	80	421
120	441	150	456	120	438	150	399
190	415	220	421	190	426	220	392
260	412	290	394	260	399	290	407
330	384	360	405	330	389	360	377
400	380	430	373	400	423	430	368
600	397			600	375		
800	375			800	368		
1000	373	1000	359	1000	373	1000	355
2000	387			2000	359		
5000	336	5000	351	5000	334	5000	353
10000	338			10000	348		

Table C.23 Hardness vs depth measurements, V400 material grade, test 15000 cycles dry

Specimen No:	**V400(2)**	**Material:**	**V400**	**Test:**	**15000 dry**	**Test Name:**	**INNOT-11**
1		**2**		**3**		**4**	
Depth	**Hardness**	**Depth**	**Hardness**	**Depth**	**Hardness**	**Depth**	**Hardness**
microns	HV0.3	microns	HV0.3	microns	HV0.3	microns	HV0.3
50	499	80	435	50	499	80	453
120	444	150	450	120	450	150	435
190	462	220	429	190	432	220	435
260	402	290	392	260	415	290	405
330	387	360	373	330	397	360	392
400	380	430	384	400	397	430	380
600	359			600	353		
800	346			800	346		
1000	346	1000	348	1000	346	1000	373
2000	342			2000	359		
5000	344	5000	364	5000	336	5000	377
10000	366			10000	377		

Table C.24 Hardness vs depth measurements, V400 material grade, test 20000 cycles wet

Specimen No:	**INR40**	**Material:**	**V400**	**Test:**	**20000 wet**	**Test Name:**	**INNOT-19**
1		**2**		**3**		**4**	
Depth	**Hardness**	**Depth**	**Hardness**	**Depth**	**Hardness**	**Depth**	**Hardness**
microns	HV0.2	microns	HV0.2	microns	HV0.2	microns	HV0.2
50	405	80	395	50	383	80	411
120	402	150	428	120	438	150	428
190	414	220	421	190	386	220	431
260	432	290	398	260	358	290	425
330	369	360	411	330	395	360	398
400	383	430	399	400	411	430	408
600	386			600	361		
800	366			800	369		
1000	383	1000	378	1000	364	1000	369
2000	398			2000	361		
5000	378	5000	366	5000	358	5000	378
10000	404			10000	377		

Table C.25 Hardness vs depth measurements, V400 material grade, test 15000 cycles dry

Specimen No:	**INR41**	**Material:**	**V400**	**Test:**	**15000 dry**	**Test Name:**	**INNOT-26**
1		**2**		**3**		**4**	
Depth	**Hardness**	**Depth**	**Hardness**	**Depth**	**Hardness**	**Depth**	**Hardness**
microns	HV0.2	microns	HV0.2	microns	HV0.2	microns	HV0.2
50	480	80	446	50	453	80	453
120	421	150	446	120	461	150	425
190	442	220	390	190	415	220	418
260	439	290	404	260	424	290	402
330	383	360	404	330	421	360	364
400	389	430	383	400	399	430	378
600	386			600	435		
800	356			800	399		
1000	386	1000	363	1000	418	1000	393
2000	398			2000	431		
5000	374	5000	363	5000	369	5000	340
10000	356			10000	404		

Table C.26 Hardness vs depth measurements, *R7, test 5000 cycles dry, INNOT-07*

Specimen No:	**INW14**	**Test Name:**	**INNOT-07**
1		**2**	
Depth	**Hardness**	**Depth**	**Hardness**
microns	HV	microns	HV
50	383	100	350
150	353	200	328
250	331	300	326
350	292	400	282
1000	258	1000	245
5000	232	5000	241
10000	238	10000	245

Table C.27 Hardness vs depth measurements, *R7,test 5000 cycles dry +5000 wet,INNOT-08*

Specimen No:	**INW13**	**Test Name:**	**INNOT-08**
1		**2**	
Depth	**Hardness**	**Depth**	**Hardness**
microns	HV	microns	HV
50	366	100	380
150	355	200	372
250	345	300	338
350	345	400	306
1000	271	1000	256
5000	253	5000	256
10000	256	10000	255

Table C.28 Hardness vs depth measurements, *R7, test 15000 cycles dry, INNOT-09*

Specimen No:	**INW9**	**Test Name:**	**INNOT-09**
1		**2**	
Depth	**Hardness**	**Depth**	**Hardness**
microns	HV	microns	HV
50	477	100	415
150	411	200	399
250	378	300	348
350	350	400	355
1000	288	1000	265
5000	263	5000	258
10000	268	10000	270

Table C.29 Hardness vs depth measurements, *R7, test 20000 cycles wet, INNOT-17*

Specimen No:	**INW10**	**Test Name:**	**INNOT-17**
1		**2**	
Depth	**Hardness**	**Depth**	**Hardness**
microns	HV0.2	microns	HV0.2
50	328	100	333
150	350	200	321
250	342	300	333
350	358	400	306
1000	251	1000	269
5000	261	5000	238
10000	269	10000	258

Table C.30 Hardness vs depth measurements, *R8T, test 15000 cycles dry, INNOT- 22*

Specimen No:	**WB35**	**Test Name:**	**INNOT-22**
1		**2**	
Depth	**Hardness**	**Depth**	**Hardness**
microns	HV0.2	microns	HV0.2
50	389	100	366
150	374	200	377
250	377	300	347
350	337	400	347
1000	261	1000	234
5000	241	5000	250
10000	240	10000	261

Table C.31 Hardness vs depth measurements, *R7, test 5000 cycles dry, INNOT-13*

Specimen No:	**INW 21**	**Test Name:**	**INNOT-13**
1		**2**	
Depth	**Hardness**	**Depth**	**Hardness**
microns	HV0.2	microns	HV0.2
50	361	100	390
150	380	200	401
250	361	300	392
350	333	400	348
1000	268	1000	284
5000	265	5000	289
10000	280	10000	245

Table C.32 Hardness vs depth measurements, *R7, test 5000 cycles dry+5000wet, INNOT-14/41*

Specimen No:	**INW16**	**Test Name:**	**INNOT-14/41**
1		**2**	
Depth	**Hardness**	**Depth**	**Hardness**
microns	HV0.2	microns	HV0.2
50	398	100	375
150	411	200	395
250	398	300	335
350	371	400	342
1000	286	1000	278
5000	248	5000	240
10000	262	10000	242

Table C.33 Hardness vs depth measurements, *R7, test 15000 cycles dry, INNOT-51*

Specimen No:	**INW20**	**Test Name:**	**INNOT-51**
1		**2**	
Depth	**Hardness**	**Depth**	**Hardness**
microns	HV0.2	microns	HV0.2
50	442	100	424
150	421	200	418
250	386	300	366
350	338	400	347
1000	261	1000	262
5000	266	5000	234
10000	261	10000	251

Table C.34 Hardness vs depth measurements, *R7, test 20000 cycles wet, INNOT-16*

Specimen No:	**INW17**	**Test Name:**	**INNOT-16**
1		**2**	
Depth	**Hardness**	**Depth**	**Hardness**
microns	HV0.2	microns	HV0.2
50	364	100	383
150	380	200	363
250	345	300	369
350	321	400	323
1000	288	1000	268
5000	249	5000	259
10000	268	10000	259

Table C.35 Hardness vs depth measurements, *R8T, test 15000 cycles dry, INNOT-23*

Specimen No:	**WB47**	**Test Name:**	**INNOT-23**
1		**2**	
Depth	**Hardness**	**Depth**	**Hardness**
microns	HV0.2	microns	HV0.2
50	386	100	404
150	408	200	395
250	377	300	398
350	345	400	340
1000	259	1000	264
5000	227	5000	251
10000	229	10000	253

Table C.36. Hardness vs depth measurements, *R7, test 5000 cycles dry, INNOT-01*

Specimen No:	**INW1**	**Test Name:**	**INNOT-01**
1		**2**	
Depth	**Hardness**	**Depth**	**Hardness**
microns	HV	microns	HV
50	402	100	380
150	345	200	375
250	375	300	353
350	338	400	333
1000	277	1000	279
5000	275	5000	260
10000	258	10000	263

Table C.37. Hardness vs depth measurements *R7,test 5000 cycles dry+5000 wet,INNOT-02*

Specimen No:	**INW2**	**Test Name:**	**INNOT-02**
1		**2**	
Depth	**Hardness**	**Depth**	**Hardness**
microns	HV	microns	HV
50	408	100	383
150	392	200	372
250	378	300	350
350	333	400	333
1000	282	1000	284
5000	270	5000	279
10000	258	10000	265

Table C.38 Hardness vs depth measurements, *R7, test 15000 cycles dry, INNOT-03*

Specimen No:	**INW3**	**Test Name:**	**INNOT-03**
1		**2**	
Depth	**Hardness**	**Depth**	**Hardness**
microns	HV	microns	HV
50	425	100	408
150	395	200	375
250	395	300	350
350	350	400	326
1000	253	1000	255
5000	244	5000	268
10000	252	10000	244

Table C.39 Hardness vs depth measurements, *R7, test 20000 cycles wet, INNOT-18*

Specimen No:	**INW15**	**Test Name:**	**INNOT-18**
1		**2**	
Depth	**Hardness**	**Depth**	**Hardness**
microns	HV0.2	microns	HV0.2
50	361	100	343
150	395	200	355
250	342	300	358
350	338	400	314
1000	269	1000	280
5000	253	5000	242
10000	257	10000	266

Table C.40 Hardness vs depth measurements, *R8T, test 15000 cycles dry, INNOT-04*

Specimen No:	**WB46**	**Test Name:**	**INNOT-24**
1		**2**	
Depth	**Hardness**	**Depth**	**Hardness**
microns	HV0.2	microns	HV0.2
50	369	100	395
150	417	200	408
250	363	300	380
350	328	400	335
1000	232	1000	250
5000	225	5000	246
10000	238	10000	212

Table C.41 Hardness vs depth measurements, *R7, test 5000 cycles dry, INNOT-24*

Specimen No:	**INW4**	**Test Name:**	**INNOT-04**
1		**2**	
Depth	**Hardness**	**Depth**	**Hardness**
microns	HV	microns	HV
50	392	100	358
150	350	200	338
250	319	300	326
350	312	400	312
1000	255	1000	266
5000	247	5000	258
10000	252	10000	239

Table C.42 Hardness vs depth measurements, *R7, test 5000 cycles dry+5000 wet, INNOT-05*

Specimen No:	**INW5**	**Test Name:**	**INNOT-05**
1		**2**	
Depth	**Hardness**	**Depth**	**Hardness**
microns	HV	microns	HV
50	395	100	389
150	383	200	389
250	369	300	361
350	343	400	331
1000	271	1000	275
5000	280	5000	270
10000	273	10000	280

Table C.43 Hardness vs depth measurements *R7, test 15000 cycles dry, INNOT-06*

Specimen No:	**INW6**	**Test Name:**	**INNOT-06**
1		**2**	
Depth	**Hardness**	**Depth**	**Hardness**
microns	HV	microns	HV
50	461	100	432
150	392	200	372
250	333	300	348
350	317	400	308
1000	265	1000	261
5000	252	5000	238
10000	239	10000	256

Table C.44 Hardness vs depth measurements, *R7, test 20000 cycles wet, INNOT-21*

Specimen No:	**INW24**	**Test Name:**	**INNOT-21**
1		**2**	
Depth	**Hardness**	**Depth**	**Hardness**
microns	HV0.2	microns	HV0.2
50	380	100	380
150	395	200	371
250	395	300	386
350	360	400	345
1000	291	1000	290
5000	266	5000	266
10000	273	10000	270

Table C.45 Hardness vs depth measurements, *R8T, test 15000 cycles dry, INNOT-25*

Specimen No:	**WB37**	**Test Name:**	**INNOT-25**
1		**2**	
Depth	**Hardness**	**Depth**	**Hardness**
microns	HV0.2	microns	HV0.2
50	424	100	418
150	424	200	398
250	383	300	383
350	358	400	358
1000	271	1000	243
5000	251	5000	253
10000	253	10000	233

Table C.46 Hardness vs depth measurements, *R7, test 5000 cycles dry, INNOT-10*

Specimen No:	**INW7**	**Test Name:**	**INNOT-10**
1		**2**	
Depth	**Hardness**	**Depth**	**Hardness**
microns	HV	microns	HV
50	368	100	387
150	361	200	359
250	351	300	340
350	317	400	312
1000	264	1000	264
5000	264	5000	245
10000	258	10000	262

Table C.47 Hardness vs depth measurements, *R7, test 5000 cycles dry+5000 wet, INNOT-12*

Specimen No:	**INW12**	**Test Name:**	**INNOT-12**
1		**2**	
Depth	**Hardness**	**Depth**	**Hardness**
microns	HV	microns	HV
50	389	100	380
150	384	200	375
250	357	300	353
350	317	400	332
1000	275	1000	244
5000	239	5000	245
10000	268	10000	250

Table C.48 Hardness vs depth measurements, *R7, test 15000 cycles dry, INNOT-11*

Specimen No:	**INW8**	**Test Name:**	**INNOT-11**
1		**2**	
Depth	**Hardness**	**Depth**	**Hardness**
microns	HV	microns	HV
50	421	100	382
150	405	200	361
250	368	300	338
350	340	400	327
1000	250	1000	266
5000	258	5000	272
10000	252	10000	253

Table C.49 Hardness vs depth measurements, *R7, test 20000 cycles wet, INNOT-19*

Specimen No:	**INW23**	**Test Name:**	**INNOT-19**
1		**2**	
Depth	**Hardness**	**Depth**	**Hardness**
microns	HV0.2	microns	HV0.2
50	340	100	361
150	350	200	361
250	355	300	330
350	328	400	312
1000	275	1000	300
5000	241	5000	289
10000	250	10000	268

Table C.50 Hardness vs depth measurements,
R8T, test 15000 cycles dry, INNOT- 26

Specimen No:	**WB45**	**Test Name:**	**INNOT-26**
1		**2**	
Depth	**Hardness**	**Depth**	**Hardness**
microns	HV0.2	microns	HV0.2
50	414	100	421
150	401	200	398
250	345	300	366
350	314	400	330
1000	261	1000	257
5000	254	5000	238
10000	264	10000	203

Table C.51 Bulk hardness measurements, rail discs, 10 kg load

Rail disc	diamond diagonal d1	diamond diagonal d2	average (d1+d2)/2	hardness HV	average hardness HV	
INR1	0.253	0.249	0.251	294		
	0.244	0.246	0.245	309	295.333	
	0.259	0.253	0.256	283		
INR2	0.230	0.227	0.229	354		
	0.232	0.227	0.229	354	354	
INR3	0.220	0.222	0.221	380		
	0.222	0.222	0.222	376	378	
INR10	0.222	0.221	0.222	376		
	0.224	0.224	0.224	370	373	
INR11	0.217	0.217	0.217	394		
	0.220	0.219	0.220	383	388.5	
INR12	0.221	0.224	0.222	376		
	0.222	0.224	0.223	373	374.5	
INR24	0.262	0.254	0.258	279		
	0.262	0.259	0.260	274	276.5	
INR23	0.256	0.253	0.254	287		
	0.260	0.255	0.258	279	283	
INR22	0.289	0.279	0.284	230		
	0.264	0.257	0.260	274	258	all three
	0.267	0.257	0.262	270	272	last two
V400(1)*				322		
				330	326	
V400(2)*				327		
				317	322	
V400(3)*				333		
				325	329	

*Note: Hardness was measured at around 10mm from outside surface.

Table C.52 Bulk hardness measurements, wheel discs, 10 kg load

Wheel disc	**hardness HV**
INW3	262
	232
	220
INW13	232
	238
INW9	217
	217
INW5	210
	212
INW1	215
	215
IN4W	213
INW4	237
	227
INW6	213
	220
INW22	202
INW2	210
INW14	203
	202
INW 7*	232
	233
INW 8*	233
	237
INW 12*	199
	203
average	220.54
average without first	218.88

* Note: Hardness was measured at around 10mm from outside surface.

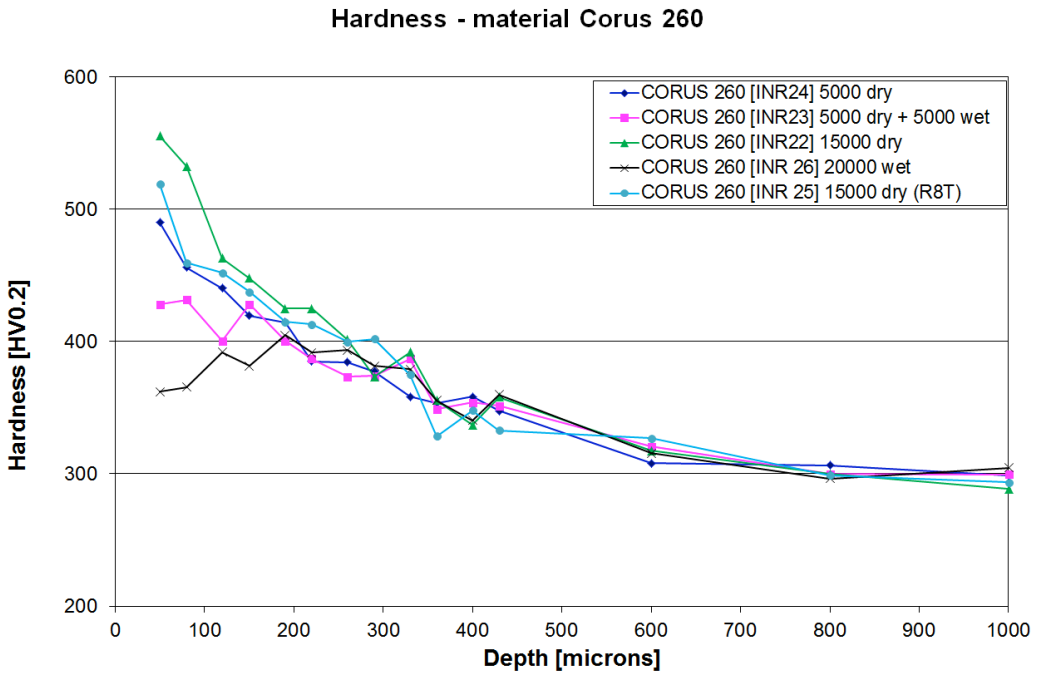

Figure C.1 Hardness vs depth, P260 material grade tests, up to 1mm

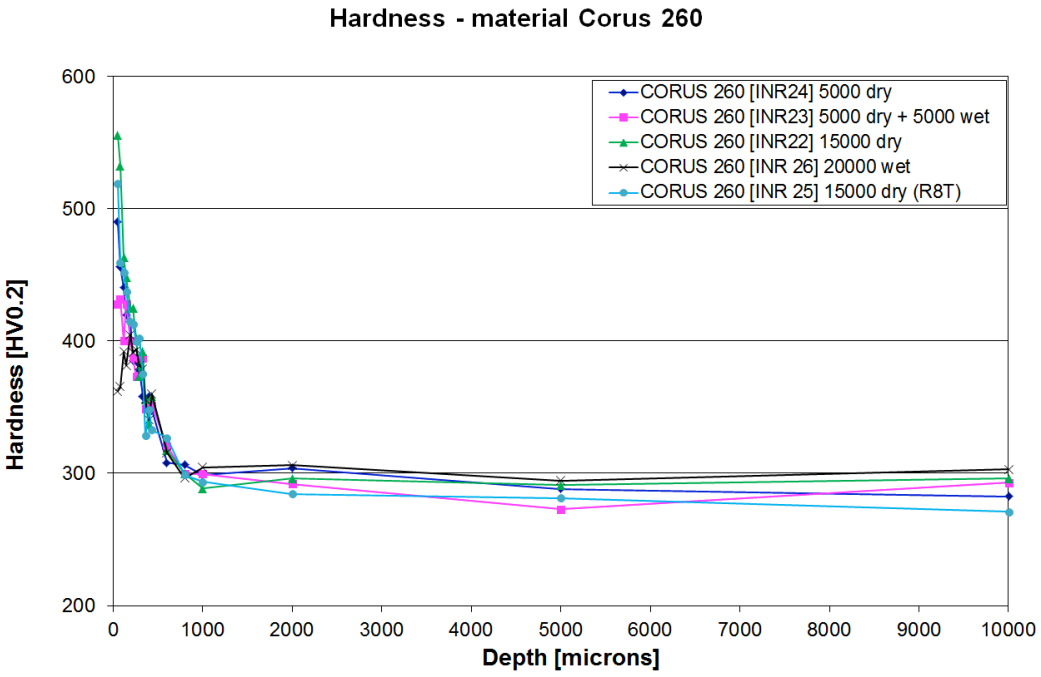

Figure C.2 Hardness vs depth, P260 material grade tests, up to 10mm

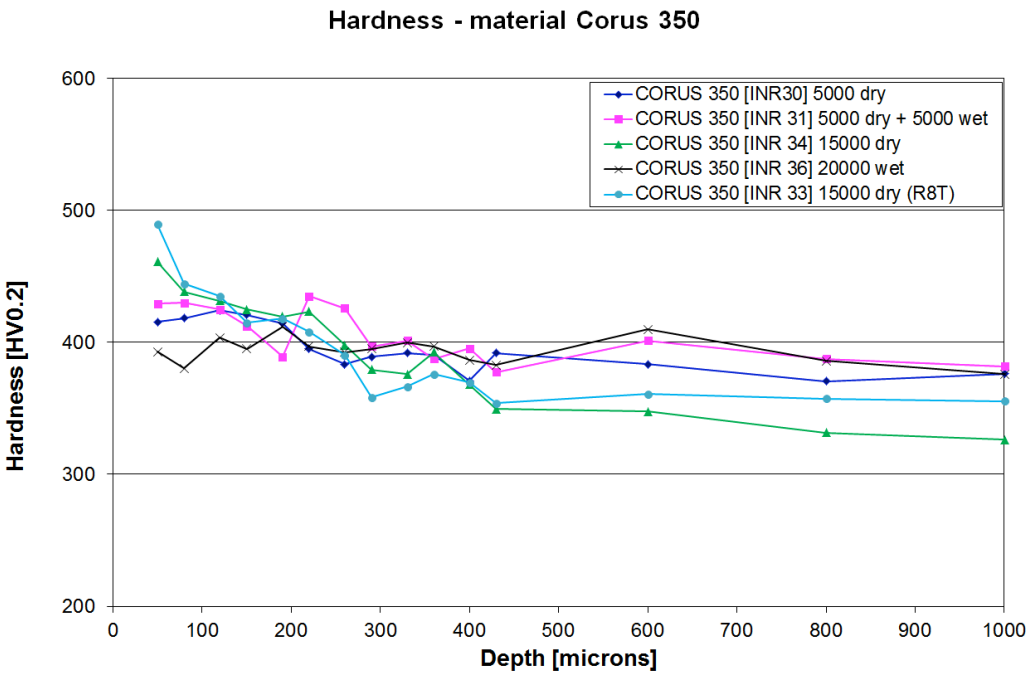

Figure C.3 Hardness vs depth, C350 material grade tests, up to 1mm

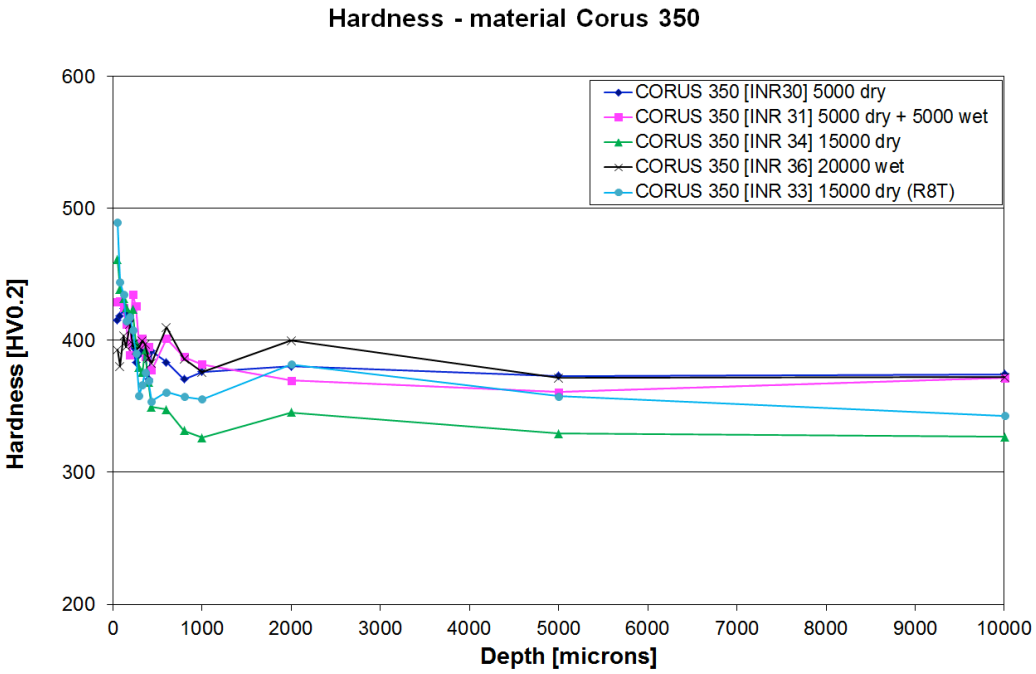

Figure C.4 Hardness vs depth, C350 material grade tests, up to 10mm

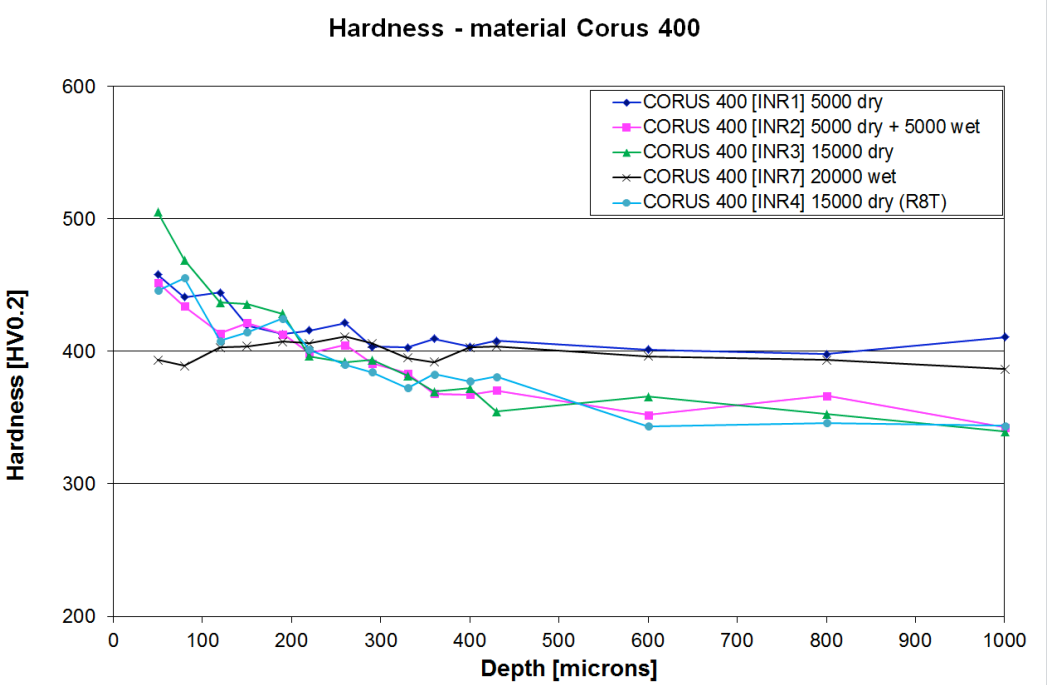

Figure C.5 Hardness vs depth, C400 material grade tests, up to 1mm

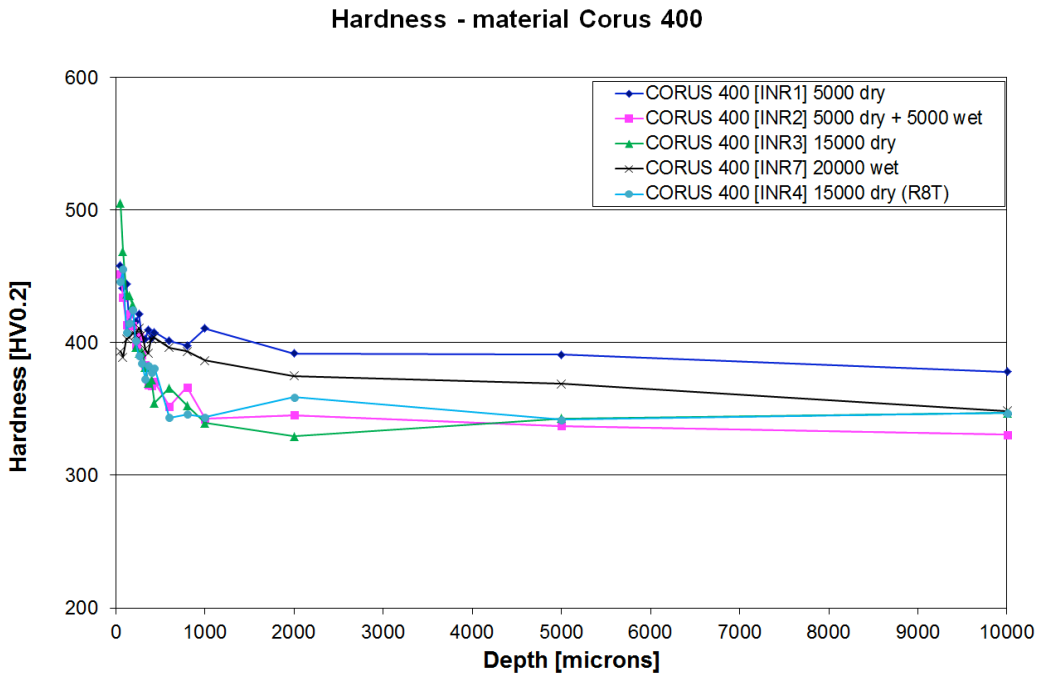

Figure C.6 Hardness vs depth, C400 material grade tests, up to 10mm

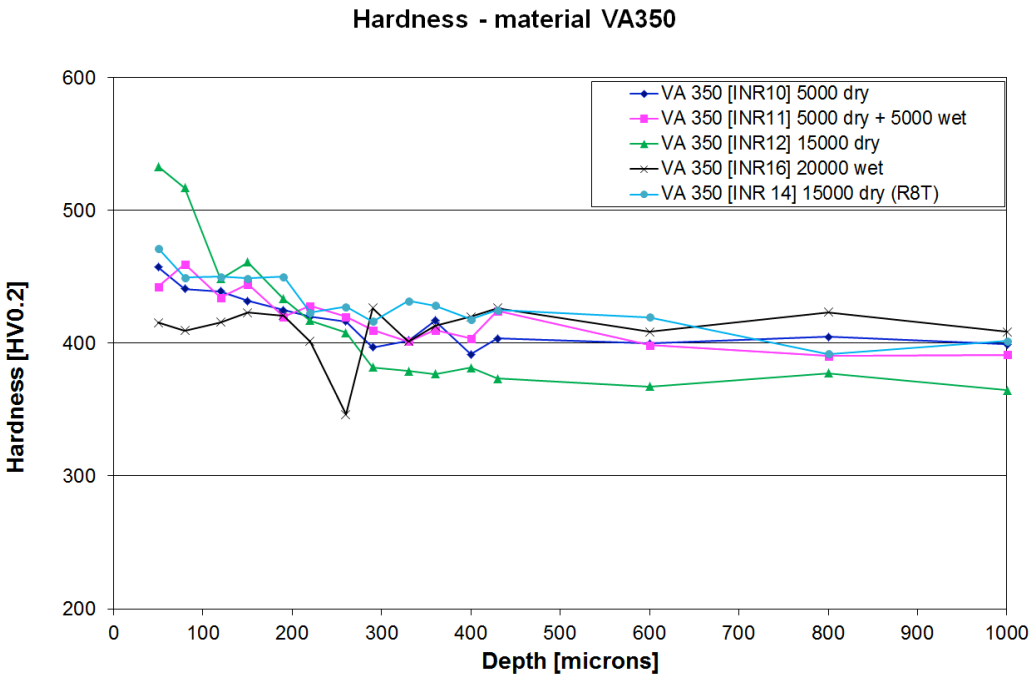

Figure C.7 Hardness vs depth, V350 material grade tests, up to 1mm

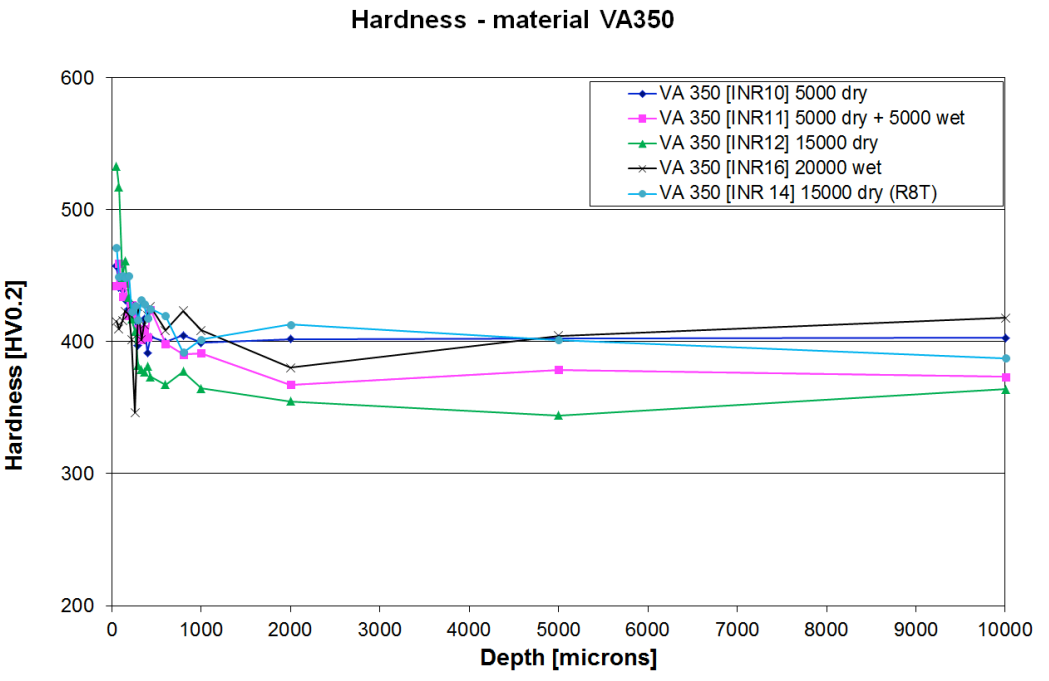

Figure C.8 Hardness vs depth, V350 material grade tests, up to 10mm

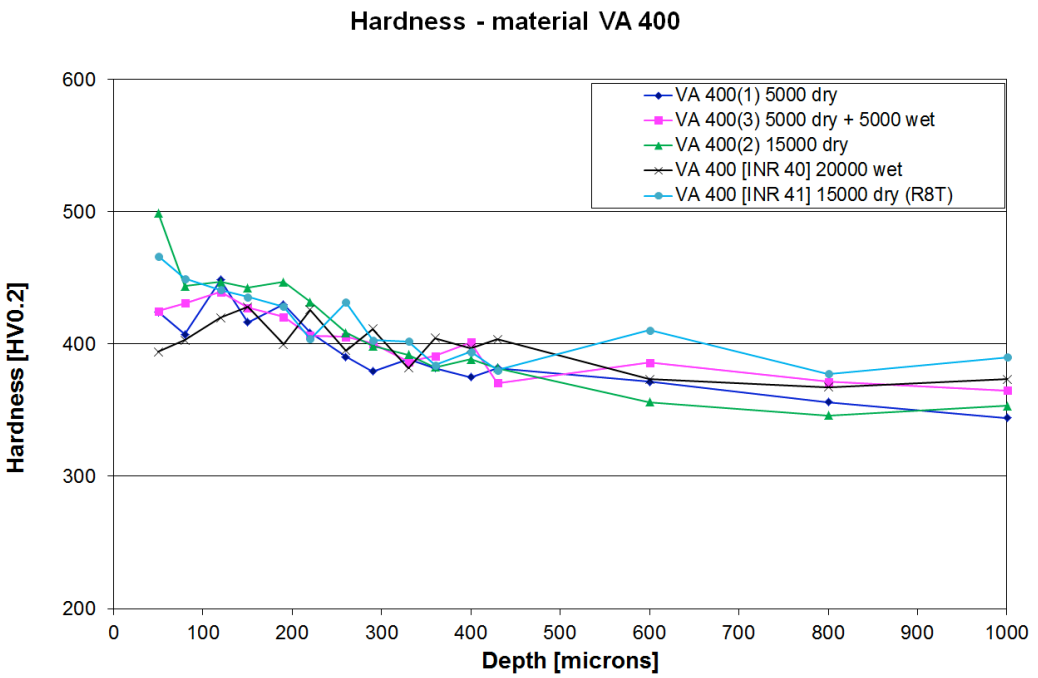

Figure C.9 Hardness vs depth, V400 material grade tests, up to 1mm

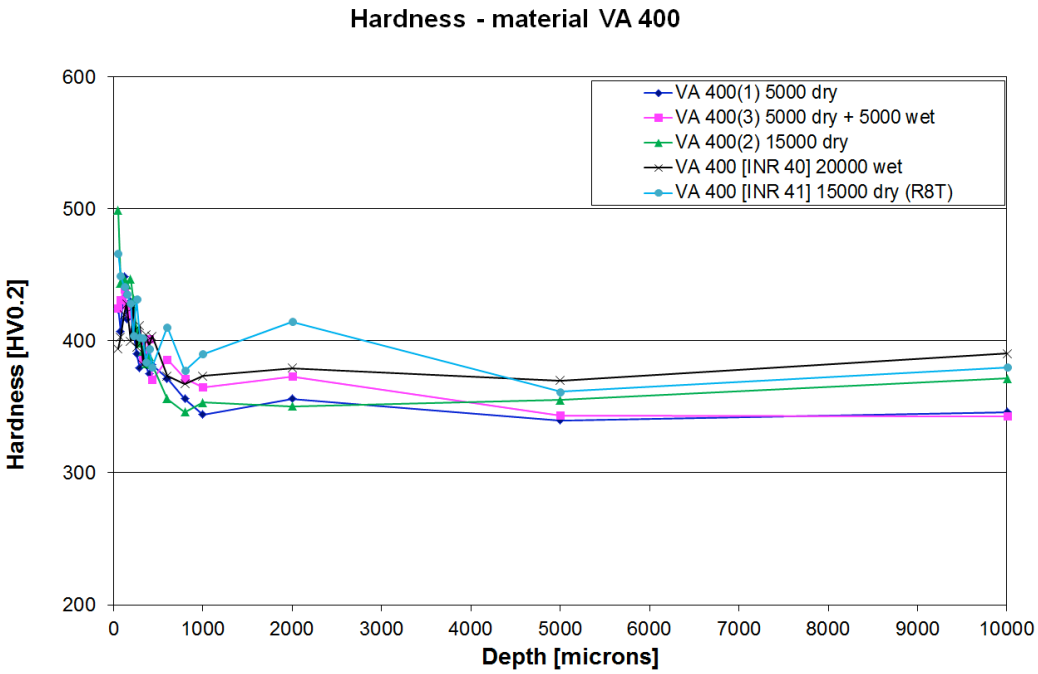

Figure C.10 Hardness vs depth, V400 material grade tests, up to 10mm

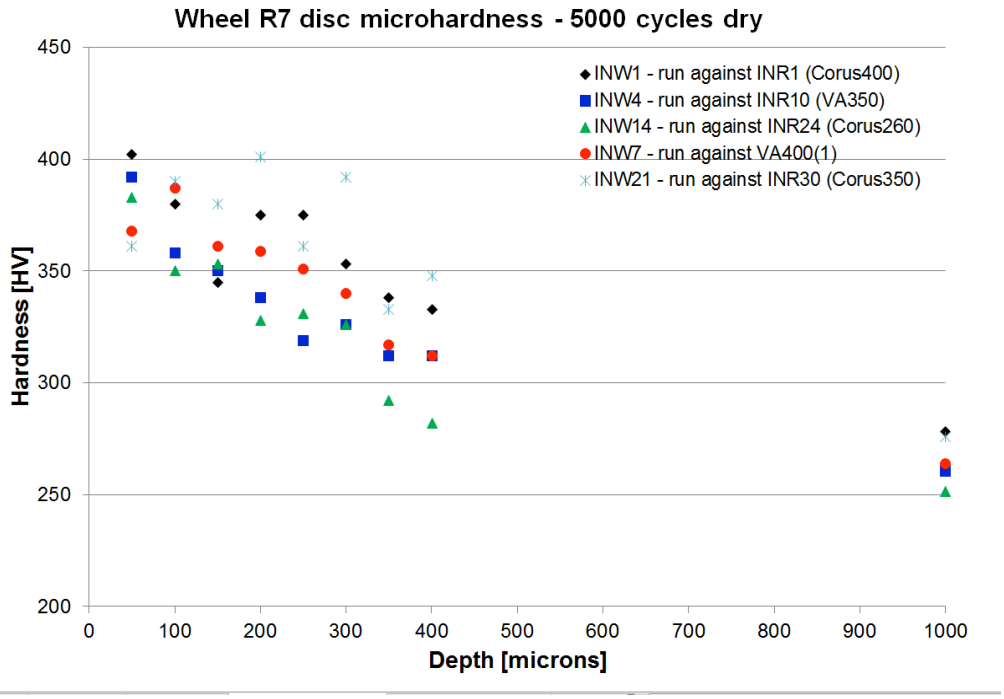

Figure C.11 Hardness vs depth, wheel R7 material, tests 5000 dry, up to 1mm

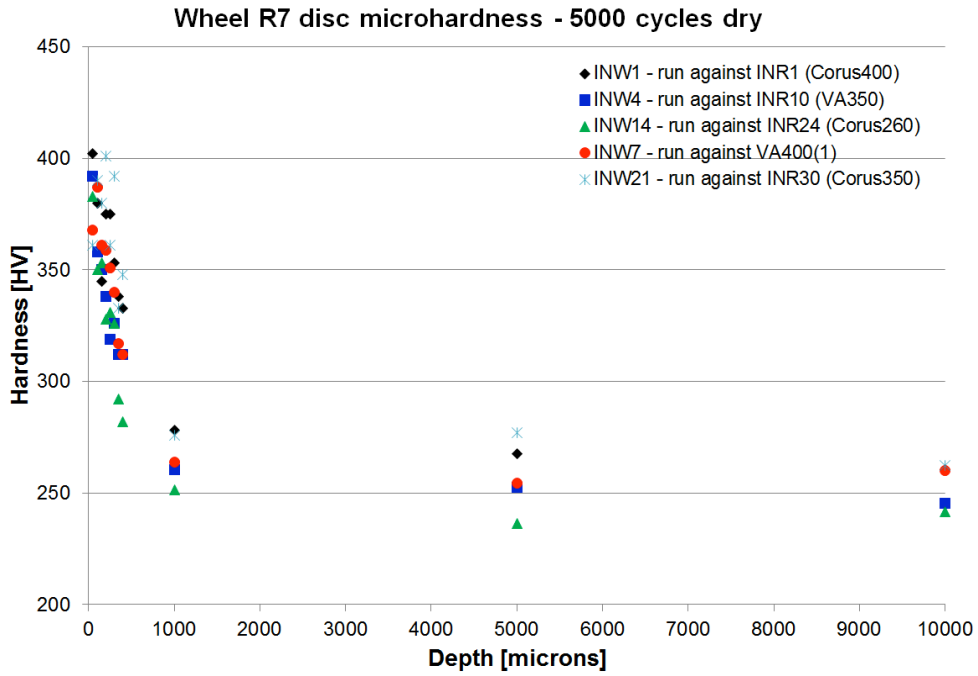

Figure C.12 Hardness vs depth, wheel R7 material, tests 5000 dry, up to 10mm

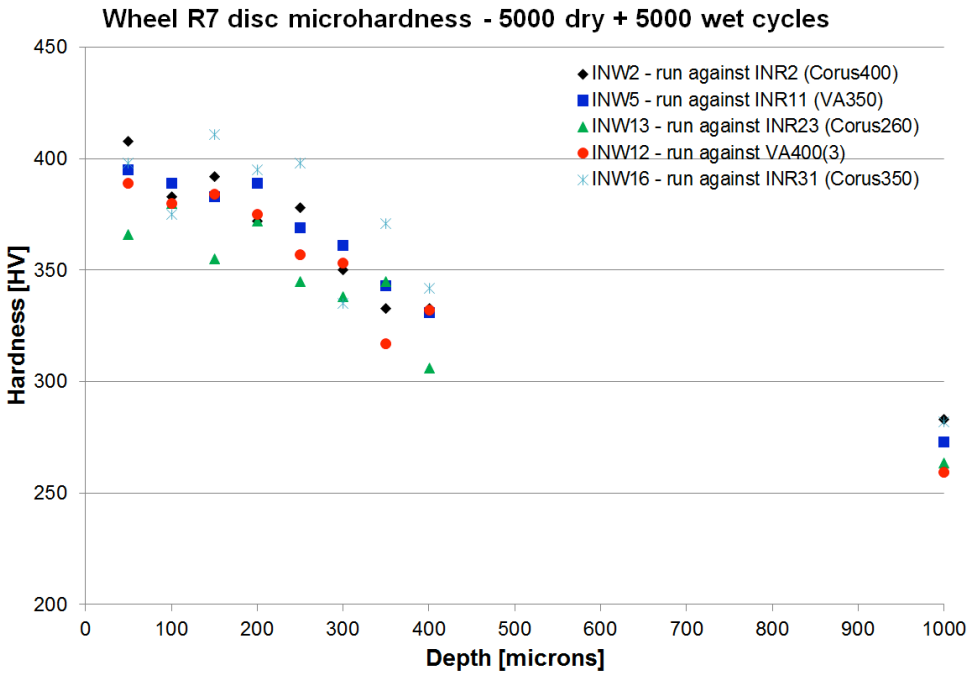

Figure C.13 Hardness vs depth, wheel R7 material, tests 5000 dry+5000wet, up to 1mm

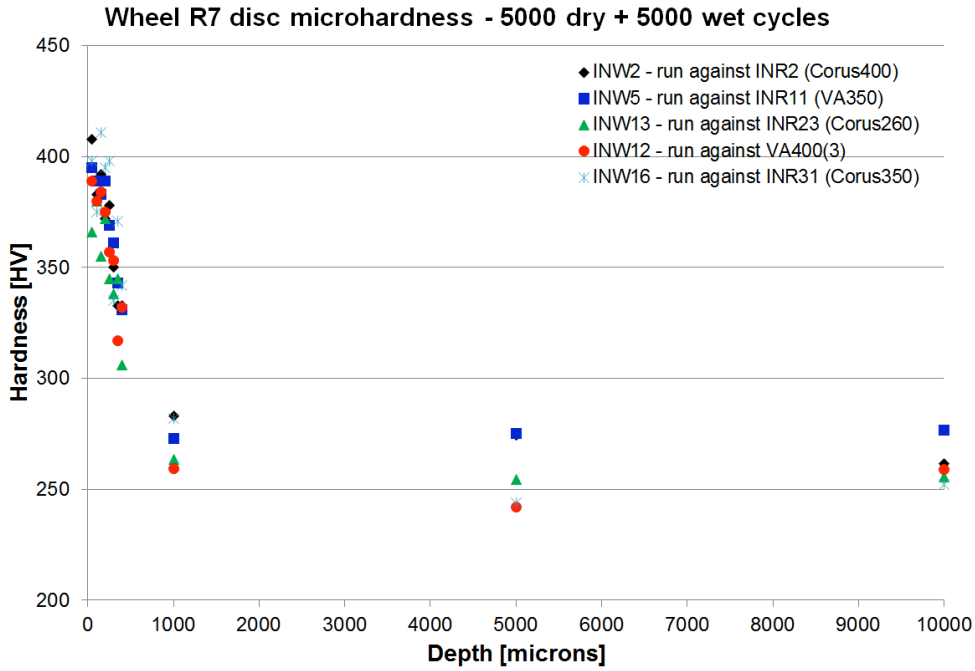

Figure C.14 Hardness vs depth, wheel R7 material, tests 5000 dry+5000wet, up to 10mm

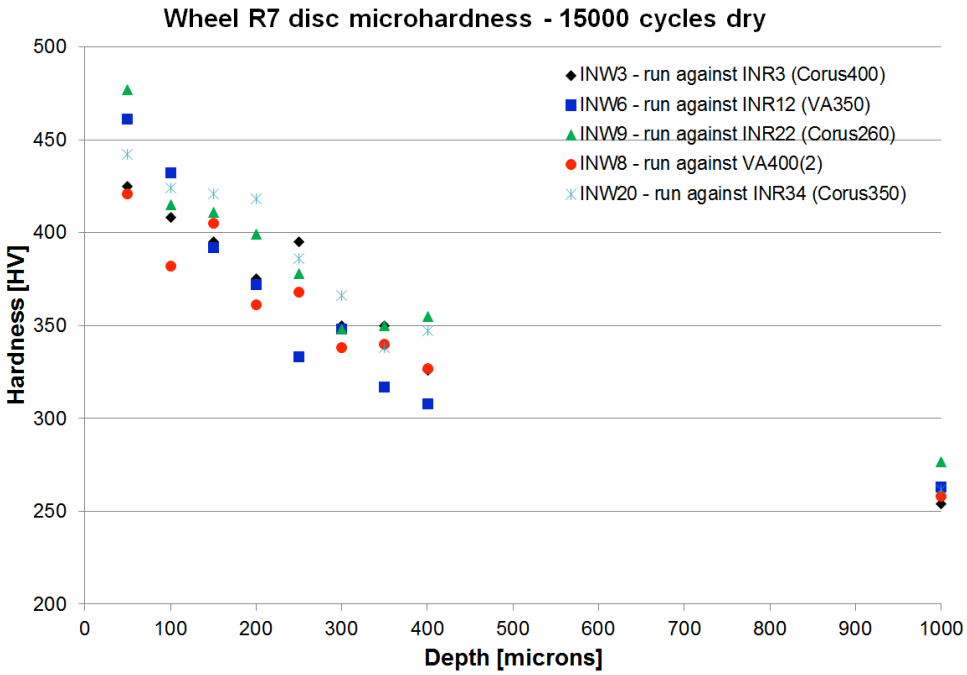

Figure C.15 Hardness vs depth, wheel R7 material, tests 15000 dry, up to 1mm

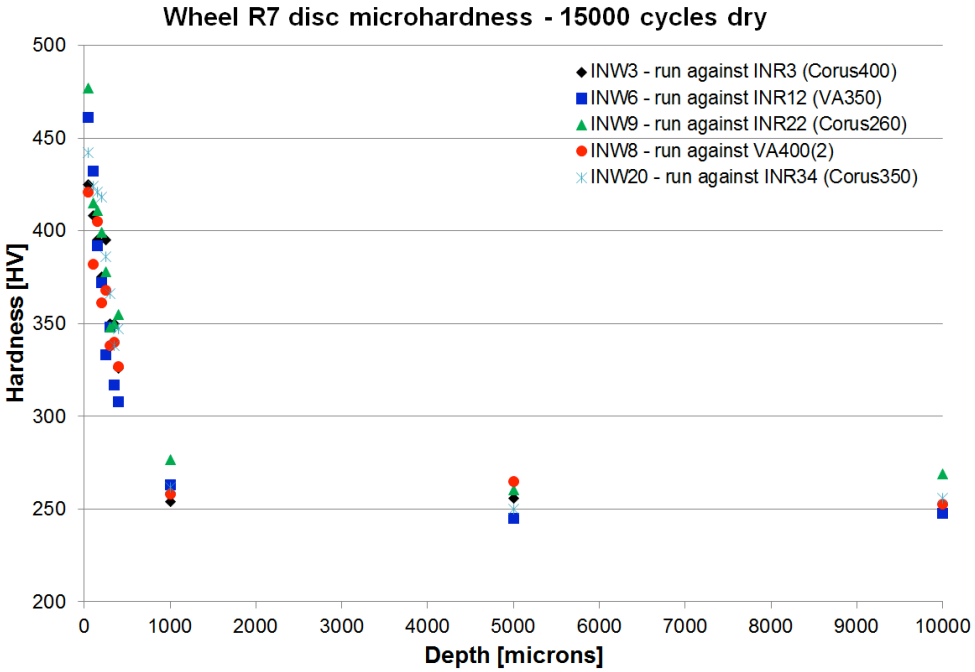

Figure C.16 Hardness vs depth, wheel R7 material, tests 15000 dry, up to 10mm

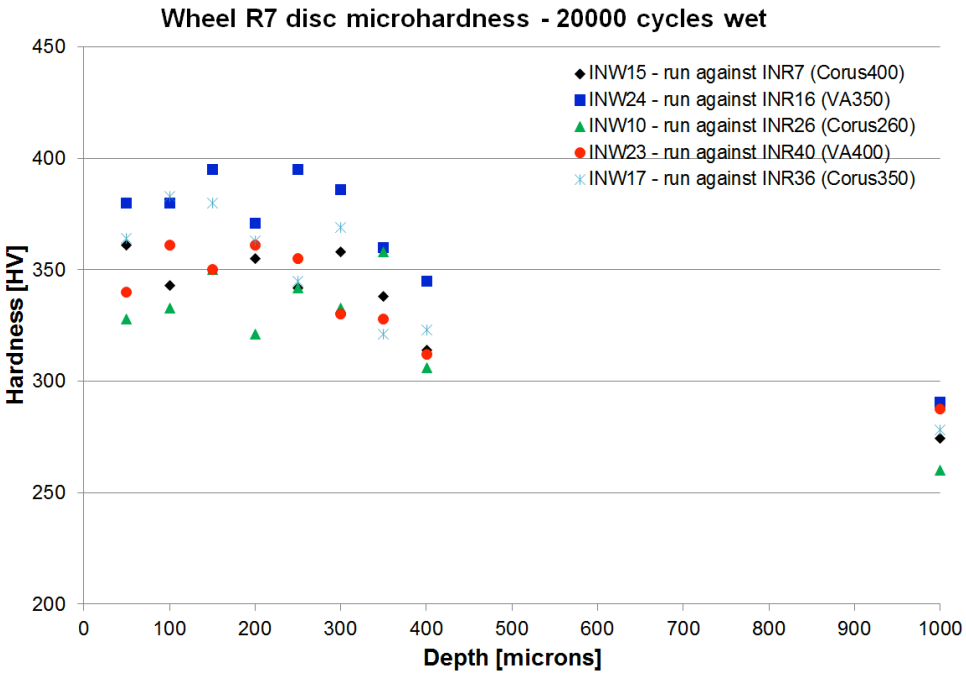

Figure C.17 Hardness vs depth, wheel R7 material, tests 20000 wet, up to 1mm

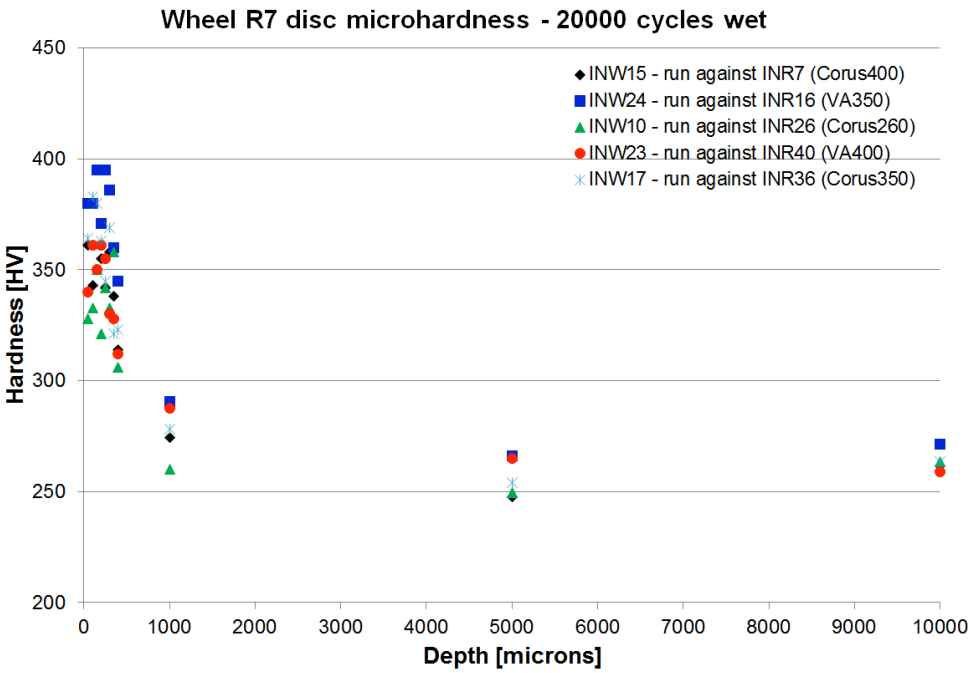

Figure C.18 Hardness vs depth, wheel R7 material, tests 20000 wet, up to 10mm

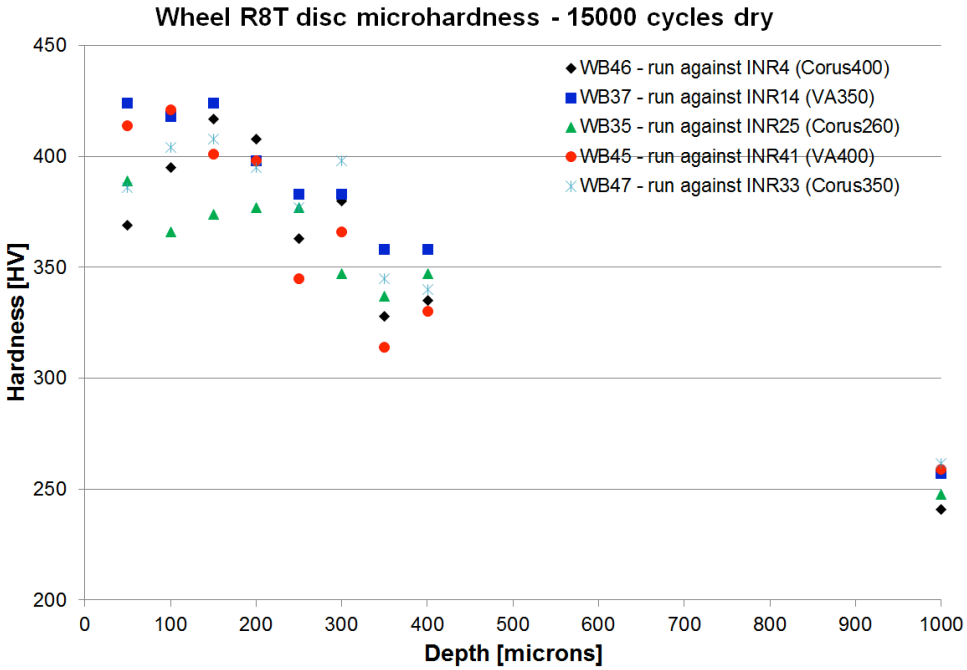

Figure C.19 Hardness vs depth, wheel R8T material, tests 15000 dry, up to 1mm

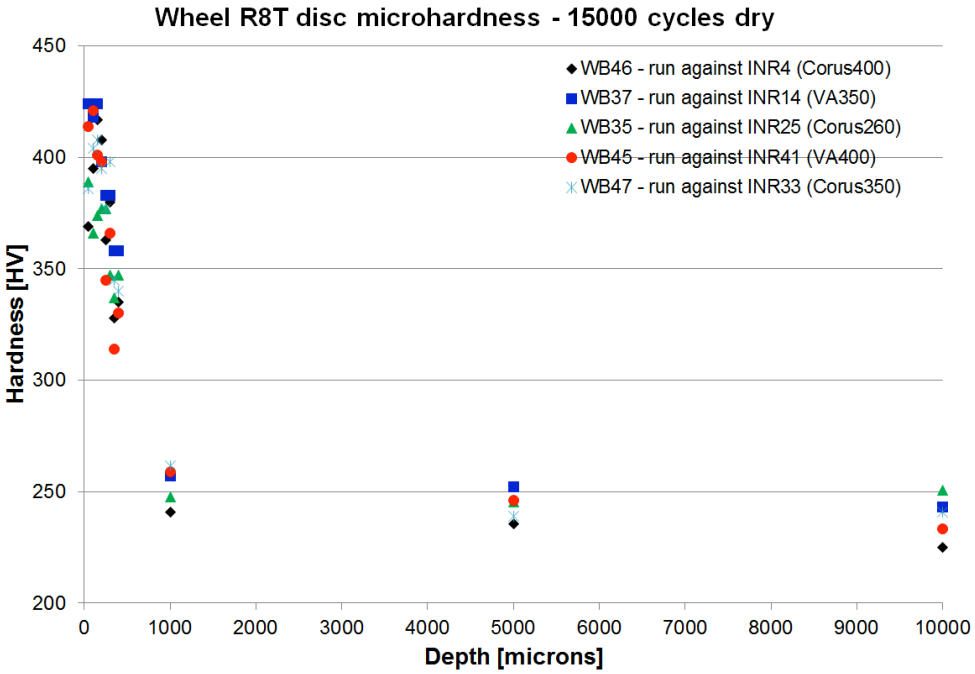

Figure C.20 Hardness vs depth, wheel R8T material, tests 15000 dry, up to 10mm

Appendix D: Twin-disc test simulations

Introduction

Dynarat simulations of laboratory SUROS twin-disc tests are presented in this Appendix D. Similar figures were published as part of Appendix 2 to Deliverable 4.2.5 of InnoTrack project that was also done by author of this Thesis.

Simulations are done for all five materials P260, C350, C400, V350 and V400 for tests: 5000 cycles dry, 5000 cycles dry + 5000 cycles wet and 15000 cycles dry. The reason why 20000 cycles wet tests were not simulated is because very small plastic deformations and strains were observed, that means, it would be very hard comparing simulations with actual material tests.

Simulation data presented here for all these materials and tests are:

- Hardness vs depth
- Strain vs depth

See Chapter 5 for analysis of these simulations.

List of figures

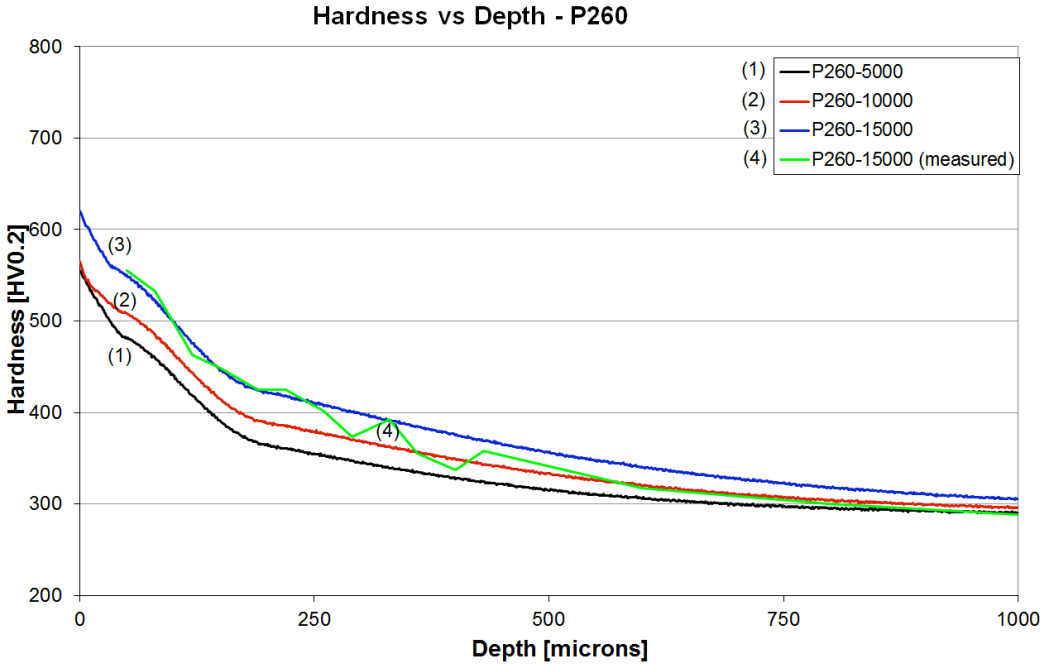

Figure D.1 Hardness vs depth, from simulations of the P260 material grade tests

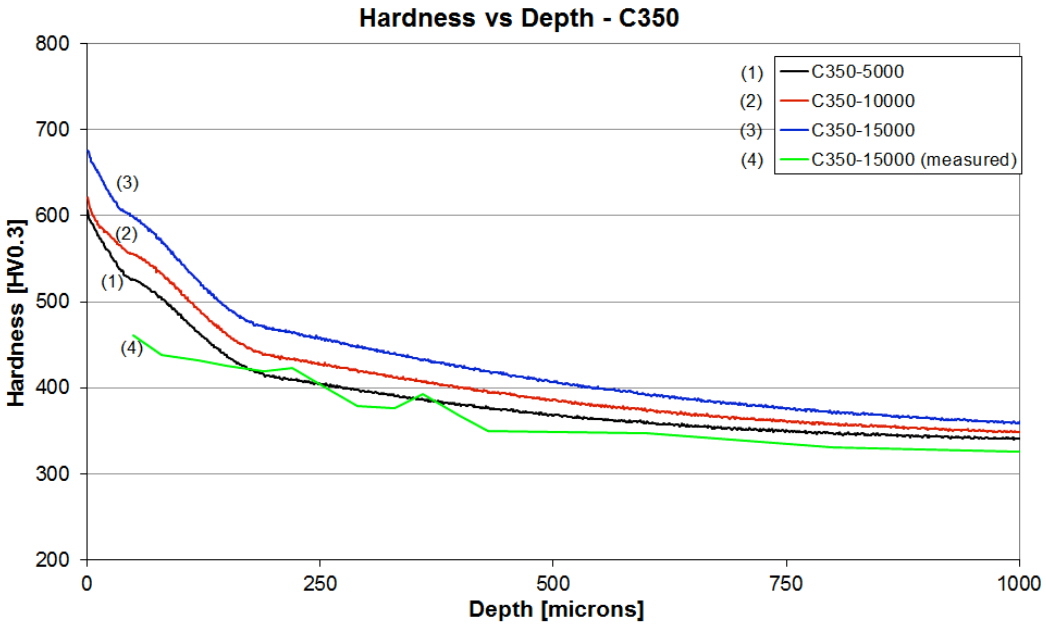

Figure D.2 Hardness vs depth, from simulations of the C350 material grade tests

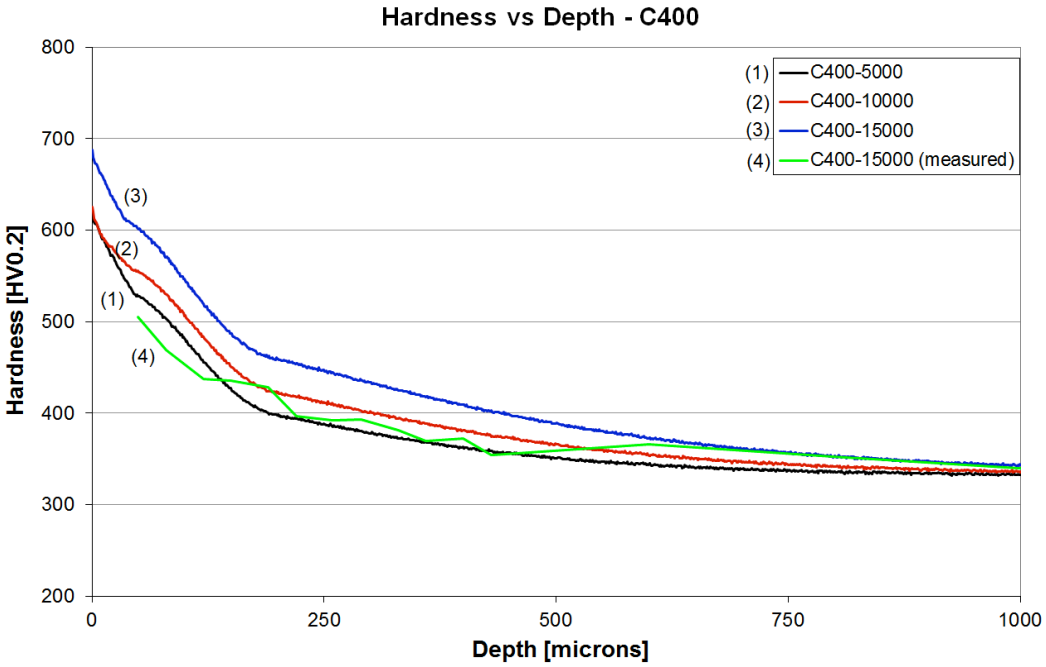

Figure D.3 Hardness vs depth, from simulations of the C400 material grade tests

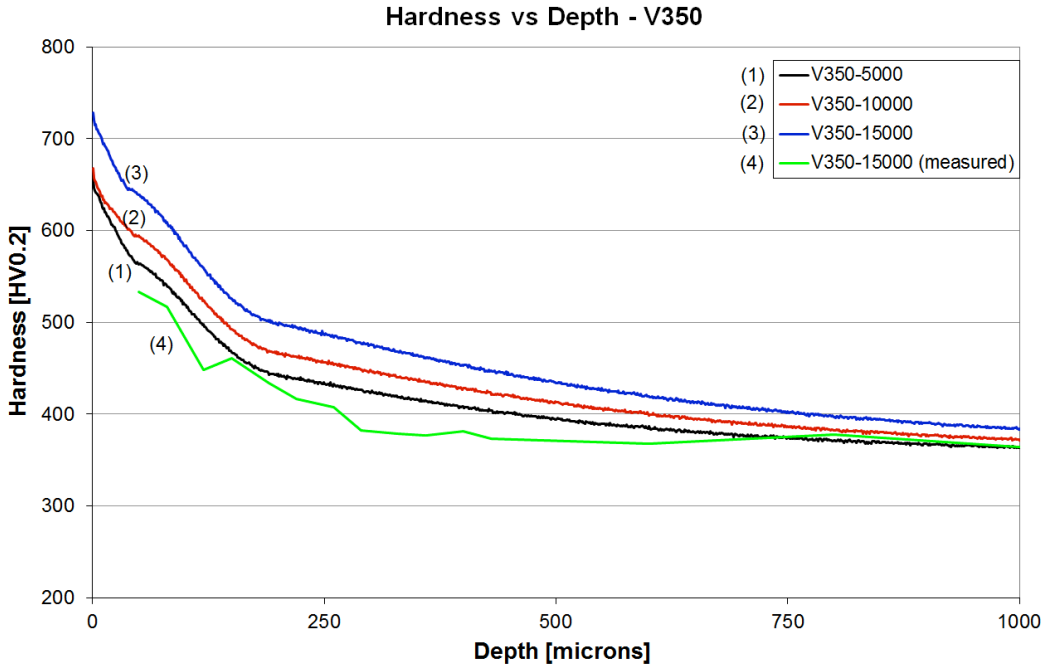

Figure D.4 Hardness vs depth, from simulations of the V350 material grade tests

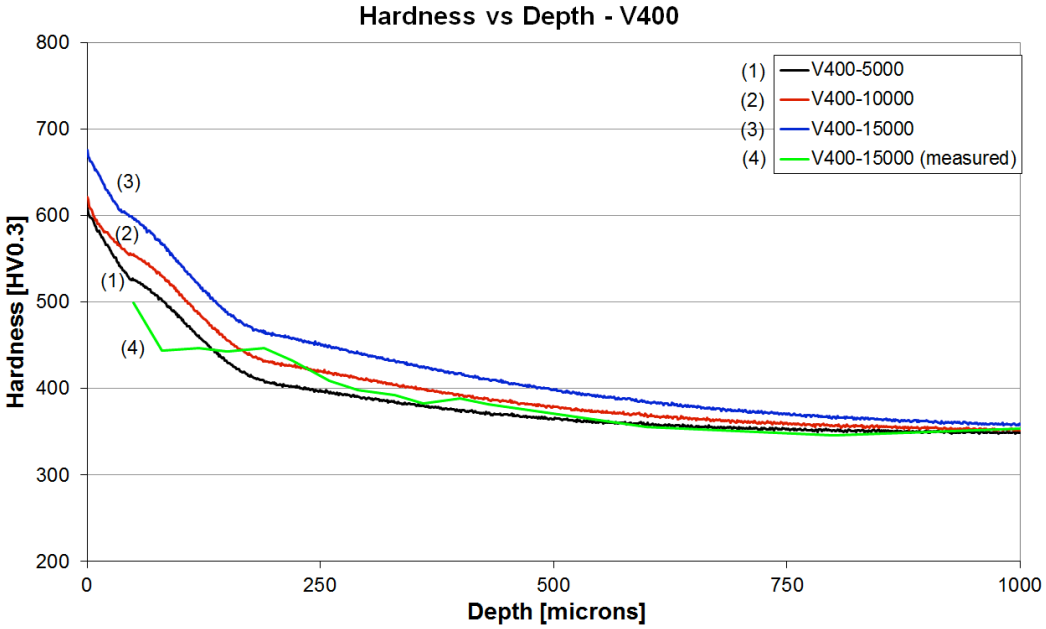

Figure D.5 Hardness vs depth, from simulations of the V400 material grade tests

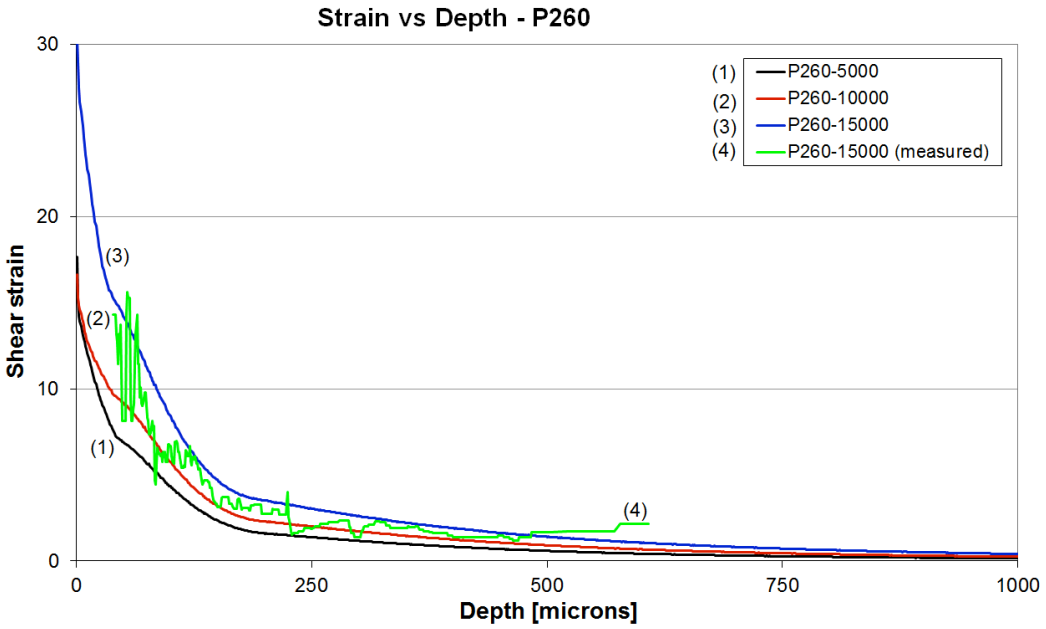

Figure D.6 Strain vs depth, from simulations of the P260 material grade tests

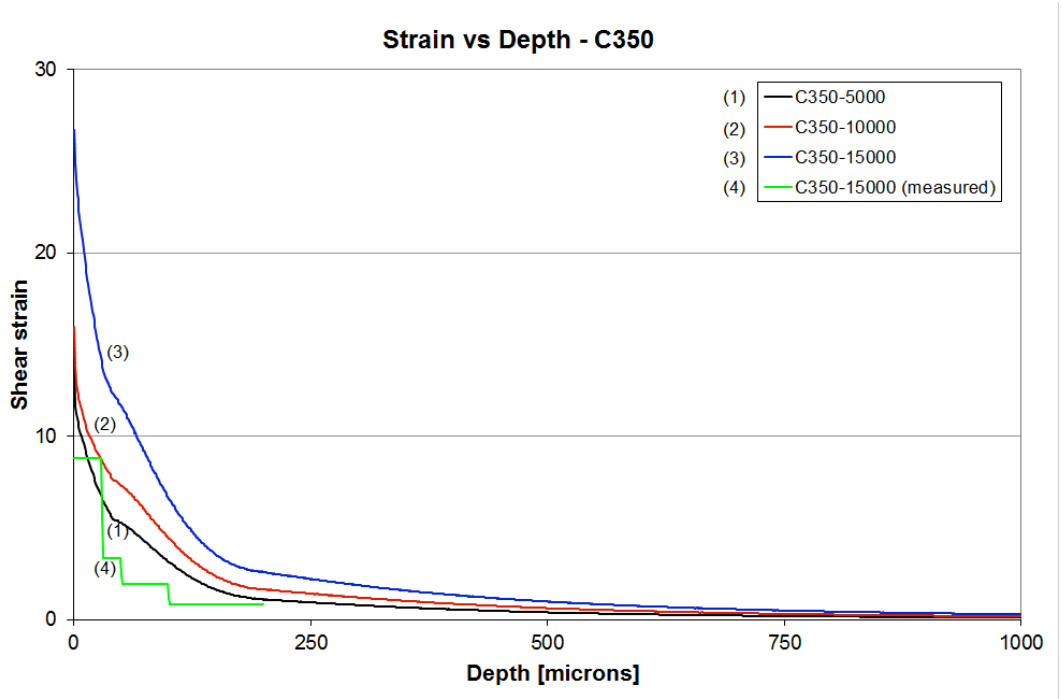

Figure D.7 Strain vs depth, from simulations of the C350 material grade tests

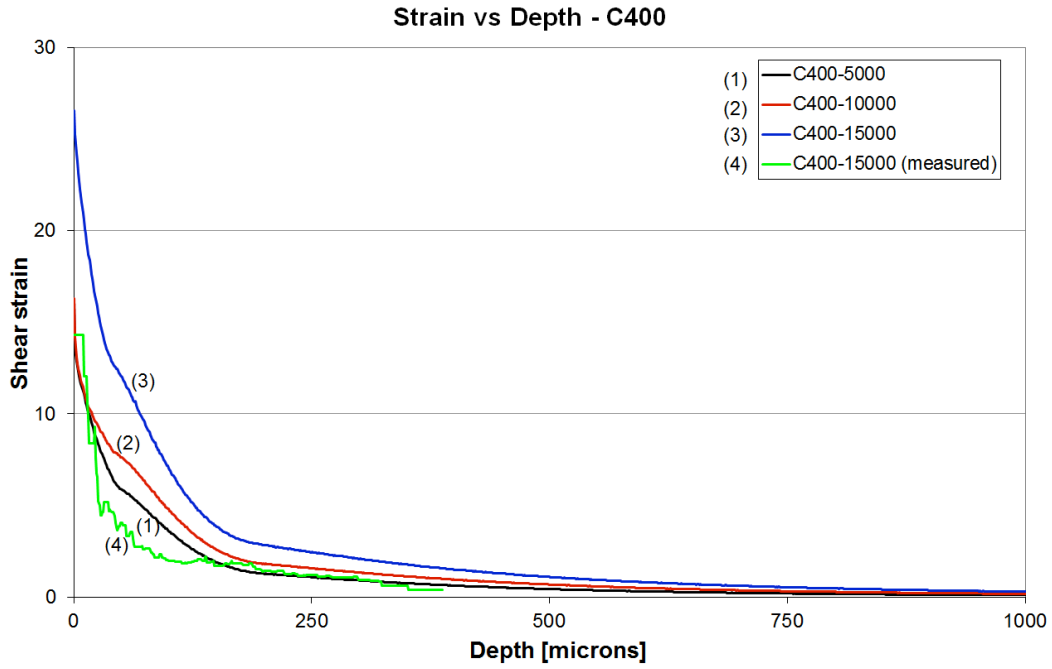

Figure D.8 Strain vs depth, from simulations of the C400 material grade tests

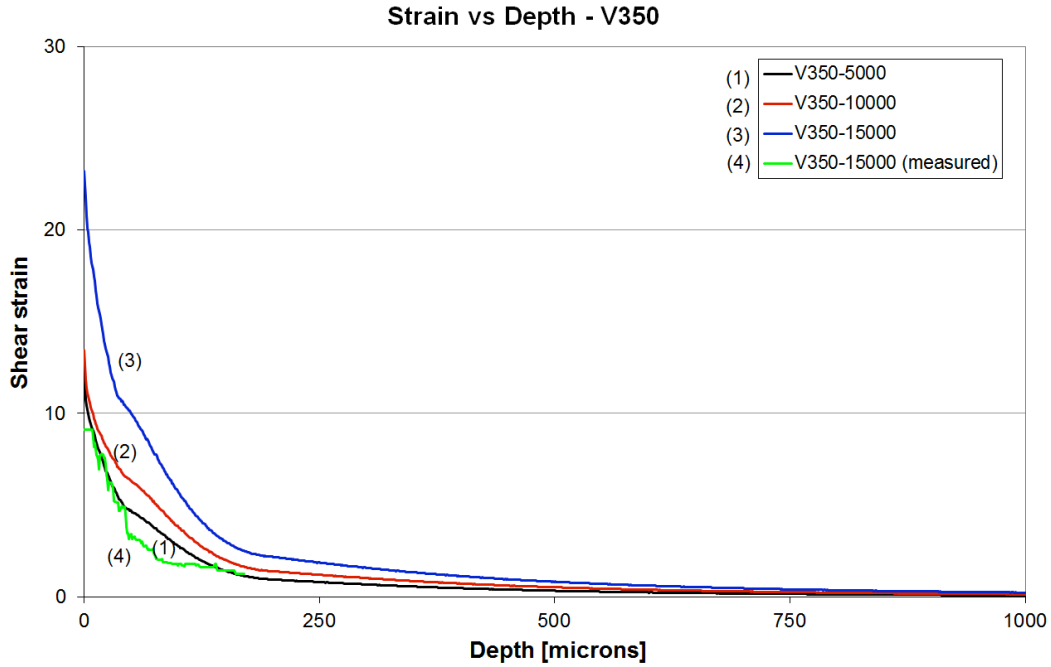

Figure D.9 Strain vs depth, from simulations of the V350 material grade tests

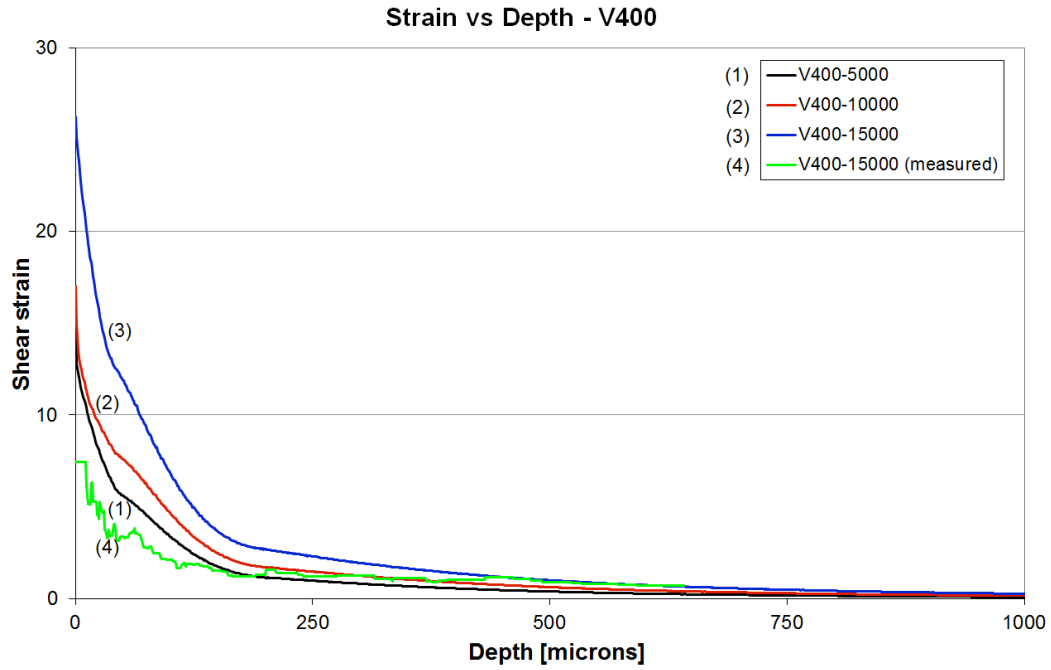

Figure D.10 Strain vs depth, from simulations of the V400 material grade tests

Appendix E: Rail Materials and Profiles

Introduction

Data in this Appendix E are from Standard: BS EN 13674-1:2011 with title:

"Railway applications - Track - Rail
Part 1: Vignole railway rails 46 kg/m and above"

"This British Standard is the UK implementation of EN 13674-1:2011.
It supersedes BS EN 13674-1:2003+A1:2007, which is withdrawn."

Steel grades

The applicable steel grades are given in Table E.1, and the steel names and steel numbers were allocated in accordance with EN 10027-1 and EN 10027-2, respectively. (taken from EN 13674-1:2011 – Railway aplications-track-rail-Part1: Vignole railway rails 46kg/m and above). The hardness ranges of the steel grades shall conform to those given in Table E.1.

Table E.1 Steel grades

Steel grade [a]		Hardness range (HBW)	Description	Branding lines
Steel name	Steel number			
R200	1.0521	200 to 240	Non-alloy (C-Mn) Non heat treated	No branding lines
R220	1.0524	220 to 260	Non-alloy (C-Mn) Non heat treated	———
R260	1.0623	260 to 300	Non-alloy (C-Mn) Non heat treated	— ———
R260Mn	1.0624	260 to 300	Non-alloy (C-Mn) Non heat treated	——— ———
R320Cr	1.0915	320 to 360	Alloy (1 %Cr) Non heat treated	——— ——— ———
R350HT	1.0631	350 to 390 [b]	Non-alloy (C-Mn) Heat treated	— ——— ———
R350LHT	1.0632	350 to 390 [b]	Non-alloy (C-Mn) Heat treated	— ——— ——— —
R370CrHT	1.0992	370 to 410	Alloy (C-Mn) Heat treated	— ——— ——— ———
R400HT	1.1254	400 to 440	Non-alloy (C-Mn) Heat treated	——— ——— ———

[a] See Table 5 a) and Table 5 b) for chemical composition/mechanical properties.
[b] See Table 6 for hardness requirements.

Table E.2 Chemical composition and mechanical properties (Table 5 a in the Standard)

Steel grade		% by mass									10^{-4} % (ppm) by mass max.		Tensile strength R_m min.	Elongation A min.	Hardness of the rail running surface, centre line[c]
Steel name	Sample	C	Si	Mn	P max.	S max.	Cr	Al max	V max	N max	O[a]	H[b]	MPa	%	HBW
R200	Liquid	0,40 to 0,60	0,15 to 0,58	0,70 to 1,20	0,035	0,035	≤ 0,15	0,004	0,030	0,009	20	3,0			
	Solid	0,38 to 0,62	0,13 to 0,60	0,65 to 1,25	0,040	0,040	≤ 0,15	0,004	0,030	0,010	20	3,0	680	14	200 to 240
R220	Liquid	0,50 to 0,60	0,20 to 0,60	1,00 to 1,25	0,025	0,025	≤ 0,15	0,004	0,030	0,009	20	3,0			
	Solid	0,48 to 0,62	0,18 to 0,62	0,95 to 1,30	0,030	0,030	≤ 0,15	0,004	0,030	0,010	20	3,0	770	12	220 to 260
R260	Liquid	0,62 to 0,80	0,15 to 0,58	0,70 to 1,20	0,025	0,025	≤ 0,15	0,004	0,030	0,009	20	2,5			
	Solid	0,60 to 0,82	0,13 to 0,60	0,65 to 1,25	0,030	0,030	≤ 0,15	0,004	0,030	0,010	20	2,5	880	10	260 to 300
R260Mn	Liquid	0,55 to 0,75	0,15 to 0,60	1,30 to 1,70	0,025	0,025	≤ 0,15	0,004	0,030	0,009	20	2,5			
	Solid	0,53 to 0,77	0,13 to 0,62	1,25 to 1,75	0,030	0,030	≤ 0,15	0,004	0,030	0,010	20	2,5	880	10	260 to 300
R320Cr	Liquid	0,60 to 0,80	0,50 to 1,10	0,80 to 1,20	0,020	0,025	0,80 to 1,20	0,004	0,18	0,009	20	2,5			
	Solid	0,58 to 0,82	0,48 to 1,12	0,75 to 1,25	0,025	0,030	0,75 to 1,25	0,004	0,20	0,010	20	2,5	1 080	9	320 to 360
R350HT	Liquid	0,72 to 0,80	0,15 to 0,58	0,70 to 1,20	0,020	0,025	≤ 0,15	0,004	0,030	0,009	20	2,5			
	Solid	0,70 to 0,82	0,13 to 0,60	0,65 to 1,25	0,025	0,030	≤ 0,15	0,004	0,030	0,010	20	2,5	1 175	9	350 to 390
R350LHT	Liquid	0,72 to 0,80	0,15 to 0,58	0,70 to 1,20	0,020	0,025	≤ 0,30	0,004	0,030	0,009	20	2,5			
	Solid	0,70 to 0,82	0,13 to 0,60	0,65 to 1,25	0,025	0,030	≤ 0,30	0,004	0,030	0,010	20	2,5	1 175	9	350 to 390
R370CrHT	Liquid	0,70 to 0,82	0,40 to 1,00	0,70 to 1,10	0,020	0,020	0,40 to 0,60	0,004	0,030	0,009	20	1,5			
	Solid	0,68 to 0,84	0,38 to 1,02	0,65 to 1,15	0,025	0,025	0,35 to 0,65	0,004	0,030	0,010	20	1,5	1.280	9	370 to 410
R400HT	Liquid	0,90 to 1,05	0,20 to 0,60	1,00 to 1,30	0,020	0,020	≤ 0,30	0,004	0,030	0,009	20	1,5			
	Solid	0,88 to 1,07	0,18 to 0,62	0,95 to 1,35	0,025	0,025	≤ 0,30	0,004	0,030	0,010	20	1,5	1.280	9	400 to 440

[a] See 9.1.3.3.

[b] See 9.1.3.2.

[c] See Figure 8.

Table E.3 Maximum residual elements, % by mass (Table 5 b in the Standard)

	Mo	Ni	Cu	Sn	Sb	Ti	Nb	Cu + 10 Sn	Others
R200, R220, R260, R260Mn	0,02	0,10	0,15	0,030	0,020	0,025	0,01	0,35	0,35 (Cr + Mo + Ni + Cu + V)
R320Cr	0,02	0,10	0,15	0,030	0,020	0,025	0,01	0,35	0,16 (Ni + Cu)
R350HT	0,02	0,10	0,15	0,030	0,020	0,025	0.04	0,35	0,25 (Cr + Mo + Ni + Cu + V)
R350LHT, R370CrHT, R400HT	0,02	0,10	0,15	0,030	0,020	0,025	0,04	0,35	0,20 (Mo + Ni + Cu + V)

Rail and wheel profiles

BS EN 13674-1:2011
EN 13674-1:2011 (E)

Dimensions in millimetres

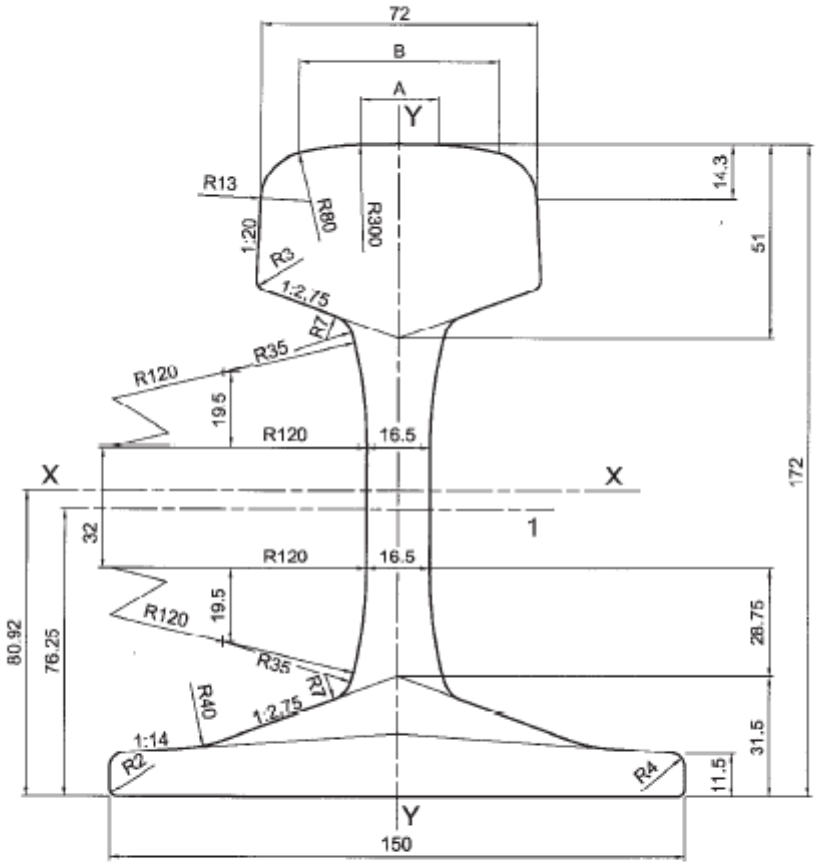

Key

1 centre line of branding

cross-sectional area	:	76,70	cm^2
mass per metre	:	60,21	kg/m
moment of inertia x-x axis	:	3 038,3	cm^4
section modulus - Head	:	333,6	cm^3
section modulus - Base	:	375,5	cm^3
moment of inertia y-y axis	:	512,3	cm^4
section modulus y-y axis	:	68,3	cm^3

indicative dimensions: *A* = 20,456 mm
B = 52,053 mm

Figure E.1 Rail profile Type 60E1 – standard BS EN 13674-1:2011 (E)

Wheel profiles are covered by European standard EN 13715:2006+A1:2010 – Railway applications – Wheelsets and bogies – Wheels – Tread profile

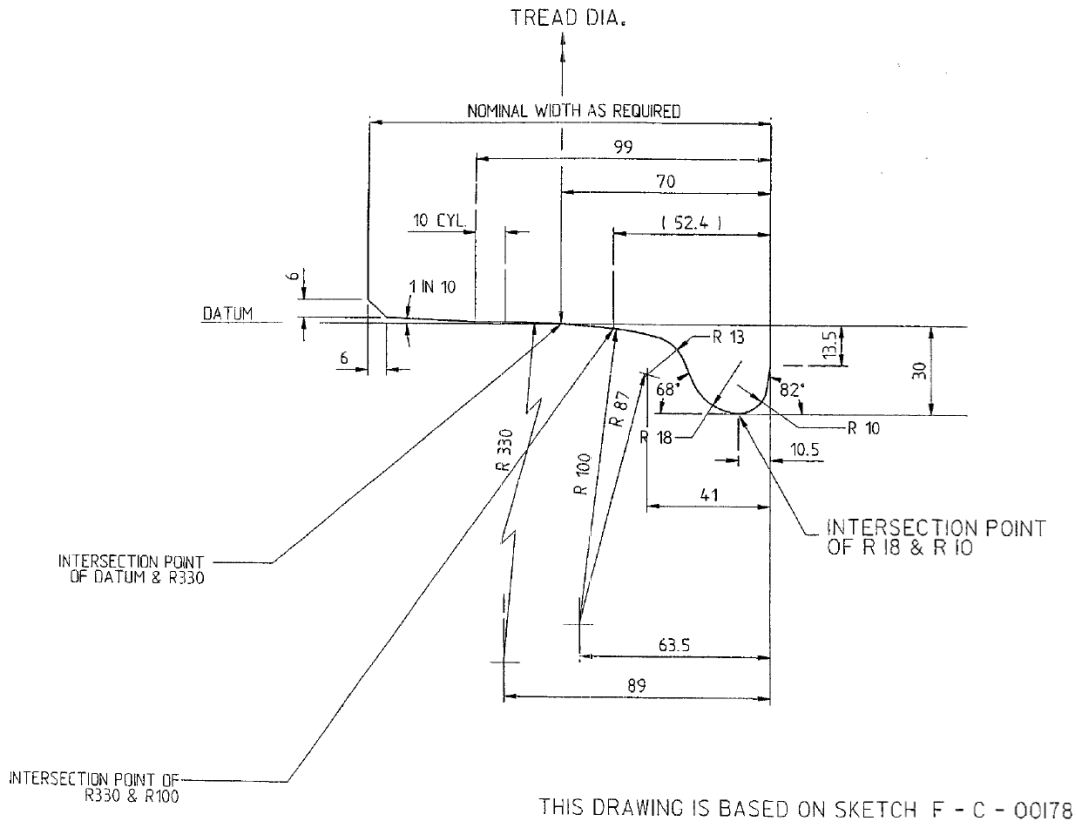

Figure E.2 P8 wheel profile, (Figure from RSSB Report: John Sinclair, 'Feasibility of reducing the number of standard wheel profile designs, 2002)